

Starchitectures

Exoplanetary System Architectures and Host Star Properties

Emil Knudstrup

PhD Thesis

Aarhus University

Emil Knudstrup

Starchitectures – Exoplanetary System Architectures and Host Star Properties

PhD thesis submitted to the Graduate School of Natural Sciences,
Aarhus University.

February 2023

PhD project supervised by Simon H. Albrecht & Mikkel N. Lund.

Typeset by the author using LuaL^AT_EX and the memoir document class.

Electronic version

Abstract

In the Solar System, the eight planets revolve on nearly circular orbits in the same direction, confined to the same orbital plane, which is only tilted by 7° relative to the Sun's equator. It is neatly ordered with four rocky planets with orbital periods of at most around 2 years, while the four gas and ice giants orbit at separations with much longer periods. Up until some 30 years ago, the Solar System was the only planetary system that we knew of. Naturally, this regularity we are seeing in the Solar System thus formed the blueprint for our theories on planetary formation, where planets form in the spinning protoplanetary disc ending up in configurations similar to the Solar System. So, how did this picture hold up as we started discovering planets outside the Solar System, so-called *exoplanets*? Do these exoplanet systems *all* resemble the Solar System?

The answer is a categorical no. The blueprint was challenged at the dawn of the exoplanet field: we see gas giants on short-period orbits, planets on extremely eccentric, almost comet-like, orbits, and the planetary orbits can be tilted with respect to the stellar spin axis—we see orbits that are well-aligned, inclined, polar, and even retrograde. Just to name a few curiosities. We are therefore tasked with finding new theories to explain this diversity and continue the exploration by discovering new systems and thoroughly characterising them in order to properly inform these theories. This not only requires excellent observations of key orbital parameters in these systems, but also intricate knowledge of the host stars harbouring the planets.

In this thesis, I will present the determination of fundamental stellar parameters, both through the study of eclipsing binaries as well as asteroseismology. Furthermore, I will be showing some new and exciting exoplanet discoveries using space-based photometry in concert with ground-based spectroscopy. Finally, I will map the system architectures in two different systems through careful analyses of key orbital parameters. This work will help expand our knowledge on how planetary systems form and evolve over time, and in this way account for the fascinating diversity of exoplanetary system architectures we are seeing.

Resumé (Dansk)

I Solsystemet kredser de otte planeter om Solen i samme retning på næsten cirkulære baner i det samme baneplan, der kun er vinklet med 7° i forhold til Solens ækvator. Inderst finder vi de fire klippeplaneter på kredsløb med omløbstider på under to år, og meget længere ude kredser gas- og isgiganterne med omløbstider på adskillelige år. Indtil for 30 år siden var Solsystemet det eneste planetsystem, vi kendte til. Derfor tog vores teorier omkring dannelsen af planetsystemer og deres udvikling afsæt i denne ordnede opbygning. Her dannes planeterne i en skive omkring stjernen bestående af støv og gas og ender i konfigurationer, der minder om den for Solsystemet. Da vi så begyndte at opdage planeter udenfor vores solsystem, *exoplaneter*, var det store spørgsmål, om vi ville genfinde denne ordnede struktur for alle andre planetsystemer.

Det skulle dog vise sig langt fra at være tilfældet. Allerede ved de første detektioner af exoplaneter blev vores ideer om, hvordan planetsystemer burde se ud sat på prøve. Vi har opdaget gasgiganter med en omløbstid på nogle få dage, planeter på ekstremt excentriske, nærmest kometlignende baner, og planeter i kredsløb, der er tiltede i forhold til stjernens rotationsakse. Derfor er vi nødt til at revidere vores teorier, imens vi fortsætter med at opdage og grundigt karakterisere nye systemer, der kan være med til at underbygge vores viden. Dette kræver både præcise observationer af særligt informative baneparametre, men også indgående kendskab til stjernerne, planeterne kredser omkring.

I denne afhandling vil jeg præsentere, hvordan vi udleder fundationale stjerneparametre, både ved at studere formørkelsesvariable og igennem asteroseismologi. Ydermere, vil jeg vise nye og bemærkelsesværdige opdagelser af planetsystemer ved at bruge rumbaseret fotometri suppleret af spektroskopiske målinger fra jorden. Endeligt, vil jeg kortlægge arkitekturen i to vidt forskellige systemer igennem udførlige analyser af nøgleparametre. Disse resultater vil hjælpe os med at udbygge vores forståelse af, hvordan planetsystemer dannes og udvikler sig over tid og på denne måde hjælpe os med at forstå den enorme diversitet af arkitekturen, vi observerer.

Contents

Abstract	iii
Resumé (Dansk)	v
Contents	vii
Preface	xiii
List of Publications	xv
Abbreviations and Acronyms	xxi
Introduction	1

I Scientific Background

1 Planetary formation, migration, and evolution	7
1.1 Stellar structure and evolution	7
1.1.1 Star formation	7
1.1.2 Main-sequence evolution	9
1.1.2.1 Energy transport	10
1.1.3 Post main-sequence evolution	12
1.1.4 Final stages of stellar evolution	14
1.2 The eccentric lifestyles of planets	16
1.2.1 Planet formation	16
1.2.2 Planetary migration	17
1.2.2.1 Disc migration	18
1.2.2.2 High-eccentricity migration	20
1.2.2.3 Why not both?	22

2 Observations and techniques	23
2.1 Spectroscopy	23
2.1.1 Ground-based spectroscopy	26
2.1.1.1 SONG	26
2.1.1.2 FIES	28
2.1.1.3 HARPS-N	28
2.2 Photometry	28
2.2.1 Space-based photometry	31
2.2.1.1 Kepler	31
2.2.1.2 K2	32
2.2.1.3 TESS	32
2.2.2 Multi-band photometry	34
2.2.3 The interplay between spectroscopy and photometry	34
2.3 Asteroseismology	35
2.3.1 Asteroseismology and stellar evolution	38
2.3.2 Exoseismology	38
2.4 Obliquity	39
2.4.1 The Rossiter-McLaughlin effect	40
2.4.1.1 Planetary shadow	43
2.4.1.2 Subplanetary velocities	43
2.4.1.3 Radial velocities	43
2.4.2 Testing planet formation and migration	44
2.4.2.1 Dynamically hot and cold systems	45
2.4.2.2 How strong is tidal alignment?	46
2.4.2.3 Preponderance of Perpendicular Planets	47
2.4.2.4 Primordial (mis)alignment	48

II Research Results

3 The age and metallicity of NGC 2506	51
3.1 Introduction	53
3.2 Targets	54
3.3 Spectroscopic observations	55
3.3.1 Radial velocity members from spectroscopy	57
3.3.2 Spectroscopic analysis of red-giant branch stars	58
3.3.2.1 Reddening from RGBs	60
3.3.3 Radial velocities for the detached eclipsing binaries	61
3.3.4 Luminosity ratios	63
3.3.5 The Spectral Energy Distribution of V4	66

3.3.5.1	T_{eff} for the components in V4	68
3.3.5.2	T_{eff} for the components in V ₂₀₃₂	70
3.4	Photometric observations	71
3.4.1	Light curves	74
3.4.2	TESS data	74
3.4.2.1	Signal Significance	76
3.4.2.2	Asteroseismology from TESS data	77
3.5	Orbital analysis: masses and radii	79
3.5.1	V ₂₀₃₂	79
3.5.2	V ₅	81
3.5.3	V ₄	81
3.5.3.1	Three-body solution for V ₄	82
3.5.3.2	The outer companion in V ₄	83
3.6	Cluster parameters	86
3.6.1	Mass-radius diagrams	86
3.6.2	The observed cluster sequence	88
3.7	Gaia distance to the cluster	90
3.8	Discussion	92
3.8.1	V ₄	94
3.8.2	V ₂₀₃₂	95
3.8.3	Future TESS observations of NGC 2506	96
3.9	Conclusions	97
4	The K2-93 Multiplanet System	99
4.1	Introduction	100
4.2	Data	102
4.3	Analysis	102
4.3.1	Asteroseismic parameters	102
4.3.2	Spectroscopy and Infrared Flux Method (IRFM) .	105
4.3.3	Asteroseismic modeling	106
4.3.4	Planetary analysis	108
4.3.4.1	Transit fitting	108
4.3.4.2	Planetary periods	112
4.3.4.3	Eccentricity	117
4.4	Discussion	121
4.5	Conclusions	124
5	A seismic study on γ Cephei A	127
5.1	Introduction	128
5.2	Observations	130

5.2.1	SONG data	130
5.2.2	TESS data	132
5.2.3	Spectroscopic analysis	132
5.2.4	Luminosity from <i>Gaia</i>	134
5.3	Seismic analysis	135
5.3.1	Filtering	135
5.3.2	Power spectra	138
5.3.3	Frequency extraction	140
5.4	Seismic modelling	143
5.4.1	MESA	143
5.4.2	BASTA	144
5.4.3	Interferometry	144
5.5	Discussion	146
5.5.1	Seismology and physical properties	146
5.5.2	The binary and planetary system	147
5.5.3	The masses	150
5.5.4	A long period signal?	152
5.5.5	Contemporaneous data	156
5.6	Conclusions	156
6	Three giant TOIs	157
6.1	Introduction	158
6.2	TESS photometry of candidate systems	160
6.2.1	TOI-1820	162
6.2.2	TOI-2025	162
6.2.3	TOI-2158	162
6.3	Ground-based observations	162
6.3.1	Speckle interferometry with SPP	164
6.3.2	Photometric follow-up	166
6.3.3	RV follow-up	168
6.4	Stellar parameters	170
6.4.1	SED	170
6.5	Joint analysis	172
6.5.1	TOI-1820	174
6.5.2	TOI-2025	174
6.5.3	TOI-2158	176
6.6	Results	176
6.6.1	The eccentricities of TOI-2025 b and TOI-1820 b . .	180
6.6.2	The obliquity of TOI-2025	181
6.7	Discussion and conclusions	181

7	TOI-1288 characterised with HARPS-N and HIRES	187
7.1	Introduction	188
7.2	Observations	190
7.2.1	Photometry	190
7.2.1.1	Light Curve Follow-up	192
7.2.2	Speckle/AO imaging	195
7.2.2.1	WIYN/NESSI	195
7.2.2.2	Gemini/'Alopeke	195
7.2.2.3	Gemini/NIRI	196
7.2.2.4	<i>Gaia</i>	198
7.2.2.5	Are the companions bound?	198
7.2.3	High-resolution spectroscopy	200
7.2.3.1	FIES	200
7.2.3.2	HARPS-N	200
7.2.3.3	HIRES	202
7.2.3.4	Periodogram analysis	202
7.2.3.5	Stellar modelling using SME and SED	205
7.2.3.6	Stellar modelling using BASTA	205
7.3	Analysis	206
7.4	Results	208
7.5	Discussion	211
7.5.1	Location in the Neptunian desert	211
7.5.2	Internal structure and atmosphere	216
7.5.3	Outer companions	219
7.6	Conclusions	220
8	The orbital alignment of HD 332231 b	223
8.1	Introduction	224
8.2	Observations	227
8.3	Determining the projected stellar obliquity	228
8.3.1	Line distortions: planet shadow	233
8.3.2	Subplanetary velocity	236
8.3.3	Radial velocities	239
8.3.4	Comparison of data and model	240
8.4	Results	241
8.5	Discussion	246
8.6	Conclusion	250
9	A puffy polar planet	251
9.1	Introduction	252

9.2	Observations	253
9.2.1	TESS photometry	253
9.2.2	HARPS spectroscopy	254
9.3	Stellar obliquity	255
9.3.1	Projected obliquity from the RM effect	256
9.3.2	Stellar inclination from TESS photometry	261
9.3.3	Stellar inclination from the empirical relation	262
9.3.4	Stellar obliquity	262
9.4	Discussion	266
9.4.1	Refined parameters for TOI-640 b	266
9.4.2	The polar orbit of TOI-640 in context	268
9.5	Conclusions	270
10	Conclusions and Outlook	273
Glossary		277
List of Figures		283
List of Tables		287
Bibliography		289
Appendices		
A	Supplementary figures	353
A.1	γ Cep	354
A.2	Trio of giants	356
A.3	TOI-1288	358
A.4	NGC 2506	360
A.5	TOI-640	361
B	Supplementary tables	365
B.1	NGC 2506	366
B.2	Trio of giants	370
B.3	γ Cep	372

Preface

In this thesis I will present the scientific research I have carried out during my PhD under the supervision of Simon H. Albrecht and Mikkel N. Lund. I was admitted to the PhD programme September 2018 and have conducted most of my research at the Stellar Astrophysics Centre (SAC). During my PhD I worked as a student support astronomer at the Nordic Optical Telescope (NOT) from September 2020 to March 2022. During this time I was (formally) on leave from the PhD.

Parts of this thesis were also presented in the progress report for the qualifying examination and is reproduced here in accordance with the rules of the Graduate School of Natural Sciences, Aarhus University.



First and foremost, I would like to express my sincere gratitude to my supervisors Simon and Mikkel for their invaluable guidance and support throughout my research in the fields of exoplanets and asteroseismology. Their expertise, insight, and dedication have been instrumental in shaping my understanding of these fascinating fields and in guiding me towards successful completion of this thesis.

Most of my research was conducted at SAC, so I would like to thank everyone who was a part of SAC during my time there for being such great colleagues, especially my fellow PhD students through the years. In this regard I, of course, would also like to thank Jørgen and Hans for creating such a fantastic and vibrant work environment.

Furthermore, I owe Mads a big thanks for his enthusiasm regarding different projects, especially projects related to SONG. A huge thanks also goes out to Frank and Karsten for their supervision during my Bachelor's and then my Master's, which motivated me to pursue a PhD. Thanks to Mark and Jakob for all their help with BASTA, and a special thanks goes out to Jakob for the L^AT_EX template. It looks great! A big thanks to the

tech-savvy Rasmus for all the technical support, and I would also like to thank Mia and Marcus for all the interesting discussions on exoplanet science.

I am extremely grateful for my time at the NOT, and I can't thank the staff there enough for making it such a great experience. A special shoutout goes to the Tinabana gang (Akke, Anni, and Paco), the peeps in el agujero de mierda (Marcelo, Sara, Emmy, Nicholas, and Julia), and Joonas, Viki, Sergio, and, of course, the ING students. Thank you all for a wonderful time!

The KESPRINT consortium has also been a vital part of my PhD, and I am very grateful for all the help I have received from the members within the consortium. Continuing on this note, I would like to express my profound gratitude to Davide for fruitful collaborations and for acting as an external advisor.

Til mine venner og min familie, særligt min kære moder, skal der lyde en kæmpe tak for deres støtte og for at sørge for, at livet også har haft andet indhold end stjerner og planeter. Den største tak af alle går til Sarah for uanede mængder kærlighed. Jeg glæder mig så meget til eventyr i Göteborg med dig og "Kirsten".

List of Publications

A full list of refereed publications can be found at the SAO/NASA Astrophysics Data System:

ui.adsabs.harvard.edu/public-libraries/FPmueuyvRyuSlH3d1qYx8g.

First Author Peer-reviewed Publications

The following five publications are included in this thesis:

- *Extremely precise age and metallicity of the open cluster NGC 2506 using detached eclipsing binaries.*
Knudstrup, E., Grundahl, F., Brogaard, K., Slumstrup, D., Orosz, J. A., Sandquist, E. L., Jessen-Hansen, J., Lund, M. N., Arentoft, T., Tronsgaard, R., Yong, D., Frandsen, S., & Bruntt, H. (2020)
— Monthly Notices of the Royal Astronomical Society, 499, 1312–1339, 28pp.
- *Confirmation and characterisation of three giant planets detected by TESS from the FIES/NOT and Tull/McDonald spectrographs.*
Knudstrup, E., Serrano, L. M., Gandolfi, D., Albrecht, S. H., Cochran, W. D., Endl, M., MacQueen, P., Tronsgaard, R., Bieryla, A., Buchhave, L. A., Stassun, K., Collins, K. A., Nowak, G., Deeg, H. J., Barkaoui, K., Safonov, B. S., Strakhov, I. A., Belinski, A. A., Twicken, J. D., Jenkins, J. M., Howard, A. W., Isaacson, H., Winn, J. N., Collins, K. I., Conti, D. M., Furesz, G., Gan, T., Kielkopf, J. F., Massey, B., Murgas, F., Murphy, L. G., Palle, E., Quinn, S. N., Reed, P. A., Ricker, G. R., Seager, S., Shiao, B., Schwarz, R. P., Srdoc, G., & Watanabe, D. (2022)
— Astronomy and Astrophysics, 667, A22, 18pp.

-  *Radial velocity confirmation of a hot super-Neptune discovered by TESS with a warm Saturn-mass companion.*
- Knudstrup, E**, Gandolfi, D., Nowak, G., Persson, C. M., Furlan, E., Livingston, J., Matthews, E., Lundkvist, M. S., Winther, M. L., Rørsted, J. L., Albrecht, S. H., Goffo, E., Carleo, I., Deeg, H. J., Collins, K. A., Narita, N., Isaacson, H., Redfield, S., Dai, F., Hirano, T., Akana Murphy, J. M., Beard, C., Buchhave, L. A., Cary, S., Chontos, A., Crossfield, I., Cochran, W. D., Conti, D., Dalba, P. A., Esposito, M., Fajardo-Acosta, S., Giacalone, S., Grunblatt, S. K., Guerra, P., Hatzes, A. P., Holcomb, R., Horta, F. G., Howard, A. W., Huber, D., Jenkins, J. M., Kabáth, P., Kane, S., Korth, J., Lam, K. W. F., Lester, K. V., Matson, R., McLeod, K. K., Orell-Miquel, J., Murgas, F., Palle, E., Polanski, A. S., Ricker, G., Robertson, P., Rubenzahl, R., Schlieder, J. E., Seager, S., Smith, A. M. S., Tenenbaum, P., Turtelboom, E., Vanderspek, R., Weiss, L., & Winn, J. (2023)
 – Monthly Notices of the Royal Astronomical Society, 519, 5637–5655, 19pp.
-  *Orbital alignment of HD 332231 b. The warm Saturn HD 332231 b/TOI-1456 b travels on a well-aligned, circular orbit around a bright F8 dwarf.*
- Knudstrup, E** & Albrecht, S. H. (2022)
 – Astronomy and Astrophysics, 660, A99, 13pp.
-  *A puffy polar planet. The low density, hot Jupiter TOI-640 b is on a polar orbit.*
- Knudstrup, E**, Albrecht, S. H., Gandolfi, D., Marcussen, M. L., Goffo, E., Serrano, L. M., Dai, F., Redfield, S., Hirano, T., Csizmadia, S., Cochran, W. D., Deeg, H. J., Fridlund, M., Lam, K. W. F., Livingston, J. H., Luque, R., Narita, N., Palle, E., Persson, C. M., & Van Eylen, V. (2023)
 – Astronomy and Astrophysics, 671, A164, 14pp.

Co-author Peer-reviewed Publications, part I

The following publication is included in this thesis:



Asteroseismology of the Multiplanet System K2-93.

Lund, M. N., **Knudstrup**, E., Silva Aguirre, V., Basu, S., Chontos, A., Von Essen, C., Chaplin, W. J., Bieryla, A., Casagrande, L., Vanderburg, A., Huber, D., Kane, S. R., Albrecht, S., Latham, D. W., Davies, G. R., Becker, J. C., & Rodriguez, J. E. (2019)
— Astronomical Journal, 158, 248, 12pp.

Co-author Peer-reviewed Publications, part II



A Hot Saturn Orbiting an Oscillating Late Subgiant Discovered by TESS.

Huber, D., Chaplin, W. J., Chontos, A., Kjeldsen, H., Christensen-Dalsgaard, J., Bedding, T. R., Ball, W., Brahm, R., Espinoza, N., Henning, T., Jordán, A., Sarkis, P., **Knudstrup**, E., Albrecht, S., Grundahl, F., Fredslund Andersen, M., Pallé, P. L., Crossfield, I., Fulton, B., Howard, A. W., Isaacson, H. T., Weiss, L. M., Handberg, R., Lund, M. N., Serenelli, A. M., Rørsted Mosumgaard, J., Stokholm, A., Bieryla, A., Buchhave, L. A., Latham, D. W., Quinn, S. N., Gaidos, E., Hirano, T., Ricker, G. R., Vanderspek, R. K., Seager, S., Jenkins, J. M., Winn, J. N., Antia, H. M., Appourchaux, T., Basu, S., Bell, K. J., Benomar, O., Bonanno, A., Buzasi, D. L., Campante, T. L., Çelik Orhan, Z., Corsaro, E., Cunha, M. S., Davies, G. R., Deheuvels, S., Grunblatt, S. K., Hasanzadeh, A., Di Mauro, M. P., García, R. A., Gaulme, P., Girardi, L., Guzik, J. A., Hon, M., Jiang, C., Kallinger, T., Kawaler, S. D., Kuszlewicz, J. S., Lebreton, Y., Li, T., Lucas, M., Lundkvist, M. S., Mann, A. W., Mathis, S., Mathur, S., Mazumdar, A., Metcalfe, T. S., Miglio, A., Monteiro, M. J. P. F. G., Mosser, B., Noll, A., Nsamba, B., Ong, J. M. J., Örtel, S., Pereira, F., Ranadive, P., Régulo, C., Rodrigues, T. S., Roxburgh, I. W., Silva Aguirre, V., Smalley, B., Schofield, M., Sousa, S. G., Stassun, K. G., Stello, D., Tayar, J., White, T. R., Verma, K., Vrard, M., Yıldız, M., Baker, D., Bazot, M., Beichmann, C., Bergmann, C., Bugnet, L., Cale, B., Carlino, R., Cartwright, S. M., Christiansen, J. L., Ciardi, D. R., Creevey, O., Dittmann, J. A., Do Nascimento, J.-D., Van Eylen, V., Fürész, G., Gagné, J., Gao, P., Gazeas, K., Giddens, F., Hall, O. J., Hekker, S., Ireland, M. J., Latouf, N., LeBrun, D., Levine, A. M., Matzko, W.,

Natinsky, E., Page, E., Plavchan, P., Mansouri-Samani, M., McCauliff, S., Mullally, S. E., Orenstein, B., Garcia Soto, A., Paegert, M., van Saders, J. L., Schnaible, C., Soderblom, D. R., Szabó, R., Tanner, A., Tinney, C. G., Teske, J., Thomas, A., Trampedach, R., Wright, D., Yuan, T. T., & Zohrabi, F. (2019)
— *Astronomical Journal*, 157, 245, 14pp.

 *The TESS-Keck Survey. I. A Warm Sub-Saturn-mass Planet and a Caution about Stray Light in TESS Cameras.*

Dalba, P. A., Gupta, A. F., Rodriguez, J. E., Dragomir, D., Huang, C. X., Kane, S. R., Quinn, S. N., Bieryla, A., Esquerdo, G. A., Fulton, B. J., Scarsdale, N., Batalha, N. M., Beard, C., Behmard, A., Chontos, A., Crossfield, I. J. M., Dressing, C. D., Giacalone, S., Hill, M. L., Hirsch, L. A., Howard, A. W., Huber, D., Isaacson, H., Kosiarek, M., Lubin, J., Mayo, A. W., Mocnik, T., Akana Murphy, J. M., Petigura, E. A., Robertson, P., Rosenthal, L. J., Roy, A., Rubenzahl, R. A., Van Zandt, J., Weiss, L. M., **Knudstrup, E.**, Andersen, M. F., Grundahl, F., Yao, X., Pepper, J., Villanueva, S., Ciardi, D. R., Cloutier, R., Jacobs, T. L., Kristiansen, M. H., LaCourse, D. M., Lendl, M., Osborn, H. P., Palle, E., Stassun, K. G., Stevens, D. J., Ricker, G. R., Vanderspek, R., Latham, D. W., Seager, S., Winn, J. N., Jenkins, J. M., Caldwell, D. A., Daylan, T., Fong, W., Goeke, R. F., Rose, M. E., Rowden, P., Schlieder, J. E., Smith, J. C., & Vanderburg, A. (2020)
— *Astronomical Journal*, 159, 241, 13pp.

 *A backward-spinning star with two coplanar planets.*

Hjorth, M., Albrecht, S., Hirano, T., Winn, J. N., Dawson, R. I., Zanazzi, J. J., **Knudstrup, E.**, & Sato, B. (2021)
— *Proceedings of the National Academy of Sciences*, 118, e2017418118, pp.

 *A Preponderance of Perpendicular Planets.*

Albrecht, S. H., Marcussen, M. L., Winn, J. N., Dawson, R. I., & **Knudstrup, E.** (2021)
— *Astrophysical Journal*, 916, L1, 8pp.

 *TOI-1431b/MASCARA-5b: A Highly Irradiated Ultrahot Jupiter Orbiting One of the Hottest and Brightest Known Exoplanet Host Stars.*

Addison, B. C., **Knudstrup, E.**, Wong, I., Hébrard, G., Dorval, P., Snellen, I., Albrecht, S., Bello-Arufe, A., Almenara, J.-M., Boisse, I., Bonfils, X., Dalal, S., Demangeon, O. D. S., Hoyer, S., Kiefer,

F., Santos, N. C., Nowak, G., Luque, R., Stangret, M., Palle, E., Tronsgaard, R., Antoci, V., Buchhave, L. A., Günther, M. N., Daylan, T., Murgas, F., Parviainen, H., Esparza-Borges, E., Crouzet, N., Narita, N., Fukui, A., Kawauchi, K., Watanabe, N., Rabus, M., Johnson, M. C., Otten, G. P. P. L., Jan Talens, G., Cabot, S. H. C., Fischer, D. A., Grundahl, F., Fredslund Andersen, M., Jessen-Hansen, J., Pallé, P., Shporer, A., Ciardi, D. R., Clark, J. T., Wittenmyer, R. A., Wright, D. J., Horner, J., Collins, K. A., Jensen, E. L. N., Kielkopf, J. F., Schwarz, R. P., Srdoc, G., Yilmaz, M., Senavci, H. V., Diamond, B., Harbeck, D., Komacek, T. D., Smith, J. C., Wang, S., Eastman, J. D., Stassun, K. G., Latham, D. W., Vanderspek, R., Seager, S., Winn, J. N., Jenkins, J. M., Louie, D. R., Bouma, L. G., Twicken, J. D., Levine, A. M., & McLean, B. (2021)
— Astronomical Journal, 162, 292, 29pp.



TOI-1136 is a Young, Coplanar, Aligned Planetary System in a Pristine Resonant Chain.

Dai, F., Masuda, K., Beard, C., Robertson, P., Goldberg, M., Batygin, K., Bouma, L., Lissauer, J. J., **Knudstrup, E.**, Albrecht, S., Howard, A. W., Knutson, H. A., Petigura, E. A., Weiss, L. M., Isaacson, H., Kristiansen, M. H., Osborn, H., Wang, S., Wang, X.-Y., Behmard, A., Greklek-McKeon, M., Vissapragada, S., Batalha, N. M., Brinkman, C. L., Chontos, A., Crossfield, I., Dressing, C., Fetherolf, T., Fulton, B., Hill, M. L., Huber, D., Kane, S. R., Lubin, J., MacDougall, M., Mayo, A., Močnik, T., Akana Murphy, J. M., Rubenzahl, R. A., Scarsdale, N., Tyler, D., Zandt, J. V., Polanski, A. S., Schwengeler, H. M., Terentev, I. A., Benni, P., Bieryla, A., Ciardi, D., Falk, B., Furlan, E., Girardin, E., Guerra, P., Hesse, K. M., Howell, S. B., Lillo-Box, J., Matthews, E. C., Twicken, J. D., Villaseñor, J., Latham, D. W., Jenkins, J. M., Ricker, G. R., Seager, S., Vanderspek, R., & Winn, J. N. (2023)
— Astronomical Journal, 165, 33, 37pp.

Selected Articles in Preparation

The following article is included in this thesis:



Solar-like oscillations in γ Cephei A as seen through SONG & TESS
Knudstrup, E., Lund, M. N., Fredslund Andersen, M., Rørsted, J. L., Hernandez, F. P., White, T. R., Grundahl, F., Pallé, P. L., Stello, D.,

- Kjeldsen, H., Vrard, M., Winther, M. L., Handberg, R., & Simón-Díaz, S.
— in prep.

Abbreviations and Acronyms

HR DIAGRAM Hertzsprung-Russell diagram; 10, 11, 144, 279

AGB asymptotic giant branch; 14, 277

BASTA BAyesian STellar Algorithm; 106–108, 137, 144–147, 154, 156, 205–207, 277

BF broadening function; 43, 61–66, 70, 74, 80, 81, 277

CCD charge-coupled device; 23, 28, 61–63, 71, 167, 195, 277

CCF cross-correlation function; 43, 44, 57, 202, 230–236, 239, 246, 248, 256, 258, 261, 278

CMD colour-magnitude diagram; 11, 12, 53, 54, 56, 69, 70, 78, 79, 86, 88–90, 93, 97, 198, 200, 211, 277, 358

DEB detached eclipsing binary; 3, 34, 51–55, 57, 61, 63, 77, 81, 86, 99, 273, 278

FIES FIber-fed Echelle Spectrograph; 28, 45, 61, 62, 64, 130, 132, 136, 156–158, 164, 168–170, 173–175, 178, 180, 200, 205, 278

GP Gaussian process; 148–152, 155, 173, 178, 179, 193, 206, 209, 229, 230, 237, 258, 261, 267, 278, 359, 362

HARPS High-Accuracy Radial Velocity Planetary Searcher; 28, 45, 188, 200–205, 212, 216, 220, 223, 224, 228, 231–233, 236, 238, 239, 241, 244–246, 248, 250, 252, 254–258, 264, 268, 275, 279, 363

KDE kernel density estimation; 35, 135, 263, 266, 279

- MCMC** Markov Chain Monte Carlo; 60, 79–83, 110, 112, 150, 151, 158, 172–176, 180–182, 206, 208, 216, 230, 236, 240, 242, 255, 258, 259, 262, 280, 356, 361, 362, 366, 368
- MS** main sequence; 9, 12, 13, 38, 53, 66–68, 83, 85–87, 90, 94, 122, 280
- NOT** Nordic Optical Telescope; 14, 15, 28, 61, 62, 64, 71, 74, 80, 82, 130, 157, 164, 168, 174, 200, 280
- PI** principal investigator; 26, 130, 157, 188, 223, 228, 254, 280
- RECON SPECTROSCOPY** reconnaissance spectroscopy; 28, 166, 170, 200, 205, 281
- RGB** red-giant branch; 9, 11, 13, 14, 51, 54–60, 77–79, 83, 86, 87, 89, 92, 96, 97, 127–129, 143, 144, 146, 156, 281, 360
- RM EFFECT** Rossiter-McLaughlin effect; 23, 40–43, 47, 48, 104, 175, 184, 216, 224, 227, 232, 234, 239, 250–256, 258, 270, 274, 275, 281, 361, 363
- RV** radial velocity; 23, 24, 26–30, 35, 42, 43, 46, 47, 52, 55–58, 61–63, 73, 79, 106, 121–123, 126–130, 132, 138, 140, 147–151, 154–158, 166, 168, 169, 171–177, 180–183, 188–190, 201–203, 206, 208, 211, 216, 220, 221, 227, 228, 230, 231, 233, 234, 239–242, 244, 246–248, 250–253, 255, 256, 258–261, 264, 266, 270, 275, 276, 281, 353, 361, 363
- SED** spectral energy distribution; 57, 66, 68–71, 170, 173, 198, 205–208, 212, 218, 219, 282, 370
- SNR** signal-to-noise ratio; 58, 59, 132, 138, 140, 143, 162, 168, 192, 202, 228, 231, 235, 236, 254, 255, 281
- SONG** Stellar Observations Network Group; 26, 27, 127, 128, 130, 131, 135, 137–140, 147–150, 152, 156, 223, 228, 232, 282, 355
- TESS** Transiting Exoplanet Survey Satellite; 28, 32–34, 37, 51, 52, 65, 74, 75, 77–80, 94, 96, 97, 102, 113, 115–117, 127, 128, 130, 132, 133, 137–140, 156–160, 162, 166, 173, 174, 178, 179, 181–183, 187–194, 202, 206, 208, 209, 212, 218–220, 224, 226–230, 232, 237, 241, 242, 244, 245, 247, 248, 250, 252, 253, 256, 258, 261, 264, 266–268, 270, 282, 354, 357, 359, 362, 370
- ZAMS** zero-age main sequence; 9, 11, 122, 282

Introduction

Up until some 30 years ago, the only planetary system that we knew of was the Solar System. Therefore, the blueprint for theories on planet formation and evolution were naturally all based on what we saw in the Solar System. Governed by the neat and ordered structure for this blueprint, where all planets are orbiting in the same plane which is more or less confined to the Sun's equator, theoreticians, such as Swedenborg (1734), Kant (1755), and Laplace (1796), devised the *nebula theory* (Perryman, 2018). Here a gaseous cloud rotates slowly, while gradually collapsing and flattening due to gravity, eventually forming the central host star, and from the remnant disc planets are formed on orbits that revolve in the same direction as the rotation of the star.

Since these early theories, the tilt between the orbital axis of the planets and the Sun's rotation axis, the so-called *obliquity*, has been measured using *helioseismology* to be $\psi = 7.155 \pm 0.002^\circ$ (Beck and Giles, 2005), confirming that it is indeed low. In addition, evidence for *protoplanetary discs* around young stars have been found (e.g., in HL Tauri; Cohen, 1975), further lending credence to this paradigm of planet formation. In these *protoplanetary discs* feeding zones are large and icy material abundant beyond the *snow line*, meaning that rocky cores can grow quickly and accrete copious amounts of gas to form massive gaseous atmospheres, thus becoming gas giants. Inside the *snow line*, which is located at a few AU from the Sun, rocky cores are too small to accrete appreciable amounts of gas, because of the small feeding zones and absence of ices, and instead they grow through impacts with other *protoplanets*. The resulting architecture is a system with circular and coplanar orbiting planets with the rocky planets inside and gas giants beyond the *snow line* (Dawson and Johnson, 2018).

However, as we started to detect planets around other stars than the Sun, *extrasolar planets* or *exoplanets*, the notion of the Solar System as a blueprint and the Sun as a typical host star were immediately challenged.

2 Introduction

We first detected exoplanets around a pulsar (Wolszczan and Frail, 1992), a very extreme and exotic host in its current evolutionary stage, but this discovery also suggests that planets can form around more massive stars, and moreover survive the later stages of stellar evolution. Things continued to get weirder when we then got to the first detection of an exoplanet around a Sun-like star, 51 Pegasi b (Mayor and Queloz, 1995), a gas giant with an orbital separation of only 0.05 AU.

In a Solar System context, eccentric orbits mainly pertain to smaller bodies like comets and asteroids. Out of the eight planets, Mercury is the only one on an orbit with an appreciable amount of eccentricity (e) at $e \sim 0.2$, the rest are on more or less circular orbits. How does this compare to the orbits of some of the exoplanet systems we have discovered? Once again things out there can be quite different, as we have discovered planets on orbits unlike the ones we see in the Solar System with extreme eccentricities of $e > 0.9$ (e.g., HD 20782 b; Jones et al., 2006). Another curiosity is that, despite its eight planets, the Solar System is lacking what appears to be the most abundant type of planet, namely super-Earths ($\gtrsim 2 R_{\oplus}$; Howard et al., 2010b; Mayor et al., 2011).

Exoplanet systems thus come in forms that are very different from the Solar System in terms of orbital separation and eccentricity, as well as the type of host star *and* planets within the systems, but what about the **obliquity** – are all systems as “flat” as the Solar System? The answer is no. In addition to prograde orbits similar to the ones in the Solar System (e.g., Queloz et al., 2000), we have found planets on orbits that are highly inclined with respect to the stellar spin axis (e.g., Hébrard et al., 2008), and we have even found retrograde orbits (e.g., Winn et al., 2009; Lund et al., 2014a).

We are thus seeing a huge diversity of planetary system architectures. A diversity beyond what we could have possibly imagined from only using the Solar System as a blueprint. This diversity is not only extraordinarily intriguing, but also poses a challenge to our understanding of planet formation and evolution. Our aim is therefore to see if we can understand the physical processes at work in shaping architectures of exoplanet systems.

How might we investigate this?

From an observer’s point of view, the main objective is to deliver key observables that can inform theories on planet formation and evolution. When it comes to understanding the formation of large planets ($\gtrsim 4 R_{\oplus}$) on short period orbits, particularly informative orbital parameters are

the eccentricity and the [obliquity](#). Information on companionship, both planetary or stellar companions, also plays a key role in the dynamical evolution of the system. As these companions can greatly influence the orbit of the inner planet, drastically shrinking its orbital separation as well as tilting it. Through these measurements we might thus be able to identify the migration pathway at work in a given system. Naturally, however, making general inferences about the origins of planets require many such measurements.

An immediate challenge in exoplanet research is the fact that the planetary parameters are intimately locked to the fundamental stellar parameters such as the mass and radius. Stellar parameters therefore not only dictate what we know about the star, but also what we can learn about the planets it might harbour. Accurate and precise stellar parameters are therefore crucial for exoplanet science, and as such a deep understanding of stellar physics is warranted to properly advance the exoplanet field. In this thesis we will therefore be probing key orbital and planetary parameters as well as fundamental stellar parameters in order to make headway in our understanding of planet formation and evolution.



Thesis outline

This thesis is composed of two parts: in Part I I will discuss the scientific background for this work before moving on to presenting research results obtained during my PhD in Part II. In Chapter 1 I will review the formation and evolution of stars as well as discuss the formation and migration of planets. In Chapter 2 I will be discussing the observational techniques used in this work, including some exciting discoveries and trends that have been unveiled.

In Chapter 3, Chapter 4 and Chapter 5 fundamental stellar parameters will be at the crux. In Chapter 3 I will present an analysis of three pairs of [detached eclipsing binary \(DEB\)](#) systems in an open cluster, NGC 2506, where the results for the masses and radii of the [DEBs](#) will be used to constrain the age and metallicity of the cluster. In Chapter 4 and Chapter 5 the stellar parameters will be derived using [asteroseismology](#). In Chapter 4 the results will be used to constrain the orbits of the planets in the multiplanet system K2-93, and in Chapter 5 the planet hosting γ Cephei system will be investigated.

I will then move on to present some discoveries of exoplanet systems in Chapter 6 and Chapter 7, where a trio of giant planets on short-period

4 Introduction

orbits will be presented in the former chapter and a hot super-Neptune with a Saturn-mass companion in the latter. In Chapter 8 and Chapter 9 I will present a thorough analysis of the planetary system architectures for two different systems through measurements of the projected obliquity. In Chapter 8 the system HD 332231 will be investigated in which the warm Saturn is on a circular and well-aligned orbit. In the TOI-640 system presented in Chapter 9, on the other hand, the orbit is highly inclined, the planet is in fact on a polar orbit. Finally, in Chapter 10 I will be summarising the work presented here as well as discussing future prospects for the exoplanet field.

Part I



Scientific Background

1

Planetary formation, migration, and evolution

In this chapter I will provide some context on the physical processes at work when shaping the architectures of planetary systems. As planet formation starts with the formation of stars, we will start with a brief introduction to the formation and evolution of stars before moving onto describing planet formation. When discussing stellar structure and evolution, I will be linking the discussion to research I have been engaged in as well as exoplanet research in general.

1.1 Stellar structure and evolution

As stars of different masses evolve quite differently, the idea here is not to describe each stellar mass category (low, intermediate, or massive) in great detail, but rather to provide a general description of stellar structure and evolution. This serves as a window into processes relevant to the exoplanet field as well as an overview into topics I have worked on. Unless explicitly cited, the following is primarily based on the works of Ryden et al. (2010), Kippenhahn et al. (2013), and Christensen-Dalsgaard (2008b). This is especially the case for the sections on stellar evolution: Section 1.1.2, Section 1.1.3, and Section 1.1.4.

1.1.1 Star formation

Stars are formed from molecular clouds, which are dense regions in the interstellar medium of very cold (~ 10 K) molecular gas. When the kinetic energy from the gas pressure in the cloud balances the potential energy from the gravitational force, the cloud is in hydrostatic equilibrium. For a

cloud with a given density and a given temperature, there is a maximum radius for which a cloud is stable against collapse. This critical radius is known as the Jeans length. If the cloud is perturbed from hydrostatic equilibrium, a dense core of typically a few solar masses will start to form. As this dense core collapses a rotationally flattened disc is formed due to conservation of angular momentum. The [protostar](#) is located in the central dense region of this disc. This process of collapsing a dense molecular cloud into a [protostar](#) only takes on the order of a few 10^4 yr (Ryden et al., 2010).

While the Sun is an isolated, single star, around half of all stars are found in binaries (e.g., Moe and Di Stefano, 2017). So, to be able to address star formation, as well as planet formation, in general, it is important to also understand the formation of binary systems. Furthermore, even though the Sun is not found in a cluster the census is that stars are formed in clusters or associations, it is worthwhile to briefly discuss stellar formation in these environments (Gounelle and Meynet, 2012).

In sufficiently massive discs, differential rotation can create spiral arms in which over-densities might lead to fragmentation. From this fragmentation one or more [protostars](#) are formed, and this is believed to be one way for binary (or higher-order) systems to form (Burkert et al., 1997). This disc fragmentation naturally takes place after the disc has formed. Alternatively, binaries can form in a turbulent cloud. Complex motion has been observed in prestellar cores (Caselli et al., 2002), where the chaotic motion leads to inhomogeneities in the velocity and density profiles of the cloud. These inhomogeneities seed the fragmentation of dense cores from which several [protostars](#) are formed (Goodwin et al., 2004).

These different ways of fragmentation should lead to different observables, with disc-fragmentation yielding smaller ($a \lesssim 100$ AU) orbits that are spin-orbit aligned. Contrary turbulent fragmentation could lead to highly eccentric, wide (100–1000 AU), misaligned orbits (Kuruwita and Haugbølle, 2022). We might therefore test the scenarios by measuring the spin-orbit angle of stars in binaries on wide as well as smaller orbits.

Hale (1994) investigated this by measuring the spin-orbit alignment of visual binaries. From this study binaries with smaller orbital separations ($\lesssim 30 - 40$ AU) were found to preferentially be aligned, while a tendency for wide orbiting binaries to be spin-orbit misaligned was found. The result was, however, disputed by Justesen and Albrecht (2020), who extended this analysis by expanding the sample, and concluded that at present the precision of the data is not sufficient to make inferences about the spin-orbit alignment of visual binaries.

Star formation on the grandest scale involves giant molecular clouds, measuring up to hundreds of light years across with masses between tens of thousands or even millions of solar masses. Stellar clusters form from these massive clouds, which has also been confirmed observationally with observations of clusters of stars embedded in these stellar nurseries (e.g., as for RCW 38; Wolk et al., 2008). Only about 4-7% of embedded clusters actually remain bound after they emerge from the molecular clouds with most disintegrating within 100 Myr (Lada and Lada, 2003), and, as mentioned, this is what has been hypothesised to have happened to the Sun and its siblings that formed from the same embedded cluster (Gounelle and Meynet, 2012).

While the birth of a planet is intimately locked to stellar formation, there is the possibility that a planet completely detaches itself from the stellar system, thus becoming a free-floating or *rogue planet* (e.g., Liu et al., 2013). Assuming this decoupling does not occur, the evolution of the planet, in terms of it surviving as a whole, its habitability, and orbital configuration, is greatly affected by the evolution of its host star.

1.1.2 Main-sequence evolution

After formation, the **protostar** radiates gravitational potential energy and contracts on the Kelvin-Helmholtz timescale, $t_{\text{KH}} = GM_\star^2/(R_\star L_\star)$, where G is the gravitational constant, M_\star is the stellar mass, R_\star the radius, and L_\star the surface luminosity. For a Sun-like star this comes out to some 30 million years. As the **protostar** contracts the central regions become hotter and denser until they reach the point where hydrogen fusion can ignite, at which point the **protostar** becomes a star on the *zero-age main sequence (ZAMS)* shown at point 1 in Figure 1.1 for the BaSTI (a Bag of Stellar Tracks and Isochrones; Hidalgo et al., 2018) track. For **protostars** with masses lower than $\sim 0.08 M_\odot$, the core never reaches a temperature sufficient for hydrogen burning, instead the **protostar** becomes a brown dwarf.

Except for the very late stages of stellar evolution, a star spends most of its life fusing hydrogen to helium in its core, and the star is thus found on the *main sequence (MS)* for the vast majority of its life. The time a star spends on the **MS** fusing hydrogen to helium, τ_H , is very dependent on the mass, on the order of $\tau_H \propto M_\star^{-2.5}$. Very massive ($> 5 M_\odot$) stars thus quickly burn through their central hydrogen reservoir, leaving the **MS** after some tens of million of years, whereas low-mass stars like the Sun spend billions of years on the **MS** before moving towards the subgiant branch and subsequently the *red-giant branch (RGB)*.

Regardless of mass, a general tendency is that during central hydrogen burning the luminosity of the star increases. As hydrogen is fused into helium in the core, the *mean molecular weight* increases simply because helium is heavier. To balance the weight of the overlying material, the pressure cannot decrease during this phase and according to the *ideal gas law*, an increase in density or an increase in temperature can compensate this increase in the mean molecular weight. Gravitational potential energy is released as the core contracts, which increases the density and temperature, resulting in an increase in the nuclear energy generation rate. The luminosity of the star therefore increases.

The increase in luminosity as a response to the changes in the core can be explained in a fairly straightforward manner. However, when it comes to describing the change in other global properties such as radius and T_{eff} , things are not so well-understood – the contraction of the core also leads to an expansion of the stellar radius. This might be part of a more general principle as described below in Section 1.1.3. The expansion rate is very dependent on mass, where for lower mass stars the expansion is quite modest. This means that the increase in luminosity leads to an increase in T_{eff} as is evident from the *Hertzsprung-Russell diagram (HR diagram)* in Figure 1.1. As is also seen is that T_{eff} for higher mass stars decreases (between point 1 and 2), because of the rapid expansion.

1.1.2.1 Energy transport

Apart from dictating the lifetime, the mass also has a profound impact on the structure of the star, which greatly influences the evolution as well. Energy transport in a star takes place either through radiation or convection. The boundary between a radiative and a convective zone is given by the *Schwarzschild criterion*, which marks the point at which energy transport through radiation requires too steep a temperature gradient, and energy transport takes place through convection.

For low-mass stars the energy transport for the core happens through radiation. In the absence of mixing, hydrogen is depleted from the core gradually with a faster depletion towards the centre as the temperature is higher here. As the core is gradually depleted, hydrogen burning continues in a shell around the depleted part of the core.

On the other hand, for more massive stars with convective cores the chemical elements are mixed. Despite the fact that the most effective burning takes place towards the center, the timescale for convective mixing is much smaller (< 1 yr) than the timescale for depleting hydrogen, meaning

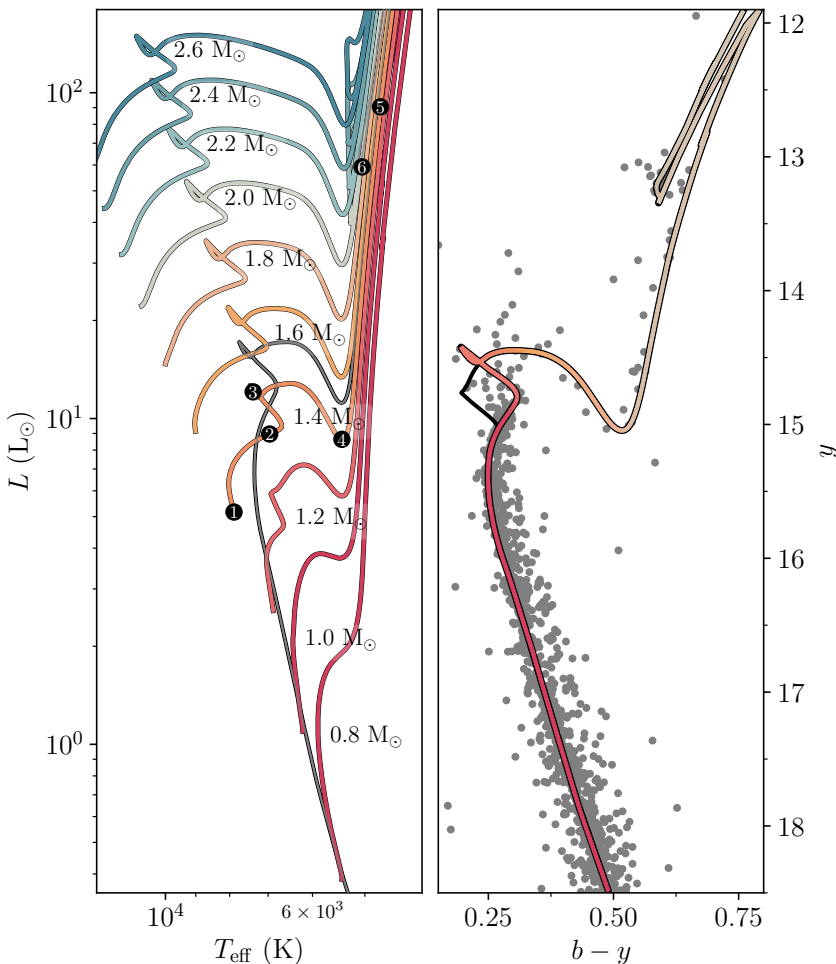


Figure 1.1 | Hertzsprung-Russell and colour-magnitude diagrams. *Left:* Evolutionary tracks of different masses from BaSTI shown in an **HR DIAGRAM**. The grey curve beneath is an **isochrone** showing how that essentially samples different masses of the same age. Some key points are highlighted for the $1.2 M_{\odot}$ track: ① the **ZAMS**, ② central hydrogen mass fraction of 0.30, ③ **turn-off**, ④ base of the **RGB**, ⑤ ignition of helium burning, and ⑥ the quiescent helium burning (see also Table 4 of Hidalgo et al., 2018). *Right:* **CMD** of NGC 2506 with grey points denoting **Gaia** proper motion members of the cluster. Overplotted are two BaSTI **isochrones** ($\tau = 2.0$ Gyr) with (colour-coded according to mass) and without (black) the inclusion of **convective core-overshooting**. The Strömgren photometry is from Knudstrup et al. (2020).

that the core is chemically homogenous, and hydrogen is thus depleted for the entire core at the same time. This is seen as the very prominent kink between point 2 and 3 in the evolutionary tracks in the left panel of Figure 1.1 for stars with masses $\gtrsim 1.2 M_{\odot}$.

For convective cores there is the added complication of [convective core-overshooting](#), which is the effect of a convective cell not stopping at the boundary given by the Schwarzschild criterion because of its inertia. Observationally, this is seen as a prolonged “hook” at the end of the [MS](#) for open clusters as in the [CMD](#) in the right panel of Figure 1.1 for NGC 2506. The amount of [convective core-overshooting](#) and its influence is still unclear, open clusters thus make up excellent test beds for comparing the theoretical [isochrones](#) to the observed sequence as we did in Knudstrup et al. (2020, Chapter 3).

The stellar structure also plays an important role in the evolution of planetary system architectures. Here the difference between a star having a convective or a radiative envelope greatly impacts the damping of the [obliquity](#), i.e., the time it takes to align the system. This distinction between convection and radiation for [tidal friction](#) was originally investigated by Zahn (1977) for close binaries, who defined two different timescales. Albrecht et al. (2012) applied these two timescales to the observed distribution of projected [obliquity](#) measurements, using a value of 6250 K for T_{eff} (the so-called [Kraft break](#)) as the division between a star having a radiative (above) or a convective (below) envelope. From this they found that in systems with convective envelopes where we expect alignment to be rapid, we find low projected [obliquities](#). Contrary, for the hotter stars with longer alignment timescales, the distribution is broad. Not only is this result evidence for planet-star tidal interactions, it also underlines the importance of understanding the internal structure of stars when studying planetary system architectures.

1.1.3 Post main-sequence evolution

After central hydrogen burning, the star is left with a core consisting of helium. For stars with masses of $\gtrsim 1.2 M_{\odot}$ this [turn-off](#) point (point 3 in Figure 1.1) corresponds to the point at maximum T_{eff} along the [MS](#). Initially there is no nuclear energy generation in the core as the temperature is far below what is required for helium burning to ignite. However, the core is surrounded by a shell of hydrogen hot enough for hydrogen burning to proceed, a so-called hydrogen shell source from which the luminosity of the star is derived. Given that this shell source converts hydrogen to

helium, the mass of the helium core increases. As outlined above this leads to a contraction of the core and as a response to the contraction the thermal energy of the core increases, up to the point where the temperature is sufficiently high for helium burning. The process is then repeated, with the star burning helium in the core until it is exhausted, while continuing to burn hydrogen in a shell. A contracting core of carbon and oxygen has now formed, which is surrounded by a helium shell source and a hydrogen shell source. Again, this process is very dependent on the mass of the star with sufficiently massive stars gradually exhausting elements in the core and subsequently in a shell all the way up to iron.

This building of layers in and around the core is seen both numerically and observationally with stars expanding during the hydrogen shell burning phase and becoming red giants. This mirroring process is known as the *shell-burning law*: when the region within a burning shell contracts, the region outside the shell expands; and when the region inside the shell expands, the region outside the shell contracts. While this very simple principle provides an intuitive understanding of the process, it is not fully understood why a contraction should be followed by an expansion.

For lower mass stars ($\sim 1 M_{\odot}$) without convective cores, the core contraction is not connected with heating, meaning that helium burning will start much later after the mass of the core has grown up to a certain limit. Given that this transitional process is quite slow, many such stars in this shell-burning phase (moving from point 3 to 5 in Figure 1.1) between central hydrogen and helium burning should be observed. The horizontal part (from 3 to 4) is the subgiant branch, which for older clusters is seen as a densely populated branch in extension of the [MS](#). For younger clusters, mass and radius determination for stars in this phase are particularly telling as this is a phase of rapid evolution, allowing one to place tight constraints on the age of the cluster. The [RGB](#) is the vertical part in Figure 1.1 starting at point 4, where the stars in response to the continued contraction of the core proceed to expand.

The expansion is so extensive that the stellar radius can reach a couple of hundreds solar radii. For the Solar System that would mean that both Mercury and Venus would be engulfed, and possibly the Earth. Needless to say, even if the Earth is not engulfed, the increase in the luminosity of the Sun would drastically change the climate on Earth.

Point 5 in Figure 1.1 denotes the time at which central helium burning sets in. For stars between 0.8 and $2.0 M_{\odot}$ this is kickstarted with the so-called *helium flash*. The star subsequently settles into more quiescent helium burning in what is observationally seen as the *red clump* at point

6. For more massive stars there are some interesting features emerging as the star moves from the [RGB](#) upwards with the blue loop becoming quite apparent for the $2.6 M_{\odot}$ track. For sufficiently massive stars the blue loops cross the instability strip, where the stars display very regular pulsation patterns as, for instance, Cepheid or δ Scuti variables.

1.1.4 Final stages of stellar evolution

As helium is now being converted into carbon and oxygen in the core, the mean molecular weight increases once again. Similar to the core hydrogen burning phase, the core contracts and heats up, which – according to the [shell-burning law](#) – means the outer envelope expands. Eventually, helium is exhausted in the core, but continues burning in a shell, meaning the star now has both helium and hydrogen shell-burning.

As was the case for hydrogen exhaustion, the carbon and oxygen core is not sufficiently hot for carbon burning to take place. The core therefore contracts and heats up. However, because of the two shell sources, the [shell-burning law](#) now acts to reverse the contraction of the core when applied to the helium shell, and thus the region between the two shells are expanded. Applying the [shell-burning law](#) to the hydrogen shell, it follows that this part along with the outer regions contract. The contraction releases gravitational potential energy, which causes the luminosity to increase.

For very massive stars ($\gtrsim 8 M_{\odot}$) the core contraction leads to temperatures sufficiently high for carbon burning to ignite, while lower mass stars enter a phase of evolution called the [asymptotic giant branch \(AGB\)](#). This is a period of thermal instability in the helium shell source, where the star alternates between having a hydrogen or a helium shell source. During this phase the star rapidly loses mass, stripping all the outer layers, while creating heavier elements through neutron capture. What is left is just the bare carbon-oxygen core. The expelled material form an initially well-defined shell around the extremely hot and luminous core, which illuminates the layers and causes it to shine as a *planetary nebula* as seen in the image taken using the [Nordic Optical Telescope \(NOT\)](#) in Figure 1.2. The remnant core, a *white dwarf*, continues to shine as it radiates away its thermal energy, gradually cooling to reach an T_{eff} of 4000 K in some 10 billion years.

As mentioned, massive stars do reach core temperatures high enough for fusing carbon. They continue fusing heavier elements and in the process building up shells of successive elements in a layered onion-like structure. This process ends with the fusion of silicon into iron at which point further



Figure 1.2 | Image of the Ring Nebula. The planetary nebula M57 also known as the Ring Nebula. Image taken with the Alhambra Faint Object Spectrograph and Camera (ALFOSC) at the NOT using Johnson-Bessell V (green) and R (orange) filters as well as $H\alpha$ (red) and OIII (blue).

fusion reactions are endothermic, meaning they require input energy, and the star is thus unable to generate energy in the core. What ensues is a violent explosion, expelling the outer layers, and a collapse of the core until it reaches nuclear densities – *core-collapse supernova*. The core now mostly consists of neutrons, and that remnant core is known as a *neutron star*. These have been detected observationally as *pulsars* as they are emitting pulses at very regular intervals, with periods between a few milliseconds and a few seconds. For the most massive stars ($\gtrsim 30 M_{\odot}$), the core-collapse

supernova does not stop at nuclear densities, but the collapse continues until a *black hole* is formed.

Speculations of whether planets could survive these violent events were put to rest at the dawn of the exoplanet field. As mentioned, the first detection of an exoplanet system was the discovery of a pair of small planets ($\sim 3 M_{\oplus}$) around a millisecond pulsar, discovered through the timing variations their orbits induce in the emitted pulses (Wolszczan and Frail, 1992). While surviving here only refers to the presence of planets, or what might be left of them, it does show that planets have some resilience to these rather disruptive events. Another remarkable discovery of a planet with an extreme object as a host, is the discovery of a gas giant around the white dwarf WD 1856+534 (Vanderburg et al., 2020). The planet in this system is significantly larger than its host star, with a planet-to-star radius ratio of around 7. This discovery suggests that giant planets can be scattered into tight orbits around white dwarves without being tidally disrupted, which was previously believed to be the case.

Even if planets were not able to survive these final stages of stellar evolution, these events are still massively important for the formation of planets, particularly seeing as numerous studies have shown a positive correlation between the host star metallicity and the occurrence rate of planets (e.g., Gonzalez, 1997; Fischer and Valenti, 2005). The heavy elements generated by these violent events are thus distributed throughout the interstellar medium, seeding the next generation of stars and planets.

1.2 The eccentric lifestyles of planets

In the following I will discuss planet formation and evolution with a particular focus on the formation of hot and warm Jupiters, based on the reviews by Dawson and Johnson (2018) and Kley and Nelson (2012). I will start with a brief introduction on the formation of planets, before moving on to discuss the migration and evolution of the planetary systems.

1.2.1 Planet formation

An accretion disc will form from the dust and gas that did not fall onto the *protostar*. This disc, known as a *protoplanetary disc*, provides the environment for planet formation, where planets are believed to form through one of the following processes: core accretion or gravitational instability. The latter is a *top-down* process, where planets form from

instabilities in the [protoplanetary disc](#), which fragment (as was the case for star formation) and collapse under their own gravity. This mechanism is faster than core accretion and can take place far away from the star (see, e.g., Boss, 1997), which is why it has been invoked to explain the formation of the wide orbiting planet around the young star AB Aurigae (Currie et al., 2022). However, as a large orbital separation is actually a criterion for these instabilities to occur, it is also why this process is generally not regarded to be the dominant process for planet formation (see, e.g., Kratter et al., 2010).

Contrary to gravitational instability, core accretion is known as a *bottom-up* process, where the planets form from the inside out. The planets form from a central core, which grows by accreting material from the [protoplanetary disc](#). Dust particles merge and form dust grains, which then combine to form pebbles, then boulders, and finally planetesimals. These planetesimals collide, eventually forming planetary cores. Given the right conditions, these cores will start to accrete gas. Sufficiently massive cores ($\sim 10 M_{\oplus}$) will be able to accrete material through runaway gas accretion leading to the formation of a gas giant (Pollack et al., 1996). This naturally necessitates the [protoplanetary disc](#) to still be present, thereby placing a limit on the timescale for the cores to form as the disc dissipates after a few million years (Fedele et al., 2010). As this process requires the presence of volatiles, it should only be able to take place beyond the [snow line](#), where the temperature is low enough for volatiles to condense, typically found at a couple of AU from the star. Furthermore, at small separations, the limiting core mass is $< 1 M_{\oplus}$.

However, Jupiter-sized planets have been observed in systems with a wide range of orbital distances. In fact, as mentioned, the very first exoplanet discovered, 51 Pegasi b, is a Jupiter-sized planet with an orbital distance of only ~ 0.05 AU (Mayor and Queloz, 1995). This clearly challenges the view of planet formation just outlined, requiring either a revision on how to form hot Jupiters *in situ* inside the [snow line](#), or a means of transportation. While *in situ* formation of hot Jupiters is still being debated, with a possible remedy coming, for instance, in the form of rapid transportation of massive cores formed at larger separations and subsequent runaway gas accretion (Batygin et al., 2016), the migratory patterns of planets will now be discussed.

1.2.2 Planetary migration

If hot Jupiters do not form *in situ*, they must have formed *ex situ* at larger orbital separations and later migrated inwards to the separations at which

we see them today. The two main migration mechanisms are *disc migration* (e.g., Goldreich and Tremaine, 1980) and *high-eccentricity migration* (e.g., Rasio and Ford, 1996). A schematic for hot Jupiter formation via either of these two as well as through *in situ* formation is provided in Figure 1.3. Which of the two processes is responsible for the population of hot Jupiters we see is actively being investigated, with the possibility of the two being able to operate in tandem in different systems (Dawson and Johnson, 2018). Each of the two mechanisms will now be discussed in more detail.

1.2.2.1 Disc migration

As the name suggests, *disc migration* refers to planetary migration through the *protoplanetary disc* through exchange of angular momentum between the gas and dust particles within the disc and the planet. Disc migration can be further divided into three types; type I, type II, and type III.

In type I migration, planets are not massive enough ($10 - 30 M_{\oplus}$) to significantly alter the global structure of the disc, but they are still able to excite spiral density waves in the gas disc. This will in turn exert a torque on the planet, which will either force the planet to migrate inwards or outwards. The timescale for this migration scales with the mass of the planet with more massive planets migrating faster. For these low-mass planets time scales are typically on the order of 10^5 years (Goldreich and Tremaine, 1980).

Planets that are sufficiently massive can fundamentally change the structure of the *protoplanetary disc*. For these massive planets angular momentum is more easily transferred to the disc, and they are able to open up gaps in the *protoplanetary disc*. This is known as type II migration. Like type I migration, the timescale here is also quite rapid, it takes on the order of 10^5 years for a Jupiter-mass planet starting at 5 AU to reach orbital separations close to the star (Nelson et al., 2000).

Type III migration, also known as *runaway migration*, is a very rapid process. It is triggered by a Saturn-mass planet's gravitational interaction with the *protoplanetary disc*, where – like in type II migration – gaps are opened in the disc. Opening gaps in the disc increases the so-called *co-orbital mass deficit*, which is the difference between the mass that would be contained in the disc surrounding the planet had it not been perturbed, and the mass actually contained in this region. If the *co-orbital mass deficit* exceeds the mass contained within the planet's *Hill sphere*, a positive feedback loop might be triggered, which leads to rapid migration. In extreme cases the semi-major axis of the planet can be halved in less than 50 orbits (Masset and Papaloizou, 2003).

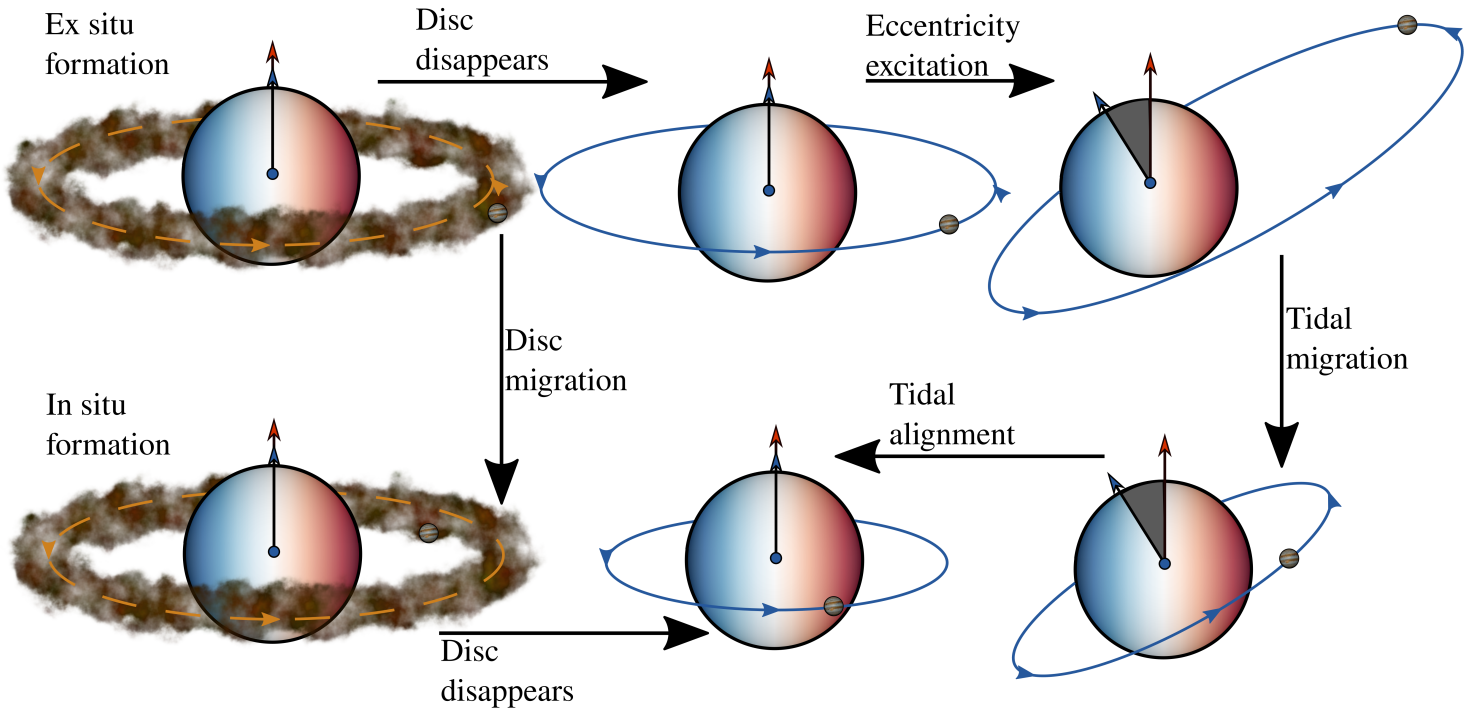


Figure 1.3 | Schematic of hot Jupiter formation. The three different scenarios for forming a hot Jupiter. The Jupiter can either form **in situ** (lower left), or **ex situ** (upper left) and migrate through **disc migration** (moving down) or **high-eccentricity migration** (moving right) with subsequent tidal migration (moving down, Equation (1.1)). In this latter the scenario the **obliquity** might also be excited seen here as the angle between the orbital axis (blue vector) and stellar spin axis (red vector), which might also subsequently be damped through tides (see Section 2.4.2.1). Figure adapted from Dawson and Johnson (2018).

Disc migration therefore offers a means of transportation for planets formed at large orbital separations to the separations at which we observe them today. Direct imaging observations have indeed found protoplanetary discs with gaps opened by the newly formed planet (again, e.g., in HL Tauri; ALMA Partnership et al., 2015) as predicted in type II migration.

1.2.2.2 High-eccentricity migration

While disc migration can transport planets from wide orbits to the inner regions of the protoplanetary disc rapidly, it is still considered a dynamically quiet process. High-eccentricity migration, on the other hand, is a much more violent process. Furthermore, contrary to disc migration, where the timescale is set by the disc lifetime, the planets in high-eccentricity migration can arrive at short period orbits much later. This is also highly relevant when it comes to close-in planets being less susceptible to photoevaporation by avoiding the star's roughly 100 Myr active stage, for instance, in the context of the Neptunian desert, a dearth of short-period Neptune-sized planets reported by (Mazeh et al., 2016), and the (few) planets that do reside there (e.g., Persson et al., 2022).

High-eccentricity migration involves multibody interactions either through scattering mechanisms or secular interactions, which – simply put – happens in a two-step process. First, a perturber extracts orbital angular momentum from the planet by exciting the planet's eccentricity. The planet's eccentricity is then subsequently damped when the planet's orbital energy is dissipated through interactions with the central star through tides raised on the planet at periapsis passages. In this second step, the tidal dissipation phase, the angular momentum of the planet is conserved, leading to a final close-in semi-major axis, a_{final} , given by

$$a_{\text{final}} = a(1 - e^2), \quad (1.1)$$

with e being the eccentricity and a the initial semi-major axis of the planet.

Close encounters between a planet and a third body, planet or star, can lead to gravitational scattering (Rasio and Ford, 1996). In planet-planet scattering differences in angular velocity between planets with different semi-major axes known as *Keplerian shear* is converted into angular momentum, changing the eccentricity and semi-major axis of the planet and potentially ejecting the perturber (a potential way of forming rogue planets). This can happen in either tightly packed systems (Jurić and Tremaine, 2008), or through a stellar fly-by exciting the orbital eccentricities of planets in the system. The latter perhaps being a relevant mechanism for forming

hot Jupiters in star clusters (Shara et al., 2016). In addition to exciting the eccentricity, gravitational scattering can also lead to highly inclined orbits with respect to its initial orbit, which presumably was in the [protoplanetary disc](#) and presumably aligned with the stellar rotation axis. The obliquity might thus be excited in this process.

The eccentricity grows as a random walk in planet-planet scattering (see, e.g., Figure 3a in Dawson and Johnson, 2018) given that each encounter induces a random kick. As the excitation mechanism relies on close encounters, eccentricities are excited on a synodic timescale at planets' conjunction with the possibility for the orbit to reach periapsis values sufficient for tidal circularisation on a timescale of thousands of years. To reach the orbital separations we see for hot Jupiters of some 0.02 AU, Equation (1.1) requires an eccentricity of $e = 0.995$ for a planet starting at the [snow line](#), $a = 2$ AU. Whether it is even possible to reach such high eccentricities has been questioned through numerical simulations by, for instance, Petrovich et al. (2014), although a more recent result from Carrera et al. (2019) can produce eccentricities of $e > 0.99$ (meaning there is no limit for the maximum eccentricity), and thus potentially offering a solution.

Secular interactions refer to the slow exchange of angular momentum between widely separated planets (or stars). Where planet-planet scattering can sufficiently excite eccentricities on a timescale of thousands of year, secular interactions take place on time scales from anywhere between thousands to millions of years, depending on the masses and separations of the bodies involved.

For secular interactions to take place the orbits are required to be significantly eccentric in the first place, and typically inclined with respect to each other. Two-body orbital resonance periodically exchanges angular momentum between two planets, leading to a periodic change in the orbital elements (Petrovich, 2015). If the planets are already on highly eccentric, highly inclined orbits, or if three planets or more are involved, this process can occur chaotically in what is known as secular chaos (e.g., Wu and Lithwick, 2011), leading to large fluctuations in the orbital parameters including highly eccentric orbits.

Widely hypothesised to trigger [high-eccentricity migration](#) for hot Jupiters (e.g., Naoz et al., 2011), Kozai-Lidov cycles (Kozai, 1962; Lidov, 1962) are a type of periodic secular interaction, usually requiring an initial mutual inclination of $> 40^\circ$. The mutual inclination for a widely separated binary could be a natural consequence of this companion forming in a different plane than the plane defined by the star-planet(s) system. In these

Kozai-Lidov cycles, angular momentum exchange also trades off mutual inclination and eccentricity, in this way driving the planet's eccentricity to high values.

Interactions between a planet and other bodies, both of planetary and stellar nature, thus also offer a way of transporting, for instance, a planet like Jupiter from a wide orbit to one much closer to its host star. Furthermore, an explanation for the hot Jupiters observed on moderately eccentric orbits (e.g., Bonomo et al., 2017a) is naturally provided by [high-eccentricity migration](#).

1.2.2.3 Why not both?

Both [disc migration](#) and [high-eccentricity migration](#) offer viable explanations for how a planet might form [ex situ](#) beyond the [snow line](#) and then subsequently migrate inwards, thus, for instance, forming a hot Jupiter. However, either mechanism falls short when it comes to accounting for the observed hot Jupiter demographic as a whole. For instance, the aforementioned population of moderately eccentric hot Jupiters can not be explained by [disc migration](#) or [in situ](#) formation, and on the other hand [high-eccentricity migration](#) has a hard time accounting for the observed hot Jupiters around T Tauri stars, which still have their [protoplanetary disc](#).

Therefore, instead of invoking just one origin channel for the formation of a hot Jupiter, the mechanisms could perhaps be working in parallel for different systems. Similarly, Fabrycky and Winn (2009) argued that having two distinct modes of planet migration could be used to explain the two components of the obliquity distribution for hot Jupiters, one accounting for the well-aligned systems and another component for the misaligned systems. In a population study Nelson et al. (2017) proposed that about 85% of hot Jupiters originated from [high-eccentricity migration](#), and the remaining 15% had migrated through [disc migration](#). Our task is thus perhaps not to find the sole origin channel, but rather to see if we can identify in which systems a given channel would be the dominant process.

2

Observations and techniques

Most of my research is driven by data acquired through both ground-based as well as space-based facilities. Therefore, this chapter is devoted to exploring some pioneering discoveries in the field of exoplanets, as well as some of the techniques used. While there is a whole suite of different ways to detect and characterise exoplanets, the vast majority of discoveries have been made through transit photometry and *radial velocity* (*RV*) measurements through spectroscopy. Section 2.1 and Section 2.2 are therefore devoted to spectroscopy and photometry, respectively.

We will also go into some detail with two very specific concepts/techniques that have played an important role in the different studies I have been involved in. These are *asteroseismology* (Section 2.3) and the *obliquity* (Section 2.4), and more specifically how to measure the *obliquity* using the *Rossiter-McLaughlin effect (RM EFFECT)* (Section 2.4.1). Finally, in Section 2.4.2 we will look at some of the trends that have emerged, and how we might test different migration scenarios and physical interactions between the planet and star.

2.1 Spectroscopy

In stellar spectroscopy we are looking at the interaction between the light emitted by a star and its atmosphere, particularly we are studying the absence (or emission) of light at very specific wavelengths, corresponding to very specific transitions in different atomic species. By dispersing the light into its constituent wavelengths, we might resolve the spectral lines and obtain a one dimensional stellar spectrum. An example of how that might look for an échelle spectrograph depicted onto a *charge-coupled device (CCD)* detector is shown in Figure 2.1. This allows us to study the

strength and profile of the absorption and emission lines as well as their wavelength shift.

The strength of the lines is governed by physical properties of the stellar atmosphere, such as temperature, density, and pressure, as well as the elemental composition. We might thus determine the effective temperature, T_{eff} , the surface gravity, $\log g$, and the metallicity, [Fe/H], by studying the spectral lines, which typically means comparing them to theoretically calculated stellar spectra. Furthermore, the line profiles can tell us about hydrodynamical conditions in the atmosphere. The lines are broadened by different mechanisms, for instance, natural and pressure broadening, but they will also be broadened by the rise and fall by material in the convective envelope, known as granulation.

The effects the motion of these convective cells have on the line profile can be divided into two categories: *micro-turbulence* and *macro-turbulence*. In the latter case the cells are larger than the unit optical depth, whereas in the former the cells are smaller than the mean free path of a photon (Gray, 2005). Finally, another very important and often very prominent contribution to line broadening is rotation. In addition to the atmospheric parameters, we might therefore also learn about the velocity fields represented by the *micro-turbulence*, ξ , and the *macro-turbulence*, ζ , as well as the projected rotation speed of the star, $v \sin i_*$.

While we know that the atomic species we find in stellar atmospheres leave their imprints at very specific wavelengths corresponding to the excitation levels of the atoms, we see the atomic fingerprints shifted in wavelength. This is due to the **RV** of the star, which is a combination of Earth's motion around the Sun and the star's projected velocity relative to the Sun. On top of these often quite big *Doppler shifts*, we might also be so lucky to detect tiny, periodic shifts induced by a planet orbiting the star.

It was exactly through high-precision **RV** surveys the first suggestions for substellar mass companions around main-sequence stars came. Among the earliest planet hosting candidates was γ Cephei A in which Campbell et al. (1988) detected small **RV** bumps superposed on the large amplitude signal of the binary orbit. Naturally, these early pioneers were cautious in announcing these findings as *bona fide* planets. Hatzes et al. (2003) later confirmed that the variations seen for γ Cephei A were indeed due to a planet mass companion. In the meantime, as mentioned, the first exoplanet had been found around another solar-like star also using high-precision **RVS** (Mayor and Queloz, 1995) with many more following. Spectroscopy thus provides an avenue for not only the determination of stellar properties, but also to detect and characterise planetary systems.

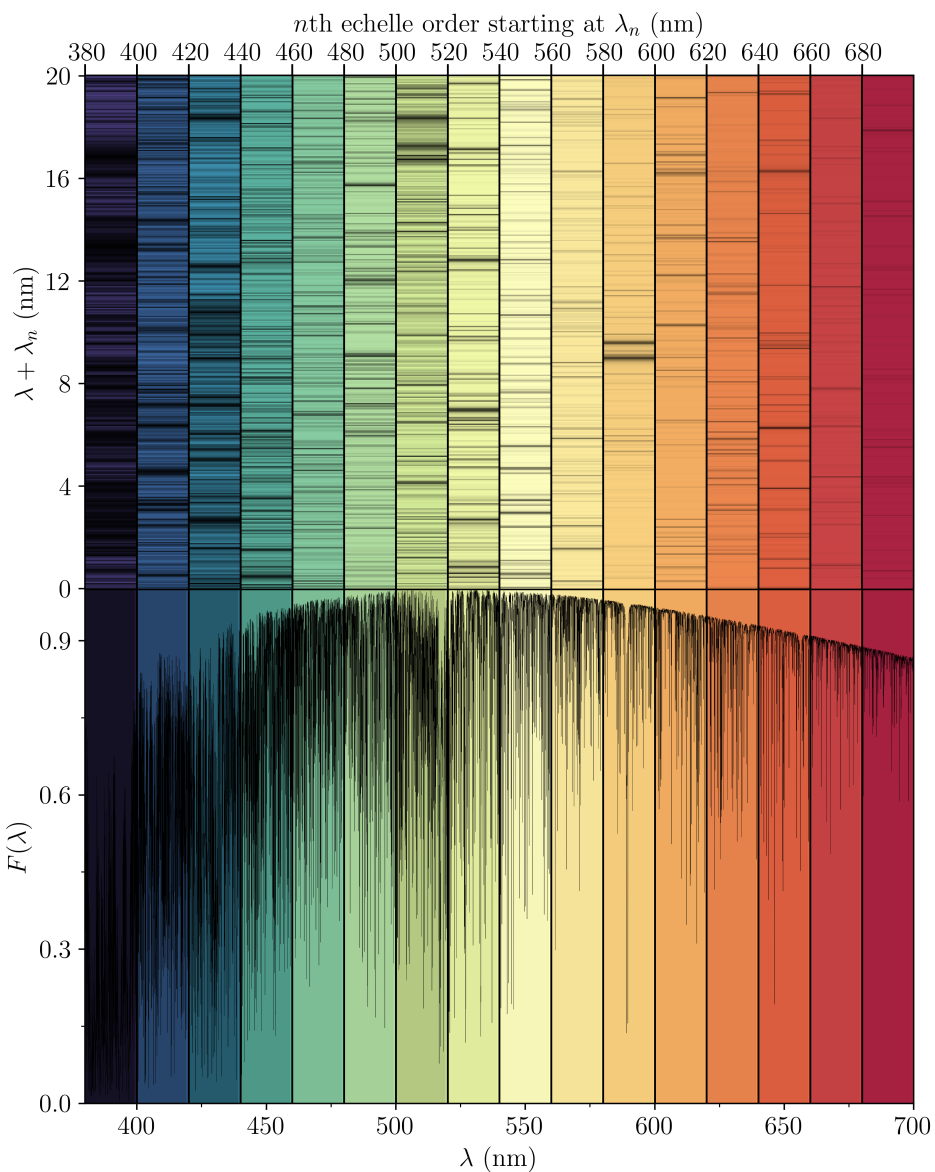


Figure 2.1 | Schematic of a stellar spectrum on a CCD. *Top:* A stellar spectrum has been divided into chunks of 20 nm similar to how spectral lines appear on a detector after passing through an échelle spectrograph. *Bottom:* The lines have been collapsed into a one dimensional stellar spectrum. Here for a model spectrum from Coelho (2014) assuming $T_{\text{eff}} = 4750$ K, $\log g = 4.5$, and $[\text{Fe}/\text{H}] = 0.0$.

The total number of planets discovered through [RV](#) surveys as of 2022 is 1023, with the growth shown in Figure 2.2. Clearly, we have been able to detect smaller and smaller [RV](#) variations – the K -amplitude – and thus lighter planets, or planets at large orbital separations, and we are also finding them in fainter systems, which in large is due to the technological advances in telescopes and instrumentation. Some of these facilities will be discussed below in Section 2.1.1. However, we have also reached a limit where improving the precision and stability might not help us detect even smaller variations as we are limited by stellar noise, or rather stellar signals. A better understanding of stellar physics and how to incorporate it into our models might help us overcome this limit.

What is also evident from Figure 2.2 is that a lot of planets discovered through [RVS](#) have been detected around cooler stars ($T_{\text{eff}} < 6200$ K). This is, at least partly, a selection effect as the precision in [RV](#) greatly depends on the number of spectral lines, and as we go to hotter and hotter stars more and more of the elements are ionised, resulting in less spectral lines (Gray, 2005).

2.1.1 Ground-based spectroscopy

As the bulk of exoplanet discoveries are made through space-telescopes (see Section 2.2.1), a huge amount of telescope time has been and is still being invested into efforts of following up the exoplanet candidates discovered by these space-based facilities. This is to, first of all, validate the planetary nature of the signal, but also to characterise the system, namely in terms of the mass of the planet and orbital eccentricity, through [RV](#) measurements. A large part of the job in the hunt for exoplanets is therefore to apply for time at these facilities harbouring high-resolution spectrographs. As such my collaborators and I have applied for time at different facilities with various sizes of telescopes, and I have been heavily involved in efforts in the detection and characterisation of exoplanet systems as the [principal investigator \(PI\)](#) for some of these.

2.1.1.1 SONG

An excellent facility to validate and characterise exoplanets around some of the brightest ($V < 9$ mag) stars is the Hertzsprung Telescope of the [Stellar Observations Network Group \(SONG\)](#) (Grundahl et al., 2014), which is located at the Observatory del Teide, at the Izaña mountain, Tenerife. The idea behind [SONG](#) is to create a network of 1 m telescopes dedicated for

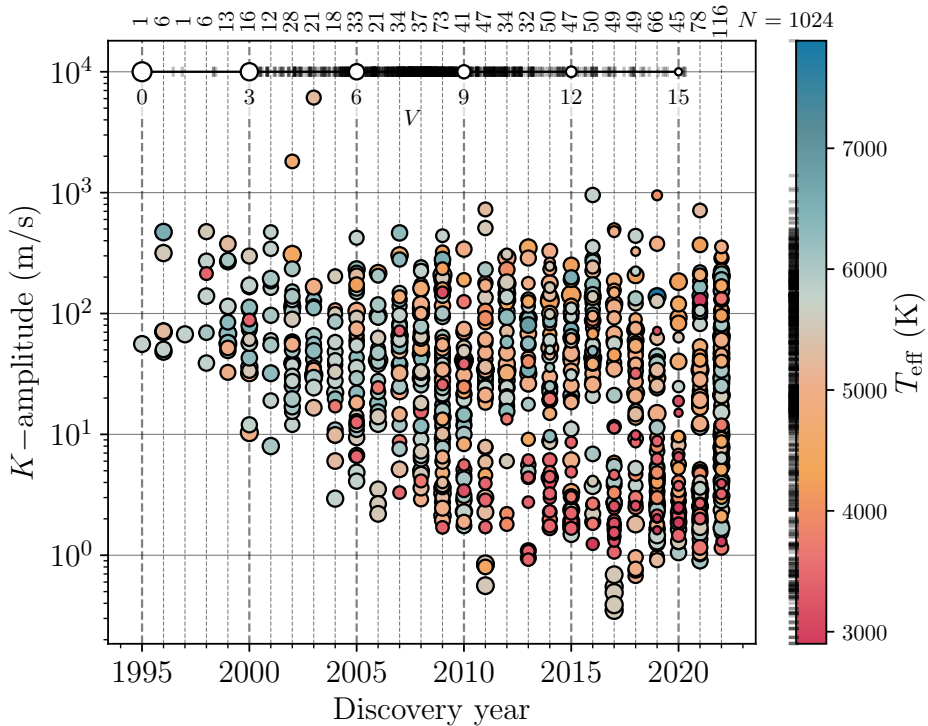


Figure 2.2 | Exoplanets detected through radial velocities. Shown here are the exoplanets detected through the years (up until 2022) using [RV](#) measurements. Their K -amplitudes is plotted as a function of discovery year with the colour coding given according to the effective temperature of the host star. A measurement at a given T_{eff} is shown as a black stripe on the colour bar. The sizes for the markers scale (with their brightnesses or) inversely with their V magnitudes as shown by the black dots. The number of planets discovered per year is given on top. Created using the NASA Exoplanet Archive through [astroquery](#) (Ginsburg et al., 2019).

observations of single targets for a very long period of time. The Tenerife node is a 1 m telescope equipped with a coudé échelle spectrograph with an iodine cell and has been a vital part of both asteroseismic (e.g., Stello et al., 2017; Arentoft et al., 2019) and exoplanetary (e.g., Talens et al., 2018; Hjorth et al., 2019a) studies. The [SONG](#) telescope has been an essential part of some of the exoplanet discovery papers I have contributed to, namely TOI-197 (Huber et al., 2019), TOI-1456 (Dalba et al., 2020), and TOI-1431 (Addison et al., 2021).

2.1.1.2 FIES

Over the years the *Fiber-fed Echelle Spectrograph* (**FIES**) (Frandsen and Lindberg, 1999; Telting et al., 2014) at the 2.56 m **NOT** (Djupvik and Andersen, 2010), which is located at the Roque de los Muchachos Observatory, La Palma, has delivered many exoplanet discoveries (e.g., Buchhave et al., 2011; Gandolfi et al., 2013). Furthermore, it has been an important instrument for the initial vetting of *Transiting Exoplanet Survey Satellite* (**TESS**) (Ricker et al., 2015) exoplanet candidates, so-called *reconnaissance spectroscopy* (**RECON SPECTROSCOPY**), where it has delivered stellar parameters for hundreds of candidates and helped rule out false positives (Bieryla et al., 2021).

The **NOT** not only served as my place of employment for 1.5 years, but has also had a significant scientific impact as we had several successful observing proposals. Using the **FIES** spectrograph we confirmed and characterised three giant planets discovered by **TESS** (TOI-1820, TOI-2025, and TOI-2158, Knudstrup et al., 2022, Chapter 6), and we have used the time for **RECON SPECTROSCOPY** as well (e.g., Serrano et al., 2022).

2.1.1.3 HARPS-N

Also located on the Roque de los Muchachos Observatory, the northern counter-part to the *High-Accuracy Radial Velocity Planetary Searcher* (**HARPS**) (Mayor et al., 2003) spectrograph, the **HARPS-N** spectrograph (Cosentino et al., 2012) offers **RV** stability and great precision. Paired with the larger collecting area as the spectrograph is mounted on the 3.6 m Telescopio Nazionale Galileo (TNG), **HARPS-N** is well-suited for detecting smaller planets or lower amplitude signals (e.g., Georgieva et al., 2021).

Another successful observing proposal for **HARPS-N** lead us to the discovery and characterisation of the TOI-1288 system (Knudstrup et al., 2023a, Chapter 7), which harbours a hot super-Neptune right in the aforementioned Neptunian desert. We furthermore found evidence for a Saturn-mass planet on a long-period orbit in the system.

2.2 Photometry

Photometric observations allow us to study the intensity variations of stars. In the beginning this was done using photographic plates, and the use of these persisted in astronomy for quite some time. Eventually, they were superseded by **CCDS**, which arguably simplified matters in terms of acquisition as well as data extraction and processing.

In exoplanet research as well as for studying eclipsing binaries, we would normally aim to acquire long, continuous time series, with many short exposures to resolve the shape of the transit or eclipse. These would typically be carried out around an epoch of interest, for instance, the mid-transit time. The principle for an eclipsing binary is outlined in Figure 2.3. If the occulting body shown in the sketch to the right did not emit any (appreciable amount of) light, this would be equivalent to a planet transiting a star.

Although, it is in principle straightforward to observe a transit of an exoplanet, there are several challenges when it comes to detecting exoplanets. First off, we do not know the mid-transit time, so we do not know when it would be a good time to carry out the observations. Secondly, the signal we are looking for is often quite small as the depth of the transit is given by the planet-to-star radius ratio, $\delta = (R_p/R_\star)^2$, which for a Jupiter-sized planet around a Sun-like star comes out to 1%.

Borucki and Summers (1984) derived the transit probability for a randomly oriented planet on a circular orbit based on the solid angle on the sphere swept out by a planet's shadow, $p_{\text{transit}} = R_\star/a$. In Solar System units this corresponds to $p_{\text{transit}} \approx 0.005(R_\star/R_\odot)(a/\text{AU})^{-1}$ (Perryman, 2018), meaning that an Earth analogue would have a transit probability of 0.5%. Adding to the difficulty is that we have to factor in the occurrence rate when we want to calculate the number of planets, we should expect to observe. A recent estimate for the occurrence rate of a hot Jupiter ($a \sim 0.05 \text{ AU}$) around a G-type star is given by Beleznay and Kunimoto (2022) who finds it to be $0.98 \pm 0.36\%$. We would thus have to observe on the order of 1000 stars to find 1 hot Jupiter.

For ground-based telescopes there is of course the additional challenge of gaps in the time series, both from the rising Sun and poor weather. Considering these challenges, it was perhaps not too surprising that the first transiting exoplanet was found in a system where we had a bit of an edge, namely the time of inferior conjunction. The first transiting exoplanet was thus a planet detected through RVS. Charbonneau et al. (2000) and Henry et al. (2000) independently detected a transit of the planet HD 209458 b (Henry et al., 2000; Mazeh et al., 2000).

Despite the challenges of detecting exoplanet transits, ground-based surveys such as the Hungarian Automated Telescope Network (HATNet; Bakos et al., 2002), the Wide Angle Search for Planets (WASP; Pollacco et al., 2006), and the Kilodegree Extremely Little Telescope (KELT; Pepper et al., 2007) were able to bring the number of exoplanets discovered through transits into the hundreds. This is seen as the great increase in Figure 2.4

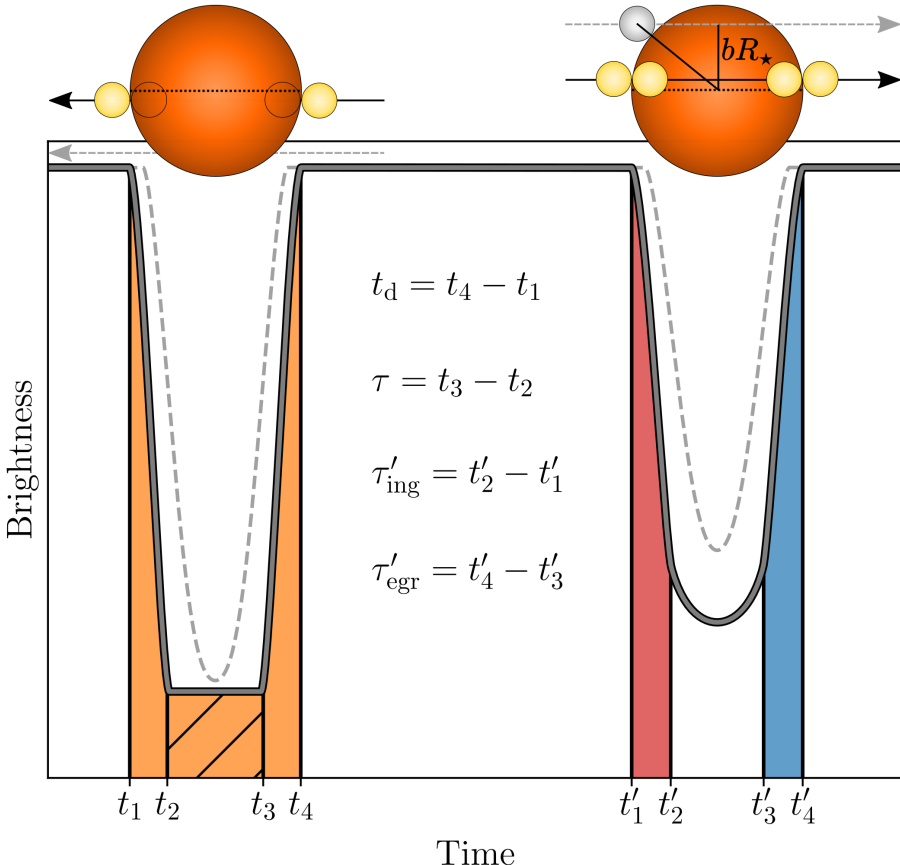


Figure 2.3 | Schematic of an eclipse. Schematic of an eclipsing binary for two different impact parameters. The primary eclipse is shown to the left and the secondary to the right. The times t_1 , t_2 , t_3 , and t_4 mark the first, second, third, and fourth contact for the primary eclipse (with primes for the secondary). The time of ingress is shown as the red band and egress in blue. The black arrow shows how the secondary star traverses (or passes behind) the primary in the low impact parameter case, modeled by the solid grey line. A case for a larger impact parameter is shown with the dashed grey line and the corresponding model is also shown with a dashed grey line.

from around 2006, which also detaches the curve for the total number of detected planets from the curve representing [RV](#) detected planets. It was, however, first with photometric surveys in space that the number of exoplanets detected through transits skyrocketed.

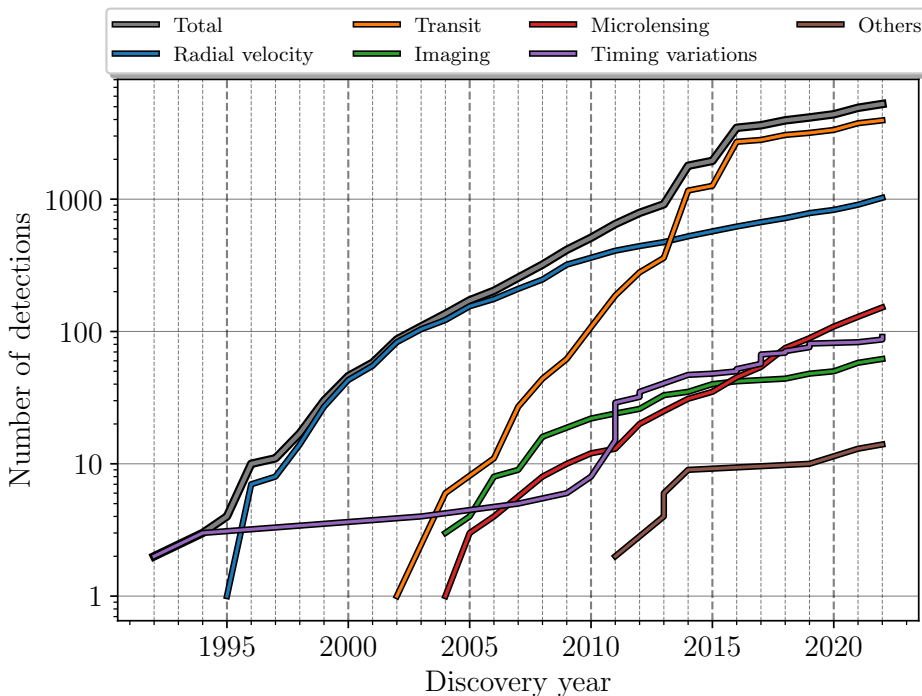


Figure 2.4 | Exoplanets detected over the years. Displayed here is the cumulative number of planets detected as a function of discovery year up until 2022. The different colours correspond to the different methods utilised for detection. Created using the NASA Exoplanet Archive through astroquery.

2.2.1 Space-based photometry

With each launch, space telescopes have helped unveil a new aspect of the mysteries of the heavens and astronomy would not be at its current state without space-based photometry. In part due to extraordinary individual discoveries owing to the quality of the data, but also simply due to the shear amount of data these space telescopes have delivered and are continuing to deliver. Three missions (distributed across two space telescopes) have had tremendous impact on the field of astronomy, but in particular when it comes to transiting planets.

2.2.1.1 *Kepler*

The *Kepler* space telescope (Borucki et al., 2010) was launched in March 2009 and started science operations in May 2009. *Kepler* was designed to

continuously monitor the same patch of the sky with the aim of exploring the structure and diversity of planetary systems. The success of the *Kepler* mission cannot be overstated, particularly in the fields of **asteroseismology** and exoplanetary science. Because of the *Kepler* mission we now know that there is at least one planet for every star in the Galaxy and rocky, Earth-like planets are common (e.g., Dressing and Charbonneau, 2013; Swift et al., 2013). Figure 2.4 clearly shows the importance of *Kepler* in the number of detected transiting planets with massive spikes in 2014 and 2016 (corresponding to large releases of planets and planet candidates). After having observed some 170,000 stars continuously for around four years, two of the spacecraft's four reaction wheels malfunctioned, marking the end of the primary *Kepler* mission.

2.2.1.2 K2

Luckily, thanks to a brilliant piece of ingenuity this was not the end of the *Kepler* spacecraft, and the *Kepler* second light mission known as *K2* (Howell et al., 2014) became a reality. With only two reaction wheels the spacecraft could no longer continuously point towards the same patch of the sky, instead observing runs were divided into campaigns each with a baseline of ~ 80 days. These campaigns were confined to the ecliptic plane. Naturally, this opened up a larger chunk of the sky in the search for exoplanets, but it has also been an important mission for, for instance, open clusters as more of these could now benefit from these 80 days of uninterrupted observations (e.g., Stello et al., 2016).

After 19 campaigns the spacecraft ran out of fuel and the mission was terminated on November 15, 2018. The *Kepler* spacecraft served 9.6 years in space, delivered more than 2,600 confirmed planets (with many more planet candidates). With this vast amount of data there could still be hidden gems and so the exploration continues.

2.2.1.3 TESS

As the *K2* mission was coming to an end, a new exoplanet hunter was launched into space, the *TESS* mission (Ricker et al., 2015). *TESS* started science operations in August 2018 with the first confirmed planet quickly following in September 2018 (Gandolfi et al., 2018; Huang et al., 2018). *TESS* is an inherently different mission than *Kepler*. Where *Kepler* focused on a single field, *TESS* is an all-sky survey, where the Northern and Southern Hemispheres are divided into 13 sectors each, with one sector being observed for 27 days, the orbital period for *TESS*. As seen in Figure 2.5, *Kepler*

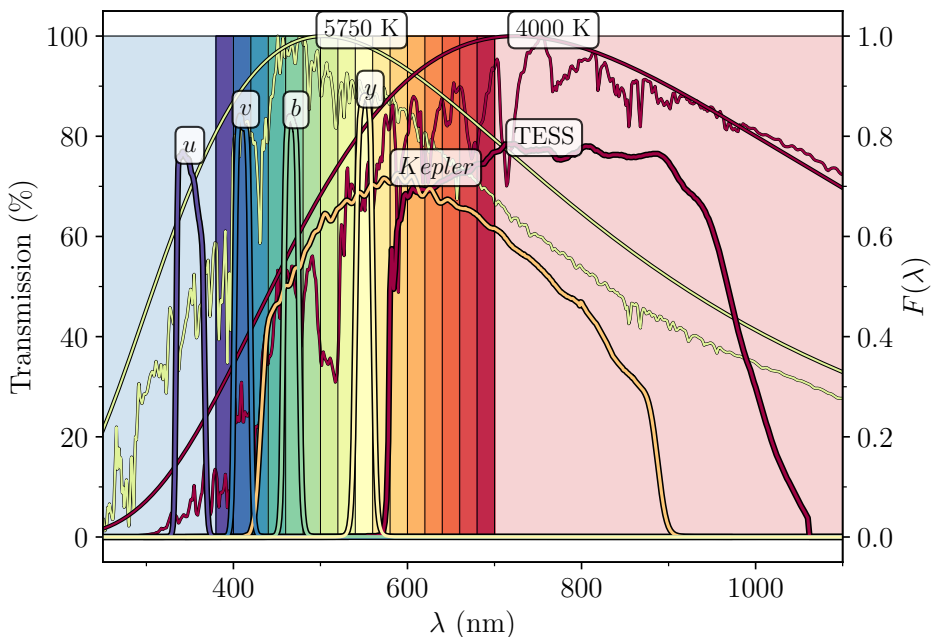


Figure 2.5 | Kepler and TESS transmission curves. The *Kepler* and *TESS* passbands compared to the Strömgren *uvby* filters. Theoretically calculated stellar spectra from Coelho (2014) are compared to black body spectra of the same temperature. The stellar model atmospheres are calculated assuming $T_{\text{eff}} = 5750 \text{ K}$ and $\log g = 4.0$ for the one to the left and $T_{\text{eff}} = 4000 \text{ K}$ and $\log g = 4.5$ for the one to the right, both have solar metallicities.

was tuned to hunt planets around solar-like (G-type) stars, whereas *TESS* is better suited for redder stars, like M-dwarfs.

The nominal mission for *TESS* was two years to cover the Southern and Northern Hemisphere, but the mission has been extended twice adding five more years of observations to the nominal mission¹. The Southern and Northern Hemisphere have been observed multiple times and now also a large part of the ecliptic has been covered, *TESS* has thus virtually combed the entire sky for exoplanets, and the total number of detected exoplanets has now surpassed 5,000.

¹: <https://heasarc.gsfc.nasa.gov/docs/tess/second-extended.html>

2.2.2 Multi-band photometry

As mentioned, in many cases we would turn to spectroscopy for more detailed information about the stellar atmosphere. From Figure 2.5 it is clear that we can certainly gain some information on the stellar properties through multi-band photometry. For instance, we could use the colour (e.g., $b - y$ as in Figure 1.1) as a proxy for the effective temperature. From Strömgren photometry one can also get an estimate for the surface gravity and the metallicity (through the Balmer-discontinuity index, $c_1 = (u - v) - (v - b)$, and the metallic-line index, $m_1 = (v - b) - (b - y)$, respectively).

Multi-band photometry is also used to vet for false-positives among the exoplanet candidates. Transit observations in different filters allow us to check if the transit depth is chromatic, which is indicative of an eclipsing binary (Collins et al., 2018). Therefore, a network of ground-based telescopes are primed to follow-up on [TESS](#) planet candidates to check for chromaticity as well as refining the ephemeris and to check if the transit is actually *on* the supposed target (due to the large pixel scale of [TESS](#), Collins, 2019).

2.2.3 The interplay between spectroscopy and photometry

While [Kepler](#) and [TESS](#) are brilliant instruments for exoplanet detection, they often only tell half the story. These photometric space-based observations need to be accompanied by ground-based spectroscopic observations, not only to validate the planetary nature of the signal, but also it is the interplay between photometric and spectroscopic observations that provides us with a complete description of the planet. Complimentary observations allow us to determine both the radius and the mass and thus the bulk density of the planet.

This naturally also applies to binary stars. Furthermore, when these supplementary measurements are applied specifically to a [*detached eclipsing binary \(DEB\)*](#) system, they allow for accurate, precise, and nearly model independent determinations of stellar masses and radii (e.g, Andersen, 1991). Generally precise and accurate stellar parameters are difficult to obtain for single, isolated stars, however, as we shall see in Section 2.3 [*asteroseismology*](#) can help.

Studies of [*DEBs*](#) can reach an accuracy of 1% in the stellar masses and radii, which provides an excellent way of testing theoretical models of stellar evolution (e.g., Southworth et al., 2005). If the [*DEB*](#) resides in an open cluster this allows for the determination of the age and metallicity for an

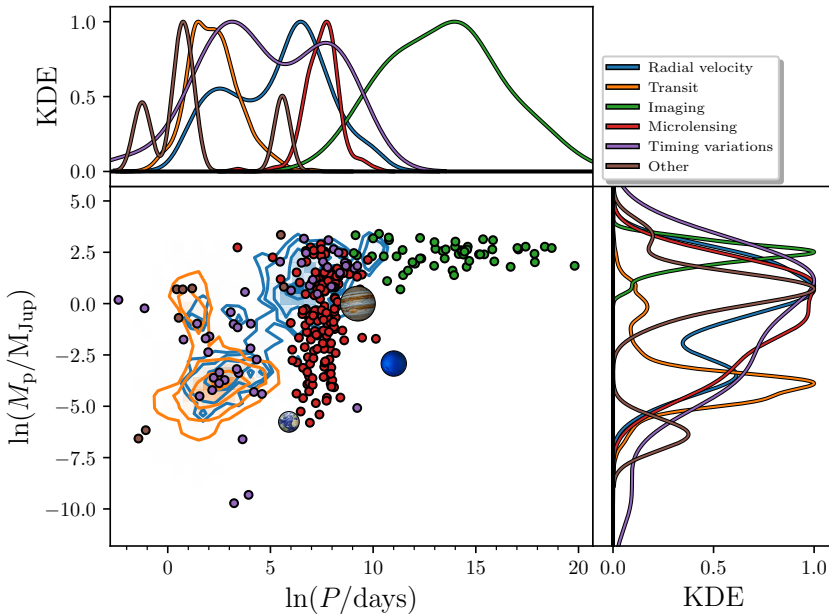


Figure 2.6 | Period-mass diagram. Shown here are the planets we have discovered through different techniques (the colour-coding is the same as in Figure 2.4) with their masses plotted against their orbital period. The detections through transits and RVS are shown as contour plots. The positions of Earth, Neptune, and Jupiter are also shown. The adjacent axes show the (peak-normed) KDE for each distribution. It is worth noting that in many cases the mass and period given here are from estimated values. Created using the NASA Exoplanet Archive through astroquery.

ensemble of stars, as they have all been formed from the same molecular cloud at the same time (e.g., Brogaard et al., 2012).

Furthermore, the different techniques also supplement each other by avoiding certain detection biases. This is clearly seen in Figure 2.6, where the masses and periods of the planets we have discovered through different methods are shown with their respective *kernel density estimation (KDE)*. Direct imaging is, for instance, probing planets on wide orbits, an area in the parameter space not as easily accessed through transit observations.

2.3 Asterosesimology

It is not only in the field of exoplanets that space-based photometry has had an astronomical impact, *asteroseismology* has also greatly benefitted

from these precise, uninterrupted photometric time series, from especially *Kepler* and *K2*.

Just like earthquakes here on Earth help us unveil the internal structure of the planet, we can study the interior of the Sun by looking at how waves propagate through it in *helioseismology* (Christensen-Dalsgaard and Gough, 1976). In the field of *asteroseismology* we probe stellar structures by observing and analysing stellar oscillations. When we are dealing with waves propagating through stars, we are mainly concerned with two types of waves: pressure modes and gravity modes known as *p-modes* and *g-modes*, respectively. The former are acoustic waves, i.e., sound waves, with pressure as the primary restoring force. For the *g-modes* buoyancy is the restoring force. In solar-like stars *g-modes* are to some degree trapped beneath the convective envelope, making them difficult to observe (Aerts et al., 2010). They are, however, more easily detected in classical pulsators such as δ Scuti stars. Here we will focus on solar-like oscillations, and we are thus mainly concerned with *p-modes*.

In the Sun the primary oscillations are caused by turbulent convective motion close to the surface. We therefore expect to see these oscillations in all stars with convective envelopes. Before any firm detection of solar-like oscillations in stars other than the Sun had been detected, Kjeldsen and Bedding (1995) suggested that the velocity amplitude should roughly scale as L_*/M_* , with L_* being the luminosity of the star. Shortly after solar-like oscillations were detected in the star η Boötis (Kjeldsen et al., 1995) and many more has followed since then, especially with the advent of the *Kepler* mission, and we now know of thousands of solar-like oscillators.

From an analysis of the overall properties of the oscillations, we can extract the global asteroseismic parameters; the *frequency of maximum power*, ν_{\max} , and the *large frequency separation*, $\Delta\nu$, shown in Figure 2.7. ν_{\max} has been suggested to scale with the *acoustic cut-off frequency* (Brown et al., 1991), which dictates the behaviour of waves near the surface, and ν_{\max} should therefore be related to the surface gravity of the star. This has also been seen empirically (e.g., Stello et al., 2009), although the theoretical foundation is still lacking. $\Delta\nu$ measures the average spacing in frequency between consecutive modes of same angular degree and scales with the inverse of the sound crossing time through the star, meaning that $\Delta\nu$ directly gives a measure for the mean stellar density.

Together with the effective temperature, these quantities can therefore be used to estimate the mass and the radius of a star via the seismic scaling relations (derived in Kjeldsen and Bedding, 1995)

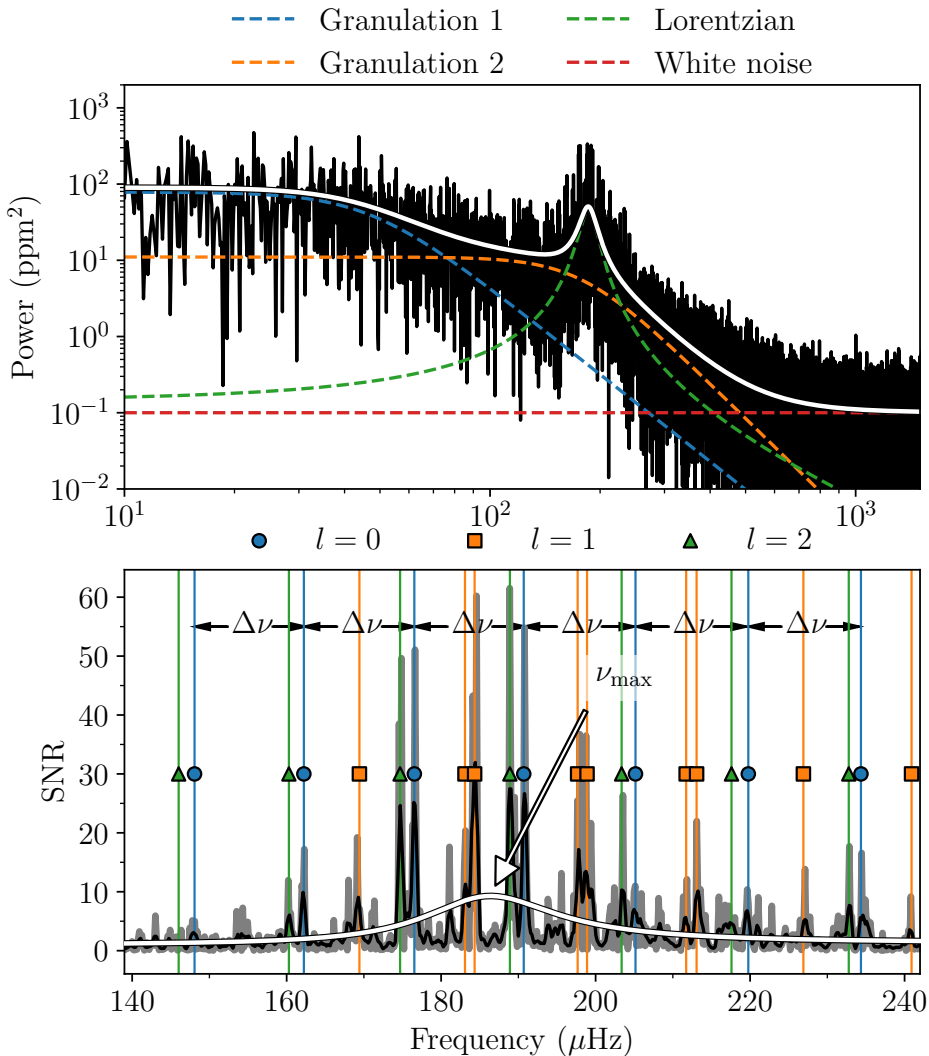


Figure 2.7 | Power spectrum. *Top:* The power spectrum of γ Cep A from TESS data (Chapter 5). Shown are the two granulation components, the white noise floor, and the Lorentzian used to capture the envelope of the oscillations as well as the sum of all these contributions (white curve). *Bottom:* Close-up around ν_{\max} of the background corrected power spectrum (black is a smoothed version of the grey power spectrum). The location of ν_{\max} has been marked, and $\Delta\nu$ is shown as the arrows between consecutive radial modes. Individual modes of different angular degree are shown with radial ($l = 0$) in blue, dipole ($l = 1$) in orange, and quadropole ($l = 2$) in green.

$$\frac{M_\star}{M_\odot} = \left(\frac{\nu_{\max}}{\nu_{\max,\odot}} \right)^3 \left(\frac{\Delta\nu}{\Delta\nu_\odot} \right)^{-4} \left(\frac{T_{\text{eff}}}{T_{\text{eff},\odot}} \right)^{3/2} \text{ and} \quad (2.1)$$

$$\frac{R_\star}{R_\odot} = \left(\frac{\nu_{\max}}{\nu_{\max,\odot}} \right) \left(\frac{\Delta\nu}{\Delta\nu_\odot} \right)^{-2} \left(\frac{T_{\text{eff}}}{T_{\text{eff},\odot}} \right)^{1/2},$$

where the subscript \odot denotes corresponding values for the Sun. We may therefore write

$$\frac{\rho_\star}{\rho_\odot} = \left(\frac{\Delta\nu}{\Delta\nu_\odot} \right)^2 \text{ and} \quad (2.2)$$

$$\frac{g_\star}{g_\odot} = \left(\frac{\nu_{\max}}{\nu_{\max,\odot}} \right) \left(\frac{T_{\text{eff}}}{T_{\text{eff},\odot}} \right)^{1/2},$$

with ρ_\star and g_\star denoting the stellar density and surface gravity, respectively. [Astroseismology](#) thus offer a way to derive key stellar parameters from the global seismic parameters for *single* stars.

2.3.1 Asteroseismology and stellar evolution

As is evident from Equation (2.1), the oscillation patterns are very sensitive to the physical properties of the star. Referring back to the discussion on stellar evolution in Section 1.1, [astroseismology](#) is therefore an excellent way to assess the evolutionary phase of the star. In fact, correctly assessing the evolutionary phase using [astroseismology](#) is exactly how Chontos et al. (2019) were able to promote the first exoplanet candidate discovered by [Kepler](#), KOI 4.01, from a false-positive to a real planet. Furthermore, observations of [g-modes](#) can be used in red giant stars to distinguish between core helium-burning and shell hydrogen-burning (Bedding et al., 2011).

For data of sufficient quality we might extract individual frequencies, instead of just the global seismic parameters. Individual frequencies allow for precise determination of key parameters with uncertainties on the order of 2% in radius, 4% in mass, and 10% in age for [MS](#) stars (Lund et al., 2017; Silva Aguirre et al., 2017).

2.3.2 Exoseismology

Obviously, precise stellar masses and radii are instrumental when determining the physical properties of exoplanets, since the planetary parameters

are derived from the stellar, and, of course, the age of the star dictates the age of the planet. However, [asteroseismology](#) can also contribute in the context of architectures of planetary systems.

The mean stellar density can be estimated from a transiting planet, assuming a circular orbit, as (Seager and Mallén-Ornelas, 2003)

$$\rho_{\star,\text{transit}} = \frac{3\pi}{GP^2} \left(\frac{a}{R_\star} \right)^3, \quad (2.3)$$

where G is the gravitational constant and P is the orbital period. As [asteroseismology](#) can provide an independent measure for the stellar density through Equation (2.2), we can express the ratio of the two density estimates as a function of the orbital eccentricity and argument of periastron, ω , as given in Dawson and Johnson (2012)

$$\frac{\rho_{\star,\text{astero.}}}{\rho_{\star,\text{transit}}} = \frac{(1 - e^2)^{3/2}}{(1 + e \sin \omega)^3}. \quad (2.4)$$

We can thus constrain the orbital eccentricity using [asteroseismology](#) as was done in, for instance, Van Eylen et al. (2014), but also what we did in Lund et al. (2019, Chapter 4) for the multiplanet system K2-93 (Vanderburg et al., 2016a).

Furthermore, as mentioned, [helioseismology](#) was used to determine the Solar System obliquity ($\psi = 7.155 \pm 0.002^\circ$; Beck and Giles, 2005), but [asteroseismology](#) might also be used to determine the [obliquity](#) of exoplanet systems. By looking at the rotational splitting of oscillation modes for HAT-P-7 (using data from [Kepler](#)), Lund et al. (2014b) were able to constrain the stellar inclination, which combined with (earlier) measurements of the projected [obliquity](#) and the orbital inclination, allowed them to confine the [obliquity](#) to be in the interval $83^\circ < \psi < 111^\circ$.

2.4 Obliquity

Before we discuss how we might measure the [obliquity](#), we should make sure to explicitly define the orientation and the terminology. While the [obliquity](#) can also refer to the inclination between the orbital axis of a planet and its rotation axis (for instance, the Earth's obliquity is 23.5°), the [obliquity](#) in this thesis always refer to the inclination between the stellar rotation axis and the orbital axis of a planet. The [obliquity](#) is also known as the spin-orbit angle. The orientation follows that of Albrecht et al. (2022) and is shown in Figure 2.8.

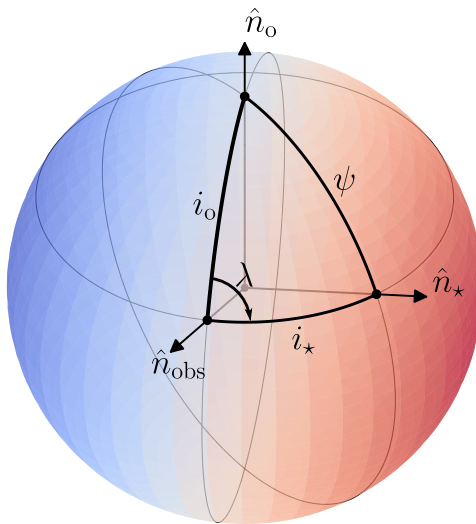


Figure 2.8 | The orientation of the system. The line-of-sight, stellar spin, and orbital angular momentum vectors are denoted as \hat{n}_{obs} , \hat{n}_* , and \hat{n}_o , respectively. i_* is the stellar inclination, i_o the orbital inclination, ψ the **obliquity**, and λ the projected **obliquity** onto the line-of-sight.

There are different ways of measuring the **obliquity**, including **asteroseismology** and tracing the movement of star spots on the stellar surface as they are obscured by planets, but most measurements of the projected **obliquity**, λ , comes from using the **RM EFFECT** (Albrecht et al., 2022). From Figure 2.8, we can see that the **obliquity** can be found from the spherical law of cosine as

$$\cos \psi = \cos_* \cos i_o + \sin_* \sin i_o \cos \lambda, \quad (2.5)$$

when the orbital and stellar inclinations are known. The former of the two is typically known quite well for these transiting systems where we would try to measure the **RM EFFECT**.

Not only is the **RM EFFECT** the method responsible for producing most of the **obliquity** measurements, it is also the method I have utilised. Therefore, we will be discussing this effect in the following.

2.4.1 The Rossiter-McLaughlin effect

Given that we know the stellar absorption lines are shaped by the stellar rotation (Section 2.1), what would we expect the absorption lines to look like if part of the stellar disc was obscured? A similar thought seemingly

grazed Holt (1893), who noted that by observing a star during an eclipse, one should be able to measure the rotation rate of the star due to the distortion of the spectral lines. This effect was later on detected (independently) by Rossiter (1924) and McLaughlin (1924), which is why it is now known as the **RM EFFECT**.

As the star is rotating, part of the stellar disc is moving towards us, meaning that it appears blueshifted, while the other part of the stellar disc is moving away from us, thus appearing redshifted. When part of the approaching stellar disc is obscured, the disc-integrated spectrum will appear redshifted, and vice versa.

The geometry of the problem is shown in Figure 2.9, which follows the convention in Albrecht et al. (2022). Here we define a coordinate axis perpendicular to the star's projected rotation axis, \hat{n}_\star . For a uniformly rotating star with an equatorial rotation speed of v and inclination i_\star along the line-of-sight, the local velocity component along this axis would then be

$$v_p = xv \sin i_\star , \quad (2.6)$$

with x being the position in units of the stellar radii.

Clearly, the projected rotation speed is largest at the limbs, meaning that the extremes during transit occur at ingress (x_1) and egress (x_2)

$$v_{\text{ing}} = x_1 v \sin i_\star , \quad v_{\text{egr}} = x_2 v \sin i_\star . \quad (2.7)$$

For a transiting planet with impact parameter b and an orbital axis, \hat{n}_o , that is inclined with λ with respect to the stellar spin axis, we have

$$\begin{aligned} x_1 &= \sqrt{1 - b^2} \cos \lambda - b \sin \lambda , \text{ and} \\ x_2 &= \sqrt{1 - b^2} \cos \lambda + b \sin \lambda , \end{aligned} \quad (2.8)$$

so we can write

$$\begin{aligned} v_{\text{ing}} + v_{\text{egr}} &= 2v \sin i_\star \cos \lambda \times \sqrt{1 - b^2} , \\ v_{\text{ing}} - v_{\text{egr}} &= 2v \sin i_\star \sin \lambda \times b . \end{aligned} \quad (2.9)$$

The amplitude of the signal thus depends on $\cos \lambda$, while the asymmetry depends on $\sin \lambda$. For systems in which we want to measure the **RM EFFECT**, we have typically already determined b and $(R_p/R_\star)^2$ — which obviously also affects the amplitude — through photometric measurements. We might therefore use the **RM EFFECT** to measure λ and $v \sin i_\star$.

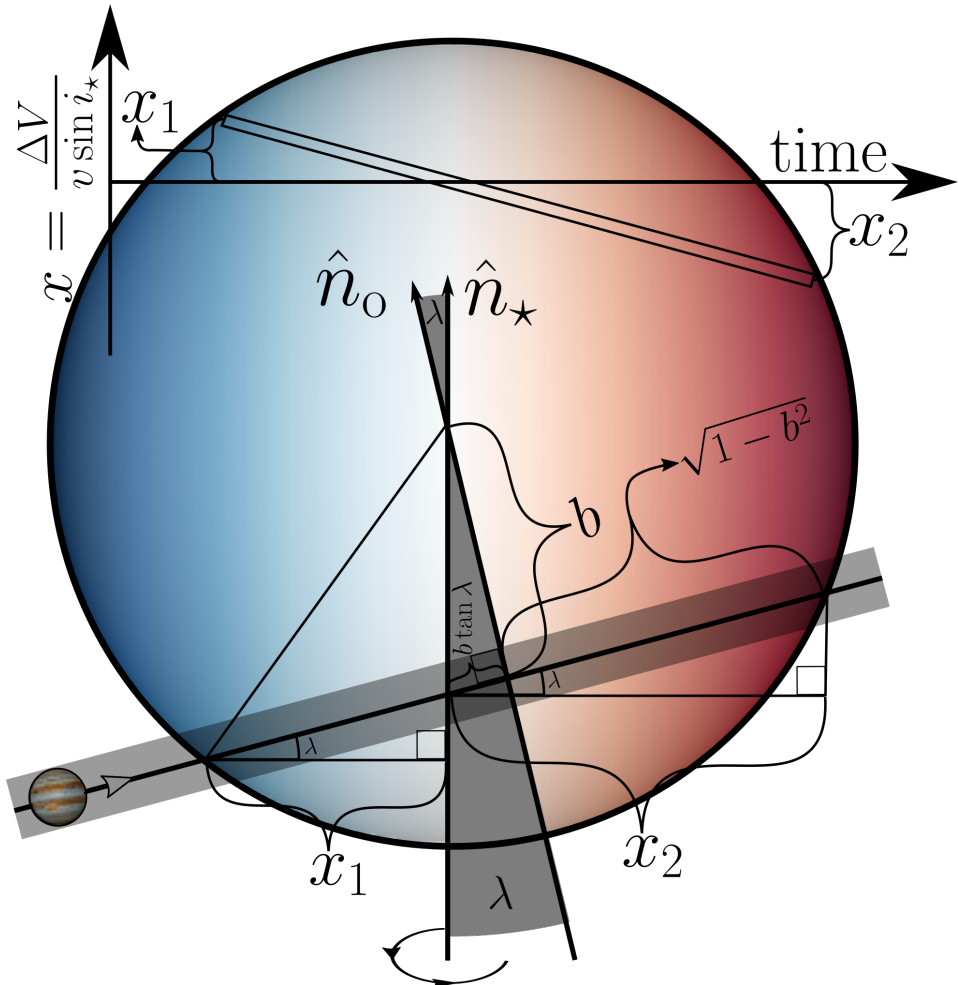


Figure 2.9 | Geometry of the RM effect. The figure illustrates a planet transiting a star with an impact parameter b and a projected obliquity λ . The graph on top shows the local rotational velocity (in units of $v \sin i_*$) obscured by the transiting planet as a function of time. Adapted from Albrecht et al. (2011) and Albrecht et al. (2022).

In the following I will briefly discuss three different ways of measuring λ from the **RM EFFECT**. We used all three methods in Knudstrup and Albrecht (2022) to measure λ for the HD 332231 system, and they are discussed in more detail in Chapter 8. All three of these methods are wrapped in `tracit`, which is a python package I have written to analyse the **RM EFFECT** as well as regular Keplerian orbits from `RVS` and transit light curves from photometry. The package is available on [GitHub](#) and the documentation can be found [here](#).

2.4.1.1 Planetary shadow

A way to represent an average of the spectral lines is through the *cross-correlation function (CCF)* (see, e.g., Horne, 1986), which is a measure of the similarity between two spectra. The *CCF* measures the lag, or displacement, between the two, which gives the *RV* of the star. Furthermore, it can be used to measure the rotational velocity of the star. Alternatively, one can make use of the *broadening function (BF)* formalism (Rucinski, 1992; Rucinski, 2002), which, for instance, avoids the effects of a non-zero baseline and distortions seen in the *CCF*.

Figure 2.10 shows a schematic of a rotating stellar disc just before ingress in the top right. The corresponding spectral line, represented by a *CCF*, is shown in the top left panel. The lower right shows the planet at ingress with the corresponding spectral line given in red compared to the out-of-transit spectral line. The lower panel to the left shows the difference between the out-of-transit and in-transit spectral line, which clearly shows the distortion of the spectral line.

The distortion of the spectral lines mentioned above is also what is known as the *planetary shadow*. A model planet shadow can be generated by creating a grid representing the stellar surface. A local velocity field is then ascribed to each pixel, taking into account the effects of *macro-turbulence* and *micro-turbulence* as well as, of course, the projected rotational speed of the star, $v \sin i_*$. This is the approach presented in Albrecht et al. (2007) and Albrecht et al. (2013b).

2.4.1.2 Subplanetary velocities

Another approach to measuring λ is to measure the subplanetary velocity, v_p , which is given in Equation (2.6). This is done by measuring the position of the distortion as seen in the bottom left of Figure 2.10, which corresponds to the local velocity field blocked by the planet as seen in the lower right of Figure 2.10. The projected obliquity can then be calculated by measuring the slope in the graph in Figure 2.9 (see, e.g., Cegla et al., 2016; Hoeijmakers et al., 2020).

2.4.1.3 Radial velocities

Finally, the *RM EFFECT* also manifests itself as an overall *RV* anomaly with the star appearing redshifted when the blueshifted part of the stellar disc and vice versa. A decent approximation for the amplitude of the *RM EFFECT* in *RV* is given by $0.7\sqrt{1 - b^2}(R_p/R_*)v \sin i_*$. The *RM EFFECT* in *RV* can be modelled by, for instance, using the code by Hirano et al. (2011).

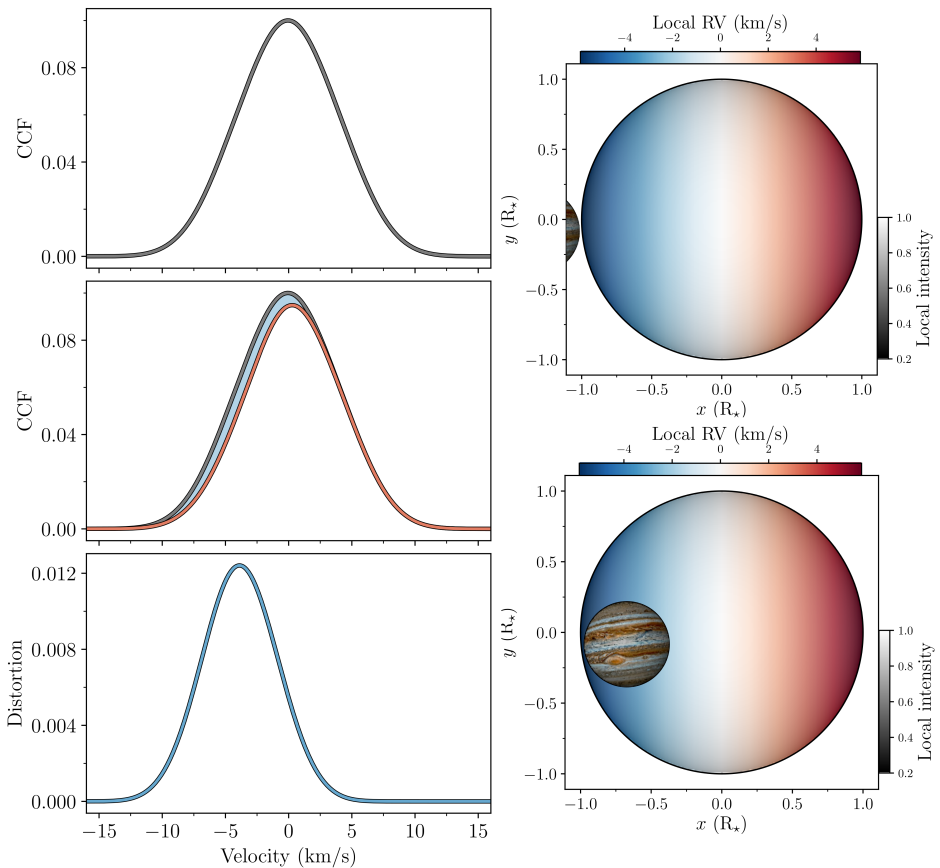


Figure 2.10 | Illustration of the RM effect. Shown on the right is a rotating, limb-darkened stellar disc in- (bottom) and out-of-transit (top) by a relatively large planet ($R_p/R_\star = 0.3$). The top panel on the left shows the stellar spectrum represented by the CCF out-of-transit. In the middle panel the out-of-transit spectral line (grey) is compared to the in-transit spectral line (red). In the bottom panel the difference between the two is shown, colour-coded to the local rotation velocity obscured by the planet.

2.4.2 Testing planet formation and migration

In Section 1.2.2 we saw how some of the different migration mechanisms could lead to different observables. In the following I will discuss some of the curious things we have learnt from studying [obliquities](#), and we will look at some of the trends we have unveiled, with a focus on investigations I have been involved in.

As for planet detection and characterisation using ground-based spectroscopy (Section 2.1.1), studying planetary system architectures in this

way involves investing a lot of telescope hours as well as investing time in applying for time. In addition to [FIES](#) (Section [2.1.1.2](#)) and [HARPS-N](#) (Section [2.1.1.3](#)), we have opted for some of the larger telescopes, namely [HARPS](#) at the ESO-3.6 m telescope at La Silla Observatory and the Echelle SPectrograph for Rocky Exoplanets and Stable Spectroscopic Observations ([ESPRESSO](#); Pepe et al., [2021](#)) spectrograph at the Very Large Telescope (VLT) at the Paranal Observatory.

2.4.2.1 Dynamically hot and cold systems

The two different, overall migration pathways discussed Section [1.2.2](#), [disc migration](#) and [high-eccentricity migration](#), should leave to distinct orbital configurations. Therefore, measuring the eccentricity and obliquity should be particularly informative and allow us to make inferences about the origin of a planet we do not think has formed [in situ](#). If we were to measure a large orbital eccentricity for this planet and a large obliquity for this star — what we could call a [dynamically hot](#) system — we would expect it to have formed through [high-eccentricity migration](#). Contrary, for a [dynamically cold](#) system (circular and well-aligned) we would expect it to have formed through [disc migration](#).

According to Rice et al. ([2022](#)), there seems to be a hint in the data of λ measurements that for cool stars, higher [obliquities](#) are found in eccentric systems. They interpret this as evidence for hot Jupiter formation through [high-eccentricity migration](#), without the need of invoking either [in situ](#) formation or [disc migration](#). Instead, they argue that the observed [dynamically cold](#) population is the result of tidal damping. As mentioned in Section [1.1.2.1](#), tides are important in shaping the architectures, but as is the case here, they also hamper the interpretation. This is shown as the steps to the right in Figure [1.3](#), where tides circularise the orbit and re-align the system.

The time it takes for tides to align the system depends on how effectively the planet can raise tides on the host star, which naturally scales with the separation between the two bodies. Winn et al. ([2010](#)) gives an estimate for this tidal alignment timescale in which the dependence scales as $(a/R_\star)^6$, meaning that we can greatly reduce the effects of tidal alignment, and thus easier interpret the results, by targeting planets at larger orbital separations.

In Knudstrup and Albrecht ([2022](#), Chapter 8) we measured the projected obliquity of the HD 332231 system; a warm ($a/R_\star \sim 24$) Saturn on a circular orbit. We found this system to be very well-aligned with a projected obliquity of $\lambda = -2 \pm 6^\circ$. [Disc migration](#) thus seems to be a likely scenario

for this system, which therefore follows this possible connection between eccentricity and [obliquity](#). However, more data are needed to fully establish the connection.

2.4.2.2 How strong is tidal alignment?

Although there is ample evidence supporting the notion of tides shaping the architectures of planetary systems, the role of tidal alignment is not fully understood yet. As the Solar System is probably thought of as a well-aligned system ($\psi = 7.155 \pm 0.002^\circ$ Beck and Giles, 2005), it would be interesting to look at the Sun's [obliquity](#) in the context of well-aligned exoplanet systems, particularly in systems for which λ has been measured precisely.

By looking at the most precise measurements ($\sigma_\lambda < 2^\circ$) for prograde, hot Jupiters around cool host stars (below the [Kraft break](#)) – exactly the systems where we would expect tides to be very effective, Albrecht et al. (2022) noted that these systems appear to be extremely well-aligned. The mean of the projected obliquity for these systems is 0.23° with a standard deviation of only 0.91° . First of all, this tells us that there is some dissipative process, like tides, at work in these systems, as we would expect a larger dispersion in the alignments from the formation of planets. Secondly, comparing the standard deviation to the mean formal measurement uncertainty (0.82°) for these systems shows us that for favourable systems (and with the right instrument), we can achieve the precision needed to study alignment to a higher degree than the Solar System alignment.

The impact of the impact parameter: The above begs the question; what constitutes a favourable system? Obviously, a large planet-to-star radius ratio amplifies the signal, so does an appreciable amount of rotation (although too much rotation can hamper the precision of the [RV](#) measurements). Furthermore, looking at Figure 2.9, for a transiting system with a low impact parameter we see the planet traverse the (perceived) stellar equator. Here it obscures a part moving at $|v \sin i_\star|$ at the stellar limbs. All else being equal, a low impact parameter should thus give rise to the largest amplitude signal.

However, for a low impact parameter there is a high degree of degeneracy because of symmetry. This greatly affects the degree of precision we can obtain for λ . Contrary for high impact parameter systems, even a small misalignment leads to a very asymmetric signal, therefore models of similar λ look very different. This means that even for small amplitude

signals, we might be able to determine λ quite precisely. This is nicely exemplified by comparing the results for the projected obliquity in HD 332231 ($\lambda = -2 \pm 6^\circ$ and $b = 0.14_{-0.12}^{+0.06}$, Chapter 8) and TOI-640 ($\lambda = 184 \pm 3^\circ$ and $b = 0.904_{-0.007}^{+0.005}$, Chapter 9), where at a first glance the **RV** curves for the **RM EFFECT** would suggest a much greater precision for the HD 332231 system.

Therefore, there is a strong case to be made for targeting high impact parameter systems for precision λ measurements. This is what we did for the WASP-50 system, which is a cool star ($T_{\text{eff}} = 5400 \pm 100$ K) harbouring a hot Jupiter ($a/R_\star = 7.51_{-0.15}^{+0.17}$) with a high impact parameter ($b = 0.687_{-0.016}^{+0.014}$; Gillon et al., 2011). Our preliminary result for this system suggests that it is very well-aligned $\lambda = 2 \pm 1.1^\circ$ as tidal interactions would predict (Albrecht et al. in prep.). In general, measuring λ for systems where we can achieve this level of precision will enable us to start deciphering the dependency of the tidal alignment on relevant parameters, for instance, as a function of a/R_\star .

2.4.2.3 Preponderance of Perpendicular Planets

While the projected **obliquity** does provide insight into the orbital configuration and evolution of the system, we need to measure the **obliquity** to get the full picture. For this we need to know the stellar inclination, which we can infer from the stellar rotation period. Recently in Albrecht et al. (2021), we sought out to determine the **obliquity** for a subset of the ~ 150 systems with projected **obliquity** measurements, and from these ~ 150 we were able to determine the stellar rotation period for a subset of 57 systems. Of these 57, 38 are well-aligned, but curiously the 18 misaligned systems are all confined in the interval $\psi = 80^\circ - 125^\circ$. These misaligned systems are not isotropically distributed, meaning that there seems to be a tendency for planets to be orbiting over the stellar poles. This trend seems to continue as we have just demonstrated for the TOI-640 system. As mentioned, we measured the **RM EFFECT**, and from these observations we found a projected **obliquity** of $184 \pm 3^\circ$. Paired with the stellar inclination, which we again derived from the rotation period, we found an **obliquity** of $\psi = 104 \pm 2^\circ$ (Knudstrup et al., 2023b, Chapter 9).

This pile up of perpendicular planets is currently not understood. The theories invoked to explain high **obliquities** in general produce distributions that are incompatible with the observed one. Recently, Vick et al. (2023) proposed that outer, binary companions can excite the star's obliquity during the dissipation of the **protoplanetary disc**. The subsequent

von Zeipel-Lidov-Kozai-driven high-eccentricity migration in their population synthesis yields a distribution with similarities to this observed preponderance of perpendicular planets.

2.4.2.4 Primordial (mis)alignment

So far there has been the implicit assumption that all systems start out in a fairly well-aligned configuration, but is that always the case? As outlined above, by invoking an initial tilt between the host star rotation axis and the orbital axis of the planet, Vick et al. (2023) might be able to explain the observed distribution of polar orbiting planets. Previous studies have also toyed with the idea of how interactions with binary companions might cause such a *primordial misalignment* (see, e.g., Bate et al., 2010; Batygin, 2012; Zanazzi and Lai, 2018).

This brings us to the K2-290 system, which was discovered and characterised by Hjorth et al. (2019b), who found it to be a triple-star system in which the primary star is orbited by an inner, hot sub-Neptune and an outer, warm Jupiter. In Hjorth et al. (2021), we subsequently measured the RM EFFECT of the warm Jupiter, finding a value of $\lambda_c = 153 \pm 8^\circ$, which spurred us on to also measure the RM EFFECT for the smaller planet. Here we found $\lambda_b = 173^{+45}_{-53}$, meaning that both planets are on retrograde orbits, and we had now defined the orientation of the protoplanetary disc. As above (Section 2.4.2.3), we measured the stellar rotation period to derive an obliquity of $\psi = 124 \pm 6^\circ$. We interpreted this as clear evidence for primordial misalignment of the planetary disk caused by the innermost companion star.

What about multiplanet systems in general? Of the 19 multiplanet systems where the projected obliquity has been measured, 15 are consistent with spin-orbit alignment. This was also what was seen in the (early) study by Albrecht et al. (2013b), who concluded that compact multiplanet systems are aligned. Recently, we measured the projected obliquity of the largest planet in the six planet system, TOI-1136, where we once again found a low projected obliquity of $\lambda = 5 \pm 5^\circ$ for this compact system (Dai et al., 2023).

The four misaligned multiplanet systems are *Kepler*-56 (Huber et al., 2013), *Kepler*-129 (Zhang et al., 2021), HD 3167 (Bourrier et al., 2021), and, of course, the K2-290 system. The difference between K2-290 and these other systems is that it is only in this system, where we can truly say we are seeing primordial misalignment, which again illustrates the uniqueness of the K2-290 system.

Part II



Research Results

3

Extremely precise age and metallicity of the open cluster NGC 2506 using detached eclipsing binaries

As we have now gone over the theoretical background of the thesis as well as the techniques we use, we will now turn to the scientific results. In the following chapters presenting research results, it has to be noted that each chapter is an independent and self-contained work. The notation might therefore deviate from the definitions given in the first part of the thesis. I have attempted to incorporate the glossary in each of the chapters to improve readability.

We will start our discussion on scientific results, where stars and planets (presumably) start their lives: in a cluster. Here I will show how to accurately and precisely determine the masses and radii of three pairs of **DEBs** with the aim of pinpointing the age and metallicity of an open cluster.

This work was started during my Master's thesis (Knudstrup, 2018), where a preliminary version of the results constituted the thesis. However, during my PhD I re-analysed all the data for the two **DEBs** presented in there (V4 in Section 3.5.3, with the exception of Section 3.5.3.1, and V2032 Section 3.5.1) and included the results for another **DEB** in the cluster (V5 in Section 3.5.2). I also added data from **Gaia** to derive an accurate distance to the cluster in Section 3.7. Furthermore, I included data from **TESS** for V2032 and V4 in Section 3.4.2 as well as for two of the **RGB** stars and many of the γ Doradus and δ Scuti stars in the cluster (Section 3.4.2.2). The altered results and conclusions are thus presented here in a significantly different version form from the initial results and conclusions in my Master's. This work has been published as

E. Knudstrup, F. Grundahl, K. Brogaard, D. Slumstrup, J. A. Orosz, E. L. Sandquist, J. Jessen-Hansen, M. N. Lund, T. Arentoft, R. Tronsgaard, D. Yong, S. Frandsen, and H. Bruntt (2020). “Extremely precise age and metallicity of the open cluster NGC 2506 using detached eclipsing binaries”. *Monthly Notices of the Royal Astronomical Society* 499.1, pp. 1312–1339

Alterations from this work are minor, mostly re-formatting of the journal version to match the layout of the thesis. Some of the long tables listing all the data that were included in the paper (Tables 3 and 6 in Knudstrup et al., 2020) as well tables and figures in the appendix (Tables A1, A2, A3, and A4 and Figures A2, A3, and A4 in Knudstrup et al., 2020) have been removed, but explicit reference is given to them when relevant.

Summary of the Chapter

Accurate stellar parameters of stars in open clusters can help constrain models of stellar structure and evolution. Here we wish to determine the age and metallicity content of the open cluster NGC 2506. To this end we investigated three [DEBS](#) (V2032, V4, and V5) for which we determined their masses and radii, as well as four red giant branch stars for which we determined their effective temperatures, surface gravities, and metallicities. Three of the stars in the [DEBS](#) have masses close to the cluster [turn-off](#) mass, allowing for extremely precise age determination. Comparing the values for the masses and radii of the binaries to BaSTI [isochrones](#) we estimated a cluster age of 2.01 ± 0.10 Gyr. This does depend on the models used in the comparison, where we have found that the inclusion of [convective core-overshooting](#) is necessary to properly model the cluster. From red giant branch stars we determined values for the effective temperatures, the surface gravities, and the metallicities. From these we find a cluster metallicity of -0.36 ± 0.10 dex. Using this value and the values for the effective temperatures we determine the reddening to be $E(b-y) = 0.057 \pm 0.004$ mag. Furthermore, we derived the distance to the cluster from [Gaia](#) parallaxes and found 3.101 ± 0.017 kpc, and we have performed a [RV](#) membership determination for stars in the field of the cluster. Finally, we report on the detection of oscillation signals in γ Dor and δ Scuti members in data from the [TESS](#) mission, including the possible detection of solar-like oscillations in two of the red giants.

3.1 Introduction

Age and metallicity determination of open clusters is of great interest since; i) it allows us to test stellar evolution theory by comparing the observed cluster sequence in a [CMD](#) to theoretically calculated [isochrones](#), ii) by combining the ages and chemical compositions with the kinematical properties of the clusters, they can be used in a much grander scheme to decipher the formation and evolution of the Galaxy in the field of Galactic Archaeology. In the latter context NGC 2506 is particularly interesting as it belongs to a group of metal-deficient clusters located just beyond the solar circle in the galactic anticenter (Anthony-Twarog et al., 2016).

In the context of stellar evolution and probing the interior of stars, NGC 2506 is an extremely promising cluster as it harbours a multitude of stellar oddballs. Arentoft et al. (2007) reported on the discovery of three oscillating blue stragglers (BSs) bringing the total in the cluster up to six, as well as the discovery of no less than 15 γ Doradus (γ Dor) stars. BSs are stars residing in a brighter and bluer region of the [MS turn-off](#) in a cluster (see Figure 3.1). The origin of BSs is still debated, but viable formation scenarios involve binary mass transfer and/or the merging of two stars, either by a direct collision or the merging of the components in a binary (e.g., Chatterjee et al., 2013; Simunovic et al., 2014; Brogaard et al., 2018). The blue stragglers are situated in the instability strip and we detect δ Scuti-like oscillations (see Section 3.4.2.2) in all of the blue stragglers. We will therefore use the terms blue stragglers and δ Scuti stars interchangeably. γ Dor stars are a type of variable stars, which as seen in Figure 3.1 can be found at or just above the [MS turn-off](#), depending on the cluster. γ Dor stars show photometric variations of up to 0.1 mag, which are caused by non-radial g-mode pulsations that allow for probing of the stellar interior. γ Dor stars can therefore be used to constrain [convective core-overshooting](#) and rotation in stellar models (Lovekin and Guzik, 2017). Precise age and metallicity determination of NGC 2506 is therefore valuable as it means constraining the parameters for these stars.

The proposed ages of NGC 2506 ranges from more than 3 Gyr in one of the earliest studies (McClure et al., 1981) to just below 2 Gyr in the more recent ones (Anthony-Twarog et al., 2016; Netopil et al., 2016). The literature seems to agree that NGC 2506 is a metal-deficient cluster with a reported upper limit of around -0.2 dex (Netopil et al., 2016), but there is no clear consensus on the metallicity.

It is possible to determine the masses and radii of the components in [DEBS](#) with great precision. Should one or both of the components turn out

to have a mass close to the cluster turn-off mass, it is possible to place a tight constraint on the age of the binary system and therefore the cluster (e.g., as for NGC 6791 in Grundahl et al., 2008; Brogaard et al., 2011, 2012).

We aim to constrain the age and metallicity of NGC 2506 by analysing three **DEBS**, meaning that we will measure the masses and radii of six stars in the cluster. To supplement our age and metallicity estimates, we will perform a spectroscopic analysis of four **RGB** stars. These will allow us to constrain the metallicity of the cluster and will allow us to firstly check if the metallicity is consistent with what is suggested by the **DEBS**, and secondly we might then choose models within a small range of this metallicity to further constrain the age.

This paper is structured as follows. In Section 3.2 we briefly introduce our target stars. In Section 3.3 and Section 3.4 we respectively present our spectroscopic and photometric data. Section 3.5 contains our orbital analysis of the **DEBS** and the stellar parameters deduced therefrom. In Section 3.6 we report on the derived cluster parameters. In Section 3.7 we present our derived distance to the cluster and membership determination using data from the **Gaia** mission (Gaia Collaboration et al., 2016). The discussion is given in Section 3.8 and finally we draw our conclusions in Section 3.9.

3.2 Targets

The names, WEBDA ID¹, and coordinates of the targets are listed in Table 3.1. Displayed in Figure 3.1 is the $b - y, y$ (data from Grundahl et al., 2000) **CMD** of NGC 2506 with the targets highlighted. Also shown in Figure 3.1 is the position of the confirmed γ Dor stars and BSs. V4 was discovered by Kim et al. (2001) and V5 by Arentoft et al. (2007). It was only very recently we detected an eclipse in V2032 and as such nothing about the system has been published yet.

From our analysis we have found that the binary V4 has an outer companion on a much wider orbit. The most massive component in V4 is close to the **turn-off** mass of the cluster, which is around $1.5 M_{\odot}$, making it one of the systems that allow for precise age determination. In this sense V2032 is an even more auspicious system as both components seem to be located on the subgiant branch – an evolutionary phase of rapid expansion making the **isochrones** almost completely vertical in the mass-radius diagram (see, e.g., Figure 3.8). Precise determination of the masses of

¹: https://webda.physics.muni.cz/cgi-bin/ocl_page.cgi?cluster=ngc+2506

Table 3.1 | Target stars in NGC 2506. Names, WEBDA ID, and coordinates of the target stars. The detached eclipsing binaries are above the solid line and the [RGB](#) stars are below. The [RGB](#) stars above the dashed lines are the ones for which we perform a spectroscopic analysis and the two listed below are the ones in which we possibly detect solar-like oscillations. The index for these (RGBXXX) refers to their index in our *uvby* photometry (Table A2 in Knudstrup et al., 2020). **Notes.** ^(a)Identifier from Anthony-Twarog et al. (2018). ^(b)No identifier found.

Name/WEBDA	α_{2000}	δ_{2000}	y	$(b - y)$
V2032/4132	08 00 00.6	-10 45 38	13.719	0.290
V4/1136	08 00 08.2	-10 45 50	14.645	0.292
V5/1335	08 00 10.3	-10 43 17	17.430	0.456
RGB231/7108 ^(a)	08 00 23.3	-10 48 48	13.622	0.612
RGB433/2375	08 00 11.5	-10 50 19	13.555	0.615
RGB913/2255	08 00 09.4	-10 48 13	13.748	0.607
RGB2358/4274	08 00 00.8	-10 44 04	13.753	0.613
RGB383/2402	08 00 20.1	-10 49 59	12.422	0.722
RGB526/- ^(b)	08 00 18.2	-10 49 21	11.077	0.975

these components will therefore completely lock the age of the cluster. The components of V5 are somewhat lower in terms of mass than the cluster [turn-off](#) mass with the lowest of the two having a mass of around $0.7 M_\odot$. This means that the masses of all the components in the binaries span a range in mass that covers the transition between stars above $\sim 1.2 M_\odot$ with a convective core and stars below with a radiative core, which will help anchor the [isochrones](#).

In addition to the [DEBS](#) we have spectra of four [RGB](#) stars. These will provide us with a firm grip on the metallicity of the cluster. Furthermore, they will allow us to probe a more evolved stage of stellar evolution in a different parameter space, namely $\log g$ and T_{eff} . Finally, the [Gaia](#) mission is providing precise parallaxes and proper motion for billions of stars, which is extremely useful in cluster studies as this allows for not only distance determination, but also membership determination.

3.3 Spectroscopic observations

Here we present our spectroscopic observations of stars in the cluster, where we first discuss the membership based on [RVS](#). We then present

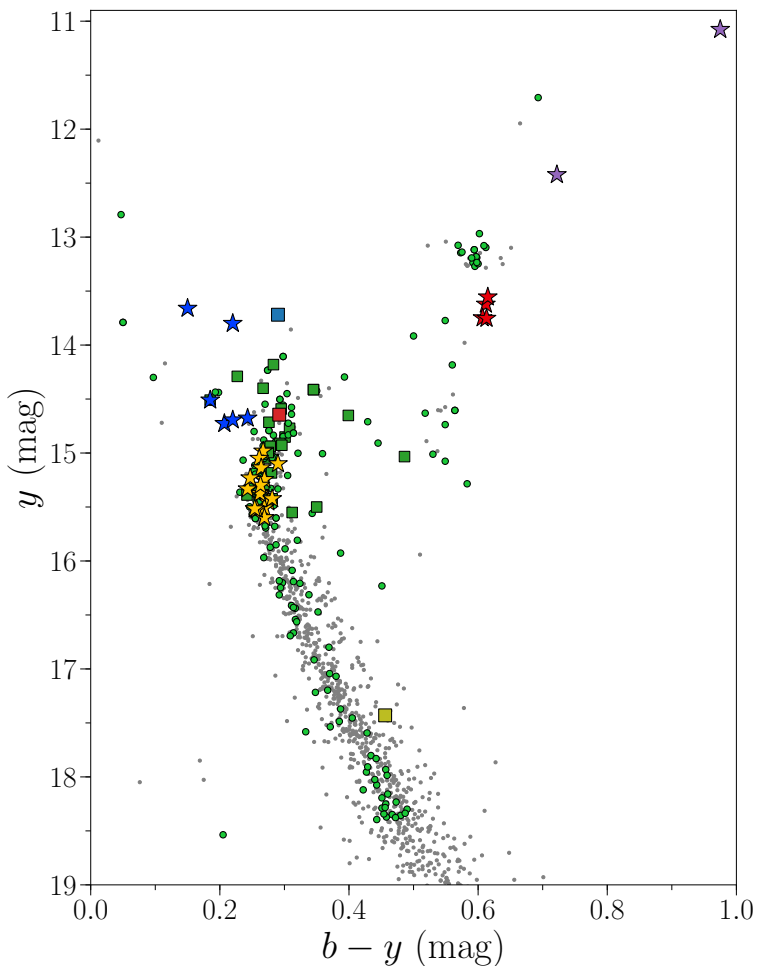


Figure 3.1 | Colour-magnitude diagram of NGC 2506. Cleansed [CMD](#) of NGC 2506. Grey dots are [Gaia](#) proper motion members of the cluster (see Section 3.7) and green dots and squares mark the confirmed [RV](#) members from spectroscopy of single and multiple systems, respectively; we have thus removed all stars we deemed non-members (see Section 3.3.1). Yellow and blue stars denote respectively the γ Dor stars and BSs reported in Arentoft et al. (2007). The blue, red, and yellow squares denote V2032, V4, and V5 listed in Table 3.1 alongside the [RGB](#) stars marked with red and purple stars in this figure. We performed a spectroscopic analysis of the [RGB](#) stars marked with red stars, and we report on the possible detection of solar-like oscillations for the stars marked with purple.

our measurements of the chemical composition of the cluster through an analysis of spectroscopic measurements of **RGB** stars, with a subsequent derivation of the colour excess of the cluster. In Section 3.3.3 we describe how we obtained **RVS** for the **DEBS**. Finally, we present measurements for the luminosity ratios of V₂₀₃₂ and V₄, both from the spectroscopic measurements, but also from measuring the *spectral energy distribution (SED)*.

3.3.1 Radial velocity members from spectroscopy

We obtained 15 epochs of GIRAFFE spectroscopy (ESO programme 075.D-0206(B); this is the same programme as the data for the **DEB** V₄, see Table 3 in Knudstrup et al. (2020), and the **RGB** stars in Section 3.3.2) from ESOs Very Large Telescope (VLT) for NGC 2506 in order to define membership near the cluster **turn-off** region and **RGB**. The setting (HR14A) with a central wavelength near 6515 Å and a resolution of 18000 (Medusa mode) was utilised. All spectra were recovered from the <http://giraffe-archive.obspm.fr> site which provided a re-reduction of the ESO GIRAFFE data. We note, however, that at the time of writing this webpage is no longer active.

To derive the velocities we cross-correlated each obtained stellar spectrum with a solar template and calculated the average velocity, standard deviation of the individual velocities as well as the width of the fitted Gaussian. This resulted in a histogram of velocities for 122 objects, with a clear peak in the distribution at $v_{\text{rad}} = 83.8$ km/s with a Full Width Half Maximum (FWHM) of 4.7 km/s. We then assigned membership by requiring that an object has an average velocity within two FWHM of the cluster mean. Following this we inspected the 15 epochs of **RVS** for each target to make sure that binaries would be correctly assigned as members or non-members.

In Table A2 in Knudstrup et al. (2020) the basic information for each target is provided; ID (from the *uvby* photometry), y and $b - y$ in the Strömgren system, average velocity, standard deviation of the 15 **RVS**, and the Gaussian σ from the fit to the **CCF**. The two second to last columns indicate whether a significant epoch-to-epoch variability was found (0 = **RV** constant, 1 = **RV** variable) and the membership status (1 = member, 0 = non-member) based on the **RV**. This forms the basis for the colour coding used in Figure 3.1. In the very last column we list both a cross-match with the catalog created by Cantat-Gaudin et al. (2018) available in the VizieR Online Data Catalog (Cantat-Gaudin and Anders, 2019), where they assessed

cluster membership based on the *Gaia* proper motions and parallaxes, and the spectroscopic membership by Anthony-Twarog et al. (2018), where we have adopted their membership classification. The values listed in Table A2 in Knudstrup et al. (2020) are the probabilities for membership they provide. As a sanity check we also did a cross-match between our target stars in Table 3.1 and Cantat-Gaudin and Anders (2019) – all stars, with the exception of V5, were found to be members. This could be due to the faintness of the system as the *RV* curves in Figure 3.5 clearly suggest that V5 is a member of the cluster. Likewise, we cross-matched our targets with the catalog by Anthony-Twarog et al. (2018), where again all targets were listed as members, with the exception of V5 and RGB525 for which we could not find a match.

3.3.2 Spectroscopic analysis of red-giant branch stars

The spectra for the *RGB* stars were obtained using UVES under the programme with ID 075.D-0206(B). We used UVES/FLAMES in the 580 nm setting, resulting in a spectral resolution of 47,000. The atmospheric parameters of the four *RGB* stars presented in Table 3.2 were determined spectroscopically from an equivalent width analysis of Fe lines using DAOSPEC (Stetson and Pancino, 2008) to measure line strengths. The line list is from Slumstrup et al. (2019) and the methodology follows that of Slumstrup et al. (2017, 2019), who has derived the metallicities for giant stars in NGC 188, M67, NGC 6819, and NGC 6633 as well as in the Hyades (Arentoft et al., 2019) in a self-consistent way. Using this method Slumstrup et al. (2017) and Arentoft et al. (2019) finds the “canonical” values for the metallicity of M67 and the Hyades. Compared to previous studies of NGC 2506 (e.g., Friel and Janes, 1993; Carretta et al., 2004) the data presented here have significantly higher spectral resolution and spectral range as well as a higher *signal-to-noise ratio* (*SNR*), which is comparable to that of Slumstrup et al. (2017, 2019).

The atmospheric parameters were determined with the auxiliary program Abundance with SPECTRUM (Gray and Corbally, 1994) using ATLAS9 stellar atmosphere models (Castelli and Kurucz, 2004) and solar abundances from Grevesse and Sauval (1998). Non-LTE (local thermodynamic equilibrium) effects have been shown to be small for Fe in this parameter range (of the order of 0.1 dex; Asplund, 2005; Mashonkina et al., 2011) and we therefore assume LTE. The effective temperatures were determined by requiring that the Fe abundance of each absorption line has no dependency on the excitation potential, i.e., excitation equilibrium.

Table 3.2 | Red Giant Branch stars. Atmospheric parameters of the four RGB stars. The uncertainties are only internal.

	T_{eff} (K)	$\log g$ (cgs;dex)	v_{mic} (km/s)
RGB ₂₃₁	4870 ± 30	2.65 ± 0.03	1.10 ± 0.04
RGB ₄₃₃	4840 ± 30	2.60 ± 0.05	1.15 ± 0.03
RGB ₉₁₃	4920 ± 30	2.70 ± 0.05	1.10 ± 0.05
RGB ₂₃₅₈	4970 ± 70	2.80 ± 0.10	1.00 ± 0.10
	[Fe/H] (dex)	[α /Fe] (dex)	[Mg/Fe] (dex)
RGB ₂₃₁	-0.36 ± 0.01	0.10 ± 0.02	0.12 ± 0.02
RGB ₄₃₃	-0.37 ± 0.01	0.10 ± 0.02	0.13 ± 0.01
RGB ₉₁₃	-0.36 ± 0.01	0.09 ± 0.02	0.08 ± 0.02
RGB ₂₃₅₈	-0.34 ± 0.03	0.06 ± 0.05	0.10 ± 0.06
	[Si/Fe] (dex)	[Ca/Fe] (dex)	[Ti/Fe] (dex)
RGB ₂₃₁	0.13 ± 0.02	0.14 ± 0.05	-0.01 ± 0.01
RGB ₄₃₃	0.13 ± 0.05	0.13 ± 0.01	0.00 ± 0.02
RGB ₉₁₃	0.16 ± 0.05	0.11 ± 0.01	0.01 ± 0.01
RGB ₂₃₅₈	0.05 ± 0.09	0.09 ± 0.05	0.02 ± 0.03
	SNR @5000 Å	SNR @6000 Å	
RGB ₂₃₁	105	230	
RGB ₄₃₃	110	230	
RGB ₉₁₃	100	220	
RGB ₂₃₅₈	100	215	

Likewise, the micro-turbulent velocity was determined by requiring that the Fe abundances show no trend with the reduced equivalent width of the lines ($\log(\frac{\text{EW}}{\lambda})$). The surface gravities were determined by invoking ionization equilibrium - requiring that the mean abundances of the two ionization stages FeI and FeII are in agreement, because FeII lines are much more sensitive to pressure changes than FeI lines in this parameter range. This is, however, also sensitive to the effective temperature and heavy element abundance and several iterations were realised to reach agreement on every parameter.

The metallicity of NGC 2506 has been determined several times in the literature and different values have been obtained. The higher determinations are from, e.g., Mikolaitis et al. (2011) and Reddy et al. (2012) with values of $[Fe/H] = -0.24 \pm 0.05$ dex and $[Fe/H] = -0.19 \pm 0.06$ dex, respectively. These are significantly higher than our mean cluster metallicity of -0.36 dex, which is in slightly better agreement with results on the lower end of determinations as, e.g., the study of many open clusters presented by Friel et al. (2002) that gives a mean cluster metallicity of -0.44 dex. The α abundances in Table 3.2 are calculated as $[\alpha/Fe] = \frac{1}{4} \cdot ([Mg/Fe] + [Ca/Fe] + [Si/Fe] + [Ti/Fe])$. We also provide the individual elemental abundances because there are interesting systematic differences in the abundances of the standard α elements, with $[Ti/Fe]$ showing no α enhancement, whereas the other three elements show slight α enhancement for all stars. The two studies by Mikolaitis et al. (2011) and Reddy et al. (2012) do not find this same significant difference between Titanium and the other three α elements used here.

3.3.2.1 Reddening from RGBs

The intrinsic spectroscopic parameters for the RGB stars in Table 3.2, i.e., T_{eff} , $\log g$, and $[Fe/H]$, allow us to determine the reddening, $E(B - V)$, of the cluster. This was done by calculating the bolometric corrections for the *Gaia* filters, $BC_{G_{\text{BP}}}$ and $BC_{G_{\text{RP}}}$, using the spectroscopic parameters and compare these to the observed *Gaia* colour, since $BC_{G_{\text{RP}}} - BC_{G_{\text{BP}}} = G_{\text{BP}} - G_{\text{RP}}$. Any discrepancy between the two should be due to the reddening. We used the bolometric corrections from Casagrande and VandenBerg (2018a,b) with $[\alpha/Fe] = 0.0$ dex.

To incorporate the uncertainties on the spectroscopic parameters, our approach was to do an *Markov Chain Monte Carlo (MCMC)* analysis using the program emcee (Foreman-Mackey et al., 2013), where we drew from Gaussian distributions for the spectroscopic parameters (Table 3.2) and a uniform distribution for the reddening, in the sense $\mathcal{N}(\mu, \sigma)$ (μ being the mean and σ the uncertainty) and $\mathcal{U}(a, b)$ ($a = 0.0$ and $b = 0.4$), respectively. We then determined $BC_{G_{\text{RP}}}$ and $BC_{G_{\text{BP}}}$ for each draw and calculated the corresponding maximum likelihood, or rather the logarithm of the maximum likelihood:

$$\log \mathcal{L} = -\frac{1}{2} \sum_{i=1}^4 \log(2\pi\sigma_i^2) + \frac{(y_{BC,i} - y_{\text{Obs},i})^2}{\sigma_{\text{Obs},i}^2},$$

where $y_{BC} = BC_{G_{RP}} - BC_{G_{BP}}$, $y_{\text{Obs.}} = G_{BP} - G_{RP}$, and $\sigma_{\text{Obs.}}$ is the uncertainty on the observed *Gaia* colour. This yielded a value of $E(B - V) = 0.080^{+0.005}_{-0.006}$ mag, corresponding to $E(b - y) = 0.057 \pm 0.004$ mag.

This value is a bit higher than the values found in Carretta et al. (2004) of $E(b - y) = 0.042 \pm 0.012$ mag (from $E(b - y) = 0.72 \cdot E(B - V)$) and $E(b - y) = 0.042 \pm 0.001$ mag found in Anthony-Twarog et al. (2016). The value we have found for the reddening can be used to calculate the effective temperatures for the stars in the binaries, which is discussed in Section 3.3.5.

3.3.3 Radial velocities for the detached eclipsing binaries

VLT was also used to obtain all of the spectroscopic data of V₄ and V₅ as well as part of the spectroscopic data of V₂₀₃₂, where both the Ultraviolet and Visual Echelle Spectrograph (UVES; Dekker et al., 2000) and the GIRAFFE spectrographs have been used for V₄, but only GIRAFFE has been used for V₅ and V₂₀₃₂. The data from UVES were acquired in 2005 by feeding the spectrograph by the Fibre Large Array Multi Element Spectrograph (FLAMES; Pasquini et al., 2002) resulting in a medium resolution of $R = 47,000$. When UVES is fed by FLAMES the spectrum is imaged onto two beams hitting two separate CCDs – a lower CCD covering 4777 – 5750 Å and an upper one covering 5823 – 6819 Å. Likewise, the GIRAFFE spectrograph was also fed by FLAMES resulting in a resolving power of $R = 33,700$. The GIRAFFE spectra were obtained in 2009 and 2010. All the spectroscopic data from VLT are summarised in Table 3 Knudstrup et al. (2020). The second batch of spectroscopic data for V₂₀₃₂ was acquired using the NOT covering epochs from 2012 to 2015. The spectra were obtained at a resolution of $R = 46,000$ using FIES (Telting et al., 2014). This is summarised in Table 4 in Knudstrup et al. (2020).

The spectroscopic data for V₄ were reduced by the UVES data reduction pipeline described in Ballester et al. (2000), and for the GIRAFFE spectra we received the reduced data products from ESO on DVDs. The FIES spectra of V₂₀₃₂ were reduced using the instrument data reduction pipeline FIEStool (v. 1.3.2), developed in python by E. Stempels and maintained and provided by the staff at NOT. Before each observing night, calibration frames were produced from a standard data set of 7 bias and 21 halogen flats and each object exposure was preceded by a Th-Ar lamp exposure for optimal wavelength calibration.

To extract the RVS of the components in all DEBS, a python implementation of the BF formalism formulated by Rucinski (1999) was utilised. RVS

were obtained by matching the spectra to appropriate model atmospheres from Coelho et al. (2005). As the spectroscopic data have been acquired with different telescopes with quite different instruments, the approach differs from instrument to instrument.

For the GIRAFFE spectra, which cover a single order, the procedure is straightforward; each spectrum was normalised and a **BF** was calculated giving an estimate for the **RV**. The UVES/FLAMES setup gives two measurements for each of the spectra listed in the upper part of Table 3 in Knudstrup et al. (2020). The divided spectra were normalised and the **BF** was calculated individually for each, yielding two **RV** measurements for a given epoch. The mean of the two then constituted the first estimate for the **RV**, however, at a later point in our analysis (see Section 3.5), anti-correlations showed up in the residuals of the **RVS** between the primary and secondary component for V4. Therefore, we omitted **RVS** derived from spectra from the upper **CCD** of the FLAMES/UVES setup due to the absence of prominent lines in this part of the spectrum and only used the measurements from the lower part. We thus took the **RV** stemming from the lower **CCD** as our value. The error was estimated by dividing this part of the spectrum into three parts, where we calculated the **BF** for each, then calculated the standard deviation of those three. This was also the approach for the GIRAFFE spectra.

With **FIES** at the **NOT**, a spectrum is divided into 78 orders. Each order for a given epoch in Table 4 in Knudstrup et al. (2020) was processed individually, i.e., each order was normalised and for this part of the spectrum, the **BF** was calculated. Therefore, for each spectrum in Table 4 in Knudstrup et al. (2020), 78 estimates for the **RVS** of the components are available. However, seeing as some of the orders at shorter wavelenghts do not have a lot of flux and some of the redder orders contain telluric lines, not all orders are equally good. Therefore, orders we deemed bad were omitted. The **RV** estimate from a given epoch is then the mean of the **RVS** obtained from all the good orders and the corresponding error is the standard deviation of the measurements from these orders. Example **BFS** for V4 and V2032 can be seen in Figure 3.2. Note that the primary component of V4 is rotating rapidly, resulting in a broad peak and a lower signal-to-noise ratio. The peak from the primary component in the **BF** for V5 was quite prominent, whereas the peak from the secondary component was harder to locate for some epochs and we had to constrain the fit to a certain interval.

With the **RVS** in hand, we could then create the **RV** curves. We used a python implementation of the program Spectroscopic Binary Orbit Program (SBOP; Etzel, 2004) to obtain estimates of the spectroscopic orbital parameters for each system, which will be used as initial guesses for the

Table 3.3 | Initial parameters. Orbital output parameters from SBOP, which serve as initialization input for the models calculated in Section 3.5.

	V2032	V4	V5
K^p (km/s)	62.00 ± 0.15	96.5 ± 0.5	71.9 ± 1.3
K^s (km/s)	62.55 ± 0.17	114.0 ± 0.2	96.1 ± 1.3
e	0.5858 ± 0.0016	0.187 ± 0.003	0.003 ± 0.011
ω (°)	319.0 ± 0.2	272.3 ± 0.6	110 ± 5
P (days)	27.8677 ± 0.0004	2.867630 ± 0.000005	3.3570 ± 0.0014
γ (km/s)	83.26 ± 0.05	85.03 ± 0.15	84.9 ± 0.7

further analysis. The starting orbital parameters from SBOP for all the DEBS are listed in Table 3.3. Here we fit for the velocity semi-amplitudes, eccentricity (e), argument of periastron (ω), period (P), systemic velocity (γ), and the time of periastron passage T_{peri} .

Evidently, V2032 is a very eccentric system with a rather long period and, interestingly, the RV amplitudes, K^p and K^s , are very similar suggesting that the masses of the components are almost identical. The superscripts p and s will denote quantities for the primary and secondary, respectively, throughout (and in the case for V4, t denotes the tertiary component).

3.3.4 Luminosity ratios

The calculated BFS do not only hold information about the RVS of the components in the binary system, but are also an estimate for their luminosity ratio, L^s/L^p . When the stars belong to the same spectral type, then the luminosity ratio is simply the ratio of the areas under the peaks. An external constraint on the luminosity ratio for the further analysis is in general advantageous and proved to be necessary to obtain precise results for our binary systems.

The ratio is easiest to calculate when the BF peaks are well separated (as is the case in Figure 3.2), so only epochs where the components have a large difference in RV were chosen from Table 3 in Knudstrup et al. (2020) and Table 4 in Knudstrup et al. (2020). As mentioned in Section 3.3.3 due to the absence of lines in the part of the spectra imaged onto the upper CCD from the FLAMES/UVES setup, we only calculated the luminosity ratio for spectra stemming from the lower CCD. This yielded a value of $L^s/L^p = 0.40 \pm 0.02$ for V4. Because of the wavelength covered by this CCD this value corresponds to the luminosity ratio in V . We translated this

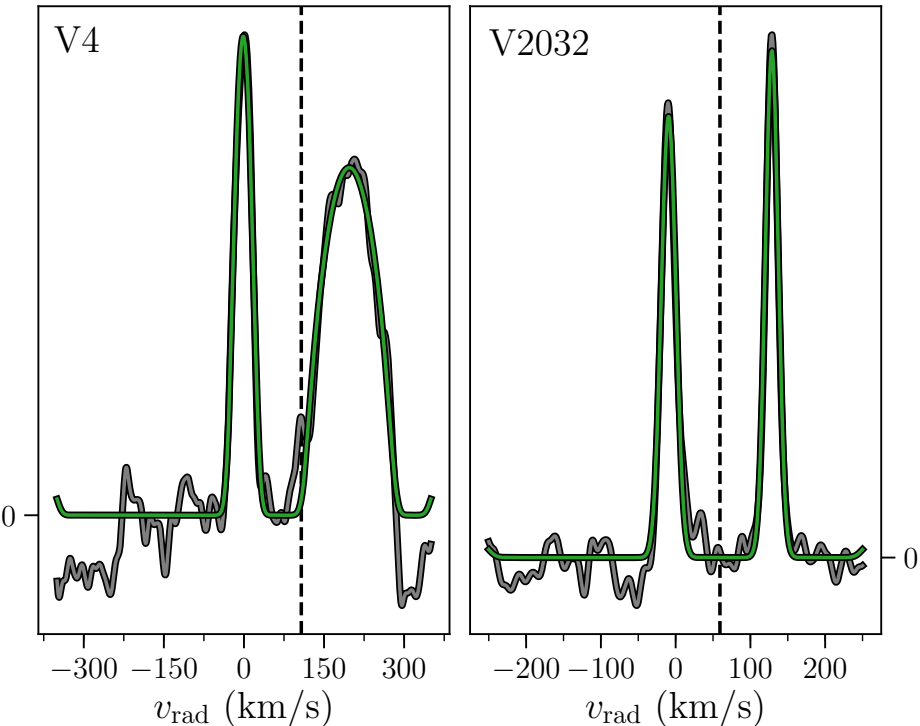


Figure 3.2 | Broadening functions. Example [BF](#) for V4 is shown to the left calculated from EP-V4 in Table 3 in Knudstrup et al. (2020). Shown to the right is an example [BF](#) for V2032 calculated from EP-V2032 in Table 4 in Knudstrup et al. (2020). The grey lines in both figures are the smoothed calculated [BFS](#) and the green lines are the fitted rotational profile (see Kaluzny et al., 2006, for details). The systemic velocity, $\gamma \sim 83 \text{ km s}^{-1}$, corrected for the BVCs for the given epochs is marked with dashed lines. The y-axis is given in arbitrary units.

ratio to corresponding values in I and B using filter transmission curves² and obtained 0.39 ± 0.02 and 0.40 ± 0.02 , respectively, corresponding to all available light curves for V4. We also calculated the luminosity ratio from the [BFS](#) for V5 using our GIRAFFE spectra and obtained a value of 0.36 ± 0.03 in V .

For V2032 we used the [FIES](#) spectra to calculate the luminosity ratio, we again only used epochs where the peaks were well separated and again

2: Filter transmission curves from [NOT](http://www.not.iac.es/instruments/filters/filters.php): <http://www.not.iac.es/instruments/filters/filters.php>.

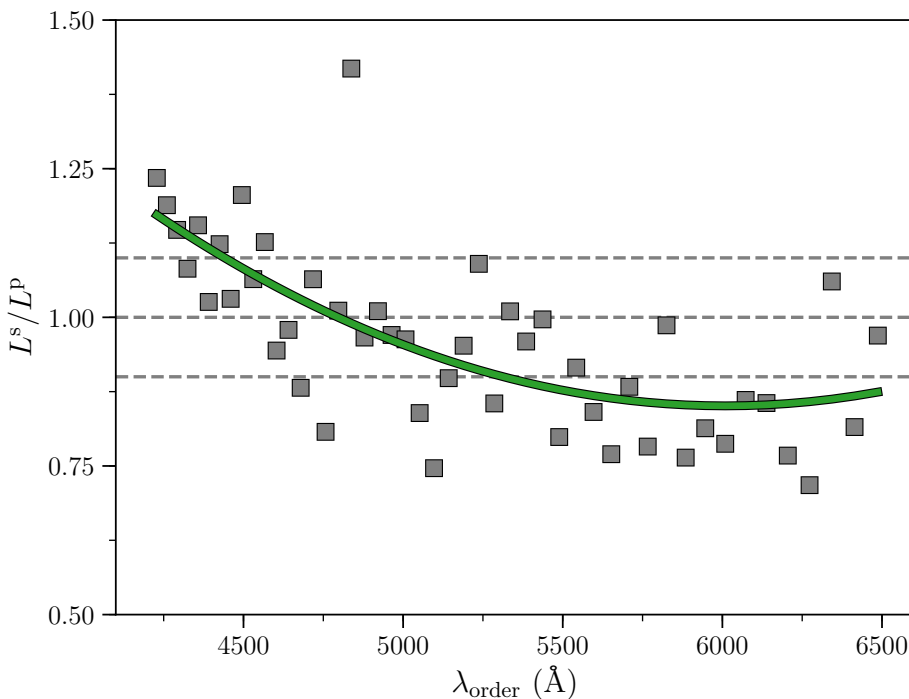


Figure 3.3 | Luminosity ratio for V2032. Luminosity ratio of V2032 as a function of order (here λ_{order} designates the midpoint of the wavelength interval for a given order). A grey square at a given order is the mean value of the luminosity ratio calculated from the [BF](#) for “good” epochs with well separated peaks (as in Figure 3.2). The green curve is a second order polynomial fit to these points, which is used to elucidate the trend.

we only used the orders that we deemed suitable. The procedure was to, for a given order, calculate L^s/L^p for all the spectra with well separated peaks and use the mean value of these as the value for this order. This was then repeated for all the good orders. This is shown with grey squares in Figure 3.3. Many of the measurements for the luminosity ratio of V2032 are very close to 1 and the overall value is 0.95 ± 0.05 , however, a small trend is apparent when the values obtained for L^s/L^p are plotted against the orders. The trend suggests that the secondary component is slightly more luminous at shorter wavelengths compared to the primary component meaning that $T_{\text{eff}}^s > T_{\text{eff}}^p$.

The luminosity ratios are used in the subsequent analysis (Section 3.5) to help constrain the radii of the components. Specifically, for V2032 where we have photometric data in V and I as well as from [TESS](#) (Section 3.4), which

has a photometric passband similar to that of I , we derived luminosity ratios corresponding to these passbands. For V this was done by simply selecting measurements of the [BF](#) from Figure 3.3 in the range 4100–6100 Å and calculate the robust mean and standard deviation of these. This resulted in a value of 0.89 ± 0.02 . For I (TESS) we utilised the same scheme as for V_4 to obtain a value of 0.84 ± 0.02 .

3.3.5 The Spectral Energy Distribution of V4

We examined the [SED](#) of V_4 to confirm the value of the luminosity ratio we have obtained from spectroscopy (see Section 3.3.4), but also to see if we can learn more about the fainter, third companion. A benefit of the binary’s membership in a cluster is that it should be possible to describe the binary’s light as the sum of the light of two single cluster stars. To that end, we compiled a database of photometric measurements from V_4 and from likely single [MS](#) stars in NGC 2506, and sought a combination of stars whose summed fluxes most closely match the fluxes of the binary. For our sample of probable single stars, we selected likely members based on [Gaia](#) proper motions, parallaxes, and photometry. Likely binaries were rejected by restricting the sample to those with [Gaia](#) photometry placing them within about 0.03 mag of the blue edge of the [MS](#) band in the $G_{\text{BP}} - G_{\text{RP}}$.

We briefly describe the photometric datasets and the conversions from magnitude to flux below. In the ultraviolet, Siegel et al. (2019) presented photometry of more than 100 open clusters (including NGC 2506) using the UVOT telescope on the *Swift* satellite (Gehrels et al., 2004). We used their magnitudes in the $uvw1$, $uvm2$, and $uvw2$ bands, and converted to fluxes.

Anthony-Twarog et al. (2016) and Grundahl et al. (2000) presented narrow-band Strömgren $uvby$ photometry for the cluster. We employed reference fluxes from Gray (1998) to convert the magnitudes to fluxes. Marconi et al. (1997) observed the cluster in 6 wide filters ($UBGVRI$). With the exception of the G filter, the magnitudes were converted to fluxes using reference fluxes from Bessell et al. (1998), taking into account the known reversal of the zero point correction rows for the observed flux, f_λ and f_ν .

There are a couple of large ground-based optical surveys that provide calibrated broad-band photometric observations. The Pan-STARRS1 survey (Kaiser et al., 2010) contains photometry in 5 filters ($grizy$), and we use their mean PSF magnitudes here. Zero points for its AB magnitude system are given in Schlafly et al. (2012). The SkyMapper survey (Data Release 1;

Wolf et al. 2018) is a six filter (*uvgriz*) Southern Hemisphere study that provides PSF magnitudes on an AB system. In addition, *Gaia* has already produced high-precision photometry extending far down the MS of the cluster as part of *Gaia* DR2. We obtained the fluxes in the G , G_{BP} , and G_{RP} bands from the *Gaia* Archive.

In the infrared, we have obtained Two-Micron All-Sky Survey (2MASS; Skrutskie et al., 2006) photometry in JHK_s from the All-Sky Point Source Catalog, and have converted these to fluxes using reference fluxes for zero magnitude from Cohen et al. (2003). The stars were observed in JK_s within the deeper VISTA survey (McMahon et al., 2013). We also used PSF magnitudes in iJ filters from the third data release of the DENIS database³.

Although we have strived to put the measurements on a consistent flux scale in order to construct spectral energy distributions, we emphasise that our procedure for decomposing the light from the two stars in a cluster binary does not depend on the exact calibration. What is important is that we are using measurements of a large number of cluster stars from uniform photometric studies, i.e., we are assuming the *relative* flux measurements are precise. The benefit of this procedure is that it is a *relative* comparison using other cluster stars with the same distance, age, and chemical composition, and not an absolute comparison. As such, it is independent of distance and reddening (as long as these are the same for the binary and comparison stars), the details of the filter transmission curves (as long as the same filter is used for observations of the different stars), and flux calibration of any of the filters (as long as the calibration is applied consistently). We can also avoid systematic errors associated with theoretical models or with the consistency of the different parts of empirical spectral energy distributions compiled from spectra.

We tested two ways of doing the decomposition of the binary's light: using well-measured NGC 2506 stars as proxies and checking all combinations of likely MS stars; and fitting all MS stars with photometry in a given filter as a function of *Gaia* G magnitude. When using sums of real stars, we are somewhat at the mercy of the photometry that is available for each star (and the binary) and of the stellar sampling, i.e., the density of stars of the MS. The use of fits allows for finer examination of the MS, although there is some risk of diverging from the photometry of real stars.

To judge the degree to which a pair of stars reproduced the binary photometry, we looked for a minimum of a χ^2 -like parameter involving fractional flux differences in the different filter bands; $\sum_i [(F_{i,\text{bin}} - (F_{i,1} +$

³: cds.u-strasbg.fr/denis.html

$F_{i,2})]/(\sigma_{i,\text{bin}} \cdot F_{i,\text{bin}})]^2$, where $F_{i,\text{bin}}$, $F_{i,1}$, and $F_{i,2}$ are the fluxes for respectively the binary and the two proxies, and $\sigma_{i,\text{bin}} = 10^{-\sigma_{i,\text{m}}/2.5} - 1$ with $\sigma_{i,\text{m}}$ being the magnitude uncertainty in the i th filter band for the binary. The uncertainty was set to 0.02 mag for photometry without quoted errors or if the quoted uncertainty was below that value. This was done in order to deweight photometry with very low uncertainties (such as [Gaia](#)) that results partly from their very wide filter bandpasses.

The best-fitting combination of cluster star [SEDS](#) depends somewhat on the filters that were employed, to the point that the redder star could switch between the brighter and fainter star. The flux ratios were somewhat more stable, however, and the two stars cannot have temperatures that are too dissimilar. Our preferred set of photometry excluded DENIS J and K_s , and WISE datasets due to low signal-to-noise, and had a goodness-of-fit value of 40.0 from measurements in 37 filters.

Top panel of Figure 3.4 shows a comparison of the [SED](#) of V4 with the best fitting pair (MHT 772 and 808 in Marconi et al., 1997, or WEBDA 4254 and 1247, respectively). A potential limiting factor is the stellar sampling available near the brighter star, but we have stars within 0.011 G mag on the bright side and within 0.007 mag on the faint side. For the faint star, other stars in the sample fall within 0.06 mag. The resulting luminosity ratio in filters similar to V (Strömgren y , Sloan g , Marconi et al. V) was 0.39.

The [MS](#) fitting procedure can be employed in any filter with a sufficient sample of stars covering the range of brightnesses for the binary's stars. In our case, this eliminates the DENIS K_s and WISE filters from consideration in fitting V4. Our fit statistic had a minimum value of 47.6 for the selection of 38 filters. We estimated the 2σ uncertainty in the fit based on where the goodness-of-fit statistic reached a value of 4 above the minimum value. For example, this returns $2\sigma(G_A) = 0.016$ and $2\sigma(G_B) = 0.05$. As expected, there is an anti-correlation between values for the primary and secondary stars because of the need to match the binary fluxes. For filters similar to V , the best-fit luminosity ratio comes out as 0.33 ± 0.02 . Overall this fit is notably poorer than the cluster star fit in infrared J , H , and K_s bands, with the computed fit being brighter than the observed binary. This appears to recommend the cluster star fit, with its slightly fainter primary star.

3.3.5.1 T_{eff} for the components in V4

We can attempt to get precise stellar temperatures for the components of V4 using the infrared flux method (IRFM; Blackwell and Shallis, 1977). With the

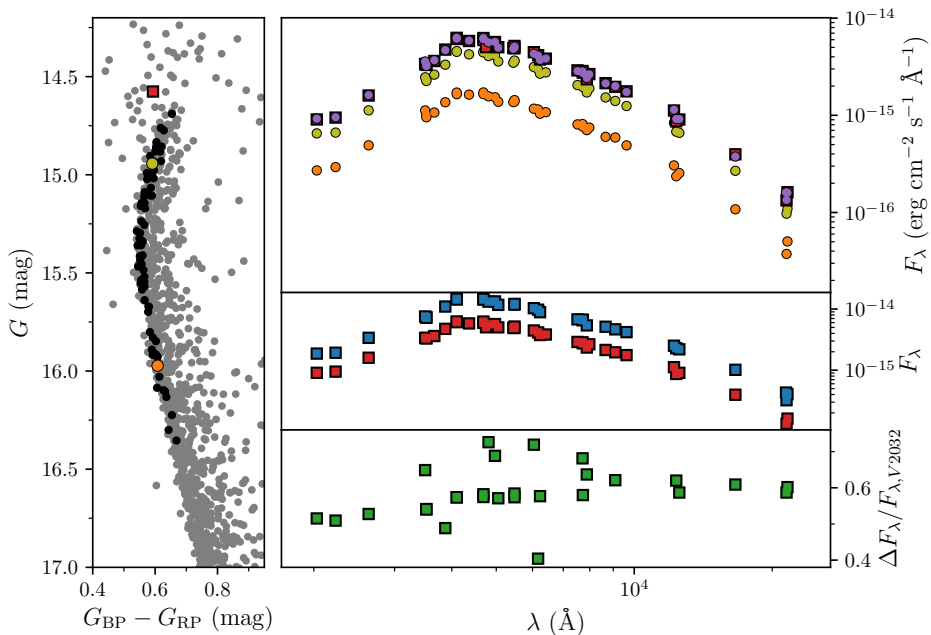


Figure 3.4 | Spectral energy distributions. *Left:* [Gaia CMD](#) for NGC 2506 cluster members in grey with the red square marking the combined photometry of V4. The yellow and orange points show the two stars identified as the best fit (MHT 772 and MHT 808, respectively). The black points are probable single cluster member stars that had photometry in all of the filter bands used in the [SED fit](#). *Top right:* [SEDS](#) of V4 (red squares, which are mostly obscured by the purple points), MHT 772 (yellow points), MHT 808 (orange points), and the combined light of the two best-fitting stars (purple points). *Middle right:* [SEDS](#) of V4 (red squares) and V2032 (blue squares). *Bottom right:* Comparison of the [SEDS](#) for V4 and V2032, $(F_{\lambda,V2032} - F_{\lambda,V4}) / F_{\lambda,V2032}$.

available photometric databases for NGC 2506, we have measurements of fluxes covering the majority of the stellar energy emission. The IRFM relies on the difference in temperature sensitivity between the bolometric flux and monochromatic fluxes in the infrared on the Rayleigh-Jeans portion of the spectrum. The ratio of the bolometric and infrared fluxes can be compared to theoretical values:

$$\frac{F_{\text{bol}}(\text{Earth})}{F_{\lambda_{\text{IR}}}(\text{Earth})} = \frac{\sigma T_{\text{eff}}^4}{F_{\lambda_{\text{IR}}}(\text{model})}$$

We used the 2MASS flux calibration of Casagrande et al. (2010) in our implementation, in part because it produced greater consistency between the temperatures derived in the three bands. VISTA J and K_s filters returned T_{eff} estimates that were within the scatter of the 2MASS values, so we considered this corroboration. Starting from a solar-metallicity ATLAS9 model that produced a good fit by eye, we adjusted the temperature of the synthetic spectrum until it matched the average IRFM temperature from the three 2MASS bands. The model surface gravity was chosen from the eclipsing binary results (Section 3.5), although the results had little sensitivity to the gravity.

For MHT 772, which was identified as the best cluster representative of the primary star of V4, we found $T_{\text{eff}} = 6830$ K, with a full range of 110 K for the estimates from different 2MASS bands. Thus, we estimate the uncertainty to be approximately 55 K. For comparison, we calculated the temperature for V4 itself, i.e., the combined light – the two stars in our SED decomposition appear to have very similar colours. We found 6820 ± 100 K (with the uncertainty estimate from half of the full range in the 2MASS measurements).

3.3.5.2 T_{eff} for the components in V2032

We were unable to decompose the light of the V2032 binary in the same way we did for V4 because the component stars appear to reside in a part of the CMD where there is rapid evolution and few single stars to be found. However, the colour of the binary’s combined light is very similar to that of V4, so we compared the SEDs of the two binaries to seek information about the component temperatures. The comparison (bottom panel Figure 3.4) showed that V4 clearly has a larger fraction of its flux in the ultraviolet, which leads us to the conclusion that the primary (more massive) star of V2032 is cooler than the stars of V4. Employing the IRFM on the SED of V2032 gives $T_{\text{eff}} = 6560 \pm 30$ K, although this should not be considered a direct measurement of the primary star’s temperature. It is, however, fairly good evidence that the primary star is evolving towards the red – if it is cooler but more luminous than the secondary star, expectations from normal single-star stellar evolution tracks would require it to be on the subgiant branch. The relative temperature difference between the components of V2032 is consistent with the results from the BFS in different spectral orders (see Section 3.3.4).

Even though we could not get a good estimate of the effective temperature of the secondary component from the SED, we can still get a good

measure for this value given that we have estimated the effective temperature of the primary component of V2032, and we have measured the metallicity and reddening, we can calculate the effective temperature of the secondary component. This was done by performing a Monte Carlo simulation, where we drew from Gaussian distributions in the sense $\mathcal{N}(\mu, \sigma)$ for the following parameters $T_{\text{eff}}^{\text{p}} = 6560 \pm 100$ K (where the 100 K is to account for any potential difference between the proxy and the primary), $E(b - y) = 0.057 \pm 0.004$ mag, $[\text{Fe}/\text{H}] = -0.36 \pm 0.10$ dex, and the colour of the combined light of V2032 $(b - y) = 0.290 \pm 0.002$ mag.

For each draw we found the colour for the primary, $(b - y)^{\text{p}}$, that minimises the difference between $T_{\text{eff}}^{\text{p}}$ estimated from the **SED** and the value resulting from using the temperature-colour-metallicity calibration in Casagrande et al. (2010) given $E(b - y)$ and $[\text{Fe}/\text{H}]$. From this it is possible to calculate the colour of the secondary component, $(b - y)^{\text{s}}$, since $(b - y) = k^{\text{p}}(b - y)^{\text{p}} + k^{\text{s}}(b - y)^{\text{s}}$, where $k^{\text{p,s}}$ is the fractional amount of light a component contributes to the system. We calculated this by drawing normally distributed values from the calculated luminosity ratio of 0.95 ± 0.05 . A measure for $(b - y)^{\text{s}}$ then yields a value for the effective temperature of the secondary component. From 5,000 draws this yielded a value of $T_{\text{eff}}^{\text{s}} = 7100 \pm 100$ K.

We caution that this is not a direct measure of the effective temperatures, rather it is a good estimate, which yields consistent results later in our analysis.

3.4 Photometric observations

As V4 has been known to be an eclipsing binary for quite some time (see, e.g., Kim et al., 2001; Arentoft et al., 2007), a lot of data have been collected through the years with the earliest stemming from 2005 and the most recent from 2017. In contrast we only recently identified V2032 as being an eclipsing binary and as such only the most recent (ground-based) photometry contains light curves of this system. Common for both systems is that the (ground-based) photometry is **CCD** observations in the Johnson system. Table 6 in Knudstrup et al. (2020) displays all the ground-based photometric data available for the two binaries – from the oldest taken with the Danish 1.54-metre to the latest stemming from the **NOT**. The observations made at the **NOT** using ALFOSC comprise all the photometric data available for V2032. The photometric data for V5 was obtained together with the earliest data for V4. All the photometric data were analysed using

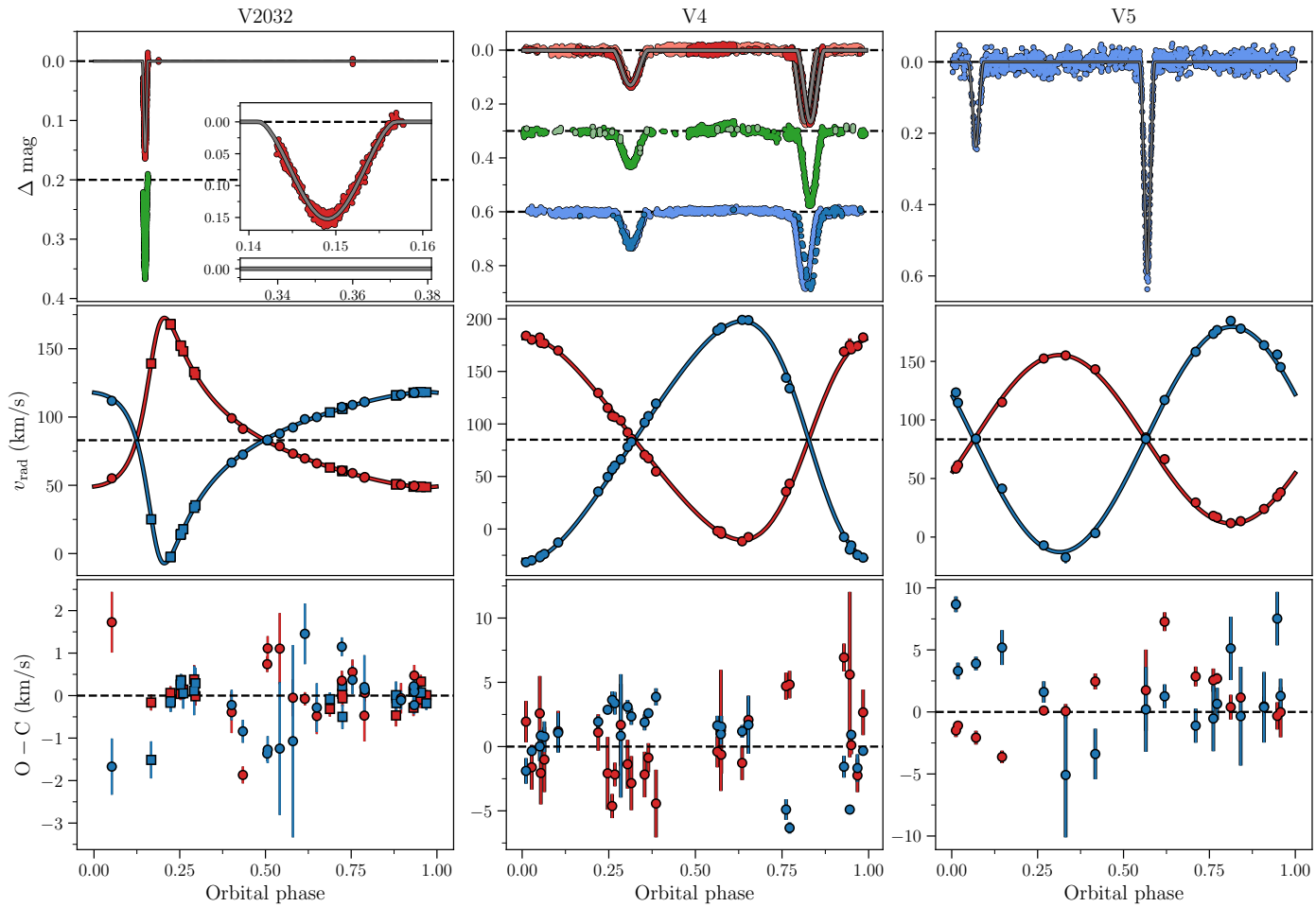


Figure 3.5 | Light and radial velocity curves. Top: Phase folded light curves of V2032, V4, and V5. For V4 we have light curves in I , V , and B marked with respectively red, green, and blue points. (Caption continued on next page.)

Figure 3.5 | Light and radial velocity curves. The green points are shifted by 0.3 mag and the blue points by 0.6 mag. Shown in the left panel are light curves for V2032 in I marked with red points and shifted by 0.2 mag in green is V . The insets show a close-up of the eclipse in I and the phase for the next conjunction, i.e., where we would expect a secondary eclipse if it was visible. In grey we have displayed a light curve model to show that our models suggest that there is only one eclipse in the system. The points in lighter colours (only for V4 and V5) are from the Danish 1.54-metre and the Flemish Mercator (see Table 6 in Knudstrup et al., 2020) and the darker points are from the other telescopes. For V5 we only show observations in B that we use in the analysis. *Middle:* Radial velocity curves for V2032, V4, and V5. The primary component is in all cases shown in red and the secondary in blue. The horizontal dashed lines denote the systemic velocity, $\gamma \sim 83$ km/s. *Bottom:* The calculated RVS subtracted from the observed ones.

the program DAOPHOT (Stetson, 1987) following the same procedure as in Grundahl et al. (2008). The Strömgren photometry presented here is the same as used in Arentoft et al. (2007) stemming from Grundahl et al. (2000). Additionally, we have obtained much more recent photometric data from [TESS](#) (Ricker et al., 2015).

3.4.1 Light curves

For the case of V₄ with observations from many different telescopes, the photometry has to be brought to match by eliminating instrumental differences between the telescopes as well as night-to-night variations, which also apply to the observations of V₂₀₃₂ and V₅. This was done by taking the mean of out-of-eclipse observations for a given night and subtract this value from the rest of the observations made that night. For observations where this was not possible (when all data points were obtained during an eclipse), the points were matched by eye. Figure 3.5 shows the phase folded light curves of V₂₀₃₂, V₄, and V₅. Evidently, the light curves of V₄ and V₅ are well-covered due to the amount of data available covering the entire phase in each, whereas the amount of observations of V₂₀₃₂ are much more sparse because of the more recent discovery of an eclipse in this system.

Something quite peculiar can be seen in the panel for V₄ in Figure 3.5. Evidently, the primary eclipse as observed by the Danish 1.54-Metre and the Flemish Mercator (published data from Arentoft et al., 2007, marked with lighter colours in Figure 3.5) is shifted from the more recent observations made with the IAC-80, LCOGT, and the [NOT](#) (darker points). These eclipse-timing variations (ETVs) are most likely caused by a third, but dimmer, companion in the V₄ system. Indications for a third body can also be seen in the [BFS](#) for V₄, where a small additional hump appeared around the systemic velocity for some epochs as in Figure 3.2, however, this is a somewhat more dubious indication.

3.4.2 TESS data

During our analysis of this cluster it was observed by [TESS](#). NGC 2506 was observed in [TESS](#)' Sector 7 and can be found in the 30 min. cadence full-frame images (FFIs) displayed in Figure A.7. From the FFIs we were able to recover the signals from V₄, V₂₀₃₂, and V₅ by making use of the [lightkurve](#) package (Lightkurve Collaboration et al., 2018). In Figure 3.6

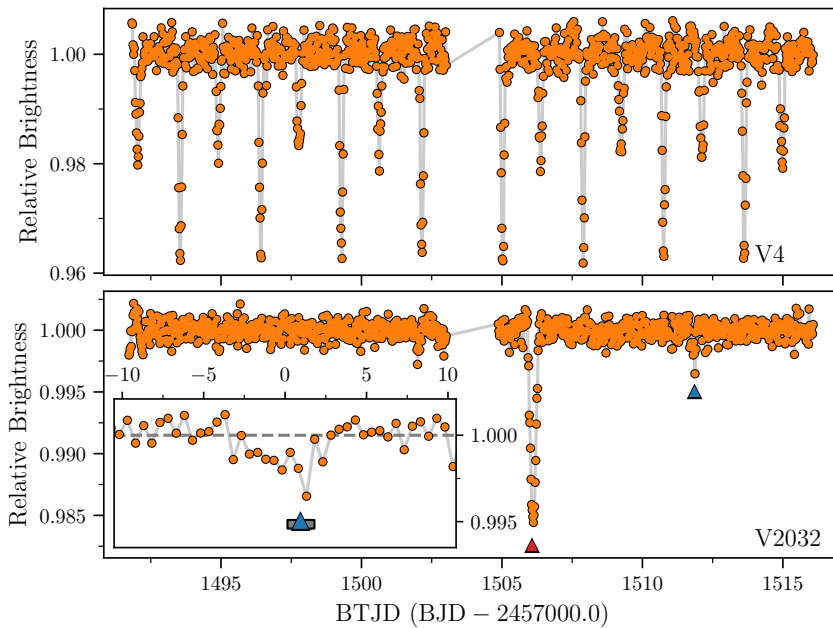


Figure 3.6 | TESS light curves. Light curves for V4 (top) and V2032 (bottom) extracted from the [TESS](#) FFIs (see Figure A.7). V4 is seen to eclipse multiple times as expected, given its ~ 2.9 d period, whereas V2032 eclipses only once, consistent with this system having an orbital period of ~ 27.9 d, which coincidentally is very close to that of [TESS](#)' orbit. The red triangle in the panel for V2032 shows the time for the primary eclipse and the blue triangle shows the expected time for the secondary eclipse (if visible) calculated from Equation (3.1). The inset is a zoomed view around the decrease in flux with the x-axis given in hours from the observed midpoint. The grey bar represents the smear in T_0^s (see Section 3.4.2.1).

we display the light curves for V2032 and V4. V5 is not shown, since we do not use the [TESS](#) light curve in our analysis.

For V4, we see multiple eclipses in Figure 3.6 and as expected V2032 only eclipses once due to the longer period. What is evident from Figure A.7, but also quite apparent when the depths seen in Figure 3.6 are compared to Figure 3.5, is how contaminated the signals are owing to the large pixel size of the [TESS](#) images (approximately 21 arcseconds per pixel; Ricker et al., 2015). Naturally, this is something we need to account for when these light curves are used to derive stellar parameters related to the depth of the eclipses.

We tried estimating the time of the secondary eclipse in V2032 as we were unsure whether this would actually be visible due to the orientation of the system. Given that the orbit of V2032 is very eccentric (see Table 3.3) the time for the secondary eclipse, T_0^s , is not just found half a period after the time for the primary eclipse, T_0^p , but can be found from (Sterne, 1940)

$$T_0^s - T_0^p = \frac{P}{\pi} \left(\frac{h(1-e^2)^{1/2}}{1-g^2} + \tan^{-1} \frac{h}{(1-e^2)^{1/2}} \right) + \frac{1}{2}P, \quad (3.1)$$

where $h = e \cos \omega$, and $g = e \sin \omega$. In Figure 3.6 we mark T_0^p with a red triangle and T_0^s as calculated from Equation (3.1) with a blue triangle. The calculated value for T_0^s seems to coincide with a decrease in flux.

3.4.2.1 Signal Significance

To assess the significance of the decrease in flux around T_0^s (blue triangle Figure 3.6) and a potential secondary eclipse in V2032, we first looked at the distribution of the data in Figure 3.6, with the exclusion of in-eclipse data, i.e., times around T_0^s and T_0^p , and tried to find a proper match. An Anderson-Darling test (Anderson and Darling, 1952) suggested that we could reject the null hypothesis of normality at a significance level of at least 1%, so clearly the data are not normally distributed. A distribution that accounts for the data much better is the Student's t distribution. Here we chose 18 degrees of freedom as this neatly captured the tails of our distribution. We then ran a Monte Carlo simulation of 5,000 draws from the Student's t distribution as a representation of our data to see how often we get a sequence of 12 (as in Figure 3.6) or more consecutive points below 1.0. This happens in around 15% of the cases. For each case of these 15% we estimated the median and created a Gaussian distribution from these. Here we find that at a 6.4σ level we can reject that these points would have a median equal to or below the median of the in-eclipse points in Figure 3.6, meaning that it is highly unlikely that this is caused by statistical fluctuations.

Finally, we looked at the timing of the signal, i.e., how likely is it that a signal of this duration (~ 6.0 h) would appear at T_0^s . Here we included a "smear" in T_0^s by incorporating the uncertainties in P , e , ω , and T_0^p (from the I column) in Table A3 in Knudstrup et al. (2020). This amounted to a spread of 1.7 h around T_0^s shown as the grey bar in Figure 3.6. Here we used 0.1 and 99.9 percentiles to be conservative resulting in a spread of 5.2 h. We then conducted another Monte Carlo simulation, where we picked out

times from the time series at random, placed our 5.2 h smear for T_0^s there, and checked if it overlapped with the observed 6.0 h signal. In 5,000 draws this happens in roughly 0.1% of the draws. Clearly, this signal cannot be ascribed to statistical fluctuations and the timing is suspicious to say the least. However, the contamination from nearby sources is so large in [TESS](#) (due to the pixel size as seen in Figure A.7) that we refrain from concluding that the observed signal in Figure 3.6 is in fact a secondary eclipse in V2032, especially seeing as our model suggests that a secondary eclipse should not be visible in the system (see Figure 3.5). Only observations around T_0^s from an instrument with a finer spatial resolution can resolve this. We therefore carry out the analysis of the system without employing additional constraints to this part of the [TESS](#) light curve.

3.4.2.2 Asteroseismology from TESS data

With the [TESS](#) data it was natural to look for solar-like oscillations in the [RGB](#) stars for which we have determined $\log g$ and T_{eff} through our spectroscopic analysis. Solar-like oscillations are standing acoustic waves stochastically driven by surface convection and are expected to be present in all cool stars with convective envelopes (Aerts et al., 2010). The reason why solar-like oscillations are interesting in the context of stellar clusters is that the oscillations a star displays are related to the physical properties of the star and are thus independent of distance, extinction, and chance alignment in space velocity making them a valuable tool for cluster membership determination (e.g., as for NGC 6791, NGC 6819, and NGC 6811 in Stello et al., 2011). Furthermore, the global seismic parameters, namely the [frequency of maximum power](#), ν_{max} , and the [large frequency separation](#), $\Delta\nu$, have been shown to scale with the mass and luminosity of the star (Kjeldsen and Bedding, 1995) meaning that these quantities can be inferred without invoking modelling of the stellar interior. These so-called asteroseismic scaling relations are, however, derived empirically necessitating thorough testing of their accuracy. The only way to test the seismically inferred masses is to compare them to model-independent masses derived from [DEBS](#). This can be done in star clusters, where masses derived from [DEBS](#) in the [turn-off](#) region can be extrapolated to the [RGB](#) and the [red clump](#) (e.g., Brogaard et al., 2012; Brogaard et al., 2015; Brogaard et al., 2016; Handberg et al., 2017).

Although it should be possible to detect solar-like oscillations in the 30 min. cadence [TESS](#) FFIs for [RGB](#) stars (e.g., Campante, 2017) at a magnitude of $y \sim 13.6$ mag these stars are, unfortunately, too faint. The

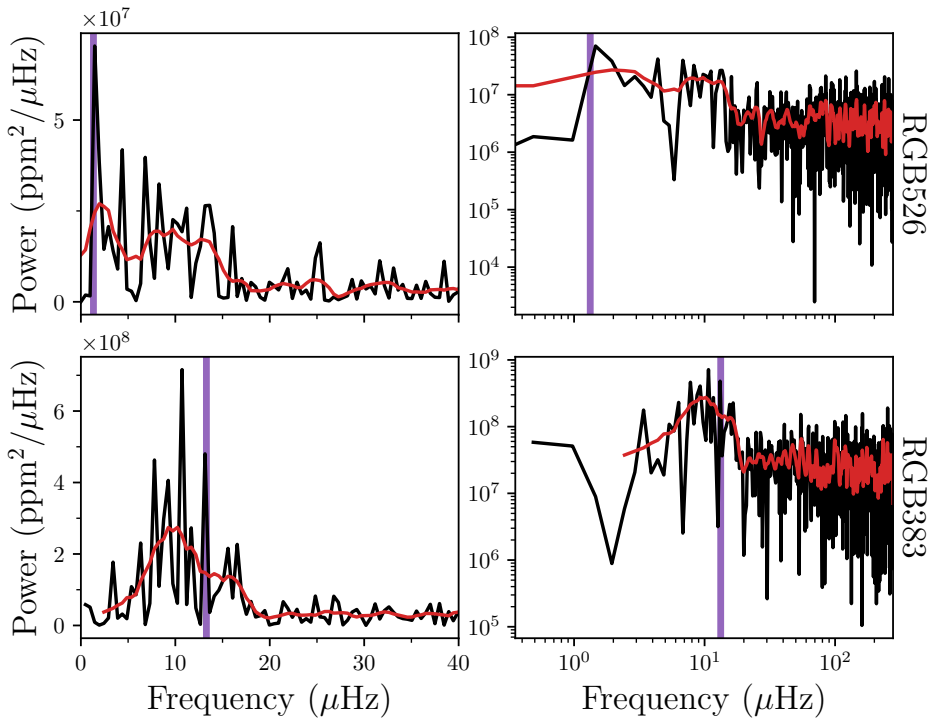


Figure 3.7 | Power spectra. Power spectra for the two [RGB](#) stars marked with purple stars in Figure 3.1 both in linear (left) and log-log plots (right). The black lines are the raw spectra and the smoothed spectra are shown in red. Top panels: The most luminous confirmed member, RGB526, of the cluster shows an excess of power at very low frequencies. Bottom panels: The third most luminous confirmed member, RGB383, shows a clear excess of power. The purple vertical lines denote ν_{max} inferred from extracting $\log g$ and T_{eff} from an [isochrone](#) fitted to the [CMD](#).

amplitude would therefore not exceed the noise level (Huber et al., 2011; Handberg and Lund, 2019) and indeed we found no evidence for solar-like oscillations in the [RGB](#) stars from the [TESS](#) FFIs.

For the classical pulsators, i.e., the δ Scuti and γ Dor stars, for which amplitudes in general are expected to be much higher (e.g., Uytterhoeven et al., 2011) we detect clear evidence for pulsations. In fact we detected clear pulsation signals for all the δ Scuti stars reported in Arentoft et al. (2007) as well for roughly half of the γ Dor stars. The γ Dor stars for which we did not detect a clear signal are mostly located towards the center of the cluster where the light is highly blended. In Table A1 in Knudstrup

et al. (2020) we list the frequency of maximum power, ν_{\max} , as well as the corresponding number of cycles per day for these. Light curves and power spectra can be found in Figures A3 and A4 in Knudstrup et al. (2020).

As mentioned our spectroscopic **RGB** stars are too faint to detect solar-like oscillations using the **TESS** data. We therefore turned towards the more luminous part of the **CMD** and looked for solar-like oscillations in all the confirmed members brighter than the aforementioned **RGB** stars. In the power spectra for two of the stars we saw an excess of power close to their expected ν_{\max} . The expected value for ν_{\max} is calculated by extracting stellar parameters from the **isochrones** in Figure 3.11 close to the stars' position in the **CMD**. These power spectra are displayed in Figure 3.7. For the brighter of the two stars, RGB526, the expected as well as the observed ν_{\max} were at a very low frequency, which makes it difficult to assess the validity of this signal. We therefore report this as an indication for solar-like oscillations in this star. However, for RGB383 for which the observed and expected ν_{\max} is at a higher frequency, we were much more convinced that what can be seen are solar-like oscillations. If this is in fact solar-like oscillations, this would (to our knowledge) be the first detection of solar-like oscillations in a cluster observed with **TESS**.

3.5 Orbital analysis: masses and radii

The orbital analysis of V2032 and V5 was done differently from V4, given the difficulties arising from the probable third companion. To obtain masses and radii of V2032 and V5 we used the program **e11c** (Maxted, 2016) to fit the light curves and the **RVS**. To obtain reliable estimates of the uncertainties we again used the program **emcee** (Foreman-Mackey et al., 2013) to do an **MCMC** sampling.

3.5.1 V2032

During our initial modelling of V2032 using the light curves in Figure 3.5, i.e., using the sparse Johnson photometry, it became evident that it was difficult to obtain consistent results for the radii between the two filters. We therefore also used the observations from **TESS** in Figure 3.6, which covers both ingress and egress of the primary eclipse, to obtain estimates for the radii. As mentioned the light curve in Figure 3.6 is from a blended signal (not from a companion to the binary, but from the nearby sources entering the large pixels), which causes a decrease in the depth of the eclipse. We

model this by including a contribution from a third (multiple) light(s) in `ellc` as $\mathcal{F}^c = l^c(\mathcal{F}^p + \mathcal{F}^s)$ with $\mathcal{F}^{p,s}$ being the flux from the primary or the secondary component (see Maxted, 2016). We estimated the contribution factor, l^c , by comparing the difference in magnitude during an eclipse in the `NOT` data (Figure 3.5) to the fractional change in flux in the `TESS` data (Figure 3.6). We found a value of $l^c = 7.6$ and we therefore adopted a Gaussian prior with this value and a width of 0.05 for this parameter during our `MCMC` run of the `TESS` light curve.

Seeing as we do not cover ingress in the light curves of V2032 in the ground-based observations, it is somewhat difficult to constrain the semi-major axis, a . However, the orbital parameters derived from our spectroscopic measurements in Table 3.3 constrain the product of the semi-major axis and inclination, i , through

$$a \sin i = \frac{P(1 - e^2)^{1/2}}{2\pi} (K^p + K^s). \quad (3.2)$$

We therefore used a Gaussian prior – in the sense $\mathcal{N}(\mu = \mu(a \sin i), \sigma = \sigma(a \sin i))$ – for this product in all cases (V , I , and `TESS`) created by drawing normally distributed samples from the parameters calculated by SBOP. Furthermore, we also incorporated Gaussian priors on the luminosity ratio of 0.89 ± 0.02 for V and 0.84 ± 0.02 for I and `TESS` (from the `BF` in Section 3.3.4). We used our estimates of the effective temperatures in Table 3.4 to estimate the surface brightness ratio, J . This was done by drawing normally distributed temperatures from these values, create corresponding Planck curves, which we multiplied by the filter transmission curves in V and I , respectively, and take the ratio between the curves resulting from each star in a system to obtain values of 1.38 ± 0.11 and 1.25 ± 0.07 . These values constituted our Gaussian priors for J , where we for each temperature draw then calculated J in the same way. We used the same value for I in the `TESS` fit due to the similarity in the passbands. The reason for adopting these constraints is that the light curves alone are not informative enough to yield fully consistent results.

For all light curves we adopted a quadratic limb darkening law with coefficients estimated using $\log g = 3.7$ dex, and $[\text{Fe}/\text{H}] = -0.3$ dex for both stars and $T_{\text{eff}}^p = 6600$ K and $T_{\text{eff}}^s = 7100$ K. We used $\xi = 2$ km/s for the `micro-turbulence`. The linear, c_1 , and quadratic, c_2 , limb darkening coefficients were found from tables by Claret (2000, 2017) for the Johnson and `TESS` filters, respectively, on which we placed Gaussian priors. We ran all our `MCMCs` with 100 walkers and for each of these we drew 20,000 times and applied a burn-in of 10,000, i.e., we rejected the first 10,000 steps

Table 3.4 | Key parameters. Key stellar parameters for the DEBS. The values for the masses and radii of V2032 and V5 are the medians and the uncertainties are from the highest posterior density (HPD) interval at a level of 68% for V2032 and V5. The results for V4 are from our DE-MCMC analysis (see Section 3.5.3.1). The effective temperatures for the individual components of V2032 and V4 are calculated from the spectral energy distributions in Section 3.3.5.

	V2032	V4	V5
M^p (M_\odot)	1.521 ± 0.005	$1.478^{+0.006}_{-0.007}$	0.945 ± 0.012
M^s (M_\odot)	1.504 ± 0.005	1.250 ± 0.010	$0.707^{+0.013}_{-0.009}$
R^p (R_\odot)	$3.10^{+0.07}_{-0.20}$	$2.300^{+0.013}_{-0.014}$	$0.68^{+0.22}_{-0.15}$
R^s (R_\odot)	$2.44^{+0.07}_{-0.10}$	$1.534^{+0.019}_{-0.018}$	$0.61^{+0.17}_{-0.06}$
\bar{T}_{eff}^p (K)	6560 ± 100	6830 ± 100	5700 ± 400
T_{eff}^s (K)	7100 ± 100	6830 ± 100	4940^{+340}_{-190}

of each walker. In Table 3.4 we display our final results for the masses and radii of the components, which we have created by drawing from the posteriors of our MCMC for each passband in Table A3 in Knudstrup et al. (2020) and created a joint posterior.

3.5.2 V5

For the modelling of V5 we employed the same strategy as for V2032 by using a prior on $a \sin i$ from Equation (3.2) and we used a Gaussian prior for the luminosity ratio, where we found $L^s/L^p = 0.36 \pm 0.03$ (stemming from the BF in Section 3.3.4). Again we adopted a quadratic limb darkening law using coefficients from the table in Claret (2000) and included them with Gaussian priors. As before the values and uncertainties are listed in Table 3.4. To get an estimate of the temperatures we drew uniformly distributed temperatures for both components, $\mathcal{U}(a, b)$ with $a = 4200$ K and $b = 6200$ K, which we then translated into a surface brightness ratio in B again using a filter transmission curve. The results for V5 are summarised in Table A3 in Knudstrup et al. (2020) with key parameters in Table 3.4.

3.5.3 V4

As mentioned, we strongly suspect a third body to be present in V4, which causes the shift we see in the eclipse times in Figure 3.5. We therefore

dealt with this system in a manner different to that for V2032 and V5. First we tried dividing the data into different intervals in time so that we only used spectroscopic and photometric data obtained within a relatively short time of each other in our fits. This was done by combining photometric data from the Danish 1.54-metre and the Mercator telescope (Table 6 in Knudstrup et al., 2020) with spectroscopic data from UVES only (Table 3 in Knudstrup et al., 2020), as well as a fit using the same photometric data with the inclusion of spectroscopic data from GIRAFFE. We also tried combinations that included all the spectroscopic data, but only included the photometry from IAC-80, LCOGT, and NOT as well as one that excluded the photometric data from NOT. All of these fits were performed using JKTEBOP (Southworth, 2013) and we invoked the constraints on the luminosity ratio of 0.40 ± 0.02 , 0.39 ± 0.02 and 0.40 ± 0.02 for the fits using data in V , I , and B , respectively.

The reason for carrying out all of these different fits is that we wanted to see how consistent our results would be if we ignored the ETVs and treated the system as only being comprised of two bodies. We prefer the solutions that utilise as much of the data as possible, but still avoid including data with variations in the eclipse times. Therefore we report the results for two of the aforementioned fits that both made use of all the spectroscopic data; the one that only includes the newer photometry, i.e., from the IAC-80, LCOGT, and NOT, and the one using the older photometric data from the Danish 1.54-metre and the Mercator. The results for the masses and radii for these five different runs can be found in Table A4 in Knudstrup et al. (2020). Our results here are in reasonable agreement, but they are not completely consistent and it would therefore be interesting to see what the consequences of not just treating the outer companion as a nuisance would be.

3.5.3.1 Three-body solution for V4

Therefore, we did a full three-body solution of the system following the approach in Orosz et al. (2019) using the ELC code (Orosz and Hauschildt, 2000) to model the light and velocity curves. To sample the parameter space we used the Differential Evolution MCMC (DE-MCMC) algorithm (Ter Braak, 2006). Our first runs resulted in a radius for the secondary component that was significantly larger ($R^s \sim 1.74 R_\odot$) than that from our JKTEBOP runs.

It is not unusual to have an inflated secondary component in close-in binaries (e.g., Brewer et al., 2016; Sandquist et al., 2016), which can be explained by magnetic activity inhibiting convection. Given the smaller

mass of the secondary component, it has a larger convective envelope, which generates strong magnetic fields. In turn these magnetic fields slow down the convective motion and thus make convection less effective. As a result the star has to expand to radiate away the excess heat that can not be transported by the inefficient convection, leading to radii increased by as much as 10% above the expected theoretical value (Torres et al., 2006). Radius inflation due to convective inhibition could therefore play a role in the secondary component of V₄, however, it does not explain the discrepancy between the results presented above and those stemming from the three-body fits.

We were able to identify that the discrepancy between the results were caused by the limb darkening coefficients. In our JKTEBOP runs these were fixed, which underestimates systematic errors, whereas in our DE-[MCMC](#) runs we sampled for these coefficients using the formulation in Kipping (2013b), but with the result that they would wander into a physically unrealistic territory. We therefore made a range for the coefficients to sample from, limited by the values we found for $\log g$ (± 0.05 dex) and T_{eff} (± 100 K) in our previous runs and for [Fe/H] (± 0.1 dex) based on our analysis of the [RGB](#) stars. Again we used values from Claret (2000, 2017) and invoked a constraint on the luminosity ratio of $L^s/L^p = 0.40 \pm 0.02$.

The results for the masses and radii from the DE-[MCMC](#) were $M^p = 1.478_{-0.007}^{+0.006} M_{\odot}$, $M^s = 1.250 \pm 0.010 M_{\odot}$, $R^p = 2.300_{-0.014}^{+0.013} R_{\odot}$, and $R^s = 1.534_{-0.018}^{+0.019} R_{\odot}$ for the primary and secondary component. Evidently, the secondary component is still slightly inflated compared to the results from JKTEBOP and compared to the theoretical models in Figure 3.8, but overall the results are in much better agreement. Our final results for the masses and radii for the primary and secondary components of V₄ are listed in Table 3.4. All other parameters form the fit can be found in Table B.1.

3.5.3.2 The outer companion in V₄

Our models suggest that the body orbiting the inner binary is in an eccentric ($e \sim 0.5$) 443 d orbit. From our modelling the mass of the third component is fairly well-determined, but as we have very little information of the radius, we are only able to place an upper limit of the amount of light this third body contributes to the system. This amounts to some 2% of the total light. Given the mass suggested by our models, this can come about by having a very hot, compact object, i.e., a white dwarf, but it is also consistent with a [MS](#) star similar to the components of V₅. Therefore, for a given solution we imposed a χ^2 penalty if the mass and radius of the

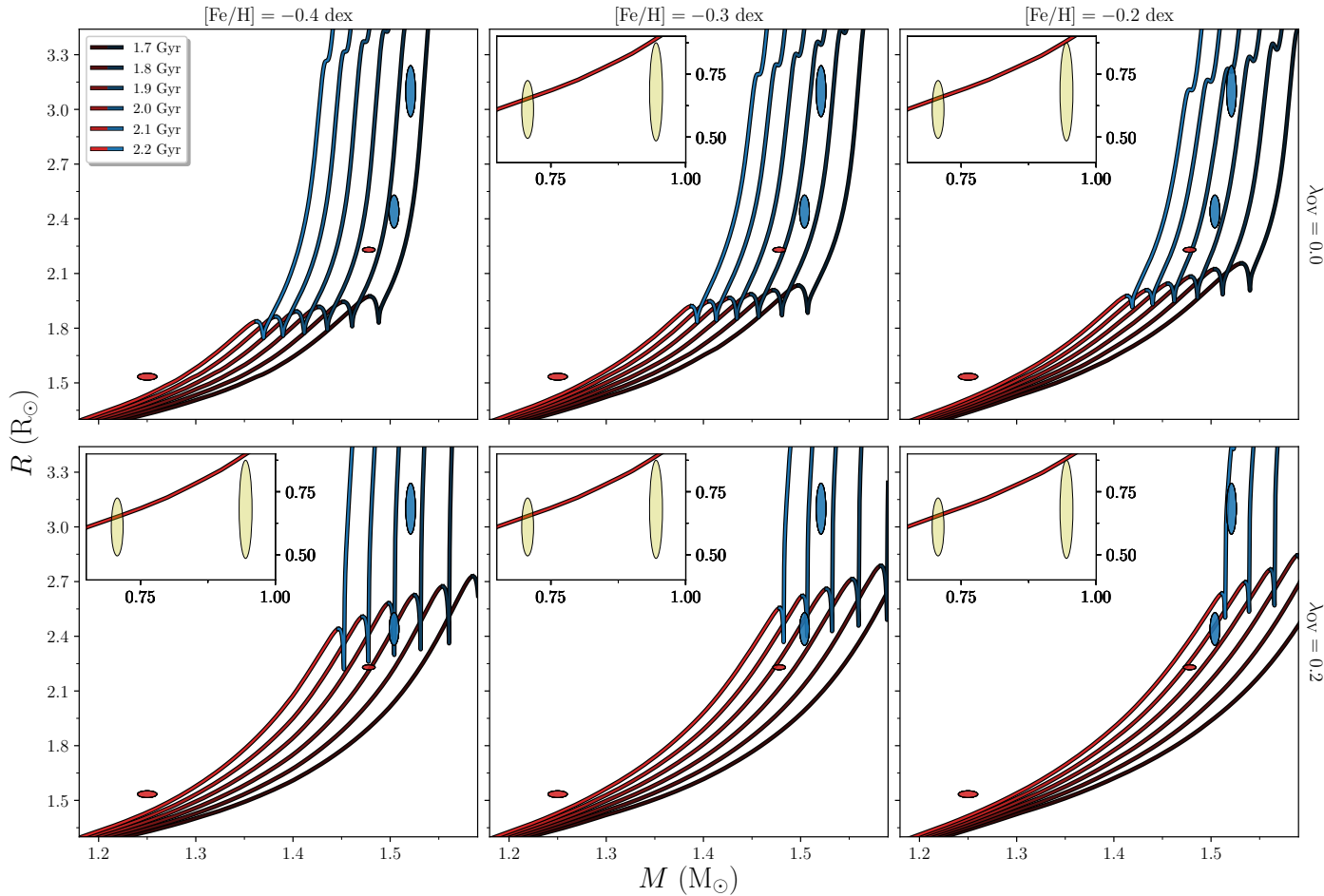


Figure 3.8 | Mass-radius diagrams. MR diagrams for the components in V2032, V4, and V5 marked with blue, red, and yellow 1σ ellipses, respectively. (Caption continued on next page.)

Figure 3.8 | Mass-radius diagrams. The red (before the terminal age MS) and blue (after) coloured lines are BaSTI [isochrones](#) at different ages. Columns separate the [isochrones](#) in metallicity and rows are for different assumptions on model physics, where the [isochrones](#) in the bottom row take [convective core overshooting](#) into account. Overshooting beyond the Schwarzschild boundary is parametrised in terms of the pressure scale height, H_P , as $\lambda_{OV} H_P$, where λ_{OV} is set to 0.2 for models that include convective core overshooting. None of the models treat diffusion or mass-loss. $[\alpha/\text{Fe}] = 0.0$ dex for all models. Mass-temperature diagrams are available in Fig. A2 in Knudstrup et al. (2020), showing that the effective temperatures and the theoretical values from the BaSTI [isochrones](#) are consistent.

third star fell outside the region in the mass-radius plane defined by BaSTI (a Bag of Stellar Tracks and Isochrones; Hidalgo et al., 2018) **isochrones** for a **MS** star. From this we find the mass to be $M^t = 0.74 \pm 0.03 M_\odot$ and if the star were to be a (well-behaved) **MS** star its radius would be similar to that of the components in V5.

3.6 Cluster parameters

To obtain cluster parameters for NGC 2506 we used the newly updated BaSTI **isochrones**. We compare these models to the masses and radii of the **DEBS**, the observed cluster sequence in Strömgren photometry, and the properties we derived for the spectroscopic **RGB** stars as well as the observed properties of the **RGB** stars potentially displaying solar-like oscillations.

3.6.1 Mass-radius diagrams

In Figure 3.8, we compare our measurements of the masses and radii of the 6 stars in V2032, V4, and V5 listed in Table 3.4 to the BaSTI **isochrones**. The models in the top row do not include **convective core-overshooting**, whereas the models in the bottom row do. We have colour-coded the **isochrones** so that blue corresponds to stars found after the terminal age **MS** (TAMS), where the components in V2032 are most likely found, and red denotes stars before the TAMS. None of the models treat atomic diffusion or mass loss (see Hidalgo et al. (2018) for details regarding the input physics).

Our analysis of the **RGB** stars suggested that the metallicity or more precisely the iron abundance is around -0.40 dex and with a value of $[\alpha/\text{Fe}] = 0.10$ dex, but since the **isochrone** grid we used does not include α -enhanced **isochrones**, we accounted for this by making use of the formula for the actual metallicity in Sharma et al. (2019)

$$[\text{M}/\text{H}] = [\text{Fe}/\text{H}] + \log(0.694 \cdot 10^{[\alpha/\text{Fe}]} + 0.306), \quad (3.3)$$

which was originally formulated by Salaris and Cassisi (2005). In the present case the metallicity would be $[\text{M}/\text{H}] = -0.29 \pm 0.12$ dex. We therefore used **isochrones** with an iron abundance close to this value to infer the age of the cluster, i.e., the middle panels in Figure 3.8. Evidently, the inclusion of **convective core-overshooting** has significant impact on the evolutionary stage of the secondary component in V2032 and the primary component of V4. In the non-overshoot scenario the primary component of V4 is found at a post **MS** evolutionary stage, but clearly the **CMD** in Figure 3.9 suggests that

Table 3.5 | Cluster parameters for NGC 2506. The age is determined from the binaries in Section 3.6.1. The metallicity and α -enhancement are based on the RGB stars in Section 3.3.2, where we have calculated a weighted average and then added the systematic uncertainties (0.1 dex) in quadrature. Again using these stars we estimated the reddening in Section 3.3.2.1. The distance is estimated from the *Gaia* data in Section 3.7. **Notes.** ^(a)From Equation (3.3).

NGC 2506	
t	2.01 ± 0.10 Gyr
[Fe/H]	-0.36 ± 0.10 dex
[α /Fe]	0.10 ± 0.10 dex
[M/H] ^(a)	-0.29 ± 0.12 dex
r	3.101 ± 0.017 kpc
$E(b - y)$	0.057 ± 0.004 mag
$E(B - V)$	$0.080^{+0.005}_{-0.006}$ mag

the component is still on the MS and therefore models including overshoot should be favoured.

Given that the stars in V2032 are at such an auspicious phase (as well as considering the difficulties for the radius of the secondary component in V4 and given the less informative stage of the components in V5) our age estimate is mostly hinged on this system and the primary component of V4. It is clear that these three components completely lock the **isochrones**, allowing for extremely precise age determination. It is also clear that if both components of V2032 are found after the TAMS, a smaller value than 0.2 is needed for λ_{OV} , and as such V2032 and V4 can be used to not only distinguish between models with and without overshoot, but also assess the amount of overshoot needed quite precisely. However, the BaSTI **isochrones** only have the two options, 0.0 or 0.2.

Our age estimate is based on the **isochrones** in Figure 3.8 with a metallicity of -0.3 dex and which include **convective core-overshooting**. From these we estimate the age of the cluster to be $t = 2.01 \pm 0.10$ Gyr, where the main source of error comes from the uncertainty of 0.1 dex on [Fe/H]. As argued the value for λ_{OV} should probably be a bit lower than 0.2 to bring the primary component of V4 and both components of V2032 to lie on the same **isochrone**. A crude estimate of how much smaller λ_{OV} should be is to consider the hooks on the **isochrones** in the middle panels ([Fe/H] = -0.3 dex) of Figure 3.8. The hook in the lower panel ($\lambda_{\text{OV}} = 0.0$)

should be decreased by around $0.1 R_{\odot}$ to capture all three stars and the difference between the hook in the top panel and the bottom is about $0.5 R_{\odot}$, which means λ_{OV} should be decreased by about 20%, i.e., to a value of around 0.16. There is roughly a 0.2 Gyr difference in the age estimate between the two middle panels meaning that a change of 20% in λ_{OV} would make the cluster around 0.04 Gyr younger. The best age estimate of the cluster with core-overshoot adjusted to match both the primary star of V4 and both components of V2032 would thus be 2.01 Gyr, since the best fitting [isochrone](#) without such a correction (in the lower middle panel of Figure 3.8) is 2.05 Gyr. Note the error for the age is the internal error and as such does not include deficiencies in the stellar models.

3.6.2 The observed cluster sequence

From the MR diagrams in Figure 3.8 it was clear that the primary component of V2032 should be found at a phase of rapid expansion and cooling. However, it is not as clear whether the secondary component is also found at this phase. Taking [isochrones](#) with $[Fe/H] = -0.3$ dex as the ones most representative of the cluster metallicity, Figure 3.8 shows that the primary component of V2032 is definitely at a stage of rapid expansion, regardless of whether [convective core-overshooting](#) is included or not. The secondary could be located on either side of the TAMS depending on the inclusion of overshooting and also the value used for λ_{OV} , even for the value available in the grid the secondary component could still be located before or after TAMS.

In the [CMD](#) in Figure 3.9, we show the [Gaia](#) proper motion members (see Section 3.7) compared to the BaSTI [isochrones](#), where we for each metallicity only show the two ages that best capture the components of V2032 and the primary component in V4 in Figure 3.8. In the [CMD](#) we have decomposed the light from the binaries V2032 and V4. This was done by using the luminosity ratios in V of 0.89 ± 0.02 and 0.40 ± 0.02 , respectively, with the observed G magnitudes and translate this into a G magnitude for each component. The colours were calculated from the surface gravities (from the radii and masses) and effective temperatures in Table 3.4 and the reddening and metallicity in Table 3.5 from which we calculated the bolometric corrections, $BC_{G_{RP}} - BC_{G_{BP}} = G_{BP} - G_{RP}$, from Casagrande and Vandenberg (2018a,b). The errors were created from drawing normally distributed values 500 times for each parameter that enters, then calculating the magnitude and colour, and subsequently measuring the spread of the resulting distributions. In Figure 3.9 these are shown as blue and red dots

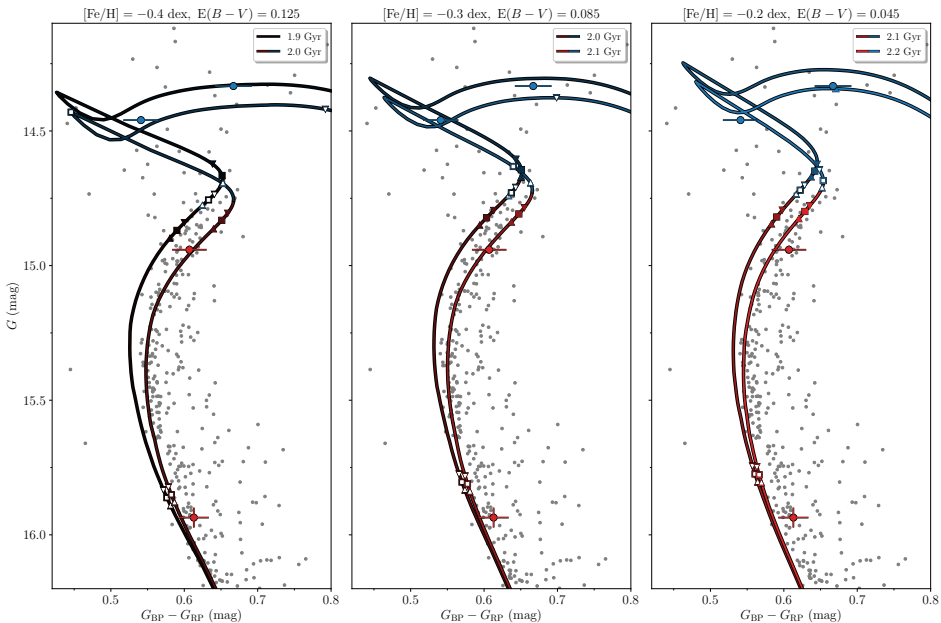


Figure 3.9 | Colour-magnitude diagrams. The [CMD](#) of NGC 2506 in [Gaia](#) colours compared to BaSTI [isochrones](#) at different metallicities and assuming different values for $E(B - V)$ and consequently slightly different values for μ for each metallicity. The colour coding for the [isochrones](#) is the same as in Figure 3.8. The blue and red dots with errorbars are the components of V2032 and V4, respectively, which have been decomposed by firstly calculating the G magnitudes based on the luminosity ratios in V of 0.89 ± 0.02 respectively 0.40 ± 0.02 . The colour for each star has been calculated from the bolometric corrections from Casagrande and VandenBerg (2018a,b) using the radii and effective temperatures in Table 3.4 and the colour excess from Table 3.5. The squares denote interpolated values for the masses in the [isochrones](#) closest to those in Table 3.4 and the upwards (downwards) facing triangles mark the lower (upper) 1σ level. For the secondary components in both V2032 and V4 we have added white markers to distinguish these points from those corresponding to the primary components. For the [isochrones](#) where the interpolated mass corresponds to the observed evolutionary stage of V2032, we match them to these values (to the extent possible). For [isochrones](#) where this is not possible we match them to the primary component of V4. Note that for some [isochrones](#) the markers for the interpolated values for the primary and secondary components are not visible. They are either towards or on the [RGB](#).

with errorbars for V2032 and V4, respectively. As argued the primary component of V4 is clearly found on the [MS](#) in the [CMD](#), which from the MR diagrams is only consistent with the inclusion of overshooting. Thus, we only consider those [isochrones](#) here. Adding to this is that the [isochrones](#) without overshooting clearly diverged from the observed cluster sequence.

We used the radii and effective temperatures for V2032 and V4 in Table 3.4 to calculate the distance to the cluster. This was done by first calculating the total luminosity of the system, $L^{\text{tot}} = L^{\text{p}} + L^{\text{s}}$, translating that to an absolute magnitude, M_V , to get the distance modulus, $\mu = m_V - M_V$, while again accounting for the extinction, A_V . We did a Monte Carlo simulation with 5,000 draws, where in each draw we drew normally distributed values (as in Section 3.5.1) for the effective temperatures, radii, apparent V -magnitude, and reddening. The resulting values for the distance was 2.92 ± 0.12 kpc and 3.17 ± 0.08 kpc for V2032 and V4, respectively.

We calculated and applied the true distance modulus, $\mu = 5 \log r - 5 + A_V$ with $A_V = 3.1 \cdot E(B - V)$ being the interstellar absorption and $r = 3.04$ kpc being the mean of the values for the distance calculated from V2032 and V4. For each pair of [isochrones](#) in Figure 3.9 we assumed values for $E(B - V)$ of 0.125, 0.085, and 0.045 and values for the metallicity of -0.4 dex, -0.3 dex, and -0.2 dex, respectively.

On each of the [isochrones](#) we have highlighted the interpolated mass from Table 3.4 with blue squares for the components in V2032 and red for those in V4. The upwards facing triangles denote the 1σ lower limit and the downwards facing triangles mark the upper limit. To make it easier to distinguish between the components we have added smaller white markers on top of the symbols for both of the secondary components.

3.7 *Gaia* distance to the cluster

With the [Gaia](#) DR2 (Gaia Collaboration et al., 2018) data we can estimate the distance to the cluster with great precision. However, estimating the distance, r , to the cluster is not as simple as taking the inverse of the parallax, i.e., $r = 1/\varpi$. This is because the measured parallax can be zero or even negative, while the distance is, of course, constrained to be positive (Luri et al., 2018). Furthermore, the distance has a non-linear relationship to the measurement $1/\varpi_{\text{True}}$. To resolve this we therefore follow the approach recommended by Luri et al. (2018), which is to treat this as a Bayesian inference problem.

First, we selected stars within a 1 degree radius of the cluster. We then located the cluster in proper motion space as shown in the top left corner of

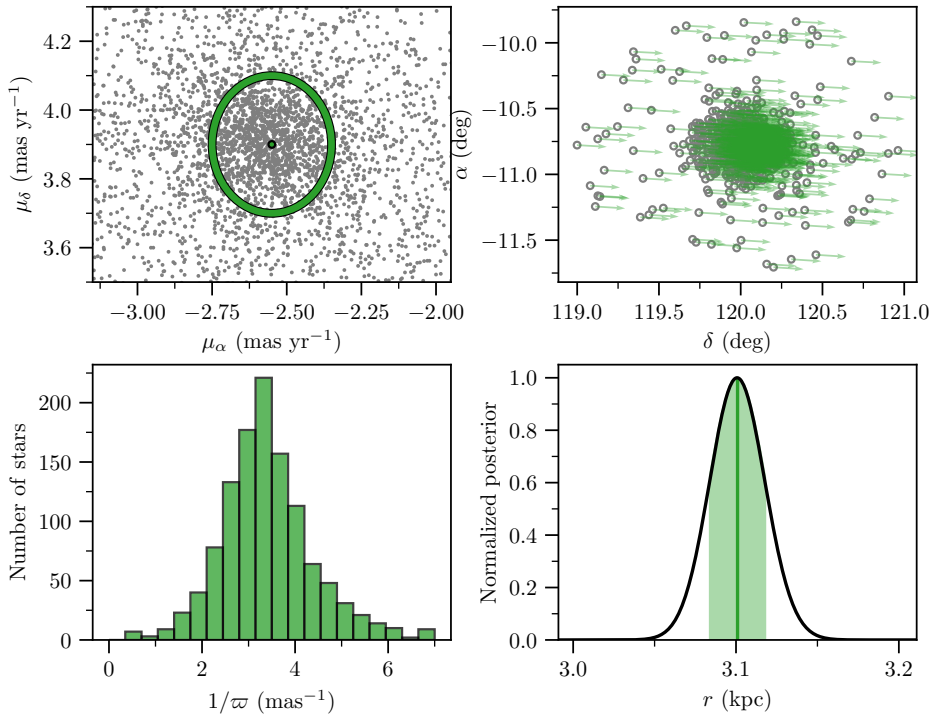


Figure 3.10 | Gaia view of NGC 2506. *Top left:* Stars in NGC 2506 as seen in proper motion space by *Gaia*, where the ring marks the stars included in the distance estimate. *Top right:* Stars in α, δ with their proper motion vectors drawn (scaled for clarity). *Bottom left:* Histogram of $1/\varpi$ for the stars used in the distance estimate. *Bottom right:* The resulting posterior from Equation (3.5).

Figure 3.10. Here we located the densest region, which should correspond to NGC 2506, and deemed stars within 0.2 mas/yr of the center of this dense region to be members of NGC 2506 (as a sanity check we plot the selected stars in α, δ in the top right corner with their proper motion vector scaled for clarity). From this sample we only included the stars with relatively well-determined parallaxes, i.e., $|\sigma_\varpi/\varpi| < 0.25$. These are displayed in the histogram of Figure 3.10.

We adopt the exponentially decreasing space density prior in distance

$$P(r|L) = \begin{cases} \frac{1}{2L^3} r^2 \exp(-r/L) & \text{if } r > 0 \\ 0 & \text{otherwise,} \end{cases} \quad (3.4)$$

where L is a length scale to the cluster set to 3.55 kpc (Anthony-Twarog et al., 2016). We estimate the likelihood as

$$P(r_i | \{\varpi\}, \{\sigma_\varpi\}, L) = \prod_{n=1}^N \int \frac{1}{\sqrt{2\pi}\sigma_{\varpi_n}} \times \exp \left[-\frac{(\varpi_n - \varpi_{\text{zp}} - 1/r_i)}{2\sigma_{\varpi_n}^2} \right] dr_i, \quad (3.5)$$

where the subscript n refers to the parallax and uncertainty in parallax of the n th star in the histogram of Figure 3.10 and r_i is the proposed distance to the cluster, i.e., we created linearly spaced values for r in the range 2 to 4.5 kpc. ϖ_{zp} is the global offset in parallax of -0.029 mas reported in Bailer-Jones et al. (2018), which we adopt. Here we have assumed that all N parallax measurements are independent and exploited that the angular extent of the cluster is small. The resulting posterior can be seen in the lower right panel of Figure 3.10, where we have displayed our result. The distance we found was $r = 3.101 \pm 0.017$ kpc. This value is in good agreement with the value of 3.04 kpc we obtained from the binaries and in excellent agreement with the value of 3.112 kpc reported in Cantat-Gaudin et al. (2018). Omitting the offset from Bailer-Jones et al. (2018) in our analysis resulted in a distance of $r = 3.41 \pm 0.02$ kpc. An offset of around -0.05 mas was reported in Khan et al. (2019) when comparing the *Gaia* distances to stars in the *Kepler* field with distances determined using asteroseismology. This means that in addition to the statistical error of 0.017 kpc that we report there is potentially a systematic error, which is significantly larger.

Finally, we note that the *Gaia* data can be used to identify potential δ Scuti and γ Dor stars in clusters. This is done by first identifying cluster members as in Section 3.3.5 and Figure 3.10, and then by plotting their uncertainty in magnitude against their magnitude. This is shown for the *Gaia* G magnitude in Figure 3.11, where a clear spread in magnitude is seen at the place where these stars reside.

3.8 Discussion

NGC 2506 is a very interesting open cluster, harbouring a multitude of rare stellar systems. Over the years we have amassed a considerable amount of data for this cluster. Data stemming from many different telescopes and instruments, both ground-based and space-based. The spectroscopic data of the RGB stars allowed us to determine the metallicity of the cluster with

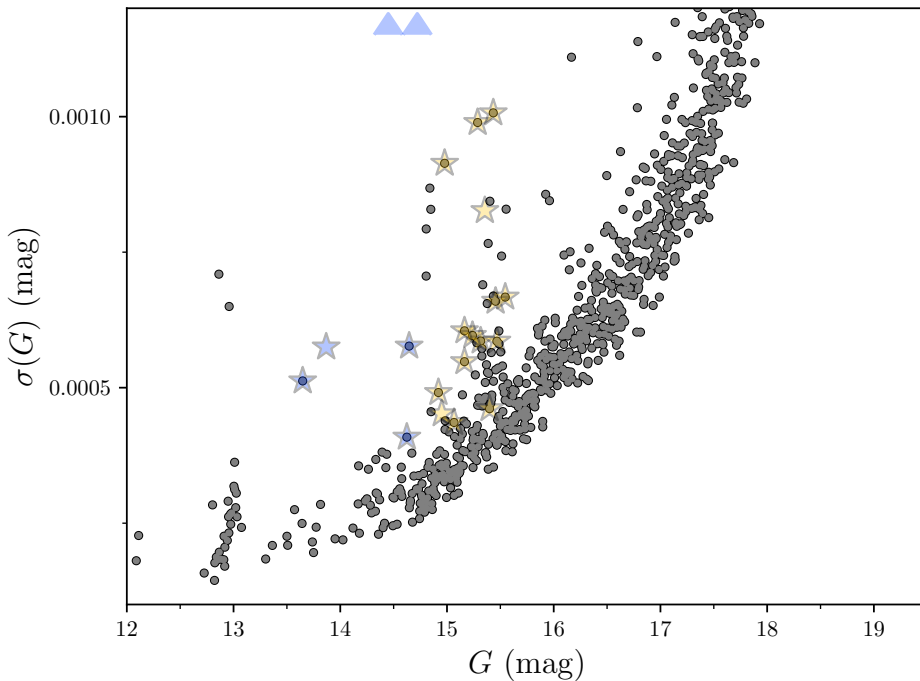


Figure 3.11 | Gaia photometric variability in NGC 2506. Cluster members (Section 3.3.1) with the uncertainty on their *Gaia* G magnitude against their G magnitude. The δ Scuti and γ Dor stars from Arentoft et al. (2007) have been marked with respectively blue and yellow stars, but here they are transparent to make the underlying spread visible, which suggests that there are more of these type of stars in the cluster. The upwards pointing triangles denote the position of two δ Scuti stars at $(G, \sigma(G)) = (14.722, 0.002)$ and $(G, \sigma(G)) = (14.450, 0.003)$.

high precision. This narrows the parameter space of the possible [isochrones](#) to choose from in the MR diagrams as well as in the [CMD](#), enabling us to put a tight constraint on the age of the cluster.

Accurately determining the parameters of a cluster such as NGC 2506 is extremely valuable for several astrophysical reasons. First off, modelling stellar evolution is, of course, relying on having accurately determined parameters for a large number of stars to test against. Secondly, if the power excess seen in Figure 3.7 is indeed due to solar-like oscillations, NGC 2506 could help to test the asteroseismic scaling relations by comparing the results for the dynamically inferred properties from the binaries to those that can be inferred from [asteroseismology](#). Furthermore, NGC 2506 can

be used as a benchmark for modelling γ Dor and δ Scuti stars, where again age and metallicity are key parameters, but here we would also have a firm grasp on the masses and radii of these stars. The power spectra for the δ Scuti stars in Figure A3 in Knudstrup et al. (2020) look very convincing in terms of detecting oscillations, whereas the power spectra for the solar-like oscillators in Figure 3.7 and for some of the γ Dor stars in Figure A4 in Knudstrup et al. (2020) are a bit more dubious. This is why it would be interesting to see what could be achieved with difference imaging specifically designed for clusters in the [TESS](#) data (e.g., Bouma et al., 2019) as this might significantly enhance the signal for the variable stars.

3.8.1 V4

V₄ is a testimony to the fact that sometimes acquiring more data can lead to unforeseen challenges and serendipitous discoveries. The exact nature of the third component of V₄ is to some extent still uncertain. As mentioned the mass is constrained to be around $0.60 M_{\odot}$, but we really have no constraints on its radius, except that our models suggested that the star should only contribute about 2% to the total light of the system. Having a body that contributes about 2% of the total light in the system is consistent with it either being a hot and compact object or a [MS](#) star similar to the components of V₅. If the third companion is a white dwarf its (final) mass suggests that the initial mass was around $3 M_{\odot}$ (e.g., Cummings et al., 2018). Given the cluster age of 2.05 Gyr, a $3 M_{\odot}$ star would have had sufficient time to evolve into a white dwarf (e.g., Kippenhahn et al., 2013). Looking through a table of nearby white dwarfs by Giammichele et al. (2012) with masses similar to that of the companion and with ages in the range 1.3-1.7 Gyr, we find that if the star is a white dwarf it should have a temperature of around 8,000 K (or hotter if the white dwarf is younger). This is significantly hotter than the components of the inner binary and could therefore be detected as an excess flux in UV. However, we did not detect such an excess (see Section 3.3.5), which is not to say that a white dwarf can be ruled out, but it does speak in favour of the scenario with a V₅-like component to the inner binary.

Regardless of the size of the third companion, it is massive enough to influence the orientation of the orbit of the inner binary. The wobble around the barycenter induced by the orbit of the third component to the inner binary is sufficiently large with a sufficiently short period that [Gaia](#) will be able to detect it in the full astrometric data release. The diameter of this orbit is around 0.3 mas as seen in Figure 3.12. It is also interesting that

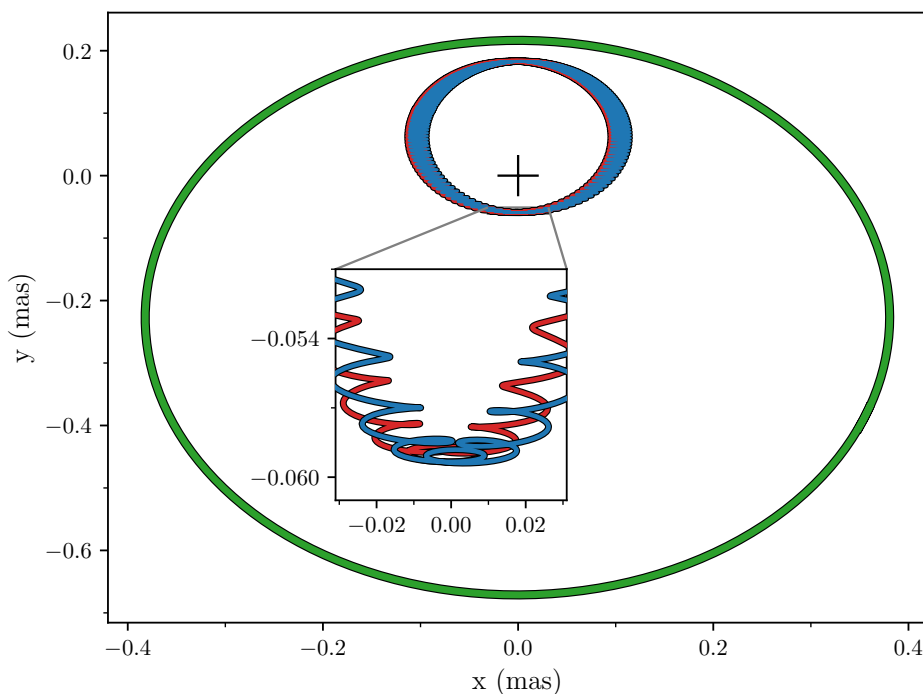


Figure 3.12 | The orbit of V4. Orbit of the V4 system if the system was viewed face-on. The red and blue lines denote the orbits of the primary and secondary component, respectively, and the green line marks the orbit of the tertiary component. The orbit around the barycenter (black plus) of the inner binary has a diameter of around 0.3 milliarcseconds and should thus be easily detectable with *Gaia*. This figure is created using REBOUND (with the IAS15 integrator; Rein and Spiegel, 2015) using the parameters in Table B.1.

given an inclination of around 90° (Table B.1) for the third body it could potentially at some point eclipse the stars in the inner binary. Observing this would be extremely valuable as this would yield the radius of this component, but it would also allow for a tighter constraint of the radii of the inner binary and ultimately the cluster parameters.

3.8.2 V2032

For V2032 more photometry of the system would really help solidify the measurements of the radii, especially observations around ingress of the primary eclipse with pre-ingress well covered could make a significant

improvement. What is perhaps even more interesting to investigate is the potential secondary eclipse seen in Figure 3.6. We have already assessed that this decrease in flux can not be assigned to statistical fluctuations and the timing of the signal is striking. The signal is, of course, dependent on the aperture mask chosen and diminishes with certain choices, however, this signal seems to persistently follow the primary eclipse. As our current models and data suggest that the secondary eclipse should not be visible, it would be extremely interesting to observe this system around T_0^s with an instrument with a better resolution to see whether a secondary eclipse can be detected. This could alter the inclination somewhat, which in turn would affect our radii, but it should not have major implications for the masses and thus would not change the cluster parameters drastically.

Given the strong constraints presented in this paper on the cluster metallicity, membership, distance and precision masses and radii for three eclipsing systems an obvious next step would be to explore the model parameters in greater detail, i.e., calculate models which include alpha enhancement and has a finer grid in the overshoot parameter, which could potentially be stronger constrained in this way.

3.8.3 Future TESS observations of NGC 2506

In the extended [TESS](#) mission the plan is for the spacecraft to revisit many of the already observed sectors and NGC 2506 should be observed again in [TESS](#)' Sector 34⁴ (primo 2021). This is extremely interesting for several reasons; firstly, we would acquire even more ephemerides for the V4 system, and might be able to place tighter constraints on the third body and we might be able to see if the potential secondary eclipse in V2032 persists (although as we have discussed we would probably require validation from instruments with higher spatial resolution). Secondly, the cadence of the FFIs in the extended mission will be changed from 30 min to 10 min, which could be of major importance for the detectability of solar-like oscillations further down the [RGB](#) (again the stars might be too faint), but a finer sampling will also aid in capturing the shape of the eclipses for the binaries. In addition, a new 20 s cadence mode will be opened for selected targets (as opposed to the current 2 min cadence mode).

⁴: <https://heasarc.gsfc.nasa.gov/cgi-bin/tess/webtess/wtv.py>

3.9 Conclusions

In this paper, we presented spectroscopic and photometric data of three detached eclipsing binaries – V2032, V4, and V5 – as well as spectroscopic data of four **RGB** stars; RGB231, RGB433, RGB913, and RGB2358. All of these stars are members of the open cluster NGC 2506 and we used the parameters derived from the data to determine the age and metallicity of the cluster. The spectroscopic data of the **RGB** stars allowed us to determine the metallicity of the cluster to be $[{\rm Fe}/{\rm H}] = -0.36 \pm 0.10$ dex with $[\alpha/{\rm Fe}] = 0.10 \pm 0.10$ dex. A value we used with our results for the masses and radii of the binaries to determine the age of the cluster to be $t = 2.01 \pm 0.10$ Gyr when we compared these results to the BaSTI **isochrones**. To properly model the cluster it is necessary to use models which include convective core-overshooting, although the value for the overshooting parameter of 0.2 available in the grid we used seems to be a bit too large. It should thus be possible to really quantify the value for the overshooting parameter in NGC 2506 using models specifically tailored to this cluster.

We found these values to be consistent with what is observed in the **CMD** of the cluster, which we have cleaned to only contain cluster members using **Gaia** DR2 data and additional spectroscopic observations. We find a very nice agreement between the distance to the cluster determined by **Gaia** and the distance we get from calculating the luminosity of the binaries V2032 and V4. We therefore conclude that the distance to the cluster is $r = 3.101 \pm 0.017$ kpc. Using the effective temperature of the **RGB** stars, we estimated the colour excess of the cluster to be $E(b-y) = 0.057 \pm 0.004$ mag, which is in good agreement with the values required to fit the model **isochrones** to the observed sequence.

We furthermore report on the possible detection of solar-like oscillations in two of the most luminous members of the cluster using data from **TESS**. Namely, the **RGB** stars we have dubbed RGB526 and RGB383, with the latter showing quite prominent features in the power spectra in Figure 3.7 around the expected ν_{\max} . If this detection is confirmed, it would to our knowledge be the first detection of solar-like oscillations in an open cluster detected by **TESS**. Much more prominent oscillations are seen in the power spectra of the δ Scuti stars (Figure A3 in Knudstrup et al., 2020) and for some of the γ Dor stars (Figure A4 in Knudstrup et al., 2020).

4

Asteroseismology of the Multiplanet System K2-93

As was discussed in Section 2.3, DEBS are not the only way we might obtain precise stellar parameters. We might also use [asteroseismology](#) to precisely determine the stellar mass and radius, and thus the density of the star. In this chapter we shall see how we might use this to constrain the orbital parameters for the planets orbiting the star.

Here we will be investigating the K2-93 (HIP 41378) system, which is a multiplanet system discovered by the [K2](#) mission and is harbouring (at least) five planets. The work reproduced in this chapter was originally published as

M. N. Lund, E. Knudstrup, V. Silva Aguirre, S. Basu,
A. Chontos, C. Von Essen, W. J. Chaplin, A. Bieryla, L.
Casagrande, A. Vanderburg, D. Huber, S. R. Kane, S. Albrecht,
D. W. Latham, G. R. Davies, J. C. Becker, and J. E. Rodriguez
(2019). “Asteroseismology of the Multiplanet System K2-93”.
Astronomical Journal 158.6, 248

The only alteration from the journal version is reformatting to match the layout of the thesis, except for Table 4.3 in which the orbital separation in AU has been removed. For this work I did and wrote the section on the transit fitting (Section 4.3.4.1) and the subsequent analyses constraining the periods (Section 4.3.4.2), the eccentricities (Section 4.3.4.3), and the velocity semi-amplitude (Section 4.4).

Summary of the Chapter

We revisit the analysis of the bright multiplanet system K2-93, discovered with data taken by the [K2](#) mission. This system contains five identified planets ranging in size from sub-Neptune to Jupiter size. The [K2](#) data available at the discovery of the system only showed single transits for the three outer planets, which allowed weak constraints to be put on their periods. As these planets are interesting candidates for future atmospheric studies, a better characterisation of the host star and tighter constraints on their orbital periods are essential. Using new data from the [K2](#) mission taken after the discovery of the system, we perform an asteroseismic characterisation of the host star. We are able to place strong constraints on the stellar parameters and obtain a value for the stellar mass of $1.22^{+0.03}_{-0.02} M_{\odot}$, a stellar radius of $1.30 \pm 0.01 R_{\odot}$, and an age of $2.07^{+0.36}_{-0.27}$ Gyr. Put together with the additional transits identified for two of the three outer planets, we constrain the orbital periods of the outer planets and provide updated estimates for the stellar reflex velocities induced by the planets.

4.1 Introduction

The K2-93 system was first discovered by Vanderburg et al. (2016a) (hereafter [V16a](#)) from data obtained during Campaign 5 (C5) of the [K2](#) mission (Howell et al., 2014). This analysis revealed a system with five transiting planets, two inner sub-Neptune-sized planets, and three outer planets ranging from Neptune to Jupiter size. The three outer planets only showed a single transit in the C5 data, hence their periods could only be loosely predicted based on the available stellar parameters and dynamical stability considerations. Based on [K2](#) data from Campaign 18 (C18), Berardo et al. (2019) and Becker et al. (2019) discovered additional transits for two (“d” and “f”) of the three outer planets, which allowed stronger constraints to be placed on their periods.

The system is particularly interesting because the stellar host, HIP 41378 (EPIC 211311380), is relatively bright, with a *V*-band magnitude of 8.93 (and JHK_s magnitudes from 7.7 – 8.0), enabling follow-up studies from ground. In contrast, the only other multi-planet transiting systems with periods beyond that of the outermost planet “f”, of which there are four from the [Kepler](#) mission¹, all have JHK_s magnitudes of the order ~ 12 .

¹: found from searching the NASA exoplanet archive (<https://exoplanetarchive.ipac.caltech.edu/index.html>) on 12 April 2019.

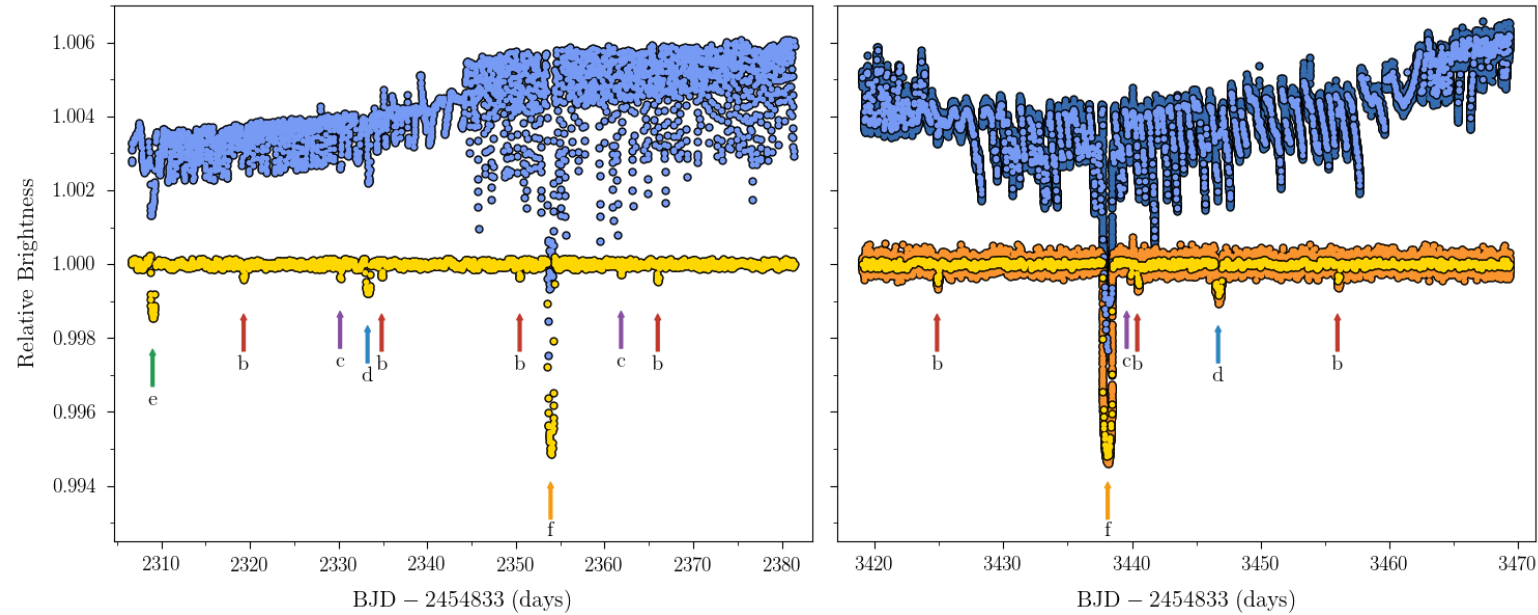


Figure 4.1 | K2 light curve of K2-93. Light curve for HIP 41378 obtained during C5 (left) and C18 (right). The blue points show the raw photometry (offset by 0.04), while the yellow points show the light curve after correcting for the K2 systematics. Light coloured points show data in LC, dark points (only in C18) show the SC data. Each of the identified transits of the five planets have been indicated with arrows.

Only one of these is also a confirmed multi-planet system. The fact that the star is bright and that the Jupiter-sized “f” planet orbits far from its host means that in addition to causing a deep transit it is an ideal target for transit transmission spectroscopy. As discussed by V16a it may even be possible to measure the planetary oblateness, because the planetary orbit will not have synchronised with the orbital period.

In this paper we present the detection of solar-like oscillations in K2-93 using the C18 short-cadence data. Using [asteroseismology](#) (Aerts et al., 2010) we provide a significant improvement in the characterisation of the host star of this benchmark system, including the planet radii and orbital periods for planets “d” and “f”. We also use data from [TESS](#) to provide additional constraints on the period of planet “e”.

4.2 Data

HIP 41378 was first observed by the [K2](#) mission during C5 in long-cadence mode (LC; $\Delta t \sim 30$ min). The star was observed again in LC in C18, and was also observed in short-cadence (SC; $\Delta t \sim 1$ min) mode² to search for asteroseismic signals.

Light curves were constructed from pixel-data downloaded from the KASOC database³, extracted using the *K2P*² pipeline (Lund et al., 2015) and corrected using the KASOC filter (Rodrigues et al., 2014), which iteratively corrects for both known planetary transits, long-term trends, sharp features, and the characteristic \sim 6-hour systematic of the [K2](#) mission (Stumpe et al., 2014; Van Cleve et al., 2016).

Figure 4.1 shows the raw and corrected light curve for HIP 41378, though without correcting for the planetary transits as done for the seismic analysis. As seen, the outer planets “d” and “f” transit again in C18, where only a single transit was available before from C5. Planet “e” unfortunately does not transit again. Our planetary analysis is described in Section 4.3.4.

4.3 Analysis

4.3.1 Asteroseismic parameters

We determined values for the average asteroseismic parameters $\Delta\nu$, the [large frequency separation](#), and ν_{\max} , the [frequency of maximum power](#).

2: <https://keplerscience.arc.nasa.gov/k2-approved-programs.html#campaign-18>

3: www.kasoc.phys.au.dk

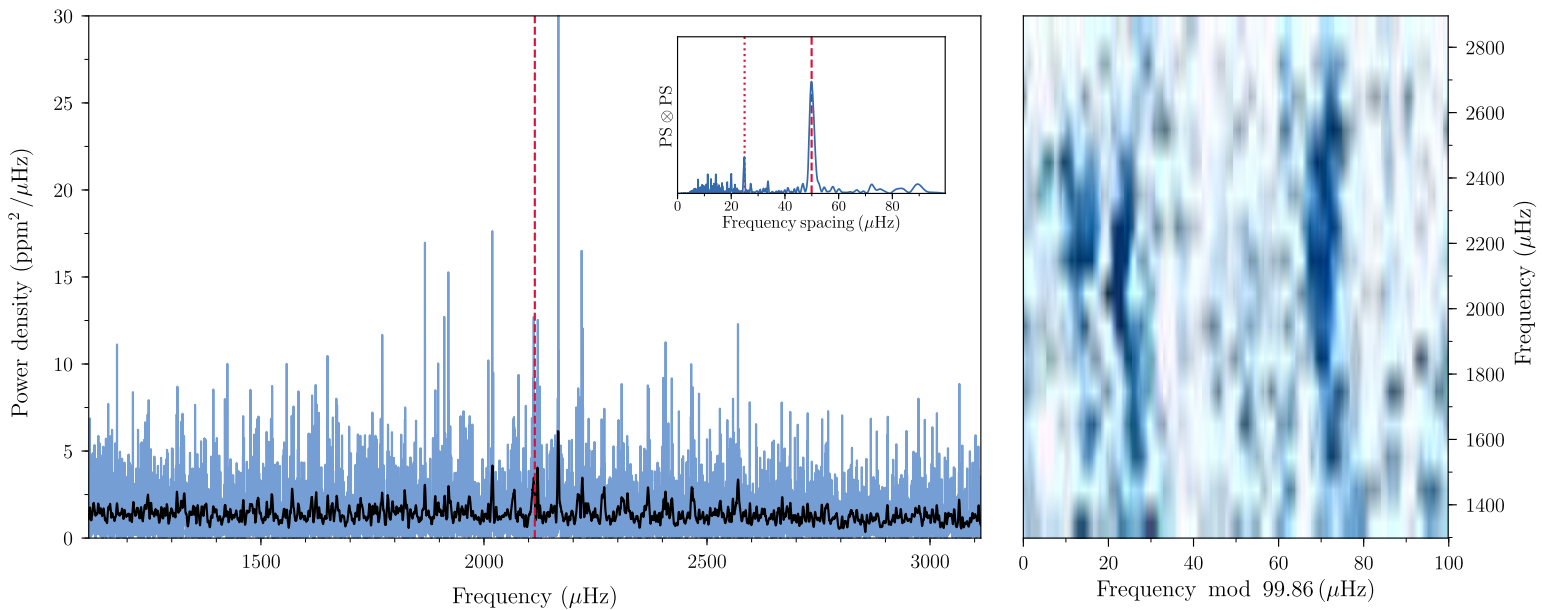


Figure 4.2 | Power spectrum and échelle diagram. Power density spectrum (PDS; left) and échelle diagram (right) of HIP 41378. The black line shows a smoothed version of the PDS and the red dashed line indicates the value of ν_{\max} . The insert in the PDS shows the $\text{PS} \otimes \text{PS}$ of a region centered on the measured ν_{\max} ; the peak in the $\text{PS} \otimes \text{PS}$ marked by a dashed red line gives the identified value for $\Delta\nu/2$, while the dotted line shows the value of $\Delta\nu/4$.

The value of ν_{\max} was determined following the procedure of Lund et al. (2016) using a fit to the stellar granulation background including a Gaussian power hump to account for the excess power from oscillations; we determine a value of $\nu_{\max} = 2114 \pm 38 \mu\text{Hz}$. $\Delta\nu$ was determined from the $\Delta\nu/2$ peak of the power-of-power spectrum centered on ν_{\max} , after first having corrected for the stellar granulation background; we determine a value of $\nu = 99.86 \pm 2.48 \mu\text{Hz}$ (see Figure 4.2).

As seen from Figure 4.2, especially clear from the échelle diagram in the right panel (Bedding, 2011), individual modes of oscillation are readily visible for this star. We extracted information on the individual modes using the peak-bagging procedure outlined in Lund et al. (2017) (see also Davies et al. (2016)). The mode identification was done by visual inspection of the power density spectrum (PDS), but we note that the obtained value $\epsilon \approx 1.29$ (observationally $\Delta\nu(\epsilon-1)$) gives the horizontal position of the $l = 0$ ridge in the échelle diagram) from our preferred identification matches predictions from Deheuvels et al. (2012) based on the stellar T_{eff} .

As part of the peak-bagging, values are determined for the stellar inclination and the mode splitting from the stellar rotation (Van Eylen et al., 2014), the former of which is particularly important to assess the **obliquity** of the planetary system (Lund et al., 2014b; Campante et al., 2016). We fitted these parameters in projected splitting and in $\cos i_{\star}$ on which we adopted a flat prior consistent with an isotropic distribution. Figure 4.3 shows the correlation map between the projected splitting and the stellar inclination, here a horizontal line corresponds to a specific value for the projected rotational velocity $v \sin i_{\star}$ when taking into account the stellar radius. We determine a posterior median value for the projected splitting of $\nu_s \sin i_{\star} = 0.90 \pm 0.32 \mu\text{Hz}$ (with the splitting ν_s given by the inverse of the stellar rotation period), and an inclination of $i_{\star} \geq 45^\circ$ as the lower limit of the 68% highest probability density interval. The projected rotational velocity $v \sin i$ found from combining the fitted projected splitting with the asteroseismic radius has a value of $5.1 \pm 1.8 \text{ kms}^{-1}$ – this is consistent with the spectroscopic value from the Stellar Parameters Classification tool (SPC; see Buchhave et al., 2012b), especially considering that the SPC value for $v \sin i_{\star}$ will contain a contribution from **macro-turbulence**. Assuming a contribution from **macro-turbulence** of $\sim 5 \text{ kms}^{-1}$ (Doyle et al., 2014), and subtracting this in quadrature from the reported SPC value, results in a $v \sin i_{\star}$ from rotation of $\sim 5.1 \text{ kms}^{-1}$, in full agreement with the seismic value. Only a weak constraint can be placed on the stellar inclination, which is inconsistent with a highly misaligned system, and a projected **obliquity**, e.g., by measuring the **RM EFFECT**, is required to fully constrain the system geometry (Winn et al., 2005; Albrecht et al., 2013b).

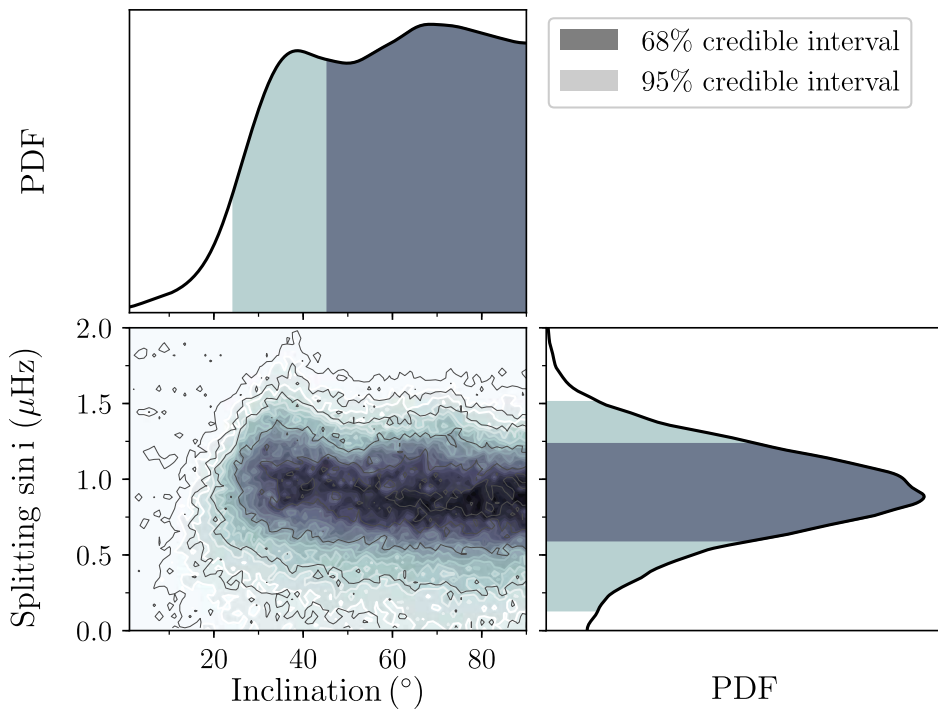


Figure 4.3 | Correlation between inclination and splitting. Correlation map of the stellar inclination and projected splitting from the peak-bagging analysis.

4.3.2 Spectroscopy and Infrared Flux Method (IRFM)

We rederived spectroscopic parameters using spectra from the 1.5 m Tillinghast telescope at the F. L. Whipple Observatory, which were obtained for the original analysis by V16a. The spectra from TRES were analysed using the SPC where the value of $\log g$ was iterated based on ν_{\max} (see Brown et al., 1991; Campante et al., 2014) to decrease the impact on uncertainties from correlations between T_{eff} , $\log g$, and $[\text{Fe}/\text{H}]$. Following Torres et al. (2012) we add systematic uncertainties of ± 59 K and ± 0.062 dex in quadrature to the derived uncertainties on T_{eff} and $[\text{Fe}/\text{H}]$. The updated spectroscopic parameters are listed in Table 4.1. The main change is seen for T_{eff} which with the seismic $\log g$ is 91 K higher than the solution of V16a.

As a sanity check of the spectroscopic T_{eff} we also determined this using the IRFM (Casagrande et al., 2014). We follow the procedure outlined in Lund et al. (2016), and fix in the determination $[\text{Fe}/\text{H}]$ to the spectroscopic

Table 4.1 | Spectroscopic and IRFM parameters. The $\log g$ values from SPC and the IRFM are obtained using the T_{eff} values combined with ν_{max} . **Notes** ^(a)The $v \sin i$ from SPC also contain a broadening contribution from **macro-turbulence**, likely resulting in a $v \sin i$ of the order $\sim 5.1 \text{ kms}^{-1}$.

Parameter	Value
Effective temperature from SPC, T_{eff} (K)	6290 ± 77
Metallicity from SPC, [Fe/H] (dex)	-0.05 ± 0.10
Projected rotation speed, ^(a) $v \sin i$ (kms^{-1})	7.1 ± 0.5
Surface gravity from SPC, $\log g$ (cgs)	4.29 ± 0.10
Effective temperature IRFM, T_{eff}	6347 ± 70
Angular diameter, θ (mas)	0.114 ± 0.002

value and adopt an interstellar reddening of zero. Uncertainties in the reddening and metallicity are propagated to the IRFM parameters using a Monte Carlo analysis. The derived parameters are listed in Table 4.1 – as seen, the agreement between the two determinations of T_{eff} is excellent and for both estimates within their $1 - \sigma$ uncertainty.

4.3.3 Asteroseismic modeling

Before proceeding with the modeling of the extracted individual frequencies it is important to consider Doppler shifts of the frequencies from the **RV** of the star (Davies et al., 2014). Based on **Gaia** DR2 (Gaia Collaboration et al., 2018), the star has an **RV** of $50.42 \pm 0.37 \text{ km s}^{-1}$, which for the range of oscillation frequencies observed would result in Doppler shifts from 0.26 to $0.45 \mu\text{Hz}$. In our case this is below the general uncertainty on the frequencies, but as the shift is systematic we account for it and thereby ensure that the uncertainty on the **RV** measurement is propagated to the adopted frequency values. We note that the shifts had a negligible effect in our case, and will in general have minimal importance when modeling frequency difference ratios rather than the frequencies themselves.

We model the star using the **B**ayesian **S**tellar **A**lgorithm (**BASTA**) (Silva Aguirre et al., 2015, 2017) with evolution models computed with the Garching Stellar Evolution Code (GARSTEC; Weiss and Schlattl, 2008) and frequencies computed with the Aarhus adiabatic oscillation package (ADIPLS; Christensen-Dalsgaard, 2008a). With **BASTA**, modeling was run using both frequency separation ratios r_{010} and r_{02} (Roxburgh and Vorontsov, 2003)

and individual frequencies with a correction for the surface term by Ball and Gizon (2014). The results from these approaches are in full agreement.

Information on the stellar distance is incorporated (Silva Aguirre et al., 2018) to constrain the stellar modeling. We use the *Gaia* DR2 parallax combined with JHK_s photometry from the Two Micron All Sky Survey (2MASS; Cutri et al., 2003; Skrutskie et al., 2006) and extinction from the Green et al. (2019) dust map to determine absolute magnitudes, which are then fitted to the grid.

Table 4.2 gives the results from the **BASTA** run using ratios and incorporating information on the distance. We have added in quadrature to the uncertainties the difference between using ratios and individual frequencies in the modeling.

As a sanity check of the modeling, a grid-based model was computed using the Yale-Birmingham code (YB; Basu et al., 2010; Gai et al., 2011; Basu et al., 2012), which takes a different approach than **BASTA** and uses different grids of stellar models – see Lund et al. (2016) for further details. The results from this approach agree fully within uncertainties with the **BASTA** results.

As a further check we also compare the distance from *Gaia* with that obtained by combining the stellar radius with the angular diameter from the IRFM (Table 4.1). For the **BASTA** results a distance of 106.0 ± 1.9 pc is obtained, in agreement with the Bailer-Jones et al. (2018) *Gaia* distance of $d = 106.29^{+0.68}_{-0.67}$ pc.

To estimate the size of a potential systematic uncertainty from different approaches and input physics in the modeling, besides the check using the YB code, we used the results from the *Kepler* LEGACY study (Lund et al., 2017; Silva Aguirre et al., 2017) and determined the median of the scatter in central parameter values for stars similar to HIP 41378 (masses from 1.05 to $1.35 M_\odot$ and radii from 1.15 to $1.45 R_\odot$). We find median relative systematic differences of 1.8% in mass, 0.5% in radius, 0.3% in density, 0.06% in $\log g$, and 4% in age. These systematic differences are all below our quoted statistical uncertainties from **BASTA** of 2.5% in mass, 0.7% in radius, 1.0% in density, 0.1% in $\log g$, and 17% in age. Given the minor contribution such systematic uncertainties would have on our reported estimates if joined with our statistical uncertainties and the uncertainty in their estimation (based here only on 17 similar stars from *Kepler*), we do not include a systematic term on our quoted parameters nor in our further analysis.

Table 4.2 | Results from the asteroseismic modeling. Here we compare our results from [BASTA](#) to the ones given in [V16a](#).

	BASTA	V16a
Mass (M_{\odot})	$1.22^{+0.03}_{-0.02}$	1.15 ± 0.064
Radius (R_{\odot})	1.300 ± 0.009	1.4 ± 0.19
Density (g/cm^3)	0.785 ± 0.008	–
$\log g$ (cgs; dex)	4.298 ± 0.004	4.18 ± 0.1
Age (Gyr)	$2.07^{+0.36}_{-0.27}$	–
Distance (pc)	106.8 ± 1.0	116 ± 18
T_{eff} (K)	6290 ± 77	6199 ± 50
[Fe/H] (dex)	-0.05 ± 0.10	-0.11 ± 0.08

4.3.4 Planetary analysis

The periods of the two innermost planets (“b” and “c”) were already well-determined by [V16a](#) from C5 data. For the short period planet “b” we again detect multiple transits in C18, whereas planet “c” only transits once (see Figure 4.2). Planets “d” and “f” both show a single transit in C18, while “e” does not transit during C18 (Becker et al., 2019; Berardo et al., 2019). Using the asteroseismic stellar parameters derived in this study, we can further improve on the properties of the planets in the system.

4.3.4.1 Transit fitting

For fitting the transits we used the Mandel and Agol (2002) model, calculated using the batman package (Kreidberg, 2015). For the optimization of transit parameters this was combined with the Affine Invariant Markov Chain Monte Carlo sampler emcee (Foreman-Mackey et al., 2013). batman was used adopting a quadratic limb-darkening law with Gaussian priors for the limb-darkening coefficients using the values from [V16a](#) with a width of 0.1.

The orbital parameters, i.e., period, semi-major axis (a/R_{\star}), mid-transit time (T_0), radius ratio (R_p/R_{\star}), and inclination, were fitted using uninformative flat priors. The starting point for the adopted 100 walkers were values close to those found in [V16a](#), except for the periods of planets “d”, “e”, and “f” as described below. To account for the [K2](#) cadence and the difference in cadence between the data used from the two campaigns (LC in C5 and SC in C18), the model light curves were oversampled by factors of 10 (SC) and 300 (LC) and then binned to the cadence of the observations.

Table 4.3 | Planetary parameters from the joint transit fit. For the limb-darkening coefficients we find $c_1 = 0.410_{-0.014}^{+0.013}$ and $c_2 = 0.12 \pm 0.02$. Value of a for planet “c” is constrained from the period and assuming a zero eccentricity orbit. **Notes.** ^(a) Value constrained from Equation (4.2) (see Figure 4.5). We note that the uncertainty on the period for planets “d” and “f” does not reflect the width of the distributions in Figure 4.5, because the period should correspond to one of the discrete periods given by Equation (4.3). For planet “d”, a value of $n = 4 \pm 1$ (Equation (4.3)) better represents the uncertainty in the predicted period. For “e” we estimate the period from the distribution in Figure 4.5.

Planet	P (days)	R_p (R_\star)	a (R_\star)	i (deg)	b	t_d (hours)	T_0 (BJD-2454833)
“b”	15.57209 ± 0.00002	$0.0180_{-0.0003}^{+0.0002}$	$22.8_{-1.0}^{+1.3}$	$89.2_{-0.3}^{+0.7}$	$0.31_{-0.22}^{+0.18}$	5.06 ± 0.03	$2319.283_{-0.002}^{+0.001}$
“c”	$31.7061_{-0.0002}^{+0.0001}$	0.0182 ± 0.0008	36_{-9}^{+6}	88.6 ± 0.4	$0.90_{-0.03}^{+0.06}$	3.21 ± 0.19	2330.162 ± 0.003
“d”	$278.360 \pm 0.001^{(a)}$	$0.0260_{-0.0006}^{+0.0004}$	190 ± 20	89.8 ± 0.1	$0.58_{-0.09}^{+0.14}$	$12.44_{-0.16}^{+0.10}$	2333.273 ± 0.004
“e”	$260_{-60}^{+160}(a)$	0.037 ± 0.001	112_{-13}^{+14}	89.7 ± 0.1	$0.52_{-0.15}^{+0.19}$	$13.00_{-0.15}^{+0.12}$	2309.020 ± 0.001
“f”	$542.0793 \pm 0.0002^{(a)}$	0.0664 ± 0.0001	$230.6_{-1.1}^{+1.3}$	89.96 ± 0.01	0.17 ± 0.03	$18.906_{-0.016}^{+0.015}$	2353.9162 ± 0.0003

In our fitting we assumed an eccentricity of zero, but discuss in Section 4.3.4.3 possible constraints on the eccentricity. We adopted a zero eccentricity, because the asymmetry from an eccentric orbit would be too small to properly constrain from the [K2](#) photometry, as also noted in [V16a](#). Following Winn (2010) the difference in ingress (τ_{ing}) and egress (τ_{egr}) time, causing the transit to appear asymmetric, can to leading order in R_\star/a and e be given as

$$\mathcal{A} \equiv \frac{\tau_{\text{egr}} - \tau_{\text{ing}}}{\tau_{\text{egr}} + \tau_{\text{ing}}} \sim e \cos \omega \left(\frac{R_\star}{a} \right)^3 (1 - b^2)^{3/2}. \quad (4.1)$$

As an example, the innermost planet “b” of the system with an $R_\star/a \approx 0.04$ will have $\mathcal{A} < 1 \times 10^{-4} e$. For planet “f”, with $R_\star/a \approx 0.0043$ (assuming the period found in Section 4.3.4.2) the value for the asymmetry will be $\mathcal{A} < 8.3 \times 10^{-8} e$. Additionally, from our assessment in Section 4.3.4.3 of the constraints that can be put on e from having the asteroseismic value for the stellar density, we find that the argument of periastron (ω) in the eccentric cases would be close to $\sim 270^\circ$. In this case $\cos \omega$ would tend to zero, further decreasing the asymmetry of the transit.

Initially, each planet was fitted independently. For each iteration of the fitting we added a step to eliminate possible residual systematics from the light curve detrending, by fitting a linear slope in addition to the model light curve for each transit for a given planet. For the initial fits we ran the sampler for 10,000 steps with a burn-in of 5000 steps.

For planets “d” and “f” there are several allowed periods (see Equation (4.3)). We fitted the transits assuming each of these allowed periods to test the impact on other transit parameters. To prevent a walker from jumping to an allowed period other than the one being tested, we constrained the period to a small interval around the tested value. We further adopted a parallel tempering approach in the [MCMC](#), with 10 different temperatures for each of the walkers.

A final joint fit including all planets was run after having constrained the starting values from the individual fits. The convergence and mixing of the walkers for this final run was assessed by visual inspection, and making use of the Gelman-Rubin convergence diagnostic (Gelman and Rubin, 1992) and checking the effective sample size (Geyer, 1992). For this we used the routines available in PyMC3 (Salvatier et al., 2016). Final planetary parameters are given in Table 4.3. Figure 4.4 shows a phase plot for the planets together with the fitted transit light curve. In each panel the signal from the other planets have been removed.

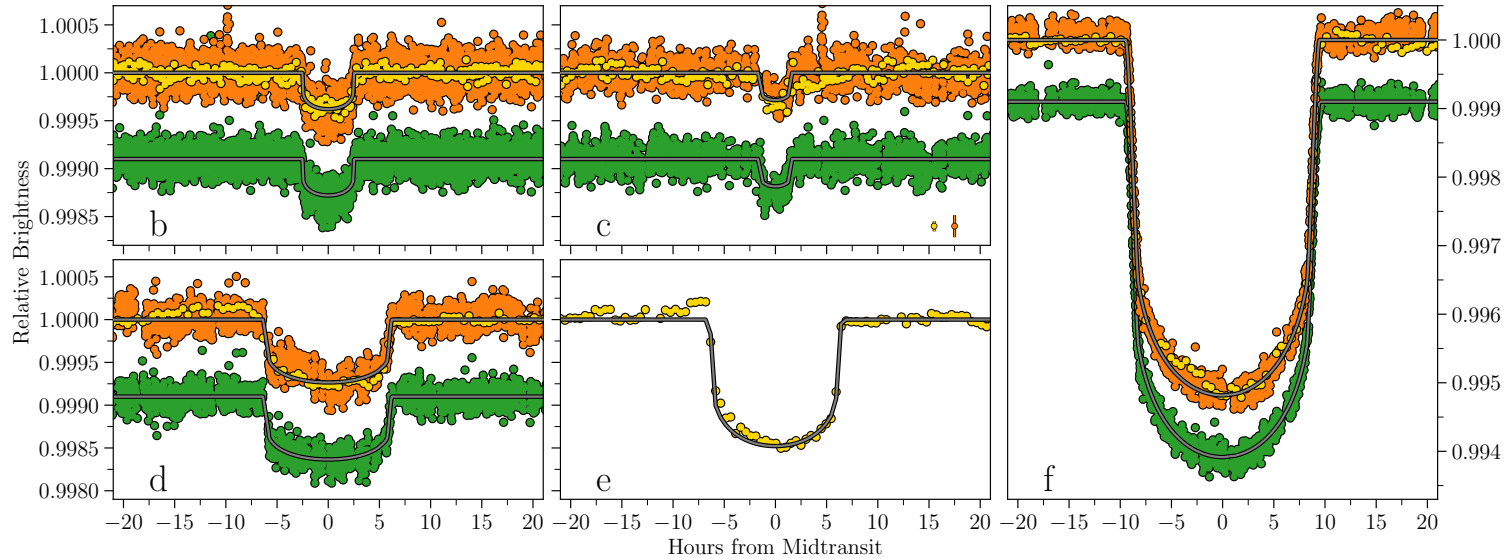


Figure 4.4 | Transit light curves. Phased light curves for all five planets using the parameters in Table 4.3, and with the fitted model overplotted. Data from $K2P^2$ are displayed in yellow, with C5 LC data given in light colours and C18 SC in dark. The data shown in green, and offset vertically from the yellow points, shows the C18 SC data from the K2SFF pipeline (Vanderburg and Johnson, 2014) – the fitted model (applied to the yellow points) has been offset by the same amount for a more direct comparison. Planets “b” and “c” are displayed in the top panels and “d” and “e” are in the bottom panels. Shown to the right is planet “f”. Denoted in the panel for planet “c” are representative photometric uncertainties for the LC and SC data.

A study by Grunblatt et al. (2016) showed that planet parameters modelled from K2 light curves can widely vary depending on the pipeline used to reduce the data. Therefore, we checked the consistency of our derived parameters by fitting for the planet properties on a light curve produced with *K2SFF* (Vanderburg and Johnson, 2014) with the systematics correction fit rederived by fitting simultaneously with the transits (Vanderburg et al., 2016b). The *K2SFF* short-cadence light curve is shown in Figure 4.4 in green, with a slight offset from the *K2P²* light curves for a direct, visual comparison.

First described by Chontos et al. (2019), this independent analysis fitted for the following parameters: orbital period (P), time of mid-transit (T_0), linear (c_1) and quadratic (c_2) limb-darkening coefficients, mean stellar density assuming a circular orbit ($\rho_{\star,\text{circ}}$), impact parameter (b), ratio of the planetary radius to the stellar radius (R_p/R_\star), and the photometric zero-point (z). To keep the two analyses consistent, the same priors are imposed and the MCMC samplers are run with the same amount of walkers and steps, including the same burn-in. When using light curves reduced through two different pipelines and modelled through two independent analyses, the parameters still agree to within 1σ for all derived quantities and thus provides further evidence for the validity of the derived planet properties.

4.3.4.2 Planetary periods

As done by V16a we predict the planetary periods from information of the star and parameters from the transit fit. The planetary period can be obtained by solving the following relation:

$$t_{d,i} = \frac{P_i}{\pi} \arcsin \left[\left(\frac{G(M_\star + m_{p,i}) P_i^2}{4\pi^2} \right)^{-1/3} \times \sqrt{(R_{p,i} + R_\star)^2 - b_i^2 R_\star^2} \right] \frac{\sqrt{1 - e_i^2}}{1 + e_i \cos \omega_i}, \quad (4.2)$$

where t_d is the transit duration, m_p is the mass of the planet, b is the impact parameter, ω is the argument of periastron, e is the eccentricity, and the subscript i refers to a given planet. By drawing samples from a normal distribution created from each of the stellar and transit parameters and their errors, we can thus build a distribution for the period. The obtained period distributions are shown in Figure 4.5. For the eccentricity we adopt a β -distribution (with parameters $\alpha = 0.867$ and $\beta = 3.03$ from

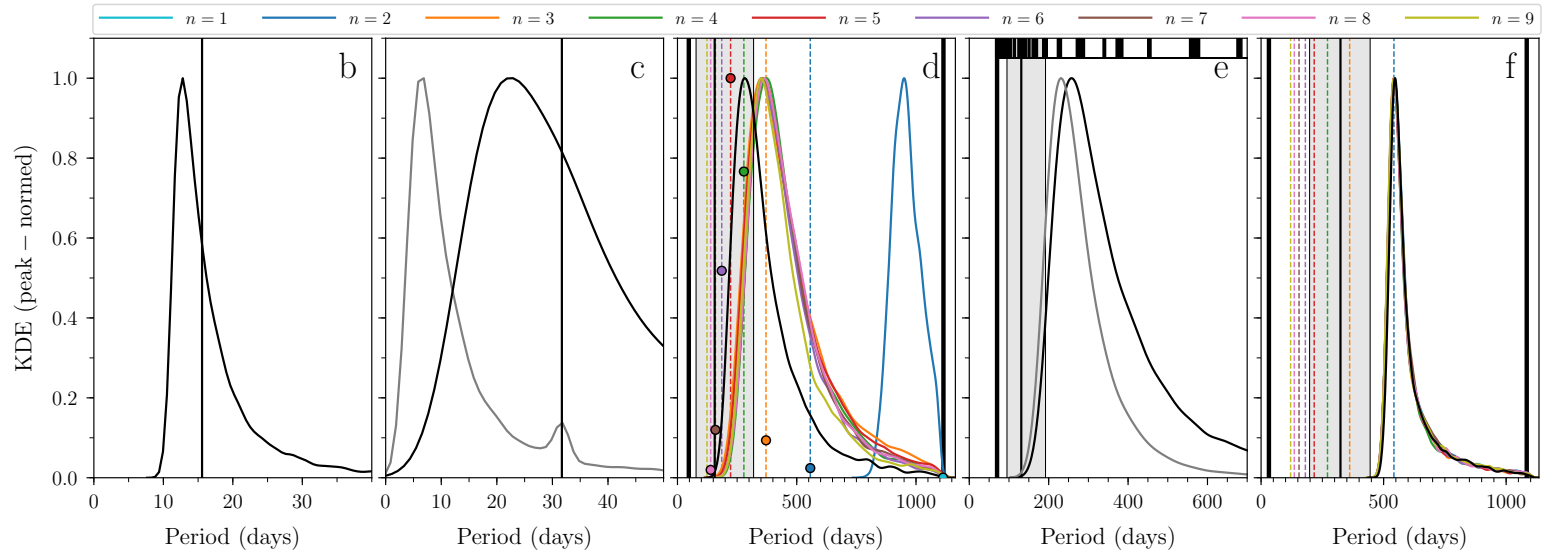


Figure 4.5 | Period distributions. Period distributions resulting from solving Equation (4.2) for all five planets going from “b” in the leftmost panel to “f” in the rightmost. The vertical black lines in the gray shaded areas mark the values from V16a. The thick black lines denote the minimum and maximum allowed value for the periods of “d”, “e”, and “f”. The black curves have been made using the parameters from the joint fit in Table 4.3. The gray curve for “c” has been created using parameters from a fit without constraints on a/R_* . The colour coding for “d” and “f” refers to the assumed period when performing the individual fits to obtain values for the parameters entering in Equation (4.2) and the dashed vertical lines denote the period assuming a value for n . For “d” the markers indicate the relative posterior probabilities evaluated at the positions of the discrete periods after applying the normalised prior probabilities by Becker et al. (2019) (their Table 2). For “e” the horizontal bar in the top shows the allowed periods in white, whereas the black areas are the forbidden periods as these would have resulted in a transit in C18 or in sector 7 of TESS (see Figure 4.6); the gray line shows the period distribution after applying a prior on the period probability following Becker et al. (2019, their Eq. 1).

Kipping, 2013a) and fixed ω to $3\pi/2$ (see Section 4.3.4.3). The masses in Equation (4.2) are estimated using the mass-radius relation in Wolfgang et al. (2016) with two different power laws, one for planets with $R_p < 4R_\oplus$ and another for planets in the range $4R_\oplus < R_p < 8R_\oplus$. For planets larger than $8R_\oplus$ we uniformly draw samples from a Jovian density distribution, i.e., $\rho = 1.3 \pm 0.5 \text{ g cm}^{-3}$ consistent with the radius anomaly reported in Laughlin et al. (2011) which should not be relevant for the present case.

For the two inner planets for which the period is well-established, the period prediction serve as a sanity check of the fitted transit parameters. For planet “b” the measured and predicted period are seen to be in good agreement. For planet “c” we obtain transit parameters from the **K2** data that result in a period distribution which poorly matches the measured period. We attribute this inconsistency to the quality of data at the transit times for planet “c”, leading to a rather uncertain estimation of a/R_\star . We note that adopting the a/R_\star and stellar parameters from V16a leads to a similar distribution. Assuming an orbit with zero eccentricity the a/R_\star should be ~ 39 rather than the value of 73 reported in V16a. We therefore confined a/R_\star to be in the interval [25, 53] for planet “c” in the final fit. This added constraint leads to a predicted period in better agreement with the measured value (see Figure 4.5).

For planets “d” and “f” we can constrain the periods to be the difference between the mid-transit times in C5 and C18 divided by an integer, i.e.,

$$P_n = \frac{T_{0,\text{C18}} - T_{0,\text{C5}}}{n}, \quad n = 1, 2, 3, \dots, \quad (4.3)$$

where $T_{0,\text{C18}}$ and $T_{0,\text{C5}}$ are the mid-transit times observed in C18 and C5. Given the ~ 3 yr gap between C5 and C18 this gives some 20 possible periods for each, with a lower boundary from the lack of additional transits in the individual time series.

The importance of the precision of the stellar parameters for the resulting distributions for the period and eccentricity differs from planet to planet. The impact is, for instance, much more pronounced for planet “f”, where the parameters t_d , b , and R_p can be determined with great precision (see Table 4.3).

We see the that the predicted period from the individual planet fits is stable against the use of transit-fit parameters based on different input periods. With the exception of one, the resulting periods for planet “d” all end up at a period corresponding to a value of $n = 3$ ($P \simeq 371$ days), which suggests two missed transits between C5 and C18. The same is true for planet “f”, where the periods match the allowed period corresponding

to $n = 2$ ($P \simeq 542$ days), indicating that a single transit has been missed between C5 and C18. From the final joint fit, the parameters for planet “d” results in a period that is lower than from the individual fits, corresponding to a value of $n = 4$ ($P \simeq 278$ days). The change in period is attributed to a change in transit parameters from the better constraint on limb-darkening parameters in the joint fit, where we find $c_1 = 0.410_{-0.014}^{+0.013}$ and $c_2 = 0.12 \pm 0.02$ for the linear and quadratic limb-darkening coefficients, respectively. We note that these coefficients are in good agreement with table values from Claret (2018). This is especially true for the linear limb-darkening coefficient. While $n = 4$ provides the best match for planet “d” the predicted period distribution is relatively broad, meaning that periods of 223 days ($n = 5$) and 371 days ($n = 3$) cannot be excluded. The periods we report in Table 4.3 for planet “d” and “f” are thus to be taken as given this value for n (corresponding to an orbit with low eccentricity) what would then be the precision with which the period can be determined. A value of $n = 4 \pm 1$ better represents the uncertainty for the period of planet “d”.

We note that the $n = 4$ period for “d” and $n = 2$ period for “f” both correspond to low-eccentricity orbits (see Figure 4.7 and Section 4.3.4.3), consistent with the circular orbits adopted in the transit fit. We did also try adopting eccentricity distributions derived in Section 4.3.4.3 for the period distributions – this causes small shifts in the individual distributions, leaving only the low-eccentricity solutions with predicted periods consistent with the input period.

The periods corresponding to $n = 2$ for “f” and $n = 4$ for “d” that we use for our final fit are not the most likely periods according to Becker et al. (2019), however, this configuration is found to be dynamically stable in both Becker et al. (2019) and Berardo et al. (2019) and as such are consistent with their results. The same goes for having $n = 3$ or $n = 5$ in Equation (4.3) for “d”.

Stability calculations for configurations similar to the one we report in Table 4.3 have been carried out by Becker et al. (2019) and Berardo et al. (2019), but as both have used different stellar parameters we used our parameters and tested the stability of the orbital solution using the Mercury6 N -body integrator (Rappaport et al., 2012). We found that this solution was stable for at least the integrated 100 Myr years.

As mentioned by Becker et al. (2019) the K2-93 system was to be observed by TESS. Figure 4.6 shows the light curve, with a 2 minute cadence, extracted from TESS sector 7 data. The light-curve extraction and a simple detrending was done using the lightkurve (Lightkurve Collaboration et al., 2018) module. The scatter in the TESS data is much higher than for K2,

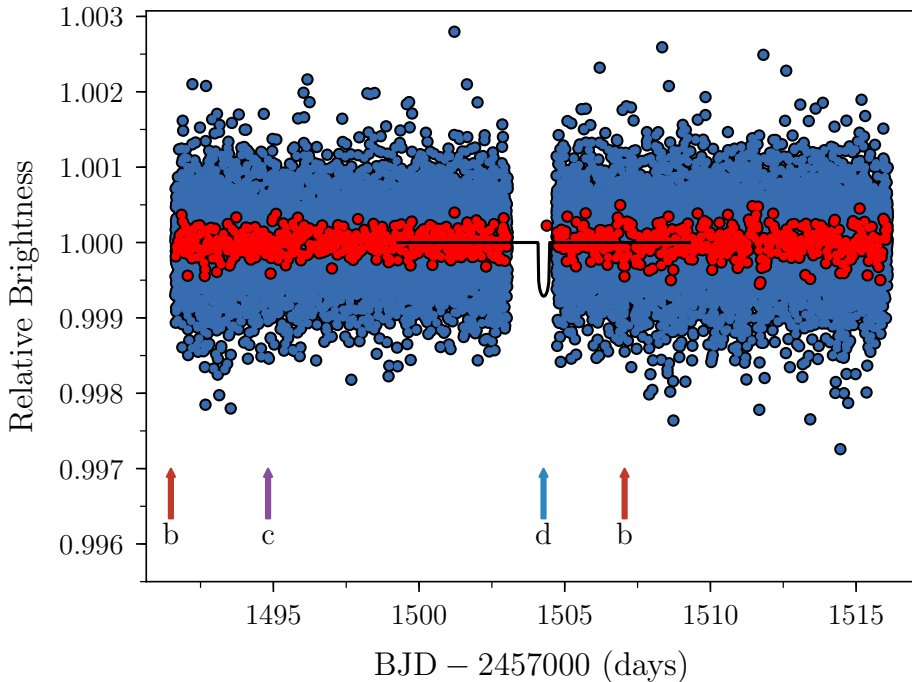


Figure 4.6 | TESS light curve. Light curve for HIP 41378 obtained during sector 7 of the [TESS](#) mission. The blue points show the 2-minute cadence photometry, having only applied a simple detrending to the data using the `lightkurve` module. The red points show the data when binned to a cadence of 30 minutes. Using the ephemerides and possible periods from [K2](#) the corresponding transit times for each planet have been indicated with arrows. For planet “d” the only possible period that would result in a transit during the sector 7 baseline is that of $n = 5$. The black transit model shows transit shape for planet “d” based on the [K2](#) analysis.

and while difficult to see, planets “b” and “c” both transit once. In Figure 4.6 we have also indicated the possible transit time for planet “d” according to Equation (4.3) and the T_0 from the [K2](#) data. Of the outer planets, planet “d” is the only one of the outer planets with a possible transit during the sector, with a period corresponding to $n = 5$ (~ 223 days). Unfortunately, the mid-time for this transit falls within the [TESS](#) downlink gap. As also indicated by the black transit model, which is based on the transit fit to the [K2](#) data, the entire transit is contained within the gap, i.e., one should not expect to see the egress in the [TESS](#) data. In sum, the [TESS](#) data cannot exclude nor confirm any of the possible periods for planets “d” and “f”. An

extra constraint on allowed periods can, however, be placed for planet “e”, which we have included in Figure 4.5.

Having only observed a single transit for planet “e” in both campaigns, we obtain a range of possible periods, as opposed to the discrete set for “d” and “f”. Furthermore, these extend beyond the difference in time between the two campaigns. We have a lower limit for the period given as the difference between the mid-transit time and the end of C5. Also, periods that would result in a transit in C18 or in sector 7 of the NASA [TESS](#) mission (Ricker et al., 2015) can be excluded (see Figure 4.5 and Figure 4.6). In the transit fitting we adopted the predicted period from Equation (4.2) of ~ 260 days, because this is the allowed period from Equation (4.2) consistent with a low-eccentricity orbit.

As noted by Becker et al. (2019) not all of the possible periods governed by Equation (4.3) are equally likely, because it is more likely that we would observe transits for “d” and “f” in C18 for larger values of n . For planet “d” Becker et al. (2019) provides normalised probabilities for the discrete periods, considering both the likelihood of the periods given the number of observed transits combined with the observation baseline and the dynamical stability of the orbits (their Table 2). If we apply these probabilities to the period distribution from our joint fit evaluated at the discrete periods we find that the posterior probability of the $n = 5$ solution becomes slightly higher than $n = 4$ where our distribution peaks (see Figure 4.5). The result from this is thus still consistent with the conservative estimate on the period uncertainty of $n = 4 \pm 1$ for planet “d”. We caution that the dynamical stability calculations of Becker et al. (2019) used stellar parameters different from the ones provided by the asteroseismic analysis which could influence the prior period probabilities. For planet “e” we applied only the prior based on the baseline (Becker et al., 2019, their Eq. 1), which moved the distribution peak slightly lower – the resulting period of 230^{+120}_{-60} days is fully consistent with the quoted period in Table 4.3. For planet “f” the period distribution from Equation (4.2) is so well-constrained around $n = 2$ that the application of prior probabilities has no effect on the favored period.

4.3.4.3 Eccentricity

While we have assumed $e = 0$ in our transit fitting, based on arguments presented in Section 4.3.4.1, it is interesting to see which constraints can be put on the eccentricity from having an asteroseismic estimate of the stellar density.

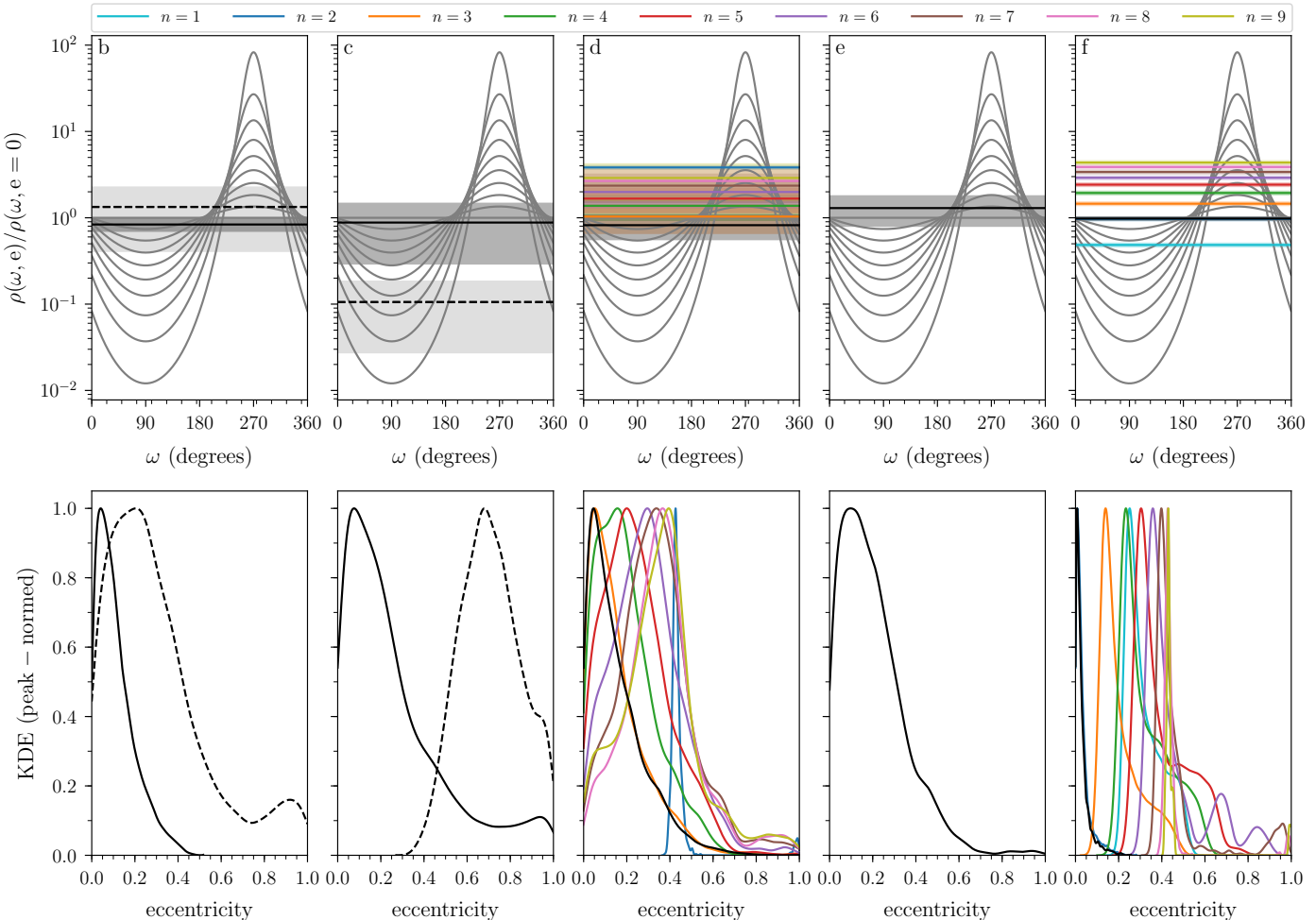


Figure 4.7 | Density ratios and eccentricity distributions. Gray solid lines in the top panels display the curves governed by Equation (4.5). (Caption continued on next page.)

Figure 4.7 | Density ratios and eccentricity distributions. The horizontal line and corresponding shaded area is our result for a planet in a given configuration. The resulting eccentricity distributions are shown in the panel below. The black solid lines show our results using parameters from the parameters in Table 4.3 and the black dashed lines in “b” and “c” are the results obtained using the stellar parameters from V16a. As in Figure 4.5 the coloured solid lines for “d” and “f” show the results from trying periods governed by Equation (4.3) and only fitting for these particular planets. Note that results for smaller periods ($n > 9$) are not displayed, since the ratio in Equation (4.5) was significantly different from 1, making it difficult to obtain reasonable eccentricity distributions when marginalizing over ω . The same is true for the $n = 1$ case for planet “d”.

Assuming a circular orbit, the mean stellar density from a transiting planet, $\rho_{\star,\text{transit}}$, can be estimated as (Seager and Mallén-Ornelas, 2003):

$$\rho_{\star,\text{transit}} = \frac{3\pi}{GP^2} \left(\frac{a}{R_{\star}} \right)^3, \quad (4.4)$$

where G is the gravitational constant. With an independent estimate of the stellar density, as the one obtained through the asteroseismic modeling, the ratio to the density in Equation (4.4) can be written as (Dawson and Johnson, 2012; Van Eylen et al., 2014; Van Eylen and Albrecht, 2015):

$$\frac{\rho_{\star,\text{astero.}}}{\rho_{\star,\text{transit}}} = \frac{(1 - e^2)^{3/2}}{(1 + e \sin \omega)^3}, \quad (4.5)$$

that is, as a function of the orbital eccentricity e and argument of periastron ω . Figure 4.7 shows for each planet the curves described by Equation (4.5) for different values of e . The values obtained for the density ratio are indicated by horizontal lines – for the outer planets “d” and “f” each of the obtained ratios from different assumed periods (and thus different a/R_{\star} ; Equation (4.3)) are given. We do not show all ratios for “d” and “f”, because the ratio in Equation (4.5) for periods with $n > 9$ all correspond to highly eccentric orbits ($e > 0.5$). This is also true for the case of a single missed transit for planet “d”, i.e., $n = 1$. Furthermore, as reported by Becker et al. (2019) periods for “f” corresponding to $n > 6$ are very unlikely as they should have been detected by their ground-based observations.

Based on the density ratio we can compute the resulting probability density for the eccentricity by marginalizing over the possible values for ω . This is done by a Monte Carlo sampling in ω , where for each draw we also draw from the density ratio and then solve for the eccentricity that matches this value – these distributions are shown in the bottom panels of Figure 4.7. In addition to a distribution we also obtain a range of possible ω values.

Note that we cannot readily obtain a distribution for the eccentricity of planet “e” because the information on the period of the planet is not precise enough. The distribution shown in Figure 4.7 is therefore obtained from assuming the period distribution from Equation (4.2) (see Figure 4.5).

Our initial fit for planet “c” with no constraints on a/R_{\star} resulted in a distribution, which was centered at a very high eccentricity for a close-in orbit ($P \simeq 31.7$ days) in a near 2 : 1 resonance with planet “b”. Assuming that the eccentricity should be close to 0, as seen for planet “b”, indicates

that the $\frac{a}{R_\star}$ is underestimated. We note also, that if we adopt the value for $\frac{a}{R_\star}$ from V16a the resulting value for the eccentricity of planet “c” is even higher, with a value of $e \simeq 0.7$ as seen in Figure 4.7. As also mentioned in Section 4.3.4.2 we attribute this likely underestimation of $\frac{a}{R_\star}$ to a poor quality of the K2 data for the three transits obtained for this planet. Berardo et al. (2019) observed transits of planets “b” and “c” with the *Spitzer Space Telescope* (Werner et al., 2004) between C5 and C18. While their planetary parameters from K2 and Spitzer for “b” are well-determined and in agreement (also with the values we report in Table 4.3), a/R_\star and i for planet “c” are, as is the case for our fit, rather poorly constrained.

Since the eccentricity cannot be properly constrained from the photometry alone, we cannot draw any firm conclusions on the possibility of non-zero eccentric orbits in the K2-93 system. We note, however, that when assuming a low eccentricity, periods consistent with the allowed periods can be obtained for planets “d” and “f”. While the likelihood of eccentric solutions could be appraised from stability calculations, the sheer number of possible parameter combinations in a five-planet system, including a sampling of starting orbital phases, makes the problem somewhat intractable – and, in any case, beyond the scope of this paper. Proper constraints on the eccentricity should rather be obtained from RV follow-up, which would also place better constraints in the planetary masses.

4.4 Discussion

The K2-93 system is very interesting for RV follow-up, both because it is bright but also because systems with 5 or more planets are rare. With new stellar and planetary parameters we can update the estimate by V16a for the RV amplitude of the star, K , induced by the planets. This amplitude can be estimated using the following relation:

$$K = \frac{1}{(1 - e^2)^{1/2}} \left(\frac{2\pi G}{P} \right)^{1/3} \frac{m_p \sin i}{(M_\star + m_p)^{2/3}}, \quad (4.6)$$

which we do using Monte Carlo sampling. For planets “b” and “c”, where we have well-determined periods, we sample from a normal distribution using the periods in Table 4.3. For “d”, “e” and “f” we sample from the distributions obtained from the final fit in Figure 4.5. For the eccentricities we draw from the distributions in Figure 4.7 (again, respectively, using $n = 4$ and $n = 2$ for “d” and “f”), except for planet “c”, where we draw from a β -distribution due to the complications mentioned in Section 4.3.4.2.

The resulting distributions for the K -amplitude induced by each planet is seen in Figure 4.8. The planetary masses are obtained from the mass-radius relation in Wolfgang et al. (2016). For planets “b” and “c” our estimate of the RV semi-amplitude is similar to that of V16a, with values of the order $1.5 - 2.2 \text{ m/s}$. For the outer planets we predict lower amplitudes, because our predicted periods are in all cases larger than those estimated by V16a. Even though the semi-amplitudes are lower the tighter constraints on the periods should aid in the isolation of the RV contributions from the individual planets. The rather small semi-amplitudes for the planets “b” through “e” is still achievable with the current generation of high-precision RV spectrographs.

Using the improved stellar properties from Table 4.2 and derived planetary properties from Table 4.3, we calculate the extent of the Habitable Zone (HZ) and place the planetary orbits within that context, see Figure 4.9. Such calculations are important given the combination of revised stellar properties and improved stellar distances (Kane et al., 2019). To calculate the HZ boundaries, we use the formalism described by Kopparapu (2013) and Kopparapu et al. (2014). These boundaries include optimistic (using assumptions regarding past surface liquid water on Venus and Mars) and conservative (runaway greenhouse and maximum greenhouse) scenarios (Kane et al., 2014; Kasting et al., 2014; Kane et al., 2016). We calculate the boundaries for the K2-93 inner optimistic HZ, inner conservative HZ, outer conservative HZ, and outer optimistic HZ as $1.12, 1.42, 2.48$, and 2.61 AU , respectively. Most of the planets lie interior to the inner optimistic HZ boundary, the so-called “Venus Zone” dominated by runaway greenhouse atmospheres for terrestrial planets (Kane et al., 2014). The outermost planets (“d” and “f”) lie within the inner part of the optimistic HZ based on these revised calculations. During the evolution of the K2-93 host the HZ boundaries have shifted compared to when the star was on the ZAMS. The increase in luminosity and decrease in T_{eff} has the net effect of gradually moving the HZ boundaries outward, particularly when the star moves off the MS (Gallet et al., 2017). Since the outermost planets lie within the inner regions of the HZ, they are likely to have occupied the conservative HZ early in the MS lifetime of the star. The planets range in size from mini-Neptune to Jupiter (planet “f”) and thus are likely giant planets. However, giant planets within the HZ are interesting from the perspective of potential exomoon habitability (Hinkel and Kane, 2013; Heller et al., 2014) and the occurrence rates of HZ giant planets have been shown to be relatively low (Hill et al., 2018). The detection of exomoons is a difficult endeavour and has been undertaken using transit signatures in the precision photometry from the

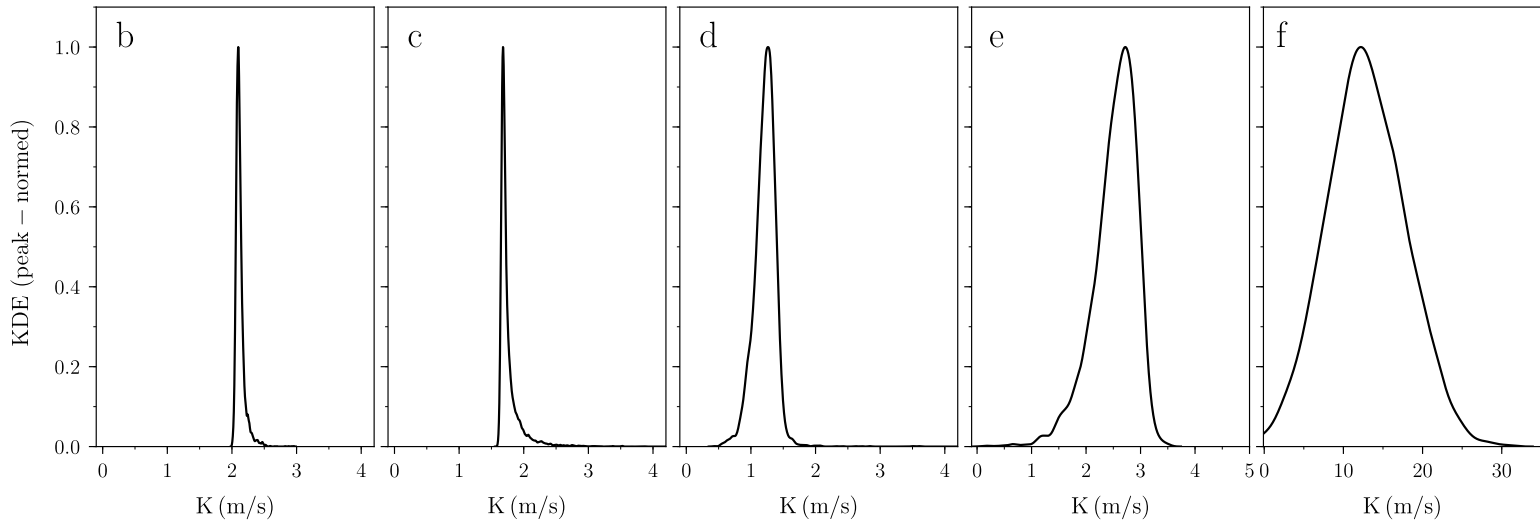


Figure 4.8 | Expected K -amplitudes. Distributions for the RV amplitude estimated from Equation (4.6) for each planet again going from “b” on the left to “f” on the right. All curves have been created using the period distributions in Figure 4.5 resulting from the parameters in Table 4.3.

Kepler mission (Kipping et al., 2009; Kipping et al., 2012). However, such exomoon searches lie at the threshold of detectability and can lead to ambiguous interpretations of the data (Teachey and Kipping, 2018; Kreidberg et al., 2019). Hill et al. (2018) provide estimates for the expected angular separation of exomoons from their host planets, the detection requirements of which are beyond the capabilities of present facilities. Significant consideration has been applied to the theory and methodology of biosignature detection for terrestrial planets (Fujii et al., 2018; Schwieterman et al., 2018), but the techniques of transmission spectroscopy and direct imaging will be likewise inhibited by low signal-to-noise observations in the near future.

The question arises as to whether the presence of the giant “f” planet located at the inner boundary of the optimistic and conservative HZ regions excludes stable orbits for HZ terrestrial planets in the system. To estimate this, we calculate the mutual Hill radii (of the [Hill spheres](#)) for adjacent planet pairs:

$$R_{H,M_p} = \left[\frac{M_{p,in} + M_{p,out}}{3M_\star} \right]^{\frac{1}{3}} \frac{(a_{in} + a_{out})}{2} \quad (4.7)$$

where “in” and “out” refer to the inner and outer planets in an adjacent pair (Crossfield et al., 2015; Simukoff et al., 2016). Using the stability criterion of $\Delta = (a_{out} - a_{in})/R_H > 9$ for adjacent planets (Smith and Lissauer, 2009), we estimated the smallest semi-major axis for an Earth-mass planet exterior to planet “f” that can fulfill the criterion, assuming a Jupiter mass for planet “f”. Our calculations show that this minimum semi-major axis is located at ~ 2.52 AU, placing such a hypothetical planet in the outer part of the optimistic HZ region (see Figure 4.9). Thus it is still (barely) possible for a terrestrial planet to retain orbital integrity within the HZ of the system.

4.5 Conclusions

We have re-analysed the K2-93 multi-planet system, which was discovered and first analysed by V16a based on long-cadence data from K2 Campaign 5. Short-cadence data obtained during K2 C18 have enabled us to perform an asteroseismic analysis of the host star, placing strong constraints on the stellar parameters. From the asteroseismic modeling we obtain a value for the stellar mass of $1.22^{+0.03}_{-0.02} M_\odot$, a stellar radius of $1.30 \pm 0.01 R_\odot$, and an age of $2.07^{+0.36}_{-0.27}$ Gyr. The asteroseismic analysis further suggests that a high [obliquity](#) can be ruled out, but the stellar inclination can only be weakly constrained.

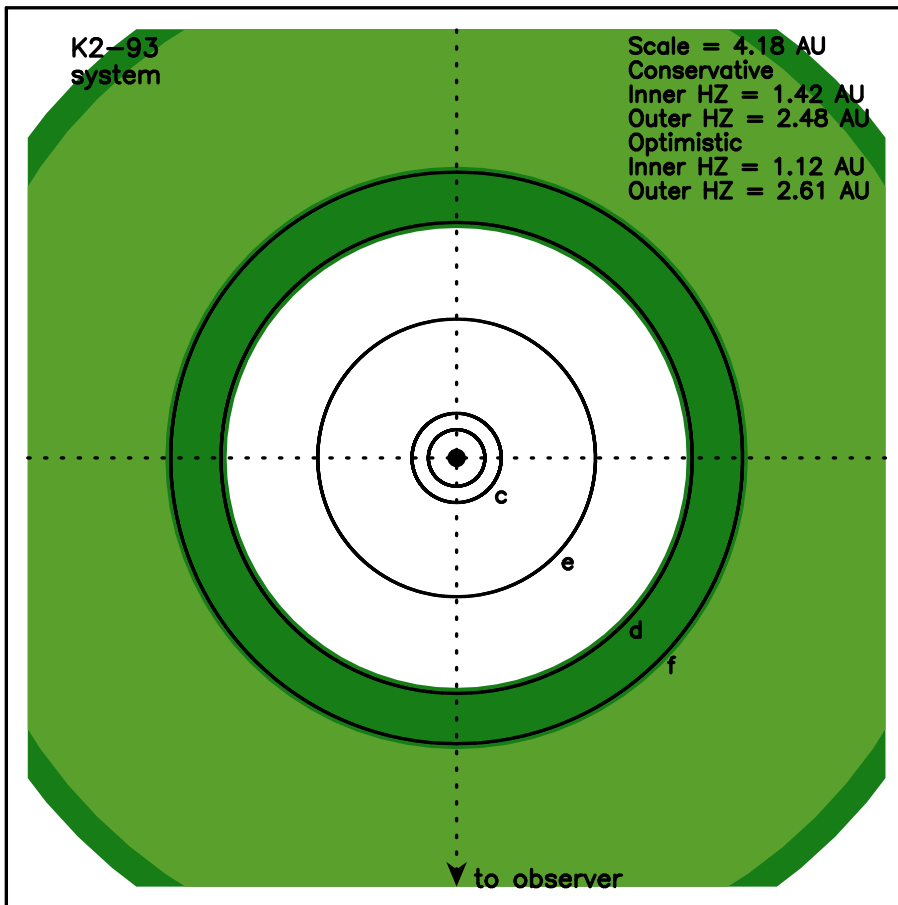


Figure 4.9 | Habitable zone estimate. A top-down view of the K2-93 planetary system spanning 4.18 AU across, where the orbits of the planets are shown as solid circles. The conservative HZ is shown in light green, and the optimistic extension to the HZ is shown below in dark green.

The updated stellar parameters from our asteroseismic analysis have enabled an improved prediction of the periods of planets “d” and “f”, which for both planets match one of their allowed periods. We predict the period of planet “d” to be ~ 278 days, but note that the value of n in equation Equation (4.3) has an uncertainty of ± 1 . For planet “f” we predict the period to be ~ 542 days, while for planet “e” (which did not transit again in C18) we predict a period of $\sim 260^{+160}_{-60}$ days. To appraise the impact on the planetary analysis from the adopted data reduction, we applied an independent analysis (Chontos et al., 2019) to the C18 data obtained from the *K2SFF* pipeline (Vanderburg and Johnson, 2014). This independent

analysis returned parameters in agreement with the results reported in Table 4.3.

We found that the transit parameters of planet “c” are poorly determined using the [K2](#) data, resulting in an unrealistic value for the orbital eccentricity and a predicted period that does not match the measured period. Comparing with [V16a](#), we find that their reported transit parameters appear to suffer the same problem. It would therefore be interesting to observe the transit of planet “c” from a ground-based facility, which should be possible given the period of only \sim 31.7 days though the shallow transit for this planet would make it difficult to detect.

By comparing the stellar density determined from [asteroseismology](#) with that obtained from the transit fit we computed distributions for the orbital eccentricities of the planets. For all planets we predict low-eccentricity orbits, and find in particular for planets “d” and “f” that the low-eccentricity solution results in a predicted period consistent with an allowed period. A better constraint on the orbital eccentricities, and the planetary masses, should be obtained from [RV](#) observations.

Based on our updated stellar and planetary parameters we found that planets “d” and “f” fall within the inner part of the optimistic habitable zone, making these planets interesting in terms of potential exomoon habitability.

5

Solar-like oscillations in γ Cephei A as seen through SONG & TESS

In the previous chapter we saw an asteroseismic analysis of the K2-93 system using photometry from [K2](#), however, as discussed in Section [2.2.1.3](#), the inheritor to [Kepler](#) and [K2](#) is the [TESS](#) mission. Therefore, in this chapter I will present the results of an asteroseismic analysis using photometry from [TESS](#) as well as [RVS](#) from the [SONG](#) network.

This analysis is carried out for the future North Star, γ Cephei (γ Cep). As mentioned (Section [2.1](#)), γ Cep A was among the earliest planet hosting candidates. In addition to hosting a planet, γ Cep is also a binary system, composed of the [RGB](#) star γ Cep A and an M-dwarf, γ Cep B. Clearly, the γ Cep system is an interesting system both in terms of stellar physics through [asteroseismology](#) as well as the dynamics of the system, particularly how γ Cep B might have influenced the formation and evolution of the planetary system around γ Cep A. This work is in preparation for submission as

E. Knudstrup, M. N. Lund, M. Fredslund Andersen, J. L. Rørsted, F. P. Hernandez, T. R. White, F. Grundahl, P. L. Pallé, D. Stello, H. Kjeldsen, M. Vrard, M. L. Winther, R. Handberg, and S. Simón-Díaz. “Solar-like oscillations in γ Cephei A as seen through SONG & TESS”. In prep.

The text presented here is a slightly modified version of the current manuscript. In this work I did the spectral analysis (Section [5.2.3](#)) and the initial data analysis, i.e., the de-trending and cleaning of the time series as well as preparing the power spectra (Section [5.3.1](#) and Section [5.3.2](#)). I also did the orbital analysis (Section [5.5.2](#)) and subsequent analysis in Section [5.5.4](#). Mikkel N. Lund and I wrote most of the paper.

Summary of the Chapter

Fundamental stellar parameters such as mass and radius are some of the most important building blocks in astronomy, both when it comes to understanding the star itself, but also when it comes to deriving properties of the exoplanets they host. *Asteroseismology* of solar-like oscillations allows us to determine these parameters with high precision. Here we investigate the solar-like oscillations of the **RGB** star γ Cep A, which harbours a giant planet on a wide orbit. We do this utilising both ground-based **RVS** from the **SONG** network as well as space-borne photometry from the NASA **TESS** mission. From the **RVS** and photometric observations we create a combined power spectrum, which we use in an asteroseismic analysis to extract individual frequencies. We clearly identify several radial and quadrupole modes as well as multiple mixed, dipole modes. We use these frequencies along with spectroscopic and astrometric constraints to model the star. Here we find a mass of $1.27^{+0.05}_{-0.07} M_{\odot}$, a radius of $4.74^{+0.07}_{-0.08} R_{\odot}$, and an age of $5.7^{+0.8}_{-0.9}$ Gyr. We use the mass of γ Cep A and our **SONG RVS** to derive masses for γ Cep B and γ Cep Ab of $0.328^{+0.009}_{-0.012} M_{\odot}$ and $6.6^{+2.3}_{-2.8} M_{\text{Jup}}$, respectively.

5.1 Introduction

Owing to its brightness the Gamma Cephei (γ Cep) system has a long and rich history in the astronomical literature. In their high-precision **RV** survey for planetary companions around nearby stars Campbell et al. (1988) found γ Cep to be a single-lined spectroscopic binary. On top of the large-scale **RV** signal induced by the binary orbit of the secondary companion, Campbell et al. (1988) found an additional variation with a periodicity of around 2.7 yr and an amplitude of some 25 m s^{-1} , which they suspected to be due to a third body in the system orbiting the primary star. As such γ Cep was amongst one of the first systems proposed to harbour an extra-solar planet (exoplanet). The planetary nature of this third body, γ Cep Ab or Tadmor¹, was confirmed by Hatzes et al. (2003), who found a period of around 906 d and an amplitude of 27.5 m s^{-1} , corresponding to a minimum mass of $1.7 M_{\text{J}}$.

In Reffert and Quirrenbach (2011) the astrometric orbit of γ Cep was investigated using *Hipparcos* data (van Leeuwen, 2007). This enabled the authors to place constraints on the orbital inclination of the planet, finding

¹: Following the 2015 edition of the IAU NameExoWorlds initiative (<https://www.iau.org/news/pressreleases/detail/iau1514/>).

minimum and maximum values of $i = 3.7^\circ$ and $i = 15.5^\circ$, corresponding to $28.1 M_J$ respectively $6.6 M_J$. The mass range for γ Cep Ab thus transitions the border between the planetary and brown dwarf regimes from $\sim 13 - 80 M_J$ (Baraffe et al., 2002; Spiegel et al., 2011). Neuhäuser et al. (2007) found an orbital inclination for the binary orbit of $i_{AB} = 119.3 \pm 1.0^\circ$, meaning that the planetary orbit is perpendicular to the binary orbit. In addition, they determined the masses of the stars to be $M_A = 1.40 \pm 0.12 M_\odot$ for the primary and $M_B = 0.409 \pm 0.018 M_\odot$ for the secondary, hence the primary component is consistent with it being a “retired” A star, while the secondary is an M dwarf.

A stellar fly-by after the formation of the planet has been suggested to be responsible for tilting the binary orbit (Martí and Beaugé, 2012). Recently, Huang and Ji (2022) employed the eccentric Kozai-Lidov (EKL; Kozai, 1962; Lidov, 1962) mechanism to explain the high mutual inclination. The exact orbital configurations and the masses involved have significant consequences for how the system might have formed and since evolved. For instance, Jang-Condell et al. (2008) argue that γ Cep B should have truncated the protoplanetary disc around γ Cep A, which could have limited planet formation in the disk.

Clearly, γ Cep is an intriguing system in the context of planet formation, dynamical evolution, and system architectures. Understanding these processes requires intricate knowledge of the fundamental properties of the host star. Asteroseismology is an important tool in stellar characterisation, directly linking the observed oscillation frequencies to the stellar properties such as mass, radius, and age (Aerts et al., 2010). Solar-like oscillations are very prevalent in subgiant and RGB stars with amplitudes of several hundreds ppm as observed in photometry (e.g., Huber et al., 2019; Stokholm et al., 2019; Li et al., 2020) and several $m s^{-1}$ in RV (e.g., Stello et al., 2017), which can easily be detected with modern photometers and spectrographs. With periods of a few hours it is not only possible, but also viable to do asteroseismic studies of RGB stars with ground-based facilities (see, e.g., Grundahl et al., 2017).

While the mass of γ Cep A would suggest it to be an A-type star of origin, the star has been known to be an evolved star for many years (e.g., Eggen, 1955) and it has thus transitioned into a K-type star, making it a viable target for asteroseismic studies of solar-like oscillations. The oscillations in γ Cep A were investigated in Stello et al. (2017) as part of the retired A-star controversy in which there appears to be an overabundance of relatively massive planet hosting stars (Johnson et al., 2014; Campante, 2017; Hjørringgaard et al., 2017; North et al., 2017). For this they made use

of observations from the **SONG** (Grundahl et al., 2017) project. This was further investigated with additional **SONG** observations in Malla et al. (2020) who found a mass of $1.32 \pm 0.12 M_{\odot}$ from the average seismic parameters: the large frequency separation, $\Delta\nu$, and the frequency of maximum power, ν_{\max} .

Here we expand the asteroseismic and orbital analysis of γ Cep A through additional ground-based observations from the **SONG** network as well as space-based photometry from the **TESS** (Ricker et al., 2015) mission. The paper is structured as follows: in Section 5.2 we present the observations and spectroscopic analysis. Our asteroseismic data analysis is detailed in Section 5.3, and our modelling is described in Section 5.4. We discuss our results in Section 5.5, and conclude in Section 5.6.

5.2 Observations

To detect oscillations of the primary star in the system, γ Cep has been closely monitored with both the 1-m fully robotic Hertzsprung **SONG** telescope (Fredslund Andersen et al., 2019) on Observatorio del Teide, Tenerife, Spain, and the Chinese **SONG** node (Deng et al., 2013) at the Delingha Observing Station, China. In addition to the ground-based data γ Cep has also been observed by **TESS** in three sectors. In addition to the **SONG** and **TESS** data, we observed γ Cep with the **NOT** at the Roque de los Muchachos, La Palma, Spain, using **FIES** (Frandsen and Lindberg, 1999; Telting et al., 2014).

5.2.1 SONG data

The **SONG** data were obtained under the programmes Poo-02 (PI Pere Pallé, IAC), Po6-06 (PI Dennis Stello, UNSW), and P10-01 (PI Mads Fredslund Andersen, AU) during Autumn of 2014, 2017, and 2019. The observations were carried out with an iodine cell for precise wavelength calibration, an exposure time of 120 seconds, and using slit number 6 which corresponds to a resolving power ($\lambda/\Delta\lambda$) of 90,000. Each 1D spectrum covering the wavelength range from 4400 to 6900 Å was extracted, and the **RVS** obtained following the procedures outlined in Grundahl et al. (2017) using the **iSONG** reduction code (Corsaro et al., 2012; Antoci et al., 2013). All **RVS** were obtained using the same high resolution template to ensure no unwanted shifts in **RVS** were introduced between the different data sets. In Figure 5.1 we show the **RVS** from the three **SONG** campaigns. The inset shows one night of observations in the 2014 campaign with error bars.

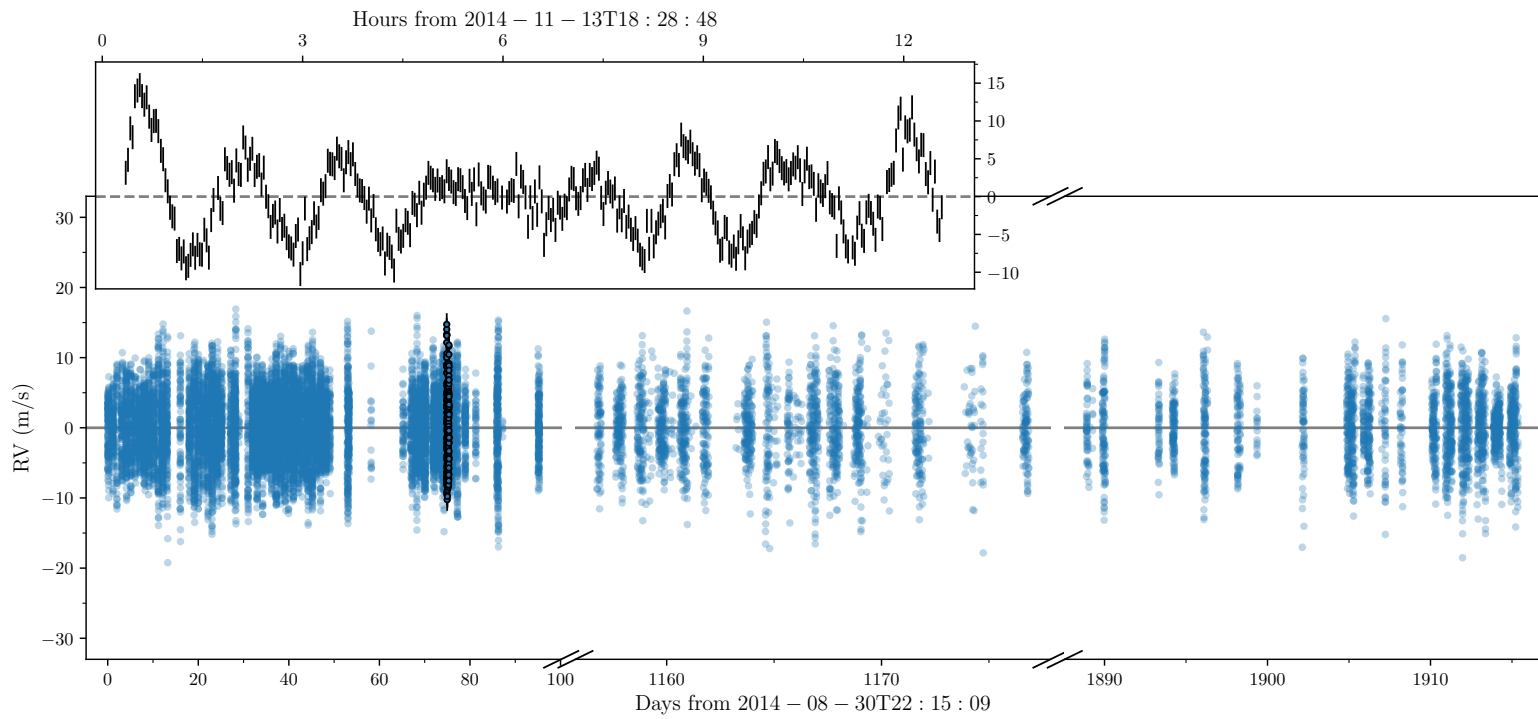


Figure 5.1 | SONG campaigns. The three different seismic [SONG](#) campaigns of γ Cep after filtering and subtracting a nightly median (Section 5.3.1). The error bars in the inset is one night of observations from the 2014 campaign. The insert is displayed in the main plot as black circles with error bars.

5.2.2 TESS data

γ Cep was observed by **TESS** in Sectors 18 (November 2019), 24-25 (mid-April to start-June 2020), and 52 (mid-May to mid-June 2022). In all four sectors γ Cep was observed in **TESS**' 2 min cadence mode. We downloaded the extracted **TESS** light curves of γ Cep from the Mikulski Archive for Space Telescopes (MAST) created by the Science Processing Operations Center (SPOC; Jenkins et al., 2016) which uses Simple Aperture Photometry (SAP; Twicken et al., 2010; Morris et al., 2020). Common instrumental systematics were removed through the Presearch Data Conditioning (PDCSAP; Smith et al., 2012; Stumpe et al., 2012) algorithm and we used these PDCSAP light curves in our analysis. We also tested a photometric extraction using the K2P² pipeline (Lund et al., 2015) with custom apertures, but with a similar quality to the PDCSAP data we chose to adopt the latter for better reproducibility.

5.2.3 Spectroscopic analysis

The observations of γ Cep using **FIES** (carried out in 2021) were obtained to get high **SNR** spectra to extract spectroscopic parameters. For the spectral analysis we used all our **FIES** spectra with the programme iSpec (Blanco-Cuaresma et al., 2014; Blanco-Cuaresma, 2019). First, we normalised the spectra by fitting the continuum using splines. We then calculated the **RV** of the star at each epoch and shifted the spectra into the restframe. To derive the stellar parameters we used iSpec with the code SPECTRUM (Gray and Corbally, 1994), which creates a synthetic stellar spectrum to compare our spectra against. We opted for the MARCS (Gustafsson et al., 2008) grid of model atmospheres as the template for the synthetic spectrum.

We follow the approach described in Lund et al. (2016) in which the spectroscopic parameters are determined through an iterative process due to degeneracies in the estimates of T_{eff} (the effective temperature), $\log g$ (surface gravity), and [Fe/H] (metallicity) (Smalley, 2005; Torres et al., 2012). We used our measured value of ν_{max} of 185.6 μHz (Table 5.2) with the T_{eff} from Mortier et al. (2013) of 4764 ± 122 K as an initial value to estimate the seismic $\log g$

$$g \simeq g_{\odot} \left(\frac{\nu_{\text{max}}}{\nu_{\text{max},\odot}} \right) \left(\frac{T_{\text{eff}}}{T_{\text{eff},\odot}} \right)^{1/2}, \quad (5.1)$$

with $\nu_{\text{max},\odot} = 3090 \pm 30$ μHz , $T_{\text{eff},\odot} = 5777$ K, and $g_{\odot} = 27,402$ cm s^{-1} (Brown et al., 1991; Kjeldsen and Bedding, 1995; Huber et al., 2011; Chaplin

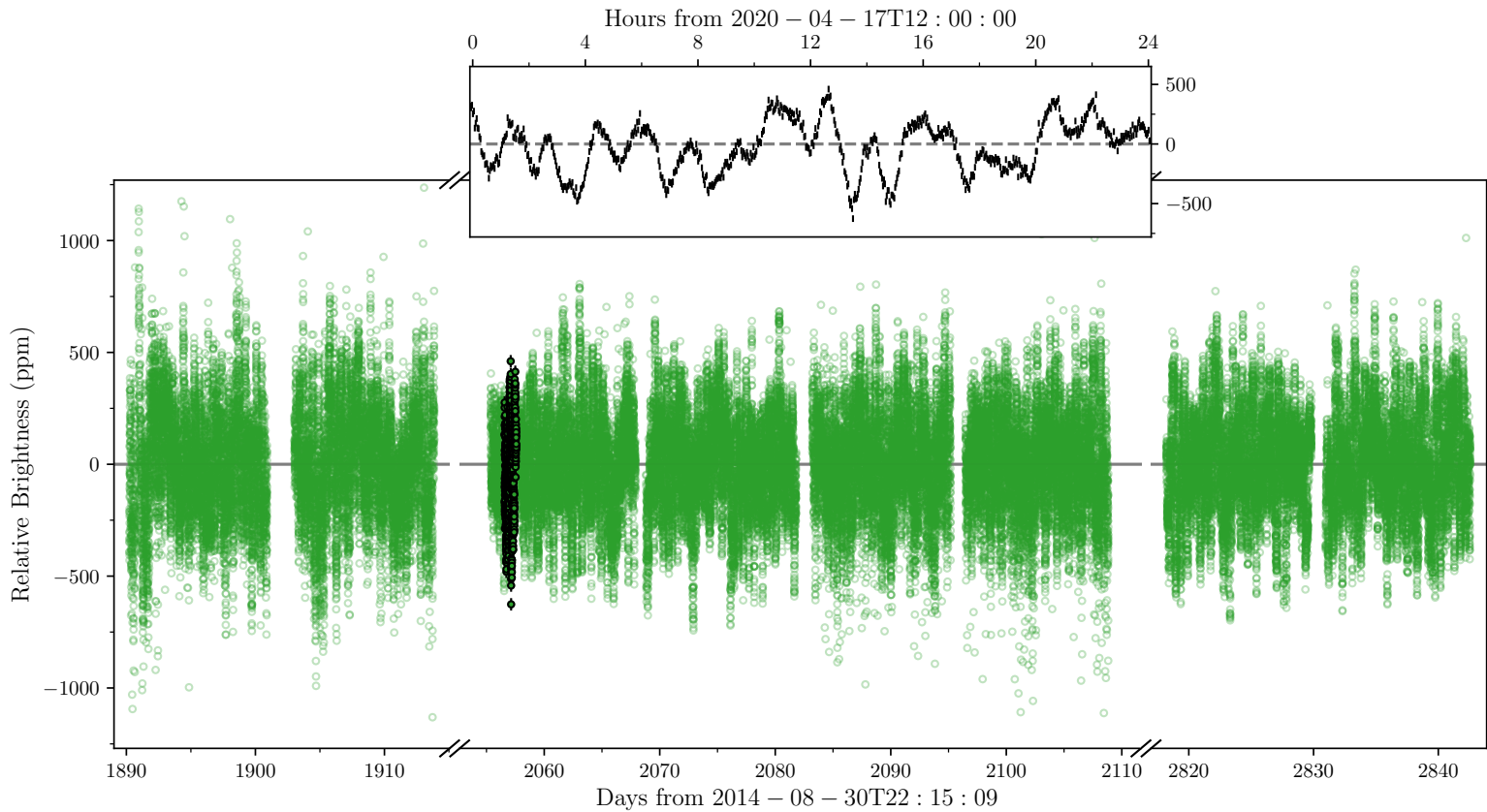


Figure 5.2 | TESS observations. The γ Cep light curve as observed by [TESS](#) in Sectors 18, 24, 25, and 52. Here we have removed outliers and normalised the light curve as described in Section 5.3.1. The error bars in the inset show a 24 hr interval. The data shown in the inset are highlighted in the main plot as black circles with error bars.

et al., 2014). Initially, we used those values as starting values in a fit for each epoch where all parameters were free to vary. From this initial fit we got $T_{\text{eff}} = 5094$ K as the median for all epochs, which yields a $\log g$ of 3.19. In the second iteration we thus fixed $\log g$ at 3.19, while letting T_{eff} , [Fe/H], $v \sin i_A$ (projected rotation speed), ζ (macro-turbulence), and ξ (micro-turbulence) free to vary. The resulting median T_{eff} across epochs was 4806 K, which gives a $\log g$ of 3.18. We thus considered the fit to have converged.

We find the results to be very consistent from epoch to epoch, which leads to very precise measurements of the parameters. These do not account for any systematic uncertainties, which are undoubtedly present. We therefore follow the approach of Torres et al. (2012) and add (in quadrature) uncertainties for T_{eff} , [Fe/H], and $v \sin i_A$ of 59 K, 0.062 dex, and 0.85 km s^{-1} , respectively. The results are summarised in Table 5.1. We also find that our spectroscopic results agree well with the range of values found in the literature – Figure 5.3 shows the distribution of results for T_{eff} , [Fe/H], and $\log g$ from the literature after year 2000, as collected from the SIMBAD database (Wenger et al., 2000).

5.2.4 Luminosity from *Gaia*

As an additional constraint for the seismic modelling we compute the stellar luminosity from combining a distance measure with the *Gaia* DR3 G -band magnitude following (see, e.g., Torres et al., 2010):

$$L/L_{\odot} = 10^{0.4(5 \log_{10}(d) - G + A_G - BC_G + V_{\odot} + 26.572 + BC_{V,\odot})}, \quad (5.2)$$

where d is the distance in pc, G is the apparent *Gaia* EDR3 G -band magnitude, A_G is the extinction in the G -band, and BC_G is the bolometric correction. We use the photogeometric distance from Bailer-Jones et al. (2021, see Table 5.1), adopt values of $V_{\odot} = -26.74 \pm 0.01$ mag and $BC_{V,\odot} = -0.078 \pm 0.005$ mag from analysis of empirical solar spectra (Lund et al., in prep.), and make saturation corrections to the *Gaia* photometry following Riello et al. (2021). For the bolometric correction BC_G we use the interpolation routines of Casagrande and Vandenberg (2018a). Based on the *Stilism*² 3D reddening map (Lallemand et al., 2014; Capitanio et al., 2017; Lallemand et al., 2019) we adopt a zero extinction, which is consistent with the close proximity of the system at a distance of only ~ 13.2 pc. The resulting luminosity is provided in Table 5.1.

2: <https://stilism.obspm.fr/>

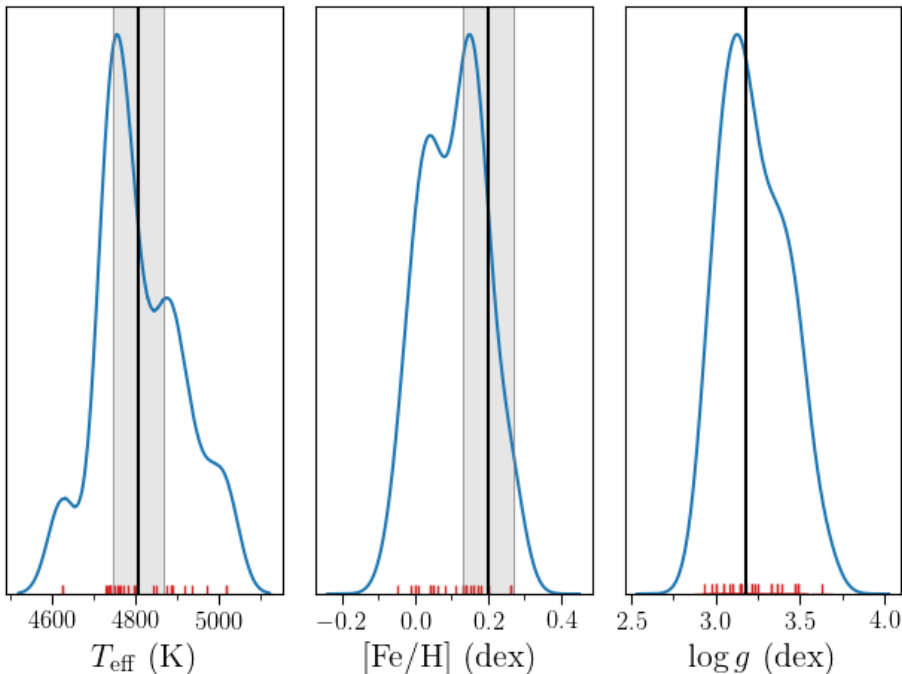


Figure 5.3 | Literature comparison of γ Cep A. The panels show the KDEs of the values for T_{eff} , $[\text{Fe}/\text{H}]$, and $\log g$ obtained from the literature after year 2000 via the SIMBAD database. The reported values of the individual studies are indicated with red markers. The vertical full lines and shaded regions indicate our values and associated uncertainties.

5.3 Seismic analysis

5.3.1 Filtering

For the asteroseismic analysis we filtered the [SONG](#) data on a night-by-night basis using a Locally Weighted Scatterplot Smoothing (LOWESS; Seabold and Perktold, 2010) filter, which takes both the duration of the observations and the fill factor on a given night into account. Firstly, we filter out the worst outliers by crudely removing all points with a median absolute deviation (MAD) > 6 . We then used the LOWESS filter to smooth the data, thereby removing the oscillations. We define the fill factor as $f \equiv N\delta t/\tau$ with δt being the sampling (2 min.), τ the duration of the night, and N the number of data points. For nights with $N < 20$ or $f < 0.3$ we simply use the median to flatten the time series. In this flat(ter) time series

Table 5.1 | System parameters for γ Cep. Catalog IDs, coordinates, magnitudes, spectral type, and spectroscopic parameters. Notes. ^(a)<https://exofop.ipac.caltech.edu/tess/>. ^(b)Gaia Collaboration et al. (2022). ^(c)Mermilliod (1997). ^(d)Bailer-Jones et al. (2021) (photogeometric). ^(e)Keenan and McNeil (1989). ^(f)This work from FIES spectra using iSpec. ^(g)Corrected following Riello et al. (2021).

γ Cep A		
Parameter	Value	Description
TIC ^(a)	367912480	
HD	222404	
<i>Gaia</i> DR3 ^(b)	2281778105594488192	
α (J2000) ^(b)	23 39 20.59	Right ascension (R.A.)
δ (J2000) ^(b)	+77 37 59.25	Declination (Dec.)
μ_α (mas yr ⁻¹) ^(b)	-64.86 ± 0.14	Proper motion R.A.
μ_δ (mas yr ⁻¹) ^(b)	171.16 ± 0.14	Proper motion Dec.
ϖ (mas) ^(b)	72.52 ± 0.15	Parallax
dist (pc) ^(d)	13.78 ± 0.03	Distance
G ^(b)	$2.9456 \pm 0.031^{(g)}$	<i>Gaia</i> G magnitude
L_G (L_\odot)	10.48 ± 0.23	Lum. from <i>Gaia</i> G -band
V ^(c)	3.212 ± 0.008	Tycho V magnitude
$B - V$ ^(c)	1.028 ± 0.004	Tycho colour
SpT ^(e)	K1III-IV	Spectral type
T_{eff} (K) ^(f)	4806 ± 60	Effective temperature
$\log g$ (cgs; dex) ^(f)	3.18	Surface gravity
[Fe/H] (dex) ^(f)	0.20 ± 0.07	Metallicity
$v \sin i_A$ (km s ⁻¹) ^(f)	0.0 ± 0.9	Projected rotation
ζ (km s ⁻¹) ^(f)	3.77 ± 0.04	Macro-turbulence
ξ (km s ⁻¹) ^(f)	1.14 ± 0.02	Micro-turbulence

Table 5.2 | Stellar parameters of γ Cep A. Physical properties for γ Cep A derived from [asteroseismology](#) from the literature and in this work. **Notes.** ^(a)Derived from spectroscopic parameters in Mortier et al. (2013). ^(b)From Mortier et al. (2013). ^(c)From the full time series.

	Stello et al. (2017)	Malla et al. (2020)	SONG ^(c)	TESS ^(c)	MESA	BASTA
Mass (M_{\odot})	1.32 ± 0.20	1.32 ± 0.12	-	-	1.33 ± 0.04	$1.27^{+0.05}_{-0.07}$
Radius (R_{\odot})	$4.88 \pm 0.22^{(a)}$	4.88 ± 0.22	-	-	4.83 ± 0.06	$4.74^{+0.07}_{-0.08}$
Age (Gyr)	-	-	-	-	4.3 ± 0.6	$5.7^{+0.8}_{-0.9}$
T_{eff} (km s $^{-1}$)	$4764 \pm 122^{(b)}$	-	-	-	4821 ± 14	4775^{+33}_{-31}
$\log g$ (cgs; dex)	3.17 ± 0.08	-	-	3.194 ± 0.002	$3.189^{+0.007}_{-0.008}$	
[Fe/H] (dex)	$0.13 \pm 0.06^{(b)}$	-	-	-	-	0.18 ± 0.06
ν_{max} (μ Hz)	185 ± 28	185 ± 9	190.1 ± 0.7	$185.6^{+1.0}_{-0.9}$	-	191^{+3}_{-4}
$\Delta\nu$ (μ Hz)	-	14.28 ± 0.58	-	-	-	$14.59^{+0.06}_{-0.05}$

we removed all points with a $MAD > 3$. We furthermore use the nightly MAD as the uncertainties for the data acquired on that night. The resulting time series can be seen in Figure 5.1.

Equivalently for the **TESS** data we use a LOWESS, but on a **TESS** orbit-to-orbit basis, i.e., in intervals of around 13.7 d. Again we started out by removing all data points with a $MAD > 6$, then applied the filter to flatten the time series, and removed the outliers, however, using a more conservative rejection criterion and only removing points with a MAD of more than 6 as opposed to 3 for the **RVS** (as the **SONG** data were more prone to outliers, e.g., because of poor weather). To ensure that the uncertainties on the two data sets (**RVS** and photometry) were derived in a consistent way, we estimated the uncertainties as the daily (24 hr) MAD as shown in Figure 5.2.

5.3.2 Power spectra

As we have multiple campaigns of **SONG** data, as well as multiple sectors of **TESS** observations, there are multiple ways of combining the data. We used a number of different power spectra in our analysis of the seismic content, especially for oscillation mode identification. Figure 5.4 shows for **SONG** and **TESS** the power spectra from either the full time series, or weighted averaged power spectra from yearly (**SONG**) or sector-wise power spectra, with the weighting given by the inverse variance ($1/\sigma^2$) of the median spectral white noise level from 3,800 μHz to 3,900 μHz – the average spectra are useful for the detection of oscillations from their higher signal-to-noise ratio, while the full spectra have superior frequency resolution (see Figure 5.4).

Finally, we produced product spectra between the **SONG** and **TESS** data. The benefit of the product spectra is the significantly reduced aliasing effect of the spectral window of **SONG** data. To combine the spectra we first fit and remove their granulation background signal, and then normalise to the peak power.

To account for the granulation background we modelled the power spectra as being composed of a series of Lorentzian functions as

$$\mathcal{P}(\nu) = \eta^2(\nu) (L(\nu) + N(\nu)) + W, \quad (5.3)$$

where L is the Lorentzian accounting for the oscillation power excess, centred on ν_{\max} and with a width Γ and amplitude A . Traditionally, the power excess is modelled by a Gaussian function, but high **SNR** spectra

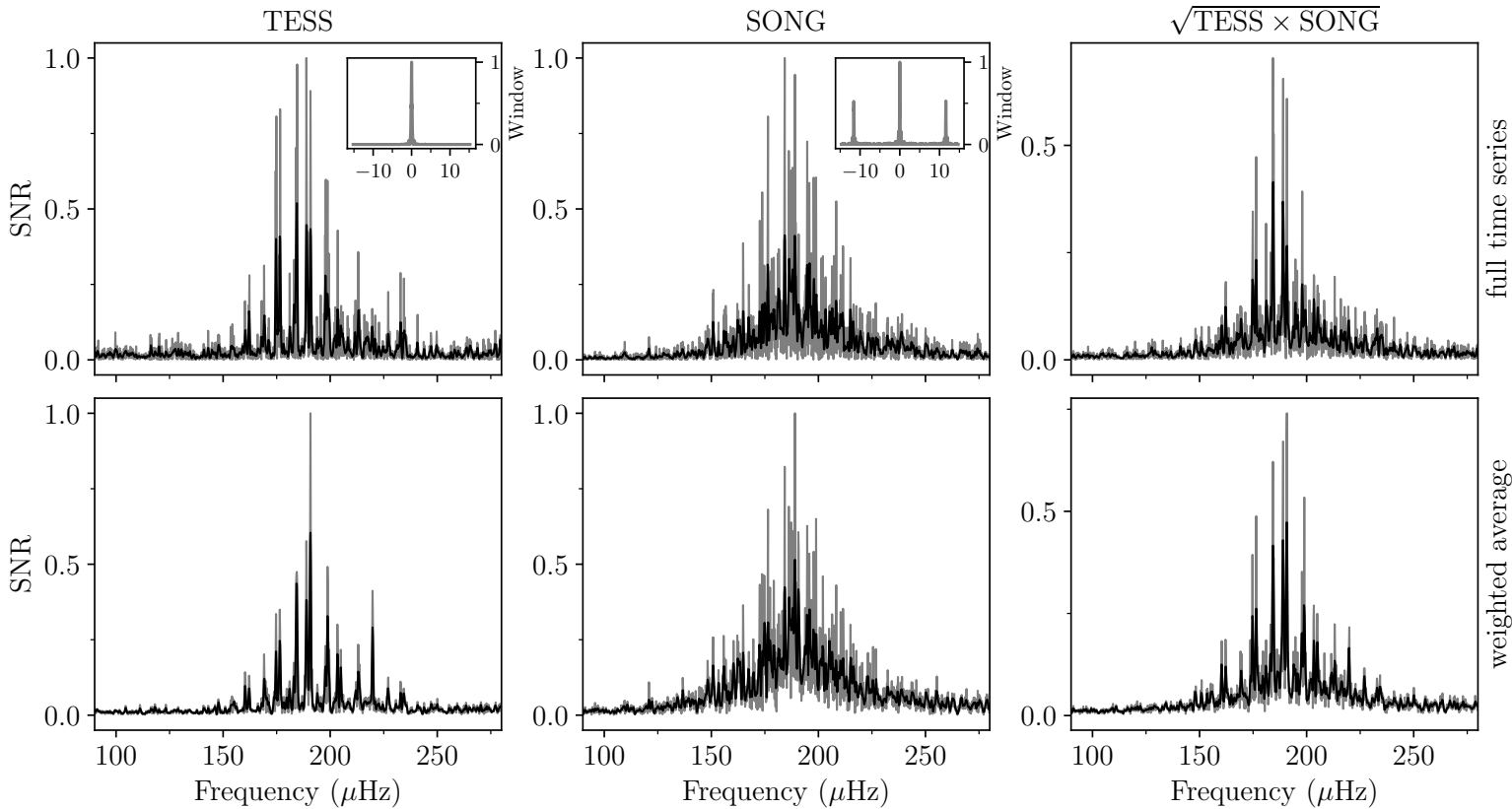


Figure 5.4 | TESS and SONG power spectra. The background corrected power spectra from [TESS](#) (left column) and [SONG](#) (middle) in grey and a smoothed (box-kernel) version shown in black. The bottom row shows the weighted average power spectra, where we have taken the power spectrum for each sector or campaign, subtracted the fitted background, and created a weighted average. In the top row we have simply removed (divided) the background from the power spectra resulting from combining all sectors or all campaigns into the time series. The right column shows the product power spectra created from the full time series (top) and the weighted average power spectra (bottom). The insets in the top left and middle columns show the spectral window from the full time series from [TESS](#) and [SONG](#), respectively.

suggest the envelope is better approximated by a Lorentzian (Lund et al., in prep.). W is the contribution from white noise, and $\eta^2(\nu)$ is the apodisation of the signal power at frequency ν from the 2-minute sampling of the temporal signal (e.g., Chaplin et al., 2011; Kallinger et al., 2014; Lund et al., 2017) given as $\eta^2(\nu) = \sin^2(x)/x^2$ with $x = \pi\nu\delta t$, where δt is the integration time here given as the **TESS** 2 min. cadence. The granulation background is parametrised as (Harvey et al., 1993; Andersen et al., 1994; Lund et al., 2017)

$$N(\nu) = \sum_{i=1}^2 \frac{\xi_i \sigma_i^2 \tau_i}{1 + (2\pi\nu\tau_i)^{\alpha_i}}, \quad (5.4)$$

corresponding to an exponentially decaying autocorrelation function, with a power of the temporal decay rate $-2/\alpha_i$. τ_i and σ_i are respectively the characteristic timescale and the root-mean-square (rms) in the time domain of the i th background component.

We employed a similar strategy to remove the background in the **SONG** data. However, as the granulation background is much less visible in **RV**, as is evident from Figure A.2, we only included one term in the granulation background, meaning $i = 1$ in Equation (5.4). We furthermore only included frequencies above 35 μ Hz because of the low **SNR** below this value. The resulting background fits are shown in Figure A.1 for **TESS** and Figure A.2 for **SONG**.

5.3.3 Frequency extraction

The extraction of individual oscillation mode frequencies, i.e. peakbagging, was performed on the full time series product power spectrum described above. The procedure followed that outlined in the LEGACY project by Lund et al. (2017). The identification of oscillation modes was straightforward for the radial ($l = 0$) and quadrupole ($l = 2$) modes from the échelle diagram and a value for $\Delta\nu$. As a sanity check we also tried the PBJam tool (Nielsen et al., 2021) which confirmed our selection. For the mixed dipole ($l = 1$) modes we first manually identified the prominent peaks in the power spectrum that could not be associated with $l = 0, 2$, these are shown in the power spectrum in Figure 5.5 and the échelle diagram in Figure 5.6. To evaluate the likelihood of a given peak actually being a mixed-mode, we tried to match the asymptotic relation for mixed modes by Shibahashi (1979), including the curvature of the variation in the large separation to be as in Appourchaux (2020). With values for the coupling strength (q), $\Delta\nu$, the phase factors ϵ_g and ϵ_p , the strength of the $\Delta\nu$ variation/curvature

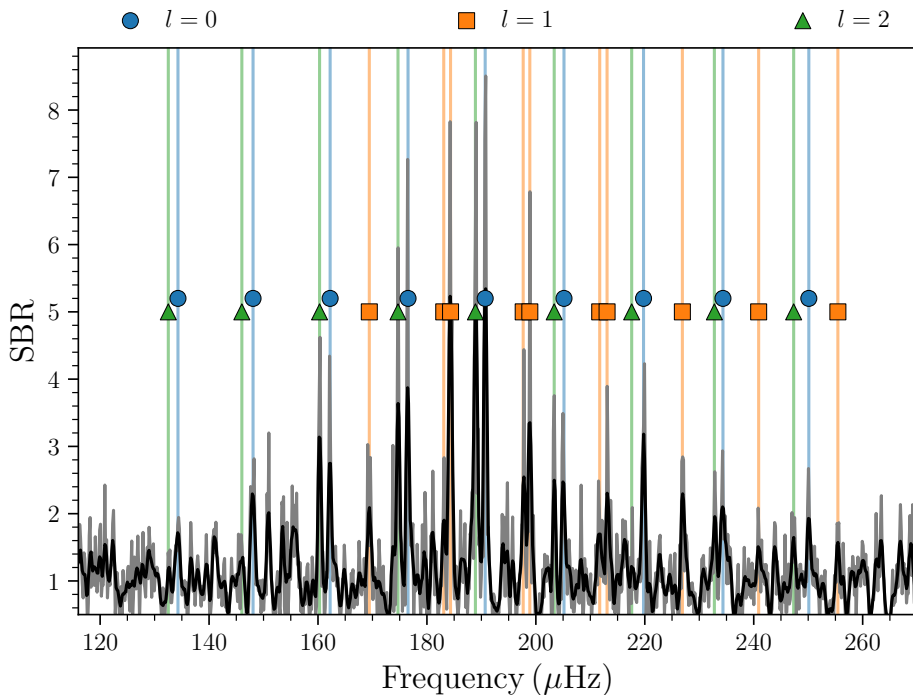


Figure 5.5 | Observed power spectrum. Signal-to-Background ratio of the product power spectrum ($\sqrt{\text{SONG} \times \text{TESS}}$) used for the peakbagging. The black spectrum is a smoothed version of the corresponding grey spectrum. The markers and vertical lines indicate the frequencies of the extracted oscillation modes.

(α) , $\delta\nu_{01}$ from the asymptotic p-mode relation, and the asymptotic period spacing ($\Delta\Pi_1$) one can solve for the frequencies of the mixed modes. The parameters pertaining to the p-mode ($\Delta\nu$, ϵ_p , α) are obtained from a fit to the identified radial modes following Lund et al. (2017). A good first guess on $\Delta\Pi_1$ can be obtained from its proportionality to $\Delta\nu$ before the star enters the red clump phase (Bedding, 2011; Mosser et al., 2014), leading to a value of $\Delta\Pi_1 \sim 84$ s. An estimate of the coupling factor of $q \sim 0.15 \pm 0.03$ is obtained from the results of Mosser et al. (2017). From Mosser et al. (2018) we find $\epsilon_g \sim 0.25 \pm 0.05$, and lastly we estimate $\delta\nu_{01} \sim -0.3 \pm 0.1$ μHz from Huber et al. (2010).

To further aid the identification of potential dipole mixed-modes we compute a proxy for the expected relative amplitudes of the asymptotically derived modes. This follows from the prescription of Benomar et al. (2014), who finds that the dipole amplitude (A_1) can be found in units of the radial

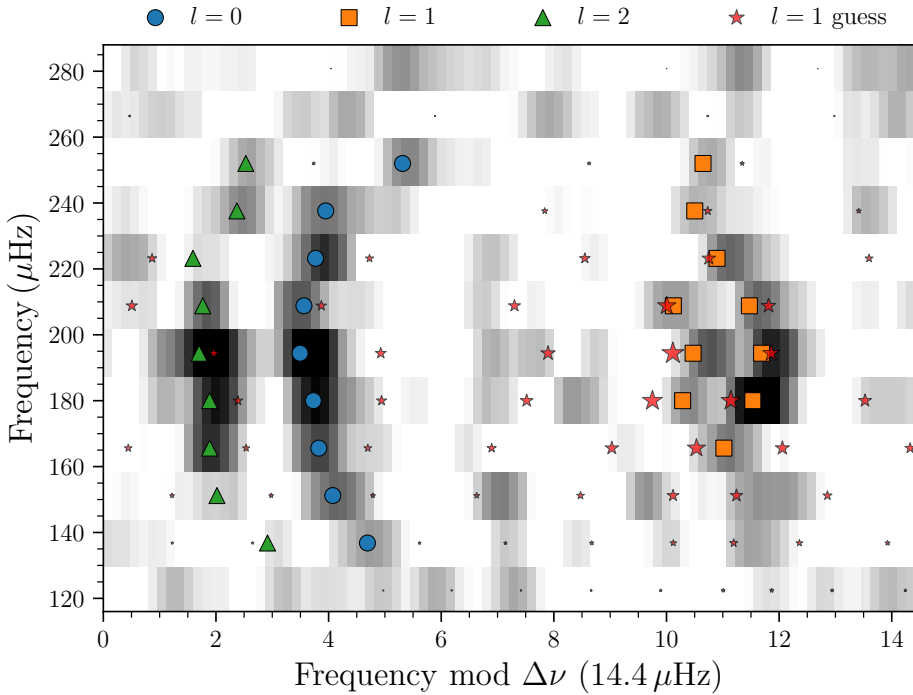


Figure 5.6 | Observed échelle diagram. Échelle diagram of the smoothed (black) spectrum in the left panel. The markers indicate, as in the left panel, the extracted modes. The red stars give the frequencies estimated from the asymptotic mixed-mode relation, with their size showing the expected relative amplitude of the modes.

mode amplitudes (A_0) as $A_1 \approx A_0 V_1 (I_0/I_1) \sqrt{\Gamma_0/\Gamma_1}$. Here I_0/I_1 denotes the ratio of mode inertias, Γ_0/Γ_1 gives the ratio in mode line-widths, while V_1 gives the relative mode visibility (Ballot et al., 2011), where we adopt $V_1^2 = 1.5$ (see Li et al., 2020). This relation can be rewritten in terms of the stretch function ζ introduced by Mosser et al. (2014), quantifying the degree of mode trapping (see also Jiang and Christensen-Dalsgaard, 2014; Mosser et al., 2015; Hekker and Christensen-Dalsgaard, 2017), as $A_1 = A_0 V_1 \sqrt{1 - \zeta}$. We model $A_0(\nu)$ as a Gaussian with a FWHM of 60 μ Hz

For the peakbagging we took the conservative approach and only selected potential modes where we could find an expected mode from the asymptotic relation in near proximity, and where the amplitude followed the expected pattern. We note that the spectrum contains a number of additional peaks that we could not easily associate with mixed-modes.

Figure 5.6 shows the frequencies and expected relative amplitudes for the mixed modes obtained from the asymptotic relation, in addition to the frequencies extracted from the peakbagging. Considering the known imprecision of the asymptotic mixed-mode relation for evolved stars (Deheuvels et al., 2014; Ong and Basu, 2019; Appourchaux, 2020) we find the match between extracted and expected frequencies quite convincing. The extracted frequencies are provided in Table B.4.

5.4 Seismic modelling

To derive physical properties for γ Cep A, we compared our measured frequencies to those calculated from stellar modelling. Furthermore, when extracting frequencies it can be instructive to compare the low SNR frequencies to model frequencies iteratively to ensure their validity. We therefore modelled our frequencies using two approaches to cross-check both the measured frequencies and the final resulting parameters. We describe these two approaches below.

5.4.1 MESA

We first modelled our frequencies using the MESA code (Modules for Experiments in Stellar Astrophysics; Paxton et al., 2011, 2013, 2015), version 15140. As this was our first iteration, this was done using a subset of the frequencies listed in Table B.4 as input, furthermore no dipole modes were included.

In MESA the model fitting is based on a set of grids of stellar models evolved from the pre-main sequence to the RGB. The standard input physics from MESA were used. The grid is composed of evolutionary sequences with different masses M , initial abundances [M/H] and mixing length parameters. The helium abundance Y were constrained by taking a Galactic chemical evolution model with $\Delta Y / \Delta Z = (Y_{\odot} - Y_0) / Z_{\odot} = 1.33$. Eigenfrequencies were computed in the adiabatic approximation using the ADIPLS code (Christensen-Dalsgaard, 2008a). The stellar parameters are found through a χ^2 minimization that compares observed values to the grid of models discussed above. The general procedure is similar to that described in Pérez Hernández et al. (2019). The results are summarised in Table 5.2.

5.4.2 BASTA

As mentioned in Section 5.3.3, mode identification for the mixed dipole modes is not as straightforward as for the $l = 0, 2$ modes. Therefore, we extracted and modelled our frequencies, namely the dipole modes, in an iterative manner. For this we used **BASTA** (Silva Aguirre et al., 2015; Aguirre Børnsen-Koch et al., 2022).

BASTA fits a star using a grid of stellar models calculated from the Garching Stellar Evolution Code (GARSTEC; Weiss and Schlattl, 2008) along with Bayesian statistics in search of the best-fitting parameters. To accurately reflect the expected distribution of stars with lower mass stars being more abundant, the Salpeter initial mass function (Salpeter, 1955) is applied. Frequency fitting is with the inclusion of a two-term surface correction as given by Ball and Gizon (2014).

We ran **BASTA** with the observed frequencies listed in Table B.4, using the spectroscopic parameters (T_{eff} , $\log g$, and [Fe/H]) from Table 5.1 along with the *Gaia* magnitudes and parallax from Table 5.1 as constraints. For the final iteration, we ran **BASTA** both with and without an additional constraint from our calculated luminosity. The two runs were in agreement, but the luminosity constraint naturally provided smaller uncertainties on the resulting parameters. We therefore adopt the values from this run as our final results.

The resulting fit to the models and their frequencies from **BASTA** is shown in Figure 5.7. We find a mass of $1.27^{+0.05}_{-0.07} M_{\odot}$, a radius of $4.74^{+0.07}_{-0.08} R_{\odot}$, and an age of $5.7^{+0.8}_{-0.9}$ Gyr, which we have tabulated in Table 5.2 along with the spectroscopic parameters (mainly reflecting the input). γ Cep A is clearly located on the RGB as seen in the HR DIAGRAM in Figure 5.8. For the global seismic parameter **BASTA** finds $\nu_{\text{max}} = 191^{+3}_{-4} \mu\text{Hz}$ and $\Delta\nu = 14.59^{+0.06}_{-0.05} \mu\text{Hz}$.

5.4.3 Interferometry

We can obtain an independent measurement of the stellar radius by combining the angular diameters from interferometry (θ_{IF}) with the distance from *Gaia* as:

$$\frac{R_{\text{IF}}}{R_{\odot}} = \frac{D_{\text{Gaia}} \times \text{AU}}{2R_{\odot}} \theta_{\text{IF}}, \quad (5.5)$$

with θ_{IF} in arcseconds, the distance D_{Gaia} in parsec (Table 5.1), and with AU giving the astronomical unit³ (see Silva Aguirre et al., 2012; Lund et al.,

³: We adopt $1 \text{ AU} = 149.5978707 \times 10^9 \text{ m}$ (IAU 2012 Resolution B2) and $R_{\odot} = 6.957 \times 10^8 \text{ m}$ (IAU 2015 Resolution B3; Mamajek et al., 2015).

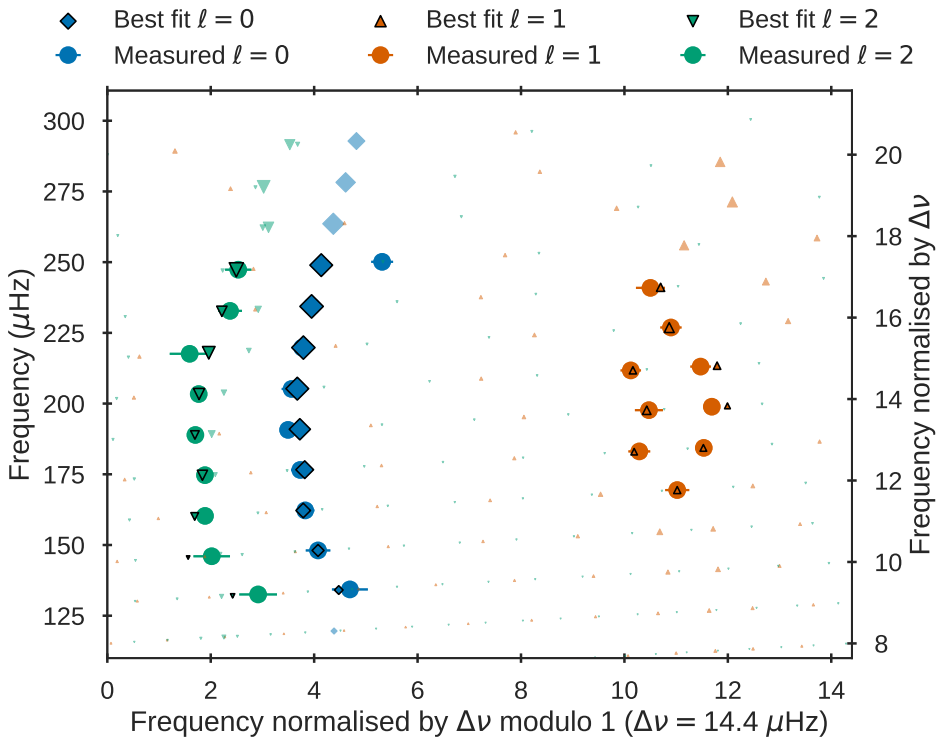


Figure 5.7 | BASTA échelle diagram. Échelle diagram showing our measured $\ell = 0$ (orange), $\ell = 1$ (green), and $\ell = 2$ (blue) frequencies as circles with error bars compared to our model frequencies from BASTA shown with black outlines. Transparent markers with no black outline denote frequencies we have not detected. As in Figure 5.6 marker sizes show the expected relative amplitude of the modes.

2016). In Table 5.3 we list the different available values from the literature together with the resulting stellar radius when adopting the *Gaia* DR3 value for the distance by Bailer-Jones et al. (2021).

We note that the *Gaia* data provides a high RUWE (Renormalised Unit Weight Error; Lindegren et al., 2018) parameter for γ Cep A, that at a value of 3.212 is significantly higher than the suggested threshold of 1.4. This suggests that the *Gaia* distances might be affected by a suboptimal astrometric solution, likely because of the orbital motion induced by the binary companion.

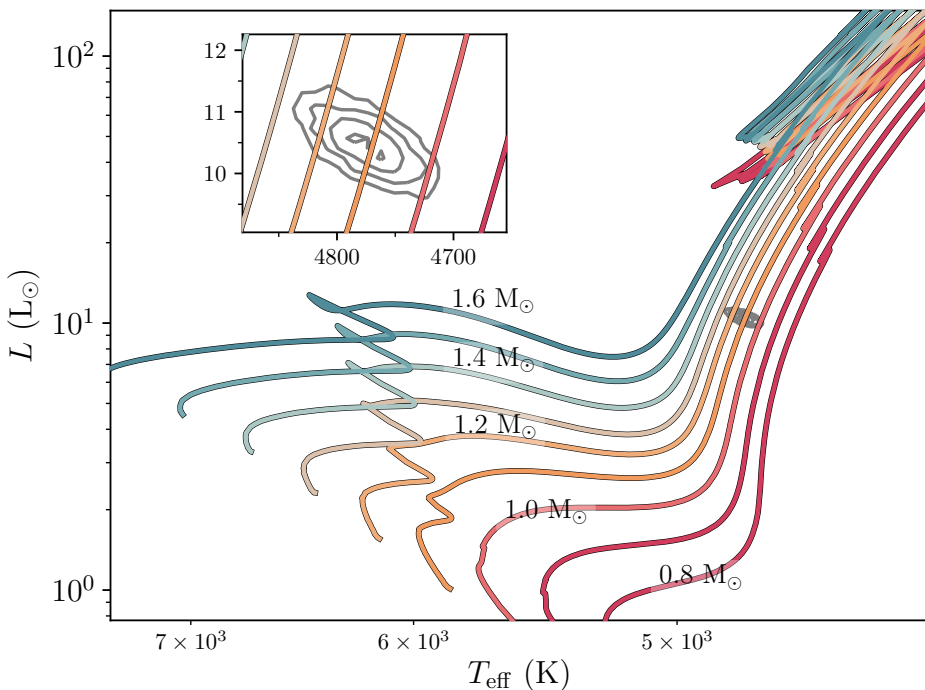


Figure 5.8 | Hertzsprung-Russell diagram for γ Cep A. Here we compare the output from [BASTA](#) (T_{eff}, R_A from Table 5.2) to evolutionary tracks from BaSTI (a Bag of Stellar Tracks and Isochrones; Hidalgo et al., 2018) with $[\text{Fe}/\text{H}] = 0.15$ and with the inclusion of diffusion and [convective core-overshooting](#). The tracks span masses from $0.8-1.6 M_{\odot}$, but only every other track is labeled.

5.5 Discussion

5.5.1 Seismology and physical properties

As is characteristic for subgiants and [RGB](#) stars, the power spectrum of γ Cep A shows mixed modes, which appears when the central region of the star starts to contract and the gravitational acceleration near the core increases. This increases the frequencies of the [g-modes](#), and they will start to couple strongly to the [p-modes](#). Although this complicates the frequency extraction, as the modes no longer follow the asymptotic relation for pure acoustic modes (and as mentioned the mixed-mode asymptotic relation for [RGB](#) stars is imprecise), the mixed-modes also allow us to probe the internal properties as they provide useful information about the core.

Table 5.3 | Interferometry. Angular diameters obtained from interferometry and the associated stellar radius (Equation (5.5)) when adopting the *Gaia* DR3 distance from Bailer-Jones et al. (2021) (see Table 5.1). **Notes.** NPOI: Navy Prototype Optical Interferometer. CHARA: Center for High Angular Resolution Astronomy.

Source	Instrument	θ (mas)	Radius (R_\odot)
Baines et al. (2018)	NPOI	3.254 ± 0.020	4.81 ± 0.03
Hutter et al. (2016)	NPOI	3.329 ± 0.042	4.92 ± 0.06
Baines et al. (2009)	CHARA	3.302 ± 0.029	4.88 ± 0.04
Nordgren et al. (1999)	NPOI	3.24 ± 0.03	4.79 ± 0.05

We find an excellent agreement between the observed dipole modes and those calculated by **BASTA** (Figure 5.7), despite the strong mixing. Furthermore, the radial and quadrupole modes also agree very well with model, with the exception of the highest order ($n = 17$) observed $l = 0$ mode. The excellent agreement allows us to place rather tight constraints on parameters such as the mass ($\sim 5\%$), the radius ($\sim 2\%$), and the age ($\sim 14\%$). Furthermore, the stellar parameters we find using **BASTA** agree well with the ones from MESA.

5.5.2 The binary and planetary system

In an attempt to refine the orbital parameters for both the binary and the planetary orbit, we modelled the orbit in a fit using our **RVS** from the different **SONG** campaigns. When we initially started modelling the orbit we noticed a prominent signal of around 90 d after having subtracted the **RV** signals of the companion star, γ Cep B, and planet, γ Cep Ab, as reported in Hatzes et al. (2003). A number of instrumental effects could introduce a signal of a few meters per second. Temperature and pressure changes being obvious candidates are however unlikely given the use of an Iodine cell for wavelength calibration. Long term trends are known to be present for a number of stars observed with **SONG** as mentioned in Arentoft et al. (2019). These show a velocity change of typically non-sinusoidal nature with a periodicity of 1 yr. The exact morphology and amplitude is strongly dependent on the sky position of the objects, namely the proximity to the ecliptic.

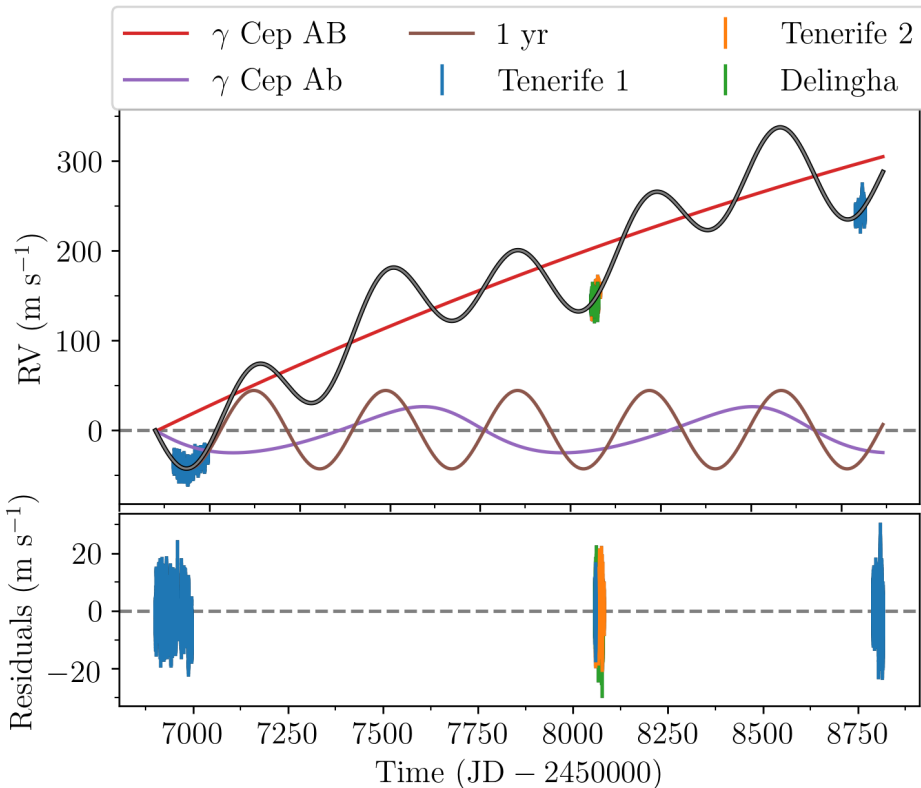


Figure 5.9 | Orbital motion. *Top:* The two *Keplerian* orbits from γ Cep B and γ Cep Ab are shown in red and blue, respectively, and the 1 yr signal is shown as the brown curve. The sum of the signals are shown as the grey model. Here they have all been shifted to start in 0.0 to make it easier to compare them. The Tenerife data are shown in blue and orange, and the Delingha data are shown in green. *Bottom:* The residuals after subtracting the model.

The variations for γ Cep, however, looked more sinusoidal, which might be because we have mainly been sampling the same phase of the 1 yr signal, namely around Autumn. The 90 d signal is thus an artefact of the known 1 yr signal. Therefore, we included an additional term in our model with a period fixed to 365.25 d, but allowing the phase and amplitude to vary. As we have data from Tenerife that was obtained with two different iodine cells (only in 2017), we include two separate **RV** offsets, Γ , for these, and we naturally apply a third offset for the Delingha data.

As the oscillations are clearly seen in the **SONG** data, we modelled these using **Gaussian process (GP)** regression utilising the library **celerite**

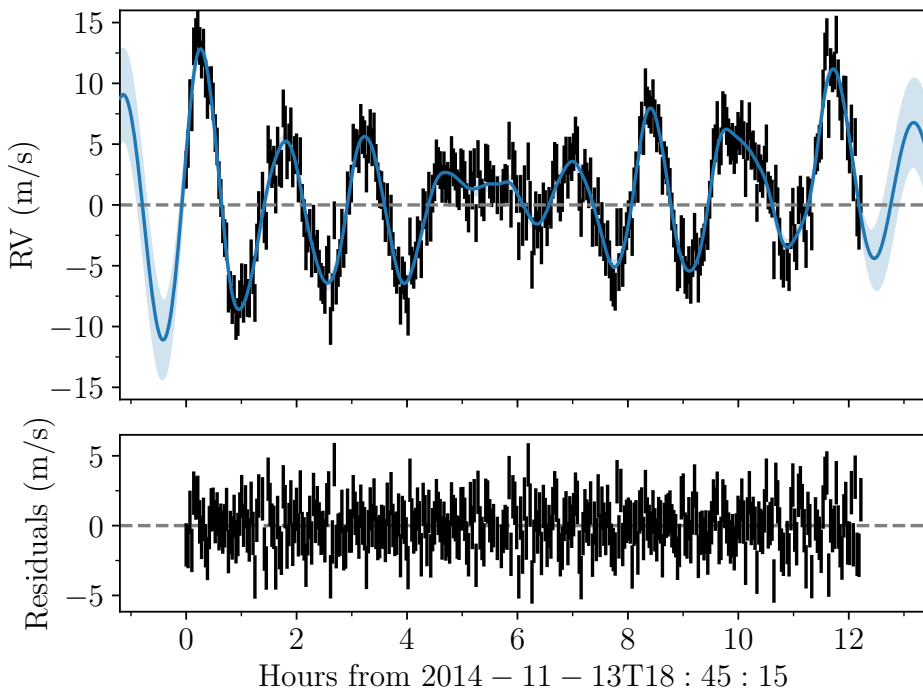


Figure 5.10 | GP detrended SONG data. *Top:* A snippet of `SONG` data from the 2014 campaign (same snippet as in Figure 5.1) after subtracting the signals shown in Figure 5.9. The blue line is the `GP` model included in the fit with the transparent band showing the 1σ confidence interval. *Bottom:* The residuals after subtracting the `GP` model.

(Foreman-Mackey et al., 2017). Our `GP` kernel is composed of two SHOTerm components in `celerite`, which are stochastically-driven, damped harmonic oscillators. The SHOTerm is characterised by three hyperparameters governing the behaviour of the kernel; the power, S_0 , the quality factor or line width, Q , and the undamped angular frequency, ω_0 , which here is directly related to ν_{\max} . The first term in our kernel is meant to capture the oscillation signals, and the second term is designed to capture any longer term variability, like granulation, although we do not expect that to be prominent in the `RVS`.

Following Pereira et al. (2019) we fix the quality factor in our granulation SHOTerm term (`SHO2`) to $Q_2 = 1/\sqrt{2}$, and we further found it necessary to fix the amplitude for this term, S_2 – the amplitude is weakly constrained by, generally, being lower than that of the oscillations and only dominate the data at the longest timescales (lowest frequencies; see

Figure 5.10). This term had a tendency to pick-up on the 1 yr signal, resulting in a significantly poorer fit when subtracting the orbital motion from γ Cep B and γ Cep Ab as well as the resulting amplitude and phase for the 1 yr signal (as done for a fit with a fixed value for S_2 in Figure 5.9). The amplitude, S_2 , thus seemed to over-compensate as the overall residuals were seemingly identical between having this parameter fixed or free to vary (as seen in Figure 5.10 again for a fixed value for S_2). Finally, we also include a white noise or jitter term, where we fix the value for the hyperparameter, σ (see Table 5.4).

In our fit we used priors from Huang and Ji (2022, their $\chi^2 = 1.44$ solution) for the binary and planetary orbit. These priors along with all parameters are summarised in Table 5.4. We sampled the posterior distribution through an MCMC analysis using emcee (Foreman-Mackey et al., 2013) with 100 walkers. We ran the MCMC until convergence, which we assessed through the rank normalised \hat{R} diagnostic test (Vehtari et al., 2019) as implemented in ArviZ (Kumar et al., 2019).

The results are given in Table 5.4, and we show the resulting orbit in Figure 5.9. We furthermore show a close-up of a single night of observations in Figure 5.10, where the oscillations and GP model are clearly seen. The rms for the residuals in Figure 5.10 comes out to around 1.56 m s^{-1} , and calculating the rms for every night of observations we find a median nightly rms of around 1.36 m s^{-1} . The typical rms reported in Hatzes et al. (2003, Table 6) is around 15 m s^{-1} . If we do not remove the oscillations from our RVS, we get an rms of 4.75 m s^{-1} .

In the context of exoplanet detection and characterisation it is important to be able to properly account for stellar oscillations and granulation, given that the limiting factor is not the precision of the (modern) spectrograph, but rather the intrinsic stellar signal. Here we are able to achieve this high precision because of the unique capabilities of SONG being dedicated to high-cadence monitoring. Sparsely sampled RVS, however, will be affected more strongly by this intrinsic stellar signal, although there are ways to partly circumvent the effects by optimising the integration time (Chaplin et al., 2019). This optimisation does, however, require knowledge of ν_{\max} .

5.5.3 The masses

From our mass measurement of γ Cep A in Table 5.2 and the orbital elements in Table 5.4 we can estimate the mass of γ Cep Ab using the mass function

Table 5.4 | Orbital and hyperparameters. Orbital and GP hyper parameters in our MCMC analysis. The priors are denoted by $\mathcal{N}(\mu, \sigma)$ for a Gaussian prior with mean, μ , and width, σ , $\mathcal{U}(a, b)$ for a uniform prior in the interval from a to b , and $\mathcal{F}(c)$ for a parameter with a fixed value of c .

Parameter	Description	Prior	Value
K_{AB} (m s ⁻¹)	Binary RV semi-amplitude	$\mathcal{N}(1699.94, 3.32)$	1711 ± 3
P_{AB} (d)	Binary orbital period	$\mathcal{N}(20731.68, 58.36)$	21170^{+48}_{-58}
$T_{0,AB}$ (JD – 2400000)	Time of inferior conjunction for binary orbit	$\mathcal{N}(48435.04, 0.67)$	$48435.2^{+0.6}_{-0.7}$
e_{AB}	Eccentricity of binary orbit	$\mathcal{N}(0.3605, 0.0026)$	0.333 ± 0.002
ω_{AB} (°)	Argument of periastron of binary orbit	$\mathcal{N}(158.90, 0.2)$	$157.07^{+0.18}_{-0.15}$
K_{Ab} (m s ⁻¹)	Planetary RV semi-amplitude	$\mathcal{N}(26.40, 1.30)$	25.6 ± 1.3
P_{Ab} (d)	Planetary orbital period	$\mathcal{N}(901.46, 2.84)$	913 ± 3
$T_{0,Ab}$ (JD – 2400000)	Time of inferior conjunction for planetary orbit	$\mathcal{N}(53107.63, 28.19)$	53117^{+18}_{-16}
e_{Ab}	Eccentricity of planetary orbit	$\mathcal{N}(0.0856, 0.075)$	$0.15^{+0.07}_{-0.05}$
ω_{Ab} (°)	Argument of periastron for planetary orbit	$\mathcal{N}(55.37, 6.7)$	49^{+6}_{-7}
P (d)	Period of 1 yr signal	$\mathcal{F}(365.25)$	-
$\log_{10} t$ (\log_{10} JD)	Phase of 1 yr signal	$\mathcal{U}(3, 7)$	5.0681 ± 0.0013
K (m s ⁻¹)	Amplitude of 1 yr signal	$\mathcal{U}(5, 50)$	$43.6157^{+0.0009}_{-0.0011}$
Γ_1 (m s ⁻¹)	Velocity offset Tenerife 1	$\mathcal{U}(25059, 33259)$	28708 ± 6
Γ_2 (m s ⁻¹)	Velocity offset Tenerife 2	$\mathcal{U}(25059, 33259)$	28944^{+5}_{-6}
Γ_3 (m s ⁻¹)	Velocity offset Delingha	$\mathcal{U}(-1300, 0)$	-874 ± 6
$\ln S_1$ (\ln m ² s ⁻²)	Amplitude	$\mathcal{U}(-5, 5)$	-3.48 ± 0.05
$\ln \omega_1$ (\ln d ⁻¹)	Angular frequency	$\mathcal{U}(0, 8)$	4.654 ± 0.005
$\ln Q_1$	Quality factor	$\mathcal{U}(-2, 5)$	$1.91^{+0.06}_{-0.08}$
$\ln S_2$ (\ln m ² s ⁻²)	Amplitude	$\mathcal{F}(-1.0)$	-
$\ln \omega_2$ (\ln d ⁻¹)	Angular frequency	$\mathcal{U}(0, 8)$	$2.48^{+0.07}_{-0.08}$
$\ln Q_2$	Quality factor	$\mathcal{F}(\ln 1/\sqrt{2})$	-
$\ln \sigma$ (\ln m s ⁻¹)	Jitter term	$\mathcal{F}(-9.4)$	-

$$\frac{M_{\text{Ab}}^3 \sin^3 i_{\text{Ab}}}{(M_{\text{Ab}} + M_{\text{A}})^2} = \frac{K_{\text{Ab}}^3 P_{\text{Ab}} (1 - e_{\text{Ab}}^2)^{3/2}}{2\pi G}, \quad (5.6)$$

with G being the gravitational constant. We did this by drawing normally distributed values from our measurements in Table 5.2 and Table 5.4, while solving for M_{Ab} in Equation (5.6) in each of the 1,000 draws we did. From this we calculated the lower limit for the mass ($i_{\text{Ab}} = 90^\circ$), but we also expanded it to get an estimate for the actual mass. For the orbital inclination, i_{Ab} , we took a conservative approach by drawing values uniformly between the boundaries from Reffert and Quirrenbach (2011) who provided a lower limit of $i_{\text{Ab}} = 3.8^\circ$ and an upper limit of $i_{\text{Ab}} = 20.8^\circ$ (at 3σ confidence). Similarly, we calculated the mass for γ Cep B using the orbital inclination from Neuhäuser et al. (2007) of $i_{\text{AB}} = 119.3 \pm 1.0^\circ$, where this time we drew normally distributed values. The results are given in Table 5.5.

We furthermore list mass estimates from the literature for all three bodies. These are determined from different approaches, where the mass of the primary has been determined spectroscopically as well as in combination with photometry, dynamically, and using [asteroseismology](#). The secondary has typically been derived from the mass function assuming a mass for the primary, but has also been determined dynamically. The mass of γ Cep Ab has exclusively been derived from the mass function.

5.5.4 A long period signal?

In Figure 5.11 we show the power spectrum of both the observations and the GP model. Evidently, there is a hint of an excess at frequencies around $0.23 \mu\text{Hz}$ (0.02 d^{-1}) corresponding to a period of 50 d. An additional source of variation in the system has been discussed previously, though at a significantly longer timescale. Hatzes et al. (2003) discuss the variation of the CaII $\lambda 8662$ equivalent widths obtained by Walker et al. (1992). As the variation is seen only in a specific time interval (1986.5-1992) over the course of the data acquisition up until that point, Hatzes et al. (2003) argue that it could be due to a period activity cycle of some 10-15 yr. While this could coincide with the SONG 2014, 2017, and 2019 campaigns, we find it unlikely that this could give rise to the signal we are seeing in the SONG data given that their period is 781 days and is only apparent in the CaII $\lambda 8662$ equivalent width.

Another possibility is rotation. The studies by, e.g., García et al. (2014), Ceillier et al. (2017), and Santos et al. (2021), have investigated the rotational properties of stars observed by [Kepler](#), including stars with solar-like

Table 5.5 | Literature masses in γ Cep. Masses of the bodies in γ Cep found in the literature. Here we only report on values explicitly reported in any of the given papers. The method denotes the approach used to derive the quantity, the masses of M_B and M_{Ab} are typically derived from the mass function, with the exception of dynamically determined masses. Hatzes et al. (2003) have used the mass estimate from Fuhrmann (2004), who states that typical errors for the mass are less than 10% for the stars in that study.

	Fuhrmann (2004)	Hatzes et al. (2003)	Torres (2007)	Neuhäuser et al. (2007)
Method (M_A)	Spectroscopy	Fuhrmann (2004)	Spectroscopy & photometry	Dynamical
M_A (M_\odot)	1.59	1.59 ± 0.12	1.18 ± 0.11	1.40 ± 0.12
Method (M_B)	-	-	Derived	Dynamical
M_B (M_\odot)	-	-	0.362 ± 0.022	0.409 ± 0.018
Method (M_{Ab})	-	Derived	-	-
$M_{Ab} \sin i_{Ab}$	-	1.7 ± 0.4	1.43 ± 0.13	1.60 ± 0.13
	Mortier et al. (2013)	Baines et al. (2018)	Malla et al. (2020)	This work
Method (M_A)	Spectroscopy	Interferometry	Asteroseismology	Asteroseismology
M_A (M_\odot)	1.26 ± 0.14	1.41 ± 0.08	1.32 ± 0.12	$1.27^{+0.05}_{-0.07}$
Method (M_B)	-	-	-	Derived
M_B (M_\odot)	-	-	-	$0.36^{+0.02}_{-0.03}$
Method (M_{Ab})	-	-	-	Derived
M_{Ab} (M_{Jup})	-	-	-	$6.6^{+2.3}_{-2.8}$
$M_{Ab} \sin i_{Ab}$	-	-	-	1.41 ± 0.08

oscillations. Their studies suggest typical rotation periods of 10–30 d for low-luminosity red giants (or subgiants), but with a good fraction of stars with longer periods, and 50 d is not uncommon.

In the following we will explore the implications if the 50 d is due to rotation. In that case the period of the signal would be given by

$$P_{\text{rot}} = \frac{2\pi R_A}{v}, \quad (5.7)$$

where v is the rotation speed at the equator. If we then assume that $P_{\text{rot}} = 50 \pm 5$ d, and assume that the spots causing the rotational modulation are concentrated towards the equator, we can get the stellar inclination by substituting Equation (5.7) in

$$\begin{aligned} i_A &= \sin^{-1} \left(\frac{v \sin i_A}{v} \right), \\ &= \sin^{-1} \left(\frac{v \sin i_A}{2\pi R_A / P_{\text{rot}}} \right). \end{aligned} \quad (5.8)$$

We followed the approach in Masuda and Winn (2020) to account for the fact that v and $v \sin i_A$ are not independent. Using $R_\star = 4.67 \pm 0.15 R_\odot$ from [BASTA](#) (Table 5.2) and $v \sin i_A$ from Table 5.1 of $0.0 \pm 0.9 \text{ km s}^{-1}$ (truncated at 0.0 km s^{-1}), we get a value for the stellar inclination of $i_A = 13^{+9}_{-6}$, meaning that we are close to seeing the star pole-on.

Our measurement of a low $v \sin i_A$ is broadly consistent with previous studies, such as Walker et al. (1992, $v \sin i_A < 0.3 \text{ km s}^{-1}$) and Jofré et al. (2015, $v \sin i_A = 1.63 \pm 0.23 \text{ km s}^{-1}$). We caution that at this level of projected rotation, disentangling rotation from especially [macro-turbulence](#) becomes challenging (Gray, 2005), but note that our value for ζ is in agreement with predictions from Hekker and Meléndez (2007) (see also Gray, 1989, 2005) covering the range $3.156 - 5.419 \text{ km s}^{-1}$ for the temperature and luminosity class of γ Cep A.

In any event, the imprint of rotation on the [RV](#) timeseries should be of low amplitude as the peak-to-peak variability from activity in [RV](#) can be approximated by the product of the corresponding photometric variability (over the same spectral band) and the projected rotation (Aigrain et al., 2012; Vanderburg et al., 2016a). With photometric variability ranges from García et al. (2014) and Santos et al. (2021) covering everything from a few hundred to a few 10^5 ppm (and likely with a bias towards higher variability with increasing period) it is difficult to estimate what the expected intrinsic and projected variability should be for a star like γ Cep A. Our asteroseismic

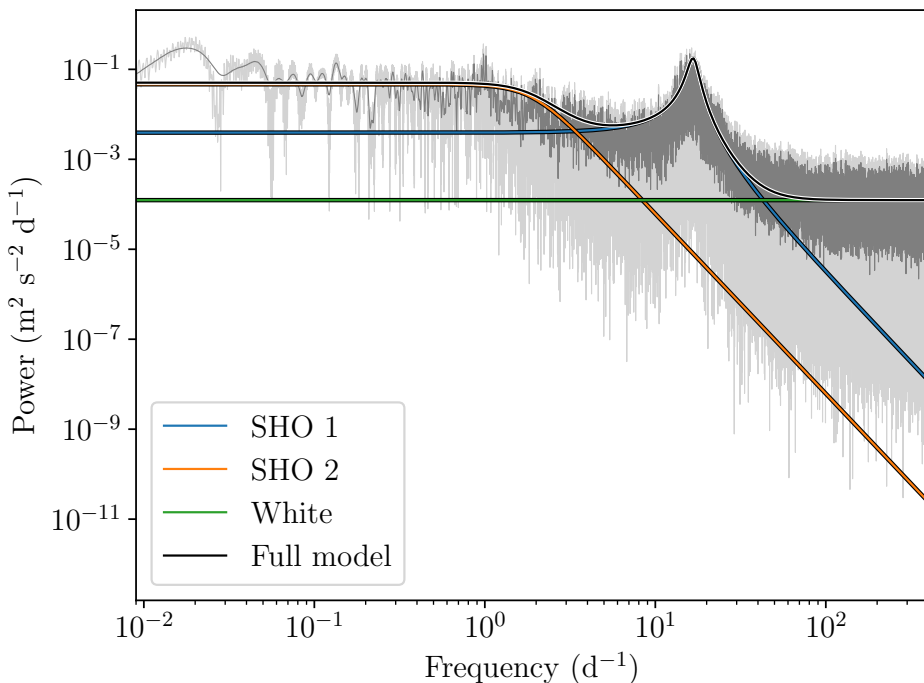


Figure 5.11 | GP power spectrum from radial velocities. The power spectrum of our GP model (black) compared to the observed power spectrum (light grey) from our RVS after subtracting the orbital motion and 1 yr signal (Figure 5.9 bottom). In darker grey we show the observed power spectrum smoothed with a box-kernel. The orange and blue curves show our harmonic GP terms, while the green line show our white noise term.

analysis did not allow us to place any strong constraints on the stellar inclination nor rotation (as we did not see evidence of rotationally split oscillation modes Lund et al., 2014a; Campante et al., 2016), but is consistent with a low projected rotation.

The exact orientation of γ Cep A is very interesting in the context of the dynamic history of the system, where a pole-on configuration place some rather tight constraints on the tilt between the stellar spin axis of γ Cep A and the orbital plane of γ Cep Ab, the obliquity. With the constraint of the orbital inclination by Reffert and Quirrenbach (2011) in the interval $3.7\text{--}15.5^\circ$, γ Cep A and γ Cep Ab would (if γ Cep A is seen pole-on) either be aligned or anti-aligned.

5.5.5 Contemporaneous data

The study we carried out here is in many ways similar to the one conducted by Arentoft et al. (2019) for the planet hosting red giant ϵ Tauri, where data from the **K2** mission (Howell et al., 2014) were paired with **SONG** data. In Arentoft et al. (2019) they derived the amplitude difference of the oscillations between the space-based photometry and the ground-based **RVS**. However, as the **K2** and **SONG** data were not collected simultaneously, the interpretation of the amplitude difference was slightly hampered.

While we do not investigate the amplitude difference here, we do have simultaneous photometry and **RVS** from 2019. This will be used in a forthcoming paper, which will also include **SONG RVS** obtained simultaneously with two additional **TESS** sectors, and in addition to amplitude differences, phase differences will also be investigated.

5.6 Conclusions

Through long-term, high cadence monitoring utilising both ground-based spectroscopic observations from the **SONG** network as well as space-borne photometry from **TESS**, we presented an in-depth asteroseismic study of the planet hosting, binary, **RGB** star γ Cep A.

In our seismic analysis we obtained both global seismic parameters, ν_{\max} and $\Delta\nu$, as well as individual frequencies, which are tabulated in Table B.4. To provide additional constraints when modelling the frequencies, we performed a spectral analysis using data from the **FIES** spectrograph to obtain values for T_{eff} , $\log g$, and [Fe/H], and we derived a luminosity using the distance and G band magnitude from **Gaia**. We modelled the frequencies with the aforementioned constraints using both **MESA** and **BASTA**. From **BASTA** we obtained a mass of $1.27^{+0.05}_{-0.07} M_{\odot}$, a radius of $4.74^{+0.07}_{-0.08} R_{\odot}$, and an age of $5.7^{+0.8}_{-0.9}$ Gyr.

We used our **SONG RVS** to fit the binary as well as the planetary orbit. Using literature values for the inclinations of the orbits and our derived orbital parameters with our mass for γ Cep A, we obtain masses of $M_B = 0.328^{+0.009}_{-0.012} M_{\odot}$ and $M_{Ab} = 6.6^{+2.3}_{-2.8} M_{\oplus}$ for γ Cep B and γ Cep Ab, respectively.

Finally, amplitude and phase differences between **SONG** and **TESS** data will be analysed in a forthcoming paper. This will be done using the simultaneous **SONG** and **TESS** data we have presented here as well as additional, simultaneous **SONG** and **TESS** data, spanning two **TESS** sectors.

6

Confirmation and characterisation of three giant planets detected by TESS from the FIES/NOT and Tull/McDonald spectrographs

In the previous chapters we saw different ways of determining stellar parameters with great precision, and how we might use those parameters to constrain the orbital parameters of exoplanets around the star. Clearly, stellar parameters are extremely important in the context of exoplanet science, however, exoplanet studies naturally starts with the detection and discovery of these systems. In the following chapters, I will present two discovery papers where I have led the efforts.

In this project, we report on the discovery and confirmation of three transiting hot and warm Jupiters detected by [TESS](#). Through our intense and long baseline [RV](#) monitoring, we constrained the eccentricities with great precision as well as revealing the presence of long-term trends in two of the systems, indicating the presence of an outer companion, thus alluding to potential migration scenarios (discussed in Section [1.2](#)).

The [RV](#) follow-up conducted here was a collaboration between the Tull and the [FIES](#) spectrographs (see Section [6.3.3](#)), where I was the [PI](#) (alongside L. M. Serrano) of the observing programme for the latter facility. Furthermore, as most of this work was conducted while I was a support astronomer at the [NOT](#), I carried out a lot of the [FIES](#) observations. I was in charge of the data analysis in Section [6.5](#) and Section [6.6](#), and I have been involved in most of the writing. The work reproduced here was originally published as

E. Knudstrup, L. M. Serrano, D. Gandolfi, S. H. Albrecht, W. D. Cochran, M. Endl, P. MacQueen, R. Tronsgaard, A. Bieryla, L. A. Buchhave, K. Stassun, K. A. Collins, G. Nowak, H. J. Deeg, K. Barkaoui, B. S. Safonov, I. A. Strakhov, A. A. Belinski, J. D. Twicken, J. M. Jenkins, A. W. Howard, H. Isaacson, J. N. Winn, K. I. Collins, D. M. Conti, G. Furesz, T. Gan, J. F. Kielkopf, B. Massey, F. Murgas, L. G. Murphy, E. Palle, S. N. Quinn, P. A. Reed, G. R. Ricker, S. Seager, B. Shiao, R. P. Schwarz, G. Srdoc, and D. Watanabe (2022). “Confirmation and characterisation of three giant planets detected by TESS from the FIES/NOT and Tull/McDonald spectrographs”. *Astronomy and Astrophysics* 667, A22

Once again, the layout has been reformatted. Further alterations include the removal of the [RV](#) and light curve follow-up tables in the appendix as well as tables containing limb-darkening coefficients and priors applied in [MCMC](#) (Tables A1-A7 in Knudstrup et al., [2022](#)).

Summary of the Chapter

We report the confirmation and characterisation of TOI-1820 b, TOI-2025 b, and TOI-2158 b, three Jupiter-sized planets on short-period orbits around G-type stars detected by [TESS](#). Through our ground-based efforts using the [FIES](#) and Tull spectrographs, we have confirmed these planets and characterised their orbits, and find periods of around 4.9 d, 8.9 d, and 8.6 d for TOI-1820 b, TOI-2025 b, and TOI-2158 b, respectively. The sizes of the planets range from 0.96 to 1.14 Jupiter radii, and their masses are in the range from 0.8 to 4.4 Jupiter masses. For two of the systems, namely TOI-2025 and TOI-2158, we see a long-term trend in the [RVS](#), indicating the presence of an outer companion in each of the two systems. For TOI-2025 we furthermore find the star to be well-aligned with the orbit, with a projected [obliquity](#) of 9^{+33}_{-31} °. As these planets are all found in relatively bright systems ($V \sim 10.9\text{--}11.6$ mag), they are well-suited for further studies, which could help shed light on the formation and migration of hot and warm Jupiters.

6.1 Introduction

Giant planets on short-period orbits (also called hot Jupiters) were the first planets to be discovered, and their numbers increased quickly during the

first years of exoplanetary science. Their existence itself immediately posed a challenge to planet formation theories, which at the time only had one example, the Solar System. Despite almost three decades of discoveries of hot Jupiters, there is still no consensus on their exact origin channel (Dawson and Johnson, 2018). While it is still unclear whether hot Jupiters can form *in situ* or not (Batygin et al., 2016), *ex situ* formation processes require a mechanism responsible for transporting these giant planets from larger separations to the current close-in orbits.

The two leading hypotheses for such large-scale migration that have been put forward are [disc migration](#) and [high-eccentricity migration](#). In the former scenario, the planets exchange angular momentum with the gas and dust particles in the circumstellar disc. As a result, the semi-major axis slowly shrinks, while the orbit remains circular (e.g. Lin et al., 1996; Baruteau et al., 2014). In contrast, the latter scenario could result in very eccentric and misaligned orbits, since it involves gravitational interactions with other bodies in the system (e.g. Chatterjee et al., 2008; Nagasawa et al., 2008).

The advent of space-based transit search missions has led to the discovery of thousands of new exoplanet candidates (see, e.g. Borucki et al., 2010; Huang et al., 2013; Livingston et al., 2018; Kruse et al., 2019). Combining these discoveries with ground-based spectroscopic follow-up observations leads to a large sample of well-characterised exoplanet systems, including the bulk density of the transiting planets, host star properties, orbital eccentricities, stellar [obliquities](#), and companionship of outer planets or stars (see, e.g. Gandolfi et al., 2019; Van Eylen et al., 2019; Carleo et al., 2020; Albrecht et al., 2021; Knudstrup and Albrecht, 2022; Smith et al., 2022).

Here we report on the discovery of three transiting hot Jupiters: TOI-1820b, TOI-2025b, and TOI-2158b. The transit-like features associated with these systems were detected by [TESS](#) (Ricker et al., 2015). We have confirmed these as bona fide planets, and we have characterised the planets and their host systems in terms of masses and orbital eccentricities. For one system (TOI-2025), we additionally performed spectroscopic transit observations and used them to determine the sky-projected spin-orbit [obliquity](#). During the preparation of this manuscript, we became aware of the efforts of another team to announce the discovery of TOI-2025 b (Rodriguez et al., 2022). The results were determined independently, and the communication between the teams were strictly related to the coordination of the manuscripts.

In Section 6.2 we describe the [TESS](#) photometry and data extraction. We present our ground-based observations, which include both additional

photometry and spectroscopic follow-up, as well speckle interferometry, in Section 6.3. In Section 6.4 we explain how we obtained stellar parameters for the three systems. The methodology behind our analysis is described in Section 6.5. We discuss our results in Section 6.6, before placing these planets in the context of the population from the literature and drawing our conclusions in Section 6.7.

6.2 TESS photometry of candidate systems

The transiting planet candidates TOI-1820, TOI-2025, and TOI-2158 were identified by the Massachusetts Institute of Technology (MIT) Quick Look Pipeline (QLP; Huang et al., 2020) in a search of light curves extracted from the 30-minute cadence Full Frame Images (FFIs) using the box-least-squares (BLS; Kovács et al., 2002; Hartman and Bakos, 2016) algorithm. Transit signals were detected for all three systems, which were then identified as TESS Objects of Interest (TOIs) by the TESS Science Office at MIT (Guerrero et al., 2021).

All three targets were subsequently put on the target list for 2-minute cadence. The 2-minute cadence data are processed by the Science Processing Operation Center (SPOC; Jenkins et al., 2016) team at the NASA Ames Research Center, where light curves are extracted through simple aperture photometry (SAP; Twicken et al., 2010; Morris et al., 2020) and processed using the Presearch Data Conditioning (PDC; Smith et al., 2012; Stumpe et al., 2012; Stumpe et al., 2014) algorithm.

We downloaded and extracted all the TESS light curves from the target pixel files using the `lightkurve` (Lightkurve Collaboration et al., 2018) package, where we use the implemented `RegressionCorrector` to correct for any background noise. We excluded cadences with severe quality issues¹. We also removed outliers. First we removed the transits from the light curve through a light-curve model using parameters from an initial fit. Next we applied a Savitzky-Golay filter and identified outliers through 5σ sigma clipping, which we then excluded from the unfiltered light curve with transits. For all three systems, we confirmed the presence of the transit-like features identified by QLP, by performing an independent search using the BLS and the Transit Least Squares (TLS; Hippke and Heller, 2019) algorithm. We furthermore searched for additional transits, without finding hints of any.

¹: 'default' in `lightkurve.SearchResult.download`

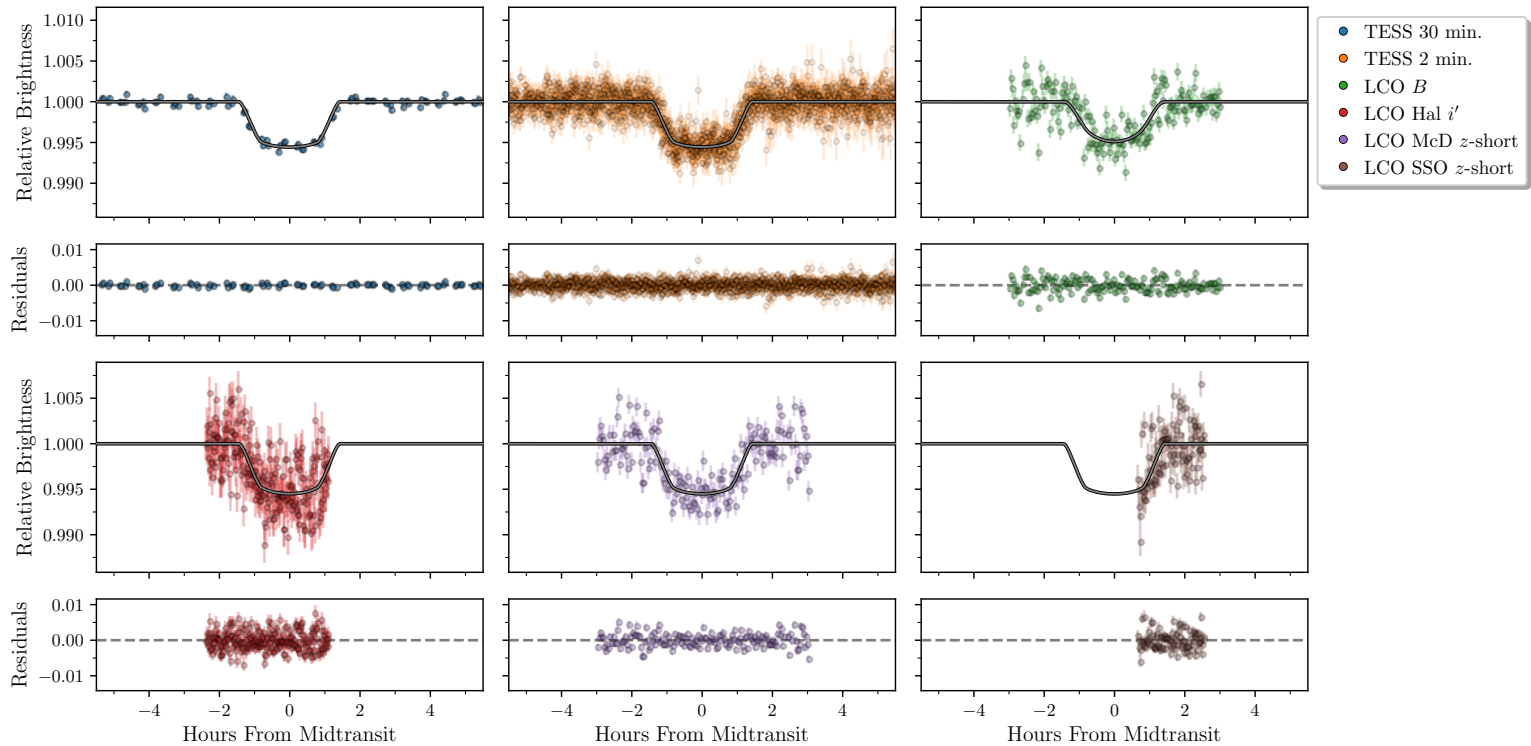


Figure 6.1 | Photometry for TOI-1820. Our different photometric observations of TOI-1820 with the best-fitting transit model are shown with a grey line, and the residuals, following the subtraction of the best-fitting model, are shown below.

6.2.1 TOI-1820

TOI-1820 was observed in Sector 22 (February 18, 2020 and March 18, 2020), with [TESS](#)' camera 1 with a cadence of 30 minutes. TOI-1820 was identified on April 17, 2020 with a [SNR](#) of 53. TOI-1820 was observed again in Sector 49 (February 26, 2022 and March 26, 2022) with camera 1, this time with a cadence of 2 minutes. In the top left of Figure 6.1, we show the [TESS](#) light curve phase folded to the periodic transit signal occurring every 4.860674 d with a depth of \sim 0.6%.

6.2.2 TOI-2025

TOI-2025 was observed with a 30-minute cadence using [TESS](#)' camera 3 in Sector 14 (July 18, 2019 to August 15, 2019), Sectors 18-20 (November 2, 2019 to January 21, 2020), Sectors 24-26 (April 16, 2020 to July 4, 2020), as well as in 2-minute cadence in Sector 40 (June 24, 2021 to July 23, 2021) and Sector 47 (December 30, 2021 to January 28, 2022), also with camera 3. Since the [TESS](#) light curves of TOI-2025 display a periodic 8.872078 d dip of \sim 0.7% with a [SNR](#) of 151, the candidate was announced as a TOI on June 19, 2020. The two panels on the top left of Figure 6.2 shows the phase-folded [TESS](#) light curves.

6.2.3 TOI-2158

TOI-2158 was observed with [TESS](#)' camera 1 during Sector 26 (June 8, 2020 to July 4, 2020) with a cadence of 30 minutes, and in Sector 40 (June 24, 2021 to July 23, 2021) with a 2-minute cadence. On August 10, 2020, TOI-2158 was announced as a TOI with a [SNR](#) of 59. The [TESS](#) light curve for TOI-2158 can be seen in the top of Figure 6.3, phase folded onto the 8.60077 d signal showing the \sim 0.5% decrease in flux. A close-up of the [TESS](#) light curves for all three systems can be found in Figure A.4.

6.3 Ground-based observations

In addition to [TESS](#) space-based photometry, we gathered ground-based photometry via the Las Cumbres Observatory Global Telescope (LCOGT; Brown et al., 2013), as well as ground-based spectroscopic measurements from different telescopes. Reconnaissance spectroscopy was acquired with the High Resolution Echelle Spectrometer (HIRES; Vogt et al., 1994) located at the Keck Observatory, the Tillinghast Reflector Echelle Spectrograph

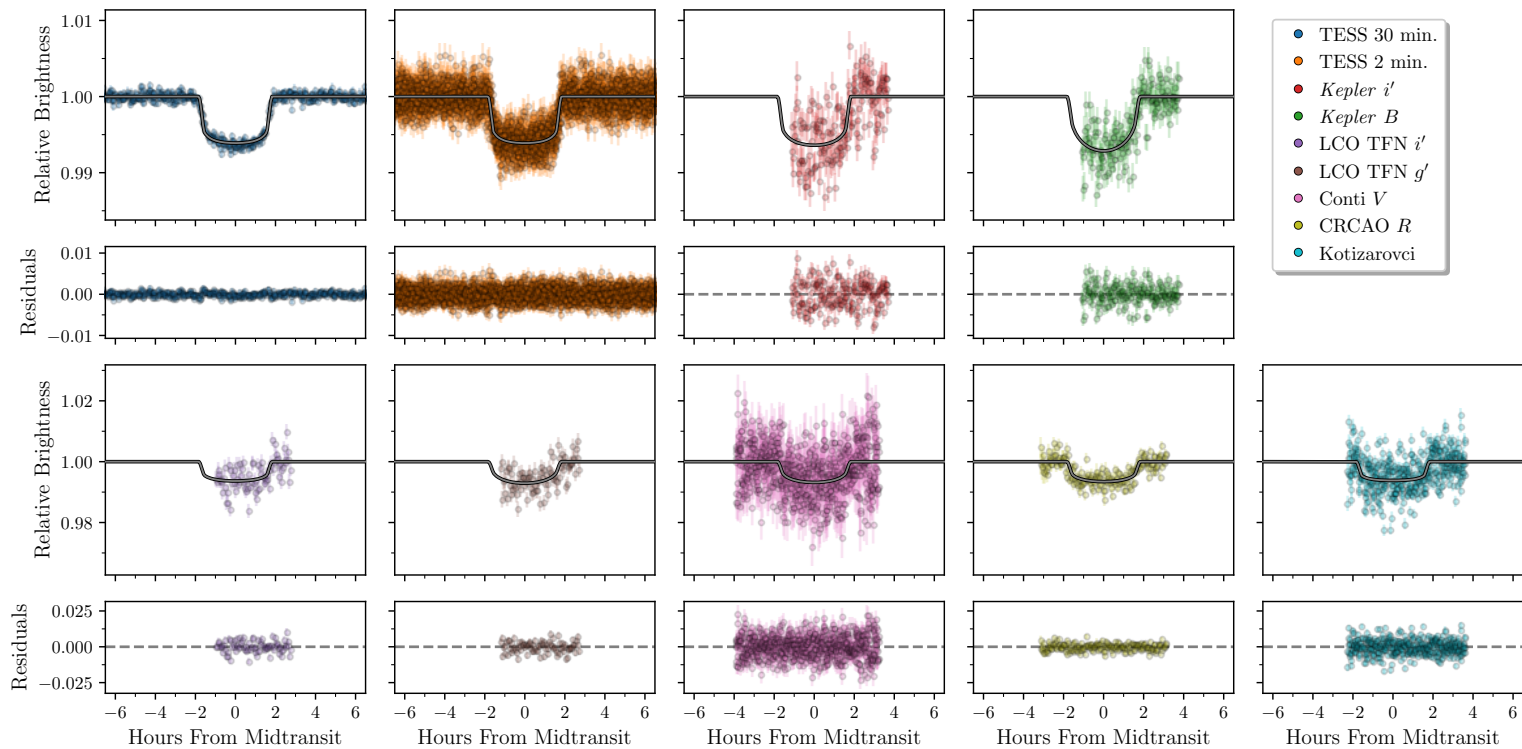


Figure 6.2 | Photometry for TOI-2025. Our different photometric observations of TOI-2025 with the best-fitting transit model shown with a grey line, and the residuals following the subtraction of the best-fitting model shown below.

(TRES; Fűrész, 2008) situated at the Fred L. Whipple Observatory, Mt. Hopkins, AZ, USA, as well as **FIES** (Frandsen and Lindberg, 1999; Telting et al., 2014) at the **NOT** (Djupvik and Andersen, 2010) of the Roque de los Muchachos observatory, La Palma, Spain.

To confirm and characterise the systems in terms of masses, bulk densities, and orbital parameters, we monitored the systems with the **FIES** spectrograph, and the Tull Coudé Spectrograph (Tull et al., 1995) at the 2.7 m Harlan J. Smith telescope at the McDonald Observatory, Texas, USA. The **FIES** and Tull spectrographs are both cross-dispersed spectrographs with resolving powers of 67,000 (in high-resolution mode) and 60,000, respectively. Finally, to investigate companionship in the systems, we obtained speckle imaging using the 2.5-m reflector at the Caucasian Mountain Observatory of Sternberg Astronomical Institute (CMO SAI; Shatsky et al., 2020).

6.3.1 Speckle interferometry with SPP

TOI-2158, TOI-2025, and TOI-1820 were observed using speckle interferometry with the SPeckle Polarimeter (SPP; Safonov et al. 2017) on the 2.5-m telescope at the Sternberg Astronomical Institute of Lomonosov Moscow State University (SAI MSU). The detector has a pixel scale of 20.6 mas px⁻¹, and the angular resolution was 83 mas. The atmospheric dispersion compensation by two direct vision prisms allowed us to use the relatively broadband I_c filter. For all targets, 4000 frames of 30 ms were obtained. The detection limits are provided in Figure 6.4. For TOI-2158 and TOI-2025, we did not detect any stellar companions, with limits for Δmag for any potential companion of 6.5 mag and 7 mag at 1'', respectively.

For TOI-1820 we detected a companion 4.0 magnitudes fainter than the primary on December 2, 2020 and July 15, 2021. The separation, position angle, and contrast were determined by the approximation of the average power spectrum with the model of a binary star (see Eq. (9) in Safonov et al., 2017). As the weight for the approximation, we took the inverse squared uncertainty of the power spectrum determination. The results are presented in Table 6.1. All binarity parameters for the two dates coincide within the uncertainties. According to **Gaia** EDR3 (Gaia Collaboration et al., 2021), the proper motion of TOI-1820 is relatively high, being $50.54 \pm 0.08 \text{ mas yr}^{-1}$ and $-33.93 \pm 0.08 \text{ mas yr}^{-1}$ along right ascension and declination, respectively. If the companion of TOI-1820 were

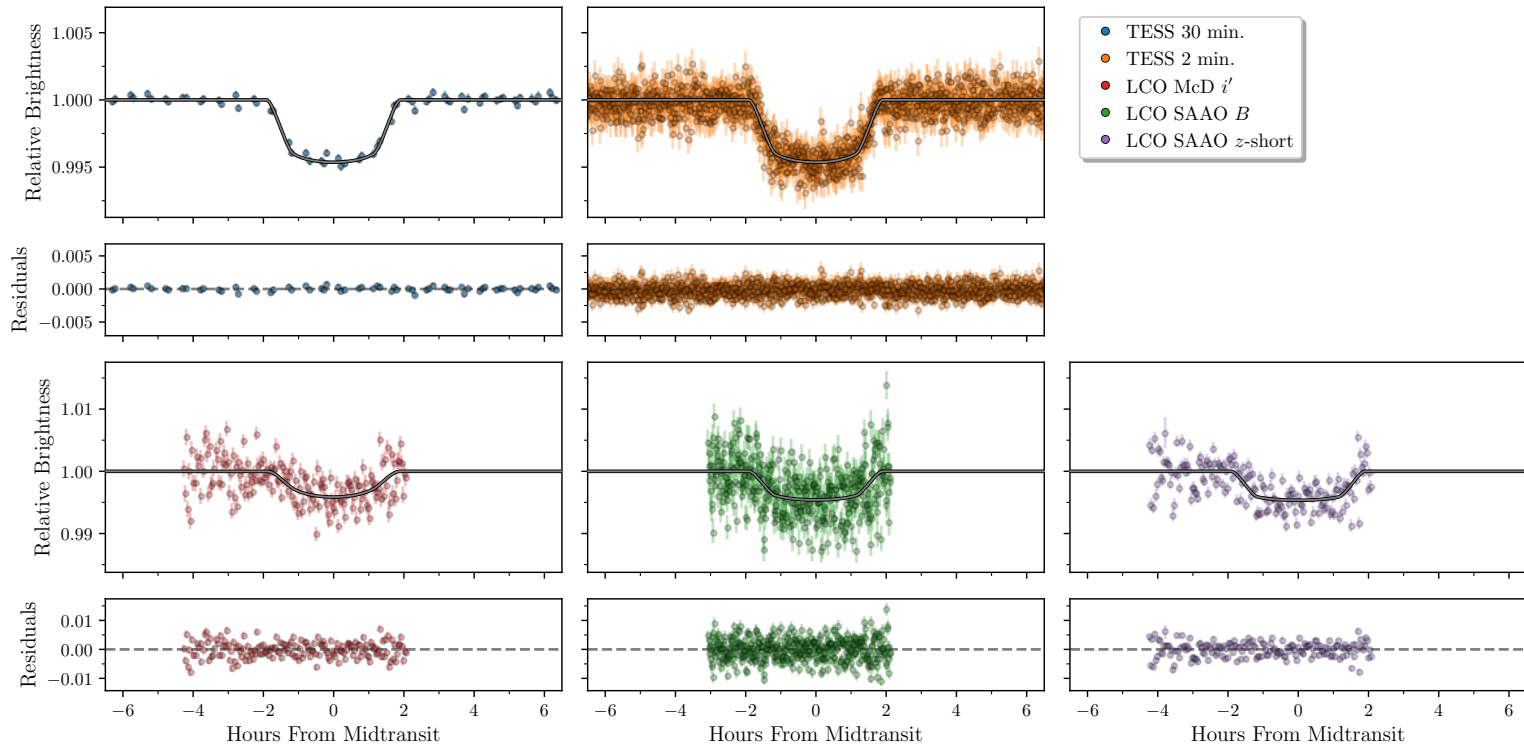


Figure 6.3 | Photometry for TOI-2158. Our different photometric observations of TOI-2158 with the best-fitting transit model are shown with a grey line, and the residuals, following the subtraction of the best-fitting model, are shown below.

Table 6.1 | Speckle observations of TOI-1820. Results from the SPP speckle interferometry of TOI-1820: separation, position angle, and contrast.

Date UT	Separation mas	P.A. °	Δm
2020-12-02	470 ± 5	102.6 ± 0.3	4.0 ± 0.1
2021-07-15	474 ± 8	101.7 ± 0.9	3.7 ± 0.1

a background star, its position with respect to TOI-1820² would change by 37.694 ± 0.051 mas between the two epochs of our observations. As long as we see a displacement much smaller than this, we conclude that TOI-1820 and its companion are gravitationally bound. With a *Gaia* parallax of 4 mas (see Table B.3), we find a physical separation between the target and the companion of ≈ 110 AU. Furthermore, from our HIRES RECON SPECTROSCOPY and using the algorithm from Kolbl et al. (2015), we can constrain this secondary companion to only contribute 1% in flux if the RV separation between the components in TOI-1820 is greater than 10 km/s. If the RV separation were less than 10 km s^{-1} , the flux of the secondary would have been unconstrained without the speckle interferometry.

6.3.2 Photometric follow-up

We acquired ground-based time-series follow-up photometry of TOI-1820, TOI-2025, and TOI-2158 as part of the *TESS* Follow-up Observing Program (TFOP; Collins, 2019)³ to attempt to: (1) rule out or identify nearby eclipsing binaries (NEBs) as potential sources of the detection in the *TESS* data; (2) detect the transit-like events on target to confirm the depth, and thus the *TESS* photometric deblending factor; (3) refine the *TESS* ephemeris; and (4) place constraints on transit depth differences across optical filter bands. We used the *TESS* Transit Finder, which is a customised version of the Tapir software package (Jensen, 2013), to schedule our transit observations. Unless otherwise noted, the images were calibrated and the photometric data were extracted using the AstroImageJ (AIJ) software

2: In the SIMBAD entry <http://simbad.u-strasbg.fr/simbad/sim-basic?Ident=TYC+1991-1863-1&submit=SIMBAD+search>, TOI-1820 is listed as a member of the cluster Melotte 111. However, the proper motion ($\mu_\alpha \sim -12 \text{ mas yr}^{-1}$, $\mu_\delta \sim -9 \text{ mas yr}^{-1}$) and parallax ($\varpi \sim 12 \text{ mas}$) are significantly different from the *Gaia* EDR3 (Gaia Collaboration et al., 2021) values listed in Table B.3.

3: <https://tess.mit.edu/followup>

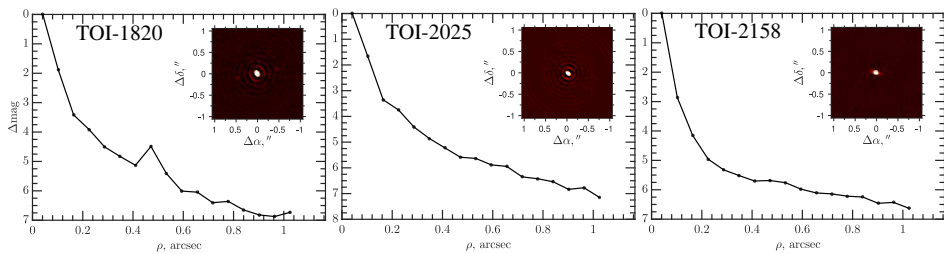


Figure 6.4 | Speckle interferometry. SAI-2.5m speckle sensitivity curve and autocorrelation function (ACF) for TOI-1820 (left panel), TOI-2025 (middle panel), and TOI-2158 (right panel). All images shown here were taken in the I -band. Only the speckle image of TOI-1820 shows evidence of a nearby companion, as can be seen by the bump in the ACF around 0.45 arcsec.

package (Collins et al., 2017). The observing facilities are described below (and the individual observations are detailed in Table A.1 in Knudstrup et al., 2022). The ground-based light curves for TOI-1820, TOI-2025, and TOI-2158 are shown in Figure 6.1, Figure 6.2, and Figure 6.3, respectively.

We observed six transits using the LCOGT 1.0-m and 0.4-m networks. Three transits were observed in alternating filter mode, resulting in a total of nine light curves. The 1-m telescopes are equipped with 4096×4096 pixel SINISTRO cameras having an image scale of $0''389$ per pixel, resulting in a $26' \times 26'$ field of view. The 0.4-m telescopes are equipped with 2048×3072 pixel SBIG STX6303 cameras having an image scale of $0''57$ pixel $^{-1}$, resulting in a $19' \times 29'$ field of view. The images were calibrated by the standard LCOGT BANZAI pipeline (McCully et al., 2018).

We observed a transit from KeplerCam on the 1.2-m telescope at the Fred Lawrence Whipple Observatory using alternating filters, resulting in two light curves. The 4096×4096 Fairchild CCD 486 detector has an image scale of $0''336$ per pixel, resulting in a $23'1 \times 23'1$ field of view.

We observed one transit each from the Kotizarovci Private Observatory 0.3-m telescope near Viskovo, Croatia, the C.R. Chambliss Astronomical Observatory (CRCAO) 0.6-m telescope at Kutztown University near Kutztown, PA, and the Conti Private Observatory 0.3-m telescope near Annapolis, MD. The Kotizarovci telescope is equipped with a 765×510 pixel SBIG ST7XME camera having an image scale of $1''2$ per pixel, resulting in a $15' \times 10'$ field of view. The CRCAO telescope is equipped with a 3072×2048 pixel SBIG STXL-6303E camera having an image scale of $0''76$ after 2×2 pixel image binning, resulting in a $13' \times 20'$ field of view. The Conti telescope is

equipped with a 2750×2200 pixel StarlightXpress SX694M camera having an image scale of $1''/0$ after 2×2 pixel image binning, resulting in a $23' \times 18'$ field of view.

6.3.3 RV follow-up

Our [NOT](#) and McDonald Observatory monitoring was carried out from May 2020 to June 2022. We reduced the [FIES](#) spectra using the methodology described in Buchhave et al. (2010) and Gandolfi et al. (2015), which includes bias subtraction, flat fielding, order tracing and extraction, and wavelength calibration. We traced the [RV](#) drift of the instrument acquiring long-exposed ThAr spectra (~ 80 s) immediately before and after each science observation. The science exposure time was set between 1800–2700 seconds, depending on the sky conditions and scheduling constraints. As our exposures were longer than 1200 s, we split the exposure in three sub-exposures to remove cosmic ray hits using a sigma clipping algorithm while combining the frames. [RVS](#) were derived via multi-order cross-correlations, using the first stellar spectrum as a template.

For Tull we used 30-minute integrations to give a [SNR](#) of 60–70 per pixel. An I_2 gas absorption was used to provide the high-precision [RV](#) metric. All Tull spectra were reduced and extracted using standard IRAF tasks. Radial velocities were extracted using the Austral code (Endl et al., 2000).

To validate the planetary nature of the transiting signal in TOI-1820 and fully characterise the system, we acquired 18 spectra with [FIES](#) and 12 spectra with Tull, shown to the left in Figure 6.5. Figure 6.6 displays the generalised Lomb-Scargle (GLS; Lomb, 1976; Scargle, 1982) periodograms with TOI-1820 to the left, in which the ~ 4.9 d transiting signal has been overplotted as the dashed line. This periodicity corresponds to the peak that we see in the GLS of the [RVS](#).

We collected a total of 46 [FIES RVS](#) to validate the planetary nature of the signal, as well as to characterise the TOI-2025 system. In the middle panel of Figure 6.5, [FIES+](#) refers to [RVS](#) collected after July 1, 2021 (see Section 6.5). As before, the transiting signal coincides with the peak in the GLS periodogram in the middle panels of Figure 6.6.

For TOI-2158 we collected 30 [FIES RVS](#) and 23 Tull [RVS](#), shown in the right panel of Figure 6.5. As for the other two systems, the peak associated with the ~ 8.6 d period planet is detected in the GLS periodogram in Figure 6.6, since it is stronger than the false alarm probability.

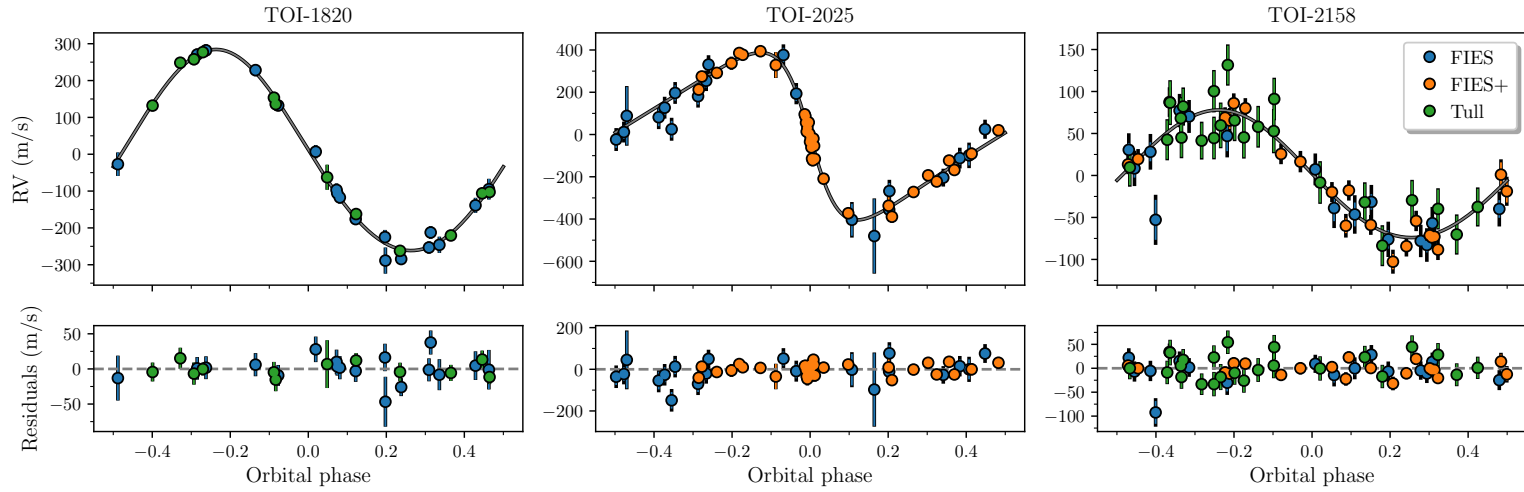


Figure 6.5 | Radial velocities. From left to right are our [FIES](#) (blue), [FIES+](#) (orange), and [Tull](#) (green) [RVS](#) for TOI-1820, TOI-2025, and TOI-2158, respectively, where the black parts of the error bars denote the jitter added in quadrature. The grey curves are the best-fitting models. In the bottom row are the residuals after subtracting the best-fitting models.

6.4 Stellar parameters

We made use of the stellar parameter classification (SPC; Buchhave et al., 2012a; Buchhave et al., 2014; Bieryla et al., 2021) tool to obtain stellar parameters, where we reduced and extracted the spectra following the approach in Buchhave et al. (2010). For TOI-2025 and TOI-2158, we used the TRES spectra as [RECON SPECTROSCOPY](#), and for TOI-1820, we used our [FIES](#) spectra. The derived stellar parameters are tabulated in Table B.3.

In addition, for TOI-1820 we also used our HIRES spectra with Specmatch-Synth to derive stellar parameters as described in Petigura et al. (2017). From the two HIRES spectra, we find $T_{\text{eff}} = 5695 \pm 100$ K, $\log g = 4.1 \pm 0.1$, $[\text{Fe}/\text{H}] = 0.01 \pm 0.06$, and $v \sin i = 3.07 \pm 0.77$ km s⁻¹. We also estimated the R'_{HK} activity indicator. As a result we obtained $\log R'_{\text{HK}} = -5.37$, a hint that the star is inactive.

6.4.1 SED

As an independent check on the derived stellar parameters, we performed an analysis of the broadband [SED](#) together with the [Gaia](#) EDR3 (Gaia Collaboration et al., 2021) parallax in order to determine an empirical measurement of the stellar radius, following the procedures described in Stassun and Torres (2016) and Stassun et al. (2017, 2018). In short, we pulled the $B_T V_T$ magnitudes from Tycho-2, the $BVgri$ magnitudes from APASS, the JHK_S magnitudes from 2MASS, the W1–W4 magnitudes from *WISE*, and the $GG_{\text{BP}}G_{\text{RP}}$ magnitudes from [Gaia](#). We also used the *GALEX* NUV flux when available. Together, the available photometry spans the stellar [SED](#) over the wavelength range 0.35–22 μm, and extends down to 0.2 μm when *GALEX* data are available (see Figure 6.7). We performed a fit using Kurucz stellar atmosphere models, with the priors on effective temperature (T_{eff}), surface gravity ($\log g$), and metallicity ($[\text{Fe}/\text{H}]$) from the spectroscopically determined values. The remaining free parameter was the extinction (A_V), which we restricted to the maximum line-of-sight value from the dust maps of Schlegel et al. (1998).

The resulting [SED](#) fits are shown in Figure 6.7 for TOI-1820, TOI-2025, and TOI-2158 with reduced χ^2 values of 1.5, 1.2, and 1.2, respectively. The resulting best-fit are summarised in Table B.3. Integrating the (unreddened) model [SED](#) gives the bolometric flux at Earth, F_{bol} , which with the T_{eff} and the [Gaia](#) EDR3 parallax (with no systematic adjustment; see Stassun and Torres, 2021) gives the stellar radius. The stellar mass can then be determined empirically from the stellar radius and the spectroscopic $\log g$, and

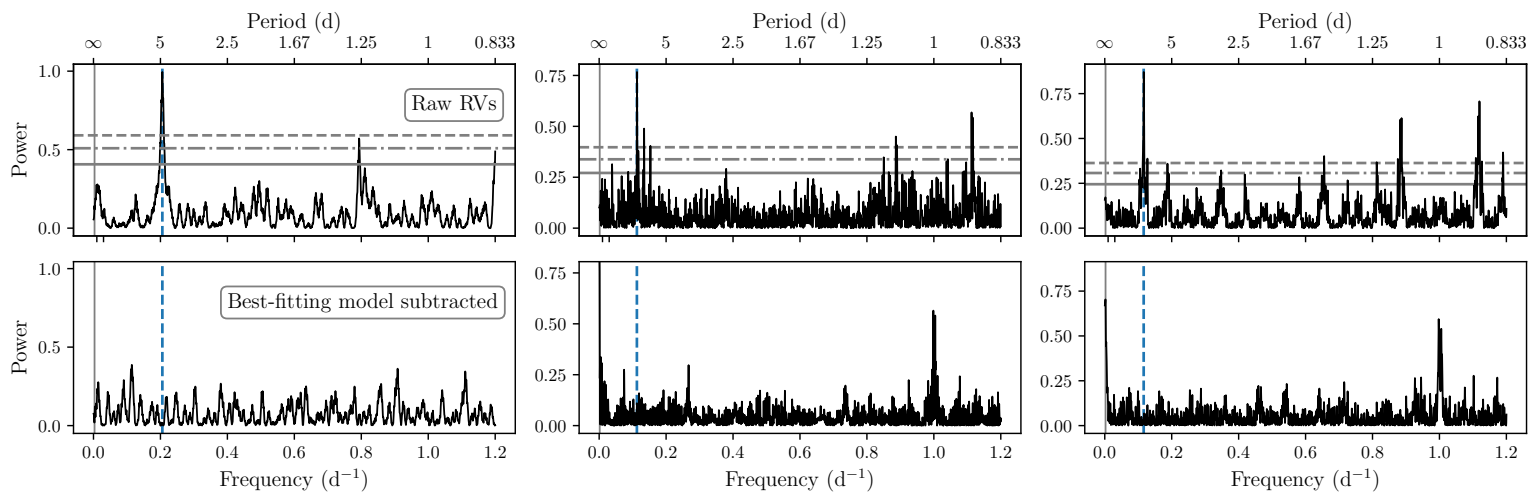


Figure 6.6 | Generalised Lomb-Scargle periodograms. From left to right are the GLS periodograms for TOI-1820, TOI-2025, and TOI-2158. In the top row, we show the GLS periodograms directly from the [RVS](#), and in the bottom we have removed the orbit of the planet. The vertical dashed lines from left to right denote the 4.9 d, 8.9 d, and 8.6 d signals seen in the photometry for TOI-1820, TOI-2025, and TOI-2158, respectively. The solid lines are our baselines, i.e. $1/(t_{\text{last RV}} - t_{\text{first RV}})$ with $t_{\text{first RV}}$ and $t_{\text{last RV}}$ being the times for the first and last acquired [RVS](#). The horizontal solid, dot-dashed, and dashed lines show the 10%, 1%, and 0.1% false alarm probabilities, respectively.

compared to the mass estimated from the empirical relations of Torres et al. (2010). Finally, we can estimate the age of the star from the spectroscopic R'_{HK} via the empirical relations of Mamajek and Hillenbrand (2008), which we can also corroborate by comparing the stellar rotation period predicted at that age from the empirical gyrochronology relations of Mamajek and Hillenbrand (2008) against that determined from the stellar radius together with the spectroscopic $v \sin i$. These parameters are also summarised in Table B.3. The rather old ages inferred for TOI-1820 and TOI-2158 would predict slow stellar rotation periods of $P_{\text{rot}} = 40 \pm 2$ d and $P_{\text{rot}} = 43 \pm 3$ d, respectively, whereas the (projected) rotational periods estimated from the spectroscopic $v \sin i$ together with R_* gives $P_{\text{rot}}/\sin i = 24.9 \pm 6.3$ d and $P_{\text{rot}}/\sin i = 19.3 \pm 3.2$ d, suggesting either somewhat younger ages, or a process that kept the stars rotating faster than expected for their ages.

It is interesting that both TOI-1820 and TOI-2158 appear to be rotating faster than what would be expected given their ages, especially seeing as both of these stars host a hot Jupiter. Discrepancy between ages inferred from [isochrone](#) fitting and gyrochronology among hot Jupiter hosts has been seen in studies by Brown (2014) and Maxted et al. (2015), and both studies suggested tidal spin-up as a possible explanation. Further evidence for this has recently been found in Tejada Arevalo et al. (2021). Tidal spin-up might, therefore, be the mechanism responsible for the discrepancy we are seeing in TOI-1820 and TOI-2158. Of course, this might also apply to the TOI-2025 system as this system also harbours a hot Jupiter, but as this system is younger, the effect might be less pronounced. We examined the residuals of the light curves from our best-fitting models (Figure A.4) to see if we could see any signs of stellar variability, for instance, rotation. However, we did not detect any signals.

6.5 Joint analysis

To estimate the planetary and orbital parameters, we fit the photometry and the [RVS](#) jointly, where we extracted confidence intervals through [MCMC](#) sampling using the [emcee](#) package by Foreman-Mackey et al. (2013). We modelled the light curves using the [batman](#) package (Kreidberg, 2015), which utilises the formalism by Mandel and Agol (2002). To account for any morphological light curve distortion (Kipping, 2010) caused by the 30-minute sampling, we oversampled our 30-minute-cadence light curves to correspond to a sampling of 2 minutes.

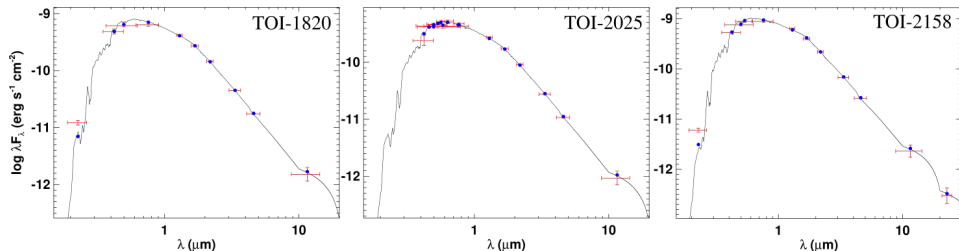


Figure 6.7 | Spectral Energy Distribution. The [SEDS](#) for TOI-1820 (left panel), TOI-2025 (middle panel), and TOI-2158 (right panel). Red symbols represent the observed photometric measurements, where the horizontal bars represent the effective width of the passband. Blue symbols are the model fluxes from the best-fit Kurucz atmosphere model (black).

In an attempt to mitigate correlated noise in the [TESS](#) photometry, we made use of [GP](#) regression through the [celerite](#) package (Foreman-Mackey et al., 2017). We used the Matérn-3/2 kernel, which includes two hyper parameters: the amplitude of the noise, A , and the timescale, τ . The only correction to the [TESS](#) data prior to the [MCMC](#) was the aforementioned background correction. For our ground-based photometry, we did not have long out-of-transit baselines. Therefore, we did not model the noise from these transits with [GPS](#), instead we used a Savitzky-Golay filter to de-trend the data with each draw in our [MCMC](#).

To fit the [RVS](#) we used a Keplerian orbit, where we naturally had different systemic velocities, γ , for the [RVS](#) stemming from [FIES](#) and Tull, when this is relevant. Due to a refurbishment of the [FIES](#) spectrograph, an offset in [RV](#) was introduced between the [RVS](#) obtained before July 1, 2021 and those obtained after. We assigned two independent systemic velocities and two independent jitter terms to [RVS](#) obtained before ([FIES](#)) and after ([FIES+](#)) this date.

Our [MCMC](#) analysis for the three systems stepped in $\cos i$ instead of i , as well as in $\sqrt{e} \cos \omega$ and $\sqrt{e} \sin \omega$ instead of e and ω . Furthermore, the code stepped in the sum of the limb darkening parameters, namely $q_1 + q_2$, where we applied a Gaussian prior with a width of 0.1. We instead fixed the difference fixed, $q_1 - q_2$, during the sampling. We retrieved the starting values of q_1 and q_2 for the [TESS](#) passband from the table Claret (2017), while we used the values from Claret et al. (2013) for the ground-based photometry. Furthermore, we used V as a proxy for our transit observations of TOI-2025 using [FIES](#).

We define our likelihood function as

$$\log \mathcal{L} = -0.5 \sum_{i=1}^N \left[\frac{(O_i - C_i)^2}{\sigma_i^2} + \log 2\pi\sigma_i^2 \right] + \sum_{j=1}^M \log \mathcal{P}_j, \quad (6.1)$$

where N indicates the total number of data points from photometry and [RVS](#). C_i represents the model corresponding to the observed data point O_i . σ_i represents the uncertainty for the i th data point, where we add a jitter term in quadrature and a penalty in the likelihood for the [RVS](#). \mathcal{P}_j is the prior on the j th parameter.

We ran our [MCMC](#) until convergence, which we assessed by looking at the rank-normalised \hat{R} diagnostic test as implemented in the `rhat` module in ArviZ (Kumar et al., 2019).

6.5.1 TOI-1820

Given the large separation of around 110 AU for the companion, the orbital period must be rather large and the expected K -amplitude must be rather small, meaning that, even if it is bound, it will not affect our [RVS](#). The companion will, however, dilute the light curve. We therefore include a contaminating factor, where we write the total flux as a function of time as $F(t) = (F_1(t) + F_2)/(F_1 + F_2)$ with $F_1(t)$ and F_1 being the flux respectively in- and out-of-transit from the planet hosting star, and F_2 is the (constant) flux from the contaminating source (or sources). Here, we included the flux from the contaminating source as a fraction of the host, F_2/F_1 , as the difference in magnitude, namely $\delta M = -2.5 \log(F_2/F_1)$. Conveniently, δM is derived from observations in the I -band, which is close to the bandpasses from [TESS](#), i' , and z -short (Figure 6.1). However, the dilution might be overestimated in the B -band. Therefore, we adopted a different value for the B -band of $\delta M = 4.5 \pm 1.0$ as the companion is most likely a cooler star.

6.5.2 TOI-2025

For TOI-2025, we have two sets of light curves with different cadences (2 min. and 30 min.), and we apply two different oversampling factors, while using the same limb darkening coefficients for both. We observed a spectroscopic transit of TOI-2025 at the [NOT](#) ([FIES+](#)) on the night starting on the August 8, 2021, allowing us to determine the projected [obliquity](#), λ , of the host star. The [RVS](#) obtained during this transit night can be

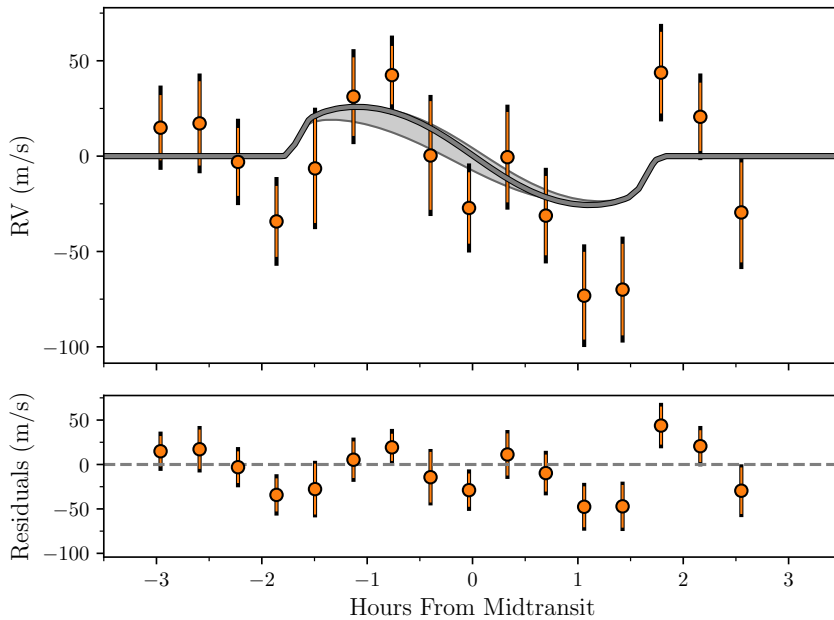


Figure 6.8 | Rossiter-McLaughlin effect in TOI-2025. Our in-transit observations of TOI-2025 with [FIES+](#). *Top:* The Keplerian orbit and quadratic trend has been subtracted from the [RVS](#) to better show the [RM EFFECT](#), with the grey line being the best-fitting model. The shaded area denotes the confidence interval in the projected [obliquity](#), $\lambda = 9^{+33}_{-31} \text{ }^\circ$. *Bottom:* Here we have further subtracted this best-fitting model from the [RVS](#).

seen in Figure 6.8. We therefore also included a model for the [RM EFFECT](#) using the algorithm by Hirano et al. (2011) for this fit. We used our SPC value in Table B.3 for $v \sin i_*$ as a prior. For the [macro-turbulence](#) and [micro-turbulence](#), we used priors stemming from the relations in Doyle et al. (2014) and Bruntt et al. (2010), respectively, along with the stellar parameters in Table B.3.

We carried out three [MCMC](#) runs for TOI-2025 to investigate the long-term trend: 1) a run where we included two additional parameters: a second order, $\ddot{\gamma}$, and a first-order acceleration parameter, $\dot{\gamma}$; 2) a run where we only included the first order parameter; and 3) a run where we did not allow for any long-term drift. These three runs are shown in Figure 6.9.

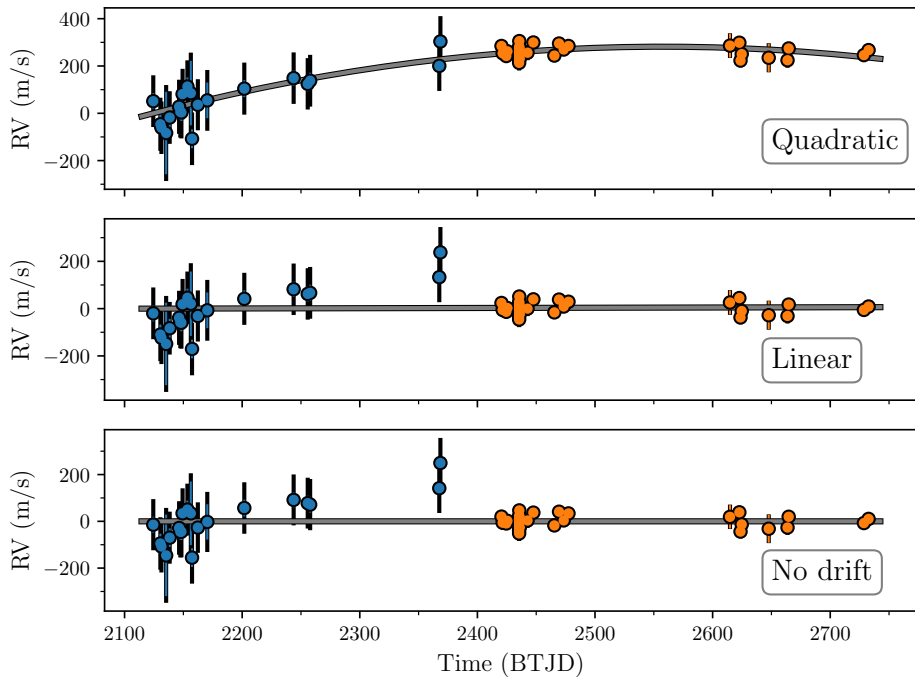


Figure 6.9 | Long-term trend in TOI-2025. The symbols are the same as in Figure 6.5, but here the RVS are plotted against time, and we have subtracted the planetary signal. *Top:* A fit where we allow for a quadratic trend. *Middle:* A fit where we only allow for a linear trend. *Bottom:* Here we do not include any long-term drift.

6.5.3 TOI-2158

Similarly to the case of TOI-2025, the RVS of TOI-2158 show a long-term trend. We therefore performed the same three runs as for TOI-2025. These are shown in Figure 6.10.

6.6 Results

The results from the MCMC for our preferred orbital configuration for each of the systems are tabulated in Table 6.2. We find that TOI-182ob is a Jupiter-sized planet, $1.14 \pm 0.02 R_J$, but significantly more massive, $2.3 \pm 0.2 M_J$. With an orbital period of 4.860674 ± 0.000005 d, it is the planet with the shortest orbital period in our sample. TOI-2025 has a similar size, $1.117 \pm 0.009 R_J$, as TOI-1820, but has about twice its mass, $4.4 \pm 0.3 M_J$. On

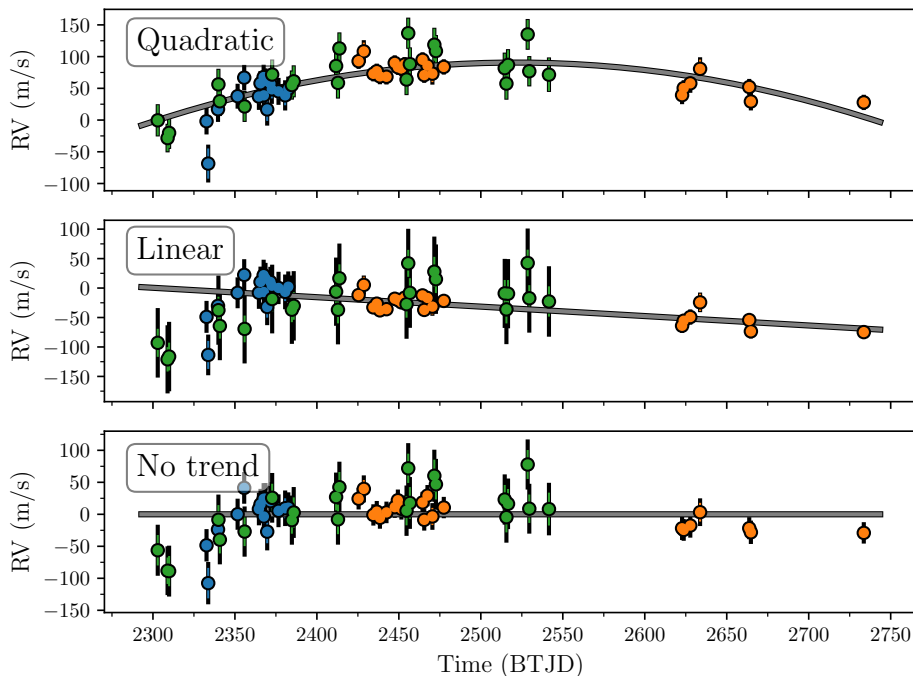


Figure 6.10 | Long-term trend in TOI-2158. The symbols are the same as in Figure 6.5, but here the **RVs** are plotted against time, and we have subtracted the planetary signal. *Top:* A fit where we allow for a quadratic trend. *Middle:* Here we only allow for a linear trend. *Bottom:* Here we do not include any long-term drift.

the other end of the mass spectrum, we find TOI-2158 b with $0.82 \pm 0.08 M_J$. TOI-2158 b is also a bit smaller than the two other planets with a radius of $0.960 \pm 0.012 R_J$.

For TOI-2025 and TOI-2158, we found evidence for long-term **RV** trends, as can be seen in Figure 6.9 and Figure 6.10. In both we also saw evidence for a curvature in the **RVs**, which we model with a quadratic term. There is no significant evidence for long-term **RV** changes in TOI-1820.

Assuming the long-term **RV** changes are due to further-out companions, we can glimpse information about their masses from some back-of-the-envelope calculations. We can therefore obtain an order of magnitude estimate for the periods of the outer companions as $P = -2\ddot{\gamma}/\dot{\gamma}$, resulting in periods of around 1870 d and 650 d for TOI-2025 and TOI-2158, respectively. Using the relation $K = \dot{\gamma}P^2/4\pi^2$ derived in Kipping et al. (2011) with

Table 6.2 | MCMC results for TOI-1820, TOI-2025, and TOI-2158. The parameters above the dashed line are the stepping parameters, and below are the derived parameters. The value given is the median and the uncertainty is the highest posterior density at a confidence level of 0.68. **Notes.** ^(a) Zero-point for TOI-2158 is $2459302.92570 \text{ BJD}_{\text{TDB}}$. ^(b) Zero-point for TOI-2025 is $2459124.41436 \text{ BJD}_{\text{TDB}}$. ^(c) Two-sided 1σ distribution $e = 0.031^{+0.013}_{-0.031}$. ^(d) Calculated from Equation (6.2). ^(e) Following Kempton et al. (2018).

Parameter		TOI-1820	TOI-2025	TOI-2158
P	Period (days)	4.860674 ± 0.000005	8.872078 ± 0.000007	8.60077 ± 0.00003
T_0	Mid-transit time (BJD)	2458903.0638 ± 0.0006	2458690.2898 ± 0.0004	$2459018.9225^{+0.0010}_{-0.0011}$
R_p/R_\star	Planet-to-star radius ratio	0.0777 ± 0.0009	0.0736 ± 0.0004	0.0700 ± 0.0009
a/R_\star	Semi-major axis to star radius ratio	8.7 ± 0.3	$12.7^{+0.5}_{-0.4}$	$11.4^{+0.6}_{-0.5}$
K	Velocity semi-amplitude (m s^{-1})	273 ± 4	396 ± 10	75 ± 4
$\cos i$	Cosine of inclination	0.097 ± 0.005	$0.023^{+0.010}_{-0.023}$	$0.075^{+0.005}_{-0.006}$
$\sqrt{e} \cos \omega$		0.20 ± 0.02	$-0.03^{+0.03}_{-0.02}$	$0.10^{+0.10}_{-0.08}$
$\sqrt{e} \sin \omega$		$0.031^{+0.016}_{-0.031}$	0.643 ± 0.016	$0.10^{+0.05}_{-0.10}$
γ_1	Systemic velocity FIES (m s^{-1})	227^{+5}_{-4}	-383 ± 19	13 ± 9
γ_2	Systemic velocity FIES+ (m s^{-1})	-	-75^{+45}_{-47}	-23^{+14}_{-15}
γ_3	Systemic velocity Tull (m s^{-1})	13947 ± 4	-	-64794^{+11}_{-13}
σ_1	Jitter FIES (m s^{-1})	7^{+3}_{-7}	45^{+12}_{-14}	19^{+5}_{-7}
σ_2	Jitter FIES+ (m s^{-1})	-	19 ± 6	15^{+3}_{-4}
σ_3	Jitter Tull (m s^{-1})	5^{+2}_{-5}	-	12^{+5}_{-11}
$\log A_1$	GP amplitude TESS 30 min.	$-6.98^{+0.09}_{-0.10}$	-8.30 ± 0.06	$-8.95^{+0.12}_{-0.13}$
$\log \tau_1$	GP timescale TESS 30 min. (log days)	$-0.77^{+0.13}_{-0.14}$	$-0.31^{+0.10}_{-0.11}$	$-1.7^{+0.5}_{-0.4}$
$\log A_2$	GP amplitude TESS 2 min.	$-7.36^{+0.10}_{-0.11}$	$-7.85^{+0.09}_{-0.10}$	$-7.271^{+0.017}_{-0.016}$

$\log \tau_2$	GP timescale TESS 2 min (log days)	-1.03 ± 0.14	$-0.23^{+0.13}_{-0.14}$	$-7.29^{+0.07}_{-0.06}$
$\dot{\gamma}^{(a,b)}$	Quadratic trend ($\text{m s}^{-1} \text{d}^{-2}$)	-	-0.0015 ± 0.0003	-0.0020 ± 0.0003
$\dot{\gamma}^{(a,b)}$	Linear trend ($\text{m s}^{-1} \text{d}^{-1}$)	-	1.4 ± 0.2	$0.87^{+0.14}_{-0.13}$
δM_I	Dilution I -band/TESS	$3.9^{+0.4}_{-0.5}$	-	-
δM_B	Dilution B -band	$4.7^{+0.8}_{-0.9}$	-	-
λ	Projected obliquity ($^\circ$)	-	9^{+33}_{-31}	-
$v \sin i_\star$	Projected rotational velocity (km s^{-1})	-	6.0 ± 0.3	-
ζ	Macro-turbulence (km s^{-1})	-	4 ± 1	-
ξ	Micro-turbulence (km s^{-1})	-	$1.3^{+0.7}_{-0.9}$	-
e	Eccentricity	0.043 ± 0.008	0.41 ± 0.02	$< 0.070 \text{ at } 3\sigma^{(c)}$
ω	Argument of periastron ($^\circ$)	9^{+4}_{-9}	93 ± 2	52^{+19}_{-52}
i	Inclination ($^\circ$)	84.4 ± 0.3	$88.7^{+1.3}_{-0.6}$	$85.7^{+0.4}_{-0.3}$
b	Impact parameter	$0.840^{+0.015}_{-0.013}$	$0.29^{+0.12}_{-0.29}$	$0.86^{+0.02}_{-0.03}$
$T_{2,1}$	Total transit duration (hours)	2.92 ± 0.04	$3.617^{+0.017}_{-0.022}$	$3.77^{+0.05}_{-0.06}$
$T_{2,1}$	Time from 1st to 2nd contact (hours)	0.61 ± 0.05	$0.255^{+0.009}_{-0.010}$	0.75 ± 0.07
R_p	Planet radius (R_J)	1.14 ± 0.02	1.117 ± 0.009	0.960 ± 0.012
$M_p^{(d)}$	Planet mass (M_J)	2.3 ± 0.2	4.4 ± 0.3	0.82 ± 0.08
ρ_p	Planet density (g cm^{-3})	2.0 ± 0.2	3.9 ± 0.3	1.14 ± 0.12
$T_{\text{eq}}^{(e)}$	Equilibrium temperature (K)(c)	1375 ± 12	1167 ± 11	1188 ± 10
a	Semi-major axis (AU)	0.061 ± 0.003	0.092 ± 0.004	0.075 ± 0.004

$$\frac{M_p \sin i}{M_J} = \frac{K \sqrt{1 - e^2}}{28.4 \text{ m s}^{-1}} \left(\frac{P}{1 \text{ yr}} \right)^{1/3} \left(\frac{M_\star}{M_\odot} \right)^{2/3}, \quad (6.2)$$

we can get an estimate of the masses of the companions. From this we get masses of $\approx 70 M_J$ and $\approx 15 M_J$ for the companions in TOI-2025 and TOI-2158, respectively.

6.6.1 The eccentricities of TOI-2025 b and TOI-1820 b

We find TOI-2025 b to travel on an eccentric orbit, 0.41 ± 0.02 . However, the argument of periastron is close to and fully consistent with 90° . This configuration can be deceptive when it comes to determining the eccentricity (e.g. Laughlin et al., 2005). This is because the **RV** curves would be symmetric for values close to $|\omega| = 90^\circ$, even for eccentric orbits.

To further investigate the orbital eccentricity, we carried out a few experiments. First, as mentioned, we ran an **MCMC** where we fixed e to 0. The best-fitting model from this run can be seen in Figure A.3, where the residuals clearly have structure in them. Our model involving a circular orbit does apparently not capture all the complexity present in the data. Consequently, the derived **RV** jitter terms for both **FIES** and **FIES+** are significantly higher, with values of $111_{-22}^{+18} \text{ m s}^{-1}$ and $82_{-13}^{+10} \text{ m s}^{-1}$, respectively, as opposed to the values of $45_{-14}^{+12} \text{ m s}^{-1}$ and $19 \pm 6 \text{ m s}^{-1}$ from the eccentric fit. As we find a modest eccentricity for TOI-1820, we carried out a similar run for TOI-1820, finding marginally higher jitter (a couple of m s^{-1}) for the $e = 0$ case.

As there might be stellar signals that are coherent on timescales of hours, but not days, and given that we have a much higher sampling during the transit night, it is worthwhile investigating if the eccentricity hinges on those measurements and to what extent. Therefore, we performed a fit in which the eccentricity was allowed to vary, but where we only included the first and the last data point from the transit night. Here, we obviously did not try to fit the **obliquity**. From this we get values of $e = 0.42 \pm 0.02$ and $\omega = 91 \pm 3^\circ$, consistent with the values from the run using all the **RV** data.

Next we performed a bootstrap experiment using the **RV** data only. In our bootstrap we used alternate realisations of our **RV** data of TOI-2025, again excluding all but the first and last data point from the transit night. After redrawing a data set from the original data, we fit for e , ω , γ_{FIES} , $\gamma_{\text{FIES+}}$, K , $\dot{\gamma}$, and $\ddot{\gamma}$. In Figure 6.11 we plot the results for e and ω for the

50,000 realisations. Evidently, we recover an eccentric orbit even when we leave out certain data points. Therefore, we conclude that our result for the eccentricity is significant and does not hinge on a few data points. Again, we did a similar exercise for TOI-1820, which also yielded consistent results with the run from the [MCMC](#), as seen in Figure 6.12. We thus conclude that the eccentricities for TOI-2025 b and TOI-1820 b are significant (at a confidence level of 20σ and 5σ , respectively), while TOI-2158 b is consistent with a circular orbit.

6.6.2 The obliquity of TOI-2025

In addition to finding an eccentric orbit for the planet, we also measured the projected [obliquity](#) of TOI-2025. We find the projected [obliquity](#) to be consistent with no misalignment, $\lambda = 9^{+33}_{-31} \text{ }^\circ$. The relevant transit [RVS](#) and our best-fitting model can be seen in Figure 6.8. Despite having only measured the projected [obliquity](#), λ , here, we can make a strong argument that it is close to the [obliquity](#), ψ , which requires the stellar inclination along the line of sight to be close to 90° . That i_* is close to 90° is supported by Figure 3 in Louden et al. (2021), where a correlation between T_{eff} and $v \sin i_*$ is plotted. From this plot we should not expect $v \sin i_*$ to be markedly different from the value of $6.0 \pm 0.3 \text{ km s}^{-1}$ given the effective temperature for TOI-2025 of $\sim 5900 \text{ K}$ that we have found. This therefore suggests that the system is aligned.

6.7 Discussion and conclusions

We validated and characterised three hot Jupiters discovered by [TESS](#): TOI-1820 b, TOI-2025 b, and TOI-2158 b. A commonality for all three systems is that we, in some way or another, see evidence for companions. The outer companions may have played a role in the migration of the gas giants, thus shaping the final architecture of the systems. Ngo et al. (2016) argue that sites hosting outer stellar companions are either more favourable environments for gas giant formation at all separations, or the presence of stellar companions might drive the inwards migration, such as through Kozai-Lidov (Kozai, 1962; Lidov, 1962), or other dynamical processes. Through our speckle interferometry of TOI-1820, we detected a ~ 4 mag fainter stellar companion at a distance of $\sim 110 \text{ AU}$ from the bright host. It would be interesting to obtain good estimates of the stellar parameters for this companion in order to assess whether it would have been able to drive Kozai-Lidov cycles responsible for the migration.

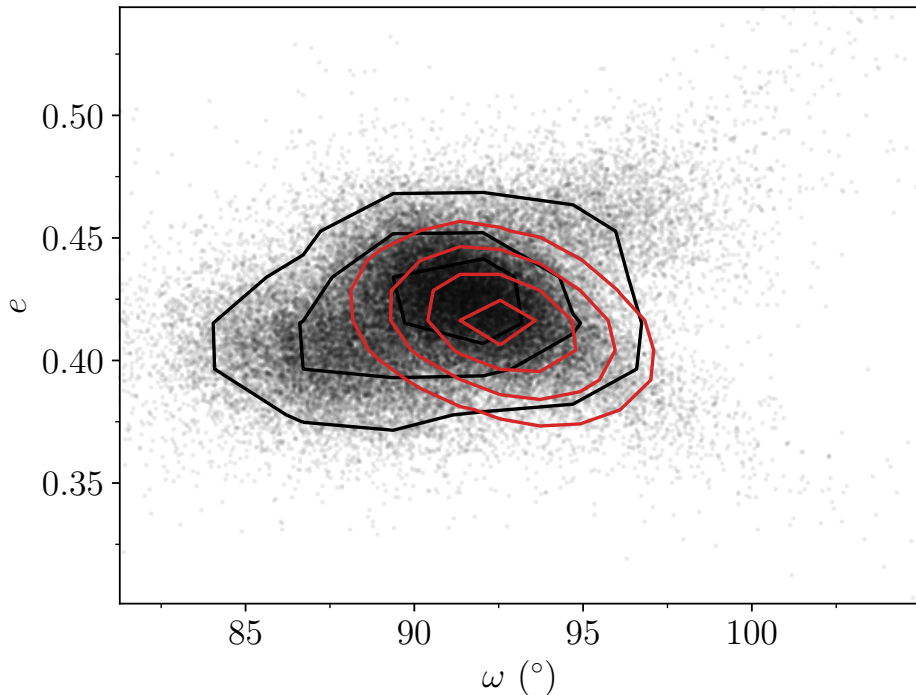


Figure 6.11 | Bootstrapping the orbit of TOI-2025 b. A 2D histogram of our bootstrap with 50,000 iterations displaying the eccentricity plotted against the argument of periastron. Each point is one iteration and the black contours denote the confidence levels. The red contours are the posteriors from our [MCMC](#) tabulated in Table 6.2.

If the outer companions are planets within ~ 1 AU from the stellar host, Becker et al. (2017) found that they should be coplanar with the inner hot Jupiters, suggesting that Kozai-Lidov migration would not be viable. However, if these companions are found at greater distances (gas giants $\gtrsim 5$ AU or stellar $\gtrsim 100$ AU), they could still be inclined and the formation of the hot Jupiter could take place through Kozai-Lidov migration (Lai et al., 2018). In the [RVS](#) for both TOI-2025 and TOI-2158, we see long-term quadratic trends. In contrast to TOI-1820, the companions in TOI-2025 and TOI-2158 might be of planetary, or at least substellar, nature and closer in (cf. the mass and period estimates in Section 6.6). As the companions in TOI-2025 and TOI-2158 are most likely found beyond 1 AU, given the (lower) estimates for their periods and the stellar masses, Kozai-Lidov migration could be a viable transport mechanism for TOI-2025 b and TOI-2158 b. [TESS](#) might be able to shed more light on these outer companions

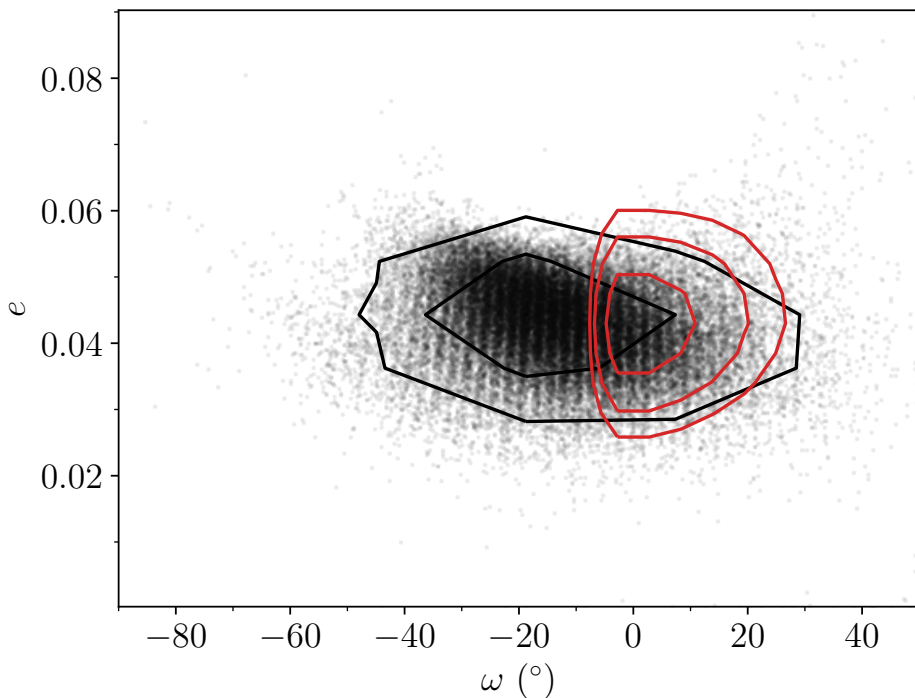


Figure 6.12 | Bootstrapping the orbit of TOI-1820 b. Same as in Figure 6.11, but for TOI-1820 b.

as more sectors become available. According to the Web **TESS Viewing Tool**⁴, TOI-2025 should be observed again in Sectors 52, 53, and 58-60, and TOI-2158 is set to be observed in Sector 53. In addition, continued **RV** monitoring will help constrain the periods and masses.

In Figure 6.13 we show the tidal diagram (left) and modified tidal diagram (right) from Bonomo et al. (2017a) with our measurements for TOI-1820 b, TOI-2025 b, and TOI-2158 b. We find that the orbital eccentricity of TOI-2158 b is consistent with $e = 0$. This planet joins the small group of planets in Bonomo et al. (2017a) with circular orbits and relatively large values for a/a_R , a_R being the Roche limit. This would allude to **disc migration**. However, given the age of 8 ± 1 Gyr for TOI-2158, the orbit of the planet might have had sufficient time to circularise, should the migration have taken place through **high-eccentricity migration**. For TOI-1820 b we find a modest eccentricity of 0.043 ± 0.008 (about three times that of Earth). In Figure 6.13 the planets with modest eccentricities are found at

4: <https://heasarc.gsfc.nasa.gov/cgi-bin/tess/webtess/wtv.py>

various relative masses and various relative distances. From the modified tidal diagram, it appears that TOI-1820 b should have a circularisation timescale of around 1-2 Gyr, and with the age of 11 ± 2 Gyr for TOI-1820, this leaves plenty of time for the system to dampen the eccentricity in the case of [high-eccentricity migration](#). However, this modest eccentricity is not irreconcilable with [disc migration](#) (Dawson and Johnson, [2018](#)). In contrast, TOI-2025 b belongs to the subgroup of systems with significant eccentricity. The planet TOI-2025 b is too massive for the star to effectively raise tides on the planet in order to circularise the orbit, meaning that the circularisation timescale is too long for the orbit to have been circularised (Dawson and Johnson, [2018](#)). The modified tidal diagram suggests that the circularisation timescale could be some 10 Gyr, which is much longer than the age of 1.7 ± 0.2 Gyr for this system.

On the same token, the planet seems to be massive enough for it to effectively raise tides on the star, while the star is sufficiently cool for tidal dissipation to be efficient (Winn et al., [2010](#); Albrecht et al., [2012](#)). The projected [obliquity](#) we find for TOI-2025 is in line with other massive planets on eccentric, aligned orbits, such as HD 147506b (Winn et al., [2007](#)), HD 17156 b (Narita et al., [2009](#)), and HAT-P-34 b (Albrecht et al., [2012](#)). Contrary to these findings, Rice et al. ([2022](#)) has found that cool stars ($T_{\text{eff}} < 6100$ K) harbouring eccentric planets tend to have higher [obliquities](#). Although, due to the sample size it is still unclear whether misalignment is associated with orbital eccentricity. Given the orbital, stellar, and planetary parameters, the low projected [obliquity](#) in TOI-2025 might be the result of tidal alignment (Albrecht et al., [2022](#)). If so it would be interesting to further reduce the uncertainty of the [obliquity](#) measurement to test if the system is aligned to within 1° as recently observed in some systems (Albrecht et al., [2022](#)). This would suggest tidal alignment, as primordial alignment would presumably lead to a certain spread, as it has apparently done in the Solar System. TOI-1820 and TOI-2158 would, for similar reasons, be excellent targets to study the [RM EFFECT](#) as well. In addition, their higher impact parameters might lead to an even higher accuracy.

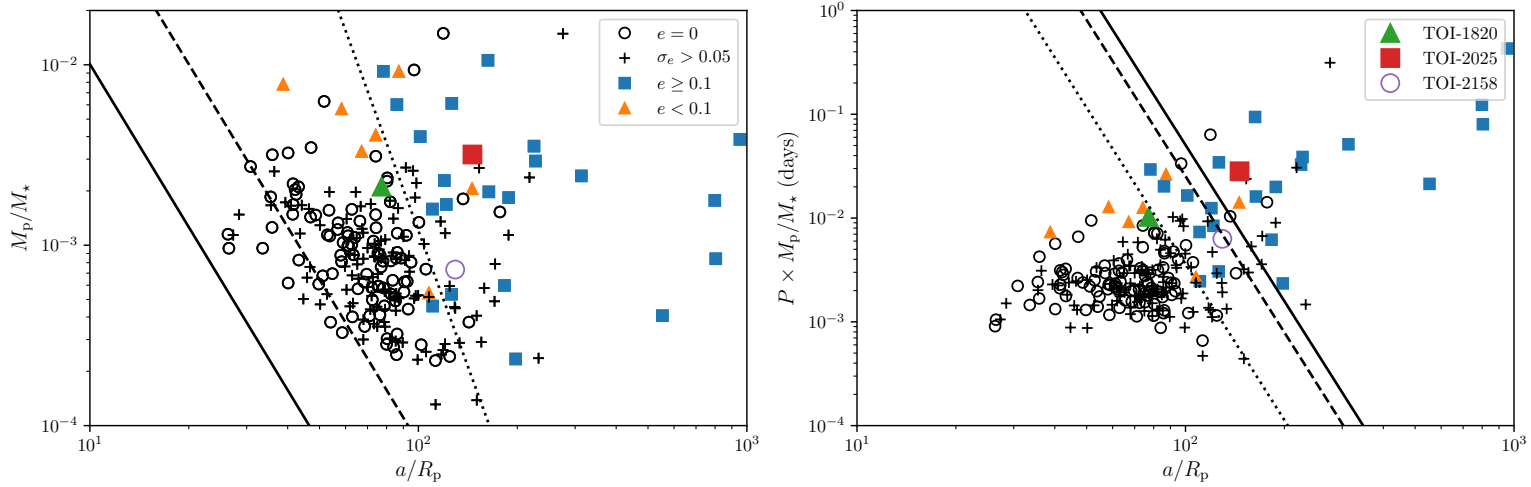


Figure 6.13 | Tidal diagrams. Tidal diagrams for transiting giant planets from Bonomo et al. (2017a). Open circles denote planets on circular orbits with $\sigma_e < 0.05$. Markers shown with pluses are planets with underdetermined eccentricities, i.e. $\sigma_e > 0.05$. Most of these are consistent with $e = 0$. Triangles represent planets with significant, but small eccentricities $e < 0.1$, and squares are eccentric systems ≥ 0.1 . Adhering to this notation we have shown the planets in our sample with the corresponding marker. However, we have colour coded them for clarity. Created from the catalogue Bonomo et al. (2017b). *Left: Tidal diagram.* The solid and dashed lines show the position of a planet with a separation of $a = a_R$ and $a = 2a_R$, respectively (a_R being the Roche limit), and radius $R_p = 1.2 R_J$. The dotted line is a circularisation **isochrone** for a planet with $P = 3$ d, $Q'_p = 10^6$, and $e = 0$. It should be noted that Eq. (1) in Bonomo et al. (2017a) used to create the dotted line should have π in the numerator instead of the denominator (A. S. Bonomo private communication). *Right: Modified tidal diagram.* The dotted, dashed, and solid lines denote the 1, 7, and 14 Gyr circularisation timescales, respectively, assuming $e = 0$ and $Q'_p = 10^6$.

7

Radial velocity confirmation of a hot super-Neptune discovered by TESS with a warm Saturn-mass companion

In the previous chapter I presented the discovery of a trio of giant planets on short-period orbits. For two of these hot and warm Jupiters we saw evidence for wide orbiting companions, and it was discussed how they might have influenced the system architectures, possibly shrinking the orbits of the transiting planets through [high-eccentricity migration](#). In this chapter, we will look at the TOI-1288 system, which also harbours an inner transiting planet discovered by [TESS](#) with a wide orbiting companion. As such this outer Saturn-mass companion might have been responsible for transporting the transiting super-Neptune to its current position, where it is residing in the so-called Neptunian “desert” (Mazeh et al., [2016](#)).

The results have been published as

E. Knudstrup, D. Gandolfi, G. Nowak, C. M. Persson, E. Furlan,
J. Livingston, E. Matthews, M. S. Lundkvist, M. L. Winther,
J. L. Rørsted, S. H. Albrecht, E. Goffo, I. Carleo, H. J. Deeg,
K. A. Collins, N. Narita, H. Isaacson, S. Redfield, F. Dai,
T. Hirano, J. M. Akana Murphy, C. Beard, L. A. Buchhave,
S. Cary, A. Chontos, I. Crossfield, W. D. Cochran, D. Conti,
P. A. Dalba, M. Esposito, S. Fajardo-Acosta, S. Giacalone, S. K.
Grunblatt, P. Guerra, A. P. Hatzes, R. Holcomb, F. G. Horta,
A. W. Howard, D. Huber, J. M. Jenkins, P. Kabáth, S. Kane,
J. Korth, K. W. F. Lam, K. V. Lester, R. Matson, K. K. McLeod,

J. Orell-Miquel, F. Murgas, E. Palle, A. S. Polanski, G. Ricker, P. Robertson, R. Rubenzahl, J. E. Schlieder, S. Seager, A. M. S. Smith, P. Tenenbaum, E. Turtelboom, R. Vanderspek, L. Weiss, and J. Winn (2023a). “Radial velocity confirmation of a hot super-Neptune discovered by TESS with a warm Saturn-mass companion”. *Monthly Notices of the Royal Astronomical Society* 519.4, pp. 5637–5655

For this project I was the [PI](#) for one of the observing programmes using the [HARPS](#)-N spectrograph, where the [RV](#) follow-up was carried out in concert with the HIRES spectrograph at the Keck Observatory. I did the data analysis in Section 7.3 and Section 7.4, and wrote most of the paper.

In the version reproduced here, the tables containing observations and nuisance parameters (Tables B1-B3 in Knudstrup et al., 2023a) have been omitted, and Figures A3 and A4 as well as one of the contrast curves in Figure 3 of Knudstrup et al. (2023a) have been removed. Other than that, the paper has only been reformatted.

Summary of the Chapter

We report the discovery and confirmation of the planetary system TOI-1288. This late G dwarf harbours two planets: TOI-1288 b and TOI-1288 c. We combine [TESS](#) space-borne and ground-based transit photometry with [HARPS](#)-N and HIRES high-precision Doppler measurements, which we use to constrain the masses of both planets in the system and the radius of planet b. TOI-1288 b has a period of $2.699835^{+0.000004}_{-0.000003}$ d, a radius of $5.24 \pm 0.09 R_{\oplus}$, and a mass of $42 \pm 3 M_{\oplus}$, making this planet a hot transiting super-Neptune situated right in the Neptunian desert. This desert refers to a paucity of Neptune-sized planets on short period orbits. Our 2.4-year-long Doppler monitoring of TOI-1288 revealed the presence of a Saturn-mass planet on a moderately eccentric orbit ($0.13^{+0.07}_{-0.09}$) with a minimum mass of $84 \pm 7 M_{\oplus}$ and a period of 443^{+11}_{-13} d. The 5 sectors worth of [TESS](#) data do not cover our expected mid-transit time for TOI-1288 c, and we do not detect a transit for this planet in these sectors.

7.1 Introduction

As the tally of exoplanets has now surpassed 5,000, we can make more informed inferences about planet formation and evolution. A wealth of

architectures and different planet types have been discovered, some of which are quite different from the planets found in the Solar System. We first learned about giant planets on short period orbits, the so-called hot Jupiters, which have been found in abundance, owing to their detection bias. The *Kepler* space mission (Borucki et al., 2010) showed us that, while super-Earths appear to be quite common (Howard et al., 2010b; Mayor et al., 2011), we see a significant dearth of Neptune mass planets on short period orbits, a paucity referred to as the Neptunian “desert” (Mazeh et al., 2016).

In addition to this paucity, studies on the planetary initial mass function (e.g., Mordasini et al., 2009) have found a minimum in the mass range where super-Neptunes reside, namely from around $30 M_{\oplus}$ to $70 M_{\oplus}$. This valley has been interpreted as the division between planets dominated by solids and gas giants that have undergone runaway gas accretion (Ida and Lin, 2004). Finding and characterising planets in this mass range could therefore help shed light on why some *protoplanets* undergo runaway accretion while others do not.

Most of the super-Neptunes were detected by *Kepler* around relatively faint stars, meaning that precise mass determinations only exist for a few of these (e.g., Kepler-101b, Bonomo et al., 2014). *TESS* (Ricker et al., 2015) along with ground-based efforts have now detected more of these super-Neptunes in brighter systems for which precise *RVS* are more viable, enabling both radius and mass determinations. Therefore, we can also determine the bulk density and make inferences about the composition. A way to gain more insight into the composition and potential migration is through atmospheric studies, which have also been used as a means to rule out certain mechanisms. For instance, as in Vissapragada et al. (2022) in which photoevaporation is ruled out as the mechanism responsible for shaping the upper edge of the Neptunian desert.

Here we report on the discovery and characterisation of the TOI-1288 planetary system. In this system we have discovered a hot super-Neptune, TOI-1288 b, with an outer Saturn mass companion, TOI-1288 c. These planets are hosted by a late G dwarf.

The paper is structured as follows. In Section 7.2 we describe our observations, which include ground-based photometry as well as that from *TESS*. We have also acquired speckle and adaptive optics (AO) imaging to search for blended companions. In addition, we have carried out extensive spectroscopic follow-up to confirm and characterise this planetary system. In Section 7.3 we present our analysis of the data in which we model the photometry and spectroscopy jointly. The results are presented

Table 7.1 | System parameters. Catalog IDs, coordinates, and magnitudes for the TOI-1288 system. **Notes.** ^(a)<https://exofop.ipac.caltech.edu/tess/>. ^(b)Gaia Collaboration et al. (2022). ^(c)Høg et al. (2000). ^(d)Cutri et al. (2003).

Parameter	Value	Name
TIC ^(a)	365733349	
Gaia DR3 ^(b)	2245652826430109184	
TYC ^(c)	4255-1629-1	
α (J2000) ^(b)	20:52:40.09	Right ascension (R.A.)
δ (J2000) ^(b)	+65:36:31.59	Declination (Dec.)
μ_α (mas yr ⁻¹) ^(b)	43.496 ± 0.017	Proper motion R.A.
μ_δ (mas yr ⁻¹) ^(b)	-68.775 ± 0.017	Proper motion Dec.
ϖ (mas) ^(b)	8.720 ± 0.013	Parallax
RV (km s ⁻¹) ^(b)	-68.1 ± 0.6	Radial velocity
G ^(b)	10.4507 ± 0.0018	Gaia G magnitude
B_P ^(b)	10.855 ± 0.006	Gaia B_P magnitude
R_P ^(b)	9.873 ± 0.003	Gaia R_P magnitude
V ^(c)	10.44 ± 0.04	Tycho V magnitude
B ^(c)	11.38 ± 0.07	Tycho B magnitude
J ^(d)	9.19 ± 0.02	2MASS J magnitude
H ^(d)	8.84 ± 0.03	2MASS H magnitude
K ^(d)	8.78 ± 0.02	2MASS K magnitude

in Section 7.4 and we discuss them in Section 7.5. Finally, we give our conclusions in Section 7.6.

7.2 Observations

The TOI-1288 system has been observed with different space- and ground-based facilities, including both photometric and spectroscopic observations, as well as high-resolution imaging. System parameters for TOI-1288 are summarised in Table 7.1.

7.2.1 Photometry

TESS observed TOI-1288 during Sectors 15, 16, 17, 18, and 24 (August 15 to November 27, 2019, and April 16 to May 13, 2020). This candidate was

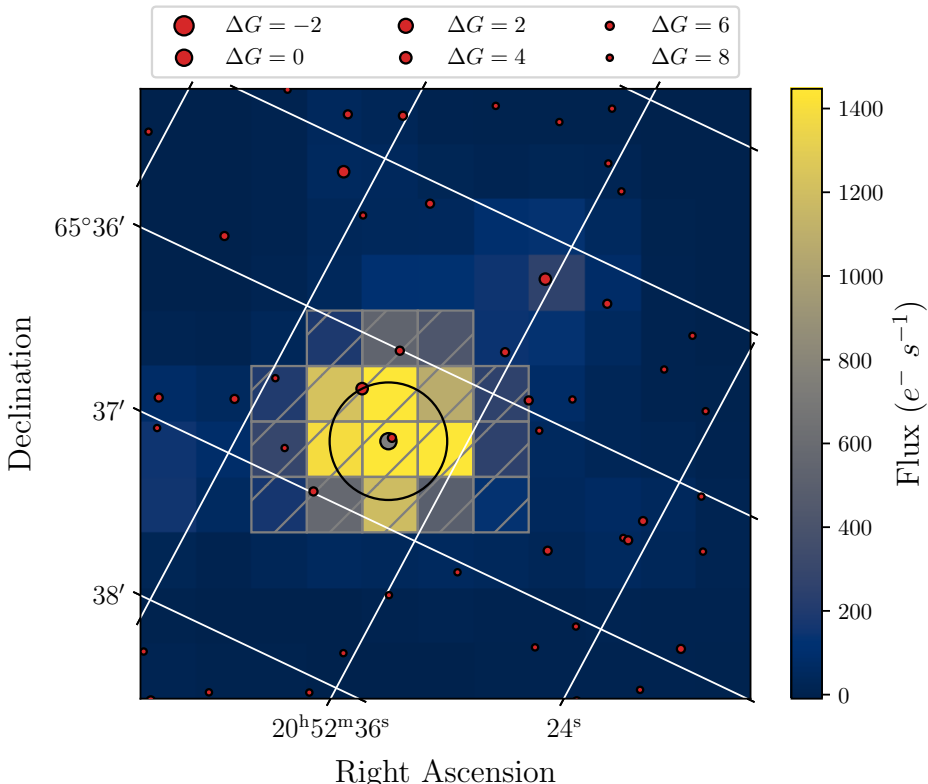


Figure 7.1 | TESS image of TOI-1288. Cutout of a [TESS](#) image of TOI-1288 from Sector 15. The red dots denote [Gaia](#) sources with their sizes scaled to the difference in G magnitude to TOI-1288. The grey dot denotes the position of TOI-1288. The hatched area shows the aperture mask we used to create the light curves, and the black circle illustrates the separation to the brightest nearby star at ~ 23 arcsec.

identified by the Science Processing Operation Center (SPOC; Jenkins et al., 2016) team at the NASA Ames Research Center, who searched the light curves, which are extracted through simple aperture photometry (SAP; Twicken et al., 2010; Morris et al., 2020) and processed using the Presearch Data Conditioning (PDC; Smith et al., 2012; Stumpe et al., 2012; Stumpe et al., 2014) algorithm. The SPOC team searches the PDCSAP light curves for transit-like signals with an adaptive, noise-compensating matched filter (Jenkins, 2002; Jenkins et al., 2010) using a pipeline that iteratively performs multiple transiting planet searches and stops when it fails to find subsequent transit-like signatures above the detection threshold of

a [SNR](#) of 7.1. The results were published in the Data Validation Report (DVR; Twicken et al., 2018; Li et al., 2019), and as the light curve shows a $\sim 0.25\%$ dip occurring every 2.7 d with an [SNR](#) of around 62, it was identified as a [TESS](#) Object of Interest (TOI; Guerrero et al., 2021) and given the ID TOI-1288. The results of the difference image centroiding test were also presented in the DVR, which located the source of the transit signal to within $1.3 \pm 2.6''$ in the Sector 14-26 multi-sector transit search.

An independent search for transit signals was performed using the Détection Spécialisée de Transits (DST; Cabrera et al., 2012) pipeline on the PDCSAP light curves. A transit signal with orbital period of 2.70 ± 0.02 days and a transit depth of $\sim 0.25\%$ was detected, consistent with the signal detected by the SPOC pipeline.

Figure 7.1 displays the [TESS](#) image in the immediate vicinity of TOI-1288 with nearby [Gaia](#) DR3 sources (Gaia Collaboration et al., 2022). All the [TESS](#) photometry from Sectors 15-18 and Sector 24 is displayed in Figure 7.2, where we show the background corrected light curve at the top. This was done using the RegressionCorrector implemented in [lightkurve](#) (Lightkurve Collaboration et al., 2018). Overplotted in grey is a model light curve created using [batman](#) (Kreidberg, 2015) with transit parameters stemming from an initial fit. We used this to remove the transit signal before removing outliers from the light curve. In the middle light curve the transits are removed, and we have applied a Savitzky-Golay filter (Savitzky and Golay, 1964) to temporarily filter the light curve. We then removed outliers through sigma clipping at 5σ , these outliers are highlighted in red. Finally, in the bottom light curve we have re-injected the transits to the unfiltered light curve as we want to account for any trend while fitting, as described in Section 7.3.

7.2.1.1 Light Curve Follow-up

We acquired ground-based time-series follow-up photometry of TOI-1288 as part of the [TESS](#) Follow-up Observing Program (TFOP; Collins, 2019)¹ using various facilities (as listed in Table B1 in Knudstrup et al., 2023a) from October 2019 to September 2021. This is done in an attempt to (1) rule out or identify nearby eclipsing binaries (NEBs) as potential sources of the detection in the [TESS](#) data, (2) detect the transit-like events on target to confirm the depth and thus the [TESS](#) photometric deblending factor, (3) refine the [TESS](#) ephemeris, and (4) place constraints on transit depth differences across optical filter bands. We used the [TESS](#) Transit Finder,

¹: <https://tess.mit.edu/followup>.

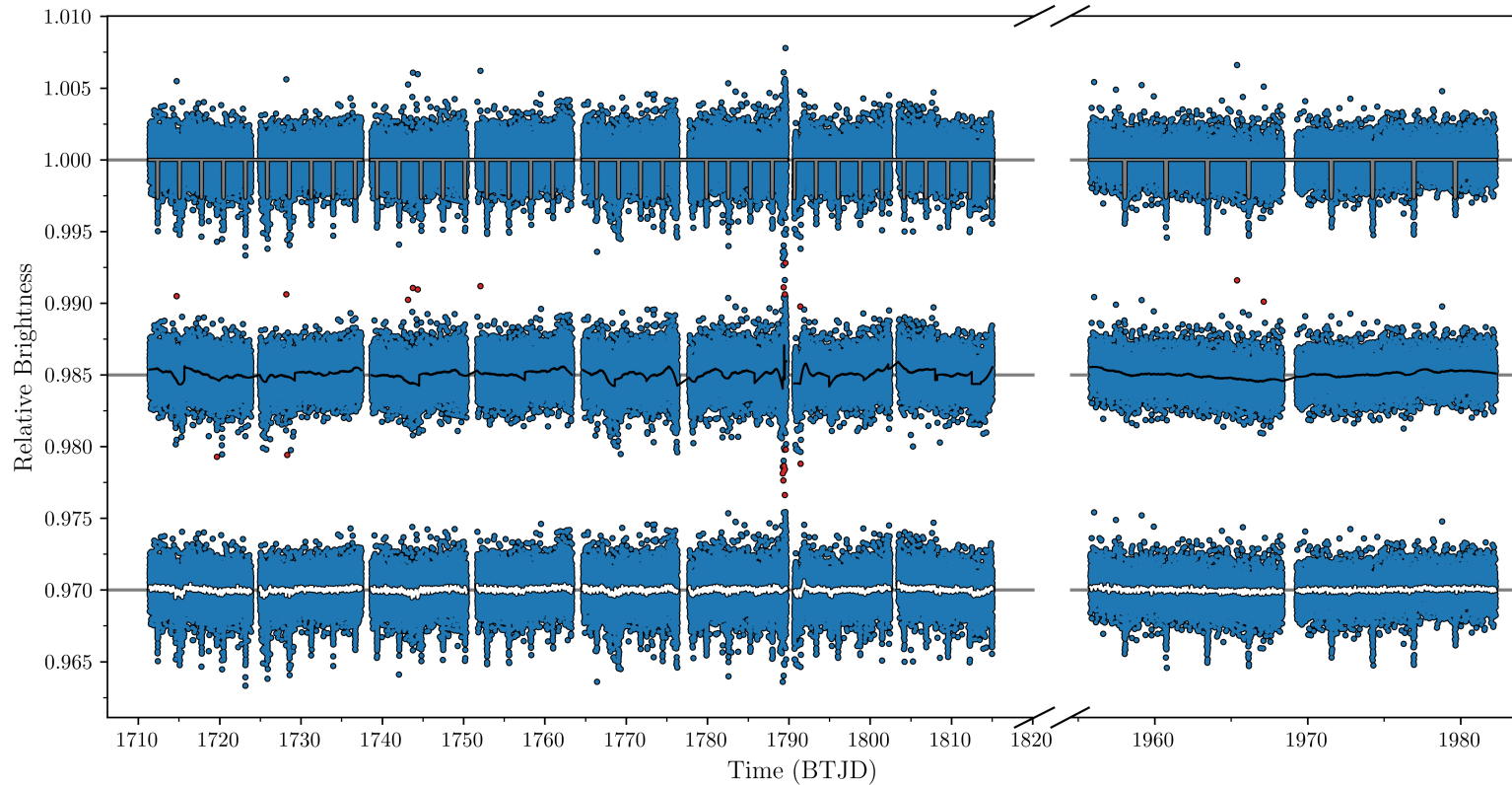


Figure 7.2 | TESS photometry. The light curve at the top shows the background corrected light curve. The grey line is a transit model created from parameters stemming from an initial fit. The transit model has been used to temporarily remove the transit in the light curve shown in the middle. Here the grey line shows a Savitzky-Golay filter (as implemented in Lightkurve Collaboration et al., 2018) used to filter and detrend the data for outlier rejection. The red points are outliers removed through a 5σ sigma clipping. The TESS data with outliers removed and the transits re-injected is shown in the light curve at the bottom. The white line is the GP we use to detrend the data (see Section 7.3).

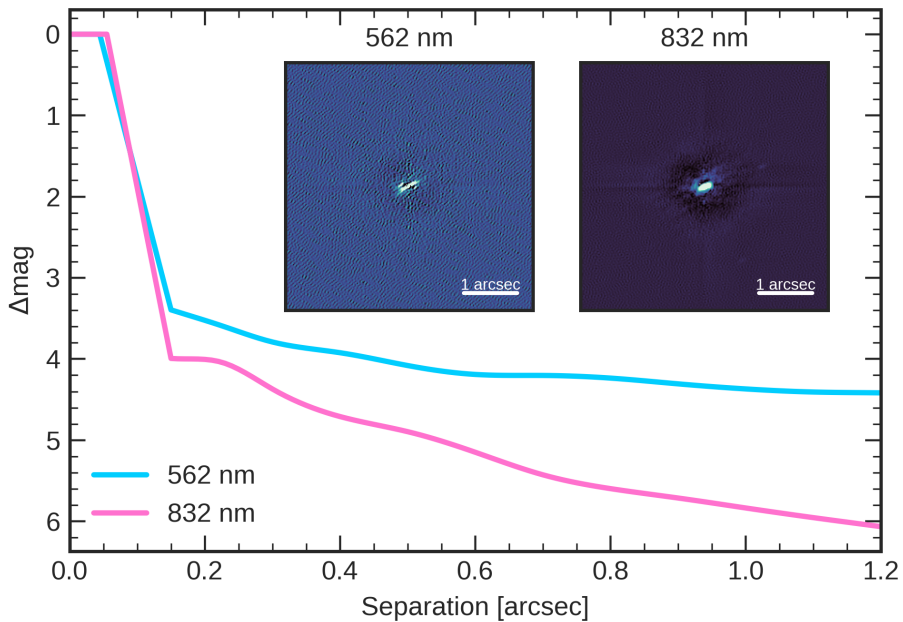


Figure 7.3 | WIYN/NESSI contrast curves from 2019. Two filter speckle imaging contrast curves for TOI-1288 from NESSI. The insets show the reconstructed 562 nm and 832 nm images with 1 arcsec scale bars.

which is a customized version of the Tapir software package (Jensen, 2013), to schedule our transit observations. The images were calibrated and the photometric data were extracted using the AstroImageJ (AIJ) software package (Collins et al., 2017), except the Las Cumbres Observatory Global Telescope (LCOGT; Brown et al., 2013) images, which were calibrated by the standard LCOGT BANZAI pipeline (McCully et al., 2018), and the Multicolor Simultaneous Camera for studying Atmospheres of Transiting exoplanets (MuSCAT; Narita et al., 2015) data, which were extracted using the custom pipeline described in Fukui et al. (2011).

The light curves are shown in Figure A.6 (and the individual observations are detailed in Table B1 in Knudstrup et al., 2023a). All photometric apertures exclude flux from all known *Gaia* DR3 stars near TOI-1288, except the *TESS*-band 16.4 magnitude neighbor 1.5'' southwest, which is nominally too faint to be capable of causing the detection in the *TESS* photometric aperture. Transit events consistent with the *TESS* TOI-1288 b transit signal were detected in each light curve and are included in the joint model described in Section 7.3.

7.2.2 Speckle/AO imaging

Nearby sources that are blended in the aperture mask used for the photometry can contaminate the light curve and alter the measured radius, it is thus important to vet for close visual companions. Furthermore, a close companion could be the cause of a false positive if the companion is itself an eclipsing binary (Ciardi et al., 2015). We therefore collected both adaptive optics and speckle imaging. The observations are described below and summarised in Table 7.2.

7.2.2.1 WIYN/NESSI

On the nights of 2019 November 17 and 2021 October 29, TOI-1288 was observed with the NESSI speckle imager (Scott, 2019), mounted on the 3.5 m WIYN telescope at Kitt Peak, AZ, USA. NESSI simultaneously acquires data in two bands centered at 562 nm and 832 nm using high speed electron-multiplying CCDs (EMCCDs). We collected and reduced the data following the procedures described in Howell et al. (2011). The resulting reconstructed image achieved a contrast of $\Delta\text{mag} \approx 5.75$ at a separation of $1''$ in the 832 nm band (see Figure 7.3).

On both nights we detected a companion at a separation of $\sim 1.2''$, however, only in the 832 nm filter. Additionally, on the night of 2021 October 29 the pipeline detected a companion at a separation of $0.065''$ (position angle of 313° and $\Delta\text{mag} = 2.57$). However, this companion is close to the detection limit (Scott, 2019), and the fit that produced it relied on image elongation (as opposed to being fully separated from the primary), which is possible to get from a mismatch between the science target and the (single) comparison star. Furthermore, it was not detected in the 2019 November 17 data (despite being of higher quality), nor was it detected in any of the other speckle or AO images (see below). We therefore conclude that the inner companion is a spurious detection most likely caused by a data artefact.

7.2.2.2 Gemini/'Alopeke

TOI-1288 was observed with the 'Alopeke speckle instrument on the Gemini North telescope, HI, USA, (Scott et al., 2021) on 2020 June 9, 2021 June 24, 2021 October 22, and 2022 May 14 (all dates in UT). Observations were obtained simultaneously in two narrow-band filters centered at 562 nm (width=54 nm) and at 832 nm (width=40 nm). Between 6 and 7 sets of 1000×0.06 s exposures were collected and then reduced with the standard

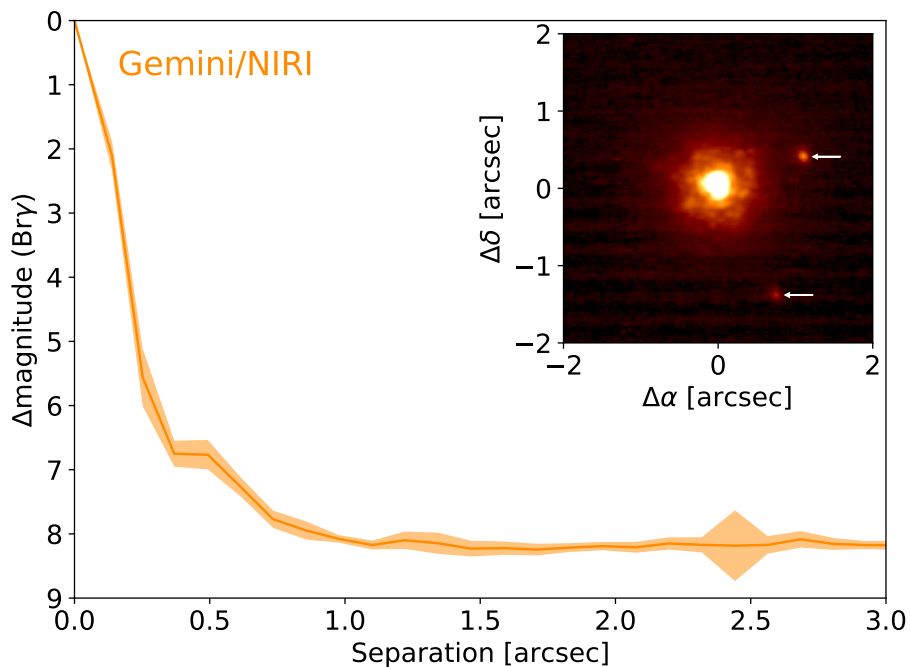


Figure 7.4 | Gemini/NIRI contrast curve. AO imaging contrast curve for TOI-1288. The inset shows the reconstructed $Br\gamma$ image with the two detected companions highlighted.

reduction pipeline using Fourier analysis (see, e.g., Howell et al., 2011, for an overview). The reduced data products include reconstructed images and 5σ contrast curves. TOI-1288 was very faint in most data sets and even not detected in one of them at 562 nm. At 832 nm, in addition to the primary star, a faint ($\Delta M \sim 5.9$) companion was detected at a projected separation of $\sim 1.2''$ - $1.3''$ in the data from 2020 June 9, 2020 June 24, 2021 October 22, and 2022 May 14. An even fainter ($\Delta M \sim 7$) companion was detected at a separation of $\sim 1.4''$ - $1.5''$ in the data from 2020 June 24, 2021 October 22, and 2022 May 14.

7.2.2.3 Gemini/NIRI

We collected adaptive optics images of TOI-1288 with the Gemini Near-Infrared Imager (NIRI; Hodapp et al., 2003) on 2019 November 8. We collected 9 science frames, each with an exposure time of 6.8 s, and dithered the telescope by $\sim 2''$ between each frame, thereby allowing for the science

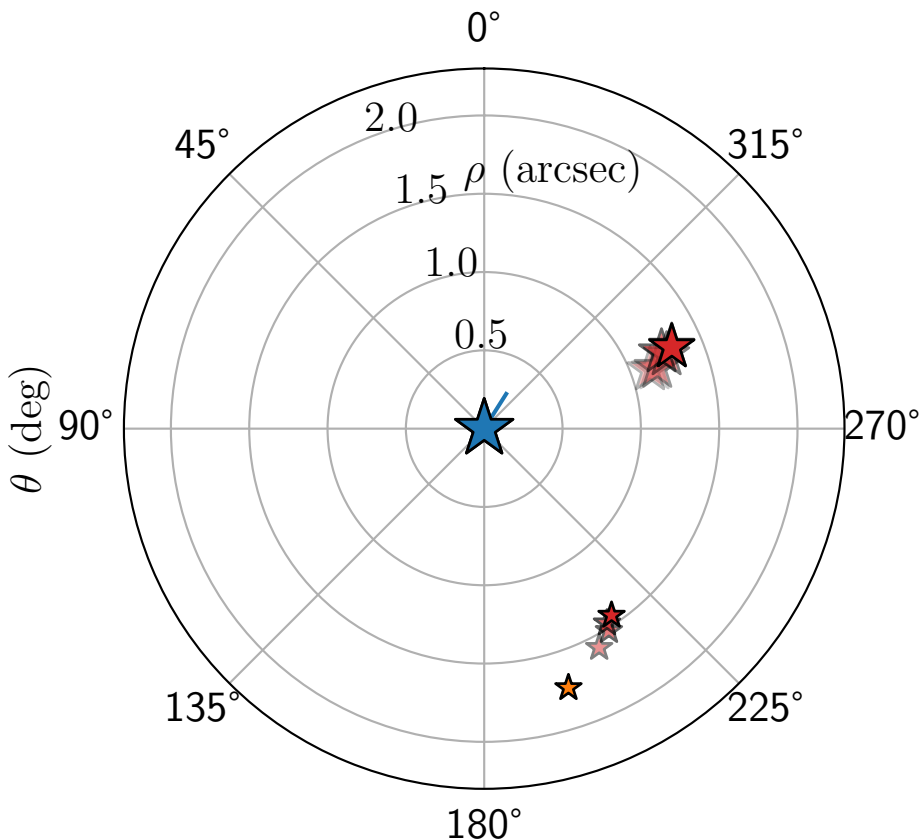


Figure 7.5 | Sky positions of blended companions. The blue star denotes TOI-1288, while red stars are the relative positions for the companions detected in the Spekle/AO images. Their sizes are scaled according to their relative brightness with the larger stars corresponding to $\Delta Br-\gamma = 4.77$ and the smaller one corresponding to $\Delta Br-\gamma = 5.88$. The transparent trails show how the companions move relative to TOI-1288 as a function of time with the opaque being the most recent position. The orange star is the relative position of the companion detected by *Gaia*, which is most likely the fainter companion. The blue line shows the proper motion of TOI-1288 over the course of 3.5 years.

frames themselves to serve as sky background frames. The target was observed in the $Br-\gamma$ filter centered at $2.166\ \mu m$. Data processing consisted of bad pixel removal, flat fielding, and subtraction of the sky background. We then aligned the frames based on the position of the primary star, and coadded the images.

The total field of view is around $26''$ square, with optimum sensitivity in the central $\sim 22''$ square. We again identified two visual candidates in the field of view. The brighter companion is at a separation of $1.152''$, a position angle of 289.3 degrees counter-clockwise of north, and is 4.77 ± 0.03 mag fainter than the host in the Br- γ band; the fainter companion is at a separation of $1.579''$, a position angle of 207.7 degrees counter-clockwise of north and is 5.88 ± 0.04 mag fainter than the host.

We measured the sensitivity of our observations as a function of radius by injecting fake companions and scaling their brightness such that they could be detected at 5σ . The contrast sensitivity is 5.56 mag fainter than the host at a separation of 250 mas, and 8.1 mag fainter than the host in the background limited regime, beyond $\sim 1''$ from the target. The contrast sensitivity as a function of radius and a high resolution image of the star are shown in Figure 7.4; we show the curve for the inner $3''$ only, but note that the data are sensitive to candidates within $13''$ in all directions. From our speckle and AO imaging we have thus identified two nearby companions.

7.2.2.4 *Gaia*

As is also apparent from Figure 7.1, one of the two aforementioned companions is also detected by *Gaia* DR3. The position of this *Gaia* companion is in good agreement with it being the fainter of the two companions seen in the Gemini 'Alopeke and AO observations. This is most likely also the companion seen in the light curve follow-up in Section 7.2.1.1. The *Gaia* detection is summarised in Table 7.2 along with the speckle and AO observations.

7.2.2.5 Are the companions bound?

In the following we will be referring to the brighter companion as star 1, and the fainter companion as star 2. To test whether these companions are bound, we study the positions of the host and the candidate companion in CMDS, loosely following the method outlined in Hirsch et al. (2017). We used the measured photometry in the 832 nm and Br- γ filters for star 1, and the *Gaia* G and Br- γ filters for star 2. In each case, we used the stellar parameters and uncertainties of the host (τ_* , [Fe/H], $\log g$, and d from the SED fit in Table 7.3) to generate a set of 1000 randomly sampled isochrones. For each filter pair, we determined a companion CMD position from the set of isochrones based on the Δ -magnitude of the companion in each filter, and then calculated a weighted average of these measurements. This can then be compared to the observed CMD position of the companion as seen in

Table 7.2 | Companions detected in Speckle, AO, and Gaia. ρ and Δ are the separation and the difference in magnitude from the central target (host), respectively. θ is the position angle from the brighter of the targets to the fainter component, measured from North through East. Star 1 is the brighter companion and star 2 the fainter one. The uncertainties for ρ and θ for the 'Alopeke data are estimated to be around 5 mas and 1 deg, respectively, while the uncertainties for Δ mag come out to around 0.5 mag for the closer companion and 1 mag for the fainter one. **Notes.**

(^a)Observations were also carried out in the 562 nm filter, but the companions were not detected in this filter.

Date (UT)	Star	ρ (arcsec)	Δ (mag)	θ (deg)	Type	Filter	Instrument	Telescope
2019-11-08	1	1.152	4.77 ± 0.03	289.3	AO	Br- γ	NIRI	Gemini
2019-11-08	2	1.579	5.88 ± 0.04	207.7	AO	Br- γ	NIRI	Gemini
2019-11-17 ^(a)	1	1.123	5.90	289.5	Speckle	832 nm	NESSI	WIYN
2020-06-09 ^(a)	1	1.172	5.94	289.5	Speckle	832 nm	'Alopeke	Gemini
2021-06-24 ^(a)	1	1.256	6.4	292.0	Speckle	832 nm	'Alopeke	Gemini
2021-06-24 ^(a)	2	1.516	6.8	211.7	Speckle	832 nm	'Alopeke	Gemini
2021-10-22 ^(a)	1	1.233	5.92	293.4	Speckle	832 nm	'Alopeke	Gemini
2021-10-22 ^(a)	2	1.468	7.34	212.3	Speckle	832 nm	'Alopeke	Gemini
2021-10-29 ^(a)	1	1.282	5.48	293.6	Speckle	832 nm	NESSI	WIYN
2022-05-14 ^(a)	1	1.306	5.83	293.5	Speckle	832 nm	'Alopeke	Gemini
2022-05-14 ^(a)	2	1.443	7.90	214.3	Speckle	832 nm	'Alopeke	Gemini
Epoch=2016.0	2	1.74	6.41	198	Photometry	<i>G</i>	-	<i>Gaia</i>

Figure A.5. For star 1, the observed and predicted positions agree to within 0.3σ , which could indicate that these objects are bound. This is further supported by their relative proximity on the sky. However, this could also be chance alignment for a background star with the right colour profile (Hirsch et al., 2017). For star 2, the observed and predicted CMD positions do not match, with a disagreement of 3.5σ . This strongly suggests that star 2 is a background star, and is not physically bound to the TOI-1288 system.

In Figure 7.5 we show the relative positions of the companions detected in Speckle/AO and the one detected in *Gaia*. Evidently, the detected companions seem to be moving over the time span covered by the different observations in a similar direction, which is more or less opposite to the proper motion of TOI-1288. This clearly suggests that neither of the two companions are bound and are likely background stars. Finally, we note that the *Gaia* position is an average of different scans taken from July 2014 to May 2017 (for DR3) and might be less reliable. Furthermore, the reason that only the fainter companion was detected in the *Gaia* data could be that at an earlier epoch TOI-1288 and the brighter companion star were likely closer on the sky, and it would thus have been more difficult for *Gaia* to detect this companion. However, as seen in the speckle/AO observations, due to the proper motion of TOI-1288, the separation between TOI-1288 and this background star is increasing, meaning that it might be possible to detect it in future data releases.

7.2.3 High-resolution spectroscopy

7.2.3.1 FIES

We performed high-resolution ($R = 67\,000$) RECON SPECTROSCOPY of TOI-1288 using **FIES** (Frandsen and Lindberg, 1999; Telting et al., 2014) mounted at the **NOT** (Djupvik and Andersen, 2010) at Roque de los Muchachos Observatory, La Palma, Spain. The **FIES** spectra were extracted following Buchhave et al. (2010), and stellar parameters were derived using the stellar parameter classification (SPC; Buchhave et al., 2012a; Buchhave et al., 2014) tool. The resulting parameters are tabulated in Table 7.3.

7.2.3.2 HARPS-N

We acquired 57 high-resolution ($R = 115\,000$) spectra of TOI-1288 utilizing the **HARPS-N** spectrograph (Cosentino et al., 2012) attached at the 3.58 m Telescopio Nazionale Galileo (TNG), also located at Roque de los Muchachos observatory. The spectra were collected between 19 November 2019 and

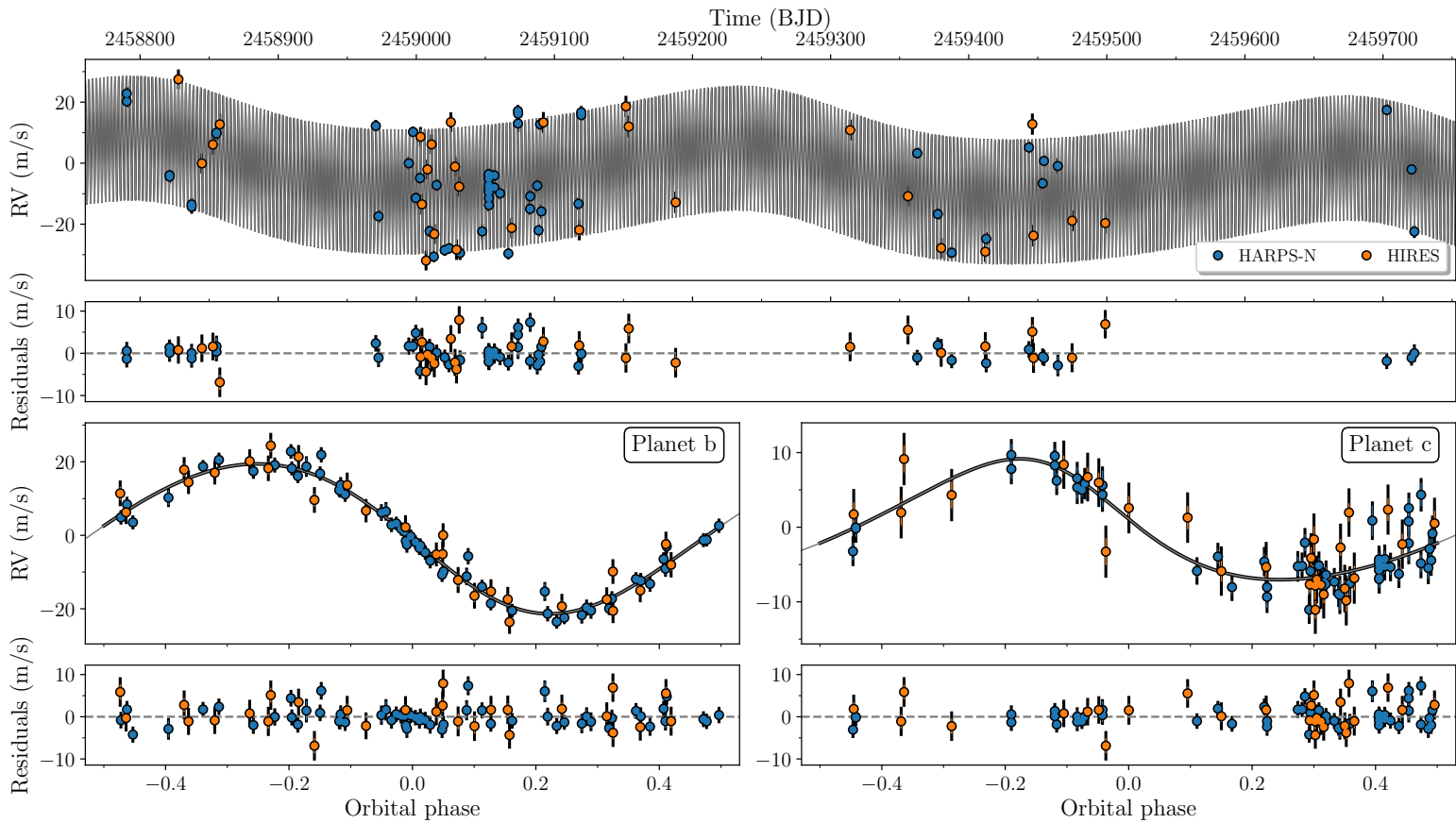


Figure 7.6 | Radial velocities of TOI-1288. *Top:* The HARPS-N (blue) and HIRES (orange) RVS as a function time. The grey model shows the combined signal for planet b and c as well as a long-term trend. *Bottom left:* The RVS phased to the period planet b with the signal from planet c and the long-term trend subtracted with the best-fitting model overplotted. *Bottom right:* The RVS phased to the period of planet c with the signal from planet b and the long-term trend subtracted with the best-fitting model overplotted.

23 May 2022. We set the exposure time to 1200–2700 s based on the sky conditions and scheduling constraints, which led to a median **SNR** of \sim 60 per pixel at 550 nm. We used the second fibre of the instrument to monitor the sky background.

The **HARPS**-N spectra were reduced and extracted using the dedicated Data Reduction Software (DRS; Lovis and Pepe, 2007) available at the telescope. The DRS also provides the full width at half maximum (FWHM) and the bisector inverse slope (BIS) of the **CCF**, which was obtained by cross-correlating the observed échelle spectra against a G2 numerical mask. In this work, we used the Template-Enhanced Radial velocity Re-analysis Application (TERRA; Anglada-Escudé and Butler, 2012) to extract precise **RV** measurements, along with additional activity indicators (namely, the H α , S-index, and Na D indexes).

7.2.3.3 HIRES

We also gathered 28 spectra with the High Resolution Echelle Spectrometer (HIRES; Vogt et al., 1994) mounted on the 10 m Keck-1 at the Keck Observatory, Hawai’i, USA. Observations were carried out between 10 December 2019 and 11 October 2021 with exposure times varying from 280–1000 s depending on sky conditions, resulting in a median **SNR** of \sim 72 near the spectral center of the image. The spectra were obtained with the iodine cell in the light path, and the **RV** extraction followed the standard HIRES forward-modelling pipeline (Howard et al., 2010a).

7.2.3.4 Periodogram analysis

All the **RVS** are shown in Figure 7.6. In Figure 7.7 we have calculated the generalised Lomb-Scargle (GLS; Lomb, 1976; Scargle, 1982) periodogram. Evidently, the \sim 2.7 d transiting signal is also detected in the **RVS**, where a peak at this frequency clearly exceeds the false-alarm probabilities (FAPs; at 0.1%, 1%, and 10%). We also see a significant peak at much lower frequencies with a period of around 443 d, which we ascribe to the presence of a further out companion. Seeing the 443 d-signal we searched the **TESS** light curve for additional transits using the box least squares (BLS; Kovács et al., 2002) algorithm after removing the transits from planet b (\sim 2.7 d), but found no evidence for additional transiting signals.

We also detected another low frequency/long period peak in the GLS which seems to be a long-term trend in the **RVS**. We have furthermore created GLS periodograms for the activity indicators from the **HARPS**-N spectra shown in Figure 7.8. Evidently, the star is inactive and the 2.7 d and

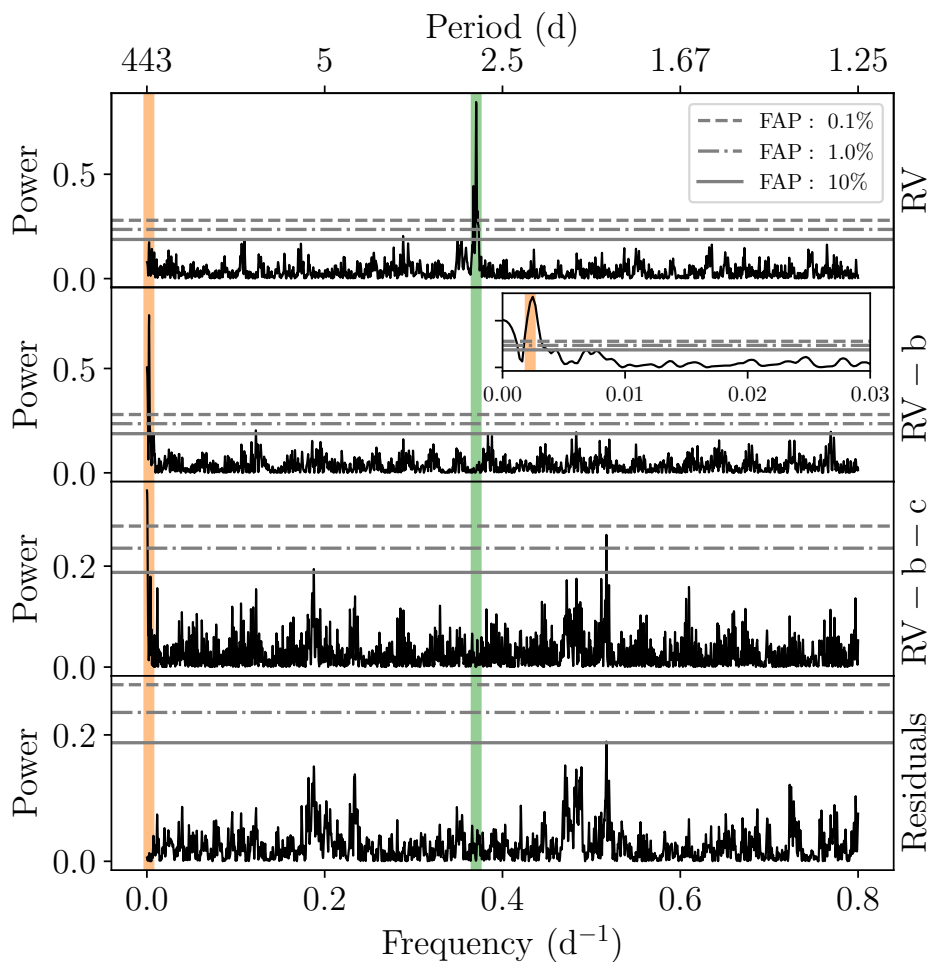


Figure 7.7 | Generalised Lomb-Scargle diagram. The GLS created from the observed [RVs](#). *Top:* The GLS after subtracting the systemic velocities for [HARPS-N](#) and [HIRES](#). The periods from Table 7.4 for planet b (green) and planet c (orange) are shown as the vertical lines. The dashed, dashed-dotted, and solid horizontal lines are the 0.1%, 1%, and 10% FAPs, respectively. *Upper middle:* The GLS after subtracting the signal from planet b. The inset shows a close-up around the period of planet c. *Lower middle:* The GLS after subtracting both the signal from planet b and c. *Lower:* The GLS after subtracting both the signal from planet b, c, and the long-term trend.

443 d do not coincide with any appreciable peak in these metrics, meaning that they are unlikely to come from stellar activity.

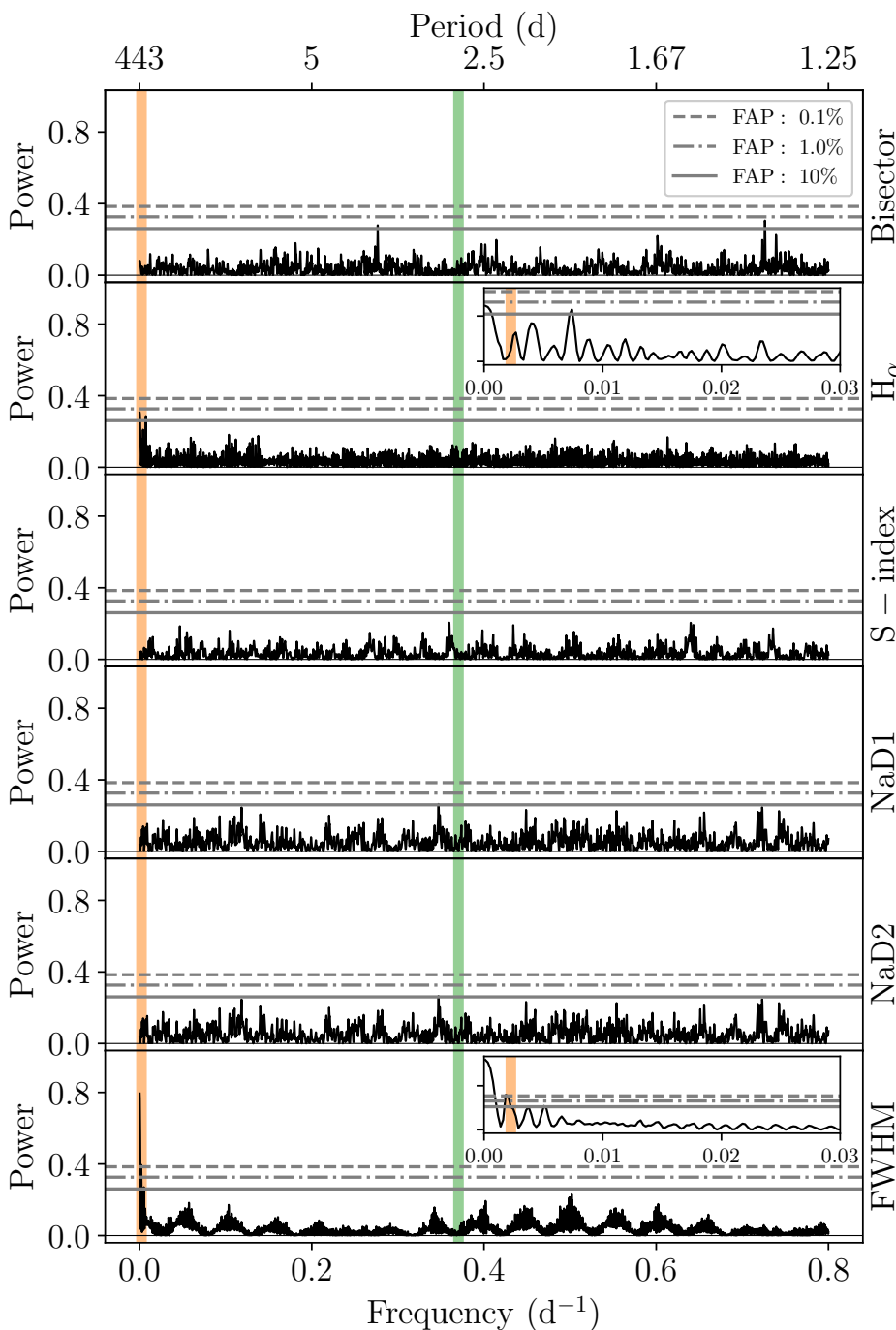


Figure 7.8 | Generalised Lomb-Scargle diagram for activity indicators. The GLS created from the activity indicators from the [HARPS-N](#) spectra. From top to bottom we show the GLS for the Bisector, H_{α} , S-index, NaD1, NaD2, and full width half maximum (FWHM). Symbols have the same meaning as in Figure 7.7.

7.2.3.5 Stellar modelling using SME and SED

In addition to the [FIES RECON SPECTROSCOPY](#) we also made use of our [HARPS-N](#) observations to derive stellar properties. We used co-added [HARPS-N](#) spectra with the software [SME²](#) (Spectroscopy Made Easy; Valenti and Piskunov, 1996; Piskunov and Valenti, 2017), a tool for fitting observations to synthetic spectra. A detailed description of the modelling can be found in Fridlund et al. (2017) and Persson et al. (2018). For this star, we held the micro- and macro-turbulent velocities, v_{mic} and v_{mac} , fixed in the modelling to 0.83 km s^{-1} (Bruntt et al., 2010), and 3.0 km s^{-1} (Doyle et al., 2014), respectively. The synthetic spectra were computed with the stellar atmosphere grid [Atlas12](#) (Kurucz, 2013), and the atomic and molecular line data were taken from [VALD³](#) (Ryabchikova et al., 2015). Our best model found an effective temperature of $T_{\text{eff}} = 5123 \pm 62 \text{ K}$, an iron abundance of $[\text{Fe}/\text{H}] = +0.10 \pm 0.11$, a surface gravity of $\log g_* = 4.23 \pm 0.09$, and a projected rotational velocity of $v \sin i_* = 1.3 \pm 1.2 \text{ km s}^{-1}$. These results were checked with the empirical code [SpecMatch-Emp](#) (Yee et al., 2017) and were found to agree within 1σ .

Using the SME results as priors, we modelled the stellar radius with [ARIADNE⁴](#) (Vines and Jenkins, 2022) fitting broadband photometry to the [SED](#). The fitted bandpasses were the Johnson B and V magnitudes (APASS), $GG_{\text{BP}}G_{\text{RP}}$ (eDR3), JHK_S magnitudes (2MASS), [WISE](#) W₁-W₂, and the Gaia eDR3 parallax. The final radius was computed with Bayesian Model Averaging from the four fitted atmospheric models grids Phoenix v2 (Husser et al., 2013), BtSettl (Allard et al., 2012), Castelli and Kurucz (2004), and Kurucz (1993) atmospheric model grids. The final stellar radius was found to be $1.010 \pm 0.015 R_\odot$, and the stellar mass $0.895^{+0.042}_{-0.023} M_\odot$ interpolated from the MIST (Choi et al., 2016) [isochrones](#). The stellar parameters are summarised in Table 7.3.

7.2.3.6 Stellar modelling using BASTA

As an independent measure for the stellar parameters we also modelled the star using the [BASTA⁵](#) (Silva Aguirre et al., 2015; Aguirre Børnsen-Koch et al., 2022). We ran [BASTA](#) using the spectroscopic parameters from the SPC analysis (T_{eff} , $[\text{Fe}/\text{H}]$, $\log g$) as input along with the [Gaia](#) magnitudes (G , B_p , R_p) and parallax. [BASTA](#)'s approach to fitting the magnitudes and

²: <http://www.stsci.edu/~valenti/sme.html>.

³: <http://vald.astro.uu.se>

⁴: <https://github.com/jvines/astroARIADNE>

⁵: <https://basta.readthedocs.io/en/latest/index.html>

parallax is described in Section 4.2.2 in Aguirre Børseth-Koch et al. (2022), where bolometric corrections are applied using the tables by Hidalgo et al. (2018), and the reddening is calculated through the dust map by Green et al. (2019). `BASTA` uses these values as constraints when fitting to a grid of BaSTI (a Bag of Stellar Tracks and Isochrones; Hidalgo et al., 2018) `isochrones`, where we opted for a science case that included both diffusion, convective core overshooting, and mass loss (see Section 3.1 in Aguirre Børseth-Koch et al., 2022). The resulting values are tabulated in Table 7.3 and are generally consistent with the other parameters, although `BASTA` found a slightly smaller stellar radius as the fit seemed to prefer a slightly larger value for $\log g$ compared to the SME and `SED` fits.

In the following we will be using stellar parameters coming from the `SED`. Therefore, derived quantities such as the planetary radius and masses will be calculated from the `SED` parameters.

7.3 Analysis

In our modelling we included both planets, where only parameters for planet b are constrained by the photometry given we have not detected any transits of planet c. We modelled the transits using `batman`, where we accounted for the correlated noise in the light curve using `GP` regression as implemented in `celerite` (Foreman-Mackey et al., 2017). We made use of the Matérn- $3/2$ kernel, which is characterised by two hyper parameters: the amplitude, A , and the time scale, τ . This model is shown at the bottom of Figure 7.2.

In addition to the `RV` signals from planet b and c, we included a first-order acceleration parameter, $\dot{\gamma}$, to account for the long-term trend. Instead of stepping in e and ω , our `MCMC` sampling was stepping in $\sqrt{e} \cos \omega$ and $\sqrt{e} \sin \omega$ for both planets. Furthermore, we were stepping in the sum of the limb-darkening coefficients, $q_1 + q_2$, while keeping the difference fixed. All stepping parameters and their priors are listed in Table 7.4.

As seen in Figure 7.1 (see also Figure A3 in Knudstrup et al., 2023a, for a DSS2 image of the field) there are multiple stars in the `TESS` aperture mask. Therefore we added a dilution term in the `MCMC`, where we only included the contribution from all sources brighter than $\Delta G = 5$, meaning that only the contribution from the south-eastern star at a separation of ~ 23 arcsec (Figure 7.1) was included. We thus did not consider the contribution from the much closer companions. The brightest of the two is found at $\Delta Br-\gamma = 4.77 \pm 0.03$ and from our measurements in Table 7.2 it

Table 7.3 | Stellar parameters for TOI-1288. The stellar parameters from our spectral analyses and stellar modelling in Section 7.2.3, Section 7.2.3.5, and Section 7.2.3.6. We also list the *Gaia* measurements. **Notes.** ^(a)Relation from Doyle et al. (2014). ^(b)Relation from Bruntt et al. (2010). ^(c)SED estimate is from MIST isochrones. ^(d)SED estimate is from $\log g$ and R_\star . ^(e) T_{eff} , $\log g$, [Fe/H], and $v \sin i_\star$ are from SPC. The rest have been derived using **BASTA**.

Parameter	Name	SME	SED	Spec-Match	SPC+ BASTA ^(e)	<i>Gaia</i> DR3
T_{eff}	Effective temperature (K)	5123 ± 62	5225^{+23}_{-27}	5220 ± 110	5367 ± 50	5300^{+20}_{-22}
$\log g$	Surface gravity	4.23 ± 0.09	4.24 ± 0.09	4.36 ± 0.12	4.36 ± 0.10	$4.447^{+0.010}_{-0.006}$
[Fe/H]	Iron abundance	0.10 ± 0.11	0.07 ± 0.09	0.30 ± 0.09	0.18 ± 0.08	$0.15^{+0.02}_{-0.03}$
[Ca/H]	Calcium abundance	0.15 ± 0.09	-	-	-	-
[Na/H]	Sodium abundance	0.25 ± 0.12	-	-	-	-
$v \sin i_\star$	Proj. rotation velocity (km s^{-1})	1.3 ± 1.2	-	-	< 2	-
ζ	Macro-turbulence (km s^{-1})	$3.0^{(a)}$	-	-	-	-
ξ	Micro-turbulence (km s^{-1})	$0.83^{(b)}$	-	-	-	-
d	Distance (pc)	-	114.7 ± 0.7	-	$112.8^{+1.6}_{-1.4}$	114.677 ± 0.013
R_\star	Stellar radius (R_\odot)	-	$1.010^{+0.015}_{-0.014}$	1.09 ± 0.18	$0.95^{+0.03}_{-0.02}$	-
$M_\star^{(c)}$	Stellar mass (M_\odot)	-	$0.89^{+0.04}_{-0.02}$	0.90 ± 0.08	$0.91^{+0.04}_{-0.05}$	-
$M_\star^{(d)}$	Stellar mass (M_\odot)	-	$0.65^{+0.14}_{-0.13}$	-	-	-
L_\star	Luminosity (L_\odot)	-	0.68 ± 0.02	-	0.65 ± 0.03	-
A_V	V band extinction	-	$0.014^{+0.015}_{-0.009}$	-	-	-
τ_\star	Age (Gyr)	-	$12.1^{+1.4}_{-3.1}$	10.05 ± 0.17	$9.8^{+4.7}_{-3.8}$	-

is clear that both companions seem to be redder than TOI-1288, meaning that the differences in magnitude are even larger in the **TESS** passband.

The total flux as a function of time is thus $F(t) = (F_1(t) + F_2)/(F_1 + F_2)$, where $F_1(t)$ is the in-transit flux and F_1 is the out-of-transit flux for TOI-1288, and F_2 is the flux from the contaminating source at ~ 23 arcsec. The flux from the contaminating source is then included as a fraction of TOI-1288, F_1/F_2 , which in magnitude translates to $\Delta\text{mag} = -2.5 \log(F_2/F_1)$. As the **TESS** passband is very close to the **Gaia** R_p passband, we used the difference in this passband as a proxy for the difference between TOI-1288 and the 23 arcsec neighbour in the **TESS** passband. Thus we sampled the dilution as a Gaussian prior with $\Delta R_p = \Delta\text{TESS} = 4.41 \pm 0.02$. The photometric apertures from the ground-based facilities are small enough so that this source does not contaminate those light curves. As such no dilution factors were included for these.

We sampled the posteriors for the transit and orbital parameters using **MCMC** sampling utilising the **emcee** package (Foreman-Mackey et al., 2013). Our likelihood function is defined as

$$\log \mathcal{L} = -0.5 \sum_{i=1}^N \left[\frac{(O_i - C_i)^2}{\sigma_i^2} + \log 2\pi\sigma_i^2 \right], \quad (7.1)$$

where N indicates the total number of data points from photometry and **RVS**. C_i represents the model corresponding to the observed data point O_i . σ_i represents the uncertainty for the i th datum, where we add a jitter term in quadrature and a penalty in the likelihood for the **RVS**. To our likelihood in Equation (7.1) we add our priors $\sum_{j=1}^M \log \mathcal{P}_j$, \mathcal{P}_j being the prior on the j th parameter, and this sum constitutes the total probability.

7.4 Results

In Figure 7.9 we show the **TESS** light curve phase-folded on the transits of planet b along with the best-fitting model. Light curves from all photometric observations can be found in Figure A.6. We find a planet-to-star radius ratio of 0.0476 ± 0.0005 , which given the stellar radius from the **SED** analysis in Table 7.3 yields a radius of $5.24 \pm 0.09 R_\oplus$. With a period of just $2.699835^{+0.000004}_{-0.000003}$ d, TOI-1288 b is thus a hot super-Neptune.

Shown in Figure 7.6 are the best-fitting models for the **RVS** for both planet b and c. This 2-planet model is heavily favoured over a 1-planet model according to the Bayesian information criterion (BIC, $\Delta\text{BIC} = 104$). To get a measure of the mass for both planets we use the relation

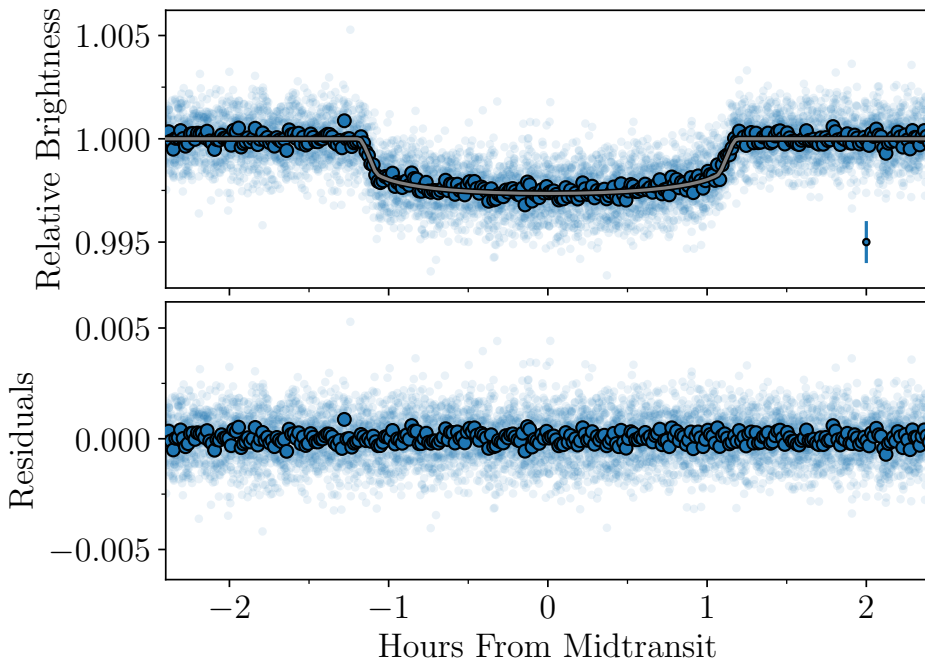


Figure 7.9 | TESS light curve of TOI-1288 b. The GP detrended TESS data from Figure 7.2 showing the phase folded transits of planet b. We show the data binned in larger, solid points, while the unbinned data are shown smaller, more transparent points. The datum with errorbar is not an actual measurement, but illustrates the median of the uncertainties of all data. The grey line is the best-fitting model.

$$M_p \sin i = \frac{K\sqrt{1-e^2}}{28.4 \text{ m s}^{-1}} \left(\frac{P}{1 \text{ yr}} \right)^{1/3} \left(\frac{M_*}{M_\odot} \right)^{2/3}, \quad (7.2)$$

where we can only get a lower limit for the mass of planet c as we do not know the inclination. For planet b we find a mass of $42 \pm 3 M_\oplus$, which combined with the radius yields a bulk density of $1.3 \pm 0.5 \text{ g cm}^{-3}$. For planet c we find a lower limit for the mass of $84 \pm 7 M_\oplus$.

For the long-term trend we have found a value for $\dot{\gamma} = -0.0086 \pm 0.0019 \text{ m s}^{-1} \text{ d}^{-1}$. This first-order acceleration parameter constitutes a lower limit for the semi-amplitude through $(t_f - t_i) \times \dot{\gamma}/2$ with t_f and t_i being the final and first timestamps. Following the Monte Carlo approach in Kane et al. (2019) (see also Pepper et al., 2020), we used our measured value for $\dot{\gamma}$ to calculate the lower limit for the companion inducing this

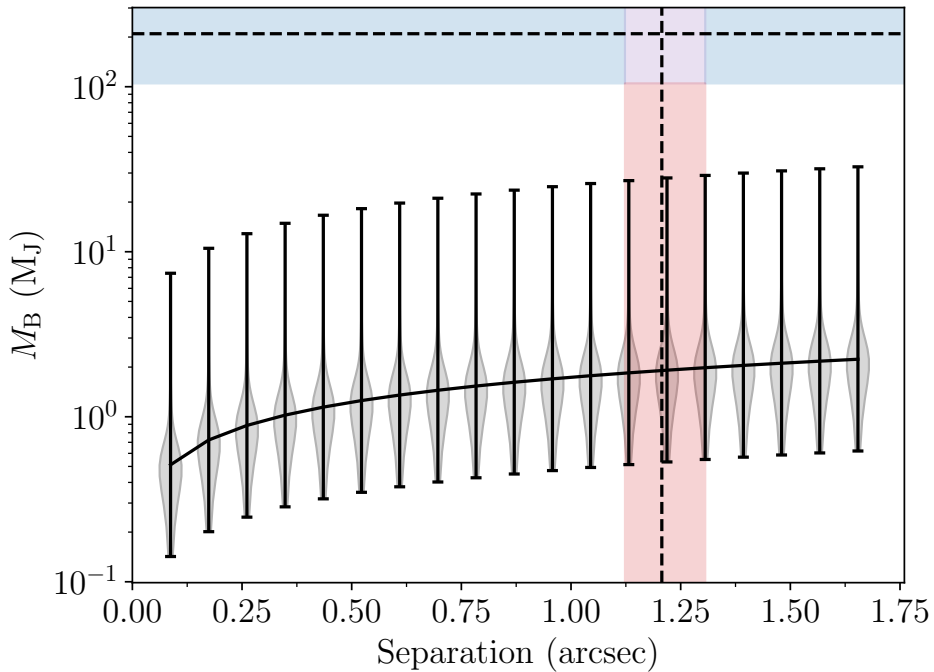


Figure 7.10 | Lower mass limit for an additional bound companion. The violinplot shows the resulting distribution for the mass of the companion for a given separation (here converted to sky-projected separation using the distance from Table 7.1). The solid black curve is the median mass for each separation. The vertical red band spans the range of the speckle and AO measurements for the separation of star 1 (Table 7.2), while the dashed vertical line is the median of these. The horizontal blue band spans the range from $0.1 M_{\odot}$ to $0.3 M_{\odot}$ with $0.2 M_{\odot}$ shown with the dashed line.

long-term trend as a function of orbital separation. Namely, we solved

$$K \leq \sqrt{\frac{G}{a_B(1 - e_B^2)}} \frac{M_B \sin i_B}{\sqrt{M_B + M_{\star}}} \quad (7.3)$$

for M_B at each a_B with e_B being drawn from a β -distribution and $\cos i_B$ from a uniform distribution.

In Figure 7.10 we show the resulting distributions for each orbital separation, here converted to a sky-projected separation. We furthermore show the observed position of the brightest of the two companions, star 1, detected in speckle and AO, if it were bound to TOI-1288. From our

analysis in Section 7.2.2.5 and its position in the CMD in Figure A.5 this companion would most likely have been an M-dwarf with a mass of around $0.2 M_{\odot}$. While this is a lower limit for the mass and could be consistent with the mass we have estimated for star 1, the median is around two orders of magnitude lower at the position for star 1. We should thus in most cases have detected a much more significant drift, if it were due to star 1. Therefore, it seems more likely that the drift we are seeing is coming from another planetary companion.

Finally, we note that the *Gaia* Renormalised Unit Weight Error (RUWE) statistic for TOI-1288 is 1.17. For a good single-star fit one would expect it to be around 1, whereas a value of $\gtrsim 1.4$ could suggest that the source is non-single or otherwise problematic for the astrometric solution. The slight departure could be because the *Gaia* astrometry is seeing the orbital motion induced by this long-term RV companion.

7.5 Discussion

7.5.1 Location in the Neptunian desert

We have found TOI-1288 b to be a hot super-Neptune with an equilibrium temperature of 1266 ± 27 K (estimated from Kempton et al., 2018, assuming zero albedo and full day-night heat redistribution). In Figure 7.11 we plot the radius (left, in Earth radii) and mass (right, in Jupiter masses) of TOI-1288 b as functions of orbital period. Evidently, TOI-1288 b falls right in the hot Neptunian desert reported by Mazeh et al. (2016). Mazeh et al. (2016) mention two processes that could account for the upper boundary. Firstly, if the planet had migrated through the disk, then stopped at the upper boundary of the desert due to a decrease in density in the disk as it moves inwards, the inner radius of the disk might be related to its mass and consequently the planetary mass. Therefore, the central hole in the disk would be smaller in a more massive disk, and hence allow for a more massive planet. Alternatively, the atmosphere of a planet moving horizontally in the diagram, i.e., migrating, might be stripped of its atmosphere due to the stellar irradiation, resulting in a smaller, lower mass planet.

In Vissapragada et al. (2022) the upper boundary of the desert was investigated by looking at the metastable helium feature in the atmospheres of the planets, which could be a tracer for any outflows. They found that this upper boundary is stable against photoevaporation, meaning that a different mechanism must be responsible for tracing out this upper edge. This is in-line with the findings of Owen and Lai (2018) in which they argue

Table 7.4 | MCMC results for TOI-1288. The median and high posterior density at a confidence level of 0.68. Subscripts b and c denote parameters for planet b and c, respectively. \mathcal{U} denotes that a uniform prior was applied during the run. **Notes.** ^(a)Barycentric TESS Julian Date (BTJD) is defined as $\text{BJD} - 2457000.0$, BJD being the Barycentric Julian Date. ^(b)From the SED stellar parameters in Table 7.3. ^(c)Following Kempton et al. (2018).

Parameter	Name	Prior	Value
Stepping parameters			
P_b	Period (days)	\mathcal{U}	$2.699835^{+0.000004}_{-0.000003}$
$T_{0,b}$	Mid-transit time (BTJD) ^(a)	\mathcal{U}	1712.3587 ± 0.0002
$(R_p/R_\star)_b$	Planet-to-star radius ratio	\mathcal{U}	0.0476 ± 0.0005
$(a/R_\star)_b$	Semi-major axis to star radius ratio	\mathcal{U}	8.5 ± 0.4
K_b	Velocity semi-amplitude (m s^{-1})	\mathcal{U}	$20.7^{+0.4}_{-0.5}$
$\cos i_b$	Cosine of inclination	\mathcal{U}	$0.030^{+0.012}_{-0.030}$
$(\sqrt{e} \cos \omega)_b$		\mathcal{U}	$-0.19^{+0.03}_{-0.04}$
$(\sqrt{e} \sin \omega)_b$		\mathcal{U}	$0.16^{+0.07}_{-0.06}$
P_c	Period (days)	\mathcal{U}	443^{+11}_{-13}
$T_{0,c}$	Mid-transit time (BTJD)	\mathcal{U}	1883^{+12}_{-14}
K_c	Velocity semi-amplitude (m s^{-1})	\mathcal{U}	$7.6^{+0.5}_{-0.6}$
$(\sqrt{e} \cos \omega)_c$		\mathcal{U}	$0.15^{+0.19}_{-0.15}$
$(\sqrt{e} \sin \omega)_c$		\mathcal{U}	$0.28^{+0.14}_{-0.13}$
$\gamma_{\text{HARPS-N}}$	Systemic velocity HARPS-N (m s^{-1})	\mathcal{U}	$7.7^{+0.8}_{-0.7}$
$\sigma_{\text{HARPS-N}}$	Jitter HARPS-N (m s^{-1})	\mathcal{U}	1.9 ± 0.3
γ_{HIRES}	Systemic velocity HIRES (m s^{-1})	\mathcal{U}	$6.2^{+0.9}_{-1.0}$

σ_{HIRES}	Jitter HIRES (m s^{-1})	\mathcal{U}	3.4 ± 0.6
$\dot{\gamma}$	Linear trend ($\text{m s}^{-1} \text{ d}^{-1}$)	\mathcal{U}	-0.0088 ± 0.0017
Derived parameters			
e_b	Eccentricity	-	$0.064^{+0.014}_{-0.015}$
ω_b	Argument of periastron ($^\circ$)	-	139^{+13}_{-17}
i_b	Inclination ($^\circ$)	-	$88.3^{+1.7}_{-0.7}$
b_b	Impact parameter	-	$0.26^{+0.10}_{-0.24}$
e_c	Eccentricity	-	$0.13^{+0.07}_{-0.09}$
ω_c	Argument of periastron ($^\circ$)	-	63^{+30}_{-33}
$T_{14,b}$	Transit duration (hours)	-	$2.37^{+0.05}_{-0.03}$
Physical parameters			
$T_{\text{eq},b}^{(c)}$	Equilibrium temperature (K)	-	1266 ± 27
$R_{p,b}$	Planet radius (R_\oplus)	-	5.24 ± 0.09
$M_{p,b}$	Planet mass (M_\oplus)	-	42 ± 3
$\rho_{p,b}$	Planet density (g cm^{-3})	-	1.3 ± 0.5
$(M_p \sin i)_c$	Lower value for planet mass (M_\oplus)	-	84 ± 7

that if photoevaporation is responsible for the upper boundary, we should see a lot of sub-Jovian mass planets in the mass-period plane at very short periods, which we do not. Rather they argue that the upper boundary is caused by [high-eccentricity migration](#).

On the other hand, Owen and Lai ([2018](#)) do find that the lower boundary could be explained by photoevaporation. This photoevaporation which leaves behind a rocky core has furthermore been used to explain the dearth of *hot super-Earths* (e.g., Sanchis-Ojeda et al., [2014](#); Lundkvist et al., [2016](#)). An alternative explanation for the lower boundary of the desert could be that as the separation increases, so does the [Hill sphere](#) of the planetesimal, the orbital path, and the dust-to-gas ratio, meaning that the core mass is increased towards the end of the first stage of formation. This would then result in more massive planets at larger separations (Mazeh et al., [2016](#)).

What is clear from Figure [7.11](#) is that the upper boundary is much more well-defined than the lower boundary. However, even if the lower boundary would be at larger radii, TOI-1288 b is still found in a very deserted area. In Figure [7.11](#) we have highlighted eight planets that are the closest to TOI-1288 b in the radius-period (distance here measured in units of $(R_\oplus^2 + \text{days}^2)^{1/2}$) plane; *Kepler*-101 b (Bonomo et al., [2014](#)), HATS-7 b (Bakos et al., [2015](#)), TOI-532 b (Kanodia et al., [2021](#)), TOI-674 b (Murgas et al., [2021](#)), TOI-1728 b (Kanodia et al., [2020](#)), NGTS-14Ab (Smith et al., [2021](#)), WASP-156 b (Demangeon et al., [2018](#)), and K2-55 b (Crossfield et al., [2016](#)). Some key parameters (Southworth, [2011](#), from <https://www.astro.keele.ac.uk/jkt/tepcat/allplanets-noerr.html>) for these systems are summarised in Table [7.5](#) along our parameters for TOI-1288 b.

Obviously, the planets are similar in terms of period and radius, but they also have quite similar masses, and thus densities. The most striking difference in Figure [7.11](#) is the insolation, which is dictated by the spectral type (T_{eff}) of the stellar host. In this context it is worth noting that the overabundance of large planets with high insolation compared to at smaller radii in Figure [7.11](#), merely reflects that it is easier to detect a larger planet around a larger (hotter) star. This is what is seen in Szabó and Kálmán ([2019](#)) (and apparent from Figure A4 Knudstrup et al., [2023a](#)).

A clustering of Neptune-sized planets with equilibrium temperatures of around 2000 K has been reported in Persson et al. ([2022](#)), which begs the question whether there could be an island of stability in the desert. However, this might also be a selection effect, and more planets in this parameter space are needed to establish this. It is an intriguing idea, and if an island of stability could exist for these slightly smaller planets on more irradiated orbits, maybe a similar island exists for TOI-1288 b and

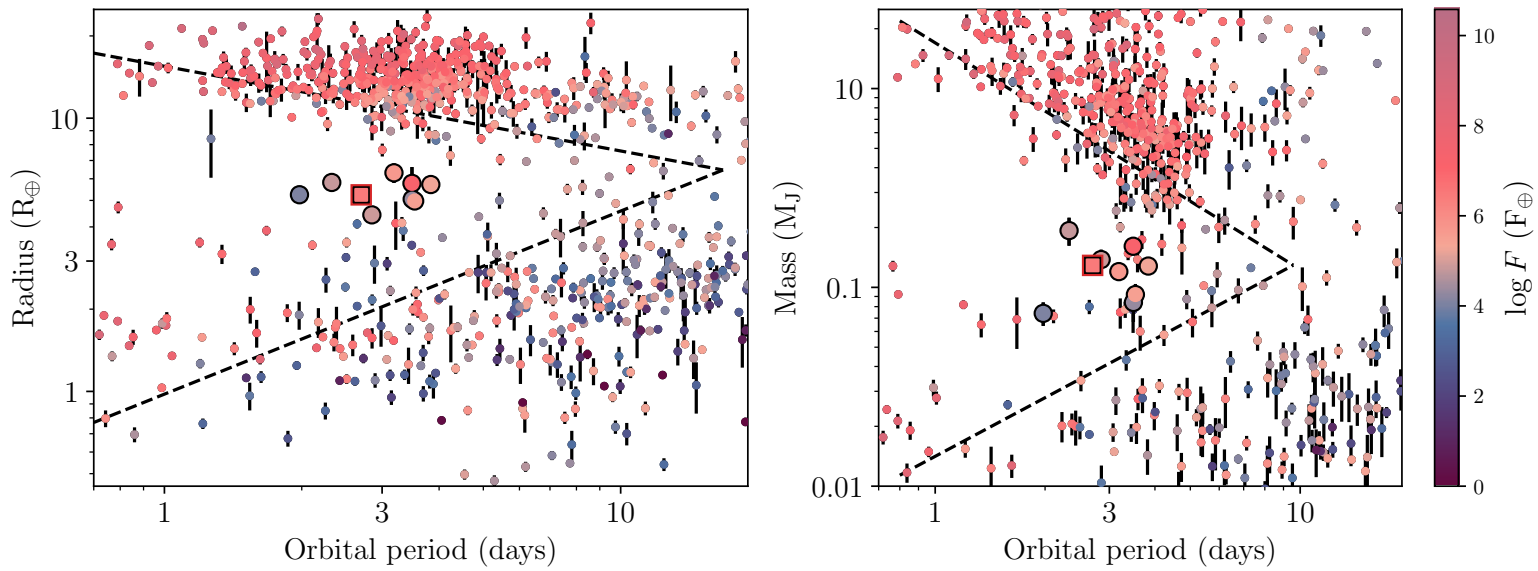


Figure 7.11 | The Neptunian desert. The hot Neptunian desert reported in Mazeh et al. (2016) shown as dashed lines. Planets (as of September 2022) from the TEPCat catalogue of "well-studied transiting planets" (Southworth, 2011, <https://www.astro.keele.ac.uk/jkt/tepcat/allplanets-noerr.html>) with uncertainties smaller than 30% in radius (left) and mass (right). The points are colour coded according to the incident flux, which is truncated at $F = 1 F_{\oplus}$. TOI-1288 b is shown as the large square with a red outline. The large circles denote the closest eight planets to TOI-1288 b in the radius-period parameter space, with their position highlighted in the mass-radius diagram as well.

Table 7.5 | Closest radius-period neighbours. The eight planets closest to TOI-1288 b in terms of radius and period (with distance in units of $(R_\oplus^2 + \text{days}^2)^{1/2}$). **Notes.** ^(a)From $(\rho_\star/\rho_\odot)^{-2/3}(P/1 \text{ yr})^{-4/3}(T_{\text{eff}}/5777 \text{ K})^4$.

	P (d)	$F^{(a)}$ (F_\oplus)	R_p (R_\oplus)	M_p (M_\oplus)	ρ_p (ρ_\oplus)	SpT
TOI-1288 b	2.6998	630	5.6	41	0.24	G
TOI-532 b	2.327	119	5.8	61	0.31	M
TOI-674 b	1.977	57	5.3	24	0.17	M
<i>Kepler</i> -101 b	3.488	1260	5.8	51	0.26	G
HATS-7 b	3.185	288	6.3	38	0.15	K
TOI-1728 b	3.492	72	5.1	27	0.21	M
NGTS-14Ab	3.536	240	5.0	29	0.25	K
WASP-156 b	3.836	186	5.7	41	0.24	K
K2-55 b	2.849	130	4.4	44	0.5	K

its neighbours, who are slightly bigger and less irradiated. It could also be a strip of pseudo stability in the desert, or it might just reflect the aforementioned less well-defined lower boundary of the desert.

7.5.2 Internal structure and atmosphere

In the mass-radius diagram in Figure 7.12 we compare TOI-1288 b to models with different compositions. The models are taken from Zeng et al. (2016, 2019). Evidently, TOI-1288 b can be described as a rocky core with a gaseous envelope at high irradiation. Probing the atmosphere of the planet through transmission spectroscopy could naturally help reveal atmospheric features, but can also provide valuable constraints on the internal structure.

We observed a transit of planet b on the night 2020 June 11 using the HARPS-N spectrograph. The RVS from this night can be seen around orbital phase 0.0 in the lower left panel of Figure 7.6, but due to the slow rotation of the star ($v \sin i_\star = 1.3 \pm 1.2 \text{ km s}^{-1}$) we do not see the RM EFFECT. For an aligned configuration a decent approximation for the amplitude is given by $0.7\sqrt{1 - b^2}(R_p/R_\star)^2 v \sin i_\star$, which comes out to just shy of 2 m s^{-1} for TOI-1288 b.

We nonetheless ran an MCMC where we included the RM EFFECT (using the code by Hirano et al., 2011). We excluded the photometry and instead applied Gaussian priors to P_b , $T_{0,b}$, $(R_p/R_\star)_b$, $(a/R_\star)_b$, and i_b using the

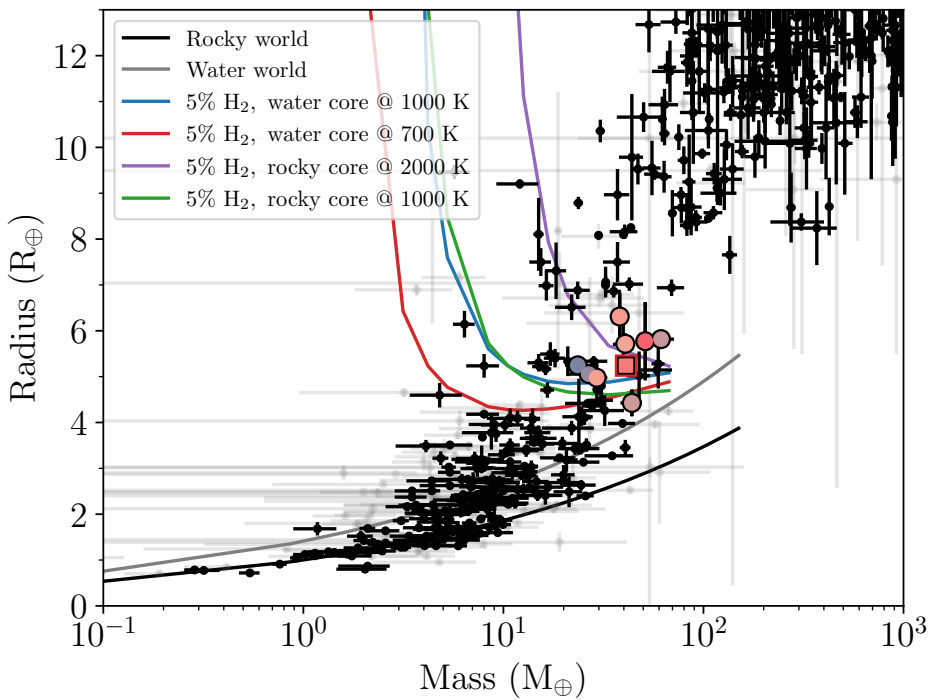


Figure 7.12 | Mass-radius diagram. Planets from the same catalogue as in Figure 7.11, but now for planets with uncertainties on both mass and radius of less (more) than 30% shown as black (grey) dots. Solid lines are composition models from Zeng et al. (2016, 2019). TOI-1288 b is again shown as the large (coloured) square with the similar (R_p , P) planets shown with large circles.

values in Table 7.4 and for $v \sin i_{\star}$ from the SME value in Table 7.3. We also applied Gaussian priors to the **macro-turbulence** and **micro-turbulence** as well as the sum of the limb-darkening coefficients (values estimated from Bruntt et al., 2010; Claret and Bloemen, 2011; Doyle et al., 2014, respectively), while applying a uniform prior to the sky-projected **obliquity**, λ_b . The rest followed the same approach as the run in Section 7.3. The resulting value for the projected **obliquity** was $\lambda_b = 70^{+110}_{-100}^{\circ}$, meaning that it is unconstrained.

Following Kempton et al. (2018) we can calculate the transmission spectroscopic metric (TSM) to assess the feasibility of transmission spectroscopy for TOI-1288 b. The TSM is given by

$$\text{TSM} = H \times \frac{R_p^3 T_{\text{eq}}}{M_p R_{\star}^2} \times 10^{-m_J/5}, \quad (7.4)$$

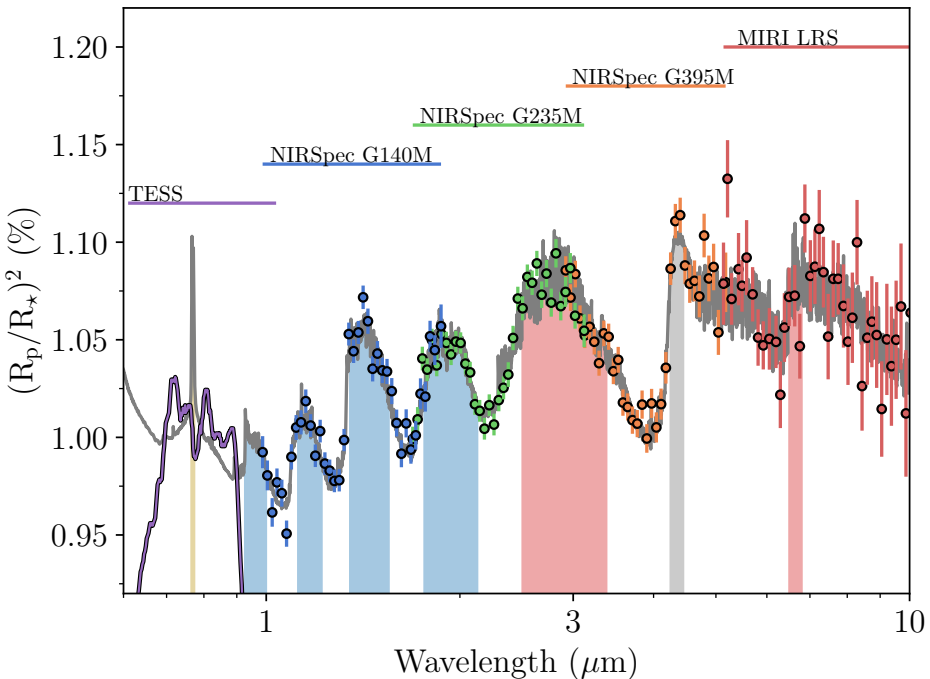


Figure 7.13 | Simulated JWST observations. A simulated transmission spectrum of TOI-1288 b in grey using petitRADTRANS. The coloured error bars are simulated JWST data from PandExo of different instruments with their wavelength coverage shown by the horizontal coloured lines and with the names of the instrument shown above. We also show the [TESS](#) transmission curve in purple. Some atomic and molecular species are highlighted in the coloured areas with K, H₂O, CH₄, and CO₂ shown with yellow, blue, red, and grey, respectively.

where m_J is the apparent magnitude of the host in the J band and H is a scale factor related to the size of the planet. For TOI-1288 b H is 1.15, while the planet, stellar, and system parameters are listed in Table 7.4, Table 7.3 (SED), and Table 7.1, respectively. This yields a TSM of ~ 87 , which is just below the suggested cutoff for follow-up efforts in Kempton et al. (2018).

While – according to this metric – TOI-1288 b is not a high priority target for JWST (Gardner et al., 2006), we still investigate what JWST might be able to detect if it were to do transmission spectroscopy. We simulated the spectrum of TOI-1288 b using petitRADTRANS (Mollière et al., 2019, 2020) assuming a cloud-free, isothermal model at 1266 K. We used PandExo (Batalha et al., 2017) to simulate the JWST data for four

different instruments. For each we assumed a total of 4 transits with a 4 hr baseline each. The resulting spectrum is shown in Figure 7.13. For this most likely quite optimistic scenario, JWST should be able to detect several molecular species, such as H₂O, CH₄, and CO₂ (if present).

7.5.3 Outer companions

According to the Web [TESS Viewing Tool](#)⁶, TOI-1288 is (at the time of writing) being re-observed in Sectors 56-58 (beginning in September 2022 and ending in November 2022). These additional sectors should help refine the transit parameters of planet b. While our current estimate for the period and ephemeris of planet c suggest a transit occurred (of course, depending on the inclination) July 2022, the uncertainties are rather large, so it is worthwhile to be on the look out for a potential transit of planet c.

Zhu and Wu (2018) and Bryan et al. (2019) found an excess of cold Jupiters in systems harbouring super-Earths/sub-Neptunes with the former stating that stars with super-Earths have roughly a 3 times higher cold Jupiter fraction compared to field stars. Furthermore, they found that this cold Jupiter fraction rises to about 60% for stars with [Fe/H] > 0.1. Given the metallicity we find for TOI-1288 of 0.07 ± 0.09 from the [SED](#) (median from all measurements in Table 7.3 is 0.15), it is perhaps not too surprising that we are seeing a cold gas giant in this system. This strong correlation between super-Earths and cold Jupiters suggests that they are not competing for the same solid material, which Zhu and Wu (2018) argue disfavours theories invoking large-scale migration.

On the other hand TOI-1288 b is a bit larger than the planets in the aforementioned studies and might have a gaseous envelope. In line with the discussion above, hot Neptunes are in danger of losing their atmospheres, especially while their stars are young and active (e.g. Lopez et al., 2012). Kozai-Lidov cycles and [high-eccentricity migration](#) can deliver Neptune-sized planets on short period orbits past this active stage (\sim 100 Myr) for the star (Dawson and Johnson, 2018). Interactions between TOI-1288 b and c could therefore be responsible for transporting TOI-1288 b to its current position. Subsequent tidal interactions with the star could then have damped the eccentricity to the current value ($0.064^{+0.014}_{-0.015}$), which compared to Earth's orbit (\sim 0.016) is still significant.

To assess whether planet c can influence the dynamics of the inner, planetary system as we see it today, we calculated the planet-star coupling

⁶: <https://heasarc.gsfc.nasa.gov/cgi-bin/tess/webtess/wtv.py>

parameter, ϵ_{*1} , given in Lai et al. (2018), which is a measure for whether an outer companion can cause the orbit of the inner planet to precess. For this we used the approximation in their Eq. (24), which is made for the case of a hot Jupiter with a gas giant companion at a separation of around 1 AU. While not exactly the case here, the approximation can still provide us with some qualitative insights.

As we need to know the stellar rotation period, P_{rot} , for this, we searched the [TESS](#) light curve using the autocorrelation method (McQuillan et al., 2013), however, we did not detect any signs of stellar rotation. Instead we estimated P_{rot} from the age, $\tau = 10.05$ Gyr (Table 7.3), and colour, $B - V = 0.94$ (Table 7.1), using the relation in Mamajek and Hillenbrand (2008), which yields a rotation period of 64 d. From this we get $\epsilon_{*1} \sim 0.5$ suggesting a strong coupling between TOI-1288 b and the star. However, it is not too far from the resonant regime of $\epsilon_{*1} \sim 1$, meaning the excitation of the spin-orbit angle, the [obliquity](#), could be possible.

In addition to TOI-1288 c for which we have constrained the orbit and thus the mass to some extent, we also see evidence for what could be a companion on an even wider orbit. However, for the time being we can only make rather crude inferences about the characteristics of this companion as was done in Section 7.4, namely Figure 7.10. For instance, if this companion were on a 10 yr coplanar (with respect to TOI-1288 b) orbit it would have a mass of around $0.3 M_J$. To decipher the dynamic influence from this companion on the architecture would require continued [RV](#) monitoring to trace out the orbit.

7.6 Conclusions

Here we presented the discovery of multiple planets in the TOI-1288 system. Using photometry from [TESS](#) as well as ground-based telescopes, we have determined that the transiting planet TOI-1288 b is a super Neptune ($5.24 \pm 0.09 R_\oplus$) on a short period orbit ($2.699835^{+0.000004}_{-0.000003}$ d). TOI-1288 b thus joins the growing population of super Neptunes that despite the drought have settled in the Neptunian desert. We have characterised the planet in terms of mass through intensive [RV](#) monitoring with the [HARPS-N](#) and [HIRES](#) spectrographs, where we find a mass of $42 \pm 3 M_\oplus$.

Combining the radius and mass for TOI-1288 b, we find that the planet can be described as a rocky core with a gaseous envelope at high radiation. Similar compositions are found for the planets most identical to TOI-1288 b in terms of orbital period and radius, meaning that the internal structure

and composition might be a crucial premise for survival in the desert. Atmospheric studies of occupants in and around the desert could help shed light on the processes, such as photoevaporation, shaping this region. TOI-1288 b is a well-suited candidate for such studies.

Furthermore, from our [RV](#) monitoring we also found evidence for an additional companion in the TOI-1288 system with an orbital period of 443_{-13}^{+11} d. We find a lower mass of $84 \pm 7 M_{\oplus}$, meaning that if this companion is close to being coplanar with TOI-1288 b, it would be a Saturn-mass planet. TOI-1288 c might have been responsible for transporting TOI-1288 b from a further out orbit to its present day location, for instance, through [high-eccentricity migration](#). Finally, we detect hints of a long-term [RV](#) trend possibly caused by another body in the TOI-1288 system.

8

The warm Saturn HD 332231 b/TOI-1456 b travels on a well-aligned, circular orbit around a bright F8 dwarf

We have now seen how to precisely and accurately determine stellar parameters and how to discover, confirm, and characterise exoplanet systems. We will now take the deep dive into planetary system architectures with some precise measurements of the projected [obliquity](#).

In this chapter I will present our results for the HD 332231 system, a system we initially followed with [SONG](#), where the discovery and characterisation of the system was published in Dalba et al. (2020). The planet is a warm Saturn on a circular orbit, so here we will be investigating the scenarios for the origins of hot and warm gas giants as put forward in Dawson and Johnson (2018, and discussed in Section 1.2).

We measured the projected [obliquity](#) using the [HARPS](#)-N spectrograph and published the results in

E. Knudstrup and S. H. Albrecht (2022). “Orbital alignment of HD 332231 b. The warm Saturn HD 332231 b/TOI-1456 b travels on a well-aligned, circular orbit around a bright F8 dwarf”. *Astronomy and Astrophysics* 660, A99

I was the [PI](#) of the proposal for the [HARPS](#)-N programme for which we obtained the transit observations, and I did the data analysis. Simon H. Albrecht and I wrote the paper together.

The version reproduced here has been reformatted, and the table in the appendix with the [HARPS](#)-N observations has been removed (Table

A.1 in Knudstrup and Albrecht, 2022). Furthermore, the individual limb-darkening parameters from Table 8.2 have been removed to limit the size of the table.

Summary of the Chapter

Contrary to the orthodox picture of planet formation resulting in a neatly ordered Solar System, exoplanet systems exhibit highly diverse orbits: short and long periods, circular and eccentric, well- and misaligned, and even retrograde orbits. In order to understand this diversity it is essential to probe key orbital parameters. Spin–orbit alignment is such a parameter and can provide information about the formation and migration history of the system. However, tidal circularisation and alignment might hamper interpretations of orbital eccentricity and **obliquities** in the context of planet formation and evolution for planets on orbits shorter than about 10 days. Here we aim to measure the projected stellar **obliquity** in the HD 332231 system in which a warm (period \approx 18.7 days) giant planet orbits a bright F star on a circular orbit. We observed the system during a transit with the **HARPS-N** spectrograph and obtained data on the **RM EFFECT**. We analysed the spectroscopic transit data together with new **TESS** photometry employing three different analysis methods. The results from the different approaches are fully consistent. We find a projected **obliquity** of $-2 \pm 6^\circ$, indicating the stellar spin axis to be well-aligned with the orbit of the planet. We furthermore find evidence for transit timing variations suggesting the presence of an additional third body in the system. Together with the low orbital eccentricity, the good alignment suggests that this warm giant planet has not undergone **high-eccentricity migration**.

8.1 Introduction

Our understanding of planet formation is intimately linked to our knowledge of the migratory patterns of giant planets. The formation of so-called hot Jupiters (HJs), gas giant planets with orbits of less than some 10 days, and warm Jupiters (WJs) found at larger separations with orbital periods of between \approx 10 and 200 days is not well understood (see Dawson and Johnson, 2018, for a review). **In situ** formation appears unlikely, at least for the inner planets. Therefore, orbital migration from their original birth orbits to the orbits we now observe them in appears to be an attractive

explanation. However, the exact route(s) for such migration remains poorly understood.

The two leading theories for orbital shrinkage are [disc migration](#) and [high-eccentricity migration](#) (Dawson and Johnson, 2018). In [disc migration](#), angular momentum is exchanged between the planet and the planetary disc, which leads to in-spiraling of the planet (e.g. Lin et al., 1996; Baruteau et al., 2014). [High-eccentricity migration](#) is the result of interactions between multiple bodies in the planetary system. Here the migration can be caused by scattering, which creates a highly eccentric orbit that subsequently shrinks via tidal circularisation (e.g. Chatterjee et al., 2008; Nagasawa et al., 2008), or by a distant stellar or planetary companion in the system, which causes secular Kozai Lidov cycles followed by tidal friction (e.g. Wu and Murray, 2003; Fabrycky and Tremaine, 2007; Naoz, 2016). In systems with three or more planets, exchange of angular momentum can drive the Jupiter's orbit to large eccentricities in a process known as secular chaos (e.g. Laskar, 2008; Wu and Lithwick, 2011; Teyssandier et al., 2019), and subsequent tidal orbital shrinking can lead to a close-in orbiting giant planet.

In general, multi-body interactions in [high-eccentricity migration](#) perturb the original orbit of the planet, leading to an elliptical or eccentric and inclined orbit with respect to its original orbital plane. Conversely, [disc migration](#) is expected to result in low-eccentricity near-circular orbits located near the midplane of the [protoplanetary disc](#) in which the planet formed. Assuming alignment between the stellar equator and the [protoplanetary disc](#), stellar [obliquities](#) (the angle between the orbital and stellar angular momenta) can be used next to eccentricity measurements to inform theories about planet formation and evolution (e.g. Fabrycky and Winn, 2009; Triaud et al., 2010; Dawson and Johnson, 2018).

However, such inference is complicated by a number of factors. It has been found that tidal interactions can significantly alter both the [obliquity](#) (Winn et al., 2010; Albrecht et al., 2012) and the eccentricity (e.g. Husnoo et al., 2012; Bonomo et al., 2017a). Furthermore, good alignment between the [protoplanetary disc](#) and stellar equator is not guaranteed, despite the fact that the former inherits its angular momentum from the latter. Chaotic accretion might lead to a misaligned stellar and [protoplanetary disc](#) spin as suggested by for example Bate et al. (2010), Thies et al. (2011), Fielding et al. (2015), and Bate (2018); but see also Takaishi et al. (2020) who suggest that moderate misalignment can also be created that way. Magnetic torques might also lead to misalignment (Foucart and Lai, 2011; Lai et al., 2011; Romanova et al., 2021). Inclined stellar or planetary companions might

Table 8.1 | HD 332231 system parameters. System and stellar parameters for HD 332231. **Notes.** ^(a)Høg et al. (2000). ^(b)Guerrero et al. (2021). ^(c)Gaia Collaboration et al. (2018). ^(d)Dalba et al. (2020).

Parameter	Value
Alternative name ^(a)	TYC 2689-70-1
Alternative name ^(b)	TOI-1456
R.A. (J2000)	20:26:57.92
Dec. (J2000)	+33:44:40.02
Parallax (mas) ^(c)	12.37 ± 0.03
V magnitude ^(a)	8.56 ± 0.01
Effective temperature (K) ^(d)	6089 ⁺⁹⁷ ₋₉₆
Surface gravity (dex) ^(d)	4.279 ^{+0.027} _{-0.034}
Metallicity (dex) ^(d)	0.036 ^{+0.059} _{-0.058}
Stellar mass (M_{\odot}) ^(d)	1.127 ± 0.077
Stellar radius (R_{\odot}) ^(d)	1.277 ^{+0.039} _{-0.036}
Age (Gyr) ^(d)	4.3 ^{+2.5} _{-1.9}
Period (days) ^(d)	18.71204 ± 0.00043
Eccentricity ^(d)	0.032 ^{+0.030} _{-0.022}
Planetary mass (M_{Jupiter}) ^(d)	0.244 ± 0.021
Planetary radius (R_{Jupiter}) ^(d)	0.867 ^{+0.027} _{-0.025}

tilt discs (see, e.g. Borderies et al., 1984; Lubow and Ogilvie, 2000; Batygin, 2012; Spalding et al., 2014; Matsakos and Königl, 2017), although Zanazzi and Lai (2018) found that HJs suppress such misalignment. While most systems observed so far suggest good primordial alignment (Albrecht et al., 2013b) at least one system appears to have had a retrograde spinning protoplanetary disc (Hjorth et al., 2021). Finally, orbits might have large inclinations relative to the stellar spin, but this is the result of precession caused by a giant orbiting a planetary companion on a wide orbit (Huber et al., 2013; Gratia and Fabrycky, 2017).

One class of systems suited to probing the evolution pathways of giant planets is the WJs, as tides may not have altered the **obliquity**, nor completely dampened the eccentricity. Depending on the presence or absence of a nearby stellar or planetary companion, a number of formation and evolution processes may be excluded or considered.

HD 332231 is one such system. It was first detected by **TESS** (Ricker et al., 2015) and was given the ID TOI-1456 (TOI: **TESS** Object of Interest; Guerrero et al., 2021). It was subsequently confirmed and characterised

by Dalba et al. (2020) through **RV** measurements. With an orbital period of ~ 18.7 d, it was determined to be a WJ, with a radius slightly larger than that of Saturn ($R_p \sim 0.87 R_{\text{Jupiter}}$), but with a significantly lower mass ($M_p \sim 0.24 M_{\text{Jupiter}}$). Key parameters for the HD 332231 system are summarised in Table 8.1.

Here we want to gain information on the **obliquity** of the host star in order to further investigate its history. We observed the system with a high-resolution spectrograph while the planet was transiting its host. Analysis of the **RM EFFECT** (e.g. Struve and Elvey, 1931; Queloz et al., 2000; Winn et al., 2005; Albrecht et al., 2007; Hébrard et al., 2008), which is a line shape distortion occurring during transits, allows us to determine λ , the sky projection of the stellar **obliquity**, ψ .

We describe our observations in Section 8.2. In Section 8.3 we use three approaches to determine the projected **obliquities** from the obtained data sets. After describing our main results in Section 8.4, we briefly discuss them in the context of measurements for similar systems in Section 8.5 before presenting our conclusions.

8.2 Observations

HD 332231 was observed by **TESS** in Sector 14 and 15 with a single transit in both sectors. An additional transit occurred in the observational gap between these two sectors. As noted by Dalba et al. (2020), the transit in Sector 14 was heavily affected by scattered light and was masked out by the presearch data conditioning (PDC) module in the Science Processing Operations Center (SPOC; Jenkins et al., 2016). We include all data and correct for this extra background using the RegressionCorrector implemented in **lightkurve** (Lightkurve Collaboration et al., 2018). The background-corrected and normalised light curve is shown in Figure 8.1. HD 332231 was observed again in the extended mission of **TESS** in Sector 41 with two consecutive transits. This allows improved determination of the ephemeris as well as other photometric transit parameters, especially as the scatter in the Sector 41 light curve is significantly lower than that in Sectors 14 and 15 as seen in Figure 8.1.

Despite correcting for the background, there are still some outliers in the light curve. In an attempt to remove these outliers, we firstly removed the transits using the best-fitting parameters from Dalba et al. (2020) as shown by the grey line in the top curve of Figure 8.1. We then applied a Savitzky-Golay filter (Savitzky and Golay, 1964), as implemented in

lightkurve, which is shown as the black line in the middle curve of Figure 8.1. Finally, we removed the outliers shown as red points in the middle curve of Figure 8.1 through 5σ sigma clipping. After having background-corrected and cleaned the light curve, we re-injected the transit, which can be seen in the bottom curve.

To determine the projected **obliquity** in HD 332231, we obtained spectroscopic transit data with **HARPS-N** (Mayor et al., 2003; Cosentino et al., 2012) mounted on the 3.58 m Telescopio Nazionale Galileo (TNG) located on Roque de los Muchachos, La Palma, Spain. We observed a transit occurring during the night of 4 August, 2020, with observations starting at 21:05 UT until 03:40 UT (programme ID: A41/TAC19, PI Knudstrup). The exposure time was set to 540 s and with an overhead of roughly 20 s, the sampling was approximately 560 s. For comparison, the total transit lasts about 6.1 h. The **RVS** and 1σ uncertainties obtained through the Data Reduction Software (DRS) of **HARPS-N** are shown in the top panel of Figure 8.2. The middle panel shows the **SNR** for each exposure for three orders, and the airmass, ranging from 1.4 to 1.0, is plotted in the lower panel along with the airmass of the Moon plotted as a dashed line. The seeing was variable with values between 0.9 and 2.0 arcsec with a median of 1.5 arcsec.

We supplement our **HARPS-N** transit observations with the **RVS** presented in Dalba et al. (2020). These include **RVS** obtained using the Levy Spectrograph (Radovan et al., 2010) at the Automated Planet Finder (APF; Radovan et al., 2014; Vogt et al., 2014), the High Resolution Echelle Spectrometer (HIRES; Vogt et al., 1994) at the Keck I telescope, and the Hertzsprung node of **SONG** (Andersen et al., 2014; Grundahl et al., 2017). The **RVS** from Dalba et al. (2020) as well as our **HARPS-N** observations are shown in Figure 8.3.

8.3 Determining the projected stellar obliquity

When part of the rotating stellar surface is blocked from view, the rotational broadened stellar absorption lines are distorted relative to their uneclipsed shape. The distortion and its time evolution are governed by the projection of the angle between the stellar spin axis and the orbital angular momentum of the occulting body.

Using the **HARPS-N** data from the night on the 4 August, 2020, supplemented by the **TESS** photometry and the publicly available **RV** data described above, we measure λ employing three different approaches. We are motivated to do so as different analysis methods can have different

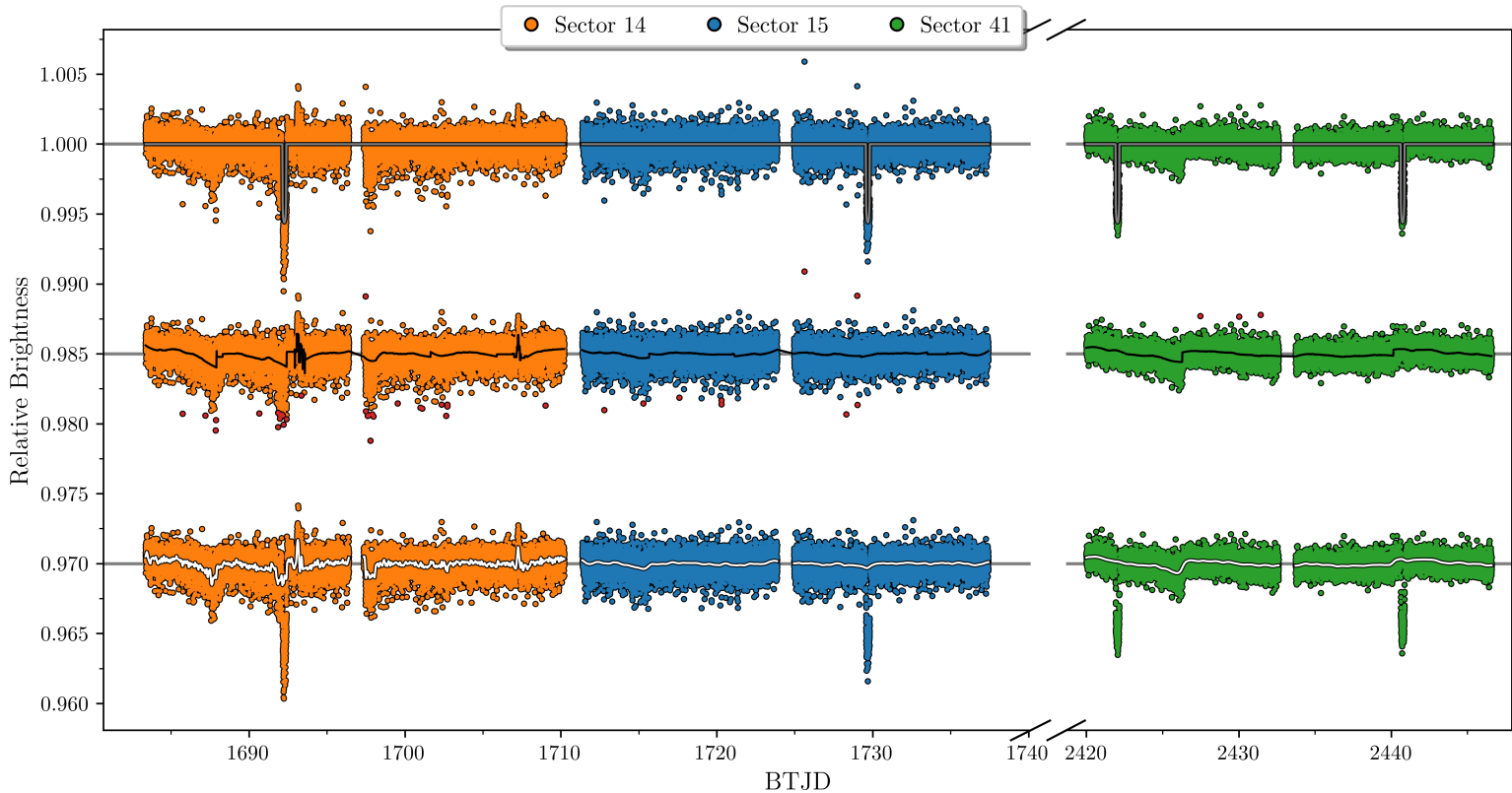


Figure 8.1 | TESS light curve for HD 332231. The top curve is a normalised but not detrended light curve of HD 332231 as observed by [TESS](#) (top curve), with orange, blue, and green points corresponding to Sectors 14, 15, and 41, respectively. The grey line is a transit model created from the parameters in [Dalba et al. \(2020\)](#). The transit model has been used to temporarily remove the transit in the light curve offset by -0.015 (denoted as the straight line below the points). Here the black line shows a Savitzky-Golay filter used to filter and detrend the data. The red points are outliers removed through a 5σ sigma clipping. The light curve with outliers removed and the transits re-injected is shown in the light curve offset by -0.03, where the white line shows the [GP](#) (see Section 8.3) used for detrending.

dependencies on systematic errors towards some system parameters; for example, timing offsets and orbital inclination. We used the following approaches: i) We analysed the stellar absorption lines and distortions thereof during the transits themselves. For this, we used the `CCF`, which serves as an "average stellar absorption line" as delivered by the DRS. ii) We also employed a procedure where we first measured the position of the `CCF` distortion in `RV` space, and then used these subplanetary velocities, v_p , to determine the projected `obliquity`. iii) Finally, we determined the projection of ψ using the anomalous stellar `RVS` occurring during transit as a result of the line distortions. As all three methods use the same data sets, they are expected to deliver fully consistent results.

Before describing the specific steps for each approach, we outline the setup common to all three approaches. In each case, we created a model which we compared to the data sets, the spectroscopic transit data, `TESS` photometry, and `RVS` taken outside transits. We extracted the confidence intervals of relevant parameters using an `MCMC` as described below.

Parameters mainly governed by photometric data are the orbital period, P , a specific mid-transit point, T_0 , the planet-to-star radius ratio, r/R , the scaled semi-major axis, a/R , the cosine of the orbital inclination, $\cos i_o$, and the quadratic limb-darkening parameters, q_1 and q_2 . For all three approaches to determining the projected `obliquity`, we modelled the `TESS` light curves with the Mandel and Agol (2002) formalism as implemented in the `batman` package (Kreidberg, 2015). As is evident from the bottom panel of Figure 8.1 the light curves are affected by systematic error. Therefore, at each step of our `MCMC` analyses, we adjusted a `GP` model to the `TESS` data, where we modelled the correlated noise with a Matérn-3/2 kernel implemented in `celerite` Foreman-Mackey et al. (2017). As the systematic error is quite different between the three sectors, we include three sets (one for each sector) of the two hyper parameters; the amplitude of the noise, A , and the timescale, τ . We furthermore include a jitter term for each light curve, $\sigma_{\text{Sector } i}$ ($i = 14, 15, 41$).

For reasons discussed in Section 8.4 we also included one additional parameter, ΔT_0 , here in our final model to data comparison. This parameter allows the spectroscopic transit midpoint to float with respect to the midpoint given by the linear ephemeris (P, T_0).

Parameters mainly determined using out-of-transit `RVS` are the orbital `RV` semi-amplitude, K , the orbital eccentricity, e , the argument of periastron, ω , and the `RV` offsets for the four spectrographs, γ_i ($i = \text{HARPS-N}$, Levy, HIRES, SONG), as well as their `RV` jitter terms added in quadrature to the `RV` uncertainties provided by the `RV` pipelines σ_i . Parameters describing the shape of the `CCFS` and any distortions during transits are the

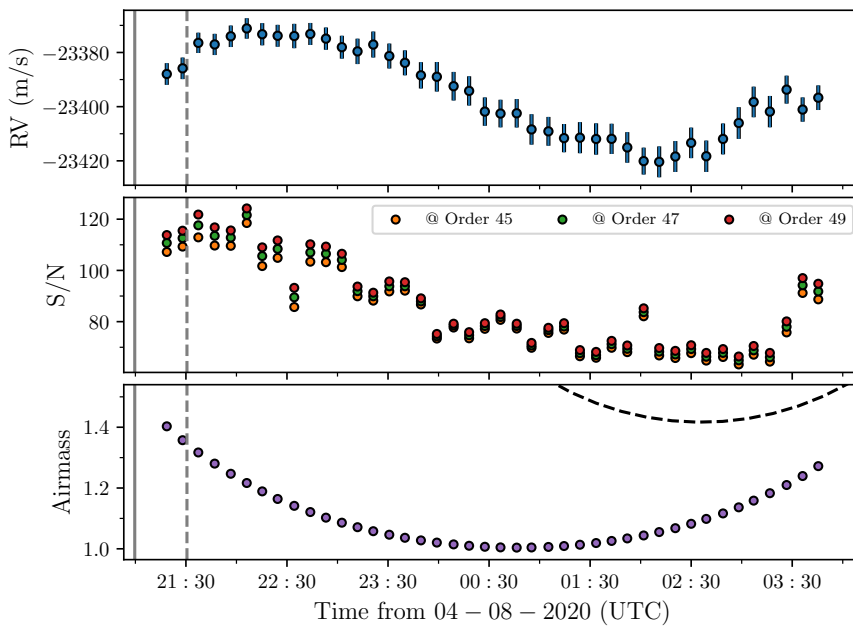


Figure 8.2 | The HARPS-N data on the transit night. *Top:* RVs extracted from the HARPS-N pipeline plotted against time. *Middle:* SNR for each exposure at three different orders, namely 45, 47, and 49. *Bottom:* Airmass for each exposure plotted with the airmass of the Moon plotted as the dashed line. In each panel, the vertical solid and dotted lines denote nautical and astronomical twilight, respectively.

projected stellar rotation speed, $v \sin i$, the stellar surface motion, which, here, is parametrised by macro-turbulence, ζ , and micro-turbulence, ξ (Gray, 2005). The HARPS-N instrument provides spectra with a resolution of $R \approx 115\,000$ resulting in a spectral point spread function (PSF) with a FWHM of $\sim 2.6 \text{ km s}^{-1}$ or a σ_{PSF} of $\sim 1.1 \text{ km s}^{-1}$. We use this value to create a Gaussian with which we convolve our model CCFs. In addition, we require two parameters with which we attempt to capture the limb darkening in the band pass of HARPS-N, $q_{1,\text{HARPS-N}}$ and $q_{2,\text{HARPS-N}}$. The deformation of the lines during the transit in our model is chiefly governed by the projected obliquity, λ (our parameter of main interest), the above-mentioned $v \sin i$, and the impact parameter $b \equiv a/R \cos i_o$, which is also controlled by the photometric data obtained during transit.

To obtain confidence intervals for our system parameters, in addition to the data described in Section 8.2, we employed prior information on

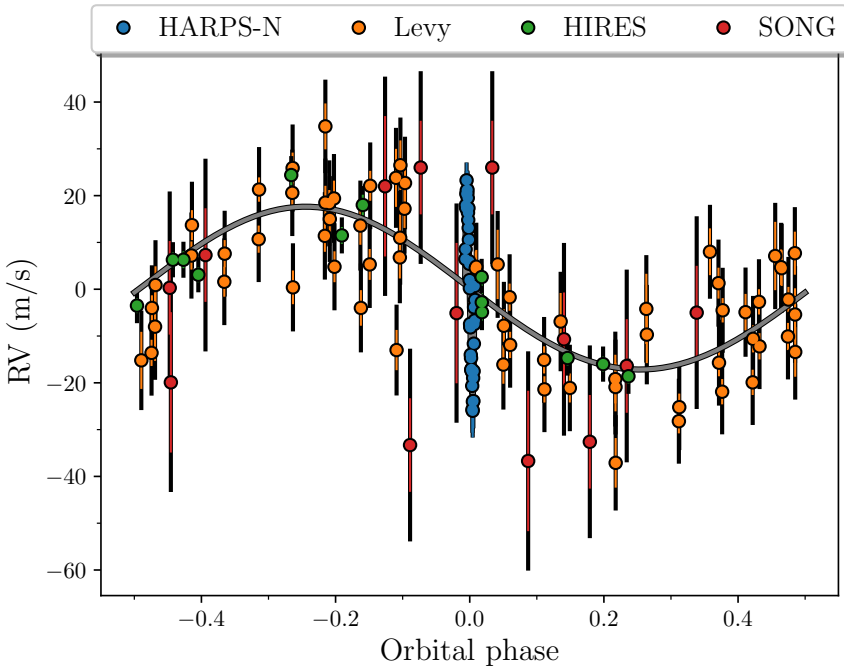


Figure 8.3 | Radial velocity curve for HD 332231 b. Radial velocities from [HARPS](#)-N, Levy, HIRES, and [SONG](#) shown with blue, orange, green, and red error bars, respectively. The grey line is the best-fitting model of the orbit modulated by the [RM EFFECT](#), which is obscured by the [HARPS](#)-N data. The coloured error bars are the nominal errors, and the black error bar is the nominal error with the jitter term added in quadrature.

stellar limb-darkening and stellar surface fields. With the stellar parameters determined by Dalba et al. (2020) and listed in Table 8.1, we queried the tables provided by Claret et al. (2013) and Claret (2017) for values for quadratic limb-darkening parameters. For the [TESS](#) passband, we find $q_1 = 0.253$ and $q_2 = 0.289$, and for the V band used for our spectroscopic transit data we obtain $q_{1,\text{HARPS-N}} = 0.513$ and $q_{2,\text{HARPS-N}} = 0.199$. From T_{eff} , $\log g$, and the relationship presented in Doyle et al. (2014), we find $\zeta = 4.46 \text{ km s}^{-1}$. Assuming a sigma of 1 km s^{-1} we use this as a Gaussian prior. For the [micro-turbulence](#) parameter ξ we assume a Gaussian prior with a mean of 2 km s^{-1} and a σ of 1 km s^{-1} , which is in line with the value given in Hirano et al. (2011). All parameters and their priors can be found in Table 8.2.

Before proceeding with creating a model and comparing it to our data, two additional steps concerning the [HARPS](#)-N [CCFS](#) were required. As

mentioned above, the PSF of **HARPS**-N has a σ_{PSF} of $\sim 1.1 \text{ km s}^{-1}$. The **CCFS** provided by the DRS are sampled on a velocity grid with a bin size of 0.25 km s^{-1} . We therefore binned the **CCFS** onto a velocity scale with bins of 1 km s^{-1} in width. Secondly, to assign the proper weight to each type of data (photometry, out-of-transit **RVS**, **HARPS**-N transit night data), the different data sets require properly scaled uncertainties. To obtain such uncertainties for the **CCFS**, we performed a fit to the last three **CCFS** obtained during the transit night, as these were obtained after egress. The averaged out-of-transit (OOT) **CCF** was fitted with the relevant parameters from above ($v \sin i$, ζ , ξ , and limb-darkening). From this best fit, and requiring a reduced chi-squared, χ^2_ν , to be ≈ 1 , we obtain uncertainties of ~ 0.0004 for each velocity point in the **CCF**. Furthermore, we normalised our **CCFS** by setting the surface area under the **CCF** to 1 for both data and model. In Figure 8.4 we display the OOT **CCFS**, the best fitting model, and the residuals of the **CCFS**. At this point, we were in a position to compare the data to the different models.

8.3.1 Line distortions: planet shadow

Here we present our analysis of the deformations of the stellar lines directly caused by the planetary transits. To perform such an analysis, we followed the approach by Albrecht et al. (2007), Albrecht et al. (2013b), and Hjorth et al. (2021), but see also for example Brown et al. (2012), Johnson et al. (2014), and Zhou et al. (2016). Our model **CCFS** were created by constructing a limb-darkened stellar grid, where we assume a quadratic limb-darkening law of the form

$$I = 1 - u_1(1 - \mu) - u_2(1 - \mu)^2 . \quad (8.1)$$

Here $\mu = \cos(\theta)$ with θ being the angle between the local normal and a line parallel to the line of sight, and I is the local intensity normalised by the intensity at the center of the disc, i.e., $\mu = 1$.

For each pixel of the stellar surface, we include the effects of **macro-turbulence** and **micro-turbulence** following Gray (2005). The local line profile in our model is given by

$$\Theta(v) = \frac{1}{2\sqrt{\pi}\zeta} \left(\frac{\exp(-v/\zeta \cos \theta)^2}{\cos \theta} + \frac{\exp(-v/\zeta \sin \theta)^2}{\sin \theta} \right) , \quad (8.2)$$

where we assume equal velocities and surface areas for tangential and radial flows.

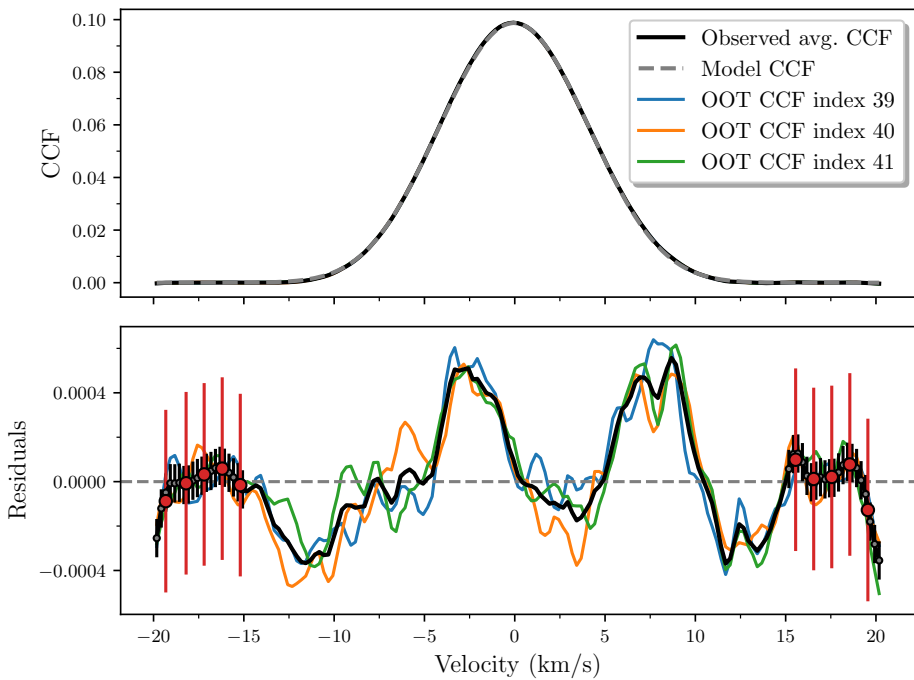


Figure 8.4 | Out-of-transit cross-correlation-functions. *Top:* Average observed CCF (created from the three OOT CCFs) shown as the solid black line with the best-fitting model overlain as the grey dashed line. The surface area under the CCF was arbitrarily set to 1. All CCFs have been shifted into the stellar rest frame. *Bottom:* Residuals between the OOT CCF and model. We also show the three epochs used to create our average out of transit CCF, i.e. the three last observations on the 4 August, 2020 (Indexing started with 0). Shown as grey error bars is the scatter on the CCFs outside of the central peak, specifically $\pm 15 \text{ km s}^{-1}$, which we have binned to 1 km s^{-1} and scaled to get $\chi^2_{\nu} \sim 1$. The binned and scaled errors are shown with red error bars, which are applied to all data points, but for illustrative purposes are only shown in the aforementioned range.

Assuming solid body rotation (no differential surface rotation), the **RV** of the stellar surface is a function of the distance from the stellar spin axis only. We tested whether or not including differential rotation into our model would change the main conclusion we draw about the projected **obliquity** and found this not to be the case. This is because differential rotation is difficult to measure via the **RM EFFECT** (Hirano et al., 2011) and would require a very well suited data set. In our case in particular, the

planet covers only a very small range in stellar latitude, and so even strong differential rotation would not change the shape of the RM signal. Still, in the presence of strong differential surface rotation, the disc-integrated $v \sin i$ might differ from the "local" $v \sin i$ as probed by v_p , but given the data at hand, this would not be noticeable.

We define a coordinate system so that the x -axis is oriented along the stellar equator and the y -axis parallel to the projected stellar spin axis. The Doppler velocity of the stellar surface below a planet v_p is then simply given by the distance from the y -axis and the projected stellar rotation speed,

$$v_p = \frac{x}{R} v \sin i . \quad (8.3)$$

The position of the planet (x_p, y_p) in this coordinate system is given by

$$\begin{pmatrix} x_p \\ y_p \end{pmatrix} = \begin{pmatrix} -\frac{\Gamma}{R} \cos(\omega + \nu) \\ -\frac{\Gamma}{R} \sin(\omega + \nu) \cos i_o \end{pmatrix} \begin{pmatrix} \cos \lambda & -\sin \lambda \\ \sin \lambda & \cos \lambda \end{pmatrix} . \quad (8.4)$$

Here, ν represents the true anomaly and Γ the distance between the centre of the planet and that of the star on the Keplerian orbit.¹ The matrix is simply the 2D rotation matrix for the angle λ .

In our model, we were at this point able to calculate for each observation whether or not parts of the rotating stellar disc are blocked from view. We performed this calculation for each observation and set the flux of pixels covered by the planet to zero when we integrated over the visible stellar surface to obtain a model of the stellar line at particular phases of the transit. The lines were then convolved with a Gaussian whose width is given by the quadrature sum of ξ and σ_{PSF} . Finally, the model [CCFS](#) were shifted in velocity space according to a Keplerian model. "Phase smearing" occurs for integration times that are sufficiently long for the planets movement over the stellar disc to be $\gtrsim r/R$. In such cases, the data should be compared to models that are integrated over such time intervals to emulate phase smearing. However, for the current set of observations, the exposure-time-to-transit-duration ratio is ≈ 0.02 , which is less than $r/R \approx 0.07$. We therefore do not take this into account here.

Now we present our comparison of the model [CCFS](#) with the observed [CCFS](#). As in Albrecht et al. (2013b), we also tried to mitigate the effect that the changes in [SNR](#) throughout the night might have on the normalisation of the spectra and resulting [CCFS](#). Such changes might lead to slightly different

¹: Normally the orbital distance is indicated by r , which we have assigned to the planetary radius.

[SNRS](#) in the [CCFS](#) and therefore slightly different [CCF](#) heights as well as small overall changes in the [CCF](#) baseline. We assigned three parameters to each [CCF](#): an intensity offset, a slope, and a scalar. These parameters were optimised every time a model was compared to the data. This approach serves to propagate the effects of any potential changes in the normalisation into the confidence intervals of the final system parameters. However, in the case of our particular data set, these parameters vary by less than 0.01% throughout the night as the transit spectra were taken under good and relatively stable conditions (Section 8.2) by a fibre fed spectrograph.

In Figure 8.5 we show the best-fitting light curve from the [MCMC](#) (Section 8.3.4), while in Figure 8.6 a) we show the [HARPS-N](#) data with the best-fitting model as well as the residuals. Here, we subtracted the OOT [CCF](#) to highlight the deformation of the [CCFS](#) due to the planetary transit. The [planetary shadow](#) first covers the blueshifted light, and during the second half of the transit covers the redshifted light, consistent with a prograde transit.

8.3.2 Subplanetary velocity

A second approach to measuring λ is to determine the subplanetary velocity, v_p , for each observation and then use a simple geometric model to determine λ from the v_p measurements (e.g. Cegla et al., 2016; Hoeijmakers et al., 2020). The results of this method do not depend directly on surface velocity fields. A dependence does remain as the OOT [CCFS](#) supply information on $v \sin i$, and that $v \sin i$ measurement does depend on the surface velocity fields. This additional information on $v \sin i$ is particularly important for our system as the impact parameter is close to zero (see Albrecht et al., 2011, for a discussion on this dependency).

The subplanetary velocities are obtained in the following way: the OOT [CCF](#), shifted to the appropriate velocities, is subtracted from the in-transit [CCFS](#). This isolates the distortion in the stellar lines, i.e. the planet shadow. The central subplanetary velocity is then measured by fitting a Gaussian to the distortions during transit, where we only searched for a distortion of the [CCFS](#) inside the interval $\pm 2 \times v \sin i$. We used the uncertainties derived from the co-variance matrix of a Levenberg-Marquardt fit and then further increased them in quadrature so $\chi^2_\nu \approx 1$. We extracted v_p for each set of system parameters afresh out of concern that any error we make in isolating the planet shadow, by for example not using the proper orbital velocity, might lead to a systematic error in the measured v_p . However, we tested that even for line parameters significantly outside our confidence

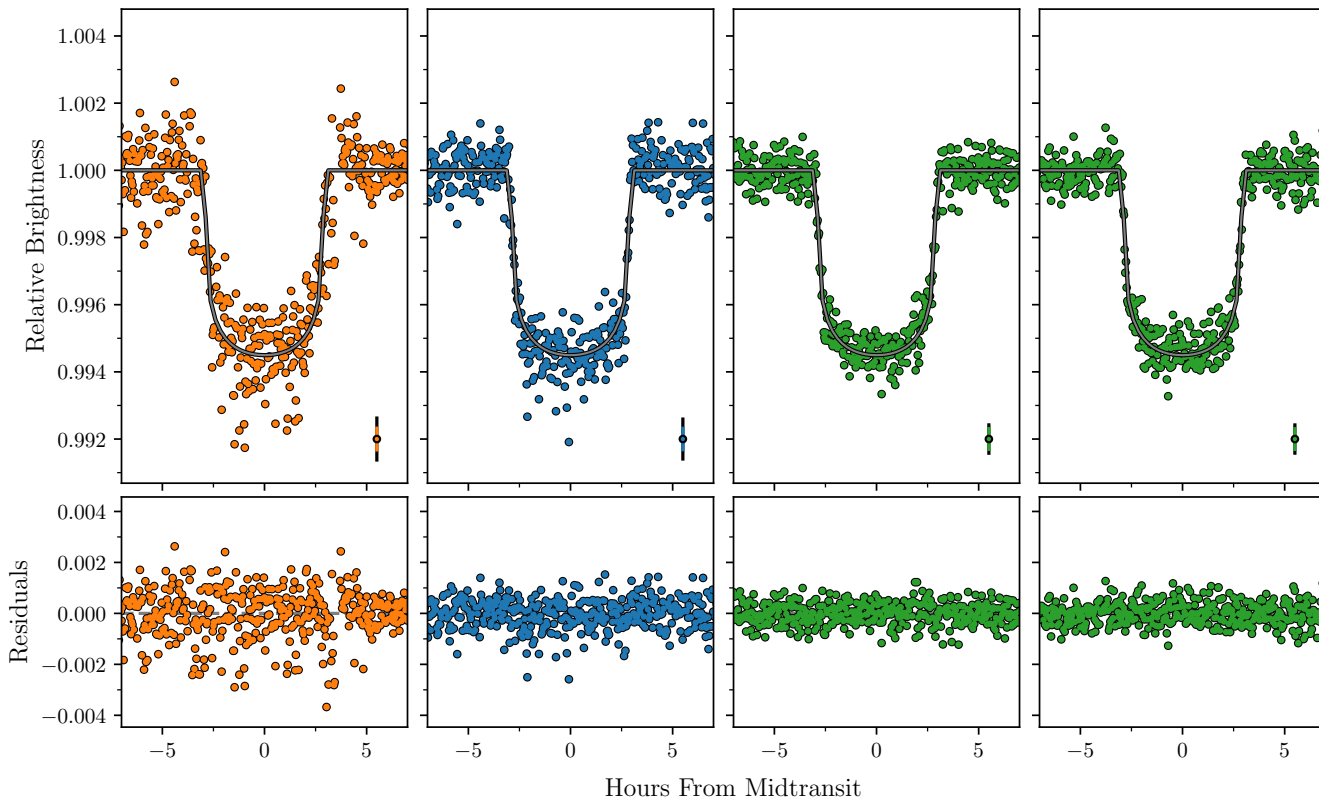


Figure 8.5 | The four transits of HD 332231 b. *Top:* Transit data points from the [TESS](#) light curve after correction using the [GP](#) model seen in Figure 8.1. The grey line is the best-fitting light curve model. *Bottom:* Residuals from subtracting the best-fitting model from the data. In each top panel, we show an error bar that is representative of the error from this particular selection of data. We added the photometric jitter in quadrature (shown in black) to the nominal error (coloured).

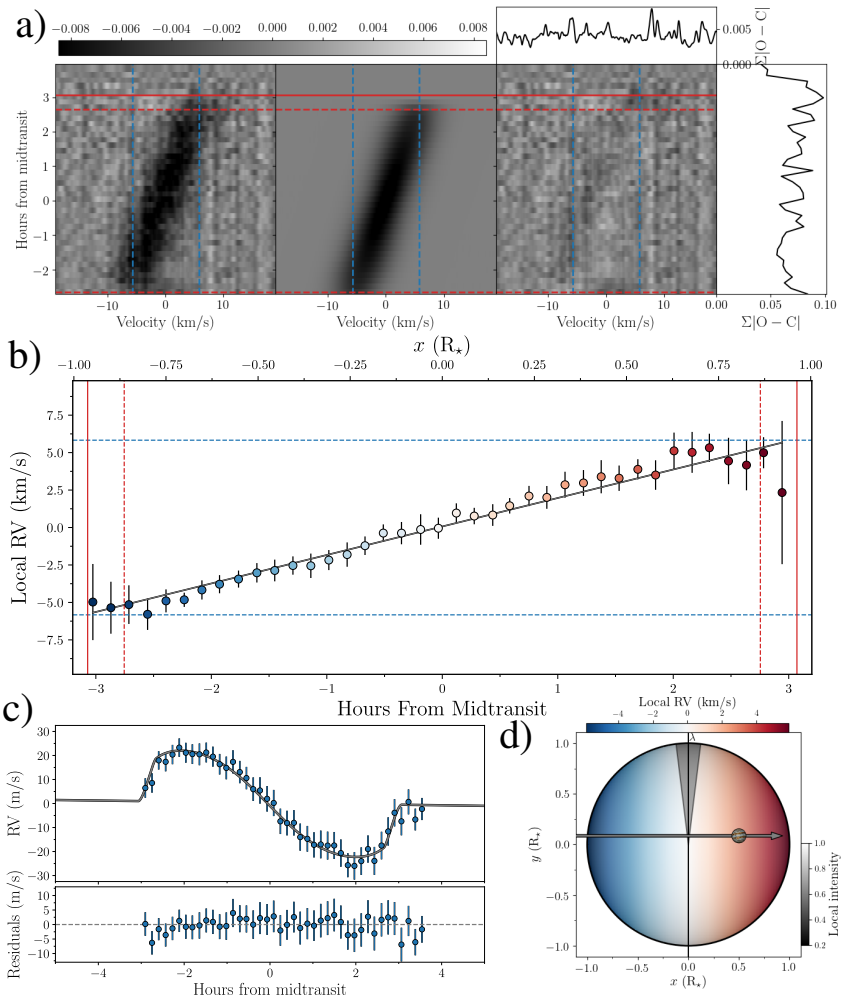


Figure 8.6 | The three approaches to measuring λ . a) *Left:* Distortion of the stellar absorption lines as observed with HARPS-N during the transit night. The vertical lines denote $\pm v \sin i$. The horizontal dashed lines are the second and third contact, i.e. the times in between is when the planet is completely within the stellar disc, and the solid line is the fourth contact, i.e. the point where the stellar and planetary discs no longer overlap. *Middle:* Best-fitting model of the distortion of the absorption lines. *Right:* Residuals from subtracting the best-fitting model from the data with the summed values displayed on top and to the right. In all panels, data and model have been shifted into the stellar rest frame, a minor effect. The horizontal colour bar at the top denotes the strength of the signal. (Caption continued on next page.)

Figure 8.6 | The three approaches to measuring λ . **b)** Subplanetary or local **RVS** created by subtracting the OOT **ccf** from the in-transit ones and measuring the position of the excess bump caused by the planet. The error bars are colour-coded according to the $v \sin i$ value they should have given their x -position in **d**), which shows the orientation of the orbit and the projected stellar rotation going from blue ($-v \sin i$) to red ($v \sin i$). As in **a**), the dashed blue line denotes the value for $v \sin i$, while the solid and dashed red lines mark the contact points. **c)** *Top:* **RVS** from **HARPS-N** used in the fit (shown with blue error bars). The grey line is the best-fitting model of the **RM EFFECT**. **c)** *Bottom:* Residuals from subtracting the best-fitting model from the data. **d)** Geometry of the system with the planet transiting the rotating and limb-darkened star, which is tilted by λ with respect to the orbit of the planet marked with the grey arrow. The horizontal colour bar shows the rotation speed at a given longitude, and the grey colour bar shows the relative intensity given going from 1.0 in the centre to around 0.16 at the limb (given the limb-darkening parameters for **HARPS-N** in Table 8.2). Here the intensity overlay has been made transparent to make the rotation colour-coding visible.

intervals, the subtraction of the overall line and subsequent determination of v_p does not change v_p outside its uncertainty interval. The extracted velocities and their uncertainties can be seen in Figure 8.6 b).

From Equation (8.3) it is clear that v_p only depends on the x -coordinate of the planet and should progress linearly with time. Therefore, in our model we can calculate v_p with a first-order polynomial, where extremes occur at ingress V_{ingress} and V_{egress} and both can be taken as positive values. The offset and amplitude of the line are given by (Albrecht et al., 2011; Albrecht et al., 2022),

$$\begin{aligned} V_{\text{egress}} - V_{\text{ingress}} &= 2 \times (v \sin i) \sin \lambda \times b, \\ V_{\text{egress}} + V_{\text{ingress}} &= 2 \times (v \sin i) \cos \lambda \times \sqrt{1 - b^2}. \end{aligned} \quad (8.5)$$

For this particular system with $b \approx 0$, good alignment would be indicated with $V_{\text{egress}} + V_{\text{ingress}} \approx 2 \times (v \sin i) \approx 11 \text{ km s}^{-1}$.

8.3.3 Radial velocities

The distortions of the spectral lines as seen in Figure 8.6 a) lead to anomalous **RVS** observed during transit, displayed in Figure 8.6 c). A first-order estimate

of the anomalous stellar [RVS](#) can be obtained from

$$\text{RV}_{\text{RM}}(t) \approx -\left(\frac{r}{R}\right)^2 v_p(t). \quad (8.6)$$

The RV_{RM} measurements relate to v_p and the radius ratio of the transiting to the occulted object. The sign change occurs as the subplanetary light is blocked from view. Any particular RV_{RM} is further modified by the stellar limb darkening at the subplanetary point on the stellar disc, Equation (8.1), and during ingress and egress by the ratio of the planetary disc in front of the star. This can be seen by comparing Figure 8.6 b) to Figure 8.6 c). For our [RV](#) model, we used the algorithm by Hirano et al. (2011) which also includes the effect of instrumental and stellar broadening. For the other two approaches, here we also include a Keplerian [RV](#) model.

8.3.4 Comparison of data and model

To extract confidence intervals for the system parameters, we used [MCMCS](#). We define our likelihood function as,

$$\log \mathcal{L} = -0.5 \sum_{i=1}^N \left[\frac{(O_i - C_i)^2}{\sigma_i^2} + \log 2\pi\sigma_i^2 \right] + \sum_{j=1}^M \log \mathcal{P}_j, \quad (8.7)$$

where N indicates the total number of data points from photometry, archival [RVS](#), and the spectroscopic data obtained during the transit night; C_i represents the model corresponding to the observed data point O_i ; σ_i is the uncertainty for the i th data point, where we add a jitter term in quadrature and a penalty in the likelihood for the [RVS](#) as well as photometry; and \mathcal{P}_j denotes the prior for the j th parameter listed in Table 8.2.

We did not step directly in the limb-darkening coefficients; rather we were stepping in the sum of the two, that is $q_1 + q_2$, where we applied a Gaussian prior with a width of 0.1. The difference, that is $q_1 - q_2$, was kept fixed during the sampling. Furthermore, our [MCMC](#) was stepping in $\sqrt{e} \cos \omega$, $\sqrt{e} \sin \omega$, and $\cos i$. We used [emcee](#) (Foreman-Mackey et al., 2013) to carry out the [MCMC](#) sampling of the posteriors. To ensure that our [MCMC](#) runs converged, we invoked the rank-normalised \hat{R} diagnostic test (Vehtari et al., 2019) using the [rhat](#) module implemented in [ArviZ](#) (Kumar et al., 2019). Our results for all three approaches are given in Table 8.2, and all clearly suggest that the stellar spin axis and the orbital axis of the planet are aligned.

8.4 Results

The additional [TESS](#) photometry from Sector 41 allows us to improve the planet-to-star radius ratio from that of the discovery paper, shrinking the uncertainty by $\sim 33\%$. We find $r/R = 0.0689 \pm 0.0003$. This is because (i) now four instead of two transits have been observed and (ii) Sector 41 photometry has a lower scatter. Using our new value for r/R with the stellar radius given in Dalba et al. (2020, (see our Table 8.1),) we find $r = 0.857 \pm 0.016 R_{\text{Jupiter}}$, which is consistent with the discovery value of $0.867^{+0.027}_{-0.025} R_{\text{Jupiter}}$.

There is a discrepancy in the systemic velocity for the [HARPS](#)-N data, $\gamma_{\text{HARPS-N}}$, between the three approaches; see Table 8.2. The shadow and slope approaches give consistent results with each other but not with the [RV](#) method. While we have not further investigated this here, we suspect that this disagreement is caused by the simple stellar line model we employ in the shadow and slope approaches. In particular, we do not model convective blueshift as done by Albrecht et al. (2012) using the approach by Shporer and Brown (2011). Therefore, our model of the line shape is fully symmetric, which is the opposite of what we expect for actual stellar absorption lines. While convective blueshift might influence all three approaches, the difference in γ probably comes about as the line and slope method fits the line itself *and* the velocity position of the distortion v_p , while the [RV](#) method only fits the [RVS](#). Given the fast rotation of the star and the quality of our data, convective blueshift might have influenced the result of γ significantly, but not the result for λ . Ideally, magnetohydrodynamics simulations of the stellar photosphere should be used to model the lines (Cegla et al., 2016; Dravins et al., 2017). We further note that the values for $v \sin i$ and $q_1 + q_2$ derived from [HARPS](#)-N data come out slightly larger for the slope compared to the values for the [RV](#) and shadow runs. These two parameters are correlated in that, for a stronger limb darkening, $v \sin i$ needs to be larger as well to fit the OOT.

Before the recent release of data from [TESS](#) Sector 41, we found in our initial runs that the three approaches of measuring λ lead to inconsistent results. Specifically, the subplanetary velocity approach found alignment ($\lambda = -7 \pm 8^\circ$), the shadow analysis indicated moderate misalignment ($\lambda = -16 \pm 4^\circ$), and the RV_{RM} measurements suggested a very significant misalignment, $\lambda = -31 \pm 6^\circ$.

Including [TESS](#) Sector 41 data, we now have photometry obtained during July and August 2019 and July and August 2021 bracketing our spectroscopic transit observations from the 4 August, 2020. From this, it

Table 8.2 | MCMC results for HD 332231. Results from the [MCMCs](#) using the [RVS](#), the planet shadow, and the local subplanetary velocity. The value is the median of the samples and the upper and lower uncertainties are estimated from the highest posterior density at a confidence level of 0.68. We denote the uniform priors as \mathcal{U} and the Gaussian priors with a mean, μ , and width, σ , as $\mathcal{N}(\mu, \sigma)$. We chose the parameters obtained from analysing the deformation in the lines (the [planetary shadow](#)) as our final parameters. T_0 is given in [TESS](#) Barycentric Julian Date (BTJD; BJD – 2457000).

Parameter	Prior	RV	Shadow	Slope
Stepping parameters				
P (days)	\mathcal{U}	18.71205 ± 0.00001	18.71205 ± 0.00001	18.71205 ± 0.00001
T_0 (BTJD)	\mathcal{U}	1729.6814 ± 0.0004	1729.6814 ± 0.0004	1729.6814 ± 0.0004
ΔT_0 (min.)	\mathcal{U}	20 ± 3	18 ± 3	22 ± 4
r/R	\mathcal{U}	0.0690 ± 0.0003	0.0689 ± 0.0003	0.0690 ± 0.0003
a/R	\mathcal{U}	$24.3^{+0.4}_{-0.3}$	$24.4^{+0.4}_{-0.3}$	$24.4^{+0.4}_{-0.3}$
$\cos i_o$	\mathcal{U}	$0.006^{+0.003}_{-0.005}$	$0.0039^{+0.0018}_{-0.0039}$	$0.0036^{+0.0015}_{-0.0035}$
λ ($^\circ$)	\mathcal{U}	-1 ± 12	-2 ± 6	0 ± 7
$v \sin i$ (km/s)	\mathcal{U}	5.64 ± 0.14	5.63 ± 0.11	$5.89^{+0.12}_{-0.13}$
ζ (km/s)	$\mathcal{N}(4.46, 1.0)$	4.8 ± 0.4	4.7 ± 0.3	4.7 ± 0.2
ξ (km/s)	$\mathcal{N}(2.0, 1.0)$	$2.7^{+0.2}_{-0.3}$	$2.71^{+0.17}_{-0.19}$	2.40 ± 0.17
K (m/s)	\mathcal{U}	$17.5^{+1.1}_{-1.2}$	17.5 ± 1.1	17.5 ± 1.1
$\sqrt{e} \cos \omega$	\mathcal{U}	$0.11^{+0.12}_{-0.09}$	$0.12^{+0.12}_{-0.08}$	$0.12^{+0.12}_{-0.08}$
$\sqrt{e} \sin \omega$	\mathcal{U}	$0.08^{+0.03}_{-0.07}$	$0.08^{+0.04}_{-0.07}$	$0.09^{+0.05}_{-0.06}$
$\gamma_{\text{HARPS-N}}$ (m/s)	\mathcal{U}	-23395.1 ± 1.1	-23346^{+12}_{-11}	-23344 ± 12
$\sigma_{\text{HARPS-N}}$ (m/s)	\mathcal{U}	$0.6^{+0.3}_{-0.6}$	-	-
γ_{Levy} (m/s)	\mathcal{U}	1.0 ± 1.1	1.1 ± 1.1	$1.1^{+1.2}_{-1.0}$

σ_{Levy} (m/s)	\mathcal{U}	$8.7^{+0.8}_{-0.9}$	$8.7^{+0.8}_{-1.0}$	$8.7^{+0.8}_{-1.0}$
γ_{HIRES} (m/s)	\mathcal{U}	$-1.6^{+1.0}_{-1.1}$	-1.6 ± 1.0	$-1.6^{+1.0}_{-1.1}$
σ_{HIRES} (m/s)	\mathcal{U}	$3.4^{+0.9}_{-1.0}$	$3.4^{+0.8}_{-1.1}$	$3.4^{+0.9}_{-1.0}$
γ_{SONG} (m/s)	\mathcal{U}	2 ± 6	2^{+5}_{-6}	2 ± 6
σ_{SONG} (m/s)	\mathcal{U}	18 ± 5	18^{+4}_{-6}	18^{+4}_{-6}
$q_1 + q_2$: TESS	$\mathcal{N}(0.542, 0.1)$	0.55 ± 0.03	0.56 ± 0.03	0.55 ± 0.03
$q_1 + q_2$: HARPS-N	$\mathcal{N}(0.7114, 0.1)$	0.78 ± 0.08	0.78 ± 0.08	$0.88^{+0.09}_{-0.10}$
$\log \sigma_{\text{Sector 15}}$	\mathcal{U}	$-7.571^{+0.008}_{-0.007}$	-7.571 ± 0.008	-7.571 ± 0.008
$\log \tau_{\text{Sector 15}}$ (log days)	\mathcal{U}	$-9.13^{+0.11}_{-0.12}$	$-9.12^{+0.10}_{-0.12}$	$-9.13^{+0.11}_{-0.12}$
$\log A_{\text{Sector 15}}$	\mathcal{U}	-1.0 ± 0.3	-1.0 ± 0.3	-1.0 ± 0.3
$\log \sigma_{\text{Sector 14}}$	\mathcal{U}	-7.502 ± 0.008	-7.502 ± 0.008	-7.503 ± 0.008
$\log \tau_{\text{Sector 14}}$ (log days)	\mathcal{U}	-7.92 ± 0.04	-7.91 ± 0.04	-7.92 ± 0.04
$\log A_{\text{Sector 14}}$	\mathcal{U}	-2.68 ± 0.11	$-2.68^{+0.10}_{-0.11}$	$-2.68^{+0.10}_{-0.11}$
$\log \sigma_{\text{Sector 41}}$	\mathcal{U}	-8.127 ± 0.012	-8.127 ± 0.012	$-8.127^{+0.012}_{-0.013}$
$\log \tau_{\text{Sector 41}}$ (log days)	\mathcal{U}	$-8.46^{+0.12}_{-0.15}$	$-8.46^{+0.13}_{-0.14}$	$-8.46^{+0.12}_{-0.15}$
$\log A_{\text{Sector 41}}$	\mathcal{U}	$-0.23^{+0.16}_{-0.15}$	$-0.23^{+0.15}_{-0.16}$	$-0.23^{+0.15}_{-0.16}$
Derived parameters				
i_o (°)		$89.67^{+0.29}_{-0.15}$	$89.78^{+0.22}_{-0.10}$	$89.80^{+0.20}_{-0.09}$
b		$0.14^{+0.06}_{-0.12}$	$0.10^{+0.04}_{-0.10}$	$0.09^{+0.04}_{-0.09}$
e		$0.026^{+0.011}_{-0.024}$	$0.029^{+0.014}_{-0.024}$	$0.029^{+0.016}_{-0.022}$
ω (°)		40^{+26}_{-40}	39^{+22}_{-39}	39^{+22}_{-39}
r (R _{Jupiter})		0.857 ± 0.016	0.856 ± 0.016	0.857 ± 0.016

now appears that the midpoint of the transit we observed with **HARPS**-N ($T_0 = 1729.6811$ in BTJD; **TESS** Barycentric Julian Date; BJD – 2457000) is shifted by ~ 20 min relative to the expected value from the linear ephemeris as derived from **TESS** photometry alone. The left panel of Figure 8.7 shows the deviation of the measured transit midpoints from these particular ephemerides.

This apparent mismatch in the mid-transit time has a more significant influence on the result obtained from the **RVS** than that from the shadow and slope. This is because the latter two methods are less governed by ingress and egress data. A shift by a few minutes will lead to a large difference between the RV_{RM} model and data (Figure 8.7). Such a difference is largest for ingress and egress data. Such data contribute less to the results for the shadow or slope methods and more importantly a shift in timing between model and data can be absorbed into the systemic velocity without significantly influencing the result for λ . RV_{RM} data—if pre-ingress and/or post-egress data have been obtained—do not allow for such a shift.

We investigated this further by plotting the posteriors for P and T_0 as obtained from photometry only. We derived these using data from Sectors 14 and 15 only, from Sector 41 only, and from all sectors combined. The results can be seen in Figure 8.8. The results from the different sectors appear to be only marginally consistent. Other parameters showed inconsistencies in addition to λ . The impact parameter was found to be 0.23 ± 0.05 . This value is inconsistent with the value obtained from photometry alone.

Given these considerations we conclude that a model employing a linear ephemeris is not adequate for modelling the system. However, we do not have enough data to constrain a physical model predicting such transit timing variations (TTVs) for the observed spectroscopic transit. We therefore decided to introduce an additional parameter ΔT_0 . This parameter allows the mid-transit time of the specific transit observed with **HARPS**-N to float freely relative to the prediction from the linear ephemeris, now only determined from the **TESS** photometry. Adding this additional parameter will reduce the precision of our final result in λ as we ask our spectroscopic data to constrain an additional parameter, which would have otherwise been constrained by the photometry. However, this is a conservative choice as any possible TTVs will now not bias our result for the projected **obliquity**.

Implementing this change to our model, the goodness of the model to data comparison improved, as measured via χ^2 for all approaches we employed to determine λ . The most noticeable improvement occurred for the χ^2 of the RM **RV** approach, where χ^2 decreased by factor of ≈ 2.8 .

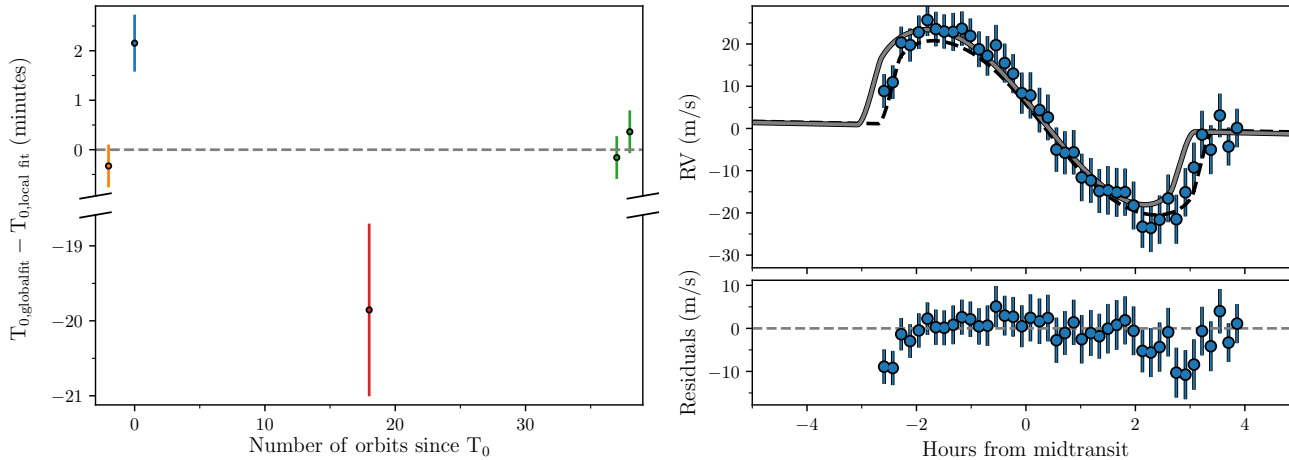


Figure 8.7 | Transit timing differences. *Left:* Timing differences between the predictions of transit midpoints derived from linear ephemeris obtained via a global fit to all photometric data and transit midpoints measured for each of the transits individually (including the spectroscopic transit), i.e., T_0 from Table 8.2. We also show a local fit, where T_0 is free to vary for each of the specific transits. The transits from [TESS](#) Sectors 14, 15, and 41 are plotted in orange, blue, and green, respectively. The transit observed with [HARPS](#)-N is plotted with a red symbol. The spectroscopic transit is offset by several σ from its expected timing. *Right:* Similar to Figure 8.6 panel c), but now assuming linear ephemeris resulting in a misaligned ($\lambda = -31 \pm 6^\circ$) orbit shown in grey. Clearly, this model does not fit the data as well as the dashed line, which is the model in panel c) of Figure 8.6. The lower panel displays the residuals between the linear ephemeris model and data. There are large systematic differences between data and model, specifically near ingress and egress, as expected if there is a timing offset.

More importantly, the functional shape of the best fitting RM **RV** model is a much better fit to the anomalous **RVS** obtained during transit. This is clearly seen when comparing the residuals of the right panel in Figure 8.7 to Figure 8.6 c). Finally, the impact parameters obtained from all three methods now agree, as expected, with the value obtained from photometry alone $b = 0.10^{+0.04}_{-0.10}$. We therefore regard this model, including a time-shift, as the most appropriate.

We have a remaining concern in regards to the **RV** data. As can be seen from the lower panel in Figure 8.6 c), almost all **RV** data points from the transit night agree within their 1σ uncertainties with the model. This suggests that the uncertainty intervals provided by the DRS² pipeline are too conservative. There are six effective parameters that are (also) controlled by the **HARPS-N RVS** (ΔT_0 , $\gamma_{\text{HARPS-N}}$, λ , $v \sin i$, $q_1 + q_2$, ζ , and ξ , of which the last four are further constrained by priors and the OOT **CCF**). There are 42 **HARPS-N RV** measurements resulting in 36 degrees of freedom. We find a χ^2 of 10.07 and a reduced χ^2 of 0.28. This would suggest that the uncertainty interval we obtain for the projected **obliquity** from the fit to the **RVS** might be overestimated. Indeed, the interval is about twice the size as for the other two methods. Another indication that the **RV** confidence interval might be overestimated comes from a comparison to the other two approaches. Given the moderate projected rotation speed of the star, the uncertainty intervals between these different methods should not differ by a factor ~ 2 , as the shadow and slope methods would benefit more from the host having a larger $v \sin i$.

In summary, we find that our results for λ —using the three different methods on the same data—are consistent with each other ($\lambda = -1 \pm 12^\circ$, $\lambda = -2 \pm 6^\circ$, $\lambda = 0 \pm 7^\circ$) as expected; see Table 8.2. Given the uncertainty interval from the fit to the anomalous **RVS** (which is probably too large as a result of overly conservative **RV** uncertainties), we use the projected **obliquity** value as derived from the fit to the shadow as a final parameter, meaning $\lambda = -2 \pm 6^\circ$ is our final value for the projected **obliquity**.

8.5 Discussion

While finalising this manuscript we became aware of a recent measurement of the projected **obliquity** in this system by Sedaghati et al. (2022). These authors observed HD 332231 during a transit night in October 2020, employing the CARMENES high-resolution spectrograph (Quirrenbach et al.,

²: The "HIERARCH TNG DRS DVRMS" entry in the FITS header.

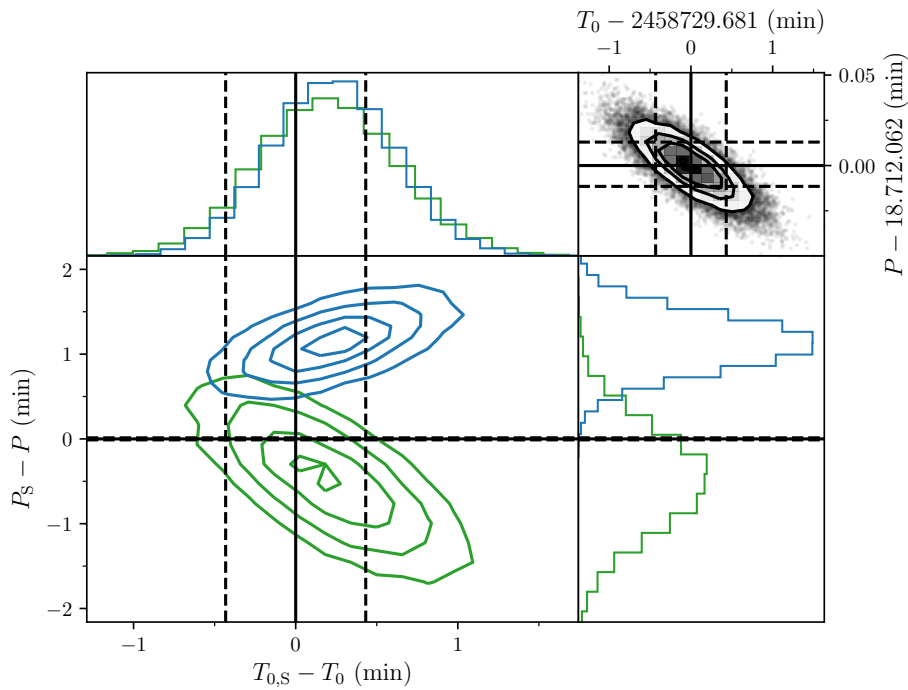


Figure 8.8 | Correlation between P and T_0 . Fit varying P and T_0 , but otherwise fixing the parameters from the [RV](#) run in Table 8.2. In blue we only fit the transits in Sectors 14 and 15, and in green we only fit the transits from Sector 41. We have subtracted P and T_0 from Table 8.2 from the results. Displayed in the top right corner are the posteriors for these, and their values and confidence intervals are shown as black lines in both correlation plots. Furthermore, we used this period to shift T_0 from Sector 41, i.e. subtracting $37 \times P$. The confidence intervals for the period, translating to different mid-transit points for different epochs, are only marginally consistent, indicating the possibility of TTVs.

[2014](#)) installed at the 3.5 m telescope at the Calar Alto Observatory, Spain. This team finds a projected obliquity of $\lambda = -42.0^{+11.3}_{-10.6} \text{ }^\circ$. This value is not in agreement with our final result, $\lambda = -2 \pm 6 \text{ }^\circ$. We suspect that there might be at least two reasons for the apparent disagreement between these two measurements. Firstly, these latter authors relied on priors solely derived from the Sector 14 and 15 [TESS](#) photometry by [Dalba et al. \(2020\)](#), and their spectroscopic transit observations were obtained about a year after these [TESS](#) observations (about two months after our spectroscopic transit observations). Therefore, their assumption of linear ephemeris might be as

erroneous as our initial assumption of linear ephemeris. Indeed, the result of their analysis of the anomalous [RVS](#) observed during transit is similar to our initial result ($\lambda = -31 \pm 6^\circ$) using the linear ephemeris derived from the [TESS](#) photometry.

A second potential reason for the mismatch might be connected to their result for the projected stellar rotation speed. They find $v \sin i = 16.3^{+6.9}_{-4.4} \text{ km s}^{-1}$. This is significantly higher than the three values ($5.3 \pm 1.0 \text{ km s}^{-1}$, $5.4 \pm 1.0 \text{ km s}^{-1}$, and $7.0 \pm 0.5 \text{ km s}^{-1}$) reported in the discovery paper (Dalba et al., 2020). That value is also difficult to reconcile with the width of the [CCFS](#) we observed; see Figure 8.4. Therefore, it is also significantly higher than what we find in our overall analysis. As discussed in Albrecht et al. (2011) for low-impact transits such as this one, a prior on $v \sin i$ can have significant influence on the derived value for λ . It would be interesting to investigate whether using a lower $v \sin i$ value, as well as allowing for a shift in transit mid-time, would not only lead to a consistent result for λ , but also to a similar result for the specific transit mid-time, as the spectroscopic transits are only two months apart.

With the data at hand, we cannot determine the cause of the departure from linear ephemeris with certainty. One possibility would be a second planet whose gravitational influence perturbs the orbit of planet b from a purely Keplerian orbit. The presence and parameters of such a potential third body may be investigated by additional RV monitoring to detect long-term RV drifts, and ground-based transit observations to measure TTVs. Also, in August 2022, the system will be observed again in [TESS](#) Sector 55. Additionally, upcoming [Gaia](#) (Gaia Collaboration et al., 2016) data releases should be able to further clarify the nature of this potential body by detecting or giving upper limits to the reflex motion of the central star caused by such a potential outer body.

Regarding the additional [RV](#) monitoring, Dalba et al. (2020) (Section 4.3) investigated the possibility of a linear trend in their [RVS](#). These authors found that a model including a first-order acceleration term is indistinguishable from a model without an acceleration parameter. As our [HARPS-N](#) transit observations do not add to the baseline given the [RV](#) offset between the spectrographs, the conclusion remains that we are currently not in a position to expand further on this.

Our result for the projected [obliquity](#), $\lambda = -2 \pm 6^\circ$, suggests that the [obliquity](#), ψ , is also low, and that the system is spin-orbit aligned. The finding that $\psi \sim \lambda$ is supported by the effective temperature of $\sim 6100 \text{ K}$ and the projected stellar rotation of $\sim 5.7 \text{ km s}^{-1}$, which according to Louden et al. (2021) is consistent with a stellar inclination of close to 90° .

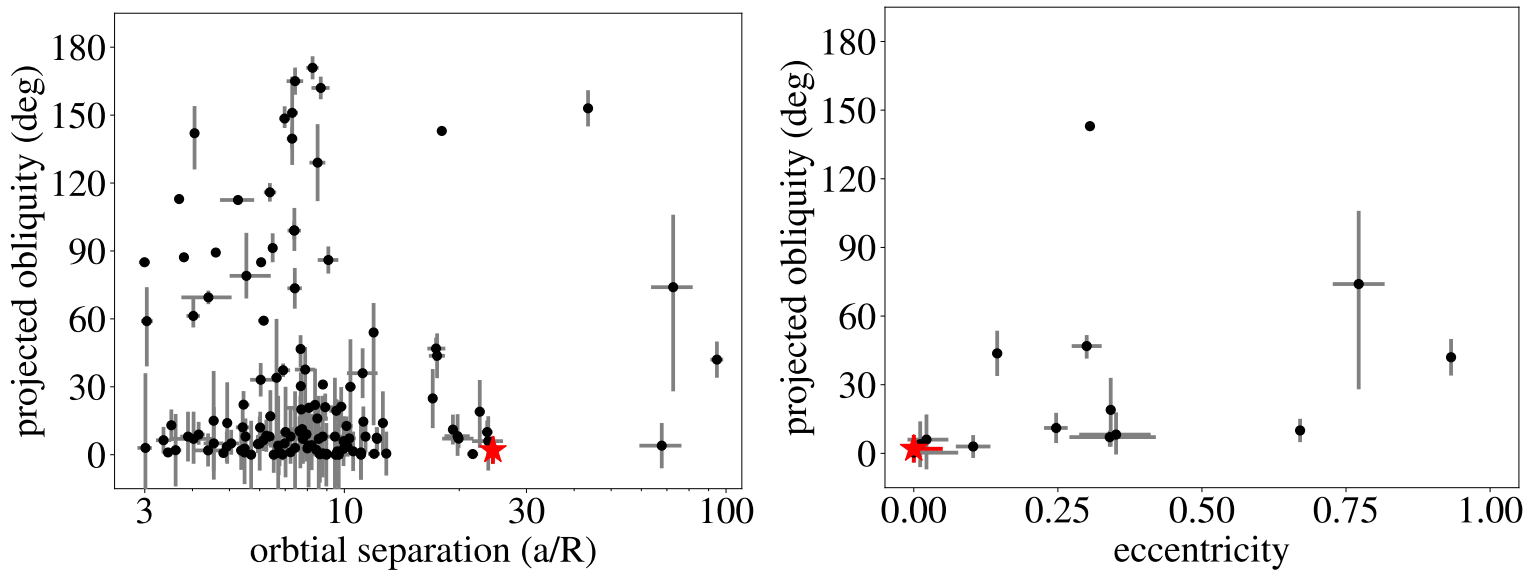


Figure 8.9 | Comparing HD 332231 to the literature. *Left:* Projected obliquities versus orbital separations *Right:* Projected obliquities versus orbital eccentricities. We only include planets more massive than $0.2 M_{\text{Jupiter}}$. In the right panel, we further only plot planets on large ($a/R > 15$) orbits and with $\sigma_{\text{ecc}} < 0.1$. HD 332231 is marked by a red star; the system belongs to the class of systems with low orbital misalignment, and low orbital eccentricity.

Given the a/R of about 24.5, this system might not have been influenced by tides. Therefore, the alignment we are seeing might be primordial. This, together with the low eccentricity of the orbit ($e = 0.029_{-0.024}^{+0.014}$), fits in a picture that orbital inclinations are often associated with high eccentricities, as illustrated in Figure 8.9. In this picture, HD 332231 b has not undergone [high-eccentricity migration](#). Dawson and Murray-Clay (2013) noticed that eccentric WJs tend to orbit metal rich ($[\text{Fe}/\text{H}] > 0$) hosts while planets on circular orbits tend to be found around stars with lower metallicities. The solar metallicity measured for HD 332231 agrees with this picture.

8.6 Conclusion

We measured the projected [obliquity](#) of the bright F8 dwarf HD 332231 using [HARPS](#)-N data acquired during transit of the warm giant planet HD 332231 b discovered by Dalba et al. (2020). We used three different approaches to analyse the [RM EFFECT](#). We model the planet shadow, the subplanetary velocities, and the anomalous in-transit [RVS](#), obtaining fully consistent results. Our measurement of the projected [obliquity](#) $\lambda = -2 \pm 6^\circ$ is consistent with alignment. Since the discovery of the planet, additional [TESS](#) photometry from Sector 41 has become available and we use this here to further refine the system parameters, specifically the planetary radius and linear ephemeris. We find an apparent shift of ≈ 20 min in the mid-transit time of the transit observed on 4 August, 2020, with [HARPS](#)-N at the TNG. This shift is relative to the linear ephemeris obtained from transits observed by [TESS](#) Summer 2019 and 2021. This shift might be explained by the presence of a third body in the system and future [RV](#), transit, and astrometric observations should be able to find such a body. While there is a non-zero probability that the system will end up in an aligned configuration through a violent dynamical process, the most probable interpretation of our findings is that the system architecture is the result of the planet having migrated to its current orbit via [disc migration](#) or that it was born [in situ](#).

9

The low density, hot Jupiter TOI-640 b is on a polar orbit

Continuing on the exoplanet system architectures, we will look at the TOI-640 system. In Albrecht et al. (2021) we discovered a tendency for planets to orbit over the stellar poles — the Preponderance of Perpendicular Planets. This is especially true for planets around hotter stars (> 6250 K), which is the case for TOI-640. Furthermore, the appreciable rotation and high impact parameter makes this a very interesting system to study through the RM EFFECT.

The paper has been accepted for publication as

E. Knudstrup, S. H. Albrecht, D. Gandolfi, M. L. Marcussen,
E. Goffo, L. M. Serrano, F. Dai, S. Redfield, T. Hirano,
S. Csizmadia, W. D. Cochran, H. J. Deeg, M. Fridlund,
K. W. F. Lam, J. H. Livingston, R. Luque, N. Narita, E. Palle,
C. M. Persson, and V. Van Eylen (2023b). “A puffy polar planet.
The low density, hot Jupiter TOI-640 b is on a polar orbit”.

Astronomy and Astrophysics 671, A164

and is in press for publication in *Astronomy and Astrophysics*. For this study, I proposed the target and scheduled the transit observations. I did the data analysis, and Simon H. Albrecht and I wrote the paper. The tables containing RVS, limb-darkening coefficients, and hyper parameters (Tables A.1-A.3 in Knudstrup et al., 2023b) and the figure showing the resulting obliquity distribution using an empirical relation (Fig. A.4 in Knudstrup et al., 2023b) have been removed in the version presented here.

As discussed in Section 2.4.2.3, we need to determine the rotation period and from that derive the stellar inclination in order to determine the obliquity. Here I would like to highlight a piece of (python) software

I have developed to do just that, which was used in this study. The code, coPsi, is available on [GitHub](#) and the documentation can be found [here](#).

Summary of the Chapter

TOI-640 b is a hot, puffy Jupiter with a mass of $0.57 \pm 0.02 M_J$ and radius of $1.72 \pm 0.05 R_J$, orbiting a slightly evolved F-type star with a separation of $6.33^{+0.07}_{-0.06} R_\star$. Through spectroscopic in-transit observations made with the **HARPS** spectrograph, we measured the **RM EFFECT**, analysing both in-transit **RVS** and the distortion of the stellar spectral lines. From these observations, we find the host star to have a projected **obliquity** of $\lambda = 184 \pm 3^\circ$. From the **TESS** light curve, we measured the stellar rotation period, allowing us to determine the stellar inclination, $i_\star = 23^{+30}_{-2}$, meaning we are viewing the star pole-on. Combining this with the orbital inclination allowed us to calculate the host star **obliquity**, $\psi = 104 \pm 2^\circ$. TOI-640 b joins a group of planets orbiting over stellar poles within the range $80^\circ - 125^\circ$. The origin of this orbital configuration is not well understood.

9.1 Introduction

Before 1992, the only planetary system we knew of was the Solar System. The neat and ordered structure we see in the Solar System therefore formed the architectural drawing for planetary formation and evolution. However, with the detection of the first exoplanet, it immediately became clear that this schematic does not apply to all systems. For instance, the very first exoplanet discovered is orbiting a pulsar (Wolszczan and Frail, 1992), the first exoplanet around a Sun-like star is a Jupiter-sized planet on a ~ 4 d orbit (Mayor and Queloz, 1995), and some systems harbour planets on wildly eccentric orbits (e.g. Cochran et al., 2008). The type of host stars, the orbital separations, and eccentricities are just some of the parameters indicating how different exoplanet systems can be from the Solar System.

Another parameter is the angle between the stellar spin axis of the host and the orbital axis of the planet, the spin-orbit angle, or the **obliquity** ψ . At $7.155 \pm 0.002^\circ$ (Beck and Giles, 2005), the **obliquity** of the Solar System is relatively low. In contrast, in exoplanet systems, measurements of ψ , or its projection on the sky λ , or the difference along the line of sight between orbital and stellar spin, display a large variety of values. The configurations range from well aligned to (moderately) misaligned, and there are even retrograde systems (see e.g. the review by Albrecht et al., 2022, and references

therein). There is also a curious trend reported by Albrecht et al., 2021; systems for which ψ has been measured are either consistent with good alignment or the planets orbit over the stellar poles. This preponderance of perpendicular planets was not evident from λ measurements alone, as without additional knowledge, meaningful inferences about ψ cannot be drawn from λ measurements (Fabrycky and Winn, 2009).

Here we aim to measure the host star [obliquity](#) in the TOI-640 system discovered and characterised by Rodriguez et al. (2021). To this end, we make use of the [RM EFFECT](#), an apparent distortion of the stellar line shapes caused by a transiting body blocking part of the rotating stellar disk. The [RM EFFECT](#) allows us to measure the sky-projected [obliquity](#), λ . To measure the stellar inclination, we use light curves from [TESS](#) (Ricker et al., 2015). Together with knowledge of the orbital inclination, we can infer the spin-orbit angle of our target system.

The paper is organised as follows. In Section 9.2, we present the observations, both photometric and spectroscopic. Section 9.3 presents the determination of the [obliquity](#) of the host star. Our new [RVS](#) and photometry allow us to also update a number of other system parameters. We discuss these together with our result on the spin-orbit angle in Section 9.4 before giving our conclusions in Section 9.5.

9.2 Observations

9.2.1 TESS photometry

Table 9.1 lists a selection of parameters determined by Rodriguez et al. (2021). These authors presented [TESS](#) data of TOI-640 from Sectors 6 and 7 taken with a cadence of 30 min. Additional [TESS](#) photometry has become available since then, as the system was observed again in Sectors 33 and 34. This time the system was observed with a cadence of 2 min. Figure A.9 displays the [TESS](#) data from all four sectors.

We downloaded and reduced the [TESS](#) data utilising the python package [lightkurve](#) (Lightkurve Collaboration et al., 2018). First, we corrected for noise induced by the motion of the spacecraft and removed scattered light using the [RegressionCorrector](#) routine. The result is shown in the top panel of Figure A.9. To exclude outliers, we then (temporarily) removed the transits from the planet using the best-fitting transit parameters, which were determined by fitting the light curve iteratively. The resulting light curves are shown in the middle panel of Figure A.9, where we also overplotted a Savitzky-Golay (Savitzky and Golay, 1964) filter to (again

Table 9.1 | TOI-640 system parameters. Selected stellar, orbital, and planetary parameters from Rodriguez et al. (2021).

Parameter	Value
Stellar mass, M_\star (M_\odot)	$1.536^{+0.069}_{-0.076}$
Stellar radius, R_\star (R_\odot)	$2.082^{+0.064}_{-0.058}$
Effective temperature, T_{eff} (K)	6460^{+130}_{-150}
Surface gravity, $\log g$ (dex)	$3.987^{+0.030}_{-0.036}$
Metallicity (dex), [Fe/H]	$0.072^{+0.085}_{-0.076}$
Age, τ (Gyr)	$1.99^{+0.55}_{-0.40}$
Proj. rotational velocity, $v \sin i_\star$ (km s $^{-1}$)	6.1 ± 0.5
Macro-turbulence, v_{mac} (km s $^{-1}$)	6.32 ± 1.37
Orbital period, P (days)	$5.0037775(48)$
Planet-to-star radius ratio, R_p/R_\star	$0.08738^{+0.00091}_{-0.00086}$
Semi-major axis / star radius, a/R_\star	$6.82^{+0.22}_{-0.24}$
Velocity semi-amplitude, K (m s $^{-1}$)	78 ± 14
Impact parameter, b	$0.8763^{+0.0063}_{-0.0067}$
Eccentricity, e	$0.050^{+0.054}_{-0.035}$
Planet radius, R_p (R_J)	$1.771^{+0.060}_{-0.056}$
Planet mass, M_p (M_J)	0.88 ± 0.16

temporarily) smooth the light curve. Points more than 5σ away from the smoothed light curves were rejected (19 out of 36,918 points were removed). The bottom panel of Figure A.9 displays the unfiltered light curves with outliers excluded, but with the transits re-injected. This is the light curve we use in the analysis for determining the projected spin-orbit angle in Section 9.3.1, whereas we use the light curve with the transits removed for determining the rotation period in Section 9.3.2.

9.2.2 HARPS spectroscopy

To measure the RM EFFECT, we observed a transit of TOI-640 b that occurred during the night 2022 February 26 UT using HARPS (Mayor et al., 2003) as part of our observing programme 106.21TJ.001 (PI: Gandolfi). HARPS is mounted at the European Southern Observatory (ESO)-3.6 m telescope at La Silla, Chile. We obtained 22 spectra on the transit night of which 4 were acquired before the beginning of ingress, 14 during transit, and 4 after egress. The average exposure time was 900 s and the median SNR

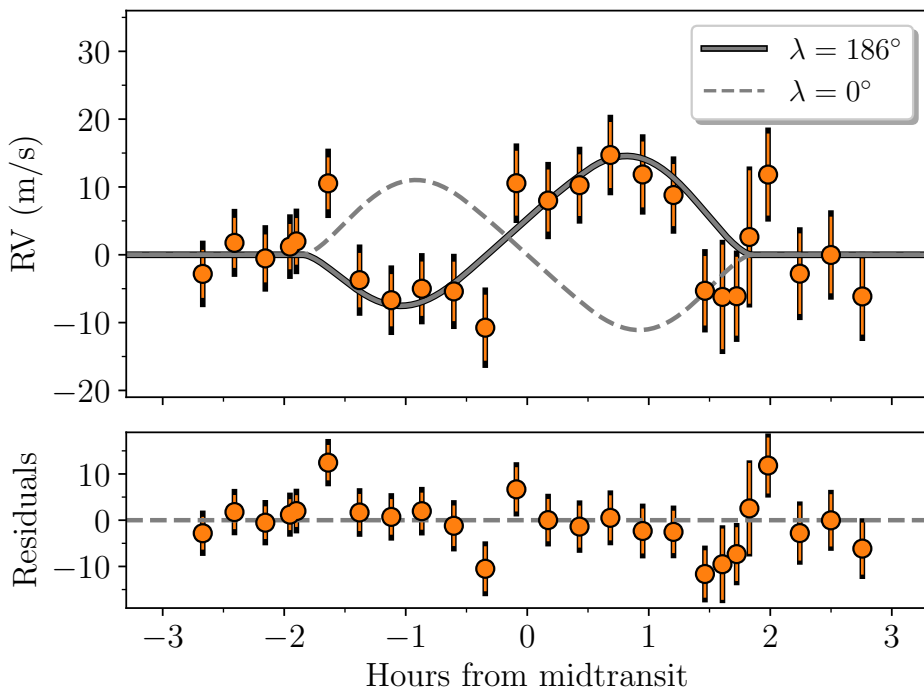


Figure 9.1 | The Rossiter-McLaughlin effect of TOI-640. The RM EFFECT as seen from HARPS RVS centred around the mid-transit time after subtracting the Keplerian motion induced by the planet. The grey line shows the RM EFFECT with the best-fitting (retrograde) model as the solid line and an aligned model as the dashed line. The error bars include the jitter term from our MCMC added in quadrature, shown as the black extension.

per pixel at 550 nm was 45. We continued to monitor the system using HARPS until 2022 November 23 UT covering a total time span of 271 days with an additional 40 RVS. For these monitoring observations, the exposure times varied between 1200 s and 1500 s depending on sky conditions, and the median SNR was 50. The extracted RVS, their associated errors, and photometric mid-times are shown in Figure A.10. Figure 9.1 shows the HARPS RVS centred on the mid-transit time, focusing in on the RM EFFECT.

9.3 Stellar obliquity

In this section, we first conduct a joint fit of both the photometric and spectroscopic data to measure the projected spin-orbit angle of TOI-640

(Section 9.3.1). We then determine the stellar inclination along the line of sight making use of **TESS** photometry (Section 9.3.2) and through the use of an empirical relation (Section 9.3.3). Together with the orbital inclination, we can then determine the stellar **obliquity** (Section 9.3.4). Our results for ψ as well as other system parameters are then discussed in Section 9.4.

9.3.1 Projected obliquity from the RM effect

Spectrally resolved stellar lines observed during transits (or eclipses) will display distortions; this is known as the **RM EFFECT**. For example, in a system where the projections of the stellar spin axis and the orbital axis of the planet are aligned (low projected **obliquity**), a transiting planet would first hide sections of the approaching stellar surface. A distortion of the lines with a negative velocity (relative to the current **RV** of the star) will appear. During later phases of the transit, further areas of the stellar surface with positive **RVS** (redshifted) will be hidden from view. This distortion can also be sensed as anomalous **RVS** during transits. In this case, first positive and later negative **RVS** are observed. However, if the spin-orbit angle is larger than 90° (a retrograde configuration) then the time evolution of the distortion and **RVS** is reversed. From a glance at Figure 9.1 and Figure 9.2, it appears as if the orbit of TOI-640 b is indeed retrograde.

Our approach to a quantitative analysis of the **RM EFFECT** is similar to the analyses performed in Knudstrup and Albrecht (2022) and Knudstrup et al. (2022), and we briefly summarise it here. Also, the following procedure is included in the python package `tracit`¹, which was used in these latter two publications.

We performed a joint fit of the photometric and spectroscopic data. Specifically, we performed two different analyses of the spectroscopic data. First, we analysed the anomalous **RVS** obtained during the transit. We then performed a second analysis where we do not use the **RVS** during transit but the underlying distortions of the line shapes, or the so-called **planetary shadow**. We did this to check for consistency between the different measurement approaches (Albrecht et al., 2007). In both cases, we also made use of the orbital **RV** measurements and the **TESS** photometry and we applied the same priors.

When determining λ through the anomalous **RVS**, we used the **RVS** obtained from the **HARPS** Data Reduction Software (DRS; Lovis and Pepe, 2007). When analysing the **planetary shadow**, we used the **CCFS** obtained

¹: <https://tracit.readthedocs.io/en/latest/>

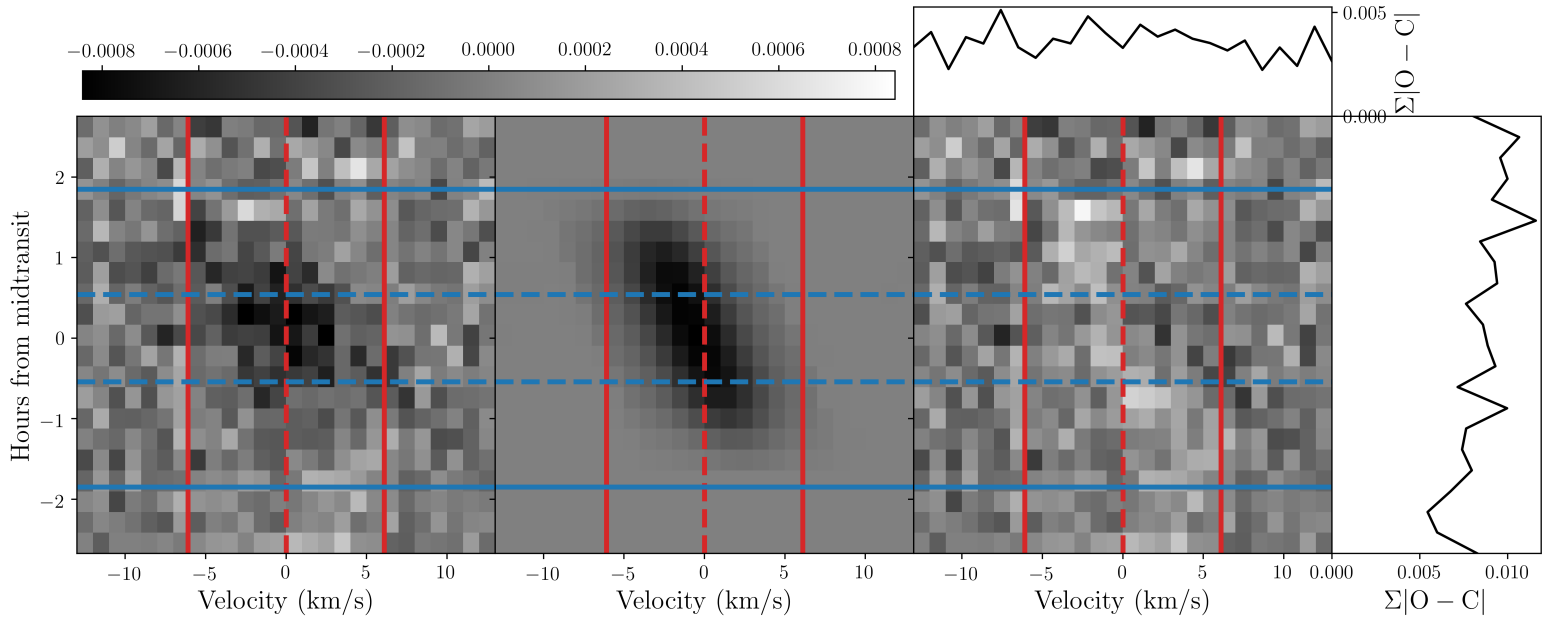


Figure 9.2 | Planetary shadow. *Left:* Distortion of the stellar absorption lines as seen for our observations with HARPS taken on the transit night. The vertical solid lines denote $\pm v \sin i_\star$, and the vertical dashed line is at $v = 0$ km s⁻¹. The horizontal dashed lines mark the points of second and third contact, which is when the planet is found completely within the stellar disk, and the solid lines denote the first and fourth contact points, where the planetary and stellar disk start to overlap. *Middle:* Best-fitting model of the distortion. *Right:* Residuals from subtracting the best-fitting model from the data. The horizontal bar on top shows the strength of the signal.

from the DRS as a proxy for the stellar absorption lines. With **HARPS**' resolution of $R = 120\,000$, the point spread function (PSF) has a full width at half maximum (FWHM) of 2.5 km s^{-1} or an equivalent dispersion of $\sigma \approx 1 \text{ km s}^{-1}$. The **CCFS** delivered by the **HARPS** DRS are over-sampled with a datum every 0.25 km s^{-1} . To account for this, we interpolated the **CCFS** onto a grid with a resolution of 1 km s^{-1} . This is the same approach as taken in Knudstrup and Albrecht, 2022 and similar to the approach taken by Cegla et al. (2016) for instance, where every fourth datum in the grid is sampled.

The relevant parameters in both approaches are the orbital period P , mid-transit time T_0 , planet-to-star radius ratio R_p/R_\star , scaled semi-major axis a/R_\star , orbital inclination i , **RV** semi-amplitude K , orbital eccentricity e , argument of periastron ω , projected stellar **obliquity** λ , projected stellar rotation speed $v \sin i_\star$, **macro-turbulence** ζ , **micro-turbulence** ξ , systemic velocity γ , and two sets of separate pairs of quadratic limb-darkening coefficients c_1, c_2 , for **TESS** and **HARPS**.

We applied Gaussian priors on $v \sin i_\star$ (from Table 9.1), as well as ζ and ξ estimated from the relations in Doyle et al. (2014) and Bruntt et al. (2010), respectively, using the parameters in Table 9.1. The Gaussian priors for the limb-darkening coefficients were obtained from the tables by Claret et al. (2013) and Claret (2018) for **HARPS** and **TESS**, respectively. Uncertainties of 0.1 were assumed. Uniform priors were applied for all other parameters.

To model the **RM EFFECT** for the **RVS**, we used the code by Hirano et al. (2011), while we used the formulation in Albrecht et al. (2007) and Albrecht et al. (2013b) to model the **planetary shadow**. We modelled the **TESS** data using the batman package (Kreidberg, 2015). This was done with the inclusion of **GP** regression –utilising the library celerite (Foreman-Mackey et al., 2017)— to characterise the photometric noise (stellar and instrumental). For our **GP**, we used a Matérn- $3/2$ kernel, which is characterised by two hyperparameters; the amplitude, A , and the timescale, τ . We sampled the posterior distribution for the parameters through **MCMC** sampling using the code emcee (Foreman-Mackey et al., 2013). In our **MCMC**, we stepped in $\sqrt{e} \cos \omega$ and $\sqrt{e} \sin \omega$ as opposed to stepping in e and ω directly. For the limb-darkening parameters, we stepped in the sum of the coefficients while keeping the difference fixed. Furthermore, we stepped in $\cos i$ instead of i , allowing us to apply a flat prior assuming an isotropic spin distribution a priori. Stepping parameters and priors are listed in Table 9.2. Our likelihood is defined as

$$\log \mathcal{L} = -0.5 \sum_{i=1}^N \left[\frac{(O_i - C_i)^2}{\sigma_i^2} + \log 2\pi\sigma_i^2 \right] + \sum_{j=1}^M \mathcal{P}_j, \quad (9.1)$$

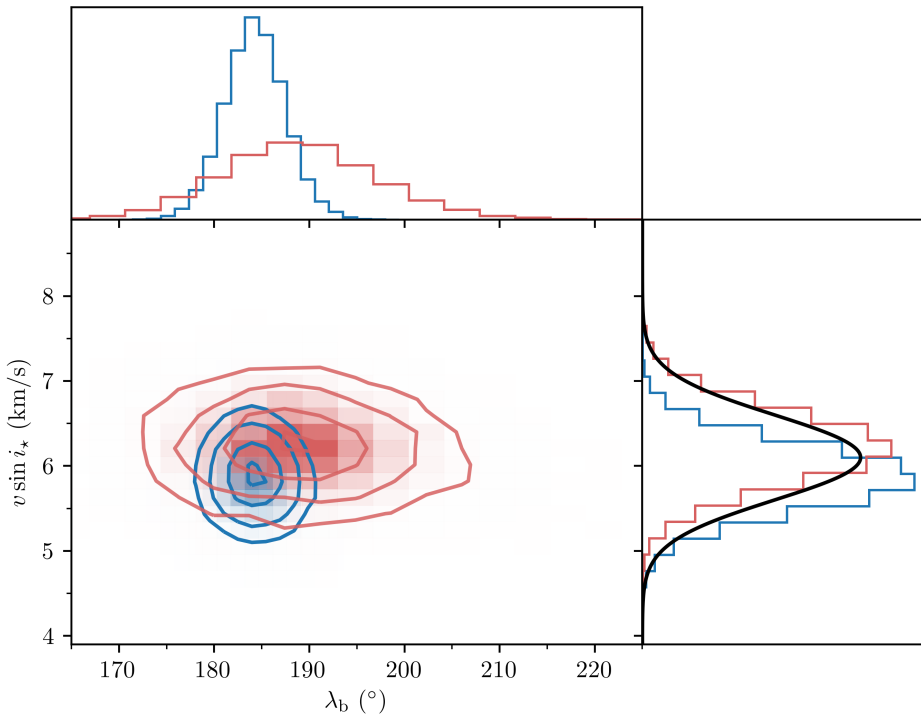


Figure 9.3 | 2D histograms. The correlation between λ and $v \sin i_*$ from our MCMCs. Blue shows the results from our RV run, while red is from the shadow run.

where N indicates the total number of data points from photometry and RVS. C_i represents the model corresponding to the observed data point O_i , and \mathcal{P}_j is the prior on the j th parameter.

Finally, before starting the joint spectroscopic photometric MCMC runs, we performed simple minimisations on each of the three data types. We then added ‘jitter’ terms in quadrature to the respective uncertainties until reduced χ^2 of 1 were obtained. This was done in an attempt to ensure proper weighting between spectroscopic and photometric data.

The observed RVS and the best-fitting model are shown in Figure 9.1, and the results are presented in the fourth column of Table 9.2. The observed shadow and best-fitting model can be seen in Figure 9.2 with the results presented in the fifth column of Table 9.2. We show the correlation plot for $v \sin i_*$ and λ for both runs in Figure 9.3. An extended correlation plot for more parameters can be found in Figure A.8.

The amplitude of the RM signal (relative to the noise) seen in Figure 9.1 and Figure 9.2 is modest; nevertheless the uncertainties in our λ measure-

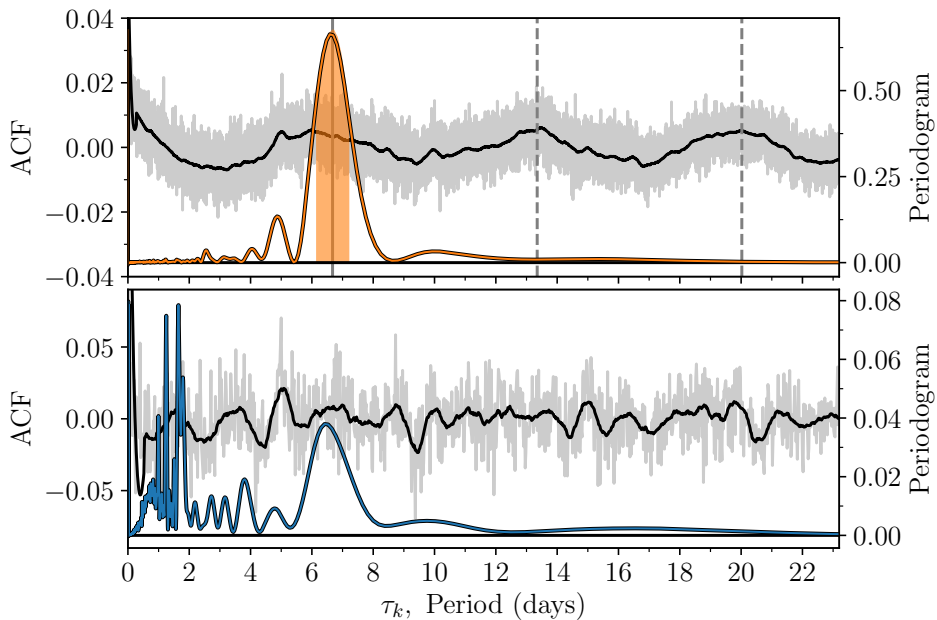


Figure 9.4 | Autocorrelation function. The ACFs are shown as the grey curves with a smoothed version in black. The (coloured) periodogram is calculated from the smoothed ACF. The *y*-axis on the left (right) is for the ACF (periodogram). *Top:* The 2 min cadence ACF with the corresponding periodogram. The vertical grey line denotes the measured rotation period, and the dashed lines are integer values of this value. Shown as the shaded area is the confidence interval for the rotation period. *Bottom:* The 30 min cadence ACF.

ments are comparably low. This is because the large impact parameter of $0.904^{+0.005}_{-0.007}$ acts as a lever. Even a small change in λ leads to a transit chord passing over stellar surface areas with substantially different rotational [RVS](#).

The λ measurement from the analysis of the [RVS](#) comes out to $184 \pm 3^\circ$, and has a lower uncertainty than the measurement from the planet shadow $189 \pm 8^\circ$. This is because the overall line width—mainly governed by $v \sin i_*$ relative to the width of the distortion—is only modest (Figure 9.2). A larger $v \sin i_*$ value would have reversed the situation as it would have lead to a more localised distortion (planet shadow) in the lines (Albrecht et al., 2022). At the same time, a larger $v \sin i_*$ leads to a larger [RV](#) uncertainty. These two advantages of analysing the line distortions relative to analysing the [RVS](#) vanish for lower $v \sin i_*$. In addition, the shadow measurement

requires alignment and normalisation of the [CCFS](#) (Knudstrup and Albrecht, 2022). This takes away some of the predictive power from the [CCFS](#) as these additional ‘hyper parameters’ (not to be confused with the [GP](#) hyper parameters) have to be determined (Albrecht et al., 2013a). This process is similar to the ‘Hyperplane Least Squares’ method described and tested by Bakos et al. (2010). Here, for the case of TOI-640, we therefore use the values obtained via the analysis of the anomalous [RVS](#) moving forward.

Up to this point, we have determined λ , the projected spin-orbit angle. Next, we determine the stellar inclination, i_* , using two different methods. Together with the orbital inclination, this allows us to determine the [obliquity](#), ψ .

9.3.2 Stellar inclination from TESS photometry

The starting point for our first inclination measurement is the rotation period of the star, P_{rot} , as determined from [TESS](#) photometry in Figure A.9. We used the light curves in the middle, where the transits have been removed by the best-fitting transit model. We measured the rotation period using the autocorrelation method (e.g. McQuillan et al., 2013). We do this by calculating the autocorrelation function (ACF) for the 2 min cadence and 30 min cadence separately. We then smoothed the ACF using a Savitzky-Golay filter from which we calculated the Generalised Lomb-Scargle (GLS; Lomb, 1976; Scargle, 1982) periodogram.

While we can clearly identify a single peak (at around 6.7 days) in the periodogram for the 2 min cadence case, we also see some additional features most likely associated with momentum dumps of the spacecraft causing ‘jumps’ in the light curves. An example of how these jumps affect the ACF and periodogram is illustrated in the third column of Fig. 2 in McQuillan et al. (2013). We therefore applied a Savitzky-Golay filter to the light curves to remove these jumps. The resulting ACFs and periodograms are shown in Figure 9.4. Evidently, the rotation is detected much more clearly for the 2 min cadence case, but it is also apparent in the 30 min cadence. We therefore proceeded with the results from the 2 min cadence periodogram.

We fitted a Gaussian to the peak in the periodogram to get an estimate of the period and the uncertainty. From this, we got a rotation period of $P_{\text{rot}} = 6.7 \pm 0.6$ d, which we can use with $R_* = 2.082 \pm 0.061 R_\odot$ to calculate the stellar inclination from

$$\sin i_* = \frac{P_{\text{rot}} v \sin i_*}{2\pi R_*}. \quad (9.2)$$

We followed the approach in Masuda and Winn (2020) to properly calculate i_* from Equation (9.2), meaning we accounted for the fact that v and $v \sin i_*$ are not independent. From this, we get a rotation speed at the equator of $v = 14 \pm 2 \text{ km s}^{-1}$ and subsequently a stellar inclination of $i_* = 23^{+3}_{-2}^\circ$.

9.3.3 Stellar inclination from the empirical relation

In the second approach, we used the results from Louden et al. (2021), who investigated the [obliquities](#) of *Kepler* planets around hot stars. This required that the authors determine the v distribution of a sample of control stars without detected transiting planets. From that sample, they obtained a relation between the mean rotation velocity of a star as a function of the effective temperature. We can use this relation with the T_{eff} from Table 9.1 to calculate i_* . We obtain $i_* = 20^{+6}_{-9} \text{ deg}$.

Using this relation from Louden et al. (2021) would not be appropriate in the case of tidal spin-up in which tides raised on the star by the planet change the rotation of the star. This effect has been suggested to take place in some hot Jupiter systems (e.g. Brown, 2014; Maxted et al., 2015; Yee et al., 2022). How effectively the planet can raise tides on the star is especially dependent on the separation, but also on the mass ratio (see e.g. Zahn, 1977). A useful metric to assess whether tides are effectively raised is given by $(M_p/M_*)(R_*/a)^3$ which for TOI-640 b is 1.4×10^{-6} , meaning that tides should not play an important role and suggesting that the use of the relation from Louden et al. (2021) is warranted. For our final result for the spin-orbit angle, we use the stellar inclination measurement from the previous section and simply note here that the two inclination measurements from this and the above section are consistent.

9.3.4 Stellar obliquity

As we now have values for i_* , i , and λ , we can use

$$\cos \psi = \sin i_* \sin i \cos \lambda + \cos i_* \cos i \quad (9.3)$$

to calculate the spin-orbit angle, ψ . Here we used our distributions for λ and i from our [MCMC](#) (Table 9.2), and we drew normally distributed values from $i_* = 23 \pm 2.5^\circ$ (determined above in Section 9.3.2) for each of these draws. There are two solutions. This is because our observations cannot distinguish between i_* and $180^\circ - i_*$; they can also not distinguish between (i, λ) and $(180^\circ - i, -\lambda)$. In the case of an exactly edge-on orbit ($i = 90^\circ$), the two solutions would collapse into one. The resulting histogram and

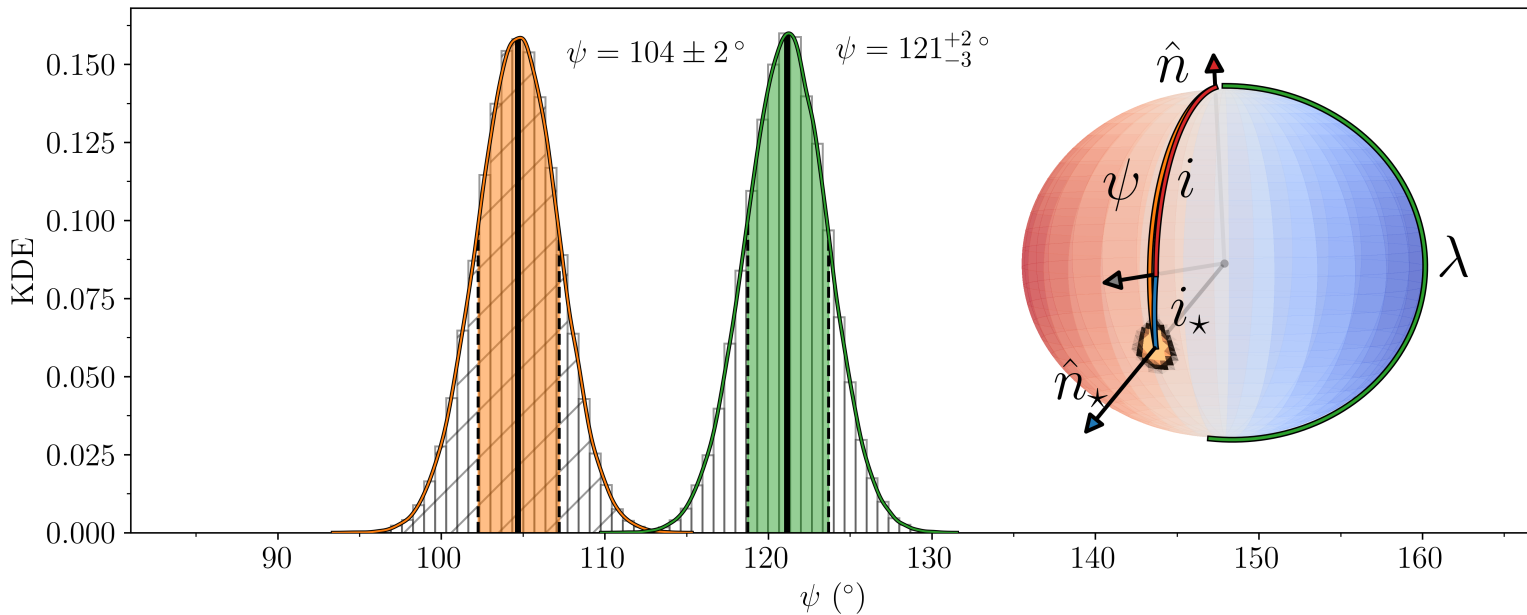


Figure 9.5 | Obliquity distributions. The histograms are the distributions for ψ calculated from the rotation period in Section 9.3.2 with the KDE overplotted as the solid lines. The coloured areas are the confidence intervals with the medians shown as the black lines. The orange distribution corresponds to using the orbital inclination, i , directly from our posteriors and the green is $i - 180^\circ$. On the sphere, we only show the “orange” distribution for ψ as the heatmap. We do this for a fixed value of i (in terms of how the sphere is oriented). The sphere is colour coded according to the perceived movement of the stellar disk with the approaching (receding) side in blue (red) for an observer along the line of sight, which is denoted by the grey arrow.

Table 9.2 | MCMC results for TOI-640. The median and highest posterior density at a confidence level of 0.68. \mathcal{U} or \mathcal{N} denotes that a uniform or a Gaussian prior, respectively, was applied during the run. Barycentric [TESS](#) Julian Date (BTJD) is defined as $\text{BJD} - 2457000.0$, BJD being the Barycentric Julian Date.

Parameter	Name	Prior	RV	Shadow
			Value	
Stepping parameters				
P	Period (days)	\mathcal{U}	$5.003777^{+0.000002}_{-0.000003}$	5.003777 ± 0.000003
T_0	Mid-transit time (BTJD)	\mathcal{U}	1459.7413 ± 0.0003	1459.7414 ± 0.0003
R_p/R_\star	Planet-to-star radius ratio	\mathcal{U}	$0.0851^{+0.0003}_{-0.0004}$	$0.0850^{+0.0004}_{-0.0003}$
a/R_\star	Semi-major axis to star radius ratio	\mathcal{U}	$6.33^{+0.07}_{-0.06}$	$6.32^{+0.08}_{-0.07}$
K	Velocity semi-amplitude (m s^{-1})	\mathcal{U}	50.1 ± 1.0	$50.0^{+1.1}_{-1.2}$
$\cos i$	Cosine of inclination	\mathcal{U}	$0.143^{+0.002}_{-0.003}$	$0.143^{+0.002}_{-0.003}$
$\sqrt{e} \cos \omega$		\mathcal{U}	$0.00^{+0.06}_{-0.07}$	0.02 ± 0.07
$\sqrt{e} \sin \omega$		\mathcal{U}	$0.06^{+0.03}_{-0.06}$	$0.07^{+0.03}_{-0.07}$
λ	Projected obliquity ($^\circ$)	\mathcal{U}	184 ± 3	189 ± 8
$v \sin i_\star$	Projected rotational velocity (km s^{-1})	$\mathcal{N}(6.1, 0.5)$	5.9 ± 0.4	6.2 ± 0.4
ζ	Macro-turbulence (km s^{-1})	$\mathcal{N}(6.65, 1.0)$	$6.6^{+0.9}_{-0.8}$	7.3 ± 0.8
ξ	Micro-turbulence (km s^{-1})	$\mathcal{N}(1.52, 1.0)$	1.7 ± 0.8	$1.6^{+0.8}_{-0.9}$
γ_{HARPS}	Systemic velocity HARPS (m s^{-1})	\mathcal{U}	40525.4 ± 0.7	$40525.6^{+0.9}_{-0.8}$
σ_{HARPS}	Jitter HARPS (m s^{-1})	\mathcal{U}	3.9 ± 0.7	4.2 ± 1.0
Derived parameters				
e	Eccentricity	-	< 0.013 (1σ)	< 0.016 (1σ)

ω	Argument of periastron ($^{\circ}$)	-	87^{+50}_{-55}	74^{+35}_{-63}
i	Inclination ($^{\circ}$)	-	$81.79^{+0.16}_{-0.12}$	$81.78^{+0.18}_{-0.14}$
b	Impact parameter	-	$0.904^{+0.005}_{-0.007}$	$0.904^{+0.006}_{-0.008}$
T_{41}	Total transit duration (hours)	-	$3.696^{+0.018}_{-0.019}$	$3.696^{+0.019}_{-0.020}$
T_{21}	Time from 1st to 2nd contact (hours)	-	1.32 ± 0.04	$1.31^{+0.04}_{-0.05}$
Physical parameters				
T_{eq}	Equilibrium temperature (K)	-	1816 ± 39	1817 ± 39
R_p	Planet radius (R_J)	-	1.72 ± 0.05	1.72 ± 0.05
M_p	Planet mass (M_J)	-	0.57 ± 0.02	0.57 ± 0.02
ρ_p	Planet density (g cm^{-3})	-	0.138 ± 0.013	0.138 ± 0.013
ρ_p	Planet density (ρ_J)	-	0.104 ± 0.010	0.104 ± 0.010

KDE are shown in orange and green in Figure 9.5. We find $104 \pm 2^\circ$ or $121^{+2}_{-3}^\circ$ for the spin-orbit angle. If the orbital inclination were exactly edge on ($i = 90^\circ$), then our result for the obliquity would be $\psi = 113^{+3}_{-2}^\circ$.

If we had not been able to determine the stellar rotation period from the TESS light curve then we could have attempted to determine ψ from the inclination measurement obtained in Section 9.3.3. In that case, we would have found a spin-orbit angle of $101^{+5}_{-9}^\circ$ or $117^{+6}_{-8}^\circ$ (the resulting histograms and KDEs for this approach are shown in Fig. A.4 in Knudstrup et al., 2023b). The results are consistent between the two inclination estimates. We report the spin-orbit angle estimated from the rotation period for the conventional orientation (i not $180^\circ - i$) as our final result, which we find to be $\psi = 104 \pm 2^\circ$.

9.4 Discussion

9.4.1 Refined parameters for TOI-640 b

From our joint fit of the photometry and the in- and out-of-transit RVS, in addition to λ , we also provide new values for other system parameters and list them in Table 9.2. Some of these new determinations differ significantly from previous determinations, and we discuss these first before we discuss the implications of our obliquity measurement.

In Figure 9.6 we show the phase-folded TESS photometry with the best-fitting transit model. We find a radius of $1.72 \pm 0.05 R_J$ for TOI-640 b. This is consistent with the value of $1.777^{+0.060}_{-0.056} R_J$ from Rodriguez et al. (2021), but is slightly more precise owing to the additional TESS photometry and increased cadence. While we find consistent results for the radius, with $0.57 \pm 0.02 M_J$ we find a roughly 2σ difference in mass from the value reported in Rodriguez et al. (2021) of $0.88 \pm 0.16 M_J$.

We find a value of $0.906^{+0.007}_{-0.009}$ for the impact parameter, differing by roughly 3σ from $0.8763^{+0.0063}_{-0.0067}$ obtained by Rodriguez et al. (2021). This then leads to a significant difference in the results for a/R_\star (our $6.31^{+0.09}_{-0.07}$ versus $6.82^{+0.22}_{-0.24}$) which is correlated with the impact parameter ($b = \cos i \frac{a}{R_\star}$). These differences in the photometric solutions may be caused by Rodriguez et al., 2021 using the then available TESS photometric data from Sectors 6 and 7 together with ground-based photometry, while we have access to Sectors 6 and 7 and Sectors 33 and 34 and do not use additional ground-based data. This discrepancy might also be caused by the difference in how the light curves have been de-trended. Furthermore, it could be due to the spectroscopic transit data as the analysis of RM data can drive the

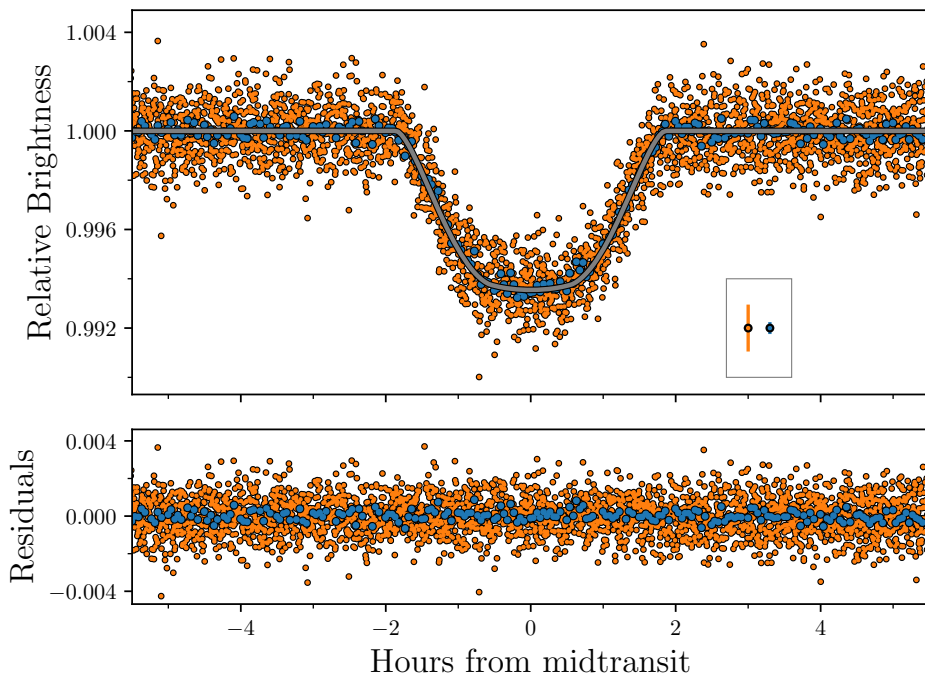


Figure 9.6 | TESS transits of TOI-640 b. TESS photometry phase folded to the period from Table 9.2 and centred on the transit. As in Figure A.9, blue and orange points are the 30 min and 2 min cadence data, respectively. The points with error bars in the box are not data, but illustrate the typical errors for the data. The data shown here have been de-trended with the GP (white line in Figure A.9). The grey curve is the best-fitting light curve.

result on b (Albrecht et al., 2022). We investigated whether or not the results for b are consistent between the different TESS observing epochs. For this, we determined b only on photometric data; first on Sectors 6 and 7 only and then on Sectors 33 and 34 only, obtaining $b = 0.917^{+0.006}_{-0.005}$ and $b = 0.911^{+0.006}_{-0.005}$, respectively. The values are consistent with each other and our final result. We note here that given the high impact parameter for the transit of TOI-640 b, any change in orbital inclination caused by for example nodal precession (see e.g. Szabó et al., 2012; Johnson et al., 2015; Watanabe et al., 2020; Stephan et al., 2022; Watanabe et al., 2022) may be picked up by future photometric (TESS) observations.

As noted in Rodriguez et al. (2021), TOI-640 b is an inflated planet. The lower mass but similar radius we find here compared to Rodriguez et al. (2021) makes it an even puffier planet with a density of $0.138 \pm 0.013 \text{ g cm}^{-3}$.

Comparing TOI-640 b to the literature, it is one of the largest and puffiest planets, but is not isolated in the mass–radius diagram as seen in Figure 9.7. The puffiness is most likely due to the rather high insolation it receives.

Finally, we investigated the light curve to see if we could see any effects of gravity darkening. However, the star does not seem to be rotating fast enough to detect this effect in the [TESS](#) photometry available.

9.4.2 The polar orbit of TOI-640 in context

Albrecht et al. (2021) derived ψ for a subset of planetary systems for which λ measurements were available. Of the 57 systems where ψ could be determined, these authors found 38 systems to be well-aligned and 18 systems misaligned in the interval between 80° and 125° , meaning that the misaligned systems are not isotropically distributed. Rather there is a tendency for planets to be orbiting the poles of the star.

With a value for ψ of $104 \pm 2^\circ$ (or $121^{+20}_{-3}{}^\circ$), TOI-640 joins this preponderance of perpendicular planets. Given the effective temperature of the star of 6460^{+130}_{-150} K, which is relatively hot in this context, one might even say that our measurement of $\psi = 104 \pm 2^\circ$ is not particularly surprising, seeing as the ‘polar-to-aligned ratio’ seems to increase with effective temperature. This might be an echo of the often larger projected [obliquities](#) found for stars with effective temperatures above 6250 K (Winn et al., 2010), as well as lower $v \sin i_*$ for spectral types of F or earlier Schlaufman (2010).

Further measurements of ψ have recently been made. Figure 9.8 shows MASCARA-1 b ($\psi = 72.1^{+2.50}_{-2.4}$; Hooton et al., 2022), GJ 3470 b ($\psi = 95^{+90}_{-8}$; Stefansson et al., 2022), KELT-7 b ($\psi = 12.4 \pm 11.7^\circ$; Tabernero et al., 2022), and TOI-640 b ($\psi = 104 \pm 2^\circ$) along with the measurements presented in Albrecht et al. (2021). Evidently, these new measurements follow the tendency of polar orbiting planets, where especially for hot stars harbour polar orbiting planets.

However, when discussing the sample of polar planets, it is important to keep in mind the various different selection effects that might play a role. For a classic example, see Figure 1 by Winn et al. (2010) and for a more recent discussion on selection effects related to spin-orbit angle measurements, see Albrecht et al. (2022). In this context, we note that we first selected TOI-640 as a system for which RM measurements, employing [HARPS](#), are likely to result in a conclusive answer concerning λ . We only started analysing the [TESS](#) light curves to establish whether or not we were able to determine the stellar rotation period from these light curves *after* the RM measurements had been taken.

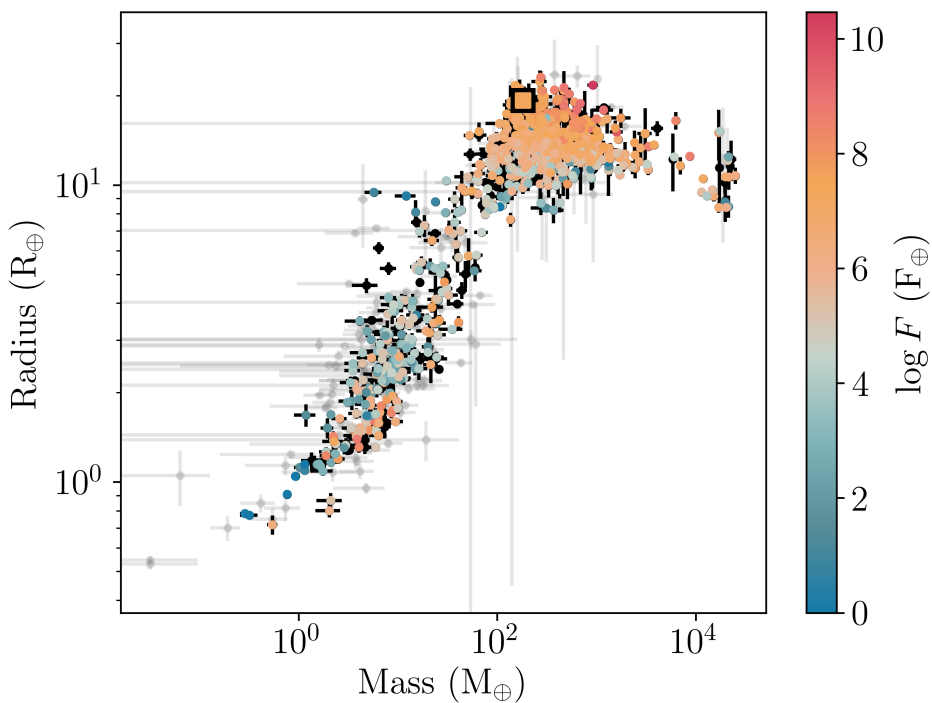


Figure 9.7 | Mass–radius diagram. Here we show planets from the TEPCat catalogue of ‘well-studied transiting planets’ (as of October 2022; Southworth, 2011, <https://www.astro.keele.ac.uk/jkt/tepcat/allplanets-noerr.html>). Grey dots are measurements with uncertainties larger than 30%, while black and coloured dots have smaller uncertainties. Points are colour coded according to the insolation, F , for those objects where it can be calculated. TOI-640 b is shown as the large square.

As to why planets should show a tendency to travel over stellar poles, Albrecht et al. (2021) briefly discuss four mechanisms, which we simply list here as 1) tidal dissipation (Lai, 2012; Rogers and Lin, 2013; Anderson et al., 2021), 2) Von Zeipel-Kozai-Lidov cycles (Fabrycky and Tremaine, 2007), 3) secular resonance crossing (Petrovich et al., 2020), and 4) magnetic warping (Foucart and Lai, 2011; Lai et al., 2011; Romanova et al., 2021). Another recent proposal was presented by Vick et al. (2023), who highlight that a binary companion (and its influence on the obliquity during disk dissipation) combined with subsequent Kozai-Lidov cycles might also produce polar orbits. While these mechanisms might be able to explain parts of the observed distribution, they do not seem to be able to fully reproduce the observations individually. It would be interesting to increase the sample

size and expand the parameter space to try to decipher whether or not these mechanisms work in tandem in different types of systems harbouring different types of planets.

9.5 Conclusions

Here we presented in-transit spectroscopic measurements for the hot Jupiter TOI-640 b. These measurements allowed us to detect the [RM EFFECT](#) both directly as the distortion of the spectral lines in the planet shadow as well as in the [RVS](#). From this, we measured a projected spin-orbit angle for the host star of $184 \pm 3^\circ$. While this would suggest that the orbit of the planet is not only retrograde, but completely anti-aligned, the rotation period we measured from the [TESS](#) light curves suggests that the [obliquity](#) is $104 \pm 2^\circ$, meaning that the orbit is actually polar.

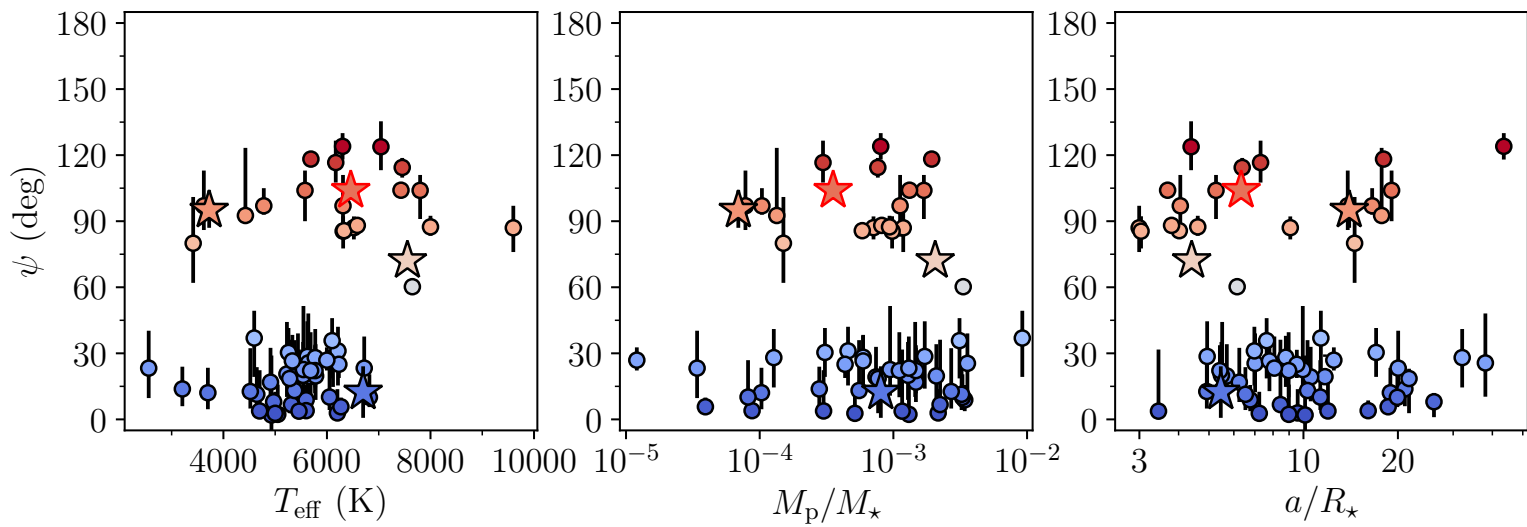


Figure 9.8 | Preponderance of perpendicular planets. Measurements of the 3D obliquity, ψ , from Albrecht et al. (2021) shown as circles with colour coding according to ψ . Recent ψ measurements not in Albrecht et al. (2021) are shown as stars, including TOI-640 (red outline). *Left:* ψ as a function of effective temperature. *Middle:* ψ as a function of planet-to-star mass ratio. *Right:* ψ as a function of orbital separation. It is worth noting that here we are only considering the results for ψ corresponding to i (and not $180^\circ - i$).

10

Conclusions and Outlook

In this thesis, I have presented the work carried out during my PhD, where the focus has been on planetary system architectures and fundamental stellar parameters. In the first part of the thesis, Part I, I provided some context into the life of stars and how their evolution might influence the planet they potentially harbour, before reviewing some of the leading theories of planetary formation and migration in Chapter 1. A more technical overview was then laid out in Chapter 2, where I discussed the tools and techniques we use to detect and characterise exoplanet systems. Here I also discussed some advances and discoveries we have made in the field.

Part II of the thesis highlighted some of the scientific results my collaborators and I have made. This began with a look into different techniques to measure fundamental stellar parameters using *detached eclipsing binary (DEB)s* in Chapter 3 and then *asteroseismology* in Chapter 4 and Chapter 5, where the asteroseismic results in the latter two chapters were used directly in the context of planetary system architectures.

I then moved on to exoplanet detection and characterisation, starting with the discovery of three giant planets on short-period orbits in Chapter 6. For two of these we detected the presence of outer companions, possibly alluding to the migration mechanism for the inner planets in these systems. An outer companion was also detected in the TOI-1288 system presented in Chapter 7. The hot super-Neptune, TOI-1288 b, is accompanied by a Saturn-mass planet on a wide orbit, TOI-1288 c. TOI-1288 c might thus have been responsible for transporting this super-Neptune after formation into the Neptunian desert, where it resides today.

Finally, I presented measurements of the projected *obliquity* in two different types of systems; the warm Saturn in the HD 332231 system in Chapter 8 and the hot Jupiter in the TOI-640 system in Chapter 9. The former system is a good example of a system that has probably undergone *disc*

migration (or formed *in situ*), whereas the latter is one of these surprisingly many polar orbiting planets.



In the immediate future we will be expanding on some of the different trends, I have presented and discussed in this thesis. In the following I will highlight some preliminary results of recent measurements, we are working on and looking to publish.

In terms of the distinction between *dynamically cold* and *dynamically hot* systems and their migration pathways, I presented a *dynamically cold* system, HD 332231. However, as was discussed in Section 2.4.2.1, more measurements are needed in order to establish this possible connection between eccentricity and (projected) *obliquity*. Recently, we detected the *Rossiter-McLaughlin effect (RM EFFECT)* in a system, which harbours a warm Jupiter on a circular orbit, TOI-892 b (Brahm et al., 2020). For this system we have measured the projected *obliquity* to be $\lambda = 4^{+10}_{-9}^\circ$ as seen in the top right panel of Figure 10.1. Furthermore, we have measured the projected obliquity of the K2-287 system, another Saturn-sized planet at an orbital separation similar to HD 332231 b, but in this system the planet is on a very eccentric orbit ($e = 0.476 \pm 0.026$, Jordán et al., 2019). We have found this eccentric system to be significantly misaligned with $\lambda = 27 \pm 6^\circ$ (top left in Figure 10.1).

These examples clearly follow the distinction between *disc migration* leading to *dynamically cold* systems and *high-eccentricity migration* leading to *dynamically hot*. Again, the former of these two processes seems to be a likely scenario for the HD 332231 and the TOI-892 systems, whereas the latter could explain the configuration for K2-287. These results will be published in a forthcoming paper (Knudstrup et al. in prep.).

In this paper, we will also be expanding on the sample of aligned, compact multiplanet systems discussed in Section 2.4.2.4. We have, for instance, measured the projected *obliquity* of the TOI-1130 system (Huang et al., 2020), which is similar to K2-290A with a inner Neptune-sized planet and a Jupiter-sized planet further out. We have measured the projected *obliquity* of planet c, the larger planet, and have found $\lambda = -4 \pm 4^\circ$ (bottom left in Figure 10.1).

While TOI-1130 resembles K2-290A in terms of the planets it harbours, the key difference might be the stellar companions, or in the case of TOI-1130, the lack thereof. It would therefore be interesting to target multiplanet systems in binary (or higher order systems) to see if the alignment of the planets is affected by the presence of a companion.

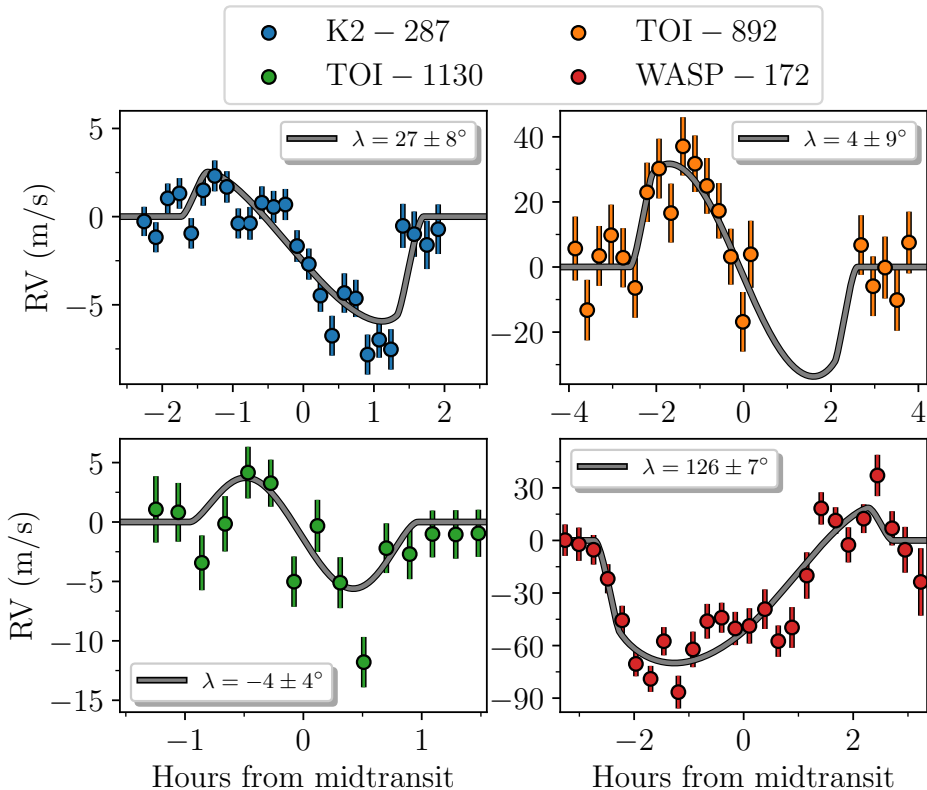


Figure 10.1 | Projected obliquity measurements. The grey curves show the best-fitting model of the RM EFFECT for the different systems. *Top left:* ESPRESSO RVS during transit of K2-287 c. *Top right:* HARPS-N RVS during transit of TOI-892 b. *Bottom left:* ESPRESSO RVS during transit of TOI-1130 c. *Bottom right:* ESPRESSO RVS during transit of WASP-172 b.

As shown in the chapter for TOI-640 (Chapter 9), the perplexing pile-up of polar orbiting seems to continue and, at least, one more measurement will be added to the tally as shown in the bottom right of Figure 10.1 for WASP-172 (Hellier et al., 2019). Our preliminary results suggest a projected obliquity of $\lambda = 126 \pm 7^\circ$, which paired with the stellar inclination derived from the rotation period of the star, yields an obliquity of $\psi = 100 \pm 6^\circ$ (Albrecht et al. in prep.).

Investigating this preponderance of perpendicular planets can, of course, be done by simply piling on more measurements. More measurements, and particularly more precise measurements, will shape up the observed distribution, making it easier to compare with theoretical calculations. However,

the possible mechanism given by Vick et al. (2023), in which primordial misalignment by a binary companion and subsequent *von Zeipel-Lidov-Kozai-driven* migration is invoked, not only leads to a distribution with similarities to the observed distribution, but also offers a fairly (in principle) straightforward way of testing this scenario. It would be extremely interesting to do an extensive study on companionship for these systems in which we have measured the *obliquity*, utilising *Gaia* as well as conducting a large-scale and long-term *RV* survey, investigating if binary companions are predominantly found in the polar systems as opposed to the aligned systems, and if these could have tilted the *protoplanetary disc*.

New and upcoming facilities will also help advance the field by providing key insights into both stellar physics and planetary system architectures. JWST (Gardner et al., 2006) is already allowing us to probe the atmospheres of exoplanets in unprecedented detail and has delivered some fantastic results of, for instance, WASP-39 b (Tsai et al., 2022), showing direct evidence for photochemistry in the atmosphere. These atmospheric measurements can also act as tracers for the migration pathways of planets (Madhusudhan et al., 2014) and how they evolve over time (Vissapragada et al., 2022). Many more exciting atmospheric measurements will certainly come in the near future.

Looking further ahead, the upcoming PLATO (PLAnetary Transits and Oscillation of stars; Rauer et al., 2014) mission (expected launch 2026) will provide numerous exoplanet detections, particularly of smaller planets on long-period orbits. Furthermore, given the precision of the photometer of PLATO, the asteroseismic yield should be very promising. The upcoming Extremely Large Telescope (ELT) with the ANDES (ArmazOnes high Dispersion Echelle Spectrograph; Marconi et al., 2022) spectrograph will also be a game-changer for the field, both in terms of atmospheric studies and the characterisation of small/long-period planets, especially when working in tandem with PLATO and its discoveries.

In conclusion, the field of exoplanets is thriving and the future looks bright. The field is developing rapidly, with many exciting theories being crafted, studies being conducted, and discoveries being made on a regular basis.

Glossary

acoustic cut-off frequency Characteristic frequency for the outer/upper turning point of pressure-modes; [36](#)

asteroseismology The study of oscillations in stars to characterise their interior; [3](#), [23](#), [32](#), [34–36](#), [38–40](#), [92](#), [93](#), [99](#), [102](#), [126–129](#), [137](#), [152](#), [153](#), [273](#)

asymptotic giant branch (AGB) Evolutionary phase with a carbon-oxygen core, helium and hydrogen fusion in a shell, and a very deep convective envelope; [xxi](#), [14](#)

BAyesian STellar Algorithm (BASTA) Flexible grid-based modelling pipeline based on Bayesian statistics and asteroseismic inference; [xxi](#), [106–108](#), [137](#), [144–147](#), [154](#), [156](#), [205–207](#)

broadening function (BF) A mathematical function that describes the shape of a spectral line in an absorption or emission spectrum; [xxi](#), [43](#), [61–66](#), [70](#), [74](#), [80](#), [81](#)

charge-coupled device (CCD) A light-sensitive integrated circuit that captures images by converting photons to electrons; [xxi](#), [23](#), [28](#), [61–63](#), [71](#), [167](#), [195](#)

co-orbital mass deficit The difference between the mass that would be contained in the protoplanetary disc surrounding the migrating planet had it not been perturbed and the mass actually contained in this region; [18](#)

colour-magnitude diagram (CMD) A variant of the Hertzsprung-Russell diagram with the colour index plotted against magnitude; [xxi](#), [11](#), [12](#), [53](#), [54](#), [56](#), [69](#), [70](#), [78](#), [79](#), [86](#), [88–90](#), [93](#), [97](#), [198](#), [200](#), [211](#), [358](#)

convective core-overshooting Overshooting refers to a convective cell in a convective region overshooting into a radiative region owing to its inertia. Here for a convective core; 11, 12, 52, 53, 85–88, 146

cross-correlation function (ccf) A measure of similarity between two sequences as a function of the displacement of one relative to the other; xxi, 43, 44, 57, 202, 230–236, 239, 246, 248, 256, 258, 261

detached eclipsing binary (DEB) An eclipsing binary system in which the stars' radii are smaller than the the Roche lobe; xxi, 3, 34, 51–55, 57, 61, 63, 77, 81, 86, 99, 273

disc migration Planetary migration through exchange of angular momentum with the particles in the protoplanetary disc; 18–20, 22, 45, 159, 183, 184, 225, 250, 273, 274

dynamically cold A system with a planet on a circular, well-aligned orbit; 45, 274

dynamically hot A system with a planet on an inclined, highly eccentric orbit; 45, 274

ex situ From Latin meaning “off site” or “away from natural location” opposite of in situ; 17, 19, 22

FIber-fed Echelle Spectrograph (FIES) The high resolution spectrograph at the NOT; xxi, 28, 45, 61, 62, 64, 130, 132, 136, 156–158, 164, 168–170, 173–175, 178, 180, 200, 205

frequency of maximum power Centre of the envelope traced by the oscillations in a power spectrum. Denoted by ν_{\max} ; 36, 77, 102

g-mode Gravity-mode. Oscillation mode where the restoring force is buoyancy; 36, 38, 146

Gaia Astrometric space mission launched in December 2013; 11, 51, 52, 54–56, 58, 60, 61, 66–69, 87–95, 97, 106, 107, 134, 136, 144, 145, 147, 156, 164, 166, 170, 191, 192, 194, 197–200, 205, 207, 208, 211, 248, 276, 360, 370

Gaussian process (GP) A type of stochastic process in which any finite collection of random variables has a joint Gaussian distribution; xxi, 148–152, 155, 173, 178, 179, 193, 206, 209, 229, 230, 237, 258, 261, 267, 359, 362

helioseismology The study of oscillations in the Sun to characterise its interior; [1](#), [36](#), [39](#)

helium flash A brief thermal runaway nuclear fusion of large quantities of helium into carbon through the triple-alpha process; [13](#)

Hertzsprung-Russell diagram (HR diagram) Diagram of stellar surface luminosity against T_{eff} ; [xxi](#), [10](#), [11](#), [144](#), [279](#)

High-Accuracy Radial Velocity Planetary Searcher (HARPS) A high resolution spectrograph located at the ESO-3.6 m telescope, with a northern counterpart, HARPS-N, at the 3.6 m Telescopio Nazionale Galileo; [xxi](#), [28](#), [45](#), [188](#), [200–205](#), [212](#), [216](#), [220](#), [223](#), [224](#), [228](#), [231–233](#), [236](#), [238](#), [239](#), [241](#), [244–246](#), [248](#), [250](#), [252](#), [254–258](#), [264](#), [268](#), [275](#), [363](#)

high-eccentricity migration Planetary migration through multi body interactions creating highly eccentric orbits with subsequent tidal capture; [18–22](#), [45](#), [48](#), [159](#), [183](#), [184](#), [187](#), [214](#), [219](#), [221](#), [224](#), [225](#), [250](#), [274](#)

Hill sphere The gravitational sphere of influence for a celestial body where the gravitational influence of the body dominates the gravitational influences of other celestial bodies; [18](#), [124](#), [214](#)

in situ From Latin meaning “on site” or “in position” opposite of ex situ; [17–19](#), [22](#), [45](#), [224](#), [250](#), [274](#)

isochrone A curve on the *Hertzsprung-Russell diagram (HR diagram)*, representing a population of stars of the same age but with different masses; [11](#), [12](#), [52–55](#), [78](#), [79](#), [85–90](#), [93](#), [97](#), [172](#), [185](#), [198](#), [205–207](#)

K2 *Kepler’s “Second Light”* mission started operations in 2014; [32](#), [36](#), [99–102](#), [108](#), [110](#), [114–116](#), [121](#), [124](#), [126](#), [127](#), [156](#)

Kepler Space telescope launched in March 2009 to perform photometric time-series measurements; [31–34](#), [36](#), [38](#), [39](#), [92](#), [100](#), [107](#), [124](#), [127](#), [152](#), [189](#), [262](#)

kernel density estimation (KDE) Kernel smoothing for probability density estimation of a random variable; [xxi](#), [35](#), [135](#), [263](#), [266](#)

Kraft break The rather abrupt decrease in the average rotation rates of stars with an T_{eff} below ~ 6250 K; [12](#), [46](#)

large frequency separation Asymptotic separation in frequency between modes of consecutive orders. Denoted by $\Delta\nu$; 36, 77, 102

macro-turbulence Large-scale motions in the stellar atmosphere that can affect the shapes and widths of spectral lines. Denoted by ζ ; 24, 43, 104, 106, 134, 136, 154, 175, 179, 207, 217, 231, 233, 254, 258, 264

main sequence (ms) The stage at which a star spends most of its life fusing hydrogen to helium in its core; xxii, 9, 12, 13, 38, 53, 66–68, 83, 85–87, 90, 94, 122

Markov Chain Monte Carlo (MCMC) Algorithms for systematic random sampling from high-dimensional probability distributions; xxii, 60, 79–83, 110, 112, 150, 151, 158, 172–176, 180–182, 206, 208, 216, 230, 236, 240, 242, 255, 258, 259, 262, 356, 361, 362, 366, 368

micro-turbulence Small-scale motions in the stellar atmosphere that can affect the shapes and widths of spectral lines. Denoted by ξ ; 24, 43, 80, 134, 136, 175, 179, 207, 217, 231–233, 258, 264

Nordic Optical Telescope (NOT) 2.56 m telescope equipped with, among other things, the FIES spectrograph and ALFOSC imager; xxii, 14, 15, 28, 61, 62, 64, 71, 74, 80, 82, 130, 157, 164, 168, 174, 200

obliquity The angle between the stellar spin axis and the orbital axis of the planet; 1–4, 12, 19, 21, 23, 39, 40, 42, 44–48, 104, 124, 155, 158, 159, 174, 175, 179–181, 184, 217, 220, 223–228, 230, 231, 234, 244, 246–253, 256, 258, 261, 262, 264, 266, 268–271, 273–276

p-mode Pressure-mode. Oscillation mode where the restoring force is the pressure gradient; 36, 141, 146

planetary shadow The observed distortions of the stellar spectral lines during transit; 43, 236, 242, 256, 258

principal investigator (PI) The individual responsible for planning and conducting the observations; xxii, 26, 130, 157, 188, 223, 228, 254

protoplanet A large planetary embryo that originated within a protoplanetary disc; 1, 189

protoplanetary disc A rotating circumstellar disc surrounding a newly formed star; 1, 16–18, 20–22, 47, 48, 129, 225, 226, 276

protostar A very young star still gathering mass from the molecular cloud; [8](#), [9](#), [16](#)

radial velocity (rv) The projected velocity of a star along the line-of-sight; [xxii](#), [23](#), [24](#), [26–30](#), [35](#), [42](#), [43](#), [46](#), [47](#), [52](#), [55–58](#), [61–63](#), [73](#), [79](#), [106](#), [121–123](#), [126–130](#), [132](#), [138](#), [140](#), [147–151](#), [154–158](#), [166](#), [168](#), [169](#), [171–177](#), [180–183](#), [188–190](#), [201–203](#), [206](#), [208](#), [211](#), [216](#), [220](#), [221](#), [227](#), [228](#), [230](#), [231](#), [233](#), [234](#), [239–242](#), [244](#), [246–248](#), [250–253](#), [255](#), [256](#), [258–261](#), [264](#), [266](#), [270](#), [275](#), [276](#), [353](#), [361](#), [363](#)

reconnaissance spectroscopy (RECON SPECTROSCOPY) Spectroscopic observations used for initial vetting of stellar parameters, typically of host stars for exoplanet candidates; [xxii](#), [28](#), [166](#), [170](#), [200](#), [205](#)

red clump Clump of stars in the HR diagram that have evolved into red giants and are now fusing helium in their cores; [13](#), [77](#)

red-giant branch (RGB) Evolutionary phase with a dense helium core, hydrogen fusion in a shell, and extended convective envelope; [xxii](#), [9](#), [11](#), [13](#), [14](#), [51](#), [54–60](#), [77–79](#), [83](#), [86](#), [87](#), [89](#), [92](#), [96](#), [97](#), [127–129](#), [143](#), [144](#), [146](#), [156](#), [360](#)

rogue planet An interstellar object of planetary-mass which is not gravitationally bound to a star; [9](#), [20](#)

Rossiter-McLaughlin effect (RM EFFECT) A distortion of the spectral lines caused by a transiting planet blocking a portion of the rotating photosphere; [xxii](#), [23](#), [40–43](#), [47](#), [48](#), [104](#), [175](#), [184](#), [216](#), [224](#), [227](#), [232](#), [234](#), [239](#), [250–256](#), [258](#), [270](#), [274](#), [275](#), [361](#), [363](#)

shell-burning law When the region within a burning shell contracts, the region outside the shell expands; and when the region inside the shell expands, the region outside the shell expands; [13](#), [14](#)

signal-to-noise ratio (SNR) The level of the desired signal compared to the level of background noise; [xxii](#), [58](#), [59](#), [132](#), [138](#), [140](#), [143](#), [162](#), [168](#), [192](#), [202](#), [228](#), [231](#), [235](#), [236](#), [254](#), [255](#)

snow line Also known as the ice line or frost line, is the particular distance in the solar nebula from the central protostar where it is cold enough for volatile compounds condense into solid ice grains; [1](#), [17](#), [21](#), [22](#)

spectral energy distribution (SED) The flux density of an object as a function of wavelength/frequency; xxii, 57, 66, 68–71, 170, 173, 198, 205–208, 212, 218, 219, 370

Stellar Observations Network Group (SONG) Fully robotic telescope with a high resolution spectrograph; xxii, 26, 27, 127, 128, 130, 131, 135, 137–140, 147–150, 152, 156, 223, 228, 232, 355

tidal friction The dissipation of energy that occurs as a result of the tidal forces exerted by one celestial body on another; 12

Transiting Exoplanet Survey Satellite (TESS) Photometric satellite mission launched in April 2018; xxii, 28, 32–34, 37, 51, 52, 65, 74, 75, 77–80, 94, 96, 97, 102, 113, 115–117, 127, 128, 130, 132, 133, 137–140, 156–160, 162, 166, 173, 174, 178, 179, 181–183, 187–194, 202, 206, 208, 209, 212, 218–220, 224, 226–230, 232, 237, 241, 242, 244, 245, 247, 248, 250, 252, 253, 256, 258, 261, 264, 266–268, 270, 354, 357, 359, 362, 370

turn-off The termination of main-sequence evolution, hydrogen in the core is exhausted; 11, 12, 52–55, 57, 77

zero-age main sequence (ZAMS) The time a star joins the main sequence by fusing hydrogen to helium in its core; xxii, 9, 11, 122

List of Figures

1.1	Hertzsprung-Russell and colour-magnitude diagrams.	11
1.2	Image of the Ring Nebula.	15
1.3	Schematic of hot Jupiter formation.	19
2.1	Schematic of a stellar spectrum on a CCD.	25
2.2	Exoplanets detected through radial velocities.	27
2.3	Schematic of an eclipse.	30
2.4	Exoplanets detected over the years.	31
2.5	<i>Kepler</i> and TESS transmission curves.	33
2.6	Period-mass diagram.	35
2.7	Power spectrum.	37
2.8	The orientation of the system.	40
2.9	Geometry of the RM effect.	42
2.10	Illustration of the RM effect.	44
3.1	Colour-magnitude diagram of NGC 2506.	56
3.2	Broadening functions.	64
3.3	Luminosity ratio for V2032.	65
3.4	Spectral energy distributions.	69
3.5	Light and radial velocity curves.	72
3.5	Light and radial velocity curves.	73
3.6	TESS light curves.	75
3.7	Power spectra.	78
3.8	Mass-radius diagrams.	84
3.8	Mass-radius diagrams.	85
3.9	Colour-magnitude diagrams.	89
3.10	<i>Gaia</i> view of NGC 2506.	91
3.11	<i>Gaia</i> photometric variability in NGC 2506.	93
3.12	The orbit of V4.	95

4.1	K2 light curve of K2-93.	101
4.2	Power spectrum and échelle diagram.	103
4.3	Correlation between inclination and splitting.	105
4.4	Transit light curves.	111
4.5	Period distributions.	113
4.6	TESS light curve.	116
4.7	Density ratios and eccentricity distributions.	118
4.7	Density ratios and eccentricity distributions.	119
4.8	Expected K -amplitudes.	123
4.9	Habitable zone estimate.	125
5.1	SONG campaigns.	131
5.2	TESS observations.	133
5.3	Literature comparison of γ Cep A.	135
5.4	TESS and SONG power spectra.	139
5.5	Observed power spectrum.	141
5.6	Observed échelle diagram.	142
5.7	BASTA échelle diagram.	145
5.8	Hertzsprung-Russell diagram for γ Cep A.	146
5.9	Orbital motion.	148
5.10	GP detrended SONG data.	149
5.11	GP power spectrum from radial velocities.	155
6.1	Photometry for TOI-1820.	161
6.2	Photometry for TOI-2025.	163
6.3	Photometry for TOI-2158.	165
6.4	Speckle interferometry.	167
6.5	Radial velocities.	169
6.6	Generalised Lomb-Scargle periodograms.	171
6.7	Spectral Energy Distribution.	173
6.8	Rossiter-McLaughlin effect in TOI-2025.	175
6.9	Long-term trend in TOI-2025.	176
6.10	Long-term trend in TOI-2158.	177
6.11	Bootstrapping the orbit of TOI-2025 b.	182
6.12	Bootstrapping the orbit of TOI-1820 b.	183
6.13	Tidal diagrams.	185
7.1	TESS image of TOI-1288.	191
7.2	TESS photometry.	193
7.3	WIYN/NESSI contrast curves from 2019.	194
7.4	Gemini/NIRI contrast curve.	196

7.5	Sky positions of blended companions.	197
7.6	Radial velocities of TOI-1288.	201
7.7	Generalised Lomb-Scargle diagram.	203
7.8	Generalised Lomb-Scargle diagram for activity indicators.	204
7.9	TESS light curve of TOI-1288 b.	209
7.10	Lower mass limit for an additional bound companion.	210
7.11	The Neptunian desert.	215
7.12	Mass-radius diagram.	217
7.13	Simulated JWST observations.	218
8.1	TESS light curve for HD 332231.	229
8.2	The HARPS-N data on the transit night.	231
8.3	Radial velocity curve for HD 332231 b.	232
8.4	Out-of-transit cross-correlation-functions.	234
8.5	The four transits of HD 332231 b.	237
8.6	The three approaches to measuring λ	238
8.6	The three approaches to measuring λ	239
8.7	Transit timing differences.	245
8.8	Correlation between P and T_0	247
8.9	Comparing HD 332231 to the literature.	249
9.1	The Rossiter-McLaughlin effect of TOI-640.	255
9.2	Planetary shadow.	257
9.3	2D histograms.	259
9.4	Autocorrelation function.	260
9.5	Obliquity distributions.	263
9.6	TESS transits of TOI-640 b.	267
9.7	Mass-radius diagram.	269
9.8	Preponderance of perpendicular planets.	271
10.1	Projected obliquity measurements.	275
A.1	TESS power spectra of γ Cep A.	354
A.2	SONG power spectra of γ Cep A.	355
A.3	Circular solution for TOI-2025 b.	356
A.4	TESS light curves.	357
A.5	Colour-magnitude diagrams for TOI-1288.	358
A.6	Light curves of TOI-1288 b.	359
A.7	NGC 2506 as seen in the FFIs of TESS.	360
A.8	Correlation plots.	361
A.9	TESS photometry of TOI-640.	362

A.10 HARPS RVs.	363
-------------------------	-----

List of Tables

3.1	Target stars in NGC 2506	55
3.2	Red Giant Branch stars.	59
3.3	Initial parameters.	63
3.4	Key parameters.	81
3.5	Cluster parameters for NGC 2506.	87
4.1	Spectroscopic and IRFM parameters.	106
4.2	Results from the asteroseismic modeling.	108
4.3	Planetary parameters from the joint transit fit.	109
5.1	System parameters for γ Cep.	136
5.2	Stellar parameters of γ Cep A.	137
5.3	Interferometry.	147
5.4	Orbital and hyperparameters.	151
5.5	Literature masses in γ Cep.	153
6.1	Speckle observations of TOI-1820.	166
6.2	MCMC results for TOI-1820, TOI-2025, and TOI-2158.	178
7.1	System parameters.	190
7.2	Companions detected in Speckle, AO, and <i>Gaia</i>	199
7.3	Stellar parameters for TOI-1288.	207
7.4	MCMC results for TOI-1288.	212
7.5	Closest radius-period neighbours.	216
8.1	HD 332231 system parameters.	226
8.2	MCMC results for HD 332231.	242
9.1	TOI-640 system parameters.	254
9.2	MCMC results for TOI-640.	264

B.1	DE-MCMC results for V ₄ in NGC 2506.	366
B.2	Results for V ₂₀₃₂ and V ₅ in NGC 2506.	368
B.3	Stellar parameters for TOI-1820, TOI-2025, and TOI-2158.	370
B.4	Mode frequencies for γ Cep A.	372

Bibliography

- Addison, B. C.; Knudstrup, E.; Wong, I.; Hébrard, G.; Dorval, P.; Snellen, I.; Albrecht, S.; Bello-Arufe, A.; Almenara, J.-M.; Boisse, I.; Bonfils, X.; Dalal, S.; Demangeon, O. D. S.; Hoyer, S.; Kiefer, F., et al. (2021). “TOI-1431b/MASCARA-5b: A Highly Irradiated Ultrahot Jupiter Orbiting One of the Hottest and Brightest Known Exoplanet Host Stars”. *Astronomical Journal* 162.6, 292.
- Aerts, C.; Christensen-Dalsgaard, J., and Kurtz, D. W. (2010). *Asteroseismology*. Astronomy and Astrophysics Library. Springer Netherlands.
- Aguirre Børnsen-Koch, V.; Rørsted, J. L.; Justesen, A. B.; Stokholm, A.; Verma, K.; Winther, M. L.; Knudstrup, E.; Nielsen, K. B.; Sahlholdt, C.; Larsen, J. R.; Cassisi, S.; Serenelli, A. M.; Casagrande, L.; Christensen-Dalsgaard, J.; Davies, G. R., et al. (2022). “The BAyesian STellar algorithm (BASTA): a fitting tool for stellar studies, asteroseismology, exoplanets, and Galactic archaeology”. *Monthly Notices of the Royal Astronomical Society* 509.3, pp. 4344–4364.
- Aigrain, S.; Pont, F., and Zucker, S. (2012). “A simple method to estimate radial velocity variations due to stellar activity using photometry”. *Monthly Notices of the Royal Astronomical Society* 419.4, pp. 3147–3158.
- Albrecht, S.; Reffert, S.; Snellen, I.; Quirrenbach, A., and Mitchell, D. S. (2007). “The spin axes orbital alignment of both stars within the eclipsing binary system V1143 Cyg using the Rossiter-McLaughlin effect”. *Astronomy and Astrophysics* 474, pp. 565–573.
- Albrecht, S. H.; Dawson, R. I., and Winn, J. N. (2022). “Stellar Obliquities in Exoplanetary Systems”. *Publications of the Astronomical Society of the Pacific* 134.1038, 082001.

- Albrecht, S. H.; Marcussen, M. L.; Winn, J. N.; Dawson, R. I., and Knudstrup, E. (2021). "A Preponderance of Perpendicular Planets". *The Astrophysical Journal Letters* 916.1, L1.
- Albrecht, S.; Setiawan, J.; Torres, G.; Fabrycky, D. C., and Winn, J. N. (2013a). "The BANANA Project. IV. Two Aligned Stellar Rotation Axes in the Young Eccentric Binary System EP Crucis: Primordial Orientation and Tidal Alignment". *Astrophysical Journal* 767.1, 32.
- Albrecht, S.; Winn, J. N.; Johnson, J. A.; Howard, A. W.; Marcy, G. W.; Butler, R. P.; Arriagada, P.; Crane, J. D.; Shectman, S. A.; Thompson, I. B.; Hirano, T.; Bakos, G., and Hartman, J. D. (2012). "Obliquities of Hot Jupiter Host Stars: Evidence for Tidal Interactions and Primordial Misalignments". *Astrophysical Journal* 757.1, 18.
- Albrecht, S.; Winn, J. N.; Johnson, J. A.; Butler, R. P.; Crane, J. D.; Shectman, S. A.; Thompson, I. B.; Narita, N.; Sato, B.; Hirano, T.; Enya, K., and Fischer, D. (2011). "Two Upper Limits on the Rossiter-McLaughlin Effect, with Differing Implications: WASP-1 has a High Obliquity and WASP-2 is Indeterminate". *Astrophysical Journal* 738.1, 50.
- Albrecht, S.; Winn, J. N.; Marcy, G. W.; Howard, A. W.; Isaacson, H., and Johnson, J. A. (2013b). "Low Stellar Obliquities in Compact Multiplanet Systems". *Astrophysical Journal* 771.1, 11.
- Allard, F.; Homeier, D., and Freytag, B. (2012). "Models of very-low-mass stars, brown dwarfs and exoplanets". *Philosophical Transactions of the Royal Society of London Series A* 370.1968, pp. 2765–2777.
- ALMA Partnership; Brogan, C. L.; Pérez, L. M.; Hunter, T. R.; Dent, W. R. F.; Hales, A. S.; Hills, R. E.; Corder, S.; Fomalont, E. B.; Vlahakis, C.; Asaki, Y.; Barkats, D.; Hirota, A.; Hodge, J. A.; Impellizzeri, C. M. V., et al. (2015). "The 2014 ALMA Long Baseline Campaign: First Results from High Angular Resolution Observations toward the HL Tau Region". *The Astrophysical Journal Letters* 808.1, L3.
- Andersen, B. N.; Leifsen, T. E., and Toutain, T. (1994). "Solar Noise Simulations in Irradiance". *Solar Physics* 152.1, pp. 247–252.
- Andersen, J. (1991). "Accurate masses and radii of normal stars". *The Astronomy and Astrophysics Review* 3.2, pp. 91–126.
- Andersen, M. F.; Grundahl, F.; Christensen-Dalsgaard, J.; Frandsen, S.; Jørgensen, U. G.; Kjeldsen, H.; Pallé, P.; Skottfelt, J.; Sørensen, A. N., and Weiss, E. (2014). "Hardware and software for a robotic network of

- telescopes - SONG". In: *Revista Mexicana de Astronomia y Astrofisica Conference Series*. Vol. 45. Revista Mexicana de Astronomia y Astrofisica Conference Series, p. 83.
- Anderson, K. R.; Winn, J. N., and Penev, K. (2021). "On a Possible Solution to the Tidal Realignment Problem for Hot Jupiters". *Astrophysical Journal* 914.1, 56.
- Anderson, T. W. and Darling, D. A. (1952). "Asymptotic Theory of Certain "Goodness of Fit" Criteria Based on Stochastic Processes". *Ann. Math. Statist.* 23.2, pp. 193–212.
- Anglada-Escudé, G. and Butler, R. P. (2012). "The HARPS-TERRA Project. I. Description of the Algorithms, Performance, and New Measurements on a Few Remarkable Stars Observed by HARPS". *The Astrophysical Journal Supplement Series* 200.2, 15.
- Anthony-Twarog, B. J.; Deliyannis, C. P., and Twarog, B. A. (2016). "WIYN Open Cluster Study. LXXII. A uvbyCaH β CCD Analysis of the Metal-deficient Open Cluster NGC 2506". *Astronomical Journal* 152, 192.
- Anthony-Twarog, B. J.; Lee-Brown, D. B.; Deliyannis, C. P., and Twarog, B. A. (2018). "WIYN Open Cluster Study. LXXVI. Li Evolution Among Stars of Low/Intermediate Mass: The Metal-deficient Open Cluster NGC 2506". *Astronomical Journal* 155.3, 138.
- Antoci, V.; Handler, G.; Grundahl, F.; Carrier, F.; Brugamyer, E. J.; Robertson, P.; Kjeldsen, H.; Kok, Y.; Ireland, M., and Matthews, J. M. (2013). "Searching for solar-like oscillations in the δ Scuti star ρ Puppis". *Monthly Notices of the Royal Astronomical Society* 435.2, pp. 1563–1575.
- Appourchaux, T. (2020). "On attempting to automate the identification of mixed dipole modes for subgiant stars". *Astronomy and Astrophysics* 642, A226.
- Arentoft, T.; De Ridder, J.; Grundahl, F.; Glowienka, L.; Waelkens, C.; Dupret, M.-A.; Grigahcène, A.; Lefever, K.; Jensen, H. R.; Reyniers, M.; Frandsen, S., and Kjeldsen, H. (2007). "Oscillating blue stragglers, γ Doradus stars and eclipsing binaries in the open cluster NGC 2506". *Astronomy and Astrophysics* 465, pp. 965–979.
- Arentoft, T.; Grundahl, F.; White, T. R.; Slumstrup, D.; Handberg, R.; Lund, M. N.; Brogaard, K.; Andersen, M. F.; Silva Aguirre, V.; Zhang, C.; Chen, X.; Yan, Z.; Pope, B. J. S.; Huber, D.; Kjeldsen, H., et al. (2019).

- “Astroseismology of the Hyades red giant and planet host \in Tauri”. *Astronomy and Astrophysics* 622, A190.
- Asplund, M. (2005). “New Light on Stellar Abundance Analyses: Departures from LTE and Homogeneity”. *Annu. Rev. Astron. Astrophys.* 43.1, pp. 481–530.
- Bailer-Jones, C. A. L.; Rybizki, J.; Fouesneau, M.; Demleitner, M., and Andrae, R. (2021). “Estimating Distances from Parallaxes. V. Geometric and Photogeometric Distances to 1.47 Billion Stars in Gaia Early Data Release 3”. *Astronomical Journal* 161.3, 147.
- Bailer-Jones, C. A. L.; Rybizki, J.; Fouesneau, M.; Mantelet, G., and Andrae, R. (2018). “Estimating Distance from Parallaxes. IV. Distances to 1.33 Billion Stars in Gaia Data Release 2”. *Astronomical Journal* 156, 58.
- Baines, E. K.; Armstrong, J. T.; Schmitt, H. R.; Zavala, R. T.; Benson, J. A.; Hutter, D. J.; Tycner, C., and van Belle, G. T. (2018). “Fundamental Parameters of 87 Stars from the Navy Precision Optical Interferometer”. *Astronomical Journal* 155.1, 30.
- Baines, E. K.; McAlister, H. A.; ten Brummelaar, T. A.; Sturmann, J.; Sturmann, L.; Turner, N. H., and Ridgway, S. T. (2009). “Eleven Exoplanet Host Star Angular Diameters from the Chara Array”. *Astrophysical Journal* 701.1, pp. 154–162.
- Bakos, G. Á.; Lázár, J.; Papp, I.; Sári, P., and Green, E. M. (2002). “System Description and First Light Curves of the Hungarian Automated Telescope, an Autonomous Observatory for Variability Search”. *Publications of the Astronomical Society of the Pacific* 114.799, pp. 974–987.
- Bakos, G. Á.; Penev, K.; Bayliss, D.; Hartman, J. D.; Zhou, G.; Brahm, R.; Mancini, L.; de Val-Borro, M.; Bhatti, W.; Jordán, A.; Rabus, M.; Espinoza, N.; Csubry, Z.; Howard, A. W.; Fulton, B. J., et al. (2015). “HATS-7b: A Hot Super Neptune Transiting a Quiet K Dwarf Star”. *Astrophysical Journal* 813.2, 111.
- Bakos, G. Á.; Torres, G.; Pál, A.; Hartman, J.; Kovács, G.; Noyes, R. W.; Latham, D. W.; Sasselov, D. D.; Sipőcz, B.; Esquerdo, G. A.; Fischer, D. A.; Johnson, J. A.; Marcy, G. W.; Butler, R. P.; Isaacson, H., et al. (2010). “HAT-P-11b: A Super-Neptune Planet Transiting a Bright K Star in the Kepler Field”. *Astrophysical Journal* 710.2, pp. 1724–1745.

- Ball, W. H. and Gizon, L. (2014). “A new correction of stellar oscillation frequencies for near-surface effects”. *Astronomy and Astrophysics* 568, A123.
- Ballester, P.; Modigliani, A.; Boitquin, O.; Cristiani, S.; Hanuschik, R.; Kaufer, A., and Wolf, S. (2000). “The UVES Data Reduction Pipeline”. *The Messenger* 101, pp. 31–36.
- Ballot, J.; Barban, C., and van’t Veer-Menneret, C. (2011). “Visibilities and bolometric corrections for stellar oscillation modes observed by Kepler”. *Astronomy and Astrophysics* 531, A124.
- Baraffe, I.; Chabrier, G.; Allard, F., and Hauschildt, P. H. (2002). “Evolutionary models for low-mass stars and brown dwarfs: Uncertainties and limits at very young ages”. *Astronomy and Astrophysics* 382, pp. 563–572.
- Baruteau, C.; Crida, A.; Paardekooper, S. .-.J.; Masset, F.; Guilet, J.; Bitsch, B.; Nelson, R.; Kley, W., and Papaloizou, J. (2014). “Planet-Disk Interactions and Early Evolution of Planetary Systems”. In: *Protostars and Planets VI*. Ed. by H. Beuther; R. S. Klessen; C. P. Dullemond, and T. Henning, p. 667.
- Basu, S.; Chaplin, W. J., and Elsworth, Y. (2010). “Determination of Stellar Radii from Asteroseismic Data”. *Astrophysical Journal* 710, pp. 1596–1609.
- Basu, S.; Verner, G. A.; Chaplin, W. J., and Elsworth, Y. (2012). “Effect of Uncertainties in Stellar Model Parameters on Estimated Masses and Radii of Single Stars”. *Astrophysical Journal* 746, 76.
- Batalha, N. E.; Mandell, A.; Pontoppidan, K.; Stevenson, K. B.; Lewis, N. K.; Kalirai, J.; Earl, N.; Greene, T.; Albert, L., and Nielsen, L. D. (2017). “PandExo: A Community Tool for Transiting Exoplanet Science with JWST & HST”. *Publications of the Astronomical Society of the Pacific* 129.976, p. 064501.
- Bate, M. R. (2018). “On the diversity and statistical properties of protostellar discs”. *Monthly Notices of the Royal Astronomical Society* 475, pp. 5618–5658.
- Bate, M. R.; Lodato, G., and Pringle, J. E. (2010). “Chaotic star formation and the alignment of stellar rotation with disc and planetary orbital axes”. *Monthly Notices of the Royal Astronomical Society* 401, pp. 1505–1513.

- Batygin, K. (2012). "A primordial origin for misalignments between stellar spin axes and planetary orbits". *Nature*.
- Batygin, K.; Bodenheimer, P. H., and Laughlin, G. P. (2016). "In Situ Formation and Dynamical Evolution of Hot Jupiter Systems". *Astrophysical Journal* 829.2, 114.
- Beck, J. G. and Giles, P. (2005). "Helioseismic Determination of the Solar Rotation Axis". *The Astrophysical Journal Letters* 621.2, pp. L153–L156.
- Becker, J. C.; Vanderburg, A.; Rodriguez, J. E.; Omohundro, M.; Adams, F. C.; Stassun, K. G.; Yao, X.; Hartman, J.; Pepper, J.; Bakos, G.; Barentsen, G.; Beatty, T. G.; Bhatti, W.; Chontos, A.; Collier Cameron, A., et al. (2019). "A Discrete Set of Possible Transit Ephemerides for Two Long-period Gas Giants Orbiting HIP 41378". *Astronomical Journal* 157, 19.
- Becker, J. C.; Vanderburg, A.; Adams, F. C.; Khain, T., and Bryan, M. (2017). "Exterior Companions to Hot Jupiters Orbiting Cool Stars Are Coplanar". *Astronomical Journal* 154.6, 230.
- Bedding, T. R. (2011). "Solar-like Oscillations: An Observational Perspective". *ArXiv e-prints* 1107.1723.
- Bedding, T. R.; Mosser, B.; Huber, D.; Montalbán, J.; Beck, P.; Christensen-Dalsgaard, J.; Elsworth, Y. P.; García, R. A.; Miglio, A.; Stello, D.; White, T. R.; De Ridder, J.; Hekker, S.; Aerts, C.; Barban, C., et al. (2011). "Gravity modes as a way to distinguish between hydrogen- and helium-burning red giant stars". *Nature* 471.7340, pp. 608–611.
- Beleznay, M. and Kunimoto, M. (2022). "Exploring the dependence of hot Jupiter occurrence rates on stellar mass with TESS". *Monthly Notices of the Royal Astronomical Society* 516.1, pp. 75–83.
- Benomar, O.; Belkacem, K.; Bedding, T. R.; Stello, D.; Di Mauro, M. P.; Ventura, R.; Mosser, B.; Goupil, M. J.; Samadi, R., and Garcia, R. A. (2014). "Asteroseismology of Evolved Stars with Kepler: A New Way to Constrain Stellar Interiors Using Mode Inertias". *The Astrophysical Journal Letters* 781.2, L29.
- Berardo, D.; Crossfield, I. J. M.; Werner, M.; Petigura, E.; Christiansen, J.; Ciardi, D. R.; Dressing, C.; Fulton, B. J.; Gorjian, V.; Greene, T. P.; Hardegree-Ullman, K.; Kane, S. R.; Livingston, J.; Morales, F., and Schlieder, J. E. (2019). "Revisiting the HIP 41378 System with K2 and Spitzer". *Astronomical Journal* 157.5, 185.

- Bessell, M. S.; Castelli, F., and Plez, B. (1998). "Model atmospheres broad-band colors, bolometric corrections and temperature calibrations for O-M stars". *Astronomy and Astrophysics* 333, pp. 231–250.
- Bieryla, A.; Tronsgaard, R.; Buchhave, L. A.; Latham, D. W.; Torres, G.; Eastman, J.; Quinn Samuel, N.; Yahalom, D. A.; Mink, J.; Esquerdo, G. A.; Calkins, M. L., and Berlind, P. (2021). "Stellar Parameter Classification of TESS recon spectra from TRES and FIES". In: *Posters from the TESS Science Conference II (TSC2)*.
- Blackwell, D. E. and Shallis, M. J. (1977). "Stellar angular diameters from infrared photometry. Application to Arcturus and other stars; with effective temperatures." *Monthly Notices of the Royal Astronomical Society* 180, pp. 177–191.
- Blanco-Cuaresma, S.; Soubiran, C.; Heiter, U., and Jofré, P. (2014). "Determining stellar atmospheric parameters and chemical abundances of FGK stars with iSpec". *Astronomy and Astrophysics* 569, A111.
- Blanco-Cuaresma, S. (2019). "Modern stellar spectroscopy caveats". *Monthly Notices of the Royal Astronomical Society* 486.2, pp. 2075–2101.
- Bonomo, A. S.; Desidera, S.; Benatti, S.; Borsa, F.; Crespi, S.; Damasso, M.; Lanza, A. F.; Sozzetti, A.; Lodato, G.; Marzari, F.; Boccato, C.; Claudi, R. U.; Cosentino, R.; Covino, E.; Gratton, R., et al. (2017a). "The GAPS Programme with HARPS-N at TNG . XIV. Investigating giant planet migration history via improved eccentricity and mass determination for 231 transiting planets". *Astronomy and Astrophysics* 602, A107.
- Bonomo, A. S.; Desidera, S.; Benatti, S.; Borsa, F.; Crespi, S.; Damasso, M.; Lanza, A. F.; Sozzetti, A.; Lodato, G.; Marzari, F.; Boccato, C.; Claudi, R. U.; Cosentino, R.; Covino, E.; Gratton, R., et al. (2017b). "VizieR Online Data Catalog: 231 transiting planets eccentricity and mass (Bonomo+, 2017)". *VizieR Online Data Catalog*, J/A+A/602/A107.
- Bonomo, A. S.; Sozzetti, A.; Lovis, C.; Malavolta, L.; Rice, K.; Buchhave, L. A.; Sasselov, D.; Cameron, A. C.; Latham, D. W.; Molinari, E.; Pepe, F.; Udry, S.; Affer, L.; Charbonneau, D.; Cosentino, R., et al. (2014). "Characterization of the planetary system Kepler-101 with HARPS-N. A hot super-Neptune with an Earth-sized low-mass companion". *Astronomy and Astrophysics* 572, A2.
- Borderies, N.; Goldreich, P., and Tremaine, S. (1984). "Excitation of inclinations in ring-satellite systems". *Astrophysical Journal* 284, pp. 429–434.

- Borucki, W. J. and Summers, A. L. (1984). "The photometric method of detecting other planetary systems". *Icarus* 58.1, pp. 121–134.
- Borucki, W. J.; Koch, D.; Basri, G.; Batalha, N.; Brown, T.; Caldwell, D.; Caldwell, J.; Christensen-Dalsgaard, J.; Cochran, W. D.; DeVore, E.; Dunham, E. W.; Dupree, A. K.; Gautier, T. N.; Geary, J. C.; Gilliland, R., et al. (2010). "Kepler Planet-Detection Mission: Introduction and First Results". *Science* 327.5968, p. 977.
- Boss, A. P. (1997). "Giant planet formation by gravitational instability." *Science* 276, pp. 1836–1839.
- Bouma, L. G.; Hartman, J. D.; Bhatti, W.; Winn, J. N., and Bakos, G. Á. (2019). "Cluster Difference Imaging Photometric Survey. I. Light Curves of Stars in Open Clusters from TESS Sectors 6 & 7". *arXiv e-prints*, arXiv:1910.01133.
- Bourrier, V.; Lovis, C.; Cretignier, M.; Allart, R.; Dumusque, X.; Delisle, J. .-B.; Deline, A.; Sousa, S. G.; Adibekyan, V.; Alibert, Y.; Barros, S. C. C.; Borsa, F.; Cristiani, S.; Demangeon, O.; Ehrenreich, D., et al. (2021). "The Rossiter-McLaughlin effect revolutions: an ultra-short period planet and a warm mini-Neptune on perpendicular orbits". *Astronomy and Astrophysics* 654, A152.
- Brahm, R.; Nielsen, L. D.; Wittenmyer, R. A.; Wang, S.; Rodriguez, J. E.; Espinoza, N.; Jones, M. I.; Jordán, A.; Henning, T.; Hobson, M.; Kossakowski, D.; Rojas, F.; Sarkis, P.; Schlecker, M.; Trifonov, T., et al. (2020). "TOI-481 b and TOI-892 b: Two Long-period Hot Jupiters from the Transiting Exoplanet Survey Satellite". *Astronomical Journal* 160.5, 235.
- Brewer, L. N.; Sandquist, E. L.; Mathieu, R. D.; Milliman, K.; Geller, A. M.; Jeffries Mark W., J.; Orosz, J. A.; Brogaard, K.; Platais, I.; Bruntt, H.; Grundahl, F.; Stello, D., and Frandsen, S. (2016). "Determining the Age of the Kepler Open Cluster NGC 6819 With a New Triple System and Other Eclipsing Binary Stars". *Astronomical Journal* 151.3, 66.
- Brogaard, K.; Bruntt, H.; Grundahl, F.; Clausen, J. V.; Frandsen, S.; Vandenberg, D. A., and Bedin, L. R. (2011). "Age and helium content of the open cluster NGC 6791 from multiple eclipsing binary members. I. Measurements, methods, and first results". *Astronomy and Astrophysics* 525, A2.

- Brogaard, K.; Christiansen, S. M.; Grundahl, F.; Miglio, A.; Izzard, R. G.; Tauris, T. M.; Sand quist, E. L.; VandenBerg, D. A.; Jessen-Hansen, J.; Arentoft, T.; Bruntt, H.; Frandsen, S.; Orosz, J. A.; Feiden, G. A.; Mathieu, R., et al. (2018). "The blue straggler V106 in NGC 6791: a prototype progenitor of old single giants masquerading as young". *Monthly Notices of the Royal Astronomical Society* 481.4, pp. 5062–5072.
- Brogaard, K.; Jessen-Hansen, J.; Handberg, R.; Arentoft, T.; Frandsen, S.; Grundahl, F.; Bruntt, H.; Sandquist, E. L.; Miglio, A.; Beck, P. G.; Thygesen, A. O.; Kjærgaard, K. L., and Haugaard, N. A. (2016). "Testing asteroseismic scaling relations using eclipsing binaries in star clusters and the field". *Astronomische Nachrichten* 337.8-9, p. 793.
- Brogaard, K.; VandenBerg, D. A.; Bruntt, H.; Grundahl, F.; Frandsen, S.; Bedin, L. R.; Milone, A. P.; Dotter, A.; Feiden, G. A.; Stetson, P. B.; Sandquist, E.; Miglio, A.; Stello, D., and Jessen-Hansen, J. (2012). "Age and helium content of the open cluster NGC 6791 from multiple eclipsing binary members. II. Age dependencies and new insights". *Astronomy and Astrophysics* 543, A106.
- Brogaard, K.; Sandquist, E.; Jessen-Hansen, J.; Grundahl, F., and Frandsen, S. (2015). "Exploiting the Open Clusters in the Kepler and CoRoT Fields". In: *Asteroseismology of Stellar Populations in the Milky Way*. Vol. 39, p. 51.
- Brown, D. J. A. (2014). "Discrepancies between isochrone fitting and gyrochronology for exoplanet host stars?" *Monthly Notices of the Royal Astronomical Society* 442.2, pp. 1844–1862.
- Brown, D. J. A.; Cameron, A. C.; Anderson, D. R.; Enoch, B.; Hellier, C.; Maxted, P. F. L.; Miller, G. R. M.; Pollacco, D.; Queloz, D.; Simpson, E.; Smalley, B.; Triaud, A. H. M. J.; Boisse, I.; Bouchy, F.; Gillon, M., et al. (2012). "Rossiter-McLaughlin effect measurements for WASP-16, WASP-25 and WASP-31". *Monthly Notices of the Royal Astronomical Society* 423, pp. 1503–1520.
- Brown, T. M.; Baliber, N.; Bianco, F. B.; Bowman, M.; Burleson, B.; Conway, P.; Crellin, M.; Depagne, É.; De Vera, J.; Dilday, B.; Dragomir, D.; Dubberley, M.; Eastman, J. D.; Elphick, M.; Falarski, M., et al. (2013). "Las Cumbres Observatory Global Telescope Network". *Publications of the Astronomical Society of the Pacific* 125, p. 1031.
- Brown, T. M.; Gilliland, R. L.; Noyes, R. W., and Ramsey, L. W. (1991). "Detection of possible p-mode oscillations on Procyon". *Astrophysical Journal* 368, pp. 599–609.

- Bruntt, H.; Bedding, T. R.; Quirion, P.-O.; Lo Curto, G.; Carrier, F.; Smalley, B.; Dall, T. H.; Arentoft, T.; Bazot, M., and Butler, R. P. (2010). “Accurate fundamental parameters for 23 bright solar-type stars”. *Monthly Notices of the Royal Astronomical Society* 405, pp. 1907–1923.
- Bryan, M. L.; Knutson, H. A.; Lee, E. J.; Fulton, B. J.; Batygin, K.; Ngo, H., and Meshkat, T. (2019). “An Excess of Jupiter Analogs in Super-Earth Systems”. *Astronomical Journal* 157.2, 52.
- Buchhave, L. A.; Bakos, G. Á.; Hartman, J. D.; Torres, G.; Kovács, G.; Latham, D. W.; Noyes, R. W.; Esquerdo, G. A.; Everett, M.; Howard, A. W.; Marcy, G. W.; Fischer, D. A.; Johnson, J. A.; Andersen, J.; Fűrész, G., et al. (2010). “HAT-P-16b: A 4 M J Planet Transiting a Bright Star on an Eccentric Orbit”. *Astrophysical Journal* 720.2, pp. 1118–1125.
- Buchhave, L. A.; Bakos, G. Á.; Hartman, J. D.; Torres, G.; Latham, D. W.; Andersen, J.; Kovács, G.; Noyes, R. W.; Shporer, A.; Esquerdo, G. A.; Fischer, D. A.; Johnson, J. A.; Marcy, G. W.; Howard, A. W.; Béky, B., et al. (2011). “Hat-P-28b and Hat-P-29b: Two Sub-Jupiter Mass Transiting Planets”. *Astrophysical Journal* 733.2, 116.
- Buchhave, L. A.; Latham, D. W.; Johansen, A.; Bizzarro, M.; Torres, G.; Rowe, J. F.; Batalha, N. M.; Borucki, W. J.; Brugamyer, E.; Caldwell, C.; Bryson, S. T.; Ciardi, D. R.; Cochran, W. D.; Endl, M.; Esquerdo, G. A., et al. (2012a). “VizieR Online Data Catalog: Stellar parameters of KOI stars (Buchhave+, 2012)”. *VizieR Online Data Catalog (other)* 0380, J/other/Nat/486.
- Buchhave, L. A.; Latham, D. W.; Johansen, A.; Bizzarro, M.; Torres, G.; Rowe, J. F.; Batalha, N. M.; Borucki, W. J.; Brugamyer, E.; Caldwell, C.; Bryson, S. T.; Ciardi, D. R.; Cochran, W. D.; Endl, M.; Esquerdo, G. A., et al. (2012b). “An abundance of small exoplanets around stars with a wide range of metallicities”. *Nature* 486, pp. 375–377.
- Buchhave, L. A.; Bizzarro, M.; Latham, D. W.; Sasselov, D.; Cochran, W. D.; Endl, M.; Isaacson, H.; Juncher, D., and Marcy, G. W. (2014). “Three regimes of extrasolar planet radius inferred from host star metallicities”. *Nature* 509.7502, pp. 593–595.
- Burkert, A.; Bate, M. R., and Bodenheimer, P. (1997). “Protostellar fragmentation in a power-law density distribution”. *Monthly Notices of the Royal Astronomical Society* 289.3, pp. 497–504.

- Cabrera, J.; Csizmadia, S.; Erikson, A.; Rauer, H., and Kirste, S. (2012). “A study of the performance of the transit detection tool DST in space-based surveys. Application of the CoRoT pipeline to Kepler data”. *Astronomy and Astrophysics* 548, A44.
- Campante, T. L.; Chaplin, W. J.; Lund, M. N.; Huber, D.; Hekker, S.; García, R. A.; Corsaro, E.; Handberg, R.; Miglio, A.; Arentoft, T.; Basu, S.; Bedding, T. R.; Christensen-Dalsgaard, J.; Davies, G. R.; Elsworth, Y. P., et al. (2014). “Limits on Surface Gravities of Kepler Planet-candidate Host Stars from Non-detection of Solar-like Oscillations”. *Astrophysical Journal* 783, 123.
- Campante, T. L.; Lund, M. N.; Kuszlewicz, J. S.; Davies, G. R.; Chaplin, W. J.; Albrecht, S.; Winn, J. N.; Bedding, T. R.; Benomar, O.; Bossini, D.; Handberg, R.; Santos, A. R. G.; Van Eylen, V.; Basu, S.; Christensen-Dalsgaard, J., et al. (2016). “Spin-Orbit Alignment of Exoplanet Systems: Ensemble Analysis Using Asteroseismology”. *Astrophysical Journal* 819, 85.
- Campante, T. L. (2017). “On the detectability of solar-like oscillations with the NASA TESS mission”. In: *European Physical Journal Web of Conferences*. Vol. 160. European Physical Journal Web of Conferences.
- Campbell, B.; Walker, G. A. H., and Yang, S. (1988). “A Search for Substellar Companions to Solar-type Stars”. *Astrophysical Journal* 331, p. 902.
- Cantat-Gaudin, T. and Anders, F. (2019). “VizieR Online Data Catalog: Gaia DR2 open clusters in the Milky Way. II (Cantat-Gaudin+, 2020)”. *VizieR Online Data Catalog*, J/A+A/633/A99.
- Cantat-Gaudin, T.; Jordi, C.; Vallenari, A.; Bragaglia, A.; Balaguer-Núñez, L.; Soubiran, C.; Bossini, D.; Moitinho, A.; Castro-Ginard, A.; Krone-Martins, A.; Casamiquela, L.; Sordo, R., and Carrera, R. (2018). “A Gaia DR2 view of the open cluster population in the Milky Way”. *Astronomy and Astrophysics* 618, A93.
- Capitanio, L.; Lallement, R.; Vergely, J. L.; Elyajouri, M., and Monreal-Ibero, A. (2017). “Three-dimensional mapping of the local interstellar medium with composite data”. *Astronomy and Astrophysics* 606, A65.
- Carleo, I.; Gandolfi, D.; Barragán, O.; Livingston, J. H.; Persson, C. M.; Lam, K. W. F.; Vidotto, A.; Lund, M. B.; Villarreal D’Angelo, C.; Collins, K. A.; Fossati, L.; Howard, A. W.; Kubyshkina, D.; Brahm, R.; Oklopčić, A., et al. (2020). “The Multiplanet System TOI-421”. *Astronomical Journal* 160.3, 114.

- Carrera, D.; Raymond, S. N., and Davies, M. B. (2019). “Planet-planet scattering as the source of the highest eccentricity exoplanets”. *Astronomy and Astrophysics* 629, L7.
- Carretta, E.; Bragaglia, A.; Gratton, R. G., and Tosi, M. (2004). “Iron abundances from high-resolution spectroscopy of the open clusters NGC 2506, NGC 6134, and IC 4651”. *Astronomy and Astrophysics* 422, pp. 951–962.
- Casagrande, L.; Portinari, L.; Glass, I. S.; Laney, D.; Silva Aguirre, V.; Datson, J.; Andersen, J.; Nordström, B.; Holmberg, J.; Flynn, C., and Asplund, M. (2014). “Towards stellar effective temperatures and diameters at 1 per cent accuracy for future surveys”. *Monthly Notices of the Royal Astronomical Society* 439, pp. 2060–2073.
- Casagrande, L.; Ramírez, I.; Meléndez, J.; Bessell, M., and Asplund, M. (2010). “An absolutely calibrated T_{eff} scale from the infrared flux method. Dwarfs and subgiants”. *Astronomy and Astrophysics* 512, A54.
- Casagrande, L. and VandenBerg, D. A. (2018a). “On the use of Gaia magnitudes and new tables of bolometric corrections”. *Monthly Notices of the Royal Astronomical Society* 479.1, pp. L102–L107.
- Casagrande, L. and VandenBerg, D. A. (2018b). “Synthetic Stellar Photometry - II. Testing the bolometric flux scale and tables of bolometric corrections for the Hipparcos/Tycho, Pan-STARRS1, SkyMapper, and JWST systems”. *Monthly Notices of the Royal Astronomical Society* 475.4, pp. 5023–5040.
- Caselli, P.; Benson, P. J.; Myers, P. C., and Tafalla, M. (2002). “Dense Cores in Dark Clouds. XIV. N_2H^+ (1-0) Maps of Dense Cloud Cores”. *Astrophysical Journal* 572.1, pp. 238–263.
- Castelli, F. and Kurucz, R. L. (2004). “New Grids of ATLAS9 Model Atmospheres”. *astro-ph/0405087*.
- Cegla, H. M.; Lovis, C.; Bourrier, V.; Beeck, B.; Watson, C. A., and Pepe, F. (2016). “The Rossiter-McLaughlin effect reloaded: Probing the 3D spin-orbit geometry, differential stellar rotation, and the spatially-resolved stellar spectrum of star-planet systems”. *Astronomy and Astrophysics* 588, A127.
- Ceillier, T.; Tayar, J.; Mathur, S.; Salabert, D.; García, R. A.; Stello, D.; Pinsonneault, M. H.; van Saders, J.; Beck, P. G., and Bloemen, S. (2017). “Surface rotation of Kepler red giant stars”. *Astronomy and Astrophysics* 605, A111.

- Chaplin, W. J.; Basu, S.; Huber, D.; Serenelli, A.; Casagrande, L.; Silva Aguirre, V.; Ball, W. H.; Creevey, O. L.; Gizon, L.; Handberg, R.; Karoff, C.; Lutz, R.; Marques, J. P.; Miglio, A.; Stello, D., et al. (2014). “Astroseismic Fundamental Properties of Solar-type Stars Observed by the NASA Kepler Mission”. *The Astrophysical Journal Supplement Series* 210.1, 1.
- Chaplin, W. J.; Cegla, H. M.; Watson, C. A.; Davies, G. R., and Ball, W. H. (2019). “Filtering Solar-Like Oscillations for Exoplanet Detection in Radial Velocity Observations”. *Astronomical Journal* 157.4, 163.
- Chaplin, W. J.; Kjeldsen, H.; Bedding, T. R.; Christensen-Dalsgaard, J.; Gilliland, R. L.; Kawaler, S. D.; Appourchaux, T.; Elsworth, Y.; García, R. A.; Houdek, G.; Karoff, C.; Metcalfe, T. S.; Molenda-Żakowicz, J.; Monteiro, M. J. P. F. G.; Thompson, M. J., et al. (2011). “Predicting the Detectability of Oscillations in Solar-type Stars Observed by Kepler”. *Astrophysical Journal* 732.1, 54.
- Charbonneau, D.; Brown, T. M.; Latham, D. W., and Mayor, M. (2000). “Detection of Planetary Transits Across a Sun-like Star”. *The Astrophysical Journal Letters* 529.1, pp. L45–L48.
- Chatterjee, S.; Ford, E. B.; Matsumura, S., and Rasio, F. A. (2008). “Dynamical Outcomes of Planet-Planet Scattering”. *Astrophysical Journal* 686, pp. 580–602.
- Chatterjee, S.; Rasio, F. A.; Sills, A., and Glebbeek, E. (2013). “Stellar Collisions and Blue Straggler Stars in Dense Globular Clusters”. *Astrophysical Journal* 777.2, 106.
- Choi, J.; Dotter, A.; Conroy, C.; Cantiello, M.; Paxton, B., and Johnson, B. D. (2016). “Mesa Isochrones and Stellar Tracks (MIST). I. Solar-scaled Models”. *Astrophysical Journal* 823.2, 102.
- Chontos, A.; Huber, D.; Latham, D. W.; Bieryla, A.; Van Eylen, V.; Bedding, T. R.; Berger, T.; Buchhave, L. A.; Campante, T. L., and Chaplin, W. J. (2019). “The Curious Case of KOI 4: Confirming Kepler’s First Exoplanet Detection”. *Astronomical Journal* 157.5, 192.
- Christensen-Dalsgaard, J. and Gough, D. O. (1976). “Towards a helioseismic inverse problem”. *Nature* 259.5539, pp. 89–92.
- Christensen-Dalsgaard, J. (2008a). “ADIPLS—the Aarhus adiabatic oscillation package”. *Astrophysics and Space Science* 316.1-4, pp. 113–120.

- Christensen-Dalsgaard, J. (2008b). *Lecture Notes on Stellar Stellar Structure and Evolution*. Sixth Edition. Institut for Fysik og Astronomi, Aarhus Universitet.
- Ciardi, D. R.; Beichman, C. A.; Horch, E. P., and Howell, S. B. (2015). “Understanding the Effects of Stellar Multiplicity on the Derived Planet Radii from Transit Surveys: Implications for Kepler, K2, and TESS”. *Astrophysical Journal* 805.1, 16.
- Claret, A. (2000). “A new non-linear limb-darkening law for LTE stellar atmosphere models. Calculations for $-5.0 \leq \log[M/H] \leq +1$, $2000 \text{ K} \leq T_{eff} \leq 50000 \text{ K}$ at several surface gravities”. *Astronomy and Astrophysics* 363, pp. 1081–1190.
- Claret, A. (2017). “Limb and gravity-darkening coefficients for the TESS satellite at several metallicities, surface gravities, and microturbulent velocities”. *Astronomy and Astrophysics* 600, A30.
- Claret, A. (2018). “VizieR Online Data Catalog: Limb-darkening for TESS, Kepler, Corot, MOST (Claret, 2018)”. *VizieR Online Data Catalog*, J/A+A/618/A20.
- Claret, A. and Bloemen, S. (2011). “Gravity and limb-darkening coefficients for the Kepler, CoRoT, Spitzer, uvby, UBVRIJHK, and Sloan photometric systems”. *Astronomy and Astrophysics* 529, A75.
- Claret, A.; Hauschildt, P. H., and Witte, S. (2013). “New limb-darkening coefficients for Phoenix/1d model atmospheres. II. Calculations for $5000 \text{ K} \leq T_{eff} \leq 10\,000 \text{ K}$ Kepler, CoRot, Spitzer, uvby, UBVRIJHK, Sloan, and 2MASS photometric systems”. *Astronomy and Astrophysics* 552, A16.
- Cochran, W. D.; Redfield, S.; Endl, M., and Cochran, A. L. (2008). “The Spin-Orbit Alignment of the HD 17156 Transiting Eccentric Planetary System”. *The Astrophysical Journal Letters* 683.1, p. L59.
- Coelho, P. R. T. (2014). “A new library of theoretical stellar spectra with scaled-solar and α -enhanced mixtures”. *Monthly Notices of the Royal Astronomical Society* 440.2, pp. 1027–1043.
- Coelho, P.; Barbuy, B.; Melendez, J.; Schiavon, R., and Castilho, B. (2005). “VizieR Online Data Catalog: High-resolution synthetic stellar library (Coelho+, 2005)”. *VizieR Online Data Catalog* 6120.

- Cohen, M. (1975). "Infrared observations of young stars - VI. A 2- to 4-micron search for molecular features." *Monthly Notices of the Royal Astronomical Society* 173, pp. 279–293.
- Cohen, M.; Wheaton, W. A., and Megeath, S. T. (2003). "Spectral Irradiance Calibration in the Infrared. XIV. The Absolute Calibration of 2MASS". *Astronomical Journal* 126.2, pp. 1090–1096.
- Collins, K. A.; Kielkopf, J. F.; Stassun, K. G., and Hessman, F. V. (2017). "AstroImageJ: Image Processing and Photometric Extraction for Ultra-precise Astronomical Light Curves". *Astronomical Journal* 153, 77.
- Collins, K. (2019). "TESS Follow-up Observing Program Working Group (TFOP WG) Sub Group 1 (SG1): Ground-based Time-series Photometry". In: *American Astronomical Society Meeting Abstracts #233*. Vol. 233. American Astronomical Society Meeting Abstracts.
- Collins, K. A.; Collins, K. I.; Pepper, J.; Labadie-Bartz, J.; Stassun, K. G.; Gaudi, B. S.; Bayliss, D.; Bento, J.; COLÓN, K. D.; Feliz, D.; James, D.; Johnson, M. C.; Kuhn, R. B.; Lund, M. B.; Penny, M. T., et al. (2018). "The KELT Follow-up Network and Transit False-positive Catalog: Pre-vetted False Positives for TESS". *Astronomical Journal* 156.5, 234.
- Corsaro, E.; Grundahl, F.; Leccia, S.; Bonanno, A.; Kjeldsen, H., and Paternò, L. (2012). "Solar-like oscillations in the G9.5 subgiant β Aquilae". *Astronomy and Astrophysics* 537, A9.
- Cosentino, R.; Lovis, C.; Pepe, F.; Collier Cameron, A.; Latham, D. W.; Molinari, E.; Udry, S.; Bezawada, N.; Black, M.; Born, A.; Buchschacher, N.; Charbonneau, D.; Figueira, P.; Fleury, M.; Galli, A., et al. (2012). "Harps-N: the new planet hunter at TNG". In: *Ground-based and Airborne Instrumentation for Astronomy IV*. Vol. 8446. Society of Photo-Optical Instrumentation Engineers (SPIE) Conference Series.
- Crossfield, I. J. M.; Petigura, E.; Schlieder, J. E.; Howard, A. W.; Fulton, B. J.; Aller, K. M.; Ciardi, D. R.; Lépine, S.; Barclay, T.; de Pater, I.; de Kleer, K.; Quintana, E. V.; Christiansen, J. L.; Schlaflly, E.; Kaltenegger, L., et al. (2015). "A Nearby M Star with Three Transiting Super-Earths Discovered by K2". *Astrophysical Journal* 804, 10.
- Crossfield, I. J. M.; Ciardi, D. R.; Petigura, E. A.; Sinukoff, E.; Schlieder, J. E.; Howard, A. W.; Beichman, C. A.; Isaacson, H.; Dressing, C. D.; Christiansen, J. L.; Fulton, B. J.; Lépine, S.; Weiss, L.; Hirsch, L.; Livingston, J., et al. (2016). "197 Candidates and 104 Validated Planets

- in K2’s First Five Fields”. *The Astrophysical Journal Supplement Series* 226.1, 7.
- Cummings, J. D.; Kalirai, J. S.; Tremblay, P.-E.; Ramirez-Ruiz, E., and Choi, J. (2018). “The White Dwarf Initial-Final Mass Relation for Progenitor Stars from 0.85 to 7.5 M”. *Astrophysical Journal* 866, 21.
- Currie, T.; Lawson, K.; Schneider, G.; Lyra, W.; Wisniewski, J.; Grady, C.; Guyon, O.; Tamura, M.; Kotani, T.; Kawahara, H.; Brandt, T.; Uyama, T.; Muto, T.; Dong, R.; Kudo, T., et al. (2022). “Images of embedded Jovian planet formation at a wide separation around AB Aurigae”. *Nature Astronomy* 6, pp. 751–759.
- Cutri, R. M.; Skrutskie, M. F.; van Dyk, S.; Beichman, C. A.; Carpenter, J. M.; Chester, T.;Cambresy, L.; Evans, T.; Fowler, J.; Gizis, J.; Howard, E.; Huchra, J.; Jarrett, T.; Kopan, E. L.; Kirkpatrick, J. D., et al. (2003). “VizieR Online Data Catalog: 2MASS All-Sky Catalog of Point Sources (Cutri+ 2003)”. *VizieR Online Data Catalog*, II/246.
- Dai, F.; Masuda, K.; Beard, C.; Robertson, P.; Goldberg, M.; Batygin, K.; Bouma, L.; Lissauer, J. J.; Knudstrup, E.; Albrecht, S.; Howard, A. W.; Knutson, H. A.; Petigura, E. A.; Weiss, L. M.; Isaacson, H., et al. (2023). “TOI-1136 is a Young, Coplanar, Aligned Planetary System in a Pristine Resonant Chain”. *Astronomical Journal* 165.2, 33.
- Dalba, P. A.; Gupta, A. F.; Rodriguez, J. E.; Dragomir, D.; Huang, C. X.; Kane, S. R.; Quinn, S. N.; Bieryla, A.; Esquerdo, G. A.; Fulton, B. J.; Scarsdale, N.; Batalha, N. M.; Beard, C.; Behmard, A.; Chontos, A., et al. (2020). “The TESS-Keck Survey. I. A Warm Sub-Saturn-mass Planet and a Caution about Stray Light in TESS Cameras”. *Astronomical Journal* 159.5, 241.
- Davies, G. R.; Aguirre, V. S.; Bedding, T. R.; Handberg, R.; Lund, M. N.; Chaplin, W. J.; Huber, D.; White, T. R.; Benomar, O.; Hekker, S.; Basu, S.; Campante, T. L.; Christensen-Dalsgaard, J.; Elsworth, Y.; Karoff, C., et al. (2016). “Oscillation frequencies for 35 Kepler solar-type planet-hosting stars using Bayesian techniques and machine learning”. *Monthly Notices of the Royal Astronomical Society* 456, pp. 2183–2195.
- Davies, G. R.; Handberg, R.; Miglio, A.; Campante, T. L.; Chaplin, W. J., and Elsworth, Y. (2014). “Why should we correct reported pulsation frequencies for stellar line-of-sight Doppler velocity shifts?” *Monthly Notices of the Royal Astronomical Society* 445, pp. L94–L98.

- Dawson, R. I. and Johnson, J. A. (2012). "The Photoeccentric Effect and Proto-hot Jupiters. I. Measuring Photometric Eccentricities of Individual Transiting Planets". *Astrophysical Journal* 756.2, 122.
- Dawson, R. I. and Johnson, J. A. (2018). "Origins of Hot Jupiters". *Annual Review of Astronomy & Astrophysics* 56, pp. 175–221.
- Dawson, R. I. and Murray-Clay, R. A. (2013). "Giant Planets Orbiting Metal-rich Stars Show Signatures of Planet-Planet Interactions". *The Astrophysical Journal Letters* 767.2, L24.
- Deheuvels, S.; Doğan, G.; Goupil, M. J.; Appourchaux, T.; Benomar, O.; Bruntt, H.; Campante, T. L.; Casagrande, L.; Ceillier, T.; Davies, G. R.; De Cat, P.; Fu, J. N.; García, R. A.; Lobel, A.; Mosser, B., et al. (2014). "Seismic constraints on the radial dependence of the internal rotation profiles of six Kepler subgiants and young red giants". *Astronomy and Astrophysics* 564, A27.
- Deheuvels, S.; García, R. A.; Chaplin, W. J.; Basu, S.; Antia, H. M.; Appourchaux, T.; Benomar, O.; Davies, G. R.; Elsworth, Y.; Gizon, L.; Goupil, M. J.; Reese, D. R.; Regulo, C.; Schou, J.; Stahn, T., et al. (2012). "Seismic Evidence for a Rapidly Rotating Core in a Lower-giant-branch Star Observed with Kepler". *Astrophysical Journal* 756, 19.
- Dekker, H.; D'Odorico, S.; Kaufer, A.; Delabre, B., and Kotzlowski, H. (2000). "Design, construction, and performance of UVES, the echelle spectrograph for the UT2 Kueyen Telescope at the ESO Paranal Observatory". In: *Proceedings of SPIE*. Ed. by M. Iye and A. F. Moorwood. Vol. 4008. Society of Photo-Optical Instrumentation Engineers (SPIE) Conference Series, pp. 534–545.
- Demangeon, O. D. S.; Faedi, F.; Hébrard, G.; Brown, D. J. A.; Barros, S. C. C.; Doyle, A. P.; Maxted, P. F. L.; Collier Cameron, A.; Hay, K. L.; Alikakos, J.; Anderson, D. R.; Armstrong, D. J.; Boumis, P.; Bonomo, A. S.; Bouchy, F., et al. (2018). "The discovery of WASP-151b, WASP-153b, WASP-156b: Insights on giant planet migration and the upper boundary of the Neptunian desert". *Astronomy and Astrophysics* 610, A63.
- Deng, L.; Xin, Y.; Zhang, X.; Li, Y.; Jiang, X.; Wang, G.; Wang, K.; Zhou, J.-L.; Yan, Z., and Luo, Z. (2013). "SONG China project - participating in the global network". *Proceedings of the International Astronomical Union* 8, pp. 318–319.

- Djupvik, A. A. and Andersen, J. (2010). "The Nordic Optical Telescope". In: *Highlights of Spanish Astrophysics V*. Vol. 14. *Astrophysics and Space Science Proceedings*, p. 211.
- Doyle, A. P.; Davies, G. R.; Smalley, B.; Chaplin, W. J., and Elsworth, Y. (2014). "Determining stellar macroturbulence using asteroseismic rotational velocities from Kepler". *Monthly Notices of the Royal Astronomical Society* 444.4, pp. 3592–3602.
- Dravins, D.; Ludwig, H.-G.; Dahlén, E., and Pazira, H. (2017). "Spatially resolved spectroscopy across stellar surfaces. I. Using exoplanet transits to analyze 3D stellar atmospheres". *Astronomy and Astrophysics* 605, A90.
- Dressing, C. D. and Charbonneau, D. (2013). "The Occurrence Rate of Small Planets around Small Stars". *Astrophysical Journal* 767.1, 95.
- Eggen, O. J. (1955). "The Masses of the Subgiants". *Publications of the Astronomical Society of the Pacific* 67.398, p. 315.
- Endl, M.; Kürster, M., and Els, S. (2000). "The planet search program at the ESO Coudé Echelle spectrometer. I. Data modeling technique and radial velocity precision tests". *Astronomy and Astrophysics* 362, pp. 585–594.
- Etzel, P. B. (2004). *SBOP: Spectroscopic Binary Orbit Program*.
- Fabrycky, D. C. and Winn, J. N. (2009). "Exoplanetary Spin-Orbit Alignment: Results from the Ensemble of Rossiter-McLaughlin Observations". *Astrophysical Journal* 696, pp. 1230–1240.
- Fabrycky, D. and Tremaine, S. (2007). "Shrinking Binary and Planetary Orbits by Kozai Cycles with Tidal Friction". *Astrophysical Journal* 669.2, pp. 1298–1315.
- Fedele, D.; van den Ancker, M. E.; Henning, T.; Jayawardhana, R., and Oliveira, J. M. (2010). "Timescale of mass accretion in pre-main-sequence stars". *Astronomy and Astrophysics* 510, A72.
- Fielding, D. B.; McKee, C. F.; Socrates, A.; Cunningham, A. J., and Klein, R. I. (2015). "The turbulent origin of spin-orbit misalignment in planetary systems". *Monthly Notices of the Royal Astronomical Society* 450, pp. 3306–3318.
- Fischer, D. A. and Valenti, J. (2005). "The Planet-Metallicity Correlation". *Astrophysical Journal* 622.2, pp. 1102–1117.

- Foreman-Mackey, D.; Agol, E.; Angus, R., and Ambikasaran, S. (2017). “Fast and scalable Gaussian process modeling with applications to astronomical time series”. *ArXiv*.
- Foreman-Mackey, D.; Hogg, D. W.; Lang, D., and Goodman, J. (2013). “emcee: The MCMC Hammer”. *Publications of the Astronomical Society of the Pacific* 125.925, p. 306.
- Foucart, F. and Lai, D. (2011). “Evolution of spin direction of accreting magnetic protostars and spin-orbit misalignment in exoplanetary systems - II. Warped discs”. *Monthly Notices of the Royal Astronomical Society* 412, pp. 2799–2815.
- Frandsen, S. and Lindberg, B. (1999). “FIES: A high resolution FIber fed Echelle Spectrograph for the NOT (poster)”. In: *Astrophysics with the NOT*. Ed. by H. Karttunen and V. Piirola, p. 71.
- Fredslund Andersen, M.; Handberg, R.; Weiss, E.; Frandsen, S.; Simón-Díaz, S.; Grundahl, F., and Pallé, P. (2019). “Conducting the SONG: The Robotic Nature and Efficiency of a Fully Automated Telescope”. *Publications of the Astronomical Society of the Pacific* 131.998, p. 045003.
- Fridlund, M.; Gaidos, E.; Barragán, O.; Persson, C. M.; Gandolfi, D.; Cabrera, J.; Hirano, T.; Kuzuhara, M.; Csizmadia, S.; Nowak, G.; Endl, M.; Grziwa, S.; Korth, J.; Pfaff, J.; Bitsch, B., et al. (2017). “K2-111 b - a short period super-Earth transiting a metal poor, evolved old star”. *Astronomy and Astrophysics* 604, A16.
- Friel, E. D. and Janes, K. A. (1993). “Metallicities and radial velocities of old open clusters.” *Astronomy and Astrophysics* 267, pp. 75–91.
- Friel, E. D.; Janes, K. A.; Tavarez, M.; Scott, J.; Katsanis, R.; Lotz, J.; Hong, L., and Miller, N. (2002). “Metallicities of Old Open Clusters”. *Astronomical Journal* 124.5, pp. 2693–2720.
- Fuhrmann, K. (2004). “Nearby stars of the Galactic disk and halo. III.” *Astronomische Nachrichten* 325.1, pp. 3–80.
- Fujii, Y.; Angerhausen, D.; Deitrick, R.; Domagal-Goldman, S.; Grenfell, J. L.; Hori, Y.; Kane, S. R.; Pallé, E.; Rauer, H.; Siegler, N.; Stapelfeldt, K., and Stevenson, K. B. (2018). “Exoplanet Biosignatures: Observational Prospects”. *Astrobiology* 18.6, pp. 739–778.
- Fukui, A.; Narita, N.; Tristram, P. J.; Sumi, T.; Abe, F.; Itow, Y.; Sullivan, D. J.; Bond, I. A.; Hirano, T.; Tamura, M.; Bennett, D. P.; Furusawa, K.; Hayashi, F.; Hearnshaw, J. B.; Hosaka, S., et al. (2011). “Measurements

- of Transit Timing Variations for WASP-5b”. *Publications of the Astronomical Society of Japan* 63, p. 287.
- Fűrész, G. (2008). “Design and Application of High Resolution and Multiobject Spectrographs: Dynamical Studies of Open Clusters”. PhD thesis. University of Szeged, Hungary.
- Gai, N.; Basu, S.; Chaplin, W. J., and Elsworth, Y. (2011). “An In-depth Study of Grid-based Asteroseismic Analysis”. *Astrophysical Journal* 730, 63.
- Gaia Collaboration; Brown, A. G. A.; Vallenari, A.; Prusti, T.; de Bruijne, J. H. J.; Babusiaux, C.; Bailer-Jones, C. A. L.; Biermann, M.; Evans, D. W.; Eyer, L.; Jansen, F.; Jordi, C.; Klioner, S. A.; Lammers, U.; Lindegren, L., et al. (2018). “Gaia Data Release 2. Summary of the contents and survey properties”. *Astronomy and Astrophysics* 616, A1.
- Gaia Collaboration; Prusti, T.; de Bruijne, J. H. J.; Brown, A. G. A.; Vallenari, A.; Babusiaux, C.; Bailer-Jones, C. A. L.; Bastian, U.; Biermann, M.; Evans, D. W.; Eyer, L.; Jansen, F.; Jordi, C.; Klioner, S. A.; Lammers, U., et al. (2016). “The Gaia mission”. *Astronomy and Astrophysics* 595, A1.
- Gaia Collaboration; Smart, R. L.; Sarro, L. M.; Rybizki, J.; Reylé, C.; Robin, A. C.; Hambly, N. C.; Abbas, U.; Barstow, M. A.; de Bruijne, J. H. J.; Bucciarelli, B.; Carrasco, J. M.; Cooper, W. J.; Hodgkin, S. T.; Masana, E., et al. (2021). “Gaia Early Data Release 3. The Gaia Catalogue of Nearby Stars”. *Astronomy and Astrophysics* 649, A6.
- Gaia Collaboration; Vallenari, A.; Brown, A.G.A.; Prusti, T., and et al. (2022). “Gaia Data Release 3. Summary of the content and survey properties”. *A&A*.
- Gallet, F.; Charbonnel, C.; Amard, L.; Brun, S.; Palacios, A., and Mathis, S. (2017). “Impacts of stellar evolution and dynamics on the habitable zone: The role of rotation and magnetic activity”. *Astronomy and Astrophysics* 597, A14.
- Gandolfi, D.; Barragán, O.; Livingston, J. H.; Fridlund, M.; Justesen, A. B.; Redfield, S.; Fossati, L.; Mathur, S.; Grziwa, S.; Cabrera, J.; García, R. A.; Persson, C. M.; Van Eylen, V.; Hatzes, A. P.; Hidalgo, D., et al. (2018). “TESS’s first planet. A super-Earth transiting the naked-eye star π Mensae”. *Astronomy and Astrophysics* 619, L10.
- Gandolfi, D.; Parviainen, H.; Deeg, H. J.; Lanza, A. F.; Fridlund, M.; Prada Moroni, P. G.; Alonso, R.; Augusteijn, T.; Cabrera, J.; Evans, T.; Geier, S.; Hatzes, A. P.; Holczer, T.; Hoyer, S.; Kangas, T., et al. (2015).

- “Kepler-423b: a half-Jupiter mass planet transiting a very old solar-like star”. *Astronomy and Astrophysics* 576, A11.
- Gandolfi, D.; Parviainen, H.; Fridlund, M.; Hatzes, A. P.; Deeg, H. J.; Frasca, A.; Lanza, A. F.; Prada Moroni, P. G.; Tognelli, E.; McQuillan, A.; Aigrain, S.; Alonso, R.; Antoci, V.; Cabrera, J.; Carone, L., et al. (2013). “Kepler-77b: a very low albedo, Saturn-mass transiting planet around a metal-rich solar-like star”. *Astronomy and Astrophysics* 557, A74.
- Gandolfi, D.; Fossati, L.; Livingston, J. H.; Stassun, K. G.; Grziwa, S.; Barragán, O.; Fridlund, M.; Kubyshkina, D.; Persson, C. M.; Dai, F.; Lam, K. W. F.; Albrecht, S.; Batalha, N.; Beck, P. G.; Justesen, A. B., et al. (2019). “The Transiting Multi-planet System HD15337: Two Nearly Equal-mass Planets Straddling the Radius Gap”. *The Astrophysical Journal Letters* 876.2, L24.
- García, R. A.; Ceillier, T.; Salabert, D.; Mathur, S.; van Saders, J. L.; Pinsonneault, M.; Ballot, J.; Beck, P. G.; Bloemen, S.; Campante, T. L.; Davies, G. R.; do Nascimento J. -D., J.; Mathis, S.; Metcalfe, T. S.; Nielsen, M. B., et al. (2014). “Rotation and magnetism of Kepler pulsating solar-like stars. Towards asteroseismically calibrated age-rotation relations”. *Astronomy and Astrophysics* 572, A34.
- Gardner, J. P.; Mather, J. C.; Clampin, M.; Doyon, R.; Greenhouse, M. A.; Hammel, H. B.; Hutchings, J. B.; Jakobsen, P.; Lilly, S. J.; Long, K. S.; Lunine, J. I.; McCaughrean, M. J.; Mountain, M.; Nella, J.; Rieke, G. H., et al. (2006). “The James Webb Space Telescope”. *Space Science Reviews* 123.4, pp. 485–606.
- Gehrels, N.; Chincarini, G.; Giommi, P.; Mason, K. O.; Nousek, J. A.; Wells, A. A.; White, N. E.; Barthelmy, S. D.; Burrows, D. N.; Cominsky, L. R.; Hurley, K. C.; Marshall, F. E.; Mészáros, P.; Roming, P. W. A.; Angelini, L., et al. (2004). “The Swift Gamma-Ray Burst Mission”. *Astrophysical Journal* 611.2, pp. 1005–1020.
- Gelman, A. and Rubin, D. B. (1992). “Inference from Iterative Simulation Using Multiple Sequences”. *Statistical Science* 7, pp. 457–472.
- Georgieva, I. Y.; Persson, C. M.; Barragán, O.; Nowak, G.; Fridlund, M.; Locci, D.; Palle, E.; Luque, R.; Carleo, I.; Gandolfi, D.; Kane, S. R.; Korth, J.; Stassun, K. G.; Livingston, J.; Matthews, E. C., et al. (2021). “Hot planets around cool stars - two short-period mini-Neptunes transiting the late K-dwarf TOI-1260”. *Monthly Notices of the Royal Astronomical Society* 505.4, pp. 4684–4701.

- Geyer, C. J. (1992). "Practical Markov Chain Monte Carlo". *Statist. Sci.* 7.4, pp. 473–483.
- Giammichele, N.; Bergeron, P., and Dufour, P. (2012). "Know Your Neighborhood: A Detailed Model Atmosphere Analysis of Nearby White Dwarfs". *The Astrophysical Journal Supplement Series* 199.2, 29.
- Gillon, M.; Doyle, A. P.; Lendl, M.; Maxted, P. F. L.; Triaud, A. H. M. J.; Anderson, D. R.; Barros, S. C. C.; Bento, J.; Collier-Cameron, A.; Enoch, B.; Faedi, F.; Hellier, C.; Jehin, E.; Magain, P.; Montalbán, J., et al. (2011). "WASP-50 b: a hot Jupiter transiting a moderately active solar-type star". *Astronomy and Astrophysics* 533, A88.
- Ginsburg, A.; Sipőcz, B. M.; Brasseur, C. E.; Cowperthwaite, P. S.; Craig, M. W.; Deil, C.; Guillochon, J.; Guzman, G.; Liedtke, S.; Lian Lim, P.; Lockhart, K. E.; Mommert, M.; Morris, B. M.; Norman, H.; Parikh, M., et al. (2019). "astroquery: An Astronomical Web-querying Package in Python". *Astronomical Journal* 157, 98.
- Goldreich, P. and Tremaine, S. (1980). "Disk-satellite interactions." *Astrophysical Journal* 241, pp. 425–441.
- Gonzalez, G. (1997). "The stellar metallicity-giant planet connection". *Monthly Notices of the Royal Astronomical Society* 285.2, pp. 403–412.
- Goodwin, S. P.; Whitworth, A. P., and Ward-Thompson, D. (2004). "Simulating star formation in molecular cloud cores. I. The influence of low levels of turbulence on fragmentation and multiplicity". *Astronomy and Astrophysics* 414, pp. 633–650.
- Gounelle, M. and Meynet, G. (2012). "Solar system genealogy revealed by extinct short-lived radionuclides in meteorites". *Astronomy and Astrophysics* 545, A4.
- Gratia, P. and Fabrycky, D. (2017). "Outer-planet scattering can gently tilt an inner planetary system". *Monthly Notices of the Royal Astronomical Society* 464, pp. 1709–1717.
- Gray, D. F. (1989). "The Rotational Break for G Giants". *Astrophysical Journal* 347, p. 1021.
- Gray, D. F. (2005). *The Observation and Analysis of Stellar Photospheres*.
- Gray, R. O. (1998). "The Absolute Flux Calibration of Strömgren UVBY Photometry". *Astronomical Journal* 116.1, pp. 482–485.

- Gray, R. O. and Corbally, C. J. (1994). "The calibration of MK spectral classes using spectral synthesis. 1: The effective temperature calibration of dwarf stars". *Astronomical Journal* 107.2, p. 742.
- Green, G. M.; Schlaflfy, E.; Zucker, C.; Speagle, J. S., and Finkbeiner, D. (2019). "A 3D Dust Map Based on Gaia, Pan-STARRS 1, and 2MASS". *Astrophysical Journal* 887.1, 93.
- Grevesse, N. and Sauval, A. J. (1998). "Standard solar composition". *Sp. Sci. Rev.* 85, pp. 161–174.
- Grunblatt, S. K.; Huber, D.; Gaidos, E. J.; Lopez, E. D.; Fulton, B. J.; Vanderburg, A.; Barclay, T.; Fortney, J. J.; Howard, A. W., and Isaacson, H. T. (2016). "K2-97b: A (Re-?)Inflated Planet Orbiting a Red Giant Star". *Astronomical Journal* 152.6, 185.
- Grundahl, F.; Clausen, J. V.; Hardis, S., and Frandsen, S. (2008). "A new standard: age and distance for the open cluster NGC 6791 from the eclipsing binary member V20". *Astronomy and Astrophysics* 492.1, pp. 171–184.
- Grundahl, F.; Fredslund Andersen, M.; Christensen-Dalsgaard, J.; Antoci, V.; Kjeldsen, H.; Hand berg, R.; Houdek, G.; Bedding, T. R.; Pallé, P. L.; Jessen-Hansen, J.; Silva Aguirre, V.; White, T. R.; Frandsen, S.; Albrecht, S.; Andersen, M. I., et al. (2017). "First Results from the Hertzsprung SONG Telescope: Asteroseismology of the G5 Subgiant Star μ Herculis". *Astrophysical Journal* 836.1, 142.
- Grundahl, F.; Vandenberg, D. A.; Stetson, P. B.; Andersen, M. I., and Briley, M. (2000). "Exploring star clusters using Strömgren uvby photometry". In: *Liege International Astrophysical Colloquia*. Ed. by A. Noels; P. Magain; D. Caro; E. Jehin; G. Parmentier, and A. A. Thoul. Vol. 35. Liege International Astrophysical Colloquia, p. 503.
- Grundahl, F.; Christensen-Dalsgaard, J.; Pallé, P. L.; Andersen, M. F.; Frandsen, S.; Harpsøe, K.; Jørgensen, U. G.; Kjeldsen, H.; Rasmussen, P. K.; Skottfelt, J.; Sørensen, A. N., and Hage, A. T. (2014). "Stellar Observations Network Group: The prototype is nearly ready". In: *Precision Asteroseismology*. Ed. by J. A. Guzik; W. J. Chaplin; G. Handler, and A. Pigulski. Vol. 301, pp. 69–75.
- Guerrero, N. M.; Seager, S.; Huang, C. X.; Vanderburg, A.; Garcia Soto, A.; Mireles, I.; Hesse, K.; Fong, W.; Glidden, A.; Shporer, A.; Latham, D. W.; Collins, K. A.; Quinn, S. N.; Burt, J.; Dragomir, D., et al. (2021). "The

- TESS Objects of Interest Catalog from the TESS Prime Mission". *The Astrophysical Journal Supplement Series* 254.2, 39.
- Gustafsson, B.; Edvardsson, B.; Eriksson, K.; Jørgensen, U. G.; Nordlund, Å., and Plez, B. (2008). "A grid of MARCS model atmospheres for late-type stars. I. Methods and general properties". *Astronomy and Astrophysics* 486.3, pp. 951–970.
- Hale, A. (1994). "Orbital CoPlanetary in Solar-Type Binary Systems: Implications for Planetary System Formation and Detection". *Astronomical Journal* 107, p. 306.
- Handberg, R.; Brogaard, K.; Miglio, A.; Bossini, D.; Elsworth, Y.; Slumstrup, D.; Davies, G. R., and Chaplin, W. J. (2017). "NGC 6819: testing the asteroseismic mass scale, mass loss and evidence for products of non-standard evolution". *Monthly Notices of the Royal Astronomical Society* 472.1, pp. 979–997.
- Handberg, R. and Lund, M. N. (2019). *T'DA Data Release Notes - Data Release 4 for TESS Sectors 1 + 2*.
- Hartman, J. D. and Bakos, G. Á. (2016). "VARTOOLS: A program for analyzing astronomical time-series data". *Astronomy and Computing* 17, pp. 1–72.
- Harvey, J. W.; Duval T. L., J.; Jefferies, S. M., and Pomerantz, M. A. (1993). "Chromospheric Oscillations and the Background Spectrum". In: *GONG 1992. Seismic Investigation of the Sun and Stars*. Ed. by T. M. Brown. Vol. 42. Astronomical Society of the Pacific Conference Series, p. 111.
- Hatzes, A. P.; Cochran, W. D.; Endl, M.; McArthur, B.; Paulson, D. B.; Walker, G. A. H.; Campbell, B., and Yang, S. (2003). "A Planetary Companion to γ Cephei A". *Astrophysical Journal* 599.2, pp. 1383–1394.
- Hébrard, G.; Bouchy, F.; Pont, F.; Loeillet, B.; Rabus, M.; Bonfils, X.; Moutou, C.; Boisse, I.; Delfosse, X.; Desort, M.; Eggenberger, A.; Ehrenreich, D.; Forveille, T.; Lagrange, A.; Lovis, C., et al. (2008). "Misaligned spin-orbit in the XO-3 planetary system?" *Astronomy and Astrophysics* 488, pp. 763–770.
- Hekker, S. and Christensen-Dalsgaard, J. (2017). "Giant star seismology". *The Astronomy and Astrophysics Review* 25.1, 1.
- Hekker, S. and Meléndez, J. (2007). "Precise radial velocities of giant stars. III. Spectroscopic stellar parameters". *Astronomy and Astrophysics* 475.3, pp. 1003–1009.

- Heller, R.; Williams, D.; Kipping, D.; Limbach, M. A.; Turner, E.; Greenberg, R.; Sasaki, T.; Bolmont, É.; Grasset, O.; Lewis, K.; Barnes, R., and Zuluaga, J. I. (2014). "Formation, Habitability, and Detection of Extrasolar Moons". *Astrobiology* 14.9, pp. 798–835.
- Hellier, C.; Anderson, D. R.; Bouchy, F.; Burdanov, A.; Collier Cameron, A.; Delrez, L.; Gillon, M.; Jehin, E.; Lendl, M.; Nielsen, L. D.; Maxted, P. F. L.; Pepe, F.; Pollacco, D.; Queloz, D.; Ségransan, D., et al. (2019). "New transiting hot Jupiters discovered by WASP-South, Euler/CORALIE, and TRAPPIST-South". *Monthly Notices of the Royal Astronomical Society* 482.1, pp. 1379–1391.
- Henry, G. W.; Marcy, G. W.; Butler, R. P., and Vogt, S. S. (2000). "A Transiting "51 Peg-like" Planet". *The Astrophysical Journal Letters* 529.1, pp. L41–L44.
- Hidalgo, S. L.; Pietrinferni, A.; Cassisi, S.; Salaris, M.; Mucciarelli, A.; Savino, A.; Aparicio, A.; Silva Aguirre, V., and Verma, K. (2018). "The Updated BaSTI Stellar Evolution Models and Isochrones. I. Solar-scaled Calculations". *Astrophysical Journal* 856.2, 125.
- Hill, M. L.; Kane, S. R.; Seperuelo Duarte, E.; Kopparapu, R. K.; Gelino, D. M., and Wittenmyer, R. A. (2018). "Exploring Kepler Giant Planets in the Habitable Zone". *Astrophysical Journal* 860.1, 67.
- Hinkel, N. R. and Kane, S. R. (2013). "Habitability of Exomoons at the Hill or Tidal Locking Radius". *Astrophysical Journal* 774.1, 27.
- Hippke, M. and Heller, R. (2019). "Optimized transit detection algorithm to search for periodic transits of small planets". *Astronomy and Astrophysics* 623, A39.
- Hirano, T.; Suto, Y.; Winn, J. N.; Taruya, A.; Narita, N.; Albrecht, S., and Sato, B. (2011). "Improved Modeling of the Rossiter-McLaughlin Effect for Transiting Exoplanets". *Astrophysical Journal* 742.2, 69.
- Hirsch, L. A.; Ciardi, D. R.; Howard, A. W.; Everett, M. E.; Furlan, E.; Saylors, M.; Horch, E. P.; Howell, S. B.; Teske, J., and Marcy, G. W. (2017). "Assessing the Effect of Stellar Companions from High-resolution Imaging of Kepler Objects of Interest". *Astronomical Journal* 153.3, 117.
- Hjørringgaard, J. G.; Silva Aguirre, V.; White, T. R.; Huber, D.; Pope, B. J. S.; Casagrande, L.; Justesen, A. B., and Christensen-Dalsgaard, J. (2017). "Testing stellar evolution models with the retired A star HD 185351". *Monthly Notices of the Royal Astronomical Society* 464.3, pp. 3713–3719.

- Hjorth, M.; Albrecht, S.; Talens, G. J. J.; Grundahl, F.; Justesen, A. B.; Otten, G. P. P. L.; Antoci, V.; Dorval, P.; Foxell, E.; Fredslund Andersen, M.; Murgas, F.; Palle, E.; Stuik, R.; Snellen, I. A. G., and Van Eylen, V. (2019a). "MASCARA-3b. A hot Jupiter transiting a bright F7 star in an aligned orbit". *Astronomy and Astrophysics* 631, A76.
- Hjorth, M.; Justesen, A. B.; Hirano, T.; Albrecht, S.; Gandolfi, D.; Dai, F.; Alonso, R.; Barragán, O.; Esposito, M.; Kuzuhara, M.; Lam, K. W. F.; Livingston, J. H.; Montanes-Rodriguez, P.; Narita, N.; Nowak, G., et al. (2019b). "K2-290: a warm Jupiter and a mini-Neptune in a triple-star system". *Monthly Notices of the Royal Astronomical Society* 484.3, pp. 3522–3536.
- Hjorth, M.; Albrecht, S.; Hirano, T.; Winn, J. N.; Dawson, R. I.; Zanazzi, J. J.; Knudstrup, E., and Sato, B. (2021). "A backward-spinning star with two coplanar planets". *Proceedings of the National Academy of Science* 118.8, 2017418118.
- Hodapp, K. W.; Jensen, J. B.; Irwin, E. M.; Yamada, H.; Chung, R.; Fletcher, K.; Robertson, L.; Hora, J. L.; Simons, D. A.; Mays, W.; Nolan, R.; Bec, M.; Merrill, M., and Fowler, A. M. (2003). "The Gemini Near-Infrared Imager (NIRI)". *Publications of the Astronomical Society of the Pacific* 115.814, pp. 1388–1406.
- Hoeijmakers, H. J.; Cabot, S. H. C.; Zhao, L.; Buchhave, L. A.; Tronsgaard, R.; Davis, A. B.; Kitzmann, D.; Grimm, S. L.; Cegla, H. M.; Bourrier, V.; Ehrenreich, D.; Heng, K.; Lovis, C., and Fischer, D. A. (2020). "High-resolution transmission spectroscopy of MASCARA-2 b with EXPRES". *Astronomy and Astrophysics* 641, A120.
- Høg, E.; Fabricius, C.; Makarov, V. V.; Urban, S.; Corbin, T.; Wycoff, G.; Bastian, U.; Schwerkendiek, P., and Wicenec, A. (2000). "The Tycho-2 catalogue of the 2.5 million brightest stars". *Astronomy and Astrophysics* 355, pp. L27–L30.
- Holt, J. R. (1893). "Spectroscopic Determination of Stellar Rotation". *Astronomy and Astro-Physics (formerly The Sidereal Messenger)* 12, p. 646.
- Hooton, M. J.; Hoyer, S.; Kitzmann, D.; Morris, B. M.; Smith, A. M. S.; Collier Cameron, A.; Futyan, D.; Maxted, P. F. L.; Queloz, D.; Demory, B. .-O.; Heng, K.; Lendl, M.; Cabrera, J.; Csizmadia, S.; Deline, A., et al. (2022). "Spi-OPS: Spitzer and CHEOPS confirm the near-polar orbit of MASCARA-1 b and reveal a hint of dayside reflection". *Astronomy and Astrophysics* 658, A75.

- Horne, K. (1986). "An optimal extraction algorithm for CCD spectroscopy." *Publications of the Astronomical Society of the Pacific* 98, pp. 609–617.
- Howard, A. W.; Johnson, J. A.; Marcy, G. W.; Fischer, D. A.; Wright, J. T.; Bernat, D.; Henry, G. W.; Peek, K. M. G.; Isaacson, H.; Apps, K.; Endl, M.; Cochran, W. D.; Valenti, J. A.; Anderson, J., and Piskunov, N. E. (2010a). "The California Planet Survey. I. Four New Giant Exoplanets". *Astrophysical Journal* 721.2, pp. 1467–1481.
- Howard, A. W.; Marcy, G. W.; Johnson, J. A.; Fischer, D. A.; Wright, J. T.; Isaacson, H.; Valenti, J. A.; Anderson, J.; Lin, D. N. C., and Ida, S. (2010b). "The Occurrence and Mass Distribution of Close-in Super-Earths, Neptunes, and Jupiters". *Science* 330.6004, p. 653.
- Howell, S. B.; Sobeck, C.; Haas, M.; Still, M.; Barclay, T.; Mullally, F.; Troeltzsch, J.; Aigrain, S.; Bryson, S. T.; Caldwell, D.; Chaplin, W. J.; Cochran, W. D.; Huber, D.; Marcy, G. W.; Miglio, A., et al. (2014). "The K2 Mission: Characterization and Early Results". *Publications of the Astronomical Society of the Pacific* 126, pp. 398–408.
- Howell, S. B.; Everett, M. E.; Sherry, W.; Horch, E., and Ciardi, D. R. (2011). "Speckle Camera Observations for the NASA Kepler Mission Follow-up Program". *Astronomical Journal* 142.1, 19.
- Huang, C. X.; Burt, J.; Vanderburg, A.; Günther, M. N.; Shporer, A.; Dittmann, J. A.; Winn, J. N.; Wittenmyer, R.; Sha, L.; Kane, S. R.; Ricker, G. R.; Vanderspek, R. K.; Latham, D. W.; Seager, S.; Jenkins, J. M., et al. (2018). "TESS Discovery of a Transiting Super-Earth in the pi Mensae System". *The Astrophysical Journal Letters* 868.2, L39.
- Huang, C. X.; Vanderburg, A.; Pál, A.; Sha, L.; Yu, L.; Fong, W.; Fausnaugh, M.; Shporer, A.; Guerrero, N.; Vanderspek, R., and Ricker, G. (2020). "Photometry of 10 Million Stars from the First Two Years of TESS Full Frame Images: Part II". *Research Notes of the American Astronomical Society* 4.11, 206.
- Huang, X.; Bakos, G. Á., and Hartman, J. D. (2013). "150 new transiting planet candidates from Kepler Q1-Q6 data". *Monthly Notices of the Royal Astronomical Society* 429.3, pp. 2001–2018.
- Huang, X. and Ji, J. (2022). "Extremely Inclined Orbit of the S-type Planet γ Cep Ab Induced by the Eccentric Kozai-Lidov Mechanism". *Astronomical Journal* 164.5, 177.

- Huber, D.; Bedding, T. R.; Stello, D.; Hekker, S.; Mathur, S.; Mosser, B.; Verner, G. A.; Bonanno, A.; Buzasi, D. L.; Campante, T. L.; Elsworth, Y. P.; Hale, S. J.; Kallinger, T.; Silva Aguirre, V.; Chaplin, W. J., et al. (2011). "Testing Scaling Relations for Solar-like Oscillations from the Main Sequence to Red Giants Using Kepler Data". *Astrophysical Journal* 743.2, 143.
- Huber, D.; Bedding, T. R.; Stello, D.; Mosser, B.; Mathur, S.; Kallinger, T.; Hekker, S.; Elsworth, Y. P.; Buzasi, D. L.; De Ridder, J.; Gilliland, R. L.; Kjeldsen, H.; Chaplin, W. J.; García, R. A.; Hale, S. J., et al. (2010). "Asteroseismology of Red Giants from the First Four Months of Kepler Data: Global Oscillation Parameters for 800 Stars". *Astrophysical Journal* 723.2, pp. 1607–1617.
- Huber, D.; Carter, J. A.; Barbieri, M.; Miglio, A.; Deck, K. M.; Fabrycky, D. C.; Montet, B. T.; Buchhave, L. A.; Chaplin, W. J.; Hekker, S.; Montalbán, J.; Sanchis-Ojeda, R.; Basu, S.; Bedding, T. R.; Campante, T. L., et al. (2013). "Stellar Spin-Orbit Misalignment in a Multiplanet System". *Science* 342.6156, pp. 331–334.
- Huber, D.; Chaplin, W. J.; Chontos, A.; Kjeldsen, H.; Christensen-Dalsgaard, J.; Bedding, T. R.; Ball, W.; Brahm, R.; Espinoza, N.; Henning, T.; Jordán, A.; Sarkis, P.; Knudstrup, E.; Albrecht, S.; Grundahl, F., et al. (2019). "A Hot Saturn Orbiting an Oscillating Late Subgiant Discovered by TESS". *Astronomical Journal* 157.6, 245.
- Husnoo, N.; Pont, F.; Mazeh, T.; Fabrycky, D.; Hébrard, G.; Bouchy, F., and Shporer, A. (2012). "Observational constraints on tidal effects using orbital eccentricities". *Monthly Notices of the Royal Astronomical Society* 422, pp. 3151–3177.
- Husser, T. .-O.; Wende-von Berg, S.; Dreizler, S.; Homeier, D.; Reiners, A.; Barman, T., and Hauschildt, P. H. (2013). "A new extensive library of PHOENIX stellar atmospheres and synthetic spectra". *Astronomy and Astrophysics* 553, A6.
- Hutter, D. J.; Zavala, R. T.; Tycner, C.; Benson, J. A.; Hummel, C. A.; Sanborn, J.; Franz, O. G., and Johnston, K. J. (2016). "Surveying the Bright Stars by Optical Interferometry. I. A Search for Multiplicity among Stars of Spectral Types F-K". *The Astrophysical Journal Supplement Series* 227.1, 4.
- Ida, S. and Lin, D. N. C. (2004). "Toward a Deterministic Model of Planetary Formation. I. A Desert in the Mass and Semimajor Axis Distributions of Extrasolar Planets". *Astrophysical Journal* 604.1, pp. 388–413.

- Jang-Condell, H.; Mugrauer, M., and Schmidt, T. (2008). "Disk Truncation and Planet Formation in γ Cephei". *The Astrophysical Journal Letters* 683.2, p. L191.
- Jenkins, J. M. (2002). "The Impact of Solar-like Variability on the Detectability of Transiting Terrestrial Planets". *Astrophysical Journal* 575, pp. 493–505.
- Jenkins, J. M.; Chandrasekaran, H.; McCauliff, S. D.; Caldwell, D. A.; Tenenbaum, P.; Li, J.; Klaus, T. C.; Cote, M. T., and Middour, C. (2010). "Transiting planet search in the Kepler pipeline". In: *Software and Cyberinfrastructure for Astronomy*. Ed. by N. M. Radziwill and A. Bridger. Vol. 7740. Society of Photo-Optical Instrumentation Engineers (SPIE) Conference Series.
- Jenkins, J. M.; Twicken, J. D.; McCauliff, S.; Campbell, J.; Sanderfer, D.; Lung, D.; Mansouri-Samani, M.; Girouard, F.; Tenenbaum, P.; Klaus, T.; Smith, J. C.; Caldwell, D. A.; Chacon, A. D.; Henze, C.; Heiges, C., et al. (2016). "The TESS science processing operations center". In: *Software and Cyberinfrastructure for Astronomy IV*. Ed. by G. Chiozzi and J. C. Guzman. Vol. 9913. Society of Photo-Optical Instrumentation Engineers (SPIE) Conference Series.
- Jensen, E. (2013). *Tapir: A web interface for transit/eclipse observability*. Astrophysics Source Code Library.
- Jiang, C. and Christensen-Dalsgaard, J. (2014). "Verification of asymptotic relation for mixed modes in red giant stars". *Monthly Notices of the Royal Astronomical Society* 444.4, pp. 3622–3631.
- Jofré, E.; Petrucci, R.; Saffe, C.; Saker, L.; Artur de la Villarmois, E.; Chavero, C.; Gómez, M., and Mauas, P. J. D. (2015). "Stellar parameters and chemical abundances of 223 evolved stars with and without planets". *Astronomy and Astrophysics* 574, A50.
- Johnson, M. C.; Cochran, W. D.; Albrecht, S.; Dodson-Robinson, S. E.; Winn, J. N., and Gullikson, K. (2014). "A Misaligned Prograde Orbit for Kepler-13 Ab via Doppler Tomography". *Astrophysical Journal* 790, 30.
- Johnson, M. C.; Cochran, W. D.; Collier Cameron, A., and Bayliss, D. (2015). "Measurement of the Nodal Precession of WASP-33 b via Doppler Tomography". *The Astrophysical Journal Letters* 810.2, L23.

- Jones, H. R. A.; Butler, R. P.; Tinney, C. G.; Marcy, G. W.; Carter, B. D.; Penny, A. J.; McCarthy, C., and Bailey, J. (2006). "High-eccentricity planets from the Anglo-Australian Planet Search". *Monthly Notices of the Royal Astronomical Society* 369.1, pp. 249–256.
- Jordán, A.; Brahm, R.; Espinoza, N.; Cortés, C.; Díaz, M.; Drass, H.; Henning, T.; Jenkins, J. S.; Jones, M. I.; Rabus, M.; Rojas, F.; Sarkis, P.; Vučković, M.; Zapata, A.; Soto, M. G., et al. (2019). "K2-287 b: An Eccentric Warm Saturn Transiting a G-dwarf". *Astronomical Journal* 157.3, 100.
- Jurić, M. and Tremaine, S. (2008). "Dynamical Origin of Extrasolar Planet Eccentricity Distribution". *Astrophysical Journal* 686.1, pp. 603–620.
- Justesen, A. B. and Albrecht, S. (2020). "The spin-orbit alignment of visual binaries". *Astronomy and Astrophysics* 642, A212.
- Kaiser, N.; Burgett, W.; Chambers, K.; Denneau, L.; Heasley, J.; Jedicke, R.; Magnier, E.; Morgan, J.; Onaka, P., and Tonry, J. (2010). "The Pan-STARRS wide-field optical/NIR imaging survey". In: *Ground-based and Airborne Telescopes III*. Edited by Stepp, Larry M.; Gilmozzi, Roberto; Hall, Helen J. *Proceedings of the SPIE*, Volume 7733, article id. 77330E, 14 pp. (2010). Vol. 7733. Society of Photo-Optical Instrumentation Engineers (SPIE) Conference Series.
- Kallinger, T.; De Ridder, J.; Hekker, S.; Mathur, S.; Mosser, B.; Gruberbauer, M.; García, R. A.; Karoff, C., and Ballot, J. (2014). "The connection between stellar granulation and oscillation as seen by the Kepler mission". *Astronomy and Astrophysics* 570, A41.
- Kaluzny, J.; Pych, W.; Rucinski, S. M., and Thompson, I. B. (2006). "Eclipsing Binaries in the Open Cluster NGC2243. II. Absolute Properties of NVCMa". *Acta Astronomica* 56, pp. 237–252.
- Kane, S. R.; Dalba, P. A.; Li, Z.; Horch, E. P.; Hirsch, L. A.; Horner, J.; Wittenmyer, R. A.; Howell, S. B.; Everett, M. E.; Butler, R. P.; Tinney, C. G.; Carter, B. D.; Wright, D. J.; Jones, H. R. A.; Bailey, J., et al. (2019). "Detection of Planetary and Stellar Companions to Neighboring Stars via a Combination of Radial Velocity and Direct Imaging Techniques". *Astronomical Journal* 157.6, 252.
- Kane, S. R.; Hill, M. L.; Kasting, J. F.; Kopparapu, R. K.; Quintana, E. V.; Barclay, T.; Batalha, N. M.; Borucki, W. J.; Ciardi, D. R.; Haghighipour, N.; Hinkel, N. R.; Kaltenegger, L.; Selsis, F., and Torres, G. (2016). "A

- Catalog of Kepler Habitable Zone Exoplanet Candidates". *Astrophysical Journal* 830.1, 1.
- Kane, S. R.; Kopparapu, R. K., and Domagal-Goldman, S. D. (2014). "On the Frequency of Potential Venus Analogs from Kepler Data". *The Astrophysical Journal Letters* 794.1, L5.
- Kanodia, S.; Cañas, C. I.; Stefansson, G.; Ninan, J. P.; Hebb, L.; Lin, A. S. J.; Baran, H.; Maney, M.; Terrien, R. C.; Mahadevan, S.; Cochran, W. D.; Endl, M.; Dong, J.; Bender, C. F.; Diddams, S. A., et al. (2020). "TOI-1728b: The Habitable-zone Planet Finder Confirms a Warm Super-Neptune Orbiting an M-dwarf Host". *Astrophysical Journal* 899.1, 29.
- Kanodia, S.; Stefansson, G.; Cañas, C. I.; Maney, M.; Lin, A. S. J.; Ninan, J. P.; Jones, S.; Monson, A.; Parker, B. A.; Kobulnicky, H. A.; Rothenberg, J.; Beard, C.; Lubin, J.; Robertson, P.; Gupta, A. F., et al. (2021). "TOI-532b: The Habitable-zone Planet Finder confirms a Large Super Neptune in the Neptune Desert orbiting a metal-rich M-dwarf host". *Astronomical Journal* 162.4, 135.
- Kasting, J. F.; Kopparapu, R.; Ramirez, R. M., and Harman, C. E. (2014). "Remote life-detection criteria, habitable zone boundaries, and the frequency of Earth-like planets around M and late K stars". *Proceedings of the National Academy of Science* 111.35, pp. 12641–12646.
- Keenan, P. C. and McNeil, R. C. (1989). "The Perkins Catalog of Revised MK Types for the Cooler Stars". *The Astrophysical Journal Supplement Series* 71, p. 245.
- Kempton, E. M. .-R.; Bean, J. L.; Louie, D. R.; Deming, D.; Koll, D. D. B.; Mansfield, M.; Christiansen, J. L.; López-Morales, M.; Swain, M. R.; Zellem, R. T.; Ballard, S.; Barclay, T.; Barstow, J. K.; Batalha, N. E.; Beatty, T. G., et al. (2018). "A Framework for Prioritizing the TESS Planetary Candidates Most Amenable to Atmospheric Characterization". *Publications of the Astronomical Society of the Pacific* 130.993, p. 114401.
- Khan, S.; Miglio, A.; Mosser, B.; Arenou, F.; Belkacem, K.; Brown, A. G. A.; Katz, D.; Casagrande, L.; Chaplin, W. J.; Davies, G. R.; Rendle, B. M.; Rodrigues, T. S.; Bossini, D.; Cantat-Gaudin, T.; Elsworth, Y. P., et al. (2019). "New light on the Gaia DR2 parallax zero-point: influence of the asteroseismic approach, in and beyond the Kepler field". *Astronomy and Astrophysics* 628, A35.

- Kim, S. .-.L.; Chun, M. .-.Y.; Park, B. .-.G.; Kim, S. C.; Lee, S. H.; Lee, M. G.; Ann, H. B.; Sung, H.; Jeon, Y. .-.B., and Yuk, I. .-.S. (2001). "Search for Variable Stars in Two Old Open Clusters: NGC₂₅₀₆ and NGC₂₄₂₀". *Acta Astronomica* 51, pp. 49–63.
- Kippenhahn, R.; Weigert, A., and Weiss, A. (2013). *Stellar Structure and Evolution*.
- Kipping, D. M. (2013a). "Parametrizing the exoplanet eccentricity distribution with the beta distribution." *Monthly Notices of the Royal Astronomical Society* 434, pp. L51–L55.
- Kipping, D. M.; Bakos, G. Á.; Buchhave, L.; Nesvorný, D., and Schmitt, A. (2012). "The Hunt for Exomoons with Kepler (HEK). I. Description of a New Observational project". *Astrophysical Journal* 750.2, 115.
- Kipping, D. M.; Hartman, J.; Bakos, G. Á.; Torres, G.; Latham, D. W.; Bayliss, D.; Kiss, L. L.; Sato, B.; Béky, B.; Kovács, G.; Quinn, S. N.; Buchhave, L. A.; Andersen, J.; Marcy, G. W.; Howard, A. W., et al. (2011). "HAT-P-31b,c: A Transiting, Eccentric, Hot Jupiter and a Long-period, Massive Third Body". *Astronomical Journal* 142.3, 95.
- Kipping, D. M. (2010). "Binning is sinning: morphological light-curve distortions due to finite integration time". *Monthly Notices of the Royal Astronomical Society* 408.3, pp. 1758–1769.
- Kipping, D. M. (2013b). "Efficient, uninformative sampling of limb darkening coefficients for two-parameter laws". *Monthly Notices of the Royal Astronomical Society* 435.3, pp. 2152–2160.
- Kipping, D. M.; Fossey, S. J., and Campanella, G. (2009). "On the detectability of habitable exomoons with Kepler-class photometry". *Monthly Notices of the Royal Astronomical Society* 400.1, pp. 398–405.
- Kjeldsen, H. and Bedding, T. R. (1995). "Amplitudes of stellar oscillations: the implications for asteroseismology." *Astronomy and Astrophysics* 293, pp. 87–106.
- Kjeldsen, H.; Bedding, T. R.; Viskum, M., and Frandsen, S. (1995). "Solarlike Oscillations in eta Boo". *Astronomical Journal* 109, p. 1313.
- Kley, W. and Nelson, R. P. (2012). "Planet-Disk Interaction and Orbital Evolution". *Annual Review of Astronomy & Astrophysics* 50, pp. 211–249.
- Knudstrup, E. (2018). "Twins, Siblings, and the Rest of the NGC 2506 Family: A Study of an Open Cluster Using Detached Eclipsing Binaries". MA thesis. Department of Physics and Astronomy, Aarhus University.

- Knudstrup, E. and Albrecht, S. H. (2022). "Orbital alignment of HD 332231 b. The warm Saturn HD 332231 b/TOI-1456 b travels on a well-aligned, circular orbit around a bright F8 dwarf". *Astronomy and Astrophysics* 660, A99.
- Knudstrup, E.; Gandolfi, D.; Nowak, G.; Persson, C. M.; Furlan, E.; Livingston, J.; Matthews, E.; Lundkvist, M. S.; Winther, M. L.; Rørsted, J. L.; Albrecht, S. H.; Goffo, E.; Carleo, I.; Deeg, H. J.; Collins, K. A., et al. (2023a). "Radial velocity confirmation of a hot super-Neptune discovered by TESS with a warm Saturn-mass companion". *Monthly Notices of the Royal Astronomical Society* 519.4, pp. 5637–5655.
- Knudstrup, E.; Grundahl, F.; Brogaard, K.; Slumstrup, D.; Orosz, J. A.; Sandquist, E. L.; Jessen-Hansen, J.; Lund, M. N.; Arentoft, T.; Tronsgaard, R.; Yong, D.; Frandsen, S., and Bruntt, H. (2020). "Extremely precise age and metallicity of the open cluster NGC 2506 using detached eclipsing binaries". *Monthly Notices of the Royal Astronomical Society* 499.1, pp. 1312–1339.
- Knudstrup, E.; Albrecht, S. H.; Gandolfi, D.; Marcussen, M. L.; Goffo, E.; Serrano, L. M.; Dai, F.; Redfield, S.; Hirano, T.; Csizmadia, S.; Cochran, W. D.; Deeg, H. J.; Fridlund, M.; Lam, K. W. F.; Livingston, J. H., et al. (2023b). "A puffy polar planet. The low density, hot Jupiter TOI-640 b is on a polar orbit". *Astronomy and Astrophysics* 671, A164.
- Knudstrup, E.; Serrano, L. M.; Gandolfi, D.; Albrecht, S. H.; Cochran, W. D.; Endl, M.; MacQueen, P.; Tronsgaard, R.; Bieryla, A.; Buchhave, L. A.; Stassun, K.; Collins, K. A.; Nowak, G.; Deeg, H. J.; Barkaoui, K., et al. (2022). "Confirmation and characterisation of three giant planets detected by TESS from the FIES/NOT and Tull/McDonald spectrographs". *Astronomy and Astrophysics* 667, A22.
- Kolbl, R.; Marcy, G. W.; Isaacson, H., and Howard, A. W. (2015). "Detection of Stars Within \sim 0.8 in of Kepler Objects of Interest". *Astronomical Journal* 149.1, 18.
- Kopparapu, R. K. (2013). "A Revised Estimate of the Occurrence Rate of Terrestrial Planets in the Habitable Zones around Kepler M-dwarfs". *The Astrophysical Journal Letters* 767.1, L8.
- Kopparapu, R. K.; Ramirez, R. M.; SchottelKotte, J.; Kasting, J. F.; Domagal-Goldman, S., and Eymet, V. (2014). "Habitable Zones around Main-sequence Stars: Dependence on Planetary Mass". *The Astrophysical Journal Letters* 787.2, L29.

- Kovács, G.; Zucker, S., and Mazeh, T. (2002). “A box-fitting algorithm in the search for periodic transits”. *Astronomy and Astrophysics* 391, pp. 369–377.
- Kozai, Y. (1962). “Secular Perturbations of Asteroids with High Inclination and Eccentricity.” *Astronomical Journal* 67, p. 579.
- Kratter, K. M.; Murray-Clay, R. A., and Youdin, A. N. (2010). “The Runts of the Litter: Why Planets Formed Through Gravitational Instability Can Only Be Failed Binary Stars”. *Astrophysical Journal* 710.2, pp. 1375–1386.
- Kreidberg, L. (2015). “batman: BAsic Transit Model cAlculatioN in Python”. *Publications of the Astronomical Society of the Pacific* 127.957, p. 1161.
- Kreidberg, L.; Luger, R., and Bedell, M. (2019). “No Evidence for Lunar Transit in New Analysis of Hubble Space Telescope Observations of the Kepler-1625 System”. *The Astrophysical Journal Letters* 877.2, L15.
- Kruse, E.; Agol, E.; Luger, R., and Foreman-Mackey, D. (2019). “Detection of Hundreds of New Planet Candidates and Eclipsing Binaries in K2 Campaigns o-8”. *The Astrophysical Journal Supplement Series* 244.1, 11.
- Kumar, R.; Carroll, C.; Hartikainen, A., and Martin, O. (2019). “ArviZ a unified library for exploratory analysis of Bayesian models in Python”. *Journal of Open Source Software* 4.33, p. 1143.
- Kurucz, R. L. (1993). “VizieR Online Data Catalog: Model Atmospheres (Kurucz, 1979)”. *VizieR Online Data Catalog*, VI/39.
- Kurucz, R. L. (2013). *ATLAS12: Opacity sampling model atmosphere program*. Astrophysics Source Code Library.
- Kuruwita, R. and Haugbølle, T. (2022). “The contribution of binary star formation on core-fragmentation scales on protostellar multiplicity”. *arXiv e-prints*, arXiv:2209.01909.
- Lada, C. J. and Lada, E. A. (2003). “Embedded Clusters in Molecular Clouds”. *Annual Review of Astronomy & Astrophysics* 41, pp. 57–115.
- Lai, D.; Foucart, F., and Lin, D. N. C. (2011). “Evolution of spin direction of accreting magnetic protostars and spin-orbit misalignment in exoplanetary systems”. *Monthly Notices of the Royal Astronomical Society* 412, pp. 2790–2798.
- Lai, D. (2012). “Tidal dissipation in planet-hosting stars: damping of spin-orbit misalignment and survival of hot Jupiters”. *Monthly Notices of the Royal Astronomical Society* 423.1, pp. 486–492.

- Lai, D.; Anderson, K. R., and Pu, B. (2018). "How do external companions affect spin-orbit misalignment of hot Jupiters?" *Monthly Notices of the Royal Astronomical Society* 475.4, pp. 5231–5236.
- Lallement, R.; Babusiaux, C.; Vergely, J. L.; Katz, D.; Arenou, F.; Valette, B.; Hottier, C., and Capitanio, L. (2019). "Gaia-2MASS 3D maps of Galactic interstellar dust within 3 kpc". *Astronomy and Astrophysics* 625, A135.
- Lallement, R.; Vergely, J. .-.L.; Valette, B.; Puspitarini, L.; Eyer, L., and Casagrande, L. (2014). "3D maps of the local ISM from inversion of individual color excess measurements". *Astronomy and Astrophysics* 561, A91.
- Laskar, J. (2008). "Chaotic diffusion in the Solar System". *Icarus* 196.1, pp. 1–15.
- Laughlin, G.; Crismani, M., and Adams, F. C. (2011). "On the Anomalous Radii of the Transiting Extrasolar Planets". *The Astrophysical Journal Letters* 729, L7.
- Laughlin, G.; Marcy, G. W.; Vogt, S. S.; Fischer, D. A., and Butler, R. P. (2005). "On the Eccentricity of HD 209458b". *The Astrophysical Journal Letters* 629.2, pp. L121–L124.
- Li, J.; Tenenbaum, P.; Twicken, J. D.; Burke, C. J.; Jenkins, J. M.; Quintana, E. V.; Rowe, J. F., and Seader, S. E. (2019). "Kepler Data Validation II-Transit Model Fitting and Multiple-planet Search". *Publications of the Astronomical Society of the Pacific* 131.996, p. 024506.
- Li, Y.; Bedding, T. R.; Li, T.; Bi, S.; Stello, D.; Zhou, Y., and White, T. R. (2020). "Asteroseismology of 36 Kepler subgiants - I. Oscillation frequencies, linewidths, and amplitudes". *Monthly Notices of the Royal Astronomical Society* 495.2, pp. 2363–2386.
- Lidov, M. L. (1962). "The evolution of orbits of artificial satellites of planets under the action of gravitational perturbations of external bodies". *Planetary and Space Science* 9.10, pp. 719–759.
- Lightkurve Collaboration; Cardoso, J. V. d. M.; Hedges, C.; Gully-Santiago, M.; Saunders, N.; Cody, A. M.; Barclay, T.; Hall, O.; Sagear, S.; Turtelboom, E.; Zhang, J.; Tzanidakis, A.; Mighell, K.; Coughlin, J.; Bell, K., et al. (2018). *Lightkurve: Kepler and TESS time series analysis in Python*. Astrophysics Source Code Library.

- Lin, D. N. C.; Bodenheimer, P., and Richardson, D. C. (1996). "Orbital migration of the planetary companion of 51 Pegasi to its present location". *Nature* 380.6575, pp. 606–607.
- Lindgren, L.; Hernández, J.; Bombrun, A.; Klioner, S.; Bastian, U.; Ramos-Lerate, M.; de Torres, A.; Steidelmüller, H.; Stephenson, C.; Hobbs, D.; Lammers, U.; Biermann, M.; Geyer, R.; Hilger, T.; Michalik, D., et al. (2018). "Gaia Data Release 2. The astrometric solution". *Astronomy and Astrophysics* 616, A2.
- Liu, M. C.; Magnier, E. A.; Deacon, N. R.; Allers, K. N.; Dupuy, T. J.; Kotson, M. C.; Aller, K. M.; Burgett, W. S.; Chambers, K. C.; Draper, P. W.; Hodapp, K. W.; Jedicke, R.; Kaiser, N.; Kudritzki, R. .-.P.; Metcalfe, N., et al. (2013). "The Extremely Red, Young L Dwarf PSO J318.5338-22.8603: A Free-floating Planetary-mass Analog to Directly Imaged Young Gas-giant Planets". *The Astrophysical Journal Letters* 777.2, L20.
- Livingston, J. H.; Endl, M.; Dai, F.; Cochran, W. D.; Barragan, O.; Gandolfi, D.; Hirano, T.; Grziwa, S.; Smith, A. M. S.; Albrecht, S.; Cabrera, J.; Csizmadia, S.; de Leon, J. P.; Deeg, H.; Eigmüller, P., et al. (2018). "44 Validated Planets from K2 Campaign 10". *Astronomical Journal* 156.2, 78.
- Lomb, N. R. (1976). "Least-Squares Frequency Analysis of Unequally Spaced Data". *Astrophysics and Space Science* 39.2, pp. 447–462.
- Lopez, E. D.; Fortney, J. J., and Miller, N. (2012). "How Thermal Evolution and Mass-loss Sculpt Populations of Super-Earths and Sub-Neptunes: Application to the Kepler-11 System and Beyond". *Astrophysical Journal* 761.1, 59.
- Louden, E. M.; Winn, J. N.; Petigura, E. A.; Isaacson, H.; Howard, A. W.; Masuda, K.; Albrecht, S., and Kosiarek, M. R. (2021). "Hot Stars with Kepler Planets Have High Obliquities". *Astronomical Journal* 161.2, 68.
- Lovekin, C. C. and Guzik, J. A. (2017). "Convection and Overshoot in Models of γ Doradus and δ Scuti Stars". *Astrophysical Journal* 849.1, 38.
- Lovis, C. and Pepe, F. (2007). "A new list of thorium and argon spectral lines in the visible". *Astronomy and Astrophysics* 468.3, pp. 1115–1121.
- Lubow, S. H. and Ogilvie, G. I. (2000). "On the Tilting of Protostellar Disks by Resonant Tidal Effects". *Astrophysical Journal* 538.1, pp. 326–340.

- Lund, M. N.; Chaplin, W. J.; Casagrande, L.; Silva Aguirre, V.; Basu, S.; Bieryla, A.; Christensen-Dalsgaard, J.; Latham, D. W.; White, T. R.; Davies, G. R.; Huber, D.; Buchhave, L. A., and Handberg, R. (2016). "Asteroseismic Properties of Solar-type Stars Observed with the NASA K2 Mission: Results from Campaigns 1-3 and Prospects for Future Observations". *Publications of the Astronomical Society of the Pacific* 128.12, p. 124204.
- Lund, M. N.; Handberg, R.; Davies, G. R.; Chaplin, W. J., and Jones, C. D. (2015). "K2P²— A Photometry Pipeline for the K2 Mission". *Astrophysical Journal* 806, 30.
- Lund, M. N.; Kjeldsen, H.; Christensen-Dalsgaard, J.; Handberg, R., and Silva Aguirre, V. (2014a). "Detection of $l = 4$ and $l = 5$ Modes in 12 Years of Solar VIRGO-SPM Data—Tests on Kepler Observations of 16 Cyg A and B". *Astrophysical Journal* 782, 2.
- Lund, M. N.; Lundkvist, M.; Silva Aguirre, V.; Houdek, G.; Casagrande, L.; Van Eylen, V.; Campante, T. L.; Karoff, C.; Kjeldsen, H.; Albrecht, S.; Chaplin, W. J.; Nielsen, M. B.; Degroote, P.; Davies, G. R., and Handberg, R. (2014b). "Asteroseismic inference on the spin-orbit misalignment and stellar parameters of HAT-P-7". *Astronomy and Astrophysics* 570, A54.
- Lund, M. N.; Silva Aguirre, V.; Davies, G. R.; Chaplin, W. J.; Christensen-Dalsgaard, J.; Houdek, G.; White, T. R.; Bedding, T. R.; Ball, W. H.; Huber, D.; Antia, H. M.; Lebreton, Y.; Latham, D. W.; Handberg, R.; Verma, K., et al. (2017). "Standing on the Shoulders of Dwarfs: the Kepler Asteroseismic LEGACY Sample. I. Oscillation Mode Parameters". *Astrophysical Journal* 835, 172.
- Lund, M. N.; Knudstrup, E.; Silva Aguirre, V.; Basu, S.; Chontos, A.; Von Essen, C.; Chaplin, W. J.; Bieryla, A.; Casagrande, L.; Vanderburg, A.; Huber, D.; Kane, S. R.; Albrecht, S.; Latham, D. W.; Davies, G. R., et al. (2019). "Asteroseismology of the Multiplanet System K2-93". *Astronomical Journal* 158.6, 248.
- Lundkvist, M. S.; Kjeldsen, H.; Albrecht, S.; Davies, G. R.; Basu, S.; Huber, D.; Justesen, A. B.; Karoff, C.; Silva Aguirre, V.; van Eylen, V.; Vang, C.; Arentoft, T.; Barclay, T.; Bedding, T. R.; Campante, T. L., et al. (2016). "Hot super-Earths stripped by their host stars". *Nature Communications* 7, 11201.

- Luri, X.; Brown, A. G. A.; Sarro, L. M.; Arenou, F.; Bailer-Jones, C. A. L.; Castro-Ginard, A.; de Bruijne, J.; Prusti, T.; Babusiaux, C., and Delgado, H. E. (2018). “Gaia Data Release 2. Using Gaia parallaxes”. *Astronomy and Astrophysics* 616, A9.
- Madhusudhan, N.; Amin, M. A., and Kennedy, G. M. (2014). “Toward Chemical Constraints on Hot Jupiter Migration”. *The Astrophysical Journal Letters* 794.1, L12.
- Malla, S. P.; Stello, D.; Huber, D.; Montet, B. T.; Bedding, T. R.; Fredslund Andersen, M.; Grundahl, F.; Jessen-Hansen, J.; Hey, D. R.; Palle, P. L.; Deng, L.; Zhang, C.; Chen, X.; Lloyd, J., and Antoci, V. (2020). “Asteroseismic masses of four evolved planet-hosting stars using SONG and TESS: resolving the retired A-star mass controversy”. *Monthly Notices of the Royal Astronomical Society* 496.4, pp. 5423–5435.
- Mamajek, E. E.; Prsa, A.; Torres, G.; Harmanec, P.; Asplund, M.; Bennett, P. D.; Capitaine, N.; Christensen-Dalsgaard, J.; Depagne, E.; Folkner, W. M.; Haberreiter, M.; Hekker, S.; Hilton, J. L.; Kostov, V.; Kurtz, D. W., et al. (2015). “IAU 2015 Resolution B3 on Recommended Nominal Conversion Constants for Selected Solar and Planetary Properties”. *arXiv e-prints*, arXiv:1510.07674.
- Mamajek, E. E. and Hillenbrand, L. A. (2008). “Improved Age Estimation for Solar-Type Dwarfs Using Activity-Rotation Diagnostics”. *Astrophysical Journal* 687.2, pp. 1264–1293.
- Mandel, K. and Agol, E. (2002). “Analytic Light Curves for Planetary Transit Searches”. *The Astrophysical Journal Letters* 580.2, pp. L171–L175.
- Marconi, A.; Abreu, M.; Adibekyan, V.; Alberti, V.; Albrecht, S.; Alcaniz, J.; Aliverti, M.; Allende Prieto, C.; Alvarado Gómez, J. D.; Amado, P. J.; Amate, M.; Andersen, M. I.; Artigau, E.; Baker, C.; Baldini, V., et al. (2022). “ANDES, the high resolution spectrograph for the ELT: science case, baseline design and path to construction”. In: *Ground-based and Airborne Instrumentation for Astronomy IX*. Ed. by C. J. Evans; J. J. Bryant, and K. Motohara. Vol. 12184. Society of Photo-Optical Instrumentation Engineers (SPIE) Conference Series.
- Marconi, G.; Hamilton, D.; Tosi, M., and Bragaglia, A. (1997). “Old open clusters: UBVRI photometry of NGC 2506”. *Monthly Notices of the Royal Astronomical Society* 291.4, pp. 763–772.
- Martí, J. G. and Beaugé, C. (2012). “Stellar scattering and the origin of the planet around γ -Cephei-A”. *Astronomy and Astrophysics* 544, A97.

- Mashonkina, L. I.; Gehren, T.; Shi, J.-R.; Korn, A. J., and Grupp, F. (2011). “A non-LTE study of neutral and singly-ionized iron line spectra in 1D models of the Sun and selected late-type stars”. *Astronomy and Astrophysics* 528, A87.
- Masset, F. S. and Papaloizou, J. C. B. (2003). “Runaway Migration and the Formation of Hot Jupiters”. *Astrophysical Journal* 588.1, pp. 494–508.
- Masuda, K. and Winn, J. N. (2020). “On the Inference of a Star’s Inclination Angle from its Rotation Velocity and Projected Rotation Velocity”. *Astronomical Journal* 159.3, 81.
- Matsakos, T. and Königl, A. (2017). “The Gravitational Interaction between Planets on Inclined Orbits and Protoplanetary Disks As the Origin of Primordial Spin-Orbit Misalignments”. *Astronomical Journal* 153, 60.
- Maxted, P. F. L. (2016). “ellc: A fast, flexible light curve model for detached eclipsing binary stars and transiting exoplanets”. *Astronomy and Astrophysics* 591, A111.
- Maxted, P. F. L.; Serenelli, A. M., and Southworth, J. (2015). “Comparison of gyrochronological and isochronal age estimates for transiting exoplanet host stars”. *Astronomy and Astrophysics* 577, A90.
- Mayor, M.; Marmier, M.; Lovis, C.; Udry, S.; Ségransan, D.; Pepe, F.; Benz, W.; Bertaux, J. .-.L.; Bouchy, F.; Dumusque, X.; Lo Curto, G.; Mordasini, C.; Queloz, D., and Santos, N. C. (2011). “The HARPS search for southern extra-solar planets XXXIV. Occurrence, mass distribution and orbital properties of super-Earths and Neptune-mass planets”. *arXiv e-prints*, arXiv:1109.2497.
- Mayor, M.; Pepe, F.; Queloz, D.; Bouchy, F.; Rupprecht, G.; Lo Curto, G.; Avila, G.; Benz, W.; Bertaux, J. .-.L.; Bonfils, X.; Dall, T.; Dekker, H.; Delabre, B.; Eckert, W.; Fleury, M., et al. (2003). “Setting New Standards with HARPS”. *The Messenger* 114, pp. 20–24.
- Mayor, M. and Queloz, D. (1995). “A Jupiter-mass companion to a solar-type star”. *Nature* 378.6555, pp. 355–359.
- Mazeh, T.; Holczer, T., and Faigler, S. (2016). “Dearth of short-period Neptunian exoplanets: A desert in period-mass and period-radius planes”. *Astronomy and Astrophysics* 589, A75.
- Mazeh, T.; Naef, D.; Torres, G.; Latham, D. W.; Mayor, M.; Beuzit, J.-L.; Brown, T. M.; Buchhave, L.; Burnet, M.; Carney, B. W.; Charbonneau, D.; Drukier, G. A.; Laird, J. B.; Pepe, F.; Perrier, C., et al. (2000). “The

- Spectroscopic Orbit of the Planetary Companion Transiting HD 209458". *The Astrophysical Journal Letters* 532.1, pp. L55–L58.
- McClure, R. D.; Twarog, B. A., and Forrester, W. T. (1981). "The old open cluster NGC 2506 and its similarity to NGC 2420." *Astrophysical Journal* 243, pp. 841–854.
- McCully, C.; Volgenau, N. H.; Harbeck, D.-R.; Lister, T. A.; Saunders, E. S.; Turner, M. L.; Siiverd, R. J., and Bowman, M. (2018). "Real-time processing of the imaging data from the network of Las Cumbres Observatory Telescopes using BANZAI". In: *Proceedings of SPIE*. Vol. 10707. Society of Photo-Optical Instrumentation Engineers (SPIE) Conference Series.
- McLaughlin, D. B. (1924). "Some results of a spectrographic study of the Algol system." *Astrophysical Journal* 60, pp. 22–31.
- McMahon, R. G.; Banerji, M.; Gonzalez, E.; Koposov, S. E.; Bejar, V. J.; Lodieu, N.; Rebolo, R., and VHS Collaboration (2013). "First Scientific Results from the VISTA Hemisphere Survey (VHS)". *The Messenger* 154, pp. 35–37.
- McQuillan, A.; Aigrain, S., and Mazeh, T. (2013). "Measuring the rotation period distribution of field M dwarfs with Kepler". *Monthly Notices of the Royal Astronomical Society* 432.2, pp. 1203–1216.
- Mermilliod, J. C. (1997). "VizieR Online Data Catalog: Homogeneous Means in the UBV System (Mermilliod 1991)". *VizieR Online Data Catalog*, II/168.
- Mikolaitis, Š.; Tautvaišienė, G.; Gratton, R.; Bragaglia, A., and Carretta, E. (2011). "Chemical composition of evolved stars in the open cluster NGC 2506". *Monthly Notices of the Royal Astronomical Society* 416.2, pp. 1092–1098.
- Moe, M. and Di Stefano, R. (2017). "Mind Your Ps and Qs: The Interrelation between Period (P) and Mass-ratio (Q) Distributions of Binary Stars". *The Astrophysical Journal Supplement Series* 230.2, 15.
- Mollière, P.; Stolk, T.; Lacour, S.; Otten, G. P. P. L.; Shangguan, J.; Charnay, B.; Molyarova, T.; Nowak, M.; Henning, T.; Marleau, G. .-.D.; Semenov, D. A.; van Dishoeck, E.; Eisenhauer, F.; Garcia, P.; Garcia Lopez, R., et al. (2020). "Retrieving scattering clouds and disequilibrium chemistry in the atmosphere of HR 8799e". *Astronomy and Astrophysics* 640, A131.

- Mollière, P.; Wardenier, J. P.; van Boekel, R.; Henning, T.; Molaverdikhani, K., and Snellen, I. A. G. (2019). “petitRADTRANS. A Python radiative transfer package for exoplanet characterization and retrieval”. *Astronomy and Astrophysics* 627, A67.
- Mordasini, C.; Alibert, Y.; Benz, W., and Naef, D. (2009). “Extrasolar planet population synthesis. II. Statistical comparison with observations”. *Astronomy and Astrophysics* 501.3, pp. 1161–1184.
- Morris, R. L.; Twicken, J. D.; Smith, J. C.; Clarke, B. D.; Jenkins, J. M.; Bryson, S. T.; Girouard, F., and Klaus, T. C. (2020). *Kepler Data Processing Handbook: Photometric Analysis*. Kepler Science Document KSCI-19081-003.
- Mortier, A.; Santos, N. C.; Sousa, S. G.; Adibekyan, V. Z.; Delgado Mena, E.; Tsantaki, M.; Israelian, G., and Mayor, M. (2013). “New and updated stellar parameters for 71 evolved planet hosts. On the metallicity-giant planet connection”. *Astronomy and Astrophysics* 557, A70.
- Mosser, B.; Benomar, O.; Belkacem, K.; Goupil, M. J.; Lagarde, N.; Michel, E.; Lebreton, Y.; Stello, D.; Vrard, M.; Barban, C.; Bedding, T. R.; Deheuvels, S.; Chaplin, W. J.; De Ridder, J.; Elsworth, Y., et al. (2014). “Mixed modes in red giants: a window on stellar evolution”. *Astronomy and Astrophysics* 572, L5.
- Mosser, B.; Gehan, C.; Belkacem, K.; Samadi, R.; Michel, E., and Goupil, M. .-.J. (2018). “Period spacings in red giants. IV. Toward a complete description of the mixed-mode pattern”. *Astronomy and Astrophysics* 618, A109.
- Mosser, B.; Pinçon, C.; Belkacem, K.; Takata, M., and Vrard, M. (2017). “Period spacings in red giants. III. Coupling factors of mixed modes”. *Astronomy and Astrophysics* 600, A1.
- Mosser, B.; Vrard, M.; Belkacem, K.; Deheuvels, S., and Goupil, M. J. (2015). “Period spacings in red giants. I. Disentangling rotation and revealing core structure discontinuities”. *Astronomy and Astrophysics* 584, A50.
- Murgas, F.; Astudillo-Defru, N.; Bonfils, X.; Crossfield, I.; Almenara, J. M.; Livingston, J.; Stassun, K. G.; Korth, J.; Orell-Miquel, J.; Morello, G.; Eastman, J. D.; Lissauer, J. J.; Kane, S. R.; Morales, F. Y.; Werner, M. W., et al. (2021). “TOI-674b: An oasis in the desert of exo-Neptunes transiting a nearby M dwarf”. *Astronomy and Astrophysics* 653, A60.

- Nagasawa, M.; Ida, S., and Bessho, T. (2008). "Formation of Hot Planets by a Combination of Planet Scattering, Tidal Circularization, and the Kozai Mechanism". *Astrophysical Journal* 678.1, pp. 498–508.
- Naoz, S. (2016). "The Eccentric Kozai-Lidov Effect and Its Applications". *Annual Review of Astronomy & Astrophysics* 54, pp. 441–489.
- Naoz, S.; Farr, W. M.; Lithwick, Y.; Rasio, F. A., and Teyssandier, J. (2011). "Hot Jupiters from secular planet-planet interactions". *Nature* 473.7346, pp. 187–189.
- Narita, N.; Fukui, A.; Kusakabe, N.; Onitsuka, M.; Ryu, T.; Yanagisawa, K.; Izumiura, H.; Tamura, M., and Yamamuro, T. (2015). "MuSCAT: a multicolor simultaneous camera for studying atmospheres of transiting exoplanets". *Journal of Astronomical Telescopes, Instruments, and Systems* 1, 045001.
- Narita, N.; Hirano, T.; Sato, B.; Winn, J. N.; Suto, Y.; Turner, E. L.; Aoki, W.; Tamura, M., and Yamada, T. (2009). "Improved Measurement of the Rossiter-McLaughlin Effect in the Exoplanetary System HD 17156". *Publications of the Astronomical Society of Japan* 61, p. 991.
- Nelson, B. E.; Ford, E. B., and Rasio, F. A. (2017). "Evidence for Two Hot-Jupiter Formation Paths". *Astronomical Journal* 154.3, 106.
- Nelson, R. P.; Papaloizou, J. C. B.; Masset, F., and Kley, W. (2000). "The migration and growth of protoplanets in protostellar discs". *Monthly Notices of the Royal Astronomical Society* 318.1, pp. 18–36.
- Netopil, M.; Paunzen, E.; Heiter, U., and Soubiran, C. (2016). "On the metallicity of open clusters. III. Homogenised sample". *Astronomy and Astrophysics* 585, A150.
- Neuhäuser, R.; Mugrauer, M.; Fukagawa, M.; Torres, G., and Schmidt, T. (2007). "Direct detection of exoplanet host star companion γ Cep B and revised masses for both stars and the sub-stellar object". *Astronomy and Astrophysics* 462.2, pp. 777–780.
- Ngo, H.; Knutson, H. A.; Hinkley, S.; Bryan, M.; Crepp, J. R.; Batygin, K.; Crossfield, I.; Hansen, B.; Howard, A. W.; Johnson, J. A.; Mawet, D.; Morton, T. D.; Muirhead, P. S., and Wang, J. (2016). "Friends of Hot Jupiters. IV. Stellar Companions Beyond 50 au Might Facilitate Giant Planet Formation, but Most are Unlikely to Cause Kozai-Lidov Migration". *Astrophysical Journal* 827.1, 8.

- Nielsen, M. B.; Davies, G. R.; Ball, W. H.; Lyttle, A. J.; Li, T.; Hall, O. J.; Chaplin, W. J.; Gaulme, P.; Carboneau, L.; Ong, J. M. J.; García, R. A.; Mosser, B.; Roxburgh, I. W.; Corsaro, E.; Benomar, O., et al. (2021). “PBjam: A Python Package for Automating Asteroseismology of Solar-like Oscillators”. *Astronomical Journal* 161.2, 62.
- Nordgren, T. E.; Germain, M. E.; Benson, J. A.; Mozurkewich, D.; Sudol, J. J.; Elias N. M., I.; Hajian, A. R.; White, N. M.; Hutter, D. J.; Johnston, K. J.; Gauss, F. S.; Armstrong, J. T.; Pauls, T. A., and Rickard, L. J. (1999). “Stellar Angular Diameters of Late-Type Giants and Supergiants Measured with the Navy Prototype Optical Interferometer”. *Astronomical Journal* 118.6, pp. 3032–3038.
- North, T. S. H.; Campante, T. L.; Miglio, A.; Davies, G. R.; Grunblatt, S. K.; Huber, D.; Kuszlewicz, J. S.; Lund, M. N.; Cooke, B. F., and Chaplin, W. J. (2017). “The masses of retired A stars with asteroseismology: Kepler and K2 observations of exoplanet hosts”. *Monthly Notices of the Royal Astronomical Society* 472.2, pp. 1866–1878.
- Ong, J. M. J. and Basu, S. (2019). “Structural and Evolutionary Diagnostics from Asteroseismic Phase Functions”. *Astrophysical Journal* 885.1, 26.
- Orosz, J. A. and Hauschildt, P. H. (2000). “The use of the NextGen model atmospheres for cool giants in a light curve synthesis code”. *Astronomy and Astrophysics* 364, pp. 265–281.
- Orosz, J. A.; Welsh, W. F.; Haghighipour, N.; Quarles, B.; Short, D. R.; Mills, S. M.; Satyal, S.; Torres, G.; Agol, E.; Fabrycky, D. C.; Jontof-Hutter, D.; Windmiller, G.; Müller, T. W. A.; Hinse, T. C.; Cochran, W. D., et al. (2019). “Discovery of a Third Transiting Planet in the Kepler-47 Circumbinary System”. *Astronomical Journal* 157.5, 174.
- Owen, J. E. and Lai, D. (2018). “Photoevaporation and high-eccentricity migration created the sub-Jovian desert”. *Monthly Notices of the Royal Astronomical Society* 479.4, pp. 5012–5021.
- Pasquini, L.; Avila, G.; Blecha, A.; Cacciari, C.; Cayatte, V.; Colless, M.; Damiani, F.; de Propris, R.; Dekker, H.; di Marcantonio, P.; Farrell, T.; Gillingham, P.; Guinouard, I.; Hammer, F.; Kaufer, A., et al. (2002). “Installation and commissioning of FLAMES, the VLT Multifibre Facility”. *The Messenger* 110, pp. 1–9.
- Paxton, B.; Bildsten, L.; Dotter, A.; Herwig, F.; Lesaffre, P., and Timmes, F. (2011). “Modules for Experiments in Stellar Astrophysics (MESA)”. *The Astrophysical Journal Supplement Series* 192.1, 3.

- Paxton, B.; Cantiello, M.; Arras, P.; Bildsten, L.; Brown, E. F.; Dotter, A.; Mankovich, C.; Montgomery, M. H.; Stello, D.; Timmes, F. X., and Townsend, R. (2013). “Modules for Experiments in Stellar Astrophysics (MESA): Planets, Oscillations, Rotation, and Massive Stars”. *The Astrophysical Journal Supplement Series* 208.1, 4.
- Paxton, B.; Marchant, P.; Schwab, J.; Bauer, E. B.; Bildsten, L.; Cantiello, M.; Dessart, L.; Farmer, R.; Hu, H.; Langer, N.; Townsend, R. H. D.; Townsley, D. M., and Timmes, F. X. (2015). “Modules for Experiments in Stellar Astrophysics (MESA): Binaries, Pulsations, and Explosions”. *The Astrophysical Journal Supplement Series* 220.1, 15.
- Pepe, F.; Cristiani, S.; Rebolo, R.; Santos, N. C.; Dekker, H.; Cabral, A.; Di Marcantonio, P.; Figueira, P.; Lo Curto, G.; Lovis, C.; Mayor, M.; Mégevand, D.; Molaro, P.; Riva, M.; Zapatero Osorio, M. R., et al. (2021). “ESPRESSO at VLT. On-sky performance and first results”. *Astronomy and Astrophysics* 645, A96.
- Pepper, J.; Kane, S. R.; Rodriguez, J. E.; Hinkel, N. R.; Eastman, J. D.; Daylan, T.; Mochnik, T.; Dalba, P. A.; Gaudi, B. S.; Fetherolf, T.; Stassun, K. G.; Campante, T. L.; Vanderburg, A.; Huber, D.; Bossini, D., et al. (2020). “TESS Reveals HD 118203 b to be a Transiting Planet”. *Astronomical Journal* 159.6, 243.
- Pepper, J.; Pogge, R. W.; DePoy, D. L.; Marshall, J. L.; Stanek, K. Z.; Stutz, A. M.; Poindexter, S.; Siverd, R.; O’Brien, T. P.; Trueblood, M., and Trueblood, P. (2007). “The Kilodegree Extremely Little Telescope (KELT): A Small Robotic Telescope for Large-Area Synoptic Surveys”. *Publications of the Astronomical Society of the Pacific* 119.858, pp. 923–935.
- Pereira, F.; Campante, T. L.; Cunha, M. S.; Faria, J. P.; Santos, N. C.; Barros, S. C. C.; Demangeon, O.; Kuszlewicz, J. S., and Corsaro, E. (2019). “Gaussian process modelling of granulation and oscillations in red giant stars”. *Monthly Notices of the Royal Astronomical Society* 489.4, pp. 5764–5774.
- Pérez Hernández, F.; García, R. A.; Mathur, S.; Santos, A. R. G., and Régulo, C. (2019). “Influence of magnetic activity on the determination of stellar parameters through asteroseismology”. *Frontiers in Astronomy and Space Sciences* 6, 41.
- Perryman, M. (2018). *The Exoplanet Handbook*.

- Persson, C. M.; Fridlund, M.; Barragán, O.; Dai, F.; Gandolfi, D.; Hatzes, A. P.; Hirano, T.; Grziwa, S.; Korth, J.; Prieto-Arranz, J.; Fossati, L.; Van Eylen, V.; Justesen, A. B.; Livingston, J.; Kubyshkina, D., et al. (2018). “Super-Earth of 8 M_⊕ in a 2.2-day orbit around the K5V star K2-216”. *Astronomy and Astrophysics* 618, A33.
- Persson, C. M.; Georgieva, I. Y.; Gandolfi, D.; Acuna, L.; Aguichine, A.; Muresan, A.; Guenther, E.; Livingston, J.; Collins, K. A.; Dai, F.; Fridlund, M.; Goffo, E.; Jenkins, J. S.; Kabáth, P.; Korth, J., et al. (2022). “TOI-2196 b: Rare planet in the hot Neptune desert transiting a G-type star”. *Astronomy and Astrophysics* 666, A184.
- Petigura, E. A.; Howard, A. W.; Marcy, G. W.; Johnson, J. A.; Isaacson, H.; Cargile, P. A.; Hebb, L.; Fulton, B. J.; Weiss, L. M.; Morton, T. D.; Winn, J. N.; Rogers, L. A.; Sinukoff, E.; Hirsch, L. A., and Crossfield, I. J. M. (2017). “The California-Kepler Survey. I. High-resolution Spectroscopy of 1305 Stars Hosting Kepler Transiting Planets”. *Astronomical Journal* 154.3, 107.
- Petrovich, C. (2015). “Hot Jupiters from Coplanar High-eccentricity Migration”. *Astrophysical Journal* 805.1, 75.
- Petrovich, C.; Muñoz, D. J.; Kratter, K. M., and Malhotra, R. (2020). “A Disk-driven Resonance as the Origin of High Inclinations of Close-in Planets”. *The Astrophysical Journal Letters* 902.1, L5.
- Petrovich, C.; Tremaine, S., and Rafikov, R. (2014). “Scattering Outcomes of Close-in Planets: Constraints on Planet Migration”. *Astrophysical Journal* 786.2, 101.
- Piskunov, N. and Valenti, J. A. (2017). “Spectroscopy Made Easy: Evolution”. *Astronomy and Astrophysics* 597, A16.
- Pollacco, D. L.; Skillen, I.; Collier Cameron, A.; Christian, D. J.; Hellier, C.; Irwin, J.; Lister, T. A.; Street, R. A.; West, R. G.; Anderson, D. R.; Clarkson, W. I.; Deeg, H.; Enoch, B.; Evans, A.; Fitzsimmons, A., et al. (2006). “The WASP Project and the SuperWASP Cameras”. *Publications of the Astronomical Society of the Pacific* 118.848, pp. 1407–1418.
- Pollack, J. B.; Hubickyj, O.; Bodenheimer, P.; Lissauer, J. J.; Podolak, M., and Greenzweig, Y. (1996). “Formation of the Giant Planets by Concurrent Accretion of Solids and Gas”. *Icarus* 124.1, pp. 62–85.

- Queloz, D.; Eggenberger, A.; Mayor, M.; Perrier, C.; Beuzit, J. L.; Naef, D.; Sivan, J. P., and Udry, S. (2000). "Detection of a spectroscopic transit by the planet orbiting the star HD209458". *Astronomy and Astrophysics* 359, pp. L13–L17.
- Quirrenbach, A.; Amado, P. J.; Caballero, J. A.; Mundt, R.; Reiners, A.; Ribas, I.; Seifert, W.; Abril, M.; Aceituno, J.; Alonso-Floriano, F. J.; Ammler-von Eiff, M.; Antona Jiménez, R.; Anwand-Heerwart, H.; Azzaro, M.; Bauer, F., et al. (2014). "CARMENES instrument overview". In: *Ground-based and Airborne Instrumentation for Astronomy V*. Ed. by S. K. Ramsay; I. S. McLean, and H. Takami. Vol. 9147. Society of Photo-Optical Instrumentation Engineers (SPIE) Conference Series.
- Radovan, M. V.; Lanclos, K.; Holden, B. P.; Kibrick, R. I.; Allen, S. L.; Deich, W. T. S.; Rivera, E.; Burt, J.; Fulton, B.; Butler, P., and Vogt, S. S. (2014). "The automated planet finder at Lick Observatory". In: *Ground-based and Airborne Telescopes V*. Ed. by L. M. Stepp; R. Gilmozzi, and H. J. Hall. Vol. 9145. Society of Photo-Optical Instrumentation Engineers (SPIE) Conference Series.
- Radovan, M. V.; Cabak, G. F.; Laiterman, L. H.; Lockwood, C. T., and Vogt, S. S. (2010). "A radial velocity spectrometer for the Automated Planet Finder Telescope at Lick Observatory". In: *Ground-based and Airborne Instrumentation for Astronomy III*. Ed. by I. S. McLean; S. K. Ramsay, and H. Takami. Vol. 7735. Society of Photo-Optical Instrumentation Engineers (SPIE) Conference Series.
- Rappaport, S.; Levine, A.; Chiang, E.; El Mellah, I.; Jenkins, J.; Kalomeni, B.; Kite, E. S.; Kotson, M.; Nelson, L.; Rousseau-Nepton, L., and Tran, K. (2012). "Possible Disintegrating Short-period Super-Mercury Orbiting KIC 12557548". *Astrophysical Journal* 752, 1.
- Rasio, F. A. and Ford, E. B. (1996). "Dynamical instabilities and the formation of extrasolar planetary systems". *Science* 274, pp. 954–956.
- Rauer, H.; Catala, C.; Aerts, C.; Appourchaux, T.; Benz, W.; Brandeker, A.; Christensen-Dalsgaard, J.; Deleuil, M.; Gizon, L.; Goupil, M. .-.J.; Güdel, M.; Janot-Pacheco, E.; Mas-Hesse, M.; Pagano, I.; Piotto, G., et al. (2014). "The PLATO 2.0 mission". *Experimental Astronomy* 38.1-2, pp. 249–330.
- Reddy, A. B. S.; Giridhar, S., and Lambert, D. L. (2012). "Comprehensive abundance analysis of red giants in the open clusters NGC 752, 1817, 2360 and 2506". *Mon. Not. R. Astron. Soc.* 419.2, pp. 1350–1361.

- Reffert, S. and Quirrenbach, A. (2011). "Mass constraints on substellar companion candidates from the re-reduced Hipparcos intermediate astrometric data: nine confirmed planets and two confirmed brown dwarfs". *Astronomy and Astrophysics* 527, A140.
- Rein, H. and Spiegel, D. S. (2015). "IAS15: a fast, adaptive, high-order integrator for gravitational dynamics, accurate to machine precision over a billion orbits". *Monthly Notices of the Royal Astronomical Society* 446.2, pp. 1424–1437.
- Rice, M.; Wang, S., and Laughlin, G. (2022). "Origins of Hot Jupiters from the Stellar Obliquity Distribution". *The Astrophysical Journal Letters* 926.2, L17.
- Ricker, G. R.; Winn, J. N.; Vanderspek, R.; Latham, D. W.; Bakos, G. Á.; Bean, J. L.; Berta-Thompson, Z. K.; Brown, T. M.; Buchhave, L.; Butler, N. R.; Butler, R. P.; Chaplin, W. J.; Charbonneau, D.; Christensen-Dalsgaard, J.; Clampin, M., et al. (2015). "Transiting Exoplanet Survey Satellite (TESS)". *Journal of Astronomical Telescopes, Instruments, and Systems* 1, 014003.
- Riello, M.; De Angeli, F.; Evans, D. W.; Montegriffo, P.; Carrasco, J. M.; Busso, G.; Palaversa, L.; Burgess, P. W.; Diener, C.; Davidson, M.; Rowell, N.; Fabricius, C.; Jordi, C.; Bellazzini, M.; Pancino, E., et al. (2021). "Gaia Early Data Release 3. Photometric content and validation". *Astronomy and Astrophysics* 649, A3.
- Rodrigues, T. S.; Girardi, L.; Miglio, A.; Bossini, D.; Bovy, J.; Epstein, C.; Pinsonneault, M. H.; Stello, D.; Zasowski, G.; Prieto, C. A.; Chaplin, W. J.; Hekker, S.; Johnson, J. A.; Mészáros, S.; Mosser, B., et al. (2014). "Bayesian distances and extinctions for giants observed by Kepler and APOGEE". *Monthly Notices of the Royal Astronomical Society* 445, pp. 2758–2776.
- Rodriguez, J. E.; Quinn, S. N.; Vanderburg, A.; Zhou, G.; Eastman, J. D.; Thygesen, E.; Cale, B.; Ciardi, D. R.; Reed, P. A.; Oelkers, R. J.; Collins, K. A.; Bieryla, A.; Latham, D. W.; Gaudi, B. S.; Hellier, C., et al. (2022). "Another Shipment of Six Short-Period Giant Planets from TESS". *arXiv e-prints*, arXiv:2205.05709.
- Rodriguez, J. E.; Quinn, S. N.; Zhou, G.; Vanderburg, A.; Nielsen, L. D.; Wittenmyer, R. A.; Brahm, R.; Reed, P. A.; Huang, C. X.; Vach, S.; Ciardi, D. R.; Oelkers, R. J.; Stassun, K. G.; Hellier, C.; Gaudi, B. S., et al. (2021). "TESS Delivers Five New Hot Giant Planets Orbiting Bright Stars from the Full-frame Images". *Astronomical Journal* 161.4, 194.

- Rogers, T. M. and Lin, D. N. C. (2013). “On the Tidal Dissipation of Obliquity”. *The Astrophysical Journal Letters* 769.1, L10.
- Romanova, M. M.; Koldoba, A. V.; Ustyugova, G. V.; Blinova, A. A.; Lai, D., and Lovelace, R. V. E. (2021). “3D MHD simulations of accretion on to stars with tilted magnetic and rotational axes”. *Monthly Notices of the Royal Astronomical Society*.
- Rossiter, R. A. (1924). “On the detection of an effect of rotation during eclipse in the velocity of the brighter component of beta Lyrae, and on the constancy of velocity of this system.” *Astrophysical Journal* 60, pp. 15–21.
- Roxburgh, I. W. and Vorontsov, S. V. (2003). “The ratio of small to large separations of acoustic oscillations as a diagnostic of the interior of solar-like stars”. *Astronomy and Astrophysics* 411, pp. 215–220.
- Rucinski, S. (1999). “Spectral Broadening Functions”. *Turkish Journal of Physics* 23, pp. 271–288.
- Rucinski, S. M. (1992). “Spectral-Line Broadening Functions of WUMa-Type Binaries. I. AW UMa”. *Astronomical Journal* 104, p. 1968.
- Rucinski, S. M. (2002). “Radial Velocity Studies of Close Binary Stars. VII. Methods and Uncertainties”. *Astronomical Journal* 124.3, pp. 1746–1756.
- Ryabchikova, T.; Piskunov, N.; Kurucz, R. L.; Stempels, H. C.; Heiter, U.; Pakhomov, Y., and Barklem, P. S. (2015). “A major upgrade of the VALD database”. *Physica Scripta* 90.5, 054005.
- Ryden, B.; Peterson, B. M., and Demianski, M. (2010). “Foundations of Astrophysics”. *American Journal of Physics* 78.1, pp. 127–127.
- Safonov, B. S.; Lysenko, P. A., and Dodin, A. V. (2017). “The speckle polarimeter of the 2.5-m telescope: Design and calibration”. *Astronomy Letters* 43.5, pp. 344–364.
- Salaris, M. and Cassisi, S. (2005). *Evolution of Stars and Stellar Populations*.
- Salpeter, E. E. (1955). “The Luminosity Function and Stellar Evolution.” *Astrophysical Journal* 121, p. 161.
- Salvatier, J.; Wieckiâ, T. V., and Fonnesbeck, C. (2016). *PyMC3: Python probabilistic programming framework*.
- Sanchis-Ojeda, R.; Rappaport, S.; Winn, J. N.; Kotson, M. C.; Levine, A., and El Mellah, I. (2014). “A Study of the Shortest-period Planets Found with Kepler”. *Astrophysical Journal* 787.1, 47.

- Sandquist, E. L.; Jessen-Hansen, J.; Shetrone, M. D.; Brogaard, K.; Meibom, S.; Leitner, M.; Stello, D.; Bruntt, H.; Antoci, V.; Orosz, J. A.; Grundahl, F., and Frandsen, S. (2016). "The Age and Distance of the Kepler Open Cluster NGC 6811 from an Eclipsing Binary, Turnoff Star Pulsation, and Giant Asteroseismology". *Astrophysical Journal* 831.1, 11.
- Santos, A. R. G.; Breton, S. N.; Mathur, S., and García, R. A. (2021). "Surface Rotation and Photometric Activity for Kepler Targets. II. G and F Main-sequence Stars and Cool Subgiant Stars". *The Astrophysical Journal Supplement Series* 255.1, 17.
- Savitzky, A. and Golay, M. J. E. (1964). "Smoothing and differentiation of data by simplified least squares procedures". *Analytical Chemistry* 36, pp. 1627–1639.
- Scargle, J. D. (1982). "Studies in astronomical time series analysis. II. Statistical aspects of spectral analysis of unevenly spaced data." *Astrophysical Journal* 263, pp. 835–853.
- Schlafly, E. F.; Finkbeiner, D. P.; Jurić, M.; Magnier, E. A.; Burgett, W. S.; Chambers, K. C.; Grav, T.; Hodapp, K. W.; Kaiser, N.; Kudritzki, R. .-.P.; Martin, N. F.; Morgan, J. S.; Price, P. A.; Rix, H. .-.W.; Stubbs, C. W., et al. (2012). "Photometric Calibration of the First 1.5 Years of the Pan-STARRS1 Survey". *Astrophysical Journal* 756.2, 158.
- Schlaufman, K. C. (2010). "Evidence of Possible Spin-orbit Misalignment Along the Line of Sight in Transiting Exoplanet Systems". *Astrophysical Journal* 719.1, pp. 602–611.
- Schlegel, D. J.; Finkbeiner, D. P., and Davis, M. (1998). "Maps of Dust Infrared Emission for Use in Estimation of Reddening and Cosmic Microwave Background Radiation Foregrounds". *Astrophysical Journal* 500.2, pp. 525–553.
- Schieterman, E. W.; Kiang, N. Y.; Parenteau, M. N.; Harman, C. E.; DasSarma, S.; Fisher, T. M.; Arney, G. N.; Hartnett, H. E.; Reinhard, C. T.; Olson, S. L.; Meadows, V. S.; Cockell, C. S.; Walker, S. I.; Grenfell, J. L.; Hegde, S., et al. (2018). "Exoplanet Biosignatures: A Review of Remotely Detectable Signs of Life". *Astrobiology* 18.6, pp. 663–708.
- Scott, N. J.; Howell, S. B.; Gnilka, C. L.; Stephens, A. W.; Salinas, R.; Matson, R. A.; Furlan, E.; Horch, E. P.; Everett, M. E.; Ciardi, D. R.; Mills, D., and Quigley, E. A. (2021). "Twin High-resolution, High-speed

- Imagers for the Gemini Telescopes: Instrument description and science verification results". *Frontiers in Astronomy and Space Sciences* 8, 138.
- Scott, N. J. (2019). "Alopeke, Zorro, and NESSI: Three dual-channel speckle imaging instruments at Gemini-North, Gemini-South, and the WIYN telescopes." In: *AAS/Division for Extreme Solar Systems Abstracts*. Vol. 51. AAS/Division for Extreme Solar Systems Abstracts.
- Seabold, S. and Perktold, J. (2010). "statsmodels: Econometric and statistical modeling with python". In: *9th Python in Science Conference*.
- Seager, S. and Mallén-Ornelas, G. (2003). "A Unique Solution of Planet and Star Parameters from an Extrasolar Planet Transit Light Curve". *Astrophysical Journal* 585, pp. 1038–1055.
- Sedaghati, E.; Sánchez-López, A.; Czesla, S.; López-Puertas, M.; Amado, P. J.; Palle, E.; Molaverdikhani, K.; Caballero, J. A.; Nortmann, L.; Quirrenbach, A.; Reiners, A., and Ribas, I. (2022). "Moderately misaligned orbit of the warm sub-Saturn HD 332231 b". *Astronomy and Astrophysics* 659, A44.
- Serrano, L. M.; Gandolfi, D.; Hoyer, S.; Brandeker, A.; Hooton, M. J.; Sousa, S.; Murgas, F.; Ciardi, D. R.; Howell, S. B.; Benz, W.; Billot, N.; Florén, H. .-.G.; Bekkelien, A.; Bonfanti, A.; Krenn, A., et al. (2022). "The HD 93963 A transiting system: A 1.04 d super-Earth and a 3.65 d sub-Neptune discovered by TESS and CHEOPS". *Astronomy and Astrophysics* 667, A1.
- Shara, M. M.; Hurley, J. R., and Mardling, R. A. (2016). "Dynamical Interactions Make Hot Jupiters in Open Star Clusters". *Astrophysical Journal* 816.2, 59.
- Sharma, S.; Stello, D.; Bland-Hawthorn, J.; Hayden, M. R.; Zinn, J. C.; Kallinger, T.; Hon, M.; Asplund, M.; Buder, S.; De Silva, G. h. M.; D'Orazi, V.; Freeman, K.; Kos, J.; Lewis, G. F.; Lin, J., et al. (2019). "The K2-HERMES Survey: age and metallicity of the thick disc". *Monthly Notices of the Royal Astronomical Society* 490.4, pp. 5335–5352.
- Shatsky, N.; Belinski, A.; Dodin, A.; Zheltoukhov, S.; Kornilov, V.; Postnov, K.; Potanin, S.; Safonov, B.; Tatarnikov, A., and Cherepashchuk, A. (2020). "The Caucasian Mountain Observatory of the Sternberg Astronomical Institute: First Six Years of Operation". In: *Ground-Based Astronomy in Russia. 21st Century*. Ed. by I. I. Romanyuk; I. A. Yakunin; A. F. Valeev, and D. O. Kudryavtsev, pp. 127–132.

- Shibahashi, H. (1979). "Modal Analysis of Stellar Nonradial Oscillations by an Asymptotic Method". *Publications of the Astronomical Society of Japan* 31, pp. 87–104.
- Shporer, A. and Brown, T. (2011). "The Impact of the Convective Blueshift Effect on Spectroscopic Planetary Transits". *Astrophysical Journal* 733, p. 30.
- Siegel, M. H.; LaPorte, S. J.; Porterfield, B. L.; Hagen, L. M. Z., and Gronwall, C. A. (2019). "The Swift UVOT Stars Survey. III. Photometry and Color-Magnitude Diagrams of 103 Galactic Open Clusters". *Astronomical Journal* 158.1, 35.
- Silva Aguirre, V.; Bojsen-Hansen, M.; Slumstrup, D.; Casagrande, L.; Kawata, D.; Ciucă, I.; Hand berg, R.; Lund, M. N.; Mosumgaard, J. R., and Huber, D. (2018). "Confirming chemical clocks: asteroseismic age dissection of the Milky Way disc(s)". *Monthly Notices of the Royal Astronomical Society* 475.4, pp. 5487–5500.
- Silva Aguirre, V.; Casagrande, L.; Basu, S.; Campante, T. L.; Chaplin, W. J.; Huber, D.; Miglio, A.; Serenelli, A. M.; Ballot, J.; Bedding, T. R.; Christensen-Dalsgaard, J.; Creevey, O. L.; Elsworth, Y.; García, R. A.; Gilliland, R. L., et al. (2012). "Verifying Asteroseismically Determined Parameters of Kepler Stars Using Hipparcos Parallaxes: Self-consistent Stellar Properties and Distances". *Astrophysical Journal* 757, 99.
- Silva Aguirre, V.; Davies, G. R.; Basu, S.; Christensen-Dalsgaard, J.; Creevey, O.; Metcalfe, T. S.; Bedding, T. R.; Casagrande, L.; Handberg, R.; Lund, M. N.; Nissen, P. E.; Chaplin, W. J.; Huber, D.; Serenelli, A. M.; Stello, D., et al. (2015). "Ages and fundamental properties of Kepler exoplanet host stars from asteroseismology". *Monthly Notices of the Royal Astronomical Society* 452.2, pp. 2127–2148.
- Silva Aguirre, V.; Lund, M. N.; Antia, H. M.; Ball, W. H.; Basu, S.; Christensen-Dalsgaard, J.; Lebreton, Y.; Reese, D. R.; Verma, K.; Casagrande, L.; Justesen, A. B.; Mosumgaard, J. R.; Chaplin, W. J.; Bedding, T. R.; Davies, G. R., et al. (2017). "Standing on the Shoulders of Dwarfs: the Kepler Asteroseismic LEGACY Sample. II. Radii, Masses, and Ages". *Astrophysical Journal* 835, 173.
- Simunovic, M.; Puzia, T. H., and Sills, A. (2014). "The Blue Straggler Star Population in NGC 1261: Evidence for a Post-core-collapse Bounce State". *Astrophysical Journal* 795.1, L10.

- Sinukoff, E.; Howard, A. W.; Petigura, E. A.; Schlieder, J. E.; Crossfield, I. J. M.; Ciardi, D. R.; Fulton, B. J.; Isaacson, H.; Aller, K. M.; Baranec, C.; Beichman, C. A.; Hansen, B. M. S.; Knutson, H. A.; Law, N. M.; Liu, M. C., et al. (2016). "Eleven Multiplanet Systems from K2 Campaigns 1 and 2 and the Masses of Two Hot Super-Earths". *Astrophysical Journal* 827, 78.
- Skrutskie, M. F.; Cutri, R. M.; Stiening, R.; Weinberg, M. D.; Schneider, S.; Carpenter, J. M.; Beichman, C.; Capps, R.; Chester, T.; Elias, J.; Huchra, J.; Liebert, J.; Lonsdale, C.; Monet, D. G.; Price, S., et al. (2006). "The Two Micron All Sky Survey (2MASS)". *Astronomical Journal* 131, pp. 1163–1183.
- Slumstrup, D.; Grundahl, F.; Brogaard, K.; Thygesen, A. O.; Nissen, P. E.; Jessen-Hansen, J.; Van Eylen, V., and Pedersen, M. G. (2017). "The [Y/Mg] clock works for evolved solar metallicity stars". *Astronomy and Astrophysics* 604, L8.
- Slumstrup, D.; Grundahl, F.; Silva Aguirre, V., and Brogaard, K. (2019). "Systematic differences in the spectroscopic analysis of red giants". *Astronomy and Astrophysics* 622, A111.
- Smalley, B. (2005). " T_{eff} and log g determinations." *Memorie della Societa Astronomica Italiana Supplementi* 8, p. 130.
- Smith, A. M. S.; Acton, J. S.; Anderson, D. R.; Armstrong, D. J.; Bayliss, D.; Belardi, C.; Bouchy, F.; Brahm, R.; Briegal, J. T.; Bryant, E. M.; Burleigh, M. R.; Cabrera, J.; Chaushev, A.; Cooke, B. F.; Costes, J. C., et al. (2021). "NGTS-14Ab: a Neptune-sized transiting planet in the desert". *Astronomy and Astrophysics* 646, A183.
- Smith, A. M. S.; Breton, S. N.; Csizmadia, S.; Dai, F.; Gandolfi, D.; García, R. A.; Howard, A. W.; Isaacson, H.; Korth, J.; Lam, K. W. F.; Mathur, S.; Nowak, G.; Pérez Hernández, F.; Persson, C. M.; Albrecht, S. H., et al. (2022). "K2-99 revisited: a non-inflated warm Jupiter, and a temperate giant planet on a 522-d orbit around a subgiant". *Monthly Notices of the Royal Astronomical Society* 510.4, pp. 5035–5049.
- Smith, A. W. and Lissauer, J. J. (2009). "Orbital stability of systems of closely-spaced planets". *Icarus* 201, pp. 381–394.
- Smith, J. C.; Stumpe, M. C.; Van Cleve, J. E.; Jenkins, J. M.; Barclay, T. S.; Fanelli, M. N.; Girouard, F. R.; Kolodziejczak, J. J.; McCauliff, S. D.; Morris, R. L., and Twicken, J. D. (2012). "Kepler Presearch Data

- Conditioning II - A Bayesian Approach to Systematic Error Correction". *Publications of the Astronomical Society of the Pacific* 124, p. 1000.
- Southworth, J. (2013). "The solar-type eclipsing binary system LL Aquarii". *Astronomy and Astrophysics* 557, A119.
- Southworth, J.; Smalley, B.; Maxted, P. F. L.; Claret, A., and Etzel, P. B. (2005). "Absolute dimensions of detached eclipsing binaries - I. The metallic-lined system WW Aurigae". *Monthly Notices of the Royal Astronomical Society* 363.2, pp. 529–542.
- Southworth, J. (2011). "Homogeneous studies of transiting extrasolar planets - IV. Thirty systems with space-based light curves". *Monthly Notices of the Royal Astronomical Society* 417.3, pp. 2166–2196.
- Spalding, C.; Batygin, K., and Adams, F. C. (2014). "Alignment of Protostars and Circumstellar Disks during the Embedded Phase". *The Astrophysical Journal Letters* 797, L29.
- Spiegel, D. S.; Burrows, A., and Milsom, J. A. (2011). "The Deuterium-burning Mass Limit for Brown Dwarfs and Giant Planets". *Astrophysical Journal* 727.1, 57.
- Stassun, K. G.; Collins, K. A., and Gaudi, B. S. (2017). "Accurate Empirical Radii and Masses of Planets and Their Host Stars with Gaia Parallaxes". *Astronomical Journal* 153.3, 136.
- Stassun, K. G.; Corsaro, E.; Pepper, J. A., and Gaudi, B. S. (2018). "Empirical Accurate Masses and Radii of Single Stars with TESS and Gaia". *Astronomical Journal* 155.1, 22.
- Stassun, K. G. and Torres, G. (2016). "Eclipsing Binaries as Benchmarks for Trigonometric Parallaxes in the Gaia Era". *Astronomical Journal* 152.6, 180.
- Stassun, K. G. and Torres, G. (2021). "Parallax Systematics and Photocenter Motions of Benchmark Eclipsing Binaries in Gaia EDR3". *The Astrophysical Journal Letters* 907.2, L33.
- Stefansson, G.; Mahadevan, S.; Petrovich, C.; Winn, J. N.; Kanodia, S.; Millholland, S. C.; Maney, M.; Cañas, C. I.; Wisniewski, J.; Robertson, P.; Ninan, J. P.; Ford, E. B.; Bender, C. F.; Blake, C. H.; Cegla, H., et al. (2022). "The Warm Neptune GJ 3470b Has a Polar Orbit". *The Astrophysical Journal Letters* 931.2, L15.

- Stello, D.; Chaplin, W. J.; Basu, S.; Elsworth, Y., and Bedding, T. R. (2009). “The relation between $\Delta\nu$ and ν_{max} for solar-like oscillations”. *Monthly Notices of the Royal Astronomical Society* 400.1, pp. L80–L84.
- Stello, D.; Huber, D.; Grundahl, F.; Lloyd, J.; Ireland, M.; Casagrande, L.; Fredslund, M.; Bedding, T. R.; Palle, P. L.; Antoci, V.; Kjeldsen, H., and Christensen-Dalsgaard, J. (2017). “Asteroseismic masses of retired planet-hosting A-stars using SONG”. *Monthly Notices of the Royal Astronomical Society* 472.4, pp. 4110–4116.
- Stello, D.; Meibom, S.; Gilliland, R. L.; Grundahl, F.; Hekker, S.; Mosser, B.; Kallinger, T.; Mathur, S.; García, R. A.; Huber, D.; Basu, S.; Bedding, T. R.; Brogaard, K.; Chaplin, W. J.; Elsworth, Y. P., et al. (2011). “An Asteroseismic Membership Study of the Red Giants in Three Open Clusters Observed by Kepler: NGC 6791, NGC 6819, and NGC 6811”. *Astrophysical Journal* 739.1, 13.
- Stello, D.; Vanderburg, A.; Casagrande, L.; Gilliland, R.; Silva Aguirre, V.; Sandquist, E.; Leiner, E.; Mathieu, R., and Soderblom, D. R. (2016). “The K2 M67 Study: Revisiting Old Friends with K2 Reveals Oscillating Red Giants in the Open Cluster M67”. *Astrophysical Journal* 832.2, 133.
- Stephan, A. P.; Wang, J.; Cauley, P. W.; Gaudi, B. S.; Ilyin, I.; Johnson, M. C., and Strassmeier, K. G. (2022). “Nodal Precession and Tidal Evolution of Two Hot Jupiters: WASP-33 b and KELT-9 b”. *Astrophysical Journal* 931.2, 111.
- Sterne, T. E. (1940). “On the Determination of the Orbital Elements of Eccentric Eclipsing Binaries”. *Proceedings of the National Academy of Science* 26.1, pp. 36–40.
- Stetson, P. B. (1987). “DAOPHOT - A computer program for crowded-field stellar photometry”. *Publications of the Astronomical Society of the Pacific* 99, pp. 191–222.
- Stetson, P. B. and Pancino, E. (2008). “DAOSPEC: an automatic code for measuring equivalent widths in high-resolution stellar spectra”, pp. 1332–1354.
- Stokholm, A.; Nissen, P. E.; Silva Aguirre, V.; White, T. R.; Lund, M. N.; Mosumgaard, J. R.; Huber, D., and Jessen-Hansen, J. (2019). “The subgiant HR 7322 as an asteroseismic benchmark star”. *Monthly Notices of the Royal Astronomical Society* 489.1, pp. 928–940.
- Struve, O. and Elvey, C. T. (1931). “Algol and stellar rotation”. *Monthly Notices of the Royal Astronomical Society* 91, p. 663.

- Stumpe, M. C.; Smith, J. C.; Van Cleve, J. E.; Twicken, J. D.; Barclay, T. S.; Fanelli, M. N.; Girouard, F. R.; Jenkins, J. M.; Kolodziejczak, J. J.; McCauliff, S. D., and Morris, R. L. (2012). “Kepler Presearch Data Conditioning I—Architecture and Algorithms for Error Correction in Kepler Light Curves”. *Publications of the Astronomical Society of the Pacific* 124, p. 985.
- Stumpe, M. C.; Smith, J. C.; Catanzarite, J. H.; Van Cleve, J. E.; Jenkins, J. M.; Twicken, J. D., and Girouard, F. R. (2014). “Multiscale Systematic Error Correction via Wavelet-Based Bandsplitting in Kepler Data”. *Publications of the Astronomical Society of the Pacific* 126.935, p. 100.
- Swift, J. J.; Johnson, J. A.; Morton, T. D.; Crepp, J. R.; Montet, B. T.; Fabrycky, D. C., and Muirhead, P. S. (2013). “Characterizing the Cool KOIs. IV. Kepler-32 as a Prototype for the Formation of Compact Planetary Systems throughout the Galaxy”. *Astrophysical Journal* 764.1, 105.
- Szabó, G. M. and Kálmán, S. (2019). “The sub-Jupiter/Neptune desert of exoplanets: parameter dependent boundaries and implications on planet formation”. *Monthly Notices of the Royal Astronomical Society* 485.1, pp. L116–L120.
- Szabó, G. M.; Pál, A.; Derekas, A.; Simon, A. E.; Szalai, T., and Kiss, L. L. (2012). “Spin-orbit resonance, transit duration variation and possible secular perturbations in KOI-13”. *Monthly Notices of the Royal Astronomical Society* 421.1, pp. L122–L126.
- Tabernero, H. M.; Zapatero Osorio, M. R.; Allende Prieto, C.; González-Álvarez, E.; Sanz-Forcada, J.; López-Gallifa, A.; Montes, D.; del Burgo, C.; González Hernández, J. I., and Rebolo, R. (2022). “HORuS transmission spectroscopy and revised planetary parameters of KELT-7 b”. *Monthly Notices of the Royal Astronomical Society* 515.1, pp. 1247–1265.
- Takaishi, D.; Tsukamoto, Y., and Suto, Y. (2020). “Star-disc alignment in the protoplanetary discs: SPH simulation of the collapse of turbulent molecular cloud cores”. *Monthly Notices of the Royal Astronomical Society* 492.4, pp. 5641–5654.
- Talens, G. J. J.; Justesen, A. B.; Albrecht, S.; McCormac, J.; Van Eylen, V.; Otten, G. P. P. L.; Murgas, F.; Palle, E.; Pollacco, D.; Stuik, R.; Spronck, J. F. P.; Lesage, A. .-.L.; Grundahl, F.; Fredslund Andersen, M.; Antoci, V., et al. (2018). “MASCARA-2 b. A hot Jupiter transiting the $m_V = 7.6$ A-star HD 185603”. *Astronomy and Astrophysics* 612, A57.

- Teachey, A. and Kipping, D. M. (2018). "Evidence for a large exomoon orbiting Kepler-1625b". *Science Advances* 4.10, eaav1784.
- Tejada Arevalo, R. A.; Winn, J. N., and Anderson, K. R. (2021). "Further Evidence for Tidal Spin-up of Hot Jupiter Host Stars". *Astrophysical Journal* 919.2, 138.
- Telting, J. H.; Avila, G.; Buchhave, L.; Frandsen, S.; Gandolfi, D.; Lindberg, B.; Stempels, H. C.; Prins, S., and NOT staff (2014). "FIES: The high-resolution Fiber-fed Echelle Spectrograph at the Nordic Optical Telescope". *Astronomische Nachrichten* 335.1, p. 41.
- Ter Braak, C. J. F. (2006). "A Markov Chain Monte Carlo version of the genetic algorithm Differential Evolution: easy Bayesian computing for real parameter spaces". *Statistics and Computing* 16.3, pp. 239–249.
- Teyssandier, J.; Lai, D., and Vick, M. (2019). "Formation of hot Jupiters through secular chaos and dynamical tides". *Monthly Notices of the Royal Astronomical Society* 486.2, pp. 2265–2280.
- Thies, I.; Kroupa, P.; Goodwin, S. P.; Stamatellos, D., and Whitworth, A. P. (2011). "A natural formation scenario for misaligned and short-period eccentric extrasolar planets". *Monthly Notices of the Royal Astronomical Society* 417, pp. 1817–1822.
- Torres, G.; Andersen, J., and Giménez, A. (2010). "Accurate masses and radii of normal stars: modern results and applications". *The Astronomy and Astrophysics Review* 18.1-2, pp. 67–126.
- Torres, G.; Fischer, D. A.; Sozzetti, A.; Buchhave, L. A.; Winn, J. N.; Holman, M. J., and Carter, J. A. (2012). "Improved Spectroscopic Parameters for Transiting Planet Hosts". *Astrophysical Journal* 757, 161.
- Torres, G. (2007). "The Planet Host Star γ Cephei: Physical Properties, the Binary Orbit, and the Mass of the Substellar Companion". *Astrophysical Journal* 654.2, pp. 1095–1109.
- Torres, G.; Lacy, C. H.; Marschall, L. A.; Sheets, H. A., and Mader, J. A. (2006). "The Eclipsing Binary V1061 Cygni: Confronting Stellar Evolution Models for Active and Inactive Solar-Type Stars". *Astrophysical Journal* 640.2, pp. 1018–1038.
- Triaud, A. H. M. J.; Collier Cameron, A.; Queloz, D.; Anderson, D. R.; Gillon, M.; Hebb, L.; Hellier, C.; Loeillet, B.; Maxted, P. F. L.; Mayor, M.; Pepe, F.; Pollacco, D.; Ségransan, D.; Smalley, B.; Udry, S., et al. (2010).

- “Spin-orbit angle measurements for six southern transiting planets. New insights into the dynamical origins of hot Jupiters”. *Astronomy and Astrophysics* 524, A25.
- Tsai, S.-M.; Lee, E. K. H.; Powell, D.; Gao, P.; Zhang, X.; Moses, J.; Hébrard, E.; Venot, O.; Parmentier, V.; Jordan, S.; Hu, R.; Alam, M. K.; Alderson, L.; Batalha, N. M.; Bean, J. L., et al. (2022). “Direct Evidence of Photochemistry in an Exoplanet Atmosphere”. *arXiv e-prints*, arXiv:2211.10490.
- Tull, R. G.; MacQueen, P. J.; Sneden, C., and Lambert, D. L. (1995). “The High-Resolution Cross-Dispersed Echelle White Pupil Spectrometer of the McDonald Observatory 2.7-m Telescope”. *Publications of the Astronomical Society of the Pacific* 107, p. 251.
- Twicken, J. D.; Catanzarite, J. H.; Clarke, B. D.; Girouard, F.; Jenkins, J. M.; Klaus, T. C.; Li, J.; McCauliff, S. D.; Seader, S. E.; Tenenbaum, P.; Wohler, B.; Bryson, S. T.; Burke, C. J.; Caldwell, D. A.; Haas, M. R., et al. (2018). “Kepler Data Validation I—Architecture, Diagnostic Tests, and Data Products for Vetting Transiting Planet Candidates”. *Publications of the Astronomical Society of the Pacific* 130.988, p. 064502.
- Twicken, J. D.; Clarke, B. D.; Bryson, S. T.; Tenenbaum, P.; Wu, H.; Jenkins, J. M.; Girouard, F., and Klaus, T. C. (2010). “Photometric analysis in the Kepler Science Operations Center pipeline”. In: *Software and Cyberinfrastructure for Astronomy*. Ed. by N. M. Radziwill and A. Bridger. Vol. 7740. Society of Photo-Optical Instrumentation Engineers (SPIE) Conference Series.
- Uytterhoeven, K.; Moya, A.; Grigahcène, A.; Guzik, J. A.; Gutiérrez-Soto, J.; Smalley, B.; Hand ler, G.; Balona, L. A.; Niemczura, E.; Fox Machado, L.; Benatti, S.; Chapellier, E.; Tkachenko, A.; Szabó, R.; Suárez, J. C., et al. (2011). “The Kepler characterization of the variability among A- and F-type stars. I. General overview”. *Astronomy and Astrophysics* 534, A125.
- Valenti, J. A. and Piskunov, N. (1996). “Spectroscopy made easy: A new tool for fitting observations with synthetic spectra.” *Astronomy and Astrophysics Supplement Series* 118, pp. 595–603.
- Van Cleve, J. E.; Howell, S. B.; Smith, J. C.; Clarke, B. D.; Thompson, S. E.; Bryson, S. T.; Lund, M. N.; Handberg, R., and Chaplin, W. J. (2016). “That’s How We Roll: The NASA K2 Mission Science Products and Their Performance Metrics”. *Publications of the Astronomical Society of the Pacific* 128.965, p. 075002.

- Van Eylen, V. and Albrecht, S. (2015). "Eccentricity from Transit Photometry: Small Planets in Kepler Multi-planet Systems Have Low Eccentricities". *Astrophysical Journal* 808, 126.
- Van Eylen, V.; Lund, M. N.; Silva Aguirre, V.; Arentoft, T.; Kjeldsen, H.; Albrecht, S.; Chaplin, W. J.; Isaacson, H.; Pedersen, M. G.; Jessen-Hansen, J.; Tingley, B.; Christensen-Dalsgaard, J.; Aerts, C.; Campante, T. L., and Bryson, S. T. (2014). "What Asteroseismology can do for Exoplanets: Kepler-410A b is a Small Neptune around a Bright Star, in an Eccentric Orbit Consistent with Low Obliquity". *Astrophysical Journal* 782, 14.
- Van Eylen, V.; Albrecht, S.; Huang, X.; MacDonald, M. G.; Dawson, R. I.; Cai, M. X.; Foreman-Mackey, D.; Lundkvist, M. S.; Silva Aguirre, V.; Snellen, I., and Winn, J. N. (2019). "The Orbital Eccentricity of Small Planet Systems". *Astronomical Journal* 157.2, 61.
- van Leeuwen, F. (2007). "Validation of the new Hipparcos reduction". *Astronomy and Astrophysics* 474.2, pp. 653–664.
- Vanderburg, A.; Becker, J. C.; Kristiansen, M. H.; Bieryla, A.; Duev, D. A.; Jensen-Clem, R.; Morton, T. D.; Latham, D. W.; Adams, F. C.; Baranec, C.; Berlind, P.; Calkins, M. L.; Esquerdo, G. A.; Kulkarni, S.; Law, N. M., et al. (2016a). "Five Planets Transiting a Ninth Magnitude Star". *The Astrophysical Journal Letters* 827, L10.
- Vanderburg, A.; Latham, D. W.; Buchhave, L. A.; Bieryla, A.; Berlind, P.; Calkins, M. L.; Esquerdo, G. A.; Welsh, S., and Johnson, J. A. (2016b). "Planetary Candidates from the First Year of the K2 Mission". *The Astrophysical Journal Supplement Series* 222, 14.
- Vanderburg, A. and Johnson, J. A. (2014). "A Technique for Extracting Highly Precise Photometry for the Two-Wheeled Kepler Mission". *Publications of the Astronomical Society of the Pacific* 126.944, p. 948.
- Vanderburg, A.; Rappaport, S. A.; Xu, S.; Crossfield, I. J. M.; Becker, J. C.; Gary, B.; Murgas, F.; Blouin, S.; Kaye, T. G.; Palle, E.; Melis, C.; Morris, B. M.; Kreidberg, L.; Gorjian, V.; Morley, C. V., et al. (2020). "A giant planet candidate transiting a white dwarf". *Nature* 585.7825, pp. 363–367.
- Vehtari, A.; Gelman, A.; Simpson, D.; Carpenter, B., and Bürkner, P.-C. (2019). "Rank-normalization, folding, and localization: An improved \widehat{R} for assessing convergence of MCMC". *arXiv e-prints*, arXiv:1903.08008.

- Vick, M.; Su, Y., and Lai, D. (2023). "High-eccentricity Migration with Disk-induced Spin-Orbit Misalignment: A Preference for Perpendicular Hot Jupiters". *The Astrophysical Journal Letters* 943.2, L13.
- Vines, J. I. and Jenkins, J. S. (2022). "ARIADNE: measuring accurate and precise stellar parameters through SED fitting". *Monthly Notices of the Royal Astronomical Society* 513.2, pp. 2719–2731.
- Vissapragada, S.; Knutson, H. A.; Greklek-McKeon, M.; Oklopčić, A.; Dai, F.; dos Santos, L. A.; Jovanovic, N.; Mawet, D.; Millar-Blanchaer, M. A.; Paragas, K.; Spake, J. J.; Tinyanont, S., and Vasisht, G. (2022). "The Upper Edge of the Neptune Desert Is Stable Against Photoevaporation". *Astronomical Journal* 164.6, 234.
- Vogt, S. S.; Allen, S. L.; Bigelow, B. C.; Bresee, L.; Brown, B.; Cantrall, T.; Conrad, A.; Couture, M.; Delaney, C.; Epps, H. W.; Hilyard, D.; Hilyard, D. F.; Horn, E.; Jern, N.; Kanto, D., et al. (1994). "HIRES: the high-resolution echelle spectrometer on the Keck 10-m Telescope". In: *Instrumentation in Astronomy VIII*. Ed. by D. L. Crawford and E. R. Craine. Vol. 2198. Society of Photo-Optical Instrumentation Engineers (SPIE) Conference Series, p. 362.
- Vogt, S. S.; Radovan, M.; Kibrick, R.; Butler, R. P.; Alcott, B.; Allen, S.; Arriagada, P.; Bolte, M.; Burt, J.; Cabak, J.; Chloros, K.; Cowley, D.; Deich, W.; Dupraw, B.; Earthman, W., et al. (2014). "APF—The Lick Observatory Automated Planet Finder". *Publications of the Astronomical Society of the Pacific* 126.938, p. 359.
- Walker, G. A. H.; Bohlender, D. A.; Walker, A. R.; Irwin, A. W.; Yang, S. L. S., and Larson, A. (1992). "Gamma Cephei: Rotation or Planetary Companion?" *The Astrophysical Journal Letters* 396, p. L91.
- Watanabe, N.; Narita, N., and Johnson, M. C. (2020). "Doppler tomographic measurement of the nodal precession of WASP-33b". *Publications of the Astronomical Society of Japan* 72.2, 19.
- Watanabe, N.; Narita, N.; Palle, E.; Fukui, A.; Kusakabe, N.; Parviainen, H.; Murgas, F.; Casasayas-Barris, N.; Johnson, M. C.; Sato, B.; Livingston, J. H.; de Leon, J. P.; Mori, M.; Nishiumi, T.; Terada, Y., et al. (2022). "Nodal precession of WASP-33b for 11 yr by Doppler tomographic and transit photometric observations". *Monthly Notices of the Royal Astronomical Society* 512.3, pp. 4404–4418.

- Weiss, A. and Schlattl, H. (2008). "GARSTEC—the Garching Stellar Evolution Code. The direct descendant of the legendary Kippenhahn code". *Astrophysics and Space Science* 316, pp. 99–106.
- Wenger, M.; Ochsenbein, F.; Egret, D.; Dubois, P.; Bonnarel, F.; Borde, S.; Genova, F.; Jasniewicz, G.; Laloë, S.; Lesteven, S., and Monier, R. (2000). "The SIMBAD astronomical database. The CDS reference database for astronomical objects". *Astronomy and Astrophysics Supplement Series* 143, pp. 9–22.
- Werner, M. W.; Roellig, T. L.; Low, F. J.; Rieke, G. H.; Rieke, M.; Hoffmann, W. F.; Young, E.; Houck, J. R.; Brandl, B.; Fazio, G. G.; Hora, J. L.; Gehrz, R. D.; Helou, G.; Soifer, B. T.; Stauffer, J., et al. (2004). "The Spitzer Space Telescope Mission". *The Astrophysical Journal Supplement Series* 154, pp. 1–9.
- Winn, J. N. (2010). "Transits and Occultations". *ArXiv e-prints*.
- Winn, J. N.; Fabrycky, D.; Albrecht, S., and Johnson, J. A. (2010). "Hot Stars with Hot Jupiters Have High Obliquities". *The Astrophysical Journal Letters* 718, p. L145.
- Winn, J. N.; Noyes, R. W.; Holman, M. J.; Charbonneau, D.; Ohta, Y.; Taruya, A.; Suto, Y.; Narita, N.; Turner, E. L.; Johnson, J. A.; Marcy, G. W.; Butler, R. P., and Vogt, S. S. (2005). "Measurement of Spin-Orbit Alignment in an Extrasolar Planetary System". *Astrophysical Journal* 631, pp. 1215–1226.
- Winn, J. N.; Johnson, J. A.; Albrecht, S.; Howard, A. W.; Marcy, G. W.; Crossfield, I. J., and Holman, M. J. (2009). "HAT-P-7: A Retrograde or Polar Orbit, and a Third Body". *The Astrophysical Journal Letters* 703.2, pp. L99–L103.
- Winn, J. N.; Johnson, J. A.; Peek, K. M. G.; Marcy, G. W.; Bakos, G. Á.; Enya, K.; Narita, N.; Suto, Y.; Turner, E. L., and Vogt, S. S. (2007). "Spin-Orbit Alignment for the Eccentric Exoplanet HD 147506b". *The Astrophysical Journal Letters* 665.2, pp. L167–L170.
- Wolf, C.; Onken, C. A.; Luval, L. C.; Schmidt, B. P.; Bessell, M. S.; Chang, S.-W.; Da Costa, G. S.; Mackey, D.; Martin-Jones, T.; Murphy, S. J.; Preston, T.; Scalzo, R. A.; Shao, L.; Smillie, J.; Tisserand, P., et al. (2018). "SkyMapper Southern Survey: First Data Release (DR1)". *Publications of the Astronomical Society of Australia* 35, e010.

- Wolfgang, A.; Rogers, L. A., and Ford, E. B. (2016). “Probabilistic Mass-Radius Relationship for Sub-Neptune-Sized Planets”. *Astrophysical Journal* 825, 19.
- Wolk, S. J.; Bourke, T. L., and Vigil, M. (2008). “The Embedded Massive Star Forming Region RCW 38”. In: *Handbook of Star Forming Regions, Volume II*. Ed. by B. Reipurth. Vol. 5, p. 124.
- Wolszczan, A. and Frail, D. A. (1992). “A planetary system around the millisecond pulsar PSR1257 + 12”. *Nature* 355.6356, pp. 145–147.
- Wu, Y. and Murray, N. (2003). “Planet Migration and Binary Companions: The Case of HD 80606b”. *Astrophysical Journal* 589, pp. 605–614.
- Wu, Y. and Lithwick, Y. (2011). “Secular Chaos and the Production of Hot Jupiters”. *Astrophysical Journal* 735.2, 109.
- Yee, S. W.; Petigura, E. A., and von Braun, K. (2017). “Precision Stellar Characterization of FGKM Stars using an Empirical Spectral Library”. *Astrophysical Journal* 836, 77.
- Yee, S. W.; Winn, J. N.; Hartman, J. D.; Bouma, L. G.; Zhou, G.; Quinn, S. N.; Latham, D. W.; Bieryla, A.; Rodriguez, J. E.; Collins, K. A.; Alfaro, O.; Barkaoui, K.; Beard, C.; Belinski, A. A.; Benkhaldoun, Z., et al. (2022). “The TESS Grand Unified Hot Jupiter Survey. II. Twenty New Giant Planets”. *arXiv e-prints*, arXiv:2210.15473.
- Zahn, J. .-.P. (1977). “Tidal friction in close binary systems.” *Astronomy and Astrophysics* 57, pp. 383–394.
- Zanazzi, J. J. and Lai, D. (2018). “Planet formation in discs with inclined binary companions: can primordial spin-orbit misalignment be produced?” *Monthly Notices of the Royal Astronomical Society* 478, pp. 835–851.
- Zeng, L.; Jacobsen, S. B.; Sasselov, D. D.; Petaev, M. I.; Vanderburg, A.; Lopez-Morales, M.; Perez-Mercader, J.; Mattsson, T. R.; Li, G.; Heising, M. Z.; Bonomo, A. S.; Damasso, M.; Berger, T. A.; Cao, H.; Levi, A., et al. (2019). “Growth model interpretation of planet size distribution”. *Proceedings of the National Academy of Science* 116.20, pp. 9723–9728.
- Zeng, L.; Sasselov, D. D., and Jacobsen, S. B. (2016). “Mass-Radius Relation for Rocky Planets Based on PREM”. *Astrophysical Journal* 819.2, 127.

- Zhang, J.; Weiss, L. M.; Huber, D.; Blunt, S.; Chontos, A.; Fulton, B. J.; Grunblatt, S.; Howard, A. W.; Isaacson, H.; Kosciarek, M. R.; Petigura, E. A.; Rosenthal, L. J., and Rubenzahl, R. A. (2021). “Long-period Jovian Tilts the Orbits of Two sub-Neptunes Relative to Stellar Spin Axis in Kepler-129”. *Astronomical Journal* 162.3, 89.
- Zhou, G.; Latham, D. W.; Bieryla, A.; Beatty, T. G.; Buchhave, L. A.; Esquerdo, G. A.; Berlind, P., and Calkins, M. L. (2016). “Spin-orbit alignment for KELT-7b and HAT-P-56b via Doppler tomography with TRES”. *Monthly Notices of the Royal Astronomical Society* 460.3, pp. 3376–3383.
- Zhu, W. and Wu, Y. (2018). “The Super Earth-Cold Jupiter Relations”. *Astronomical Journal* 156.3, 92.

Appendices

A

Supplementary figures

This appendix contains additional/supplementary figures from the different papers presented in Part II. Power spectra of γ Cep (Chapter 5) from the different sectors/campaigns are shown in Figure A.1 and Figure A.2. A circular solution for TOI-2025 is given in Figure A.3 and close-up of the transiting trio (Chapter 6) is given in Figure A.4. Supplementary figures for TOI-1288 presented in Chapter 7 are shown in Figure A.5 and Figure A.6. An FFI of NGC 2506 (Chapter 3) is shown in Figure A.7. An extended correlation plot for the analysis of TOI-640 (Chapter 9) is given in Figure A.8, and the full light and **RV** curves are given in Figure A.9 and Figure A.10.

A.1 γ Cep

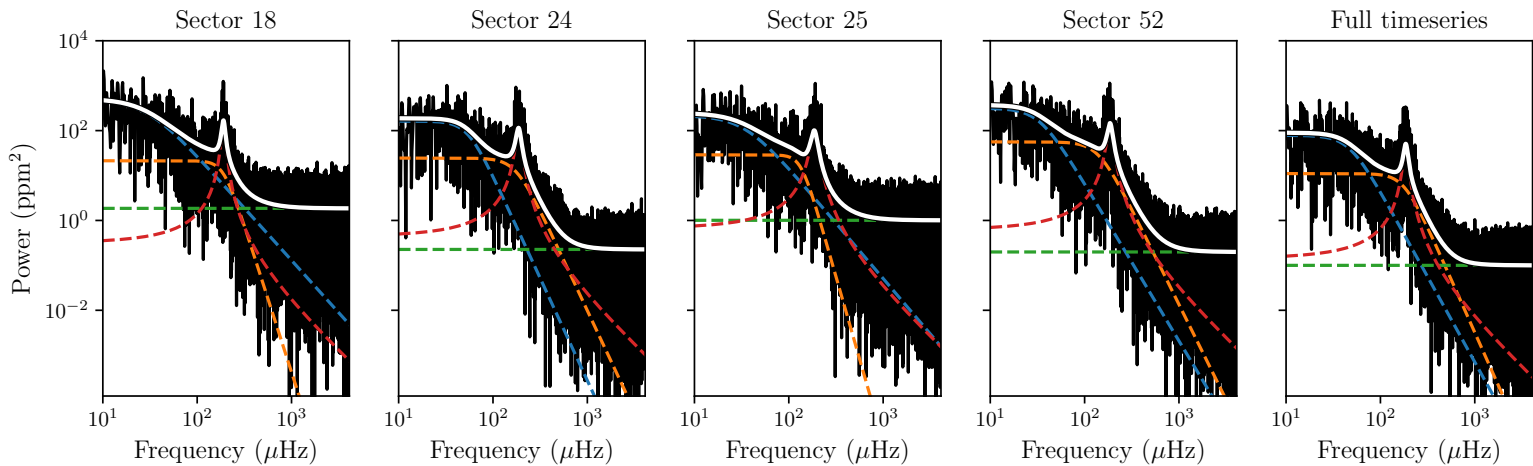


Figure A.1 | TESS power spectra of γ Cep A. Log-log plots of the power spectra resulting from the four individual TESS sectors as well as the full timeseries. The blue and orange lines are the two granulation components from Equation (5.4), shown in green is the white noise, and the oscillations are modelled as the Lorentzian shown in red. The sum of all components, i.e., Equation (5.3), is shown as the thick white lines.

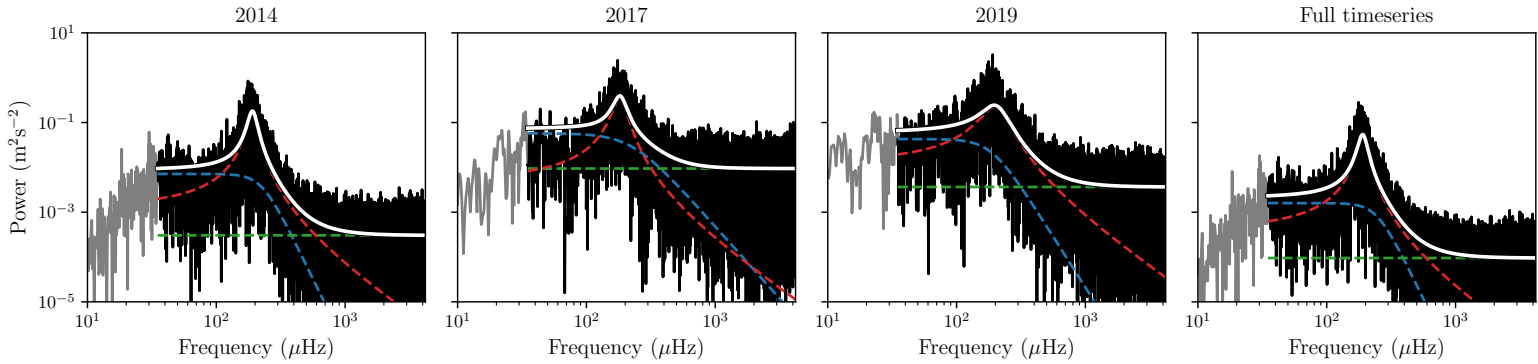


Figure A.2 | SONG power spectra of γ Cep A. Log-log plots of the power spectra resulting from the three individual [SONG](#) campaigns as well as the full time series. Here we have only included frequencies above $35 \mu\text{Hz}$, i.e., we only use the portion of the spectra shown in black. The blue line is the single granulation component from Equation (5.4), shown in green is the white noise, and the oscillations are modelled as the Lorentzian shown in red. The sum of all components, i.e., Equation (5.3), is shown as the thick white lines.

A.2 Trio of giants

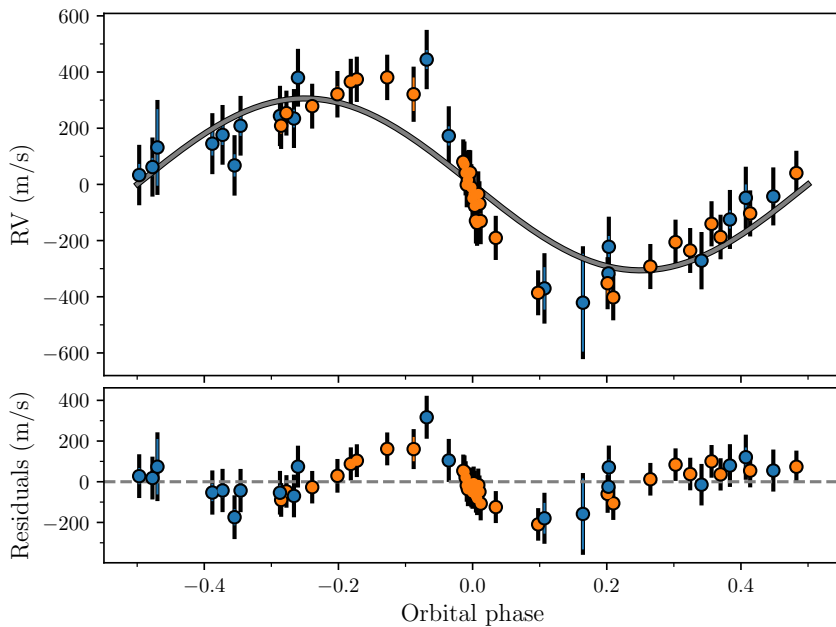


Figure A.3 | Circular solution for TOI-2025 b. Symbols are the same as in the middle panel of Figure 6.5, but here we have fixed $e = 0$ during the [MCMC](#).

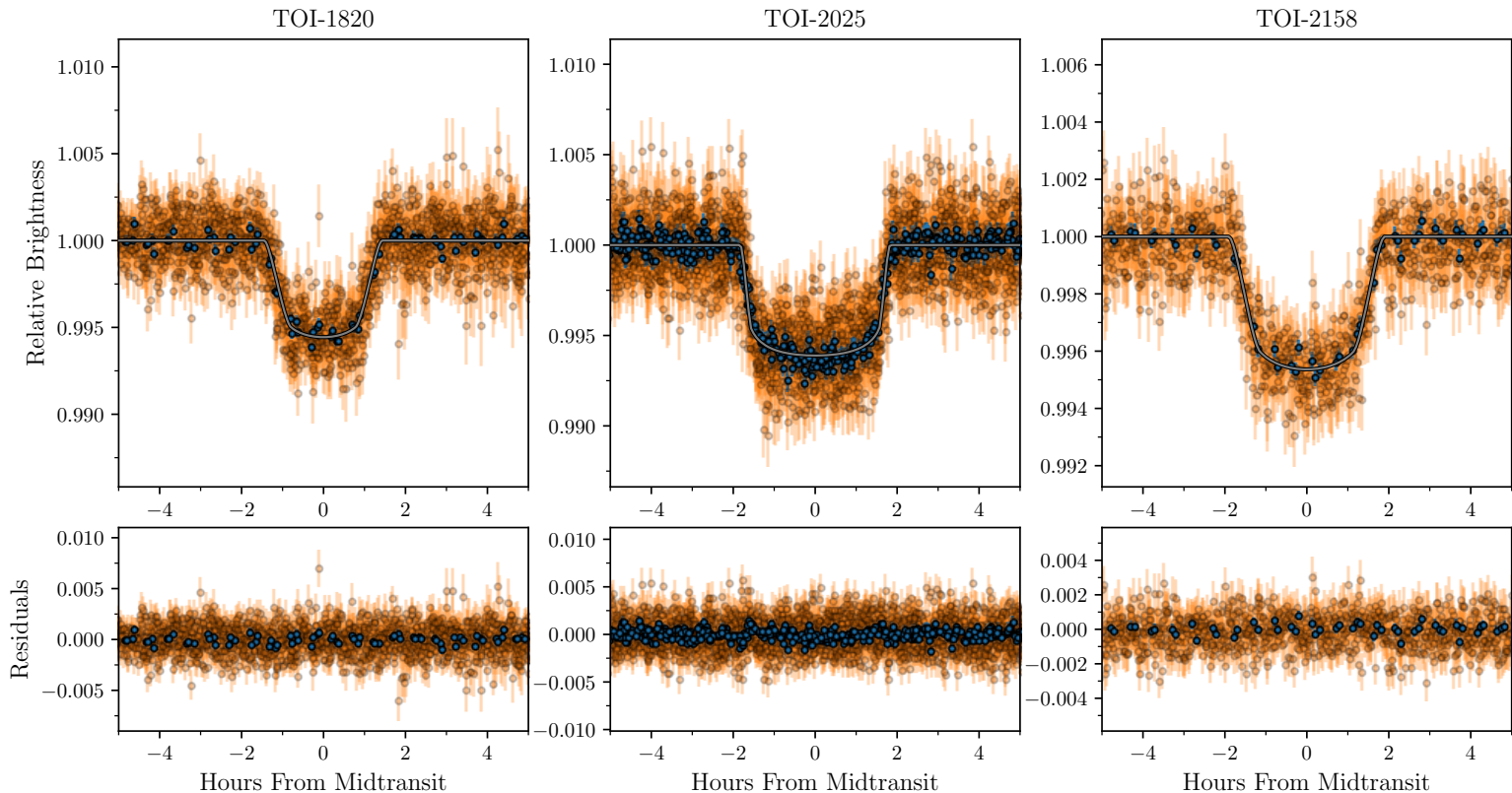


Figure A.4 | TESS light curves. A close-up of the TESS 2 min (orange) and 30 min (blue) cadence light curves for TOI-1820 (left), TOI-2025 (middle), and TOI-2158 (right). The residuals show no structure around the transits.

A.3 TOI-1288

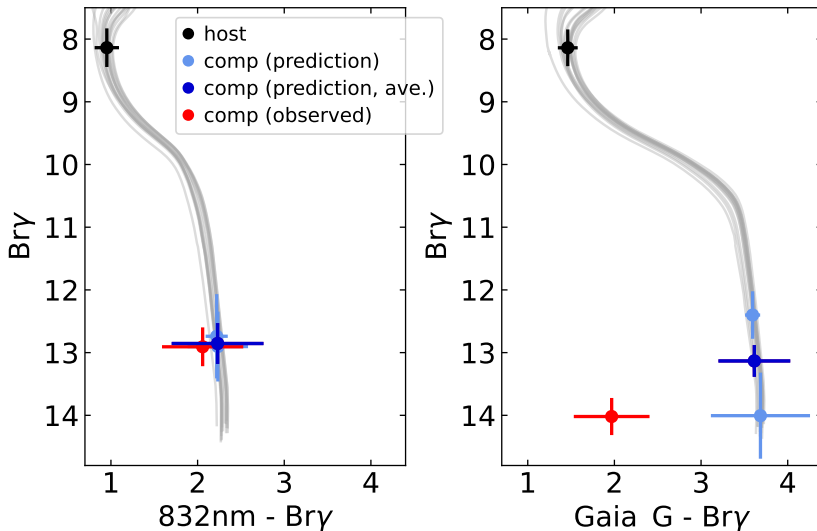


Figure A.5 | Colour-magnitude diagrams for TOI-1288. Comparison of observed photometry with predicted photometry for both candidate companions. In each case, we show the [CMD](#) position of the host (black), the predicted position of a bound companion based on each measured Δmag (light blue) and the weighted average of these predictions (dark blue), and finally the observed [CMD](#) position of the companion (red). The clear disagreement for star 2 (right) indicates that this is a background object, while the relative agreement between the red and dark blue points for star 1 (left) could indicate a bound companion. As discussed in Section 7.2.2.5 this is not the case.

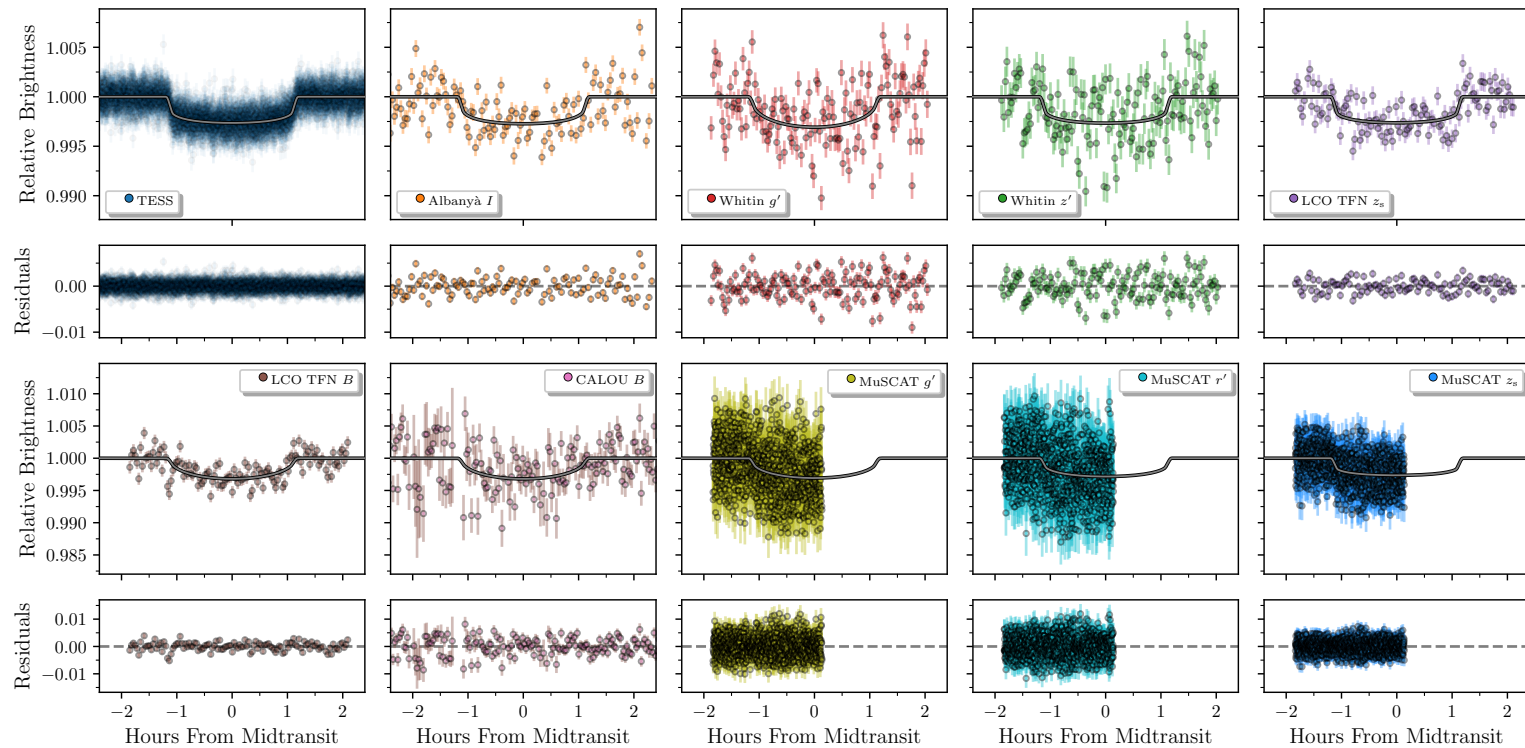


Figure A.6 | Light curves of TOI-1288 b. The phase folded transits of planet b from all the different photometers. The [TESS](#) light curve (top left) is the [GP](#) detrended data from Figure 7.2. The grey lines are the best-fitting models.

A.4 NGC 2506

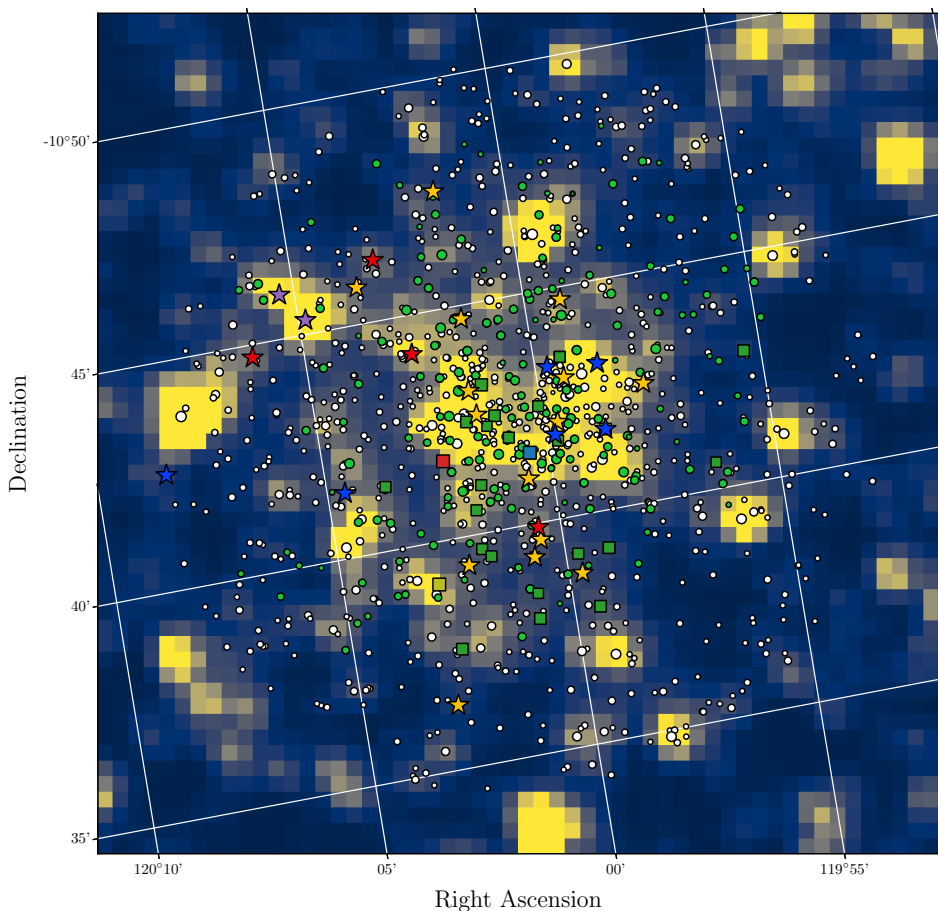


Figure A.7 | NGC 2506 as seen in the FFIs of TESS. As in Figure 3.1 yellow and blue stars denote the γ Dor stars and BSs/ δ Scuti stars, respectively. V2032, V4, and V5 are respectively marked with blue, red, and yellow squares. Red and purple stars mark the position of the [RGB](#) stars for which we have respectively performed a spectroscopic analysis or possibly detected solar-like oscillations. Again the green squares and dots denote the binaries and single members, respectively, but this time they have been scaled according to their magnitude (the brighter the bigger). The white dots are [Gaia](#) sources brighter than $G < 17$ within a 0.13° radius of the cluster center – these have also been scaled according to their magnitude.

A.5 TOI-640

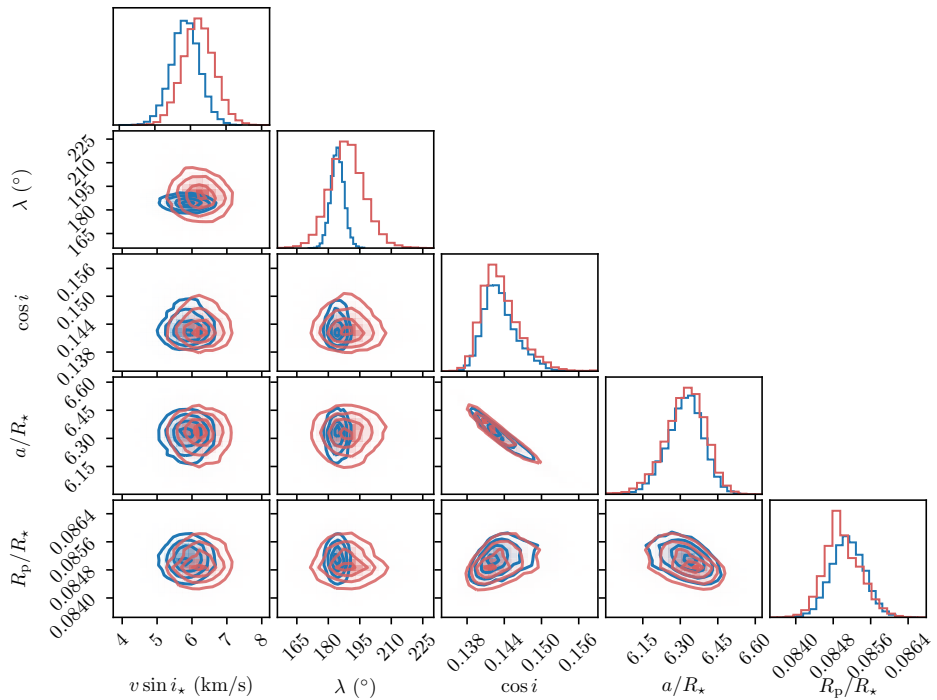


Figure A.8 | Correlation plots. Here we show the correlation between some of the stepping parameters from our MCMC (Section 9.3.1). Blue is from our run using the RVS as input for the RM EFFECT, and red is using the shadow.

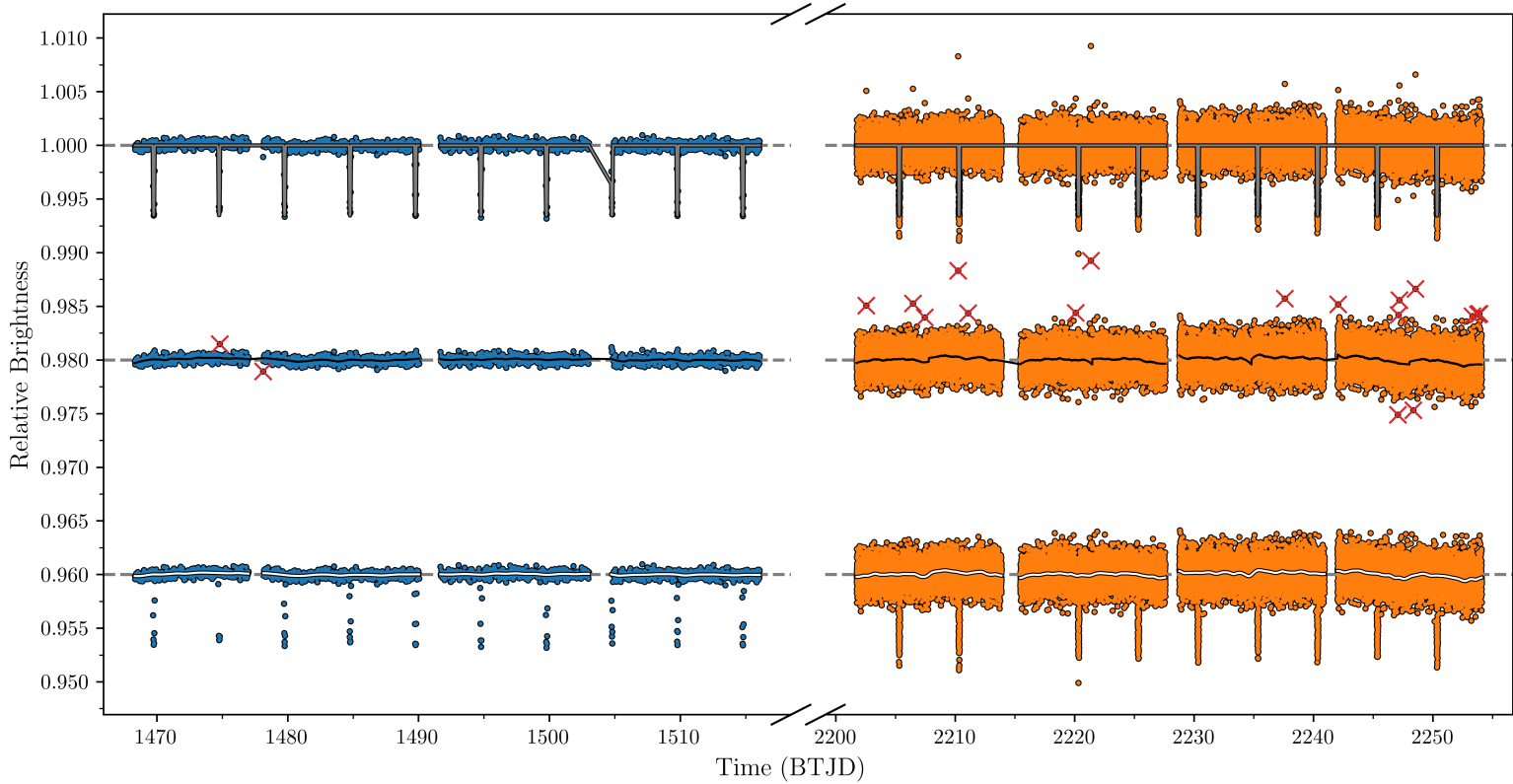


Figure A.9 | TESS photometry of TOI-640. TESS photometry of TOI-640 with Sectors 6 and 7 is shown in blue to the left and Sectors 33 and 34 in orange to the right. The light curves at the top have been corrected for scattered light. The grey curves show the best-fitting (determined iteratively) transit model. In the middle, we have subtracted this transit model. We used a Savitzky-Golay filter (black curve) to identify outliers, which are marked as red crosses. In the bottom, we have re-injected the transits into the light curves with the outliers removed. The white curves are the GPS we used to de-trend the data during our MCMC fit (see Section 9.3.1).

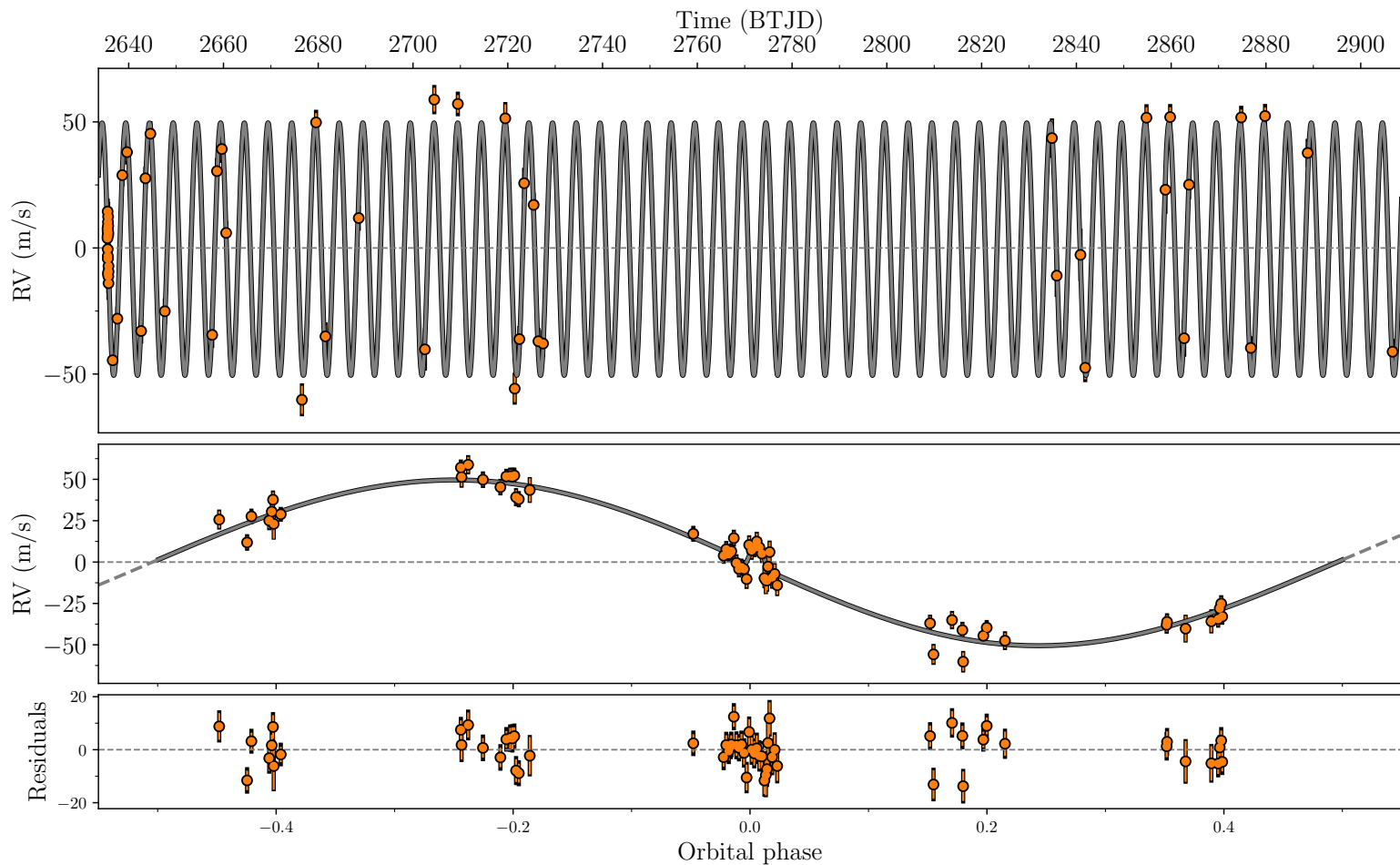


Figure A.10 | HARPS RVs. *Top:* HARPS RVs shown in orange with the best-fitting model overplotted in grey. *Middle:* HARPS RVs phase folded to the period of the planet for the values in Table 9.2. *Bottom:* Residuals after subtracting the Keplerian orbit and the RM EFFECT.

B

Supplementary tables

This appendix contains additional/supplementary tables from the different papers presented in Part II. Table B.1 and Table B.2 are supplements to the study of NGC 2506 in Chapter 3, Table B.3 lists parameters for the hosts of the trio of giant planets presented in Chapter 6, and the individual frequencies for γ Cep A in Chapter 5 are shown in Table B.4.

B.1 NGC 2506

Table B.1 | DE-MCMC results for V4 in NGC 2506. Results from the DE-MCMC run of the V4 system in which all the photometric data are included simultaneously. Here we give the median and the upper/lower 1σ result for a given parameter. i_{mutual} is the mutual inclination between the orbit of the third body and the binary orbit and Ω is the nodal angle.

	<i>I</i>	<i>V</i>	<i>B</i>	TESS
$M^{\text{p}} (M_{\odot})$			$1.478^{+0.006}_{-0.007}$	
$M^{\text{s}} (M_{\odot})$			1.250 ± 0.010	
$K^{\text{p}} (\text{km/s})$			96.3 ± 0.4	
$K^{\text{s}} (\text{km/s})$			113.84 ± 0.12	
$\gamma (\text{km/s})$			79.8 ± 0.3	
e			0.1891 ± 0.0011	
$\omega (^{\circ})$			$272.62^{+0.09}_{-0.08}$	
$P (\text{days})$			2.867623 ± 0.000002	
$R^{\text{p}} (R_{\odot})$			$2.300^{+0.013}_{-0.014}$	
$R^{\text{s}} (R_{\odot})$			$1.534^{+0.019}_{-0.018}$	
$a (R_{\odot})$			11.87 ± 0.02	
$i (^{\circ})$			80.14 ± 0.06	
$T_0^{\text{p}} (\text{BJD} - 2,450,000)$			3379.0738 ± 0.0005	
$T_{\text{eff}}^{\text{p}} (\text{K})$			6690^{+140}_{-120}	
$T_{\text{eff}}^{\text{s}}/T_{\text{eff}}^{\text{p}}$			1.0162 ± 0.0019	

c_1^p	$0.235^{+0.004}_{-0.005}$	$0.404^{+0.006}_{-0.004}$	$0.548^{+0.005}_{-0.006}$	$0.250^{+0.005}_{-0.006}$
c_2^p	$0.173^{+0.004}_{-0.007}$	$0.242^{+0.005}_{-0.003}$	0.292 ± 0.005	$0.178^{+0.005}_{-0.006}$
c_1^s	$0.230^{+0.004}_{-0.003}$	$0.414^{+0.003}_{-0.005}$	$0.547^{+0.006}_{-0.005}$	0.251 ± 0.005
c_2^p	$0.174^{+0.004}_{-0.003}$	$0.248^{+0.002}_{-0.004}$	0.292 ± 0.005	0.184 ± 0.004
l^c	0.8288 ± 0.0015			
$M^t (M_\odot)$	0.74 ± 0.03			
$R^t (R_\odot)$	$0.68^{+0.03}_{-0.02}$			
$P^t (\text{days})$	$443.4231^{+0.0017}_{-0.0022}$			
$a^t (R_\odot)$	370.7 ± 1.3			
e^t	0.512 ± 0.014			
$\omega^t (\text{°})$	221 ± 3			
$i^t (\text{°})$	$89.59^{+0.03}_{-0.02}$			
$i_{\text{mutual}} (\text{°})$	$9.45^{+0.08}_{-0.07}$			
$\Omega (\text{°})$	0.19 ± 0.19			
$T_0^t (\text{BJD} - 2,450,000)$	3210 ± 6			
$T_{\text{eff}}^t (\text{K})$	5500^{+200}_{-300}			

Table B.2 | Results for V2032 and V5 in NGC 2506. Results for V2032 (left of vertical dashed line) and V5 (right) resulting from an MCMC sampling of 20,000 steps with a burn-in of 10,000 for the different photometric data available. The parameter space was sampled using 100 walkers. The value is taken as the 50th percentile of the chain and the uncertainties are the 16th and 84th percentile. **Notes.** ^(a) $a \sin i$ constrained by Equation (3.2). ^(b)Sampled using a Gaussian prior for V2032 and a uniform prior for V5: $\sigma(T_{\text{eff}}) = 100$ K and $\mathcal{U}(4200\text{K}, 6200\text{K})$. ^(c)Sampled using a Gaussian prior: $\sigma(c_i) = 0.1$ and $\sigma(l^c) = 0.05$.

	V2032			V5
	<i>I</i>	<i>V</i>	TESS	<i>B</i>
K^p (km/s)	$61.99^{+0.10}_{-0.09}$	$62.01^{+0.10}_{-0.09}$	$61.88^{+0.10}_{-0.09}$	$71.96^{+0.18}_{-0.13}$
K^s (km/s)	62.70 ± 0.11	62.71 ± 0.11	62.61 ± 0.10	$96.18^{+0.12}_{-0.11}$
γ_{GIRAFFE} (km/s)	83.05 ± 0.04	83.05 ± 0.04	83.04 ± 0.04	$83.40^{+0.19}_{-0.13}$
γ_{FIES} (km/s)	83.28 ± 0.04	83.29 ± 0.04	83.28 ± 0.04	-
e	0.5867 ± 0.0010	0.5868 ± 0.0010	0.5860 ± 0.0010	$0.0016^{+0.0007}_{-0.0008}$
ω (°)	138.85 ± 0.10	138.84 ± 0.10	138.88 ± 0.10	$109.9^{+0.3}_{-0.7}$
P (days)	27.86780 ± 0.00015	27.86788 ± 0.00015	27.86741 ± 0.00016	$3.35852^{+0.00014}_{-0.00017}$
T_{peri} (BJD−2,450,000)	7754.495 ± 0.006	7754.498 ± 0.006	$7754.485^{+0.007}_{-0.006}$	$3387.112^{+0.014}_{-0.025}$
M^p (M_{\odot})	1.522 ± 0.004	1.519 ± 0.004	1.523 ± 0.005	$0.945^{+0.004}_{-0.003}$
M^s (M_{\odot})	1.505 ± 0.004	1.501 ± 0.004	1.505 ± 0.005	$0.707^{+0.004}_{-0.003}$
R^p (R_{\odot})	$3.11^{+0.04}_{-0.05}$	2.92 ± 0.04	3.19 ± 0.11	0.68 ± 0.04
R^s (R_{\odot})	$2.44^{+0.08}_{-0.04}$	$2.39^{+0.07}_{-0.05}$	$2.50^{+0.10}_{-0.09}$	$0.610^{+0.021}_{-0.016}$
a (R_{\odot}) ^(a)	$56.01^{+0.15}_{-0.14}$	$55.94^{+0.15}_{-0.14}$	$56.05^{+0.15}_{-0.14}$	$9.04^{+0.10}_{-0.05}$
i (°) ^(a)	83.47 ± 0.10	$84.01^{+0.13}_{-0.17}$	83.0 ± 0.3	$88.91^{+0.26}_{-0.17}$
T_0^p (BJD−2,450,000)	7781.5157 ± 0.0002	7781.5173 ± 0.0002	$7781.554^{+0.005}_{-0.006}$	$3385.6608^{+0.0005}_{-0.0004}$

$T_{\text{eff}}^{\text{p}(\bar{b})}$ (K)	6560^{+80}_{-70}	6590^{+90}_{-80}	$6560^{+80}_{-70} \pm 70$	5690^{+140}_{-120}
$T_{\text{eff}}^{\text{s}(\bar{b})}$ (K)	7100 ± 80	7080 ± 90	7100 ± 80	4940^{+110}_{-60}
$c_1^{\text{p}(c)}$	$0.38^{+0.08}_{-0.09}$	0.24 ± 0.09	0.21 ± 0.10	0.49 ± 0.09
$c_2^{\text{p}(c)}$	$0.10^{+0.10}_{-0.09}$	0.37 ± 0.10	0.32 ± 0.10	$0.36^{+0.17}_{-0.13}$
$c_1^{\text{s}(c)}$	0.31 ± 0.10	0.30 ± 0.10	$0.18^{+0.10}_{-0.09}$	$0.38^{+0.10}_{-0.15}$
$c_2^{\text{s}(c)}$	0.13 ± 0.10	0.36 ± 0.10	0.33 ± 0.10	$0.18^{+0.06}_{-0.08}$
$l^{\text{c}(c)}$	-	-	7.60 ± 0.05	-

B.2 Trio of giants

Table B.3 | Stellar parameters for TOI-1820, TOI-2025, and TOI-2158. Parameters of the stellar hosts in the three systems of this study. **Notes.** ^(a)Tycho-2 (Høg et al., 2000). ^(b)*Gaia* EDR3 (Gaia Collaboration et al., 2021). ^(c)This work: SPC. ^(d)This work: **SED**. ^(e)This work: HIRES spectra.

	TESS Object of Interest	TOI-1820	TOI-2025	TOI-2158
	TESS Input Catalogue	TIC 393831507	TIC 394050135	TIC 342642208
	TYCHO-2	TYC 1991-1863-1	TYC 4595-797-1	TYC 1577-691-1
$V^{(a)}$	Tycho V magnitude	10.90	11.60	10.89
$G^{(b)}$	Gaia G magnitude	10.97	11.36	10.67
$\alpha_{\text{J}2000}^{(b)}$	Right Ascension	12:30:44.813	18:51:10.861	18:27:14.413
$\delta_{\text{J}2000}^{(b)}$	Declination	27:27:07.206	82:14:43.492	20:31:36.793
$\mu_\alpha^{(b)}$	Proper motion in R.A. (mas yr $^{-1}$)	50.54 ± 0.08	2.79 ± 0.04	-44.00 ± 0.04
$\mu_\delta^{(b)}$	Proper motion in Dec. (mas yr $^{-1}$)	-33.93 ± 0.08	-4.52 ± 0.05	7.89 ± 0.07
$\varpi^{(b)}$	Parallax (mas)	4.00 ± 0.06	2.95 ± 0.02	5.01 ± 0.04
$\pi^{(b)}$	Distance (pc)	250 ± 4	339 ± 2	200 ± 1
$T_{\text{eff}}^{(c)}$	Effective temperature (K)	5734 ± 50	5880 ± 53	5673 ± 50
$\log g^{(c)}$	Surface gravity (dex)	4.24 ± 0.05	4.17 ± 0.06	4.19 ± 0.05
$[\text{Fe}/\text{H}]^{(c)}$	Metallicity (dex)	0.14 ± 0.15	0.18 ± 0.08	0.47 ± 0.08
$v \sin i_\star^{(c)}$	Projected rotational velocity (km s $^{-1}$)	4.5 ± 0.8	6.0 ± 0.3	3.7 ± 0.5
$A_V^{(d)}$	Extinction (mag)	0.04 ± 0.02	0.10 ± 0.03	0.24 ± 0.02
$F_{\text{bol}}^{(c)}$	Bolometric flux (erg s $^{-1}$ cm $^{-2}$)	$(1.017 \pm 0.018) \times 10^{-9}$	$(7.02 \pm 0.16) \times 10^{-10}$	$(1.540 \pm 0.018) \times 10^{-9}$
$R_\star^{(d)}$	Radius (R_\odot)	1.51 ± 0.06	1.56 ± 0.03	1.41 ± 0.03

$M_{\star}^{(d)}$	Mass (M_{\odot})	1.04 ± 0.13	1.32 ± 0.14	1.12 ± 0.12
$P_{\text{rot}} / \sin i^{(d)}$	Rotation period (days)	25 ± 6	13.2 ± 0.7	19 ± 3
$P_{\text{pred}}^{(d)}$	Predicted rotation period (days)	40 ± 2	-	43 ± 3
$\log R'_{\text{HK}}^{(e)}$	Activity	$-5.37^{(e)}$	-	-5.06 ± 0.05
$\tau^{(d)}$	Age (Gyr)	11 ± 2	1.7 ± 0.2	8 ± 1
$\rho^{(d)}$	Density (g cm^{-3})	0.43 ± 0.07	0.49 ± 0.06	0.56 ± 0.07

B.3 γ Cep

Table B.4 | Mode frequencies for γ Cep A. The observed individual mode frequencies extracted from the product power spectrum.

Order	Degree	Frequency (μ Hz)
8	2	132.5 ± 0.4
9	0	134.3 ± 0.3
9	2	146.0 ± 0.4
10	0	148.1 ± 0.2
10	2	160.29 ± 0.13
11	0	162.23 ± 0.18
11	1	169.4 ± 0.2
11	2	174.69 ± 0.13
12	0	176.53 ± 0.18
12	1	183.1 ± 0.2
13	1	184.33 ± 0.13
12	2	188.90 ± 0.11
13	0	190.69 ± 0.13
14	1	197.7 ± 0.3
15	1	198.89 ± 0.14
13	2	203.37 ± 0.15
14	0	205.16 ± 0.19
16	1	211.72 ± 0.20
17	1	213.07 ± 0.20
14	2	217.6 ± 0.4
15	0	219.77 ± 0.17
18	1	226.9 ± 0.2
15	2	232.8 ± 0.2
16	0	234.4 ± 0.2
19	1	240.9 ± 0.3
16	2	247.3 ± 0.3
17	0	250.1 ± 0.2